Oklahoma Department of Transportation
200 NE 21st Street, Oklahoma City, OK 73105-3204

FINAL REPORT ~ FHWA-OK-16-08

Precast Prestressed Concrete Pavement to Abate Settlement Problems Under Bridge Approach Slabs

Peizhi Sun, M.Sc., Ph.D. Candidate
Dan G. Zollinger, Ph.D., P.Eng
Robert Lytton, Ph.D., P.Eng
Zachary Department of Civil Engineering
Texas A&M University
Texas Transportation Institute
College Station, Texas

October 2016

The Oklahoma Department of Transportation (ODOT) ensures that no person or groups of persons shall, on the grounds of race, color, sex, religion, national origin, age, disability, retaliation or genetic information, be excluded from participation in, be denied the benefits of, or be otherwise subjected to discrimination under any and all programs, services, or activities administered by ODOT, its recipients, sub-recipients, and contractors. To request an accommodation please contact the ADA Coordinator at 405-521-4140 or the Oklahoma Relay Service at 1-800-722-0353. If you have any ADA or Title VI questions email ODOT-ada-titlevi@odot.org.

PRECAST PRESTRESSED CONCRETE PAVEMENT TO ABATE SETTLEMENT PROBLEMS UNDER BRIDGE APPROACH SLABS

FINAL REPORT ~ FHWA-OK-16-08

ODOT SP&R ITEM NUMBER 2265

Submitted to:
Dawn R. Sullivan, P.E.
Director of Capital Programs
Oklahoma Department of Transportation

Submitted by:
Peizhi Sun, Research Assistant
Dan G. Zollinger, Ph.D., P.Eng
Robert Lytton, Ph.D., P.Eng
Zachary Department of Civil Engineering
Texas A& M University
Texas Transportation Institute

October 2016

TECHNICAL REPORT DOCUMENTATION PAGE

1. REPORT NO.	2. GOVERNMENT ACCESSION NO.	3. RECIPIENT'S CATALOG NO.
FHWA-OK-16-08		

4. TITLE AND SUBTITLE	5. REPORT DATE
Precast Prestressed Concrete Pavement To Abate Settlement Problems Under Bridge Approach Slabs	Oct 2016
	6. PERFORMING ORGANIZATION CODE

7. AUTHOR(S)	8. PERFORMING ORGANIZATION REPORT
Peizhi Sun, Dan G. Zollinger, and Robert Lytton	Click here to enter text.

9. PERFORMING ORGANIZATION NAME AND ADDRESS	10. WORK UNIT NO.
Texas Transportation Institute Texas A&M University College Station, Texas 77843-3135	11. CONTRACT OR GRANT NO. ODOT SPR Item Number 2265

12. SPONSORING AGENCY NAME AND ADDRESS	13. TYPE OF REPORT AND PERIOD COVERED
Oklahoma Department of Transportation Office of Research and Implementation 200 N.E. 21st Street, Room G18 Oklahoma City, OK 73105	Final Report Nov 2014 - Oct 2016
	14. SPONSORING AGENCY CODE

15. SUPPLEMENTARY NOTES

16. ABSTRACT

The well-known bump-at-the-end-of-the-bridge often involving the joint between a bridge approach slab (BAS) and a bridge deck (as well as the associated slab cracking) has been a recurring issue over the years in many states. DOTs have reported differential settlement and cracking issues at this joint which has significantly reduced ride quality. Previous experience indicates that any "non-removal" conventional method of repair would not work well once erosion has set in; however, removing and replacing distressed BAS with cast-in-place (CIP) concrete usually require significant amount of time for curing, which leads to high costs of lane-closure and user delays. Therefore, a long-lasting and rapid repair method is needed to address this issue. This research focuses in part on the introduction of the precast concrete pavement slab for repairing distressed BASs and the elaboration of the design and construction procedures for precast BASs. Key elements within a BAS system are identified and design considerations provided for these elements for the prevention of erosion damage that may occur underneath the BASs. In addition, this research also provides a detailed design procedure for the stone column technique in order to address the potential for large settlement in the foundation of bridge embankments and proposes a procedure using non-destructive testing methods to rapidly characterize soil properties. This report contains three parts. The first part, "Final Report", consists of Chapter 1 through Appendix D; the second part, from Chapter 9 to Appendix H, is the "Bridge Approach Design Guideline"; the third part is the "Stone Column and Embankment Design Guideline" which consists of Chapter 14 to Appendix N.

17. KEY WORDS	18. DISTRIBUTION STATEMENT
Bridge Approach Slab, Settlement, Erosion, Precast Concrete, Stone Column, Non Destructive Testing	No restrictions. This publication is available from the Office of Research and Implementation, Oklahoma DOT.

19. SECURITY CLASSIF. (OF THIS REPORT)	20. SECURITY CLASSIF. (OF THIS PAGE)	21. NO. OF PAGES	22. PRICE
Unclassified	Unclassified	695	N/A

Form DOT F 1700.7 (08/72)

SI* (MODERN METRIC) CONVERSION FACTORS

APPROXIMATE CONVERSIONS TO SI UNITS

SYMBOL	WHEN YOU KNOW	MULTIPLY BY	TO FIND	SYMBOL
		LENGTH		
in	inches	25.4	millimeters	mm
ft	feet	0.305	meters	m
yd	yards	0.914	meters	m
mi	miles	1.61	kilometers	km
		AREA		
in^2	square inches	645.2	square millimeters	mm^2
ft^2	square feet	0.093	square meters	m^2
yd^2	square yard	0.836	square meters	m^2
ac	acres	0.405	hectares	ha
mi^2	square miles	2.59	square kilometers	km^2
		VOLUME		
fl oz	fluid ounces	29.57	milliliters	mL
gal	gallons	3.785	liters	L
ft^3	cubic feet	0.028	cubic meters	m^3
yd^3	cubic yards	0.765	cubic meters	m^3
		NOTE: volumes greater than 1000 L shall be shown in m^3		
		MASS		
oz	ounces	28.35	grams	g
lb	pounds	0.454	kilograms	kg
T	short tons (2000 lb)	0.907	megagrams (or "metric ton")	Mg (or "t")
		TEMPERATURE (exact degrees)		
^oF	Fahrenheit	5 (F-32)/9 or (F-32)/1.8	Celsius	^oC
		ILLUMINATION		
fc	foot-candles	10.76	lux	lx
fl	foot-Lamberts	3.426	candela/m^2	cd/m^2
		FORCE and PRESSURE or STRESS		
lbf	poundforce	4.45	newtons	N
lbf/in^2	poundforce per square inch	6.89	kilopascals	kPa

APPROXIMATE CONVERSIONS FROM SI UNITS

SYMBOL	WHEN YOU KNOW	MULTIPLY BY	TO FIND	SYMBOL
		LENGTH		
mm	millimeters	0.039	inches	in
m	meters	3.28	feet	ft
m	meters	1.09	yards	yd
km	kilometers	0.621	miles	mi
		AREA		
mm^2	square millimeters	0.0016	square inches	in^2
m^2	square meters	10.764	square feet	ft^2
m^2	square meters	1.195	square yards	yd^2
ha	hectares	2.47	acres	ac
km^2	square kilometers	0.386	square miles	mi^2
		VOLUME		
mL	milliliters	0.034	fluid ounces	fl oz
L	liters	0.264	gallons	gal
m^3	cubic meters	35.314	cubic feet	ft^3
m^3	cubic meters	1.307	cubic yards	yd^3
		MASS		
g	grams	0.035	ounces	oz
kg	kilograms	2.202	pounds	lb
Mg (or "t")	megagrams (or "metric ton")	1.103	short tons (2000 lb)	T
		TEMPERATURE (exact degrees)		
^oC	Celsius	1.8C+32	Fahrenheit	^oF
		ILLUMINATION		
lx	lux	0.0929	foot-candles	fc
cd/m^2	candela/m^2	0.2919	foot-Lamberts	fl
		FORCE and PRESSURE or STRESS		
N	newtons	0.225	poundforce	lbf
kPa	kilopascals	0.145	poundforce per square inch	lbf/in^2

*SI is the symbol for the International System of Units. Appropriate rounding should be made to comply with Section 4 of ASTM E380.
(Revised March 2003)

ACKNOWLEDGEMENTS

This research was funded by the Oklahoma Department of Transportation and this support is gratefully acknowledged. The authors are also grateful the subsurface exploration work and technical review of this report conducted by personnel from the ODOT Materials and Bridge Divisions.

The authors also would like to gratefully acknowledge the technical suggestions provided by Dan Ye from Fugro Consultants, Inc. and Randall W. Brown from URETEK, Inc.

ABSTRACT

The well-known bump-at-the-end-of-the-bridge often involving the joint between a bridge approach slab (BAS) and a bridge deck (as well as the associated slab cracking) has been a recurring issue over the years in many states. DOTs have reported differential settlement and cracking issues at this joint which has significantly reduced ride quality. Previous experience indicates that any “non-removal” conventional method of repair would not work well once erosion has set in; however, removing and replacing distressed BAS with cast-in-place (CIP) concrete usually require significant amount of time for curing, which leads to high costs of lane-closure and user delays. Therefore, a long-lasting and rapid repair method is needed to address this issue.

This research focuses in part on the introduction of the precast concrete pavement slab for repairing distressed BASs and the elaboration of the design and construction procedures for precast BASs. Key elements within a BAS system are identified and design considerations provided for these elements for the prevention of erosion damage that may occur underneath the BASs. In addition, this research also provides a detailed design procedure for the stone column technique in order to address the potential for large settlement in the foundation of bridge embankments and proposes a procedure using non-destructive testing methods to rapidly characterize soil properties.

This report contains three parts. The first part, “Final Report”, consists of Chapter 1 through Appendix D; the second part, from Chapter 9 to Appendix H, is the “Bridge Approach Design Guideline”; the third part is the “Stone Column and Embankment Design Guideline” which consists of Chapter 14 to Appendix N.

TABLE OF CONTENTS

Page

LIST OF FIGURES

Page

This page is intentionally blank.

LIST OF TABLES

Page

CHAPTER 1

INTRODUCTION

The well-known bump-at-the-end-of-the-bridge that is often associated with concrete bridge approach slabs (BASs) have been a recurring issue in many states for several decades. DOTs have reported differential settlement and cracking issues near the joint between a bridge deck and a BAS which has significantly reduced ride quality. Numerous research studies have been conducted to investigate the mechanisms that lead to the formation of the bump associated distress as well as the development of new strategies to address it. The leading mechanisms are those associated with settlement of the foundation materials due to consolidation, poor compaction during construction or the weakening of embankment fill under saturation caused by water infiltration through unsealed joints or cracks in the pavement surface. Other mechanisms relate to voiding between the slab and the base layer due to erosion coupled with poor drainage again caused by water infiltration through joints and cracks in the approach slab particularly under contractive movements caused by seasonal temperature variations.

The practitioners (i.e. the Oklahoma DOT engineers) often have to face the choices of whether maintenance/rehabilitation or new construction is needed for an existing problematic site and selecting the associated measures, which usually depends on the severity of the distress as well as the availability of funds. Sometimes, it is a less complicated but costly decision if the BAS has settled so much that leaves new construction the only option; in other situations, it can be difficult to define the level of the severity of the distress and determine what measures should be taken.

Table 1-1 attempts to provide a simple guide to help practitioners make the choice on a method of repair. As shown in the table, the severity of the distress has been categorized into four levels. One major criterion for differentiating Level 1 & 2 from Level 3 & 4 severity of distress is the location of the potential problems leading to the bump issue. For Level 1 & 2 severity, the location of the potential problems appears only at the surface of the BAS (e.g. failed joint sealing) or at the slab-base interface

(e.g. erosion underneath the BAS); for Level 3 & 4 severity, the location of the potential problems propagates into the deeper layers of the embankment (e.g. embankment settlement) or pre-exists in the foundation underneath the embankment (e.g. very compressible foundation soils). Therefore, different measures should be applied to address different levels of severity. For Level 1 and 2 severity of distress (relatively less severe conditions), maintenance/rehabilitation measures are considered adequate to correct the problematic conditions and improve the ride quality; for Level 3 and 4 severity of distress (relatively more severe conditions), where maintenance/rehabilitation measures are not sufficient or ineffective to restore the conditions, project-level rehabilitation or new construction is required to radically address the problems.

There have been a variety of maintenance or rehabilitation measures to address the potential problems associated with the Level 1 and 2 severity of distress. As shown in Table 1-1, for Level 1 severity where surface drainage issues appear, general maintenance measures such as cleaning out edge drains, resealing the joints and cracks in the BAS may effectively prevent further moisture infiltration if done on a regular basis. For Level 2 severity where noticeable bump and widening joints are present, to address the root causes of the bump distress associated with this level of severity (e.g. excessive moisture infiltration inducing erosion underneath the BAS), viable solutions consist of improving the BAS surface grading to avoid accumulation of runoff water, resealing the joints and cracks in the BAS, retrofitting widening joints with load transfer devices and injecting cementitious grout or proprietary polyurethane materials into the embankment or foundation (as a means to address the eroded and voided area in the base layer and to pressure grout a settled BAS back into position).

Table 1-1 Guidelines for evaluating severity of distress and selecting possible repair measures

	Maintenance/Rehabilitation		**Project-level Rehabilitation/Re Construction**	
Level of Severity	**Level 1**	**Level 2**	**Level 3**	**Level 4**

Settlement and Bump Condition	None	Noticeable	Apparent	Significant
Failure Stages	Blocked drainage	Standing water	Clogged drainage system	Failed drainage system
	Joint sealant debonding	Joint sealant separation	Missing joint sealant	Wide open expansion joint
	Slab cracking	Widening joints/cracks	Moving cracks	Spalled and faulted cracks
		Pumping/water on the interface	Slab staining	Base erosion
			Signs of embankment settling	Voided and saturated embankment fill
				Embankment and foundation settling
Repair Measures	Clean out edge drains	Improve grading	Reshape cross drainage	Add/clean edge or cross drainage
	Reseal the joints/cracks	Reseal the joints	Reseal the joints	Reseal the joints
		Retrofit the crack with load transfer devices	Partial/Full replacement of the approach slab	Full replacement of the BAS
		Slab undersealing/ jacking	Deep stabilization of the base layer and embankment fill	Replace the embankment fill
				Reinforce the foundation soil

In order to adequately address the Level 3 and 4 severity of distress, where the potential issues are in the deeper layers of the embankment or in the foundation soils, it may be necessary to remove at least portion of the BAS in order to repair the underlying layers applying the measures listed in Table 1-1. The reasons for partial or full slab replacement can be summarized as:

- to restore and strengthen the underlying supporting layers for the new BAS;

- to fully replace cracked segments of the BAS thus preventing further moisture infiltration;
- to fully restore the joint sealing and load transfer;
- to redesign the BAS (such as optimizing the joint spacing to avoid excessive thermal induced joint movement and redesigning the surface grading to better direct runoff away from the BAS).

However, the drawbacks of replacing the BASs are the costs of lane-closure and user delays, since it requires to allow time for curing cast-in-place (CIP) concrete.

It should also be noted that the aforementioned advantages of replacing BASs do not necessarily lead to satisfying long-term BAS performance; if the causes of the bump issue are due to voids or weakened areas in the underlying supporting layers (e.g. saturated embankment or very compressible foundation soils), only replacement of the BAS will not minimize re-occurrence of the distress. Therefore, comprehensive remedial measures may be needed to address all the possible root causes leading to the bump issues.

CURRENT PRACTICE IN OKLAHOMA

Currently, the most common remedial method applied by the Oklahoma DOT maintenance team is to place an asphalt overlay, considering its easiness and lower cost, at the location where bump occurs to smooth out the unevenness; however, several drawbacks are associated with this method:

- Asphalt materials are essentially prone to rutting therefore requiring frequent maintenance or replacement;
- It may become only a short-term fix and further bump issues may still occur if the root causes are not resolved;
- Without correctly identifying and addressing the real causes of the bump issue, it may be a waste of money to place asphalt overlay and can yield much higher life cycle cost.

Therefore, the first step for achieving successful BAS maintenance is to correctly identify the severity level of the bump issue (whether it is Level 1, 2, 3 or 4) and the root causes (whether it is only caused by the surface drainage issues or by the problems deep in the foundation soils); thorough site investigations and evaluations need to be conducted by structural and geotechnical engineers to achieve those purposes rather than simply placing a layer of asphalt overlay every time a bump is observed.

If the site is identified as Level 1 or 2 severity where the root causes of the bump issue can be treated without removing the BAS, the asphalt overlay method may be a possible option, but needs to be applied in combination with other remedial practices that address the root cause of the bump issue pertinent to that level of severity (e.g. reseal the joints and improve the drainage to avoid excessive moisture infiltration). In this case, the asphalt overlay method (although slab undersealing/jacking is more preferred) may be effective in smoothing the road surface for a certain period (depending on the quality of the asphalt material) since exacerbation of the base erosion condition is minimized through addressing the root causes.

If the site is identified as Level 3 or 4 severity where very compressible soil layers pre-exist in the foundation or the BAS has badly cracked leading to excessive moisture infiltration into deeper layers of the embankment, placing an asphalt overlay may work initially, but the overlay will not be long-lasting and new bump issues will likely develop again very soon because the root causes of the bump issue cannot be treated without removing the cracked BAS.

Currently, Oklahoma DOT applies 13 in. doubly reinforced CIP concrete slabs as the standard practice for building BASs. However, requiring significant amount of time for curing which complicates lane closures has been the major obstacle preventing the reconstruction/rehabilitation of CIP BASs. In many cases where the bump issues become urgent (e.g. after a heavy rainfall event) and need to be fixed quickly to minimize the disruption of traffic (e.g. in high traffic volume areas), the asphalt overlay method remains the only quick solution for the Oklahoma DOT maintenance team to address the Level 3 or 4 severity bump issues even if acknowledging that it will not last long nor fix the root causes of the bump, which is essentially a waste of time and money. Therefore, faster and less traffic-disruptive methods are needed for constructing

BASs as a means to replace the asphalt overlay method especially when addressing the Level 3 or 4 severity conditions. Fortunately, precast concrete pavement (PCP) technologies have been developed and facilitated in recent years, which provides a quick solution for constructing BASs.

OBJECTIVES

This document mainly focuses on elaborating the specific measures pertaining to resolving/preventing the Level 3 and 4 severity distress, which are more related to project-level rehabilitations or reconstruction. Specifically, this document will provide background information on:

- a method of using precast technologies for constructing BASs;
- designing and constructing long-lasting BASs using precast concrete pavement technologies;
- applying appropriate practices to create a favorable environment (which consists of design details of drainage, expansion joint, embankment backfill, foundation improvement measures, and etc.) in order to facilitate successful performance of the BAS;
- designing stone columns as a means to address the potential settlement issue caused by the very compressible soil layers present in the foundation of bridge embankments;
- a new methodology/procedure to expedite the process for characterizing soil properties.

The ultimate goal of this document is to provide Oklahoma DOT with a new option/tool for addressing the bump issues in a faster, more cost effective, and less traffic-disruptive manner rather than relying on applying the asphalt overlay method.

REPORT ORGANIZATION

Chapter 2 provides the results and observations made in field investigations on some BASs in Oklahoma; detailed visual distress survey, FWD and DCP testing were

conducted to evaluate the structural capacity and healthiness of the BASs (as well as the adjacent pavement slabs).

Chapter 3 provides background information of the jointed precast concrete pavement (JPrCP) and the precast prestressed concrete pavement (PPCP) and detailed design procedures and examples for designing BASs using these precast technologies especially taking into account the determination of erosion damage.

Chapter 4 provides the information regarding the construction of the precast BASs, including panel fabrication and storage, base preparation, panel installation and post-installation activities.

Chapter 5 provides information regarding the key elements within a BAS system that may affect the performance of the BAS and the evaluation of the design details selected for these elements.

Chapter 6 provides the detailed procedures and examples for designing the stone column technique for improving the foundation of the embankment as a means to address the potential large settlement when very compressible soil layers are present.

Chapter 7 provides the information regarding the use of new non-destructive testing technologies (i.e. applying methylene blue test and percometer test) to rapidly characterize the soil properties that are used for designing stone columns.

CHAPTER 2

FIELD INVESTIGATION

This chapter provides research findings of field investigations on four bridge approach slabs (BASs) in Oklahoma. The main purpose of this investigation was to identify/confirm the mechanisms behind the distress experienced by these BASs. To facilitate this investigation, this study presents the results of analysis of falling weight deflectometer (FWD) data relative to the structural capacity of the slabs as well as the slab – base bonding condition. In addition, to better understand the distress mechanisms, dynamic cone penetrometer (DCP) testing was performed to identify voiding and weak layers in the embankment. It is expected that, by periodically performing the testing, the practitioners are able to monitor the healthiness of BASs, identify the potential issues and take remedial actions accordingly before it is too late.

SITE DESCRIPTION

In this study, the sites for the field investigation were selected based on the information in bridge inspection reports and inspection photos provided by Oklahoma Department of Transportation (OKDOT). Based on the severity of the observed BAS issues, four sites were chosen for the field investigation, including one on U.S. 66 over the spring creek in Oklahoma County (named as “Spring Creek”), one on Northeast 13th street over Interstate 235 (I-235) in Oklahoma City (named as “I-235”), a third one on Hereford Lane over U.S. 69 in McAlester (named as “Hereford Lane”) and a fourth one on U.S. 70 over blue river in Bryan County (named as “Blue River”). The information below focuses on the introduction of the site background information as it may pertain to the performance of the BASs in question including the traffic loading repetitions, environmental conditions, design factors as well as adjacent pavement slabs, embankment fill and foundation soil conditions.

Spring Creek

The Spring Creek site shown in Figure 2-1 is at a very busy highway integral bridge built in 1983 where the average daily traffic (ADT) is over 29650 with 12% trucks (as of 2012). The average low temperature is 24 ˚F in January and the average high temperature is 93 ˚F in July. The highest average precipitation is 5.4 in. in June. The BASs were 13 in. doubly reinforced type concrete slabs connecting to 8 in. dowel jointed concrete pavements. Armored expansion joints were used at the BAS-bridge deck transitions. Sandy clay materials were found within approximately 40 ft. below the ground surface, packed sand layers with clay were found ranging from 40 – 90 ft. below the ground surface; sandstones can be found further down.

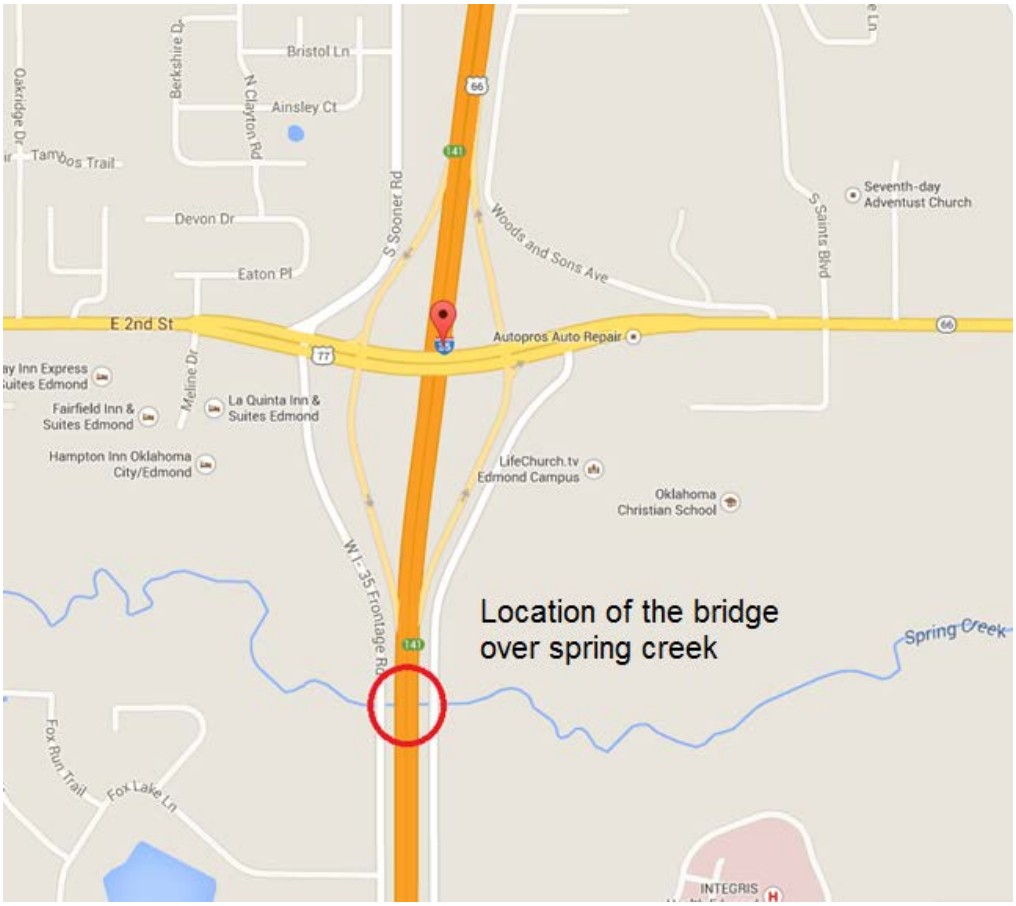

Figure 2-1 Location of the Spring Creek site

I-235

The I-235 site shown in Figure 2-2 is at a bridge connecting with a less busy city street. The non-integral bridge was built in 1988 and the ADT is only 4000 with 5% trucks (as of 2012). The average low temperature is 29 ˚F in January and the average high temperature is 94 ˚F in July. The highest average precipitation is 4.9 in. in June. The BAS and pavement slab designs were the same as the Spring Creek site; the difference is that the BASs were tied to the bridge deck slabs at the BAS-bridge deck transitions. Based on the geotechnical information, compacted granular backfill was found 0 – 10 ft. below the ground surface; below that were highly varied soil layers consisting of combinations of shale and sandstone layers from 10 – 25 ft. Sandstone layers were found 25 ft. and deeper.

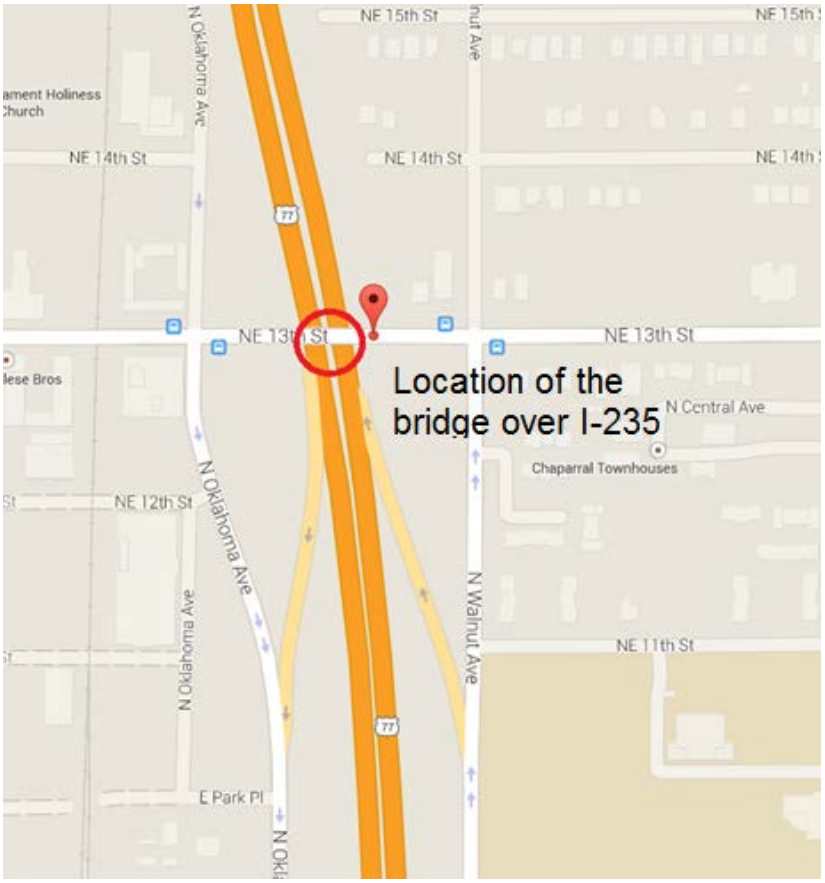

Figure 2-2 Location of the I-235 site

Hereford Lane

The Hereford Lane site shown in Figure 2-3 is at a relatively new integral bridge built in 2008 over Highway U.S. 69. The ADT is 1450 with 5% trucks (as of 2011). The average low temperature was 30 ˚F in January and the average high temperature was 93 ˚F in July. The highest average precipitation is 5.2 in. in May. The BAS design is the same as the previous projects (i.e. 13 in. doubly reinforced concrete slabs connecting to 8 in. dowel jointed concrete pavements). The BASs were also tied to the bridge deck slabs at the BAS-bridge deck transitions. The embankment fills (approximate 10 ft. high) were mainly silty clay with sandstone fragments and cobbles where the foundation soils were medium hard to stiff residual deposits [1].

Figure 2-3 Location of the Hereford Lane site

The Hereford Lane site has some new features in the design and construction of the embankment and foundation soils compared to the other two sites. In order to provide greater bearing capacity and reduce foundation soil settlement, 3 ft. diameter stone columns were used to reinforce the foundation soil and geogrid layers were placed in the compacted embankment fill at 24 in. lifts, which was expected to increase

the stability of the embankment structure. Controlled low strength material (CLSM) in the form of a wedge was placed under the BASs aiming to prevent voiding and settlement issues attributed to its greater resistance to erosion and lower compressibility compared with common embankment clay materials. These features are evaluated during the field investigation. Figure 2-4 provides an elevation view of the backfill area, where the geometry of CLSM, locations of stone columns and geogrid layers are shown.

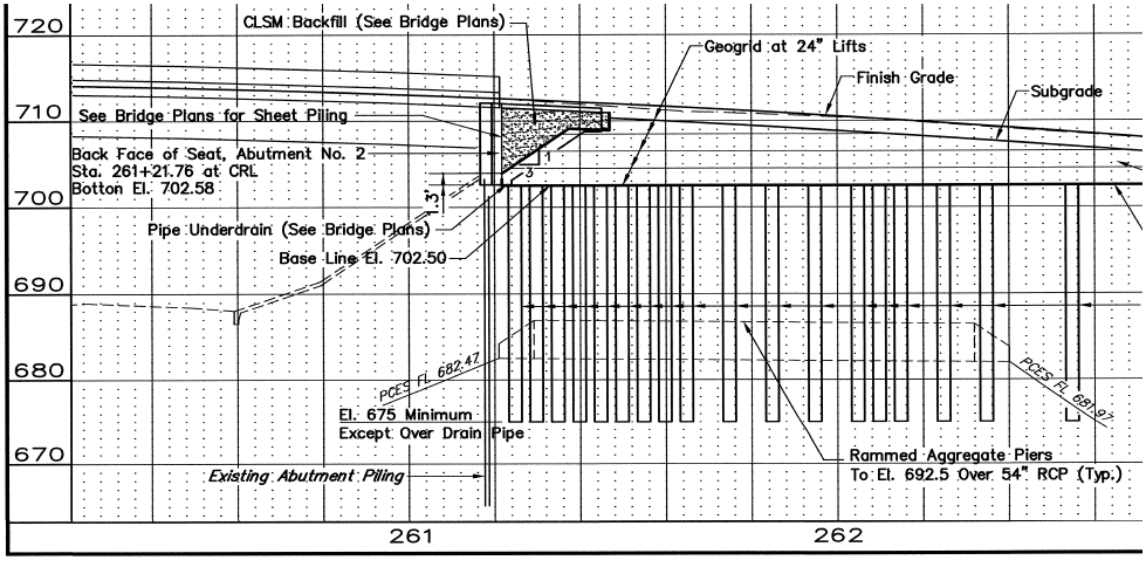

Figure 2-4 Elevation view of the backfill area [2]

Blue River

In addition to the aforementioned investigations, an additional field visit was made for the BAS of a non-integral abutment bridge built over the Blue River in Bryan County, Oklahoma (site named as “Blue River”) in 2012 (the location map is shown in Figure 2-5). The ADT was 5514 with 16% of trucks (as of 2012). The BAS was also a 13 in. doubly reinforced type concrete slab but connecting to 12 in. asphalt pavements. Again, a CLSM wedge was placed underneath the BAS (which was also tied to the bridge deck).

This site was selected because it has a similar BAS design compared to the Hereford Lane site (although no stone columns were placed in the embankment

foundation) and a similar distress type was observed at the BAS – pavement joint (subsequently discussed). Due to the scope of this visit, only visual inspections on the distresses were made (no FWD or DCP testing was involved).

Figure 2-5 The location map of the Blue River site

INVESTIGATION APPROACH

The field investigation consisted of conducting detailed visual distress survey of the BASs (as well as the adjacent pavement slabs) and carrying out FWD and DCP testing to evaluate the structural capacity of concrete slabs and the condition of the underlying layers.

Slab Distress Survey

The objective of the visual distress survey was to provide information as to the possible mechanisms and factors involved with the performance of the BASs. Many of the observed distresses were either structural or material related, whereas others reflected poor conditions of the underlying support layers.

Dynamic Cone Penetrometer Testing

The DCP is a simple and economic testing method to indicate the in-situ soil strength and to locate weak soil layers or spots in foundations or embankments. In this study, the DCP testing was conducted by Uretek, USA personnel employing a DPM 30-20 Model DCP manufactured by Pagani Geotechnical Equipment of Piacenza, Italy and detailed information of this equipment can be found elsewhere [3]. The DCP testing started with inserting sacrificial cone and rods into drilled holes in concrete slabs; the cone and rods were then driven into the embankment fill by a percussive head which was lifted by an electrical-motor-controlled mechanical arm [3]. The DCP information was useful to determine the nature of the supporting structure as it may pertain to the cracking and bump issues associated with BASs.

Falling Weight Deflectometer Testing

The falling weight deflectometer (FWD) testing has been widely used as a non-destructive method to evaluate the stiffness-related parameters of existing concrete pavements (such as modulus of pavement layers) and load transfer capacity of joints. Different from the nature of the DCP testing (which mainly focuses on evaluating the support condition at various depths), the FWD testing was performed in this study mainly to determine the structural capacity of the BASs and assess the degree of erosion of the supporting material immediately below the slab (i.e. the slab-base interface condition) since these parameters can be directly related to the performance of the BASs (in terms of the cracking and bump conditions). Even though the nature of the two testing methods are different (meaning that a comparative analysis between their results may not be applicable), performing both the tests will be helpful to evaluate the support condition in various dimensions (both at the slab-base interface and in the deeper soil layers) in order to comprehensively understand the root causes of the BAS distresses.

A Dynatest Model 8000 FWD provided by the Oklahoma DOT consisted of an 11.8-in diameter loading plate and seven deflection sensors spaced at 0, 8, 12, 24, 36, 48 and 72 inches from the center of the plate was used to carry out the field work. The

FWD contains four different loading magnitudes, which are approximately 8.5, 9, 12 and 15 kips. The testing pattern was performed using the LTPP standard test plan as a guide shown in Figure 2-6. Four testing positions were tested in this study for both concrete pavements and BASs, including the center of the slab (J_1), the slab corner (J_2), the mid-slab along the longitudinal pavement edge (J_3) and the outer wheel path near the transverse joint (J_5). It should be noted that J_0 was not used for this test (according to the guidelines [4]) and J_4 position (mainly used to determine load transfer efficiency of joints) was not tested due to the lack of a sensor behind the loading plate.

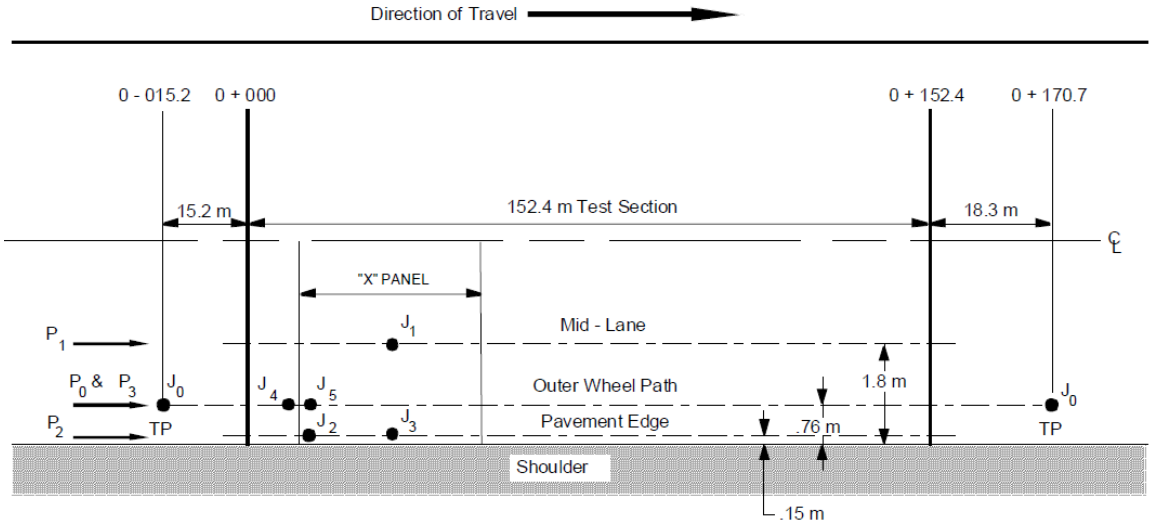

Figure 2-6 LTPP FWD testing plan for Jointed Concrete Pavement (JCP) [4]

In order to achieve the purpose of identifying weak spots and loss of support underneath BASs, the deflection data measured during the FWD testing were used to back-calculate the effective concrete slab thickness and the interlayer friction coefficient, which are two important parameters for quantitatively accessing the structure capability of the BASs.

Determination of effective slab thickness and interlayer friction coefficient

The effective slab thickness concept refers to an equivalent slab thickness based on the structural response of the pavement structure to the application of load. It is considered that, due to the erosion of the supporting layer, the slab-base interface condition may vary from no contact (base is totally unbonded/separated from slab) to

full contact (base is fully bonded to slab); with the intermediate condition being partially-bonded which could vary considerably in the presence of weak spots.

The basic approach to determining an equivalent slab thickness was outlined by Zollinger et al. [5]. Using the deflection results obtained from FWD testing, the effective slab thickness for the partially-bonded slab condition is calculated as:

$$h_e = [\ell_m^4 \cdot \frac{12(1-\nu^2)k_{dyn}}{E_c}]^{\frac{1}{3}} = h_{e-p} \quad (2\text{-}1)$$

where:

h_e = effective slab thickness (in) $= h_{e-p}$,

ℓ_m = radius of relative stiffness (in) $= 0.0284 \cdot BA^2 - 0.2891 \cdot BA + 0.992$,

ν = Poisson's ratio of the concrete,

k_{dyn} = dynamic modulus of subgrade reaction (psi/in) $= \frac{d_0^* \cdot P}{d_0 \cdot \ell_m^2} \cdot 1000$

E_c = elastic modulus of the PCC layer (psi),

d_0^* = dimensionless deflection $= \frac{1}{8}[1 + \frac{1}{2\pi}(\ln(\frac{a}{2\ell_m}) - 0.673)(\frac{a}{\ell_m})^2]$,

P = wheel load (lb),

d_0 = deflection at the loading position (mils),

a = radius of loading plate (in),

BA = basin area calculated from 7 sensors $= 6\frac{d_0 + 2(d_1 + d_2 + d_3 + d_4 + d_5) + d_6}{d_0}$

$d_1, d_2, d_3, d_4, d_5, d_6$ = deflection at 1, 2, 3, 4, 5 and 6 ft. from the loading position (mils)

An expression for the interlayer friction coefficient (μ_e) between concrete slab and the underlying subbase layer was shown to be [5]:

$$\mu_e = \frac{\sigma_{e-u} - \sigma_e[\frac{2h_{e-u}}{h_{e-p}} - 1]}{\frac{h_c}{12} + \sigma_v} \quad (2\text{-}2)$$

where:

σ_e = $\frac{s_e p}{h_e^2}$,

σ_{e-u} = $\frac{s_{e-u} P}{h_{e-u}}$

σ_{e-p} = $\sigma_e[\frac{2h_{e-u}}{h_{e-p}} - 1]$

s_e = Dimensionless stress = $a + b\ell_m + c\ell_m^2$ (for the effective pavement section),

a, b, c = 0.0006, 0.0403, and -0.0002 (for FWD plate loading),

h_c = Concrete slab thickness (in),

h_{e-u} = Unbonded slab thickness (in) = $h_1^3 + \frac{E_2}{E_1} h_2^3$,

E_i = flexural moduli of the pavement layers (1 = concrete layer, 2 = subbase layer),

h_i = thickness of the pavement layers (1= concrete layer, 2 = subbase layer),

σ_v = Load induced vertical pressure (psi) (≈ 0.7 psi).

The interlayer friction coefficient varies as the degree of bonding changes (also if the local supporting soil is separated from the concrete slab); therefore it is a useful parameter to judge the extent of voiding or erosion immediately underneath BASs.

RESULTS AND DISCUSSION

Field investigations were conducted on the outer travel lane of entrance and departure BASs for the four aforementioned sites in Oklahoma. During the investigations, slab distress surveys, DCP and FWD were conducted for the first three locations. Figure 2-7 shows schematic diagrams of the DCP locations and distress on the entrance and departure BASs as well as on the adjacent pavement slabs of the three sites. Note that the straight lines are joints or slab boundaries, the wave lines are cracks and the circles are the locations of DCP testing in Figure 2-7.

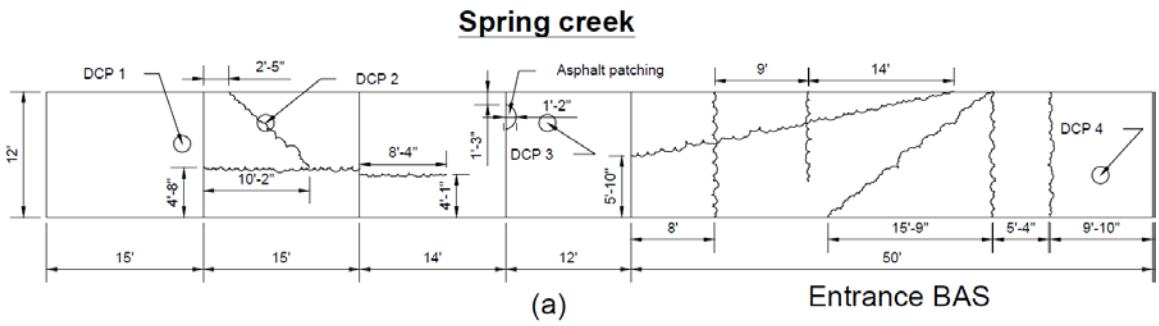
Spring creek
DCP 1
2'-5"
DCP 2
Asphalt patching
9'
14'
1'-2"
DCP 3
DCP 4
12'
1'-3"
8'-4"
10'-2"
4'-8"
4'-1"
5'-10"
8'
15'-9"
5'-4"
9'-10"
15'
15'
14'
12'
50'
(a)
Entrance BAS

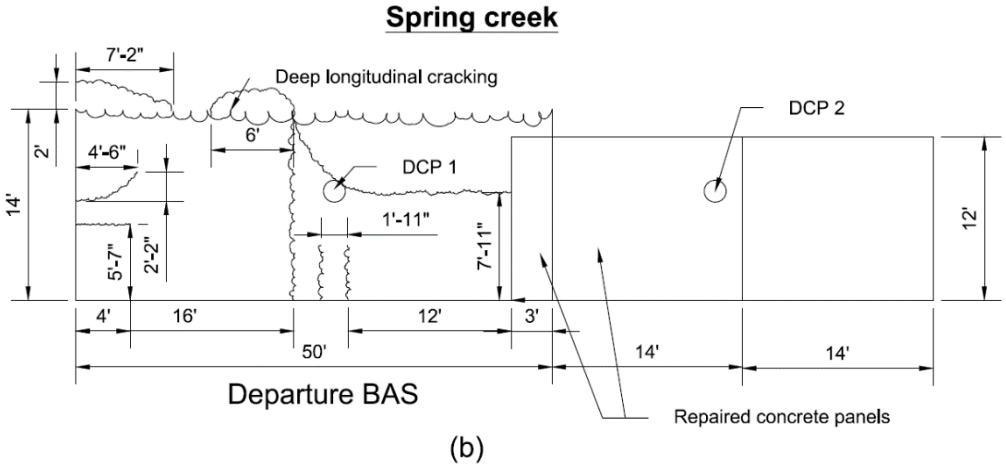
Spring creek
7'-2"
Deep longitudinal cracking
DCP 2
6'
4'-6"
DCP 1
2'
14'
1'-11"
7'-11"
12'
5'-7"
2'-2"
4'
16'
12'
3'
50'
14'
14'
Departure BAS
Repaired concrete panels
(b)

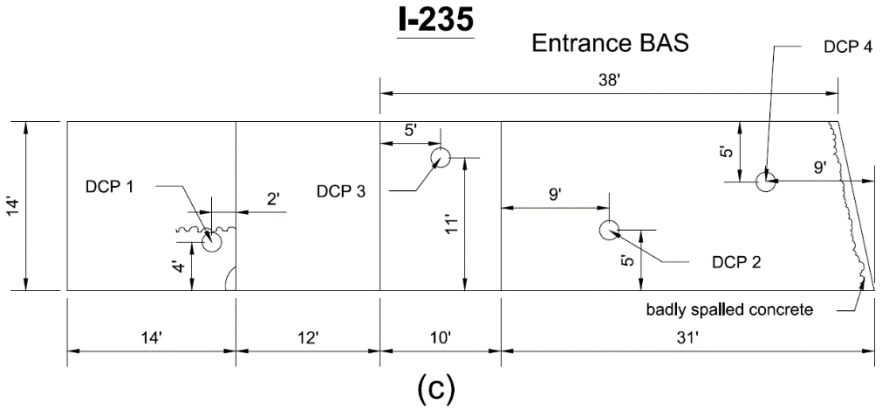
I-235
Entrance BAS
DCP 4
38'
5'
5'
9'
DCP 1
2'
DCP 3
9'
14'
11'
5'
DCP 2
4'
badly spalled concrete
14'
12'
10'
31'
(c)

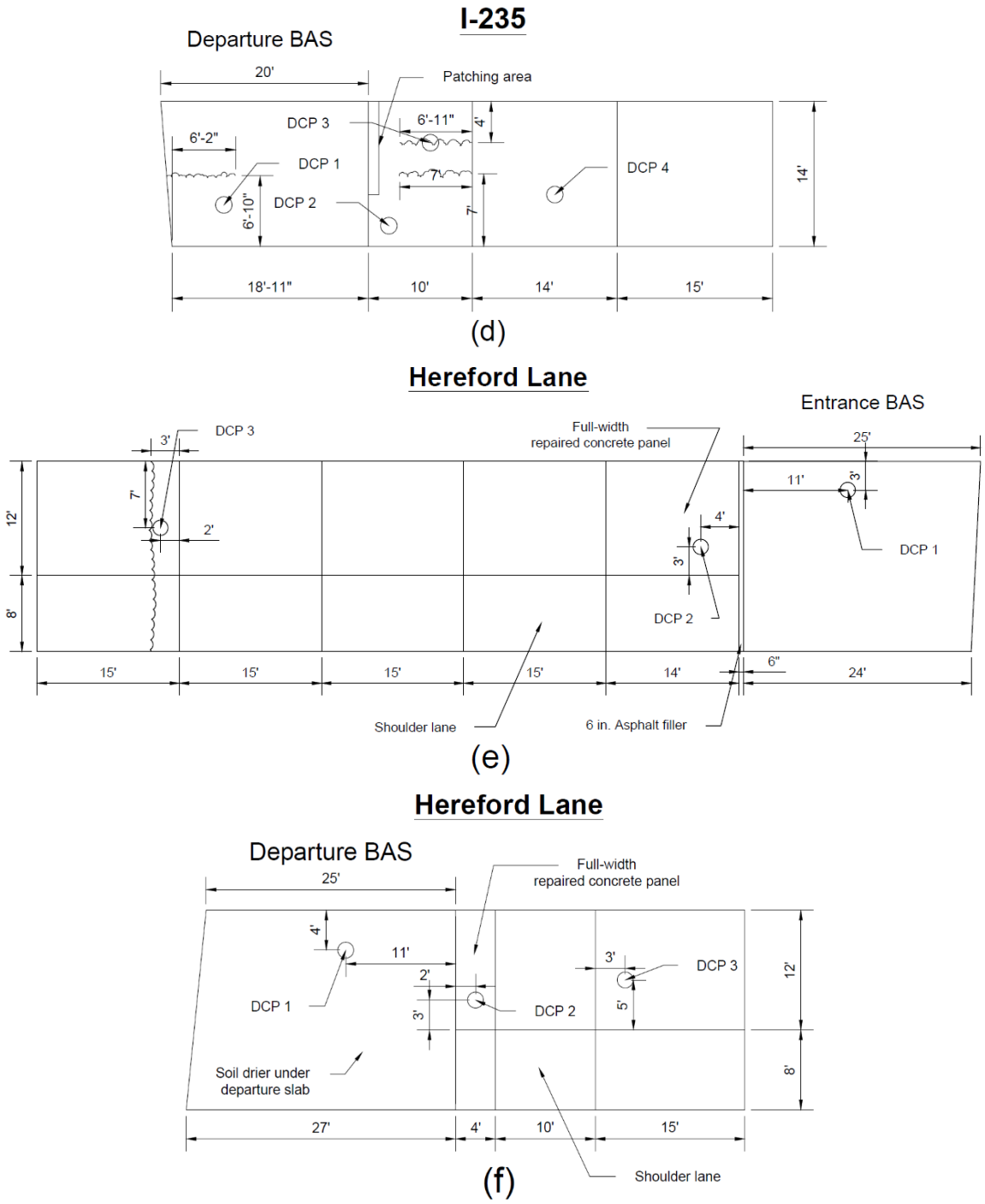

Figure 2-7 DCP locations and distress on (a) Spring Creek entrance BAS, (b) Spring Creek departure BAS, (c) I-235 entrance BAS, (d) I-235 departure BAS, (e) Hereford Lane entrance BAS, (f) Hereford Lane departure BAS and adjacent pavement slabs

Spring Creek

On the Spring Creek site, the BASs on both ends were shattered with extensive cracking (shown in Figure 2-7 (a) and (b) and Figure 2-8), which was likely due to loss of support, by erosion between the slab and the base under the effect of heavy traffic load repetitions. Although differential settlement was not obvious at the BAS-bridge deck joint, the armor expansion joints at both ends were broken, the joint seals were missing, and the adjacent concrete badly spalled (mainly on the passing lane), which appeared to be the main the cause of the roughness. It was found that lateral drainage was nearly blocked for several hundred feet in both directions from the bridge as neither the entrance nor departure BAS was properly drained.

The DCP results taken near the entrance BAS-bridge connection (DCP 4 as shown in Figure 2-7 (a)) consistently showed very low number of blow counts (3~6) within 8 ft. of the ground surface. This could be due to weakening of the embankment soil caused by water infiltration. The expansion joint sealant deterioration could also be another factor that worsened the problem.

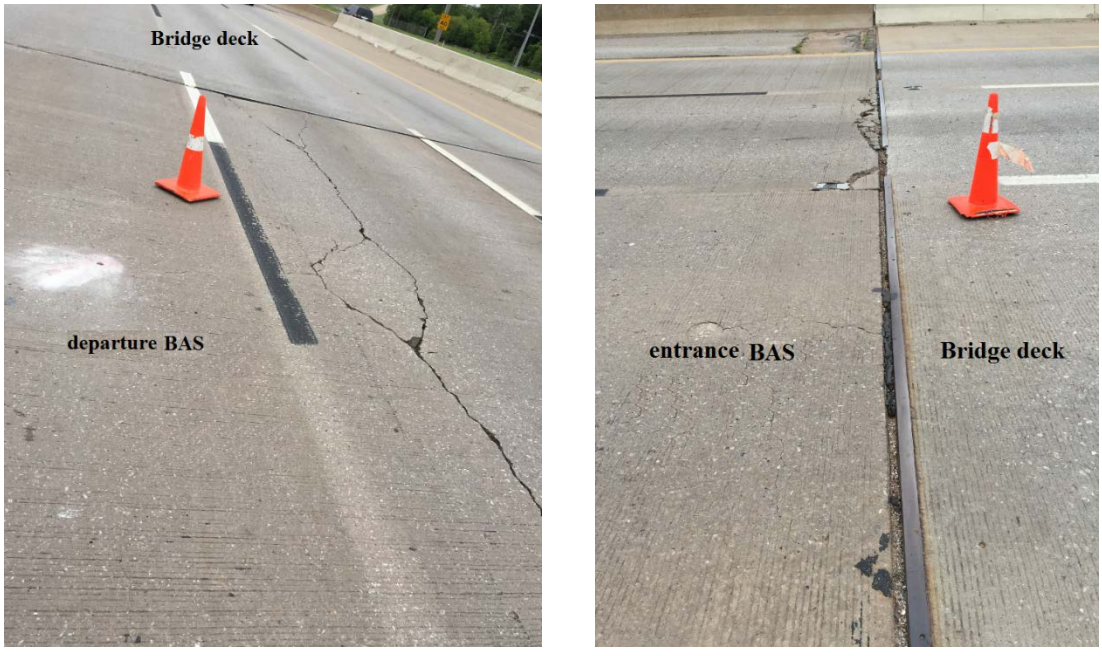

(a) (b)

Figure 2-8 Distress observed at Spring Creek site (a) entrance BAS-bridge connection and (b) departure BAS-bridge connection

As shown in Figure 2-9 (a), the effective slab thickness calculated from FWD data for the J_1 and J_3 locations generally exhibited greater values compared to the J_2 and J_5 locations indicating that center and mid-slab locations are less susceptible to erosion and pumping damage. One exception was at the corner of the departure BAS where J_2 showed the greatest effective slab thickness. This could be attributed to the contribution of the repaired concrete panel at the departure BAS-pavement connection as shown in Figure 2-7 (b). Restoration made to the underlying support at that location led to the increased effective slab thickness and interlayer friction coefficient as shown in Figure 2-9. Figure 2-9 (b) also shows that interlayer friction was almost nonexistent at the other test locations, which suggests that a severe base-slab separation condition was present as reflected by the extensive slab cracking observed in both the entrance and departure BASs.

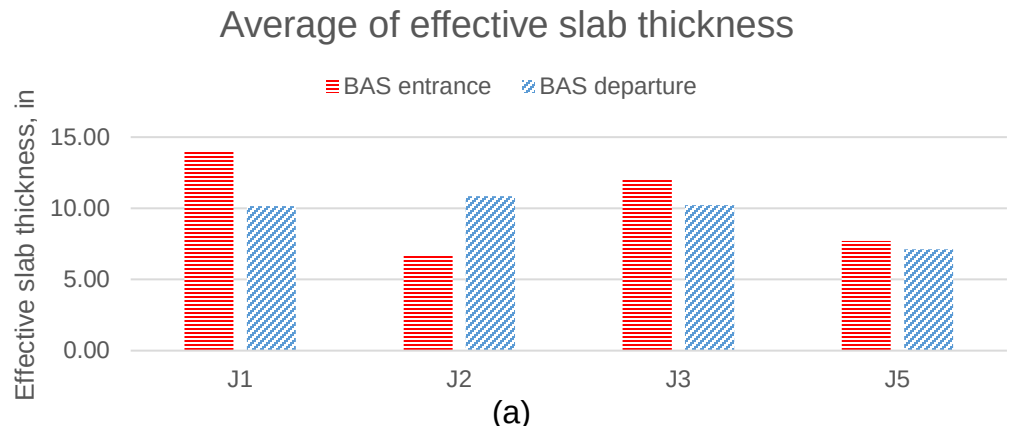

(a)

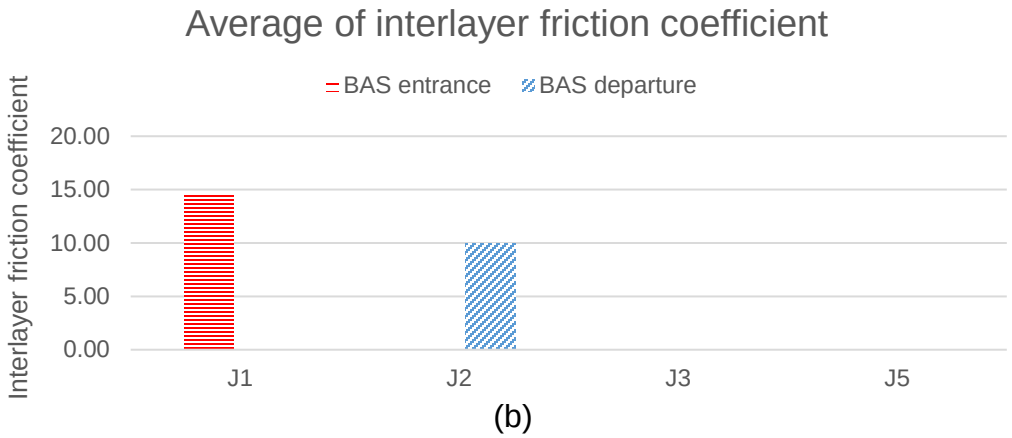

(b)

Figure 2-9 the average of (a) the effective slab thickness and (b) interlayer friction coefficient of entrance and departure BASs at Spring Creek

In summary, the poor performance (i.e. the severe erosion and slab cracking conditions) for this site is likely related to the drainage problem in association with the heavy traffic loading repetitions. Cracking in both BASs may have aggravated the drainage issue possibly weakening the embankment fill. The DCP results indicated that poor consolidation may have been present in the embankment fill also contributing to the cracking. The combination of FWD and DCP test results seemed to be very useful to define the mechanisms taking place underneath both the entrance and departure BASs responsible for the cracking at those areas.

I-235

For the I-235 site, concrete spalling parallel to the expansion joints was observed along almost the full width of the entrance/departure BAS-bridge deck joints as shown in Figure 2-10 (a) and (b). Neither differential slab settlement nor severe bump issue was experienced at these connections. However, significant slab settlements (approximate 3 in.) were observed in the sidewalk adjacent to the Entrance BAS as shown in Figure 2-10 (c).

Based on the DCP results, weak embankment soil layers (number of blow counts < 5) were encountered within 6 ft. of the ground surface underneath the entrance BAS surface (from “DCP 4” shown in Figure 2-7 (c)). The conditions were similar on the other end of the bridge where a large voided area and weak embankment soil layers (number of blow counts < 1) were found down to 6.5 ft. below the departure BAS ground surface (from “DCP 1” shown in Figure 2-7 (d)). The causes of the substantial voiding are not entirely obvious but it seems that moisture infiltration had much to do with it. It could be a combination of factors involved, such as poor embankment soil compaction and water infiltration into the joints. Although the top portion of the supporting embankment structure is weaker at this site as suggested by the DCP results, not as much slab cracking has occurred as was observed at the Spring Creek site.

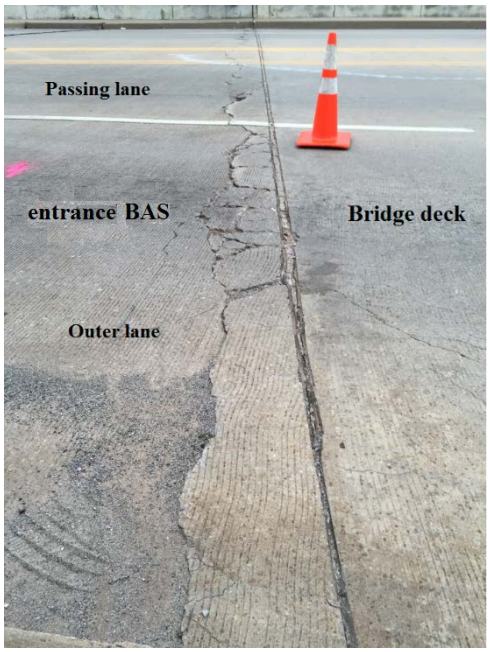

(a)

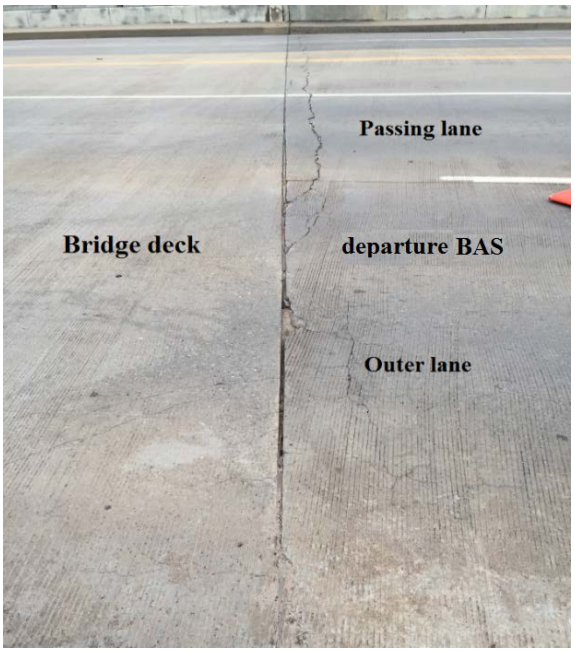

(b)

(c)

Figure 2-10 Major distress observed at I-235 site (a) entrance BAS-bridge connection, (b) departure BAS-bridge connection and (c) large settlement at the sidewalk along entrance BAS

The DCP testing results which were taken below the BASs could be the key to understanding the cause of the spalled area parallel to the entrance/departure BAS-bridge deck joint. The weak supporting soil layers suggested by the DCP results could

be a factor since they may contribute to the high shear stresses at that location created due to the restraint along the joint (due to horizontally tying the BAS to the bridge deck using steel reinforcement) against deflection bending (as a result of having one side supported by rigid abutment and the other end supported by weak and voided soil support) in the approach slab. The location of the horizontal tie bars may have also magnified the spalling condition when they are placed at a shallow depth in the concrete. Although not as likely, spalling could also been attributed to restraint of temperature expansion of the approach slab against the bridge deck; however, it appears that further investigation using ultra-sonic scanning technology would be useful to clearly identify the orientation of the spall cracking at this site and whether steel reinforcement or doweling was associated with the cracking.

"DCP 2" (location shown in Figure 2-7 (c)) was taken at the entrance BAS near the settled sidewalk shown in Figure 2-10 (c). The results also indicated again very weak soil layers (number of blow counts < 3) within the first 4 ft. below this area. The cause of such huge depression was very likely moisture related. Excessive water may have infiltrated into the sidewalk and eroded the soil support; the tree near the sidewalk may also contributed to the shrinkage of the soil – due to the suction in the soil (i.e. negative pore water pressure in the soil particles that reduces the total volume of the soil body) exacerbating the settling problem.

FWD was performed at the J_1 and J_5 locations at the outer lane of the entrance/departure BAS due to the lack of a shoulder lane at this site. As shown in Figure 2-11 (a), the average effective slab thickness for the J_1 location was greater compared to the same location at the Spring Creek site. This suggested greater structural capacity which may explain why the cracking condition at this site was far better than that at the Spring Creek site. Again, the FWD and visual cracking results seem to suggest that the length of the structural support at this site was much greater than at the Spring Creek site and the greater effective stiffness would lead to higher horizontal shear stress along the edge of BAS-bridge deck joint. Spall cracking tends to be horizontally oriented which seems to be the case here but further NDT data at the J_5 location of the entrance BAS would be useful to confirm that even though this location had a comparatively much lower effective slab thickness yielding high horizontal shear

(shown in Figure 2-11 (a)). This explanation seems to be consistent with the spalling condition along the joint with the departure BAS (shown in Figure 2-10 (a)) where the spalling distress was less severe and the support lengths were lower (shown in Figure 2-10 (b)). The average of interlayer friction coefficients for this site indicated good contact at the slab center but nearly none along the bridge joint shown in Figure 2-11 (b). This finding accorded with the aforementioned DCP results at the same location where a large voided and weak areas within the embankment were detected, which further validated the utility of the calculated results from the analysis of the FWD data.

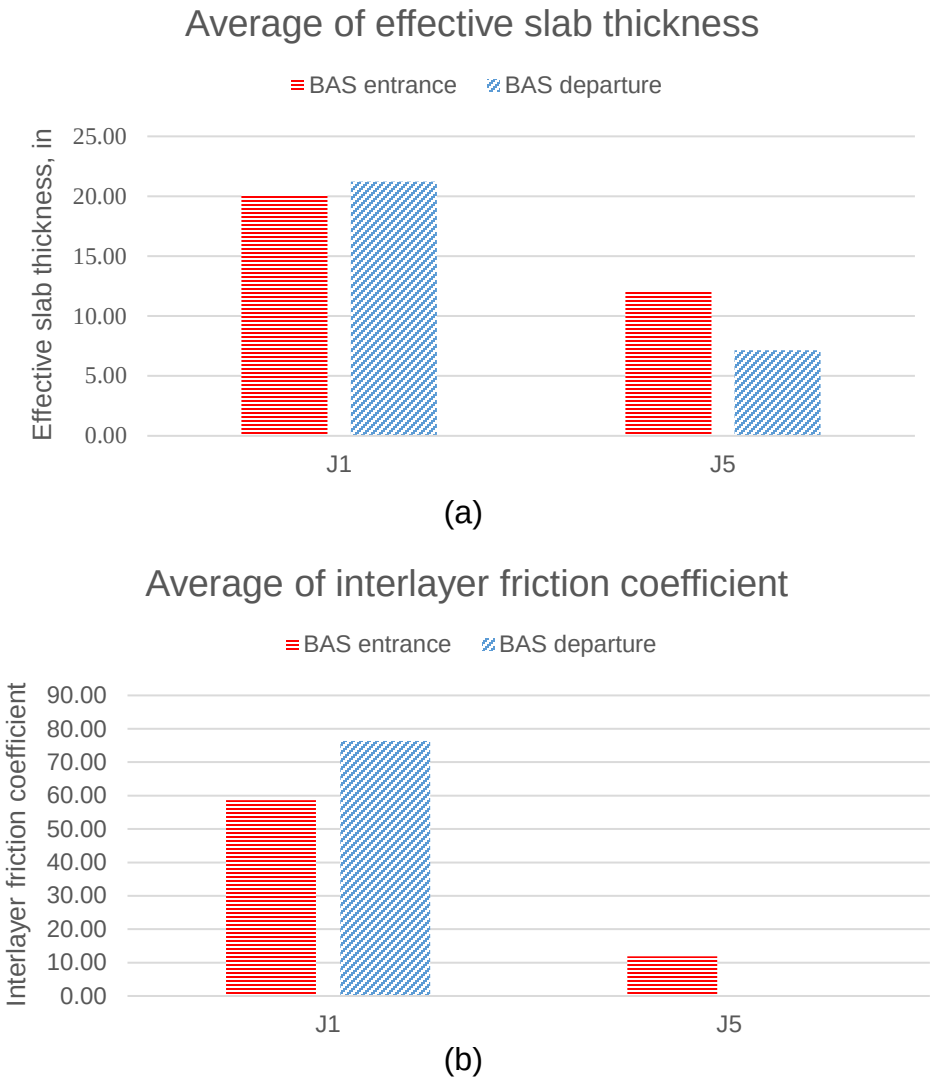

Figure 2-11 the average of (a) the effective slab thickness and (b) interlayer friction coefficient of entrance/departure BAS at I-235

In summary, the parallel spalled cracking, as a major issue at this site, was probably caused by inadequate support along the bridge joint. Although extensive slab cracking was not observed probably due to the high effective slab thicknesses that seemed to be prevalent at this site, satisfactory slab contact with the supporting base layer and low ADT volumes may also have been the factors.

Hereford Lane

No cracking or discontinuity was observed for the entrance/departure BAS at this site and the bridge deck – BAS transitions were very smooth. However, a full-depth repair (FDR) had been made on the pavement slabs adjacent to both the entrance/departure BASs as shown in Figure 2-12 (a) and (b). The width of the repaired concrete pavement panel was 14 ft. for the entrance BAS (shown in Figure 2-7 (e)) and 4 ft. for the departure BAS side (shown in Figure 2-7 (f)). The wider FDR area at the entrance BAS side is probably suggesting that, prior to the FDR, this side had more slab cracking and a greater amount of erosion compared to the departure side. The 6-in wide asphalt filler found at the entrance/departure BAS-pavement joint (as shown in Figure 2-12 (a) and (b)) was placed in lieu of the old expansion joint which had failed. As suggested by the broken segment (i.e. one end of the pavement curb) at the entrance/departure BAS–pavement joint as shown in Figure 2-12 (c), some thermally inducted movement may be involved but this may only be a secondary issue. It is speculated that, prior to placing the FDR, the failure of the expansion joint might have resulted in spalled joints and excessive water infiltration into the underlying embankment fill, creating a locally weakened area and exacerbated the slab cracking condition; eventually, FDR had to be made at the entrance/departure BAS-pavement joint.

DCP testing conducted under the FDR locations on both sides yielded results indicating that the top embankment supporting layer was very strong (total number of blow counts was about 70) within 3 ft. of the ground surface at the entrance BAS side, where a weaker top supporting layer (total number of blow counts was about 30) was discovered within 5 ft. of the pavement surface at the departure BAS side. However, the

blow counts at the entrance side were found consistently lower than those at the departure side 5 – 25 feet below the surface. Soil samples from the core holes of DCP testing showed that the embankment on the entrance side was definitely wet and holding pockets of water (very likely from the joint at the pavement-BAS) while the soil on the departure side was relatively dry. This tended to validate the notion that water getting into the joint at the entrance/departure BAS-pavement joint, weakened the embankment soil below the slab.

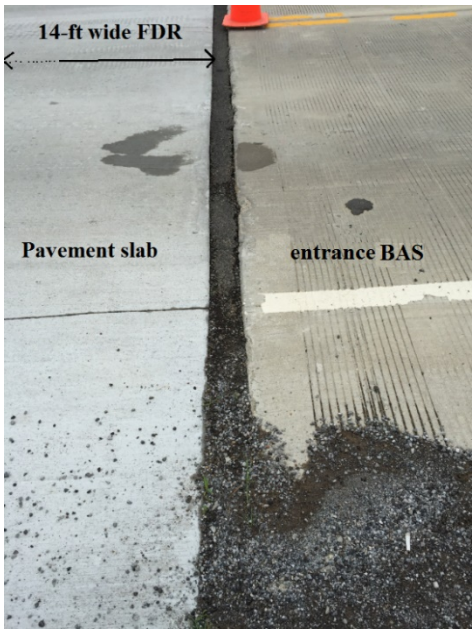

(a)

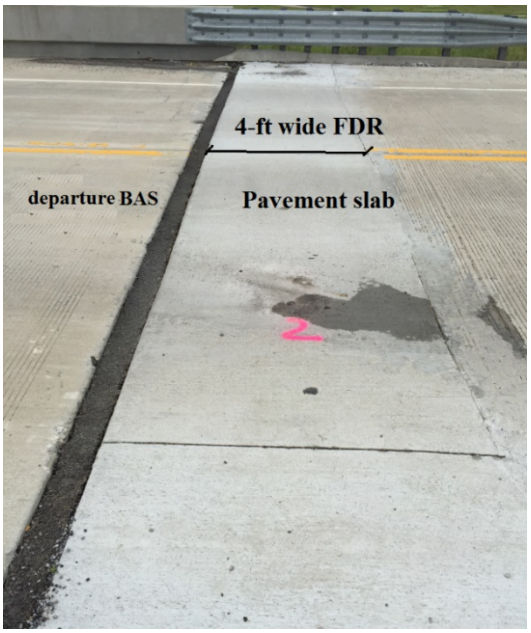

(b)

(c)

Figure 2-12 FDR at (a) Entrance BAS-Pavement connection (b) departure BAS-pavement connection and (c) broken sliver at the entrance/departure BAS–pavement connection

Figure 2-13 the average of (a) the effective slab thickness and (b) interlayer friction coefficient of the FDR adjacent to entrance/departure BAS at Hereford Lane

The FWD results and discussions for this site mainly focus on the pavement slabs where the FDR was made adjacent to the entrance/departure BAS. As shown in Figure 2-13 (a), the effective slab thickness of the FDR at the entrance side was greater in J_1 and J_3 locations (center and mid-slab locations where DCP were conducted) compared with those at the departure side. This is consistent with the DCP results where it showed stronger embankment soil layer within 3 ft. below the FDR at the entrance side, which must have contributed to the greater effective slab thickness

compared to that of the FDR at the departure side. Figure 2-13 (b) suggests that the slab/subbase contact under the FDR was better at the entrance side; whereas at the departure side, slab/subbase separation was definitely a problem at the corner (J_2) and edge (J_5) due to the absence of interlayer friction. Based on the FWD results, it seems that the FDR may not be long-lasting, unless measures are taken to minimize water infiltration through the joints to prevent further erosion at the corner and edge locations.

The positive aspect of this project was that the practices of tying the BASs to bridge deck slabs and the use of the CLSM wedge (which provided a good base support) seemed to result in minimal moisture infiltration and less potential for erosion to occur underneath the BAS-bridge deck joint (since the BAS-bridge deck joints were very smooth and no cracking was observed in the BASs). However, the bump and erosion issues seemed to shift from the BAS-bridge deck joint to the BAS-pavement joint, possibly related to the excessive moisture infiltration at the BAS-pavement joint due to failed joint sealing and the effect of repetitive traffic loads. The higher blow counts were observed at isolated locations in the DCP results, tended to validate the utility of the geo-grid layers to reinforce the embankment structure. The benefit of using stone columns to support the embankment was not obvious based on the DCP results; however, according to the soil taken from the core holes of DCP, the entire area where the embankments rest was totally saturated yet no significant settlement was observed, which indirectly suggested that the stone columns did make a difference.

Blue River

At this site, the bridge deck – BAS transition was also very smooth attributed to the use of the CLSM wedge and tying BAS to bridge deck slab. However, a longitudinal crack was found at the BAS and water stains were observed in and about the crack as shown in Figure 2-14 (a) and (c); faulting was discovered at the BAS – pavement joint leading to a moderate bump as well as spalling along the asphalt pavement edge. In addition, water stains were also found at the face of the abutment wall as shown in Figure 2-14 (b). Although DCP testing was not conducted at this site, the mechanism leading to the observed distresses was obvious. Observations indicated that the site

grading accidentally led to the accumulation of runoff water at the BAS – pavement joint (being the lowest point), resulting in excessive moisture infiltration and erosion damage underneath the joint. The nature of the BAS cracking, the water stains and the faulting distresses are indicators of the moisture infiltration and erosion damage. As the crack has propagated from the BAS – pavement joint to almost ¾ length of the BAS (shown in Figure 2-14 (c)), it is not difficult to recognize that a considerable amount of moisture had infiltrated into the crack and the joint, which may cause more erosion in the base and further aggravation of the cracking condition; the water stains found on the abutment wall face shown in Figure 2-14 (b) are also the evidences of excessive moisture infiltration and base erosion.

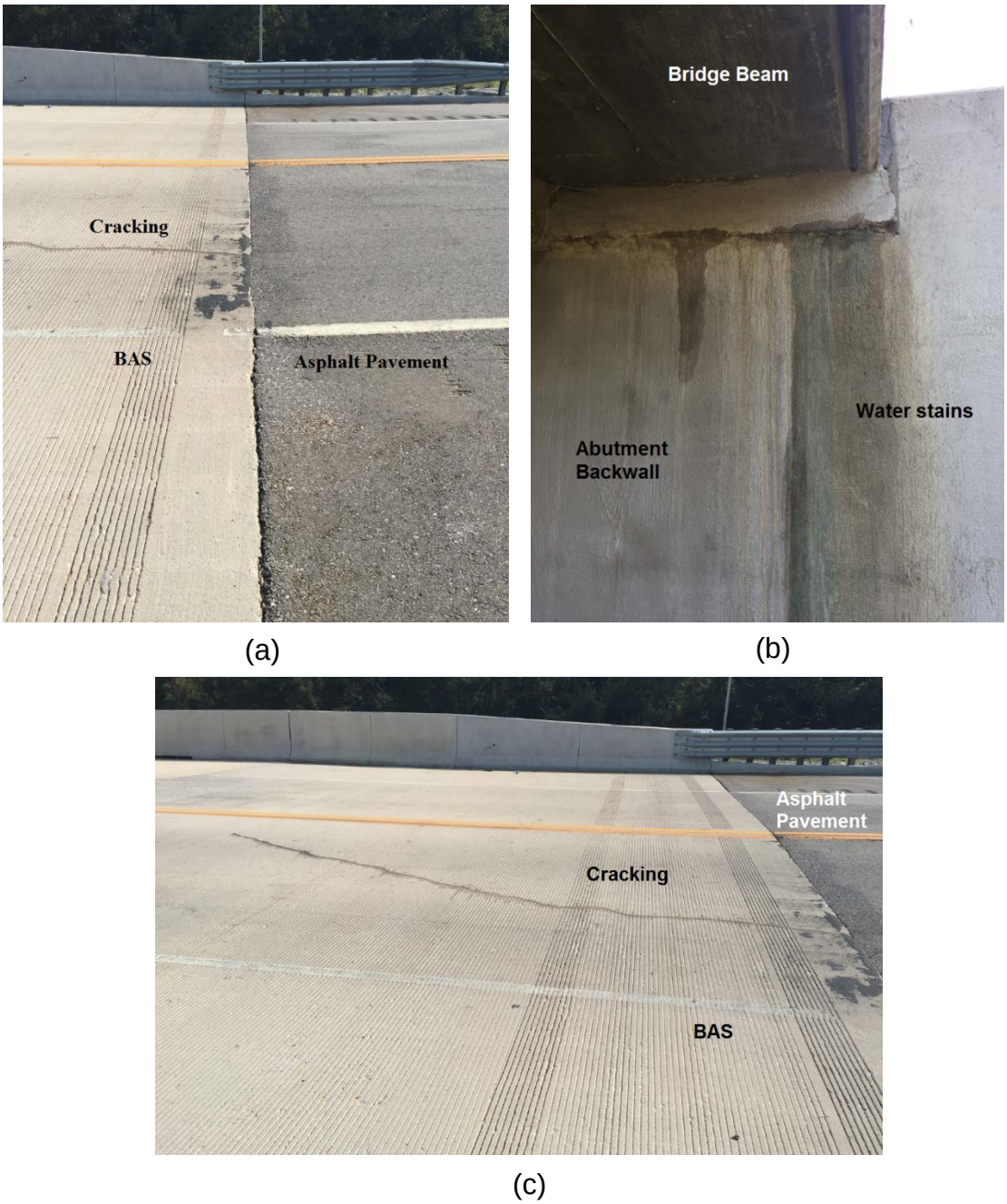

(a) (b)

(c)

Figure 2-14 (a) BAS-pavement connection at Blue River site (b) water stains on the bridge abutment wall at Blue River site (c) the longitudinal cracking on the BAS at Blue River site

FINDINGS

Field investigation was conducted for the four sites in Oklahoma, the results of the slab distress survey, DCP and FWD performed at the entrance/departure BASs and adjacent pavement slabs have led to the following findings:

- By using the FWD deflection results, the calculation of the effective slab thickness and interlayer friction coefficient provides an efficient non-destructive approach to evaluate the structural capacity of BASs and the slab-base interface condition, which is useful to monitor the healthiness of BASs and to determine whether remedial actions (e.g. injection grouting) are required to prevent the condition from getting worse;
- Many previous studies indicated that the bump-at-the-end-of-the-bridge is mainly caused by the settlement or erosion of the underlying support, the results of this investigation tend to support those findings;
- Poor drainage conditions, failed joint sealants and cracked concrete have been the three main factors leading to the excessive moisture infiltration; similar findings were also indicated by a previous field investigation conducted in Oklahoma [6];
- Drainage appears to be the leading factor affecting the BAS performance; poor drainage tends to create conditions for pumping and erosion to occur underneath joints with failed sealants which can eventually cause extensive slab cracking; the cracking will create more entry points for water infiltration, which further exacerbates the erosion condition;
- It appears that the use of geo-grids and stone columns are beneficial to support conditions under BASs;
- The bridge deck – BAS joint may not be susceptible to the bump issue when the BAS is tied to the bridge deck (which results in a minimal potential for moisture infiltration and erosion to occur underneath this joint) in combination with the use of a less compressible and erodible embankment backfill material (e.g. a CLSM wedge) to support the BAS;
- A good BAS – pavement transition design (including both load transferring and drainage considerations) is needed to insure proper functioning of the sealed

joints in order to minimize the potential for moisture infiltration to occur underneath the joint, as there was evidence showing that the bump issue may transfer from the bridge deck – BAS joint to the BAS – pavement joint (similar observations were also indicated by some previous field investigations [7-9]) due to the base erosion caused by excessive moisture infiltration and repetitive traffic loads.

CHAPTER 3

DESIGN OF BRIDGE APPROACH SLAB USING PRECAST CONCRETE PAVEMENT

This chapter mainly provides information regarding the procedures for designing bridge approach slabs (BASs) using precast technologies. First, the background information of the precast concrete pavement technologies are introduced, including the various configurations of jointed precast concrete pavements (JPrCPs) and precast prestressed concrete pavements (PPCPs). Second, detailed procedures are provided for designing the thickness of JPrCP and PPCP BASs; the erosion damage that may potentially develop underneath BASs was taken into account to better address the bump issues observed in Oklahoma. Third, design examples are elaborated to better assist practitioners for designing precast BASs.

BACKGROUND OF PRECAST CONCRETE PAVEMENT

The precast concrete pavement (PCP) is an emerging technology which provides durable and longer-lasting features that meet the needs for rapid construction and rehabilitation of existing pavements. Although the history of PCP in the U.S. has been more than 40 years, early applications of PCP were limited to small scale emergency repairs. Over the past 15 years, substantial effort has been made by highway agencies as well as industry organizations to facilitate the advancement and application of PCP; specific types of PCPs were developed and used for both intermittent repairs and project-level rehabilitations/reconstructions for highway and airfield pavements as well as BASs [10-16].

The following provides an introduction to two different types of PCPs that can potentially be used for constructing BASs – one being the jointed precast concrete pavement (JPrCP) and the other precast prestressed concrete pavement (PPCP). The specific features of the two options allow engineers to tailor the design of BASs based on key site conditions and design objectives associated with the use of BASs in

Oklahoma, which provides a more durable system to effectively minimize the bump-at-the-end-of-the-bridge.

Jointed Precast Concrete Pavement

The introduction of JPrCP comes from the need for a more appropriate and rapid method to rehabilitate distressed concrete pavement BASs. In general, a JPrCP behaves very similarly to a conventional cast-in-place (CIP) jointed concrete pavement (JCP) [10]; however, different from the conventional CIP JCP where the aggregate interlock is thought to contribute a greater portion of the load transfer capability (when the joint opening is less than 0.03 in.) at the transverse joints, the application of JPrCP heavily relies on the use of dowel bars to provide load transfer mainly because that the fabricated precast concrete slabs have smooth joint faces and lack the aggregate interlocking mechanism.

JPrCP can be made of either reinforced concrete panels or pretensioned concrete panels. As a means to facilitate the installation of dowel bars, a slot system is usually fabricated in precast panels. Currently, two options are available for making slots in precast concrete panels [10]:

1. Top slot system;
2. Proprietary bottom slot system.

Top Slot System

In a top slot system, the precast panels are equipped with three 1.5 in. diameter and 18 in. long dowel bars spaced at 12 in. at the transverse joint centered on each wheel path of the pavement slab [17] as shown in Figure 3-1. To accommodate the dowels, dowel slots are either pre-formed in precast panels or made at the edges or joints of adjacent slabs through sawing, jackhammering, air cleaning and sandblasting. Once the precast panel is installed, the dowel slots are filled with high strength concrete grout that often consists of non-shrink proprietary materials [17]. Load transfer in the top slot system is achieved through the bond resistance between the grout and the sandblasted face of the slots as shown in Figure 3-2.

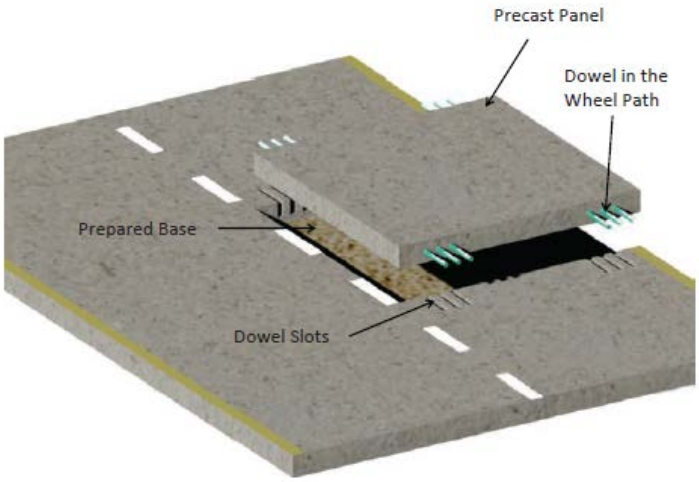

Figure 3-1 A JPrCP with top slot system [10]

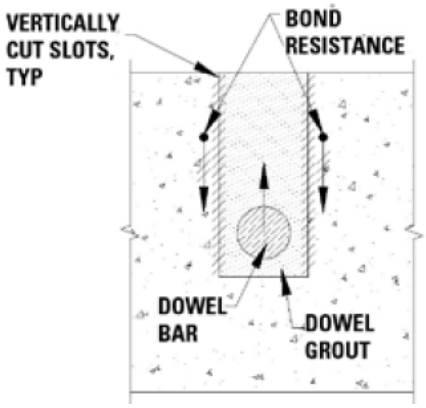

Figure 3-2 Vertical face of the joint of the top slot system [18]

A modified version of the top slot system uses only 1 in. wide narrow top surface slots as shown in Figure 3-3 (the length of the slot has been significantly reduced in a more recent version [19]) which allows for temporary traffic opening until the slots are patched. The development of this version of top slot system aims at addressing multiple lane closures that are involved during the construction, in which the original surface slots are too wide (about 2.5 – 3 in.) to be left open for traffic without being patched, which affects construction efficiency during each lane closure. In this modified version, dowel bars are inserted into the slots before the placement of the precast panels; once the panels are in place, the dowel bars are then slid into the drilled holes in the adjacent concrete panels; following that the slots are patched with rapid-setting materials [10].

Figure 3-3 A narrow-mouth top surface slot system [10]

Bottom Slot System

In a proprietary bottom slot system, the dowel slots are cast at the bottom of the precast panel along the transverse joints as shown in Figure 3-4. The dowel bars are embedded into the adjacent panels by drilling and epoxy grouting to provide load transfer [10]. Once installed, the bottom slots in the precast panel are filled with non-shrink grout through the grout holes at the surface of the panel. Similar to the top slot system, load transfer in the bottom slot system is achieved through the bond resistance; in addition, the specially designed dove-tail shape bottom slot system shown in Figure 3-5 can also provide a mechanical resistance to avoid pull-out of dowel bars [18].

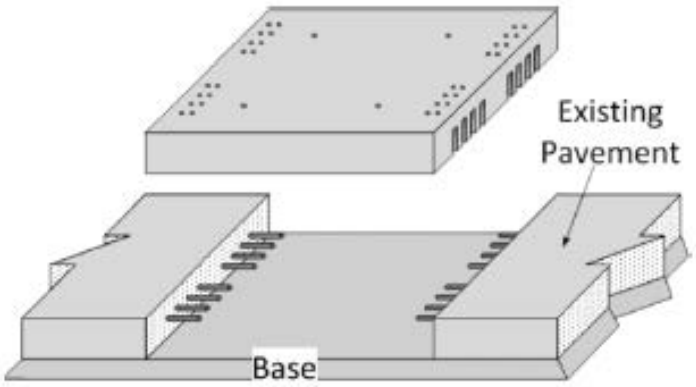

Figure 3-4 A precast concrete panel with bottom slot system [10]

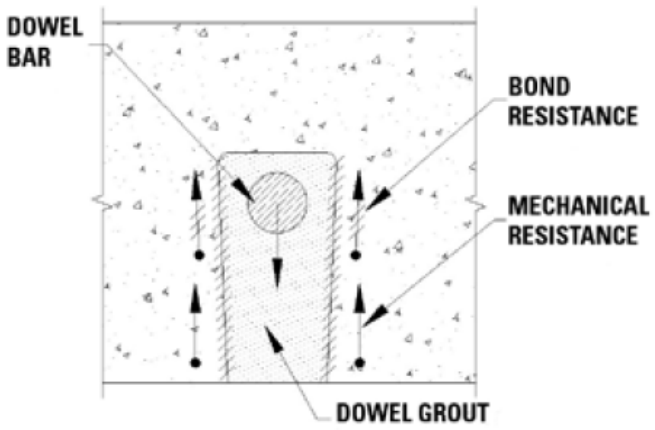

Figure 3-5 Vertical face of the joint of the bottom slot system [18]

Precast Prestressed Concrete Pavement

The concept of PPCP was developed based on the past experiences with CIP prestressed concrete pavement projects [20]. A PPCP section which usually has much longer expansion joint spacing (150 – 250 ft.) (compared with a conventional CIP JCP) is composed of a series of individual panels; each panel has a length of 8 – 10 ft. and a width of up to 38 ft. [21] (note that sometimes the width of individual panels is designed the same as the width of one lane as a means to expedite the construction [19]). The panels within a PPCP section are usually pretensioned in the transverse direction during panel fabrication stage, and are post-tensioned together in the longitudinal direction during construction stage; or they can also be post-tensioned in both the directions during the construction.

Three versions of PPCP shown in Figure 3-6 have been used in the previous projects [10, 13, 22]:

1. Central stressing system;
2. End hand hole stressing system;
3. End gap slab stressing system.

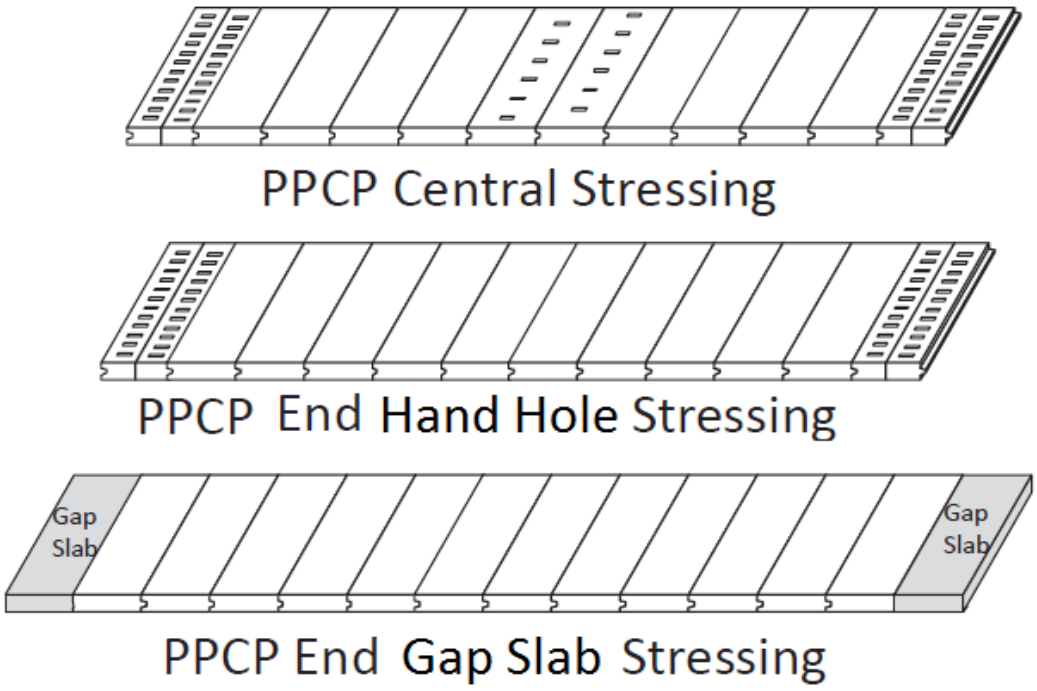

Figure 3-6 The three version of PPCP, after [10]

Central Stressing System

The original version of PPCP consists of three different types of panels, the base panels, the central stressing panel and the joint panels as shown in Figure 3-7. The three different types of panels work together to achieve successful post-tensioning throughout the entire pavement section. As indicated in the details in Figure 3-7, in addition to the pretensioning strands that transversely pre-tension the panels, each of the three different types of panels are fabricated with a continuous shear key along the joint surface to ensure a tight connection and vertical alignment of the panels, lifting anchors cast for moving and positioning the panels, and ducts mounted for post-tensioning the strands in the longitudinal direction of the PPCP [12].

Each type of panel is designed with a specific purpose in mind. A joint panel, as shown in Figure 3-7 (a), contains two half panels at the end of each PPCP segment. The expansion joint between the two half panels is designed to relieve the contraction or expansion of the pavement materials due to temperature variation. The post-tensioning (P-T) anchor access or hand holes facilitate the installation of a dead-end

anchorage system which contains a wedge attached to a bearing plate to lock the strands in place while they are being post-tensioned at the central stressing panels. The grout inlet/vent is usually cast in front of the anchorage system to allow for grouting after post-tensioning is finished. A base panel, as shown in Figure 3-7 (b), is the very generic part that constitutes the majority of a PPCP system. The main purpose of the base panels (varied number) is to fill the space between the joint panels and the central stressing panel depending on the total length of a PPCP system. Meanwhile, the base panels also provide a medium for the ducts in which to pass the post-tensioning strands through. A central stressing panel, as indicated in Figure 3-7 (c), is designed similarly as the base panels, but with central stressing pockets which allow for the installation of a coupler as shown in Figure 3-8. The couplers are designed such that the post-tensioning strands extend from both ends of the panels are held together and post-tensioned using a stressing ram at the central stressing pockets during construction. Followed by that, the pockets and the post-tensioning ducts are filled with fast setting concrete to secure the strands and minimize the traffic interruption [12].

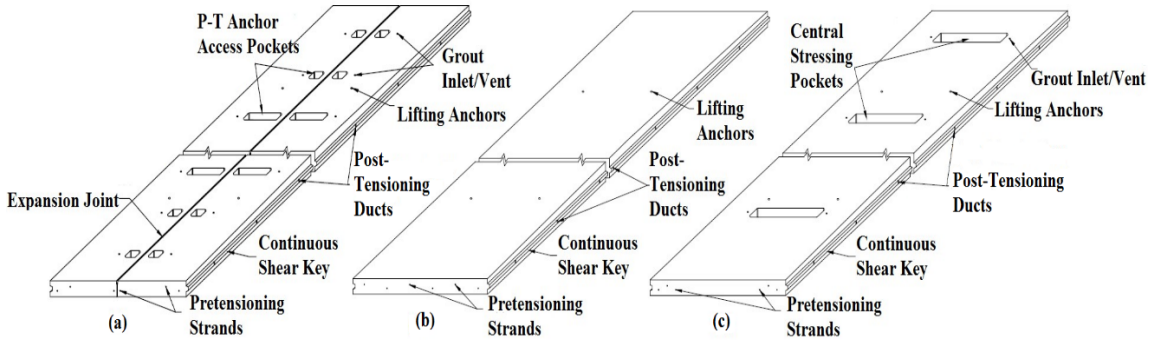

Figure 3-7 (a) Joint panel, (b) base panel and (c) central stressing panel, after [23]

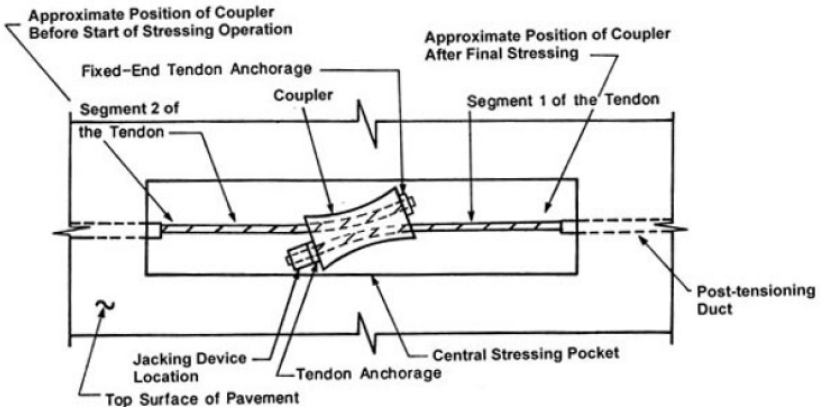

Figure 3-8 Coupler installed at the central stressing pockets [12]

End Hand Hole Stressing System

Another version of a PPCP system shown in Figure 3-9 was used in demonstration projects in Missouri in 2005 [22] and Delaware in 2009 [10].

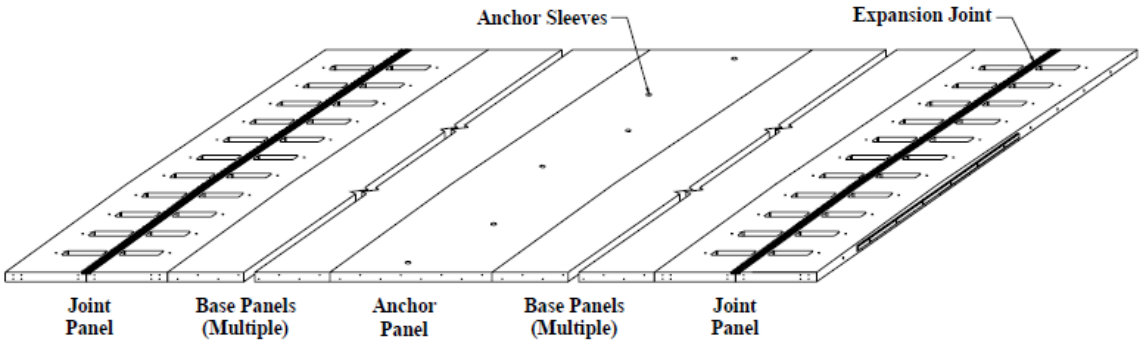

Figure 3-9 PPCP system with end stressing system at surface [22]

Different from the original version, this version of PPCP uses an anchor panel cast with anchor sleeves in place of the central stressing panel. As shown in Figure 3-10, the anchor panels will be anchored into the base and subgrade layer using anchor pins through the anchor sleeves which will be grouted afterwards. Anchoring the anchor panel into the underlying layer will be beneficial to keeping the panels from progressively moving along the direction of traffic and forcing the panels to contract towards or expand outwards from the centerline of the anchor panel, which is helpful to maintain the uniformity of the width of expansion joints.

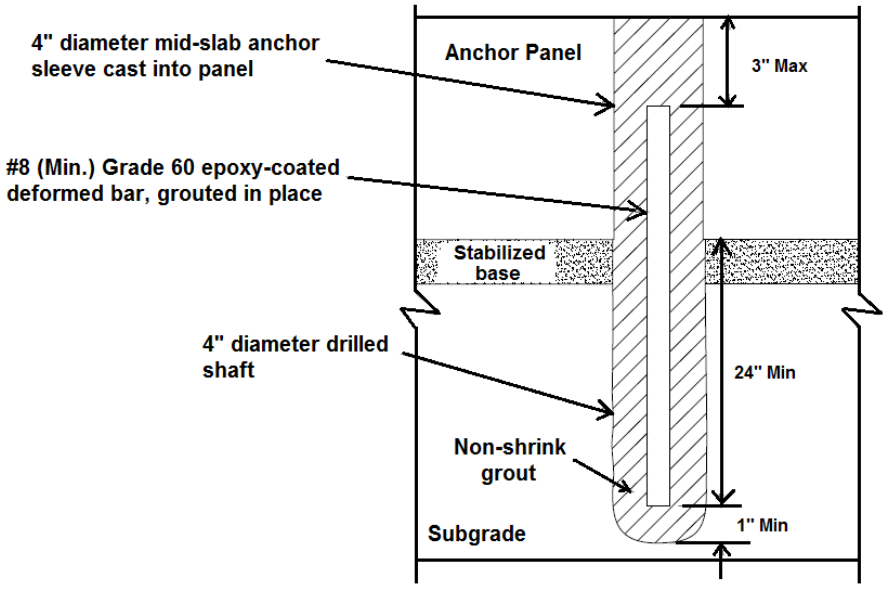

Figure 3-10 Design details of the anchor system in the anchor panels [22]

The modifications to the features at the central stressing panels are the result of the change in the post-tensioning method in later versions of this PPCP system. Instead of applying the central-stressing method at the central stressing panels, the later version uses the concept of end-stressing that allows the post-tensioning to be finished at the joint panels, which essentially eliminates the need for the stressing pockets in the central stressing panels. The size of the stressing pocket in the joint panels is also greatly reduced due to the benefit of using a “banana nose” stressing ram as shown in Figure 3-11. The nose of the special stressing ram is able to reach into the anchorage system and the post-tensioning strands from the outside without having to fit into the access pockets.

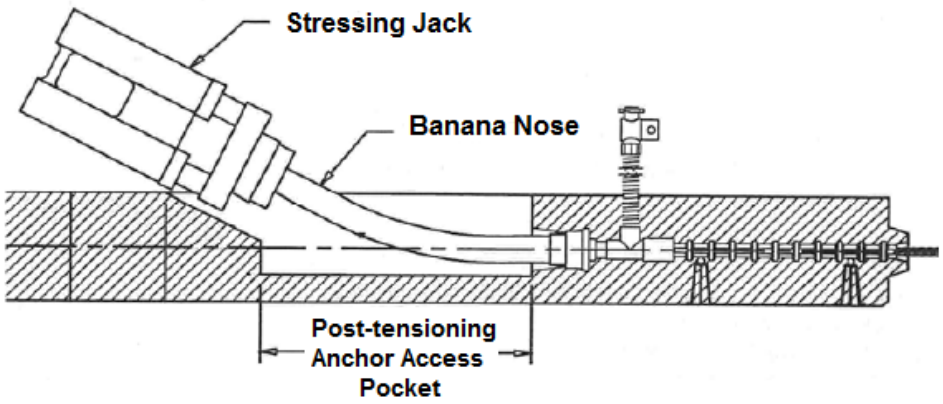

Figure 3-11 Stressing ram with a "banana nose" [22]

End Gap Slab Stressing System

The third version of PPCP was used in a project on I-680 in California in 2011 [10, 24]. Different from the previous two versions, this version, shown in Figure 3-12, consists of base panels, end joint panels and gap panels that form an expansion joint. Besides casting with dowel bars for load transfer, the end joint panels are also designed with anchorage system pockets that permit post-tensioning via the gap at each end, which avoids the need for the surface access pockets. However, the gap that is left for post-tensioning operations between two adjacent end joint panels needs to be filled with an additional panel which can be cast in place.

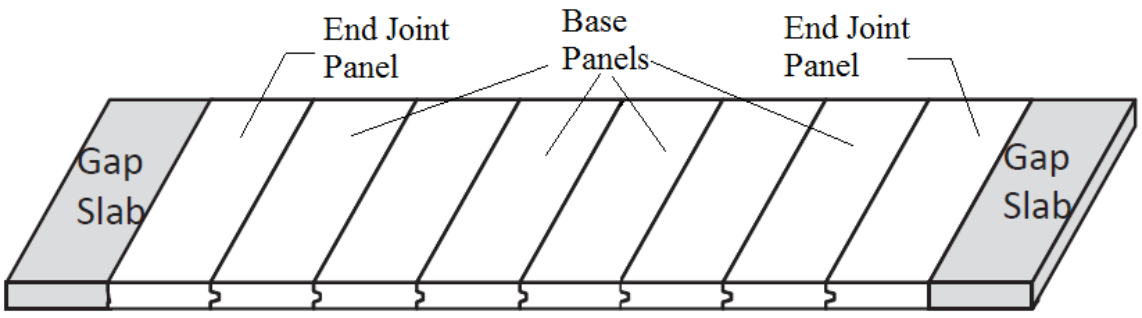

Figure 3-12 PPCP with end gap slab stressing system, after [10]

Benefits of Using Precast BAS

The benefits of using precast panels have been clearly identified as [10-12, 18, 20, 22, 23].

1. The most noticeable advantage is the short closure period. This is due to the fact that concrete panels are precast, which means that their strengths are developed off-site and panels are ready for traffic loading as soon as the panel installation is finished. This benefit allows the construction to be finished overnight or during weekends without encountering peak traffic hours, which greatly reduces the degree of traffic disruption and minimizes the user delay costs;
2. Generally speaking, the quality and performance of precast concrete panels are essentially better than the cast-in-place concrete slabs. This is because the precast panels are made at fabrication facilities in which the concrete mixture can be placed with more flexibility without accounting for curing on the job site; in addition, some other challenges associated with the placement of fresh concrete (e.g. late or shallow joint saw cutting) can be avoided;
3. More consistent quality of concrete can be assured at a fabrication facility particularly with regard to the effects of curing. Concrete pavements that are cured under a field condition can experience excessive curling and warping stresses if the curing quality is underachieved, which may produce more slab cracking and adversely affect the performance of pavements [25, 26]. Curing conditions at fabrication facilities allows the manufacture to better control the curing quality and make concrete panels with negative built-in temperature gradient, which can improve the performance of concrete (up to a certain degree). This type of pavement allows construction to be carried out during very cool or hot seasons which is often restricted in the constructions of CIP concrete pavements;
4. Precast concrete panels provide extensive flexibility and applicability under various conditions, from intermittent distressed area repair to project-level rehabilitations/new constructions for both concrete and asphalt pavements, toll plazas, intersections, freeway ramps tunnels and BASs.

BAS Type Selection

For JPrCP panels, the specific advantages are:

1. A JPrCP system is simpler and easier to design, fabricate and install comparing to a PPCP system, therefore yields lower initial cost;
2. The design method of cast-in-place JPCP which has been proved successful over years, can be directly used to design JPrCP;
3. JPrCP is more versatile, because it can not only be used for continuous repairs or new constructions like PPCP, but also is more suitable for intermittent repairs comparing to PPCP;
4. JPrCP has better applicability for various site conditions, such as horizontal curves, 3-dimensional surfaces, crown line changes, utility-intensive area and heavily-skewed BASs.

For PPCP panels, the specific advantages are related to the fact that the panels are usually pretensioned during fabrication and post-tensioned during construction:

1. By prestressing concrete panels, the pretensioned/post-tensioned tendons are able to provide compressive stress once the tension force is released, which significantly increase the tensile capacity of concrete panels and reduce the occurrence of tensile cracking which improves the performance of the concrete slab; therefore, they usually last longer;
2. Prestressing concrete can also reduce the design thickness of the panels. With the method of prestressing through post-tensioning, the compressive stress induced in the concrete panels essentially allows a thinner slab to behave like a thicker slab resulting in equivalent structural capacity, which can potentially yield lower life-cycle cost;
3. Prestressing provides greater confining pressure to the intermittent (inactive) joints which increases the joint load transfer capability;
4. Prestressing is able to maintain the tightness of pavement joints which is favorable for preventing the base layer erosion in check.

For the purpose of constructing BASs, the PPCP has additional benefits in addition to the aforementioned ones.

1. Prestressing panels provides a BAS with greater structural capacity in spite of partially supported conditions that may occur due to the settlement of the embankment or material loss due to erosion;
2. The intermittent joints of PPCP are effectively sealed by the compressive force exerted by post-tensioning strands which may reduce water infiltration into the supporting layers;
3. Once tied to the integral abutment, the PPCP BAS behaves like a single piece slab which can create a sufficiently large resistant force at the slab-base interface (if designed long enough) that inhibits the load induced movement of an integral bridge abutment structure, thus keeping the joints between the abutment back wall and BAS tight protecting the sealant and preventing infiltration issues.

Selection Criteria

Based on the aforementioned advantages of the two types of PCPs, the criteria for BAS type selection can be established as shown in Table 3-1. The criteria are divided into two categories, direct and secondary criteria. For the direct criteria, meeting either one of them will lead to the selection of the specific BAS type pertinent to that criterion. For instance, if it is an integral abutment bridge, PPCP is automatically selected as the BAS type (considering the additional benefits listed above). The secondary criteria come into play if none of the direct criterion is present and therefore both the types are viable options for building the BAS; in this case, the secondary criteria provide only recommendations (rather than requirements) to the BAS type selection. Note that when both the direct criteria for choosing JPrCP and PPCP are present (e.g. only limited initial funds are available and it is an integral abutment bridge), it is recommended that the direct criteria for JPrCP governs.

Table 3-1 BAS type selection criteria

	JPrCP	**PPCP**

Direct Criteria	Limited initial funds	Integral abutment bridge
	Intermittent repairs only	Higher structure performance standards (less slab cracking)
	Complex road surface geometry	Longer service life requirements
	Heavily-skewed bridge	\
Secondary Criteria	Shorter construction time	Potential lower life cycle cost
	\	Limited space for providing lateral drainage

DESIGN CONSIDERATIONS FOR BRIDGE APPROACH SLAB

To date, a standard procedure for designing BASs has not been established since the state-of-art of the BAS design methodology and design details vary from state to state depending on the experience of the agencies [8, 27-31]. Some state DOTs even use asphalt and non-reinforced concrete for the construction of BASs; however, previous research [32] conducted for the BASs in Wisconsin indicated that 93% of reinforced concrete BASs had good performance ratings whereas only 56% of non-reinforced concrete BASs were rated as fair; 76% of asphalt BASs earned poor ratings. The statistics emphasized the significance of using reinforced concrete to build BASs due to the greater structural rigidity comparing to other pavement types.

Boundary Condition

Although a national standard design procedure is not available, BASs can be designed using any of three methods with different assumptions for the design boundary condition [30, 33, 34]. One method considers that a BAS behaves like a simply supported beam with one end resting on the bridge abutment and the other end supported by the embankment backfill or a sleeper slab assuming no soil support is provided in between the two ends. However, this assumption is rarely valid unless

substantial settlement or erosion occurs in the embankment fill. Design under this assumption is too conservative and often uneconomical.

Another design method is based on the assumption that a BAS is fully supported by embankment backfills and behaves like a normal pavement structure; this design assumption is valid as long as no wetting-induced settlement takes place in the embankment fill or in the foundation soil (which is one reason to pay attention to properly draining runoff water away from the BAS). In other words, this assumption requires a different approach to maintenance after construction by insuring the embankment settlement is well controlled as when a controlled low strength material (CLSM) wedge is used as the embankment backfill material. The positive aspect of this approach is that it provides an economical BAS design (e.g. less reinforcement is needed or a thinner slab will suffice).

A third type of design approach is a variation of the first type and the BAS is assumed to be partially supported due to the soil settlement or erosion. Again, this may be what is usually seen to occur if the type of the backfill material is very erodible and/or compressible and the drainage is not very well taken care of. A BAS design approach of this manner assumes an effective unsupported span length being some portion (e.g. 1/4) of the full length of the BAS to account for the unsupported area underneath the BAS. However, state DOTs have various standards for selecting the effective unsupported span length, which yields different levels of design reliability. In order to account for the varied length and location of the voids, design under this assumption often requires using advanced analysis methods such as a finite difference method [27] or a finite element method [30].

Objective and Methodology

The thickness and the reinforcement ratio (although not the focus of this research) are the two main objectives when designing a BAS. State transportation agencies who adopted the first or the third assumptions regarding the design boundary condition are usually confident designing the reinforcement since the procedure is similar to that of designing the reinforcement for a bridge deck which has a solid

theoretical basis (i.e. flexure theory). However when it comes to selecting/designing the thickness of a BAS which must be completed prior to designing the reinforcement (if the flexure theory is adopted), the method is usually based on empirical equations (which are usually formulated based on one single parameter - the assumed unsupported span length) or local experience which lacks solid theoretical basis. This type of method may be appropriate for designing the thickness of structures like beams and bridge decks (which have simple boundary conditions), or for BASs supported by a highly erodible embankment and a foundation with a high potential for settlement. However, for the BASs built in Oklahoma which actually behave more like concrete pavements (whose behaviors are greatly affected by the repetitive traffic loads and the environment conditions) attributed to the presence of the solid and less erodible CLSM support, the empirical method can be inappropriate and sometimes overly conservative for designing the thickness of a BAS. Therefore, it is appealing to optimize the thickness design for BASs through the application of a more mechanistic approach accounting for the complex boundary conditions. After all, appropriately designing the BAS thickness using a more mechanistic approach will be beneficial to preventing the occurrence of fatigue cracking (identified as one of the major factors causing moisture infiltration which may potentially lead to the erosion and bump issues at BASs [35]) as well as the development of the bump conditions.

Because the BASs, benefited from the uniform support provided by embankment backfills constructed using advanced methods (e.g. the CLSM wedge used in Oklahoma), behave more like concrete pavements, it is recommended that a fully supported condition can be assumed when designing the thickness of BASs. In this regard, the thickness of BASs can be designed using any available mechanistic-empirical procedures which are developed for designing concrete pavements. Applying the mechanistic-empirical design methodology will provide practitioners more confidence when conducting a thickness design and a chance to optimize the design taking into account a variety of influencing factors (e.g. slab dimensions, traffic volume, climate effects and material properties) as opposed to simply applying an empirical equation which is usually formulated solely based on a single influencing parameter (i.e. the assumed unsupported span length).

That being said, the erosion condition that may potentially develop underneath a BAS is not excluded from the mechanistic-empirical design procedure due to the assumption of a fully supported condition. In fact, an advanced procedure that appropriately considers and calculates the potential for erosion damage is incorporated in the thickness design as subsequently elaborated. In addition, it should also be noted that assuming a fully supported condition for the thickness design does not conflict with any assumption made for the reinforcement design. Once the thickness design is complete, it is still valid to apply the flexure theory for designing the reinforcement in a BAS by assuming a partially supported condition, as a means to address the potential for sudden tensile failure that could occur if extreme conditions take place (e.g. a significant loss in the embankment support due to a hurricane).

Considerations for Precast BAS

With respect to the design for BASs made of precast/prestressed slabs, a standard design procedure is unfortunately not available either. To date, the only guidance available related to the design of precast BASs is the *Guideline for Accelerated Bridge Construction Using Precast/Prestressed Concrete Elements Including Guideline Details* published by the PCI Northeast Bridge Technical Committee [36]. This guideline recommends that a precast BAS needs not to be designed with a fully supported condition, but should be designed like a simply supported bridge deck following the latest edition of the American Association of State Highway and Transportation Officials (AASHTO) *Load Resistance Factor Design (LRFD) Bridge Design Specifications* by assuming one end supported by the abutment, the other supported by soil or a sleeper slab and no soil support present in between the two ends. The specification in the PCI published guideline appears to be written by directly adopting the design assumption made for conventional cast-in-place concrete BASs and is more pertinent to the reinforcement design. However, the thickness design was not addressed explicitly and the appropriateness for the direct adoption was not evaluated which raises a few concerns.

First, the design assumption behind the specification of this guideline can be sometimes ultra-conservative for designing the thickness of a BAS as aforementioned, since it might have underestimated or overlooked the efforts made by many state transportation agencies to improve the quality of embankment construction aiming at preventing the occurrence of the unsupported conditions (e.g. Oklahoma DOT uses a CLSM wedge underneath BASs). Second, the design approach warrants some modifications due to the fact that a precast BAS does not always behave the same way as a conventional cast-in-place concrete BAS, especially for a PPCP BAS. In a PPCP system, the entire system (including joint panels, base panels and central stressing panel or panels with an equivalent function) is post-tensioned together such that it acts in some respects like a single slab. The total length of a PPCP BAS, for instance in the Iowa demonstration project, is approximately 77 ft. at the centerline of the pavement [11], which is far longer than the span of a conventional BAS that ranges from 10 – 30 ft. [33]. If the entire length of a PPCP BAS was assumed simply supported following the specifications suggested by PCI, the design would result in an unrealistically high initial cost. In the Iowa PPCP BAS demonstration project, the simply supported boundary condition was not adopted; instead, a partially supported boundary condition was assumed (i.e. an unsupported length of 15 ft. was assumed near the abutment end) as the basis for designing the reinforcement of the PPCP BAS. The thickness of the PPCP BAS was selected as 12 in. by experience without following any detailed design procedures. To address the potential for excessive tensile stress associated with the unsupported span, the flexural strength of the assumed unsupported portion was increased by reducing the spacing of the transverse post-tensioning strands; whereas the remaining portion of the BAS was designed like a pavement, in which wider-spaced transverse post-tensioning strands were used. It appears that the thickness design of the precast BAS could be optimized since a 12 in. thick reinforced concrete pavement (referring to the assumed fully supported portion of the PPCP BAS) could be excessive for this application.

As discussed above, it is recommended that the thickness of BASs can be designed using a mechanistic-empirical procedure developed for the thickness design of concrete pavements; this recommendation also applies to the thickness design for

precast BASs. A report by Tayabji et.al [10] sponsored by the 2nd Strategic Highway Research Program (SHRP) provides the most recent and comprehensive information for the precast concrete pavement (PCP) technology including design guidelines and mechanistic-empirical design procedures for JPrCPs and PPCPs. Therefore, the procedure elaborated in that report is adopted in this research for designing the thickness of precast BASs; in addition, certain modifications and improvements are made to better account for the erosion damage that may take place underneath a BAS (the procedure is subsequently elaborated).

In order to apply the guidelines and design procedures of precast pavements for designing the thickness of precast BASs, the following prerequisites have been identified:

1. A full base support condition must be provided beneath the BAS. This requirement is satisfied due to the fact that Oklahoma DOT has adopted the use of a controlled low strength material (CLSM) as the backfill behind the abutment to support the BAS and which minimizes the potential for settlement of the CLSM as much as possible [37]. However, large settlement that invalidates the assumption could still occur if the foundation underneath the CLSM wedge is very compressible and has not been consolidated sufficiently before the construction of the embankment, or if the foundation is saturated and eroded when the subsurface drainage system does not function properly. Therefore, better drainage design details (addressed in Chapter 5) and certain foundation improvement techniques (e.g. the stone column technique addressed in Chapter 6) are suggested to prevent settlement from occurring beneath the CLSM;
2. Only minimal base erosion is allowed to occur over the design life of the BAS. The design should take into account the potential of base erosion in the design phase following the procedure elaborated in this chapter as well as applying certain techniques and design details (addressed in Chapter 5) to minimize water infiltration into the joints and facilitate better drainage around the BAS in order to minimize the potential for erosion.

The current design procedure for PCPs was developed based on the design procedures for conventional CIP concrete pavements, i.e. the Mechanistic-Empirical Pavement Design Guide (MEPDG) by American Association for State Highway and Transportation Officials (AASHTO) [38] and the associated design software named as the AASHTOWare Pavement ME Design released in 2013 (previously known as the DARWin-ME released in 2011) [39]. The following elaborates the key steps for designing a precast BAS following the procedure established in the study by Tayabji et.al [10] and certain modifications were made by incorporating a method which takes into account the determination of the erosion damage that could potentially develop underneath precast BASs into the design procedure.

DESIGN GUIDELINE FOR JPrCP [10]

The MEPDG design procedure is recommended for the design of JPrCP, considering adjusted design inputs and design criteria subsequently discussed. In addition, other available concrete pavement design procedures may be adopted and modified to design JPrCP following this guideline as well.

The general concrete pavement design procedure of MEPDG can be structured in terms of three major steps, which are summarized as follows [38]:

Step 1. Determine the trial input values for design, including the trial type and thickness of the pavement layers, material properties, joint spacing, dowel bar size and spacing, traffic ESALs and climate;

Step 2. Establish threshold limits in terms of the design performance criteria (i.e. cracking and faulting) and the associated reliability levels for the trial design; if the performance criteria predicted by the software do not meet the design criteria, the trial design inputs need to be modified until the design performance criteria are met;

Step 3. Evaluate design alternatives by utilizing engineering judgment and considering life-cycle cost analysis (LCCA); note that this step is beyond the scope of the MEPDG design procedure, LCCA should be conducted based on project needs.

Modification of Design Inputs

In ***Step 1*** of the design procedure for JPrCP, the following design aspects/inputs must be considered/adjusted to reflect the nature of the precast concrete panels and the conditions of BASs:

1. The default value of the concrete modulus of rupture is 650 psi for CIP concrete panels. For precast concrete panels, this value usually exceeds 700 psi due to the high construction quality; the level of prestress applied to the panels can also affect this input. A concrete modulus of rupture of 750 psi is recommended for JPrCP in this guideline; if the concrete panel is prestressed (i.e. through pretensioning), the effective modulus of rupture would be 850 psi (consider an additional effective pre-stress of 200 psi);
2. The default value of the permanent curl/warp effective temperature difference for CIP JCP is -10˚F. For precast concrete panels, it is expected that much less permanent temperature difference would occur since they are fabricated in manufacturing facilities with better temperature control condition. However, surface drying service to PPCP panels may effectively also lead to some permanent temperature difference. Although an extreme assumption, a -10˚F is still used for the permanent curl/warp effective temperature difference for the design of JPrCP;
3. A 50% of the actual ultimate concrete shrinkage (somewhere between 500 – 800 με (micro-strain)) is recommended because substantial shrinkage of the PPCP panels have already taken place during the storage period prior to being installed on site;
4. The default value of the contact friction time (i.e. the time that takes for the panel to lose contact with the underlying base layer) in the MEPDG is 136-month for CIP JCP. However, because the design procedure described in this chapter will incorporate a separate analysis to account for the erosion taking place at the interface between the concrete panel and the underlying base layer; therefore, the contact friction time value should be set as the design life of the BAS (e.g. if the design life is 40 years, the contact friction time should be 480-month);

5. The contact friction coefficient is considered low since the bottom of the precast panel is not expected to strongly bond with the underlying base layer as in the case of CIP JCP (due to the smooth precast panel bottom surface). Therefore, the “sliding” friction values as shown in Table 3-2 can be used in the design of precast BASs;

Table 3-2 Recommended values of coefficient of friction [40]

Subbase/Base type	Friction Coefficient		
	Low	Mean	High
Fine grained soil	0.5	1.1	2
Sand	0.5	0.8	1
Aggregate	0.5	2.5	4
Lime-stabilized clay	3	4.1	5.3
ATB	2.5	7.5	15
CTB	3.5	8.9	13
Soil cement	6	7.9	23
LCB	3	8.5	20
LCB not cured	> 36 (higher than LCB cured)		

6. The joint spacing of the BASs should be set in the range of 6 – 8 ft. in order to minimize the concrete slab movement at the joints due to thermal effects; this will help to keep the joint width narrow and the joint sealant functional, which is beneficial to preventing moisture infiltration into the joints and the associated erosion possibilities.

Adjustment of Design Criteria

Second, design criteria needs to be established prior to the design of JPrCP. The long-term failure types of JPrCPs are considered similar to the conventional CIP JCPs, including: 1. Structural distress such as a). Slab cracking; 2. Functional distress such as a). Joint faulting; b). Joint spalling; c). Poor ride quality (i.e. transition smoothness) and d). Poor surface texture (in terms of friction and noise). Similarly, the design criteria of JPrCP can be adopted from those of conventional CIP JCP; fortunately, because of the better quality precast concrete panels, the design criteria for slab cracking can be

relaxed. Table 3-3 provides the recommended design criteria for a JPrCP with an initial service life of 40 years.

Table 3-3 Recommended design criteria for JPrCP [10]

	Distress type	Value
Structural distress	Cracked slab (%)	25 - 30
Functional distress	Faulting (in)	0.15
	Spalling (length, severity)	minimal
	Smoothness (IRI) (in/mi)	150 - 180
	Surface texture (friction)	Long lasting (FN>35)
	Surface texture (noise)	Not available, but surface should produce accepted level of pavement-tire noise

DESIGN GUIDELINE FOR PPCP [10]

The design procedure for PPCP consists of the following four key steps:

1. Design the panel thickness of baseline design for conventional CIP JCP;
2. Design the PPCP panel thickness and determine the required effective prestress;
3. Design the prestressing system to achieve the required effective prestress;
4. Design the expansion joint.

The overall design procedure for PPCP can be illustrated as shown in Figure 3-13.

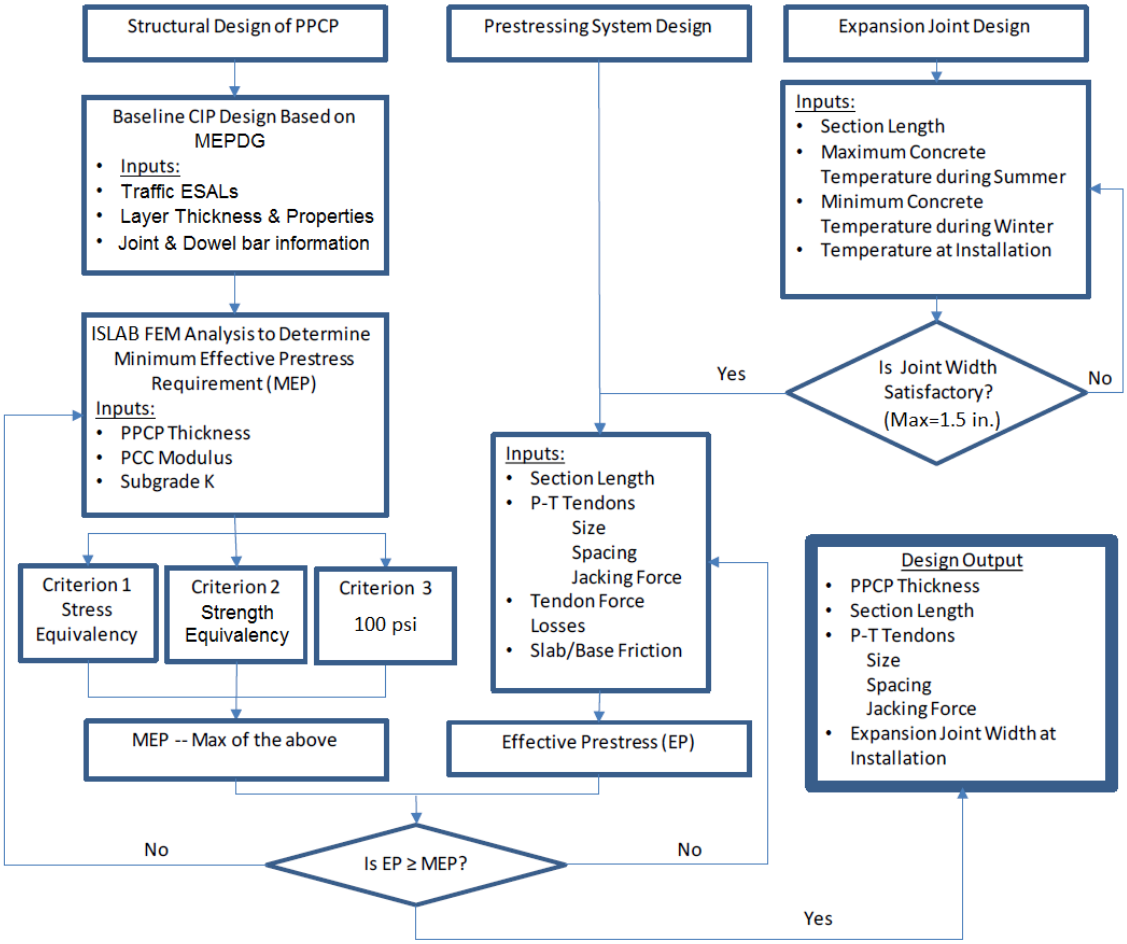

Figure 3-13 Design flow chart for PPCP, after [41]

Step 1. Baseline Panel Thickness Design

Prior to determining the required effective prestress, it is necessary to establish a baseline design for a conventional CIP JCP, which serves as a reference for the design of a PPCP BAS that is considered to have a performance equivalent to or better than the baseline design. The baseline design can be conducted using any mechanistic–empirical pavement design procedure with considering the local environmental condition, traffic loading information, subgrade type, pavement shoulder information and etc. (which are the same inputs for the design of PPCP). This guideline recommends using the MEPDG procedure and the associated design software to establish the baseline design. The design procedure for CIP JCP (i.e. baseline design) is almost

identical to the design procedure for JPrCP which has been elaborated previously, except that there is no need to modify the design inputs and criteria because the baseline design applies the default concrete material properties of the conventional CIP JCP.

Design output

It is expected that the baseline design will output the thicknesses of the JCP slab and the underlying base layers which will be used in the design of PPCP.

Step 2. PPCP Panel Thickness and Required Effective Prestress Design

This section elaborates the design of the PPCP panel thickness and the determination of the effective prestress required to provide the PPCP panel with performance equivalent to or superior than the baseline design. The concept is based on the assumption that, once installed, PPCPs will perform similarly to the CIP prestressed concrete pavements.

It is recommended that the minimum PPCP panel thickness should be at least 8 in. or enough thickness to allow for the inclusion of prestressing and reinforcing hardware (prestressing strand ducts, anchorage system, expansion sleeves for steel dowel and etc.). The thickness of the PPCP panels and the required effective prestress are designed using the criteria described in the following sections.

Criterion 1. Stress equivalency criterion

The stress equivalency criterion shown in Figure 3-14 is sometimes referred to as the thickness equivalency criterion. The main objective of this criterion is to determine the effective prestress that is sufficient to provide a compressive stress such that the critical tensile stress in a thin PPCP system is equivalent to the critical tensile stress in a thick conventional CIP JCP considering the same traffic loading condition. This criterion considers both edge and interior loading conditions to address the design for single-lane and multi-lane PPCP panels, respectively.

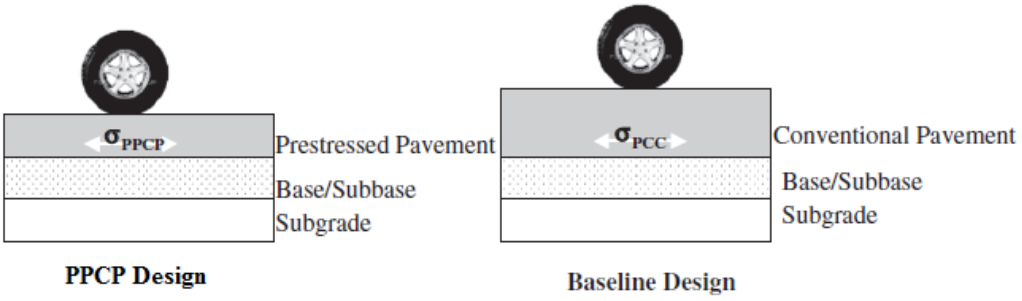

Figure 3-14 Stress equivalency criterion[10]

Depending on the specific design details of a PPCP project, the critical loading position can either be at the edge of a single-lane-wide panel (at the midway of the panel) as shown in Figure 3-15 (a) or at the interior edge of a multi-lane-wide panel (e.g. 2 ft. away from the edge) as shown in Figure 3-15 (b).

For either case, to determine the required effective prestress, the critical tensile stresses at the bottom of both the baseline design panel and the PPCP panel need to be determined using a finite-element based software (e.g. ISLAB2000), which requires design inputs such as loading magnitude, loading position, panel dimension, panel thickness and modulus of subgrade reaction.

Once the tensile stresses at the bottom of the PPCP panel and baseline design panel are determined, the effective prestress is calculated using the following equation:

$$EP_1 = \sigma_{PPCP} - \sigma_{Baseline} \quad (3\text{-}1)$$

where:

EP_1 = required effective prestress for a PPCP system considering stress equivalency criterion;

σ_{PPCP} = tensile stress at the bottom of a PPCP panel due to the design axle loading at the specified loading position (either at the edge for a single-lane-wide panel or at the interior edge for a multi-lane-wide panel); and

$\sigma_{Baseline}$ = tensile stress at the bottom of a baseline design panel due to the design axle loading at the edge loading position.

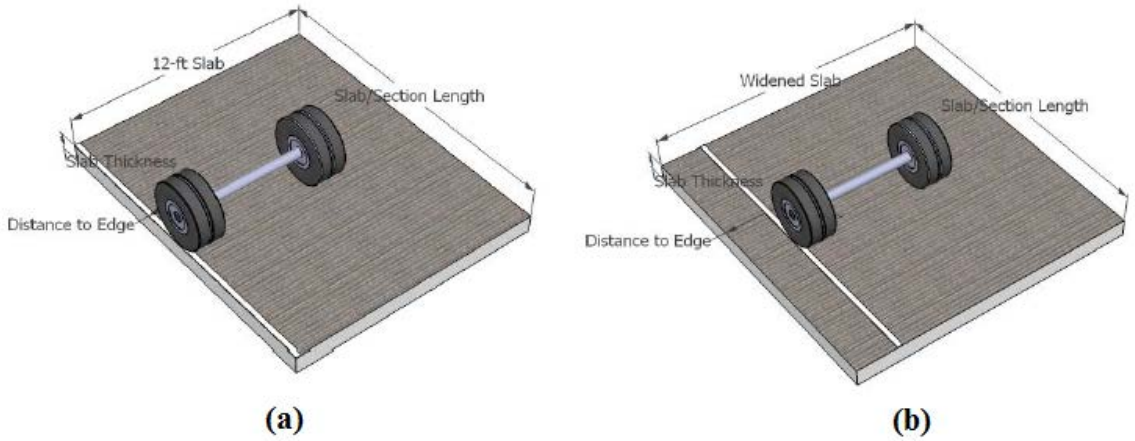

Figure 3-15 Critical loading positions for (a) a single-lane-wide panel and (b) a multi-lane-wide panel [41]

The stress equivalency criterion does have its limitations, because a strong base needs to be assumed such that deflection can be ignored in the analysis as well as the joint load transfer. Therefore, this criterion has limited utility and should only be used to generate a preliminary prestress design of a PPCP system.

Criterion 2. Strength equivalency criterion

The strength equivalency criterion assumes that the effective flexural strength (modulus of rupture) of a PPCP panel is the combination of the flexural strength of the precast concrete panel (usually 650 – 750 psi) plus the effective prestress EP_2 (typically 150 psi). The effective flexural strength can be used in any mechanistic–empirical design method that incorporates concrete flexural strength as an input to design the thickness of a concrete pavement. One example of such mechanistic–empirical design methods is the MEPDG [38].

The main purpose of the strength equivalency criterion is to design a thin PPCP system with an effective flexural strength equivalent to the flexural strength of a thick conventional JCP such that the PPCP system has a performance equivalent to or exceeds the performance criteria of the conventional JCP using the same design inputs. However, the design performance criteria of a PPCP system is somewhat different from

that of a JCP system due to the fact that the distresses do not develop in the same fashion in the two pavement systems.

Design Criteria and Inputs Adjustments

Design criteria need to be first established prior to the design of PPCP using the strength equivalent criterion.

1. Cracking criterion is the only performance criterion considered when designing a PPCP system and it was noted that even the cracking criterion for a PPCP system reaches 100%, it still yields much fewer cracks (20 – 30 cracks/mile. if assuming the length a PPCP system is about 150 – 250 ft.) than a JCP system which usually has a 15% cracking criterion (this leads to about 50 cracks/mile. if a 15-ft spacing is assumed for the JCP slabs). Therefore, the cracking criterion of a JCP system cannot be directly applied to a PPCP system.

   It is recommended to use calibrated fatigue analysis and calibrated cracking criterion (e.g. 50%) to design PPCP BAS. However, the application of this criterion can often lead to unsatisfactory design thickness (less than 8 in.) if the pavement is designed for less than 10 million ESALs traffic load repetitions with good base support. In these cases, the 8 in. minimum PPCP panel thickness requirement will govern the thickness design;
2. Deflection-based joint faulting criterion has not been established for the design of a PPCP system. Although the joint faulting criterion is applicable to a PPCP system, it is mainly set to account for the faulting of short-spaced concrete pavement (i.e. JCP which usually has a 15-ft joint spacing), whereas the expansion joint spacing for a PPCP system generally ranges from 150 – 250 ft.. Therefore, joint faulting criterion is not directly designed for, but is warranted by using a stiff base to reduce the joint deflection under heavy traffic loading as well as by providing sufficient effective level of prestress;
3. Material-related distress is also ignored in the design consideration of a PPCP system due to the fact that precast concrete panels are made in

fabrication facilities where better quality control and curing conditions are warranted comparing to the conventional cast-in-place JCP;

4. For function distress criteria, neither smoothness nor surface texture criterion were considered. However, it is expected that two cycles of diamond grinding may be performed to restore and satisfy the smoothness and texture conditions for a 40-year pavement design life. Note that it is desirable to perform a medium-heavy shot blast (i.e. meeting concrete surface profiles (CSP) 5 or 6) in order to retain adequate skid resistance.

Besides modifying design performance criteria, some of the design inputs also need to be adjusted to account for the difference between PPCP and CIP JCP. This section is similar to the modification of the inputs for design JPrCP:

1. The default value of the concrete modulus of rupture is 650 psi for CIP concrete panels. For PPCP panels, the effective flexural strength is the combination of the flexural strength of the concrete panel (usually 650 – 750 psi) plus the effective prestress (typically 150 psi);
2. A -10˚F is still used for the permanent curl/warp effective temperature difference for the design of PPCP;
3. A 50% of the actual ultimate concrete shrinkage (somewhere between 500 – 800 millionths of an inch) is recommended to design PPCP;
4. The default value of the contact friction time (i.e. the time that takes for the panel to lose contact with the underlying base layer) in the MEPDG is 136-month for CIP JCP. However, because the design procedure described in this chapter will incorporate a separate analysis to account for the erosion taking place at the interface between the concrete panel and the underlying base layer; therefore, the contact friction time value should be set as the design life of the BAS (e.g. if the design life is 40 years, the contact friction time should be 480-month; although it should be noted that the AASHTO LRFD uses a 75-year design life for BASs);
5. The contact friction coefficient is considered low since the bottom of the precast panel is not expected to strongly bond with the underlying base layer

as in the case of CIP JCP (due to the smooth precast panel bottom surface). Therefore, the “sliding” friction values as shown in Table 3-2 can be used in the design of precast BASs.

To design a PPCP following the strength equivalency criterion, the following summarizes the design criteria and inputs that are needed to be specially considered regarding their differences between PPCP and JCP as shown in Table 3-4.

Table 3-4 Design criteria and input adjustments between PPCP and JCP, after Tayabji et.al [10]

	Design Parameters	PPCP	JCP
Distress Criteria	Cracking	50%	15%
	Faulting	not applicable	0.15 in
	Smoothness	not applicable	180 in/mi
Precast Panel Inputs	Thickness	minimum 8 in	minimum 8 in
	Flexural strength	700 psi	650 psi
	Required effective prestress	150 psi	0
	Effective flexural strength	850 psi	650 psi
	ultimate drying shrinkage, 10^{-6} in	300	600

Design output

The design output of this step are the thickness of the PPCP panel and the required effective prestress. Note that the final required effective prestress can be determined based on the following function [41]:

$$EP_{required} = Max(EP_1, EP_2, EP_{\min}) \quad (3\text{-}2)$$

where $EP_{required}$ is the required effective prestress, EP_1 and EP_2 are the effective prestress determined using Criterion 1 and 2, respectively and $EP_{\min}$ is the minimum required effective prestress which has a recommended value of 100 psi [41].

Step 3. Prestressing System Design

The main purpose of designing a prestressing system for a PPCP system is to provide adequate level of effective prestress that satisfies the structural capacity requirement for the effective prestress in a PPCP system. The design procedure consists of:

1. Selecting the size, force and spacing of prestressing tendons;
2. Determining the length of a PPCP section;
3. Determining the total applied prestress based on panel thickness and tendon spacing;
4. Accounting for the prestress loss due to various factors such as the slab-base friction, concrete shrinkage and creep and etc. (these are explained in the following section);
5. Determining the effective prestress by subtracting the prestress loss from the total applied prestress.

Total applied end prestress

The total applied prestress in a PPCP system is achieved by pretensioning (usually in transverse direction) each concrete panel during fabrication and post-tensioning (usually in longitudinal direction but can also be in transverse direction) all the concrete panels within a PPCP system together during installation. In the United States, PPCP demonstration projects mainly used 0.5-in diameter, Grade 270, 7-wire strands for pretensioning and 0.6-in diameter, Grade 270, 7-wire strands for post-tensioning; strands are usually prestressed to 75% - 80% of the ultimate strength. The properties of prestressing strands (tendons) are shown in Table 3-5.

Table 3-5 Properties of prestressing strands [10]

Property	0.5-in Tendon Diameter	0.6-in Tendon Diameter
Tendon cross-sectional area (in^2)	0.153	0.217
75% of ultimate load (lbf)	31000	43000
80% of ultimate load (lbf)	33000	46900
ultimate load (lbf)	41300	58600

The spacing of prestressing strands (ranges from 18 – 36 in. based on previous experience) needs to be designed based on the length a PPCP system which usually ranges from 150 to 250 ft. (the shortest PPCP section was 110 ft. and the longest was 325 ft. from previous experience) such that the effective prestress meets the structural capacity requirement. For the construction of BAS, the length a PPCP section may be reduced and the guidance to determine the length of the BAS is subsequently elaborated. Once the spacing of prestressing strands is selected, the total applied end prestress can be determined based on the designed panel thickness as shown in Table 3-6.

Table 3-6 Total applied end prestress assuming 75% of ultimate load [10]

Panel thickness (in)	End Prestress (psi) for Strand Spacing of			
	18 in	**24 in**	**30 in**	**36 in**
8	299	224	179	149
9	265	199	159	133
10	239	179	143	119
11	217	163	130	109
12	199	149	119	100

The total applied prestress cannot be directly used in the design to meet the required level of prestress in a PPCP system, because it is also necessary to account for the prestress loss to avoid overestimation of the structural capacity of a PPCP system.

Section length determination

The length of the BASs in the U.S. generally ranges from 10 – 40 ft. [28], which are mostly determined based on empirical experience. Based on the past experience, one source that leads to the bump issue at BASs is due to the thermal induced contractive and expansive movements of the integral abutment bridge which force the BAS to also slide back and forth relative to the embankment backfill (elaborated in Chapter 5) if the BAS is tied or anchored to the bridge deck. In order to restrain the BAS from sliding, the BAS should be designed with enough length (i.e. the drag length as shown in Figure 3-16) such that sufficient resisting force can be developed at the slab-base interface to resist the force induced due to the thermal changes in the integral abutment bridge.

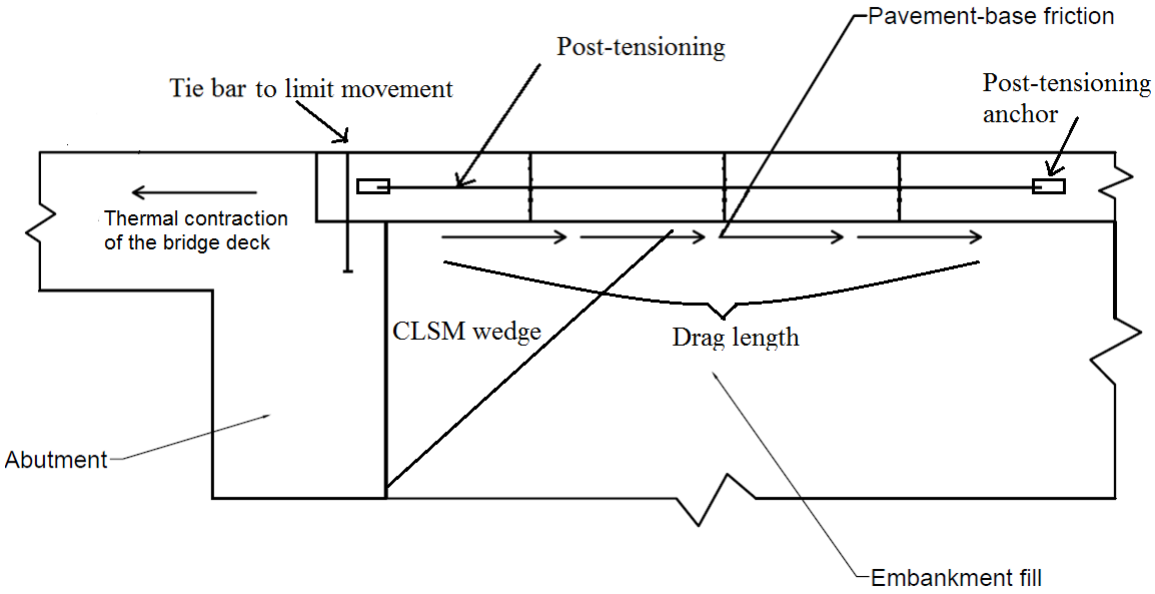

Figure 3-16 Illustration of the drag length concept

A simple analytical model as shown in Figure 3-17 is proposed to facilitate the estimation of the drag length, where Ft is the thermal force induced by the temperature change in the bridge structure, Fs is the resisting force at the slab-base interface. The BAS will not slide if the thermal force does not exceed the resisting force.

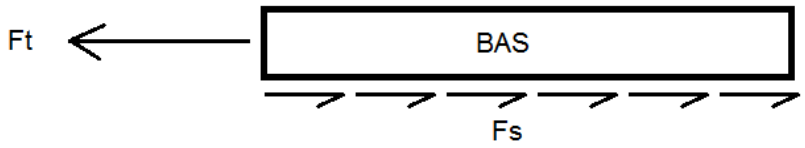

Figure 3-17 A simple analytical model for drag length determination

The thermal force Ft can be calculated by:

$$Ft = A \cdot E_c \cdot \alpha \cdot \Delta T \tag{3-3}$$

where

A = the cross section area of the BAS;

E_c = young's modulus of the concrete;

α = coefficient of thermal expansion of the concrete;

ΔT = the temperature change in the bridge deck.

The slab-base friction Fs can be calculated as:

$$Fs = \mu \cdot N = \mu \cdot \gamma \cdot h \cdot w \cdot L \tag{3-4}$$

where

μ = coefficient of friction at the slab-base interface;

γ = unit weight of concrete;

h = thickness of the BAS;

w = width of the BAS; and

L = the length of the BAS (i.e. the drag length).

Therefore, the length of the BAS can be determined as:

$$Fs \geq Ft \tag{3-5}$$

$$L \geq \frac{E_c \cdot \alpha \cdot \Delta T}{\mu \cdot \gamma} \tag{3-6}$$

where all the parameters are defined previously.

Prestress loss

Prestress losses of a PPCP system must be taken into consideration when designing the prestress provided by post-tensioning strands. It is very important that the

prestress loss is not overlooked, because it determines the level of effective prestress in a PPCP system which is not equivalent to the initial total prestress being applied to the system. Failure to consider prestress losses can result in overestimated structural capacity of a PPCP system. The factors that contribute to the prestress losses include slab-base friction, concrete shrinkage and creep, elastic shortening of concrete (often negligible), relaxation of steel tendons, slippage of steel tendons in anchorage system (extra attention being paid during post-tensioning to avoid this situation) and friction between steel tendons and ducts (often negligible for tangent pavement sections). Among these factors, the slab-base friction contributes the most to the prestress loss and can be relieved by placing a layer of polyethylene sheeting at the slab-base interface or segmentally performing post-tensioning to the system (i.e. reducing the length of post-tensioning). In general, the total prestress loss caused by the aforementioned factors can be as large as 100 psi (0.7 MPa) based on extensive testing results and experience. The following summarized the methods to predict the prestress losses due to the various factors.

Prestress loss due to slab-base friction

Prestress loss caused by the slab-base friction (σ_F) in psi is calculated as:

$$\sigma_F = \frac{\mu\gamma L}{2 \cdot 144} \tag{3-7}$$

where:

μ = coefficient of friction at the slab-base interface, which ranges from 0.5 to 1.5 for a PPCP system depending on the properties of the base layer and the bond breaker placed at the interface; a value of 1.0 is recommended;

γ = unit weight of concrete in pci; and

L = the length of the BAS (or the length of each section being segmentally post-tensioned) in ft.,

The above equation can be simplified assuming a concrete unit weight of about 142 – 146 lb./ft.^{3} as shown in the following:

$$\sigma_F = \frac{\mu L}{2} \tag{3-8}$$

Prestress loss due to concrete shrinkage

The concrete shrinkage induced prestress loss (f_s) is calculated by the following equation:

$$f_s = \varepsilon_s E_S(\frac{A_s}{A_c}) \tag{3-9}$$

where:

E_S = young's modulus of steel tendons;

A_s = area of tendons per unit width of a panel; and

A_c = area of concrete per unit width of a panel.

ε_s = concrete ultimate drying shrinkage strain which can be calculated using the following equations [42]:

$$\varepsilon_s = 1330 - 970y \tag{3-10}$$

$$y = (390z^{-4} + 1)^{-1} \tag{3-11}$$

$$z = 0.381\sqrt{f'_{c28}}[1.25\sqrt{\frac{a}{cm}} + 0.5(\frac{g}{s})^2](\frac{1+s/c}{w/cm})^{1/3} - 12 \tag{3-12}$$

where:

a/cm = aggregate-cementitious material ratio,

g/s = gravel-sand ratio,

s/c = sand-cement ratio,

w/cm = water-cementitious material ratio,

f'_{c28} = compressive strength at 28 days in ksi.

The shrinkage strain of concrete is a material property depending on the type of cement, water-to-cement ratio, type and gradation of aggregates, curing conditions and etc. For a PPCP system, concrete panel shrinkage takes place at both fabrication facilities and after being installed on site. The ultimate drying shrinkage strain for precast should be 50% of the actual value calculated from Equation (3-10).

Prestress loss due to concrete creep

The concrete creep induced prestress loss (f_{cr}) is determined by the following equation:

$$f_{cr} = C_u \frac{E_s}{E_c} f_{pe} (\frac{A_s}{A_c}) \quad (3\text{-}13)$$

where:

C_u = ultimate concrete creep coefficient which depends on many factors such as the properties and gradation of aggregates, cementitious material ratio, curing condition, concrete age at the time of stress and etc.. A value of 2.5 is recommended;

E_c = concrete modulus of elasticity; and

f_{pe} = prestress applied at the end of a PPCP system

Prestress loss due to steel relaxation

The tendon steel relaxation induced prestress loss (f_r) is determined by the following equation:

$$f_r = \rho \cdot f_{pe} \quad (3\text{-}14)$$

where:

ρ = coefficient of steel relaxation, a value of 0.04 is recommended.

Effective prestress

The long-term effective prestress at the midpoint of a PPCP system can be determined using the following equation:

$P_{effective}$=total applied end stress – prestress loss (3-15)

Design output

The main design output of this section is to finalize the design of prestressing system and obtain the effective prestress $P_{effective}$ by applying the following steps:

1. Compare the effective prestress $P_{effective}$ with the required effective prestress $EP_{required}$ determined from the last step. If $P_{effective} \geq EP_{required}$, the design is valid.
2. Otherwise, adjust the length of a PPCP section, tendon spacing and panel thickness until $P_{effective} \geq EP_{required}$

Step 4. Expansion Joint Design

An initial expansion joint width is determined at the beginning, thereafter the variation is estimated considering short-term effects due to post-tensioning and long-term effects due to temperature induced movement, creep and shrinkage of concrete. The joint width variation is determined in this step.

Panel movement calculation

This section provides procedures to determine the movement of PPCP, specifically referring to the movement at the BAS – pavement joint if the BAS is tied to the abutment.

Long-term movement of PPCP

Long term expansion joint is affected by diurnal and seasonal temperature variation as well as creep and shrinkage. The maximum seasonal temperature difference (i.e. the minimum temperature during winter subtracted from the maximum temperature during summer) is greater than the maximum daily temperature difference (i.e. daily temperature change during winter); therefore, it controls the maximum temperature difference when calculating the concrete movement due to temperature difference.

The movement (including both ends) of a PPCP section due to seasonal temperature variation is determined by the following equation:

$$dL_{Temp} = (T_{c\max} - T_{c\min}) \times CTE_c \times L \tag{3-16}$$

where:

$T_{c\max}$ = maximum concrete temperature during summer;

$T_{c\min}$ = minimum concrete temperature during winter;

The movement of a PPCP section due to concrete creep is determined by the following equation:

$$dL_{creep} = C_u \times (P_{end} + P_{effective})/2 \times (1/E_c) \times L \tag{3-17}$$

where:

C_u = ultimate concrete creep coefficient which depends on many factors such as the properties and gradation of aggregates, cementitious material ratio, curing condition, concrete age at the time of stress and etc.. A value of 2.5 is recommended;

P_{end} = prestress applied at the end of a PPCP system;

$P_{effective}$ = effective prestress = applied prestress – prestress loss; and

E_c = concrete modulus of elasticity.

The movement of a PPCP section due to concrete shrinkage ($dL_{shrinkage}$) is determined by the following equation:

$$dL_{shrinkage} = \varepsilon_s \times L \tag{3-18}$$

where:

ε_s = long-term concrete shrinkage strain, which can be calculated using Equation (3-10) – (3-12).

Total movement of PPCP

The total long-term movement (dL_{Total}) of a PPCP section due to the aforementioned considerations is determined as:

$$dL_{Total} = dL_{temp} + dL_{creep} + dL_{shrinkage} \tag{3-19}$$

Where all the terms are previously defined. Note that the traffic load induced movement may also be incorporated into the calculation of the total long-term movement of the BAS depending on the specific site condition, the practitioner may employ a structural engineer to perform that kind of calculation if necessary.

Joint width design

The following provides the calculations for designing joint width, including determining the joint width at placement and the maximum joint width.

Join width at placement

The design of initial joint width takes into consideration that a minimum joint width needs to be maintained during the first summer after construction based on the amount

of concrete expansion due to the temperature difference between the maximum summer temperature and the concrete temperature at the time of installation. The initial joint width ($JW_{Install}$) is determined by:

$$JW_{Install} = dL_{\min} + (T_{\max} - T_{Install}) \times CTE_C \times L \quad (3\text{-}20)$$

where:

$dL_{\min}$ = minimum joint width to be maintained during the first summer, assumed to be 0.25 in.;

$T_{\max}$ = maximum temperature during summer, assumed to be 120˚F;

$T_{Install}$ = concrete temperature at the time of PPCP system installation;

CTE_C = concrete coefficient of thermal expansion; and

L = total length of a PPCP system.

Long-term minimum joint width

The long-term minimum joint width ($JW_{(L-T)\min}$) takes into account the effects of concrete creep and shrinkage and can be calculated using the following equation:

$$JW_{(L-T)\min} = dL_{\min} + dL_{creep} + dL_{shrinkage} \quad (3\text{-}21)$$

Where all the terms are previously defined.

Maximum joint width

The maximum joint width ($JW_{\max}$) can be determined as:

$$JW_{\max} = dL_{\min} + dL_{total} \quad (3\text{-}22)$$

Where all the terms are previously defined.

Joint sealant design

Joint sealant systems should be designed to accommodate for the changes in the expansion joint width which fluctuates from the minimum joint width during the first summer (assumed to be 0.25 in.) to the maximum joint width (the summation of the minimum joint width during the first summer plus the total long-term movement of a PPCP system). However, the long-term maximum joint width should not be greater than 1.5 in. in order to maintain a certain level of joint load transfer capacity. Underestimation

of minimum joint width can result in early failure of joint sealant; overestimation of maximum joint width can lead to overdesign of the joint sealing system.

Design output

The main design outputs of this step which are useful for the design of PPCP are:

1. The joint width at the time of installation;
2. Long-term minimum joint width;
3. Maximum joint width.

The main criterion is that the maximum joint width should not exceed 1.5 in, otherwise load transfer capability of expansion joints cannot be well achieved. If the criterion is not met, the design inputs need to be modified, such as changing the length of the PPCP section and the level of total applied prestress and re-design starting from ***"Step 3. Prestressing System Design"***.

DESIGN CONSIDERATION OF EROSION

It has been well-recognized that erosion underneath the BAS is one of the main issues leading to the bump-at-the-end-of-the-bridge as aforementioned. In the past, engineers have made various attempts with respect to different construction methods in order to minimize erosion, such as optimizing the surface or subsurface drainage system to better drain runoff water away from the BAS, tying the BAS to the bridge deck slab to minimize water infiltration at the BAS – bridge deck joint and using controlled low strength material (CLSM) which provides a less erodible and low compressible base support. However, erosion was not well considered when designing BASs since most BASs were designed by simply assuming that a certain length of the slab near the abutment end is totally unsupported (e.g. up to 50% – 60% length of the BAS) due to the erosion (sometimes referred to as the "washout" [11, 43]) or settlement occurred in the base layer underneath the BAS – bridge deck joint as shown in Figure 3-18 (a). The recent field investigations conducted for the distressed BASs in Oklahoma indicated that this assumption may not truly reflect what was observed in the field, since in many

cases the erosion and bump issues had occurred at the BAS – pavement joints as opposed to at the BAS – bridge deck joint. Therefore, it is necessary to modify the design assumption in order to match the field observations.

In this research, the erosion condition mainly refers to the debonding condition (i.e. loss of base support) taken place underneath the BAS – pavement joint (near the edges of the slabs) based on the aforementioned field observations (elaborated in Chapter 2) as well as some previous field investigations [7-9]. As shown in Figure 3-18 (b), a more realistic scheme is used to characterize the development of erosion damage under this configuration, where the amount of erosion damage gradually increases from zero (representing a fully bonded condition at the slab-base interface) to the maximum level (representing a fully unbonded condition) at a certain stage of the design life. In this regard, a fully supported condition (only in the early years of the design life) may be assumed for designing the thickness of a BAS similar as is done in the design of a concrete pavement. That being said, in order to adequately design the thickness of a BAS that is able to provide satisfying performance throughout the entire design life, it is also necessary to take into account the erosion damage that gradually takes place at the slab-base interface underneath the BAS – pavement joint (on the basis that the potentials for large foundation and/or embankment settlements have been well addressed by applying improved construction techniques).

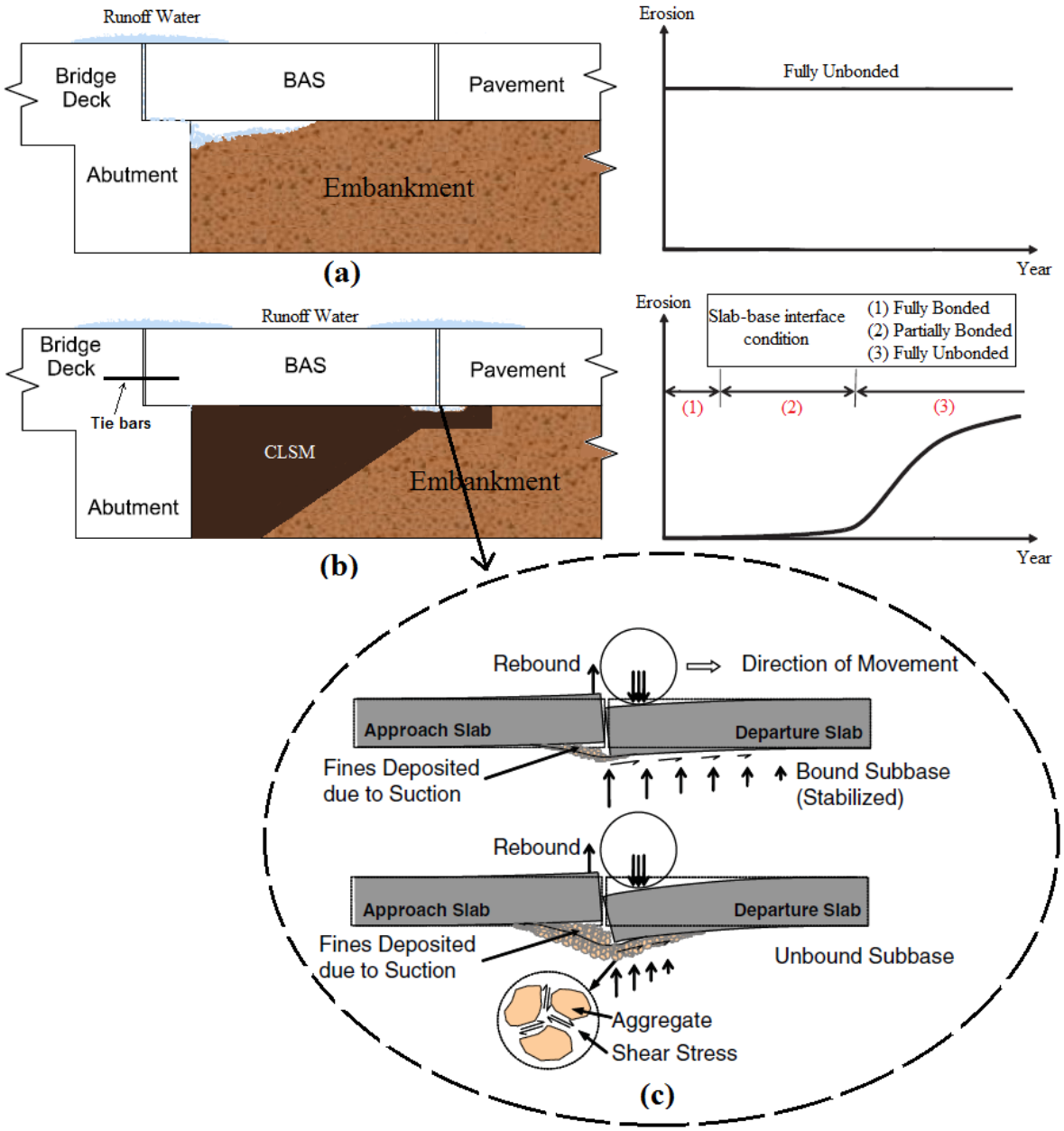

Figure 3-18 Representation of the erosion under BASs (a) the extreme condition that previous research addressed (b) the condition that this research addressed (c) the mechanism for the shear induced erosion [44]

It is pointed out that the mechanism leading to the erosion underneath the BAS – pavement joint is very similar to that causing the erosion underneath a faulted concrete pavement joint as shown in Figure 3-18 (c). The mechanism for this type of erosion is mainly related to the deflection-induced shear action at the slab-base interface caused

by repetitive traffic loads. The quantification of the erosion damage can be very difficult, because many factors are involved in the development of the distress, including the thickness of the slab, the load transfer capability at this joint, the amount of repetitive traffic, the climate condition, the base type and strength, the drainage and sealant conditions, and etc.. In this regards, a procedure which can adequately take into account these factors for quantifying the erosion damage underneath the BAS would be of great interest for the design of BASs. Efforts have been underway to develop a method for quantifying erosion damage which is briefly introduced in the following section.

As elaborated in the previous sections, the design for either the JPrCP or PPCP has been largely relying on the use of MEPDG and the associated computer software which represent the state-of-the-practice of the concrete pavement design methodology. In the MEPDG, base erosion is addressed through modeling the faulting distress and the prediction of the erosion is more related to the thickness and the stiffness of the base layers [38]. However, in addition to the base layer thickness and stiffness, field observations also indicated that other factors such as the slab-base interfacial friction and adhesion conditions which were not explicitly addressed in the current MEPDG design procedure could also affect the erosion condition and the performance of concrete pavement [45]. Essentially, the MEPDG only assumes either unbonded or fully bonded condition for the slab-base interface, which exhibits limitations to adequately consider a broad range of partially bonded conditions as shown in Figure 3-18 (b) that exists due to various levels of interfacial friction and adhesion.

The following elaborates a procedure to better model the base erosion condition for the design of BAS using precast concrete technologies. Essentially, this section provides a means to adjust the concrete slab thickness (the design output of MEPDG based on assuming either fully bonded or unbonded condition) to an “erosion-based slab thickness” (subsequently defined) taking into account the degree of slab-base bonding as a function of the erosion damage. More importantly, the procedure facilitates an adjustment of the design reliability to quantitatively reflect the effects of various construction practices or design details on the performance of the BAS with respect to

their utilities in preventing erosion damage underneath the BAS and maintaining a satisfactory structural capacity to minimize the bump issue.

The step-by-step procedure can be briefly described as:

1. Calculate the percent of erosion damage $\%E$ taken place at the end of the design period based on the following five key parameters:
    - the average daily traffic (ADT) at the start year;
    - the percent of trucks;
    - the number of wet days (min 0.1” rain);
    - the thickness of the concrete slab; and
    - the cohesion of the base.

    In order to better help practitioners perform the design calculations, the complex design procedure has been simplified and an Excel spreadsheet was developed to facilitate the determination of the erosion damage based on the five key parameters (each has 3 levels of magnitude to help with interpolating the results).

2. Determine the “erosion-based slab thickness” based on the erosion damage which dictates the degree of bonding at the slab-base interface;
3. Adjusting the reliability for the specific performance criterion (i.e. cracking or faulting) based on the “erosion-based slab thickness”.

The procedure described in this section can be incorporated into the design procedures for both JPrCP and PPCP as described in the previous sections:

- For JPrCP: this procedure should be used after the MEPDG outputs the predicted performance (i.e. cracking or faulting) that satisfy the initial design performance criteria at the design reliability using the trial design inputs (i.e. concrete and base layer thicknesses and etc.);
- For PPCP: this procedure should be used following the ***Criterion 2*** in ***Step 2*** of the “***Design guideline for PPCP***” once MEPDG outputs the predicted

performance that satisfy the initial design performance criteria at the design reliability using the trial design inputs.

Step 1. Determination of Erosion Damage

In a recently research by Bari and Zollinger [46], the effects of both the interfacial friction and adhesion are incorporated into the design of concrete pavement regarding the erosion damage. The erosion damage model can be expressed as:

$$\%E = \frac{f_i}{f_0} = e^{-(\frac{\rho}{D_i})^{\alpha}} \quad (3\text{-}23)$$

where $\%E$ is the percent of erosion, f_i is the level of faulting for load cycle i, f_0 is the ultimate faulting, ρ and α are the local calibration coefficients and D_i is the accumulated erosion damage for load cycle i along the slab-base interface which is defined as:

$$D_i = \sum \frac{N}{N_f} \times (\%\, Wet\ Days) \quad (3\text{-}24)$$

where N is the accumulated traffic ESALs (subsequently elaborated), N_f is the ultimate load to failure (subsequently elaborated) and $\%\, Wet\ Days$ is the number of days in which the precipitation is greater than 0.5 inch over the number of days in one year (365 days) for the project area (data can be retrieved from the LTPP database). For better understanding the details of this model, the readers can refer to the previous publications [40, 44, 46, 47].

Determination of accumulated traffic

In the analysis of erosion damage, the daily traffic are converted to an erosion-based equivalency in terms of the equivalent single axle load (ESAL) which is expressed as [48]:

$$ESAL_y = \sum_{i=1}^{17}(\sum_{j=1}^{10}(\sum_{k=1}^{4}(\sum_{i=1}^{39}((F_{l+1} - F_l) \cdot ELF_l) \cdot AT_k \cdot EAF_k) \cdot VC_j) \cdot TTC_i) \cdot EWF \cdot LDF \cdot \frac{ADT}{2} \cdot 365 \quad (3\text{-}25)$$

$$N = \sum_1^y ESAL_y \cdot GF \quad (3\text{-}26)$$

where $ESAL_y$ is the erosion-equivalent single axle load per year, F_l is the load group fraction (%), ELF_l is the equivalent load factor per load group l, AT_k is the percent of truck for axle type k, EAF_k is the equivalent axle factor for axle type k, VC_j is the percent of vehicle class, TTC_i is the percent of truck traffic class, EWF is the equivalent wander factor, LDF is the lane distribution factor, ADT is the average daily traffic, y is the number of design years and GF is the traffic growth factor. The expressions of the traffic equivalency factors are shown in Table 3-7.

Table 3-7 Traffic equivalency factors for erosion-based damage

Equivalency Factors	Erosion-based Damage		
	Single Axle	Tandem Axle	Tridem Axle
ELF	$\frac{DE_{load}}{DE_{18kip\,load}}$	$\frac{DE_{load}}{DE_{36kip\,load}}$	$\frac{DE_{load}}{DE_{54kip\,load}}$
EAF	1	$\frac{DE_{TA}}{DE_{SA}}$	$\frac{DE_{TR}}{DE_{SA}}$
EWF	$e^{0.049} - \frac{25.207}{\ell} - \frac{0.775}{\ln(LTE)}$		

As shown in Table 3-7, the determination of ELF and EAF relies on the calculation of the ratio of deformation energy with respect to load types or axle types. The deformation energy is expressed as:

$$DE = \frac{(P\delta^*)^2}{2k\ell^2}\left[1 - \left(\frac{LTE}{100}\right)^2\right] \quad (3\text{-}27)$$

Single: $$\ln\delta^* = -0.5567 + 0.09478\sqrt{\ell} - 0.007026LTE \quad (3\text{-}28)$$

Tandem: $$\ln\delta^* = -2.1498 + 0.0447\sqrt{\ell}\ln(\ell) - 0.01138\sqrt{LTE}\ln(LTE) \quad (3\text{-}29)$$

Tridem: $$\ln\delta^* = -2.7649 + 0.1203\frac{\ell}{\ln(\ell)} - 0.009765\sqrt{LTE}\ln(LTE) \quad (3\text{-}30)$$

where DE is the deformation energy (lb/in), P is the traffic load (lb), δ^* is the dimensionless deflection (in), k is the modulus of sublayer reaction (psi/in) and ℓ is the radius of relative stiffness (in).

The equivalent wander factor EWF is determined as:

$$\ln(EWF) = a + \frac{b}{\ell} + \frac{c}{\ln(LTE)} \tag{3-31}$$

$$a = 0.000213D^2 - 0.000538D - 0.010777 \tag{3-32}$$

$$b = -0.192D^2 - 0.9865D - 1.2295 \tag{3-33}$$

$$c = 0.0000846D^2 - 0.0199152D + 0.0247361 \tag{3-34}$$

where D is the mean distance from the edge of a slab to the outside of dual tires illustrated as shown in Figure 3-19 and other parameters are defined previously.

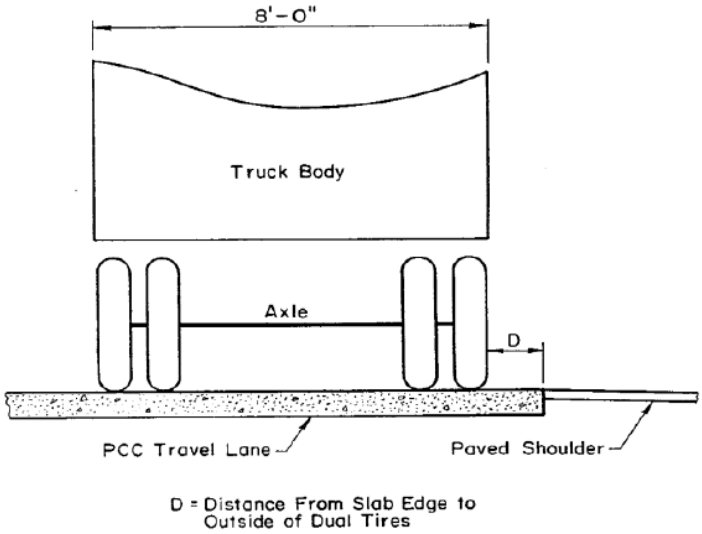

Figure 3-19 Illustration of the mean distance from the slab edge to the outside of dual tires [49]

Determination of ultimate load

The ultimate load to failure can be expressed as:

$$N_f = 10^{k_1 + k_2 . r_i} \tag{3-35}$$

where k_1 and k_2 are erosion damage calibration coefficients and r_i is defined as:

$$r_i = \frac{\tau_i}{f_e} \tag{3-36}$$

where τ_i is the interfacial shear stress and f_e is the effective interfacial frictional resistance or bond strength.

The interfacial shear stress τ_i can be determined as:

$$\tau_i = (1 - x_b)\frac{\partial \delta_{L_i}}{\partial X}\frac{E_{sb}}{2(1+\nu)}\left(\frac{1}{\psi}\right) \tag{3-37}$$

$$\frac{\partial \delta_{L_i}}{\partial X} = \frac{\partial \delta^*_{L_i}}{\partial x}\frac{P}{L^* k \ell^2} \tag{3-38}$$

$$\frac{\partial \delta^*_{L_i}}{\partial x} = b + 2dx + fy \tag{3-39}$$

where x_b is the degree of bonding (subsequently discussed), E_{sb} is the elastic modulus of the base, ν is the Poisson's ratio of the base, ψ is the load transfer factor $= a_i(LTE) + 1$, $a_i = 0.03$ for edge loading and $a_i = 0.07$ for corner loading, LTE is the load transfer efficiency (%), $\partial \delta_{L_i}$ is the loaded deflection $= \frac{\delta^*_{L_i} P}{k\ell^2}$, $\delta^*_{L_i}$ is the dimensionless deflection $= a_d + b_d\sqrt{\ell} + c_d\sqrt{y_L}\ln(y_L)$, $a_d = 0.004920832$, $b_d = 0.16834363$, $c_d = -0.025856456$, y_L is the load position in transverse direction of the slab, P is the load, ℓ is the radius of relative stiffness, k is the modulus of subgrade reaction, X is the distance from the point of loading along the diagonal from the corner or from the edge of the slab, $L^* = \frac{W}{2}$ for slab edge and $L^* = \frac{W}{\sqrt{2}}$ for slab corner, W is the slab width, $x = \frac{X}{L^*}$, b, d and f are edge or corner coefficients, $y = \frac{h_c}{\ell}$ and h_c is the slab thickness.

The effective interfacial frictional resistance or bond strength f_e can be defined as:

$$f_e = \sigma_v \mu_e = (1 - \%E)[f_\tau + f_F] = (1 - \%E)\left[\frac{K_I^2}{2Lf_t} + f_F\right] \tag{3-40}$$

where σ_v is the normal stress$= k_{eff}\Delta$, k_{eff} is the effective modulus of subgrade reaction, Δ is the loaded deflection, μ_e is the effective coefficient of friction, $\%E$ is the percent of erosion damage, f_τ is the cohesive shear strength of the weakest layer adjoining the interface$= \sigma_v\mu_\tau$, μ_τ is the cohesive coefficient of friction, K_I is the fracture toughness of the weakest layer adjoining the slab interface, L is the lift-off distance, f_t is the tensile strength of the slab-base interface $= \frac{f_\tau}{\tan\varphi}$, f_F is the frictional interfacial shear strength $= \sigma_v \tan\phi = \sigma_v\mu_F$, μ_F is the interfacial coefficient of sliding friction$= \tan\phi$, ϕ is

the internal angle of friction of the base material. Substituting the equations for f_e, f_τ and f_F in Equation (3-40), the effective coefficient of friction μ_e can be expressed as:

$$\mu_e = (1 - \%E)[\mu_\tau + \mu_F] \quad (3\text{-}41)$$

where all the parameters are defined previously.

Sensitivity analysis and model calibration

A sensitivity analysis of the model is shown in Figure 3-20 (a) as a means to demonstrate the effects of the influencing factors on the development of erosion damage. Comparisons are made for the $\%E$ at the end of the design life (e.g. 35 years) and it is found that the accumulated $\%E$ generally increases with the increase of ADT, number of wet days and flow factor (where 20% represents a lower rate of moisture infiltration and therefore a better sealant condition), and decreases with the increase of BAS thickness, the cohesion of the base material and the base permeability. Again, the figure reinforces the importance of limiting moisture infiltration at slab joints (e.g. using a better quality joint sealing material) and providing sufficient drainage (e.g. using a more drainable base) with respect to minimizing erosion damage.

Using the measured LTPP faulting data of one pavement section located in Texas, the erosion model was calibrated in terms of the faulting level (which is easily calculated using Equation (3-23) once $\%E$ is predicted) as shown in Figure 3-20 (b). The calibrated erosion model was then used to predict the faulting levels for some other pavement sections (in Texas) with similar base layer properties and the predictions were compared with the measured LTPP faulting data. Figure 3-20 (c) indicates that a good fit is achieved between the predicted and measured faulting. The result of a paired two-sample t-test also indicates that the predicted faulting match well with the observed data (a null hypothesis of zero mean difference between them is accepted) [47].

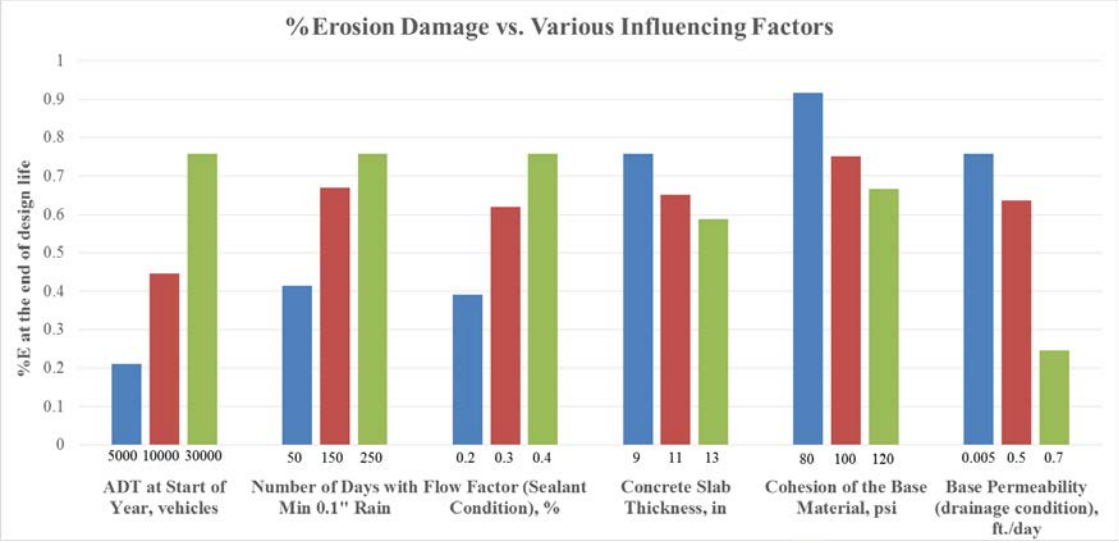

(a)

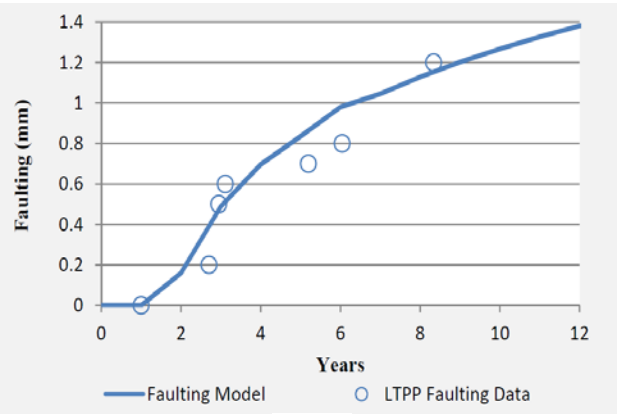

(b)

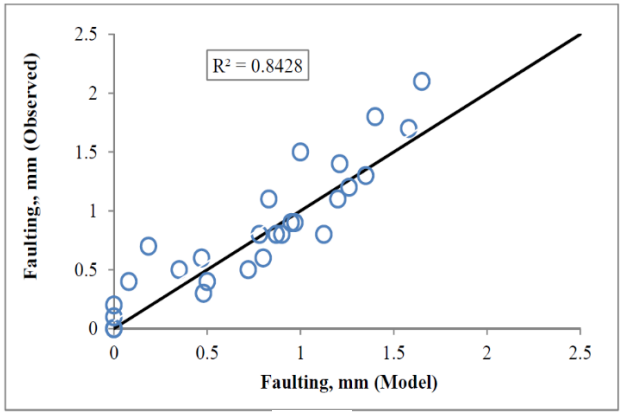

(c)

Figure 3-20 (a) Sensitivity analysis of the erosion model; (b) calibration of the model using field data [47]; (c) predicted versus measured faulting of LTPP Data [47]

Design output

The output of this step is the percent of erosion $\%E$ and the effective coefficient of friction μ_e.

Step 2. Determination of Erosion-Based Slab Thickness

This section proposes a new concept named as the “erosion-based slab thickness” and a procedure for calculating this parameter as shown in Figure 3-21. The necessary information for calculating the “erosion-based slab thickness” is:

- The thicknesses of the concrete slab and base layers (outputs of the MEPDG design);
- The predicted percent of erosion $\%E$ and the effective coefficient of friction μ_e at the slab-base interface at the end of the design life (outputs of the erosion analysis).

Before elaborating the concept of the “erosion-based slab thickness”, the “effective slab thickness” concept must be introduced to facilitate the understanding of the newly proposed concept. The “effective slab thickness” concept comes from a theoretically rigorous approach proposed by Ioannides et al. [50] focusing on transforming a multi-layered system (i.e. the concrete slab layer and the base layer) to a single composite layer system (i.e. a single effective concrete slab – base layer resting on a subgrade). In other words, the base layer is considered as a portion of the concrete slab (after transformation) rather than a portion of the subgrade. In this regard, the “effective slab thickness” refers to an effective equivalent slab thickness taking into account the structural capacities of both the concrete layer and the base layer (which can vary due to the presence of voiding as a result of base erosion).

It is considered that, due to the erosion of the supporting soil layer underneath the BAS, the slab-base interface condition varies from one extreme condition (fully bonded) to another (totally unbonded/separated) depending on the associated traffic repetitions and accumulated damage; a transitional state which exists between the two extreme conditions is referred to as the partially bonded condition and the degree of bonding is influenced by the erosion damage occurred at the slab-base interface. In general, the higher the degree of the bonding, the greater the effective slab thickness.

The thickness of the unbonded slab thickness, fully bonded slab thickness and their relation to the partially-bonded slab thickness are expressed in the following equations [50]:

$$h_{e-u} = [(h_1^3 + \frac{E_2}{E_1} h_2^3)]^{1/3} \quad (3\text{-}42)$$

$$h_{e-b} = \{h_1^3 + \frac{E_2}{E_1} h_2^3 + 12[\begin{matrix}(x_{na} - \frac{h_1}{2})^2 h_1 \\ + \frac{E_2}{E_1}(h_1 - x_{na} + \frac{h_2}{2})^2 h_2\end{matrix}]\}^{1/3} \quad (3\text{-}43)$$

$$x_{na} = \frac{E_1 h_1 \frac{h_1}{2} + E_2 h_2 (h_1 + \frac{h_2}{2})}{E_1 h_1 + E_2 h_2} \quad (3\text{-}44)$$

$$h_{e-p} = (1 - x_b) h_{e-u} + (x_b) h_{e-b} \quad (3\text{-}45)$$

Where h_{e-u} is the effective thickness of the unbonded concrete layer, h_{e-b} is the effective thickness of the bonded concrete layer, h_{e-p} is the effective thickness of the partially-bonded concrete layer, E_1, E_2 are the elastic modulus of layer 1 and 2 (psi), h_1, h_2 are the thicknesses of layer 1 and 2 (layer 1 represents the concrete slab layer and layer 2 is the base layer). Rearranging Equation (3-45), the degree of bonding x_b can be expressed as:

$$x_b = \frac{h_{e-p} - h_{e-u}}{h_{e-b} - h_{e-u}} \quad (3\text{-}46)$$

The degree of bonding x_b has been related to the effective coefficient of friction μ_e at the slab-base interface based on the analysis of FWD data and can be expressed as:

$$x_b = e^{-(\frac{A}{\mu_e})^B} \quad (3\text{-}47)$$

where $A = e^{[\frac{(3-0.2\mu_e)}{B}]}$, $B = -0.039[\ln(\mu_e)]^2$ and μ_e is the effective coefficient of friction at the slab-base interface which is correlated to the erosion damage and can be calculated as shown in Equation (3-41). Generally, the greater the percentage of the erosion damage, the smaller the effective coefficient of friction which results in less degree of bonding and thinner effective slab thickness. In this way, the practitioner should be able to determine a partially-bonded concrete layer thickness h_{e-p} taking into account the erosion damage taken place at the slab-base interface. Once the degree of bonding x_b is determined, the practitioners are able to calculate the partially-bonded concrete layer thickness h_{e-p} using Equation (3-45).

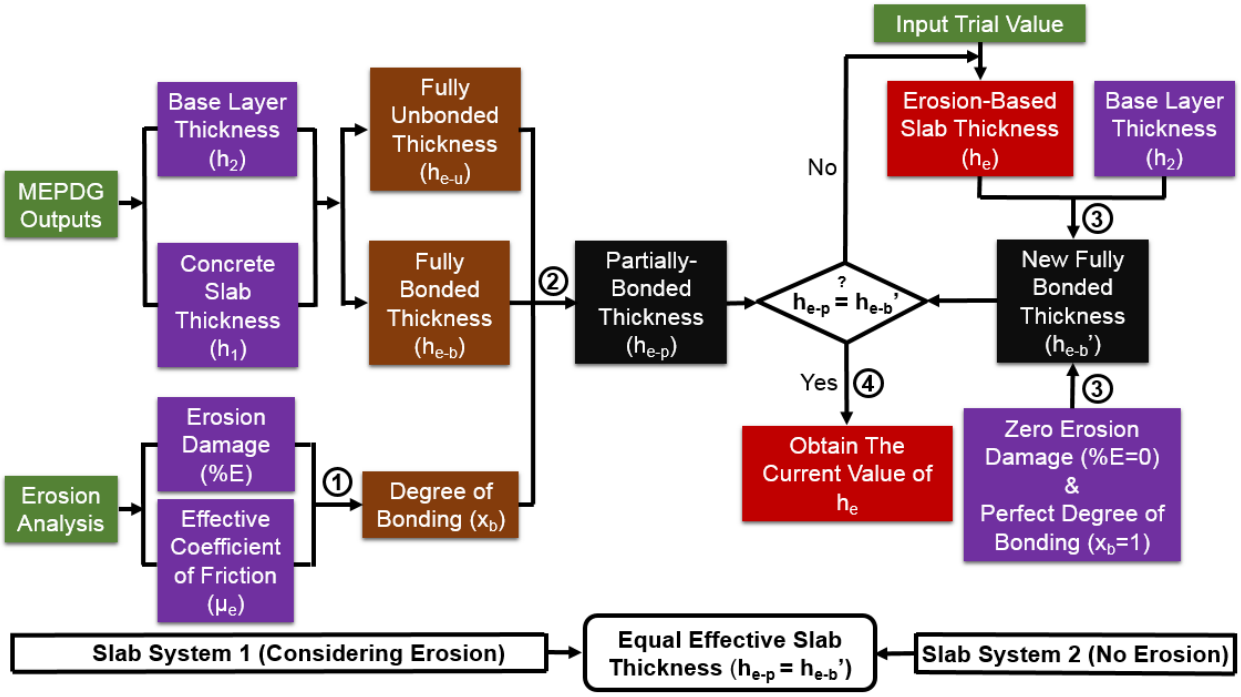

Figure 3-21 Flowchart of the procedure to determine the erosion-based slab thickness

The "erosion-based slab thickness" concept is proposed as a means to reflect how much the erosion damage could affect the structural capacity of a concrete layer only; in other words, in the single composite layer system (i.e. the effective concrete slab – base layer), the reduction in the structural capacity of the base layer due to the erosion damage is replaced by the reduction in the structural capacity of the concrete slab layer only (by reducing the concrete slab thickness and assuming zero erosion damage). The calculated erosion-based slab thickness (usually a reduced concrete slab thickness comparing to the initial design thickness) will help to facilitate determining the effect of the erosion damage on the reliability of the BAS performance, which is subsequently elaborated (see section "***Step 3. Reliability Analysis***").

As shown in Figure 3-21, where a step-by-step procedure is provided, the determination of the erosion-based slab thickness h_e relies on assuming two slab systems, which are slab system 1 (considering realistic erosion) and slab system 2 (considering zero erosion); the effective slab thicknesses of the two systems are equal to each other.

As marked in Figure 3-21, the procedure to calculate the erosion-based slab thickness h_e can be described as:

1. Calculate the degree of bonding x_b based on the percent of erosion $\%E$ and the effective coefficient of friction μ_e at the end of the BAS design life obtained by performing the erosion analysis (i.e. see section "***Step 1. Determination of Erosion Damage***");
2. Calculate the partially-bonded slab thickness h_{e-p} based on the degree of bonding x_b, fully bonded thickness h_{e-b} and fully unbonded thickness h_{e-u}; in slab system 1 where the percent of erosion $\%E$ is taken into account, the effective slab thickness is equivalent to the partially-bonded slab thickness h_{e-p};
3. In slab system 2, assume that erosion damage does not exist (i.e. $\%E = 0$) and the degree of bonding is perfect (i.e. $x_b = 1$); calculate the new fully bonded thickness $h_{e-b}{}'$; the effective slab thickness for slab system 2 is equivalent to the new fully bonded thickness $h_{e-b}{}'$;
4. The erosion-based slab thickness h_e of slab system 2 can be determined through trial and error such that the effective thicknesses of the two systems are equal to each other (i.e. $h_{e-p} = h_{e-b}{}'$).

To facilitate the calculation process, an Excel spreadsheet is made to help the practitioner determine the unknown which is the erosion-based slab thickness h_e. The inputs needed for this section are the original concrete layer and base layer thicknesses h_1, h_2, the material properties (modulus of subgrade reaction and young's modulus of each layer) and the effective coefficient of friction μ_e.

Design output

The output of this step is the erosion-based slab thickness h_e.

Step 3. Reliability Analysis

A reliability analysis is included in this procedure to account for the erosion-related factors leading to the variability in the performance of BASs. In general, increasing the design thicknesses of the pavement layers (or other design parameters such as base layer shear strength) can result in a greater level of design reliability. In this procedure, due to the consideration of erosion, a reduced concrete slab thickness (i.e. the erosion-based slab thickness) would result in a reduction in the design reliability. The following provides a method to obtain the final reliability due to the consideration of erosion and a way to adjust the BAS thickness in order to achieve the initial design reliability.

In the MEPDG, the deviations of all the factors leading to the slab cracking are assumed to be normally distributed. The predicted cracking for the design reliability can be determined as:

$$CK_p = CK_{50} + STD_{CK} \cdot Z_P \quad (3\text{-}48)$$

where CK_p is the predicted cracking at the design reliability level P (e.g. 95%), CK_{50} is the predicted cracking based on the mean inputs (corresponding to the 50% reliability), STD_{CK} is the standard deviation of the cracking and Z_P is the standardized normal deviate corresponding to the design reliability level P (one-tailed normal distribution). MEPDG finalizes the design process once the predicted cracking at the design reliability level reaches the design cracking criterion.

A design chart such as the one shown in Figure 3-22 can be developed in order to perform the reliability adjustment. The hollow points on the curves shown in Figure 3-22 represent the percentages of predicted slab cracking (a design output of MEPDG) which are obtained by varying the design concrete slab thickness (e.g. 9.5 – 10 in) at various levels of cracking reliability (e.g. 50 – 95 %) while holding the values of other design inputs constant.

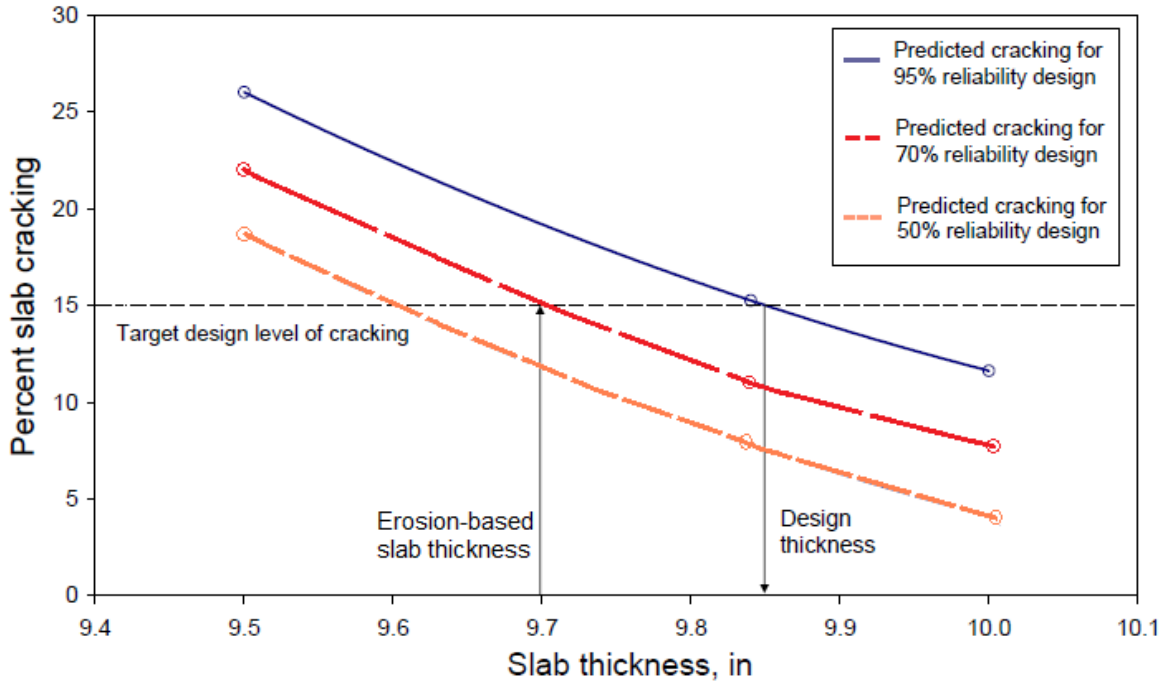

Figure 3-22 Reliability adjustment chart, modified based on [38]

Once the chart is developed, the level of reliability can be easily determined for the erosion-based slab thickness following the procedure shown in Figure 3-23. Two design purposes can be achieved by using the flowchart; Purpose 1 is to determine the final reliability due to the consideration of the erosion damage; Purpose 2 is to determine a new concrete slab thickness in order to meet the original design reliability as a result of considering erosion in the design.

For instance, if the cracking reliability is designed at 95% initially, the MEPDG outputs a design concrete slab thickness of 9.85 inches meeting the cracking criterion (e.g. 15%) as shown in Figure 3-23. Due to the consideration of the erosion damage taken place at the slab-base interface, the design thickness of the concrete slab is reduced from 9.85 to 9.7 inches (the determination of the erosion-based slab thickness was previously elaborated); accordingly, in order to meet the 15% cracking criterion (i.e. Purpose 1 as shown in Figure 3-23), the final design reliability has to be reduced from 95% to 70% (by using the reliability adjustment chart shown in Figure 3-22). The 25% reduction in the design cracking reliability is attributed to the consideration of the erosion damage.

The practitioners should also determine whether the adjusted level of reliability (i.e. 70%) will meet their design expectations; if it is determined that meeting the original 95% cracking reliability is a necessity, then a new concrete slab thickness h_1' (e.g. 10 inches) should be determined (Purpose 2 shown in Figure 3-23) through trial and error such that the new erosion-based slab thickness h_e' (e.g. 9.85 inches) is equivalent to the original design concrete slab thickness h_1 (since it is known that the original 95% reliability for 15% slab cracking can be achieved at this thickness).

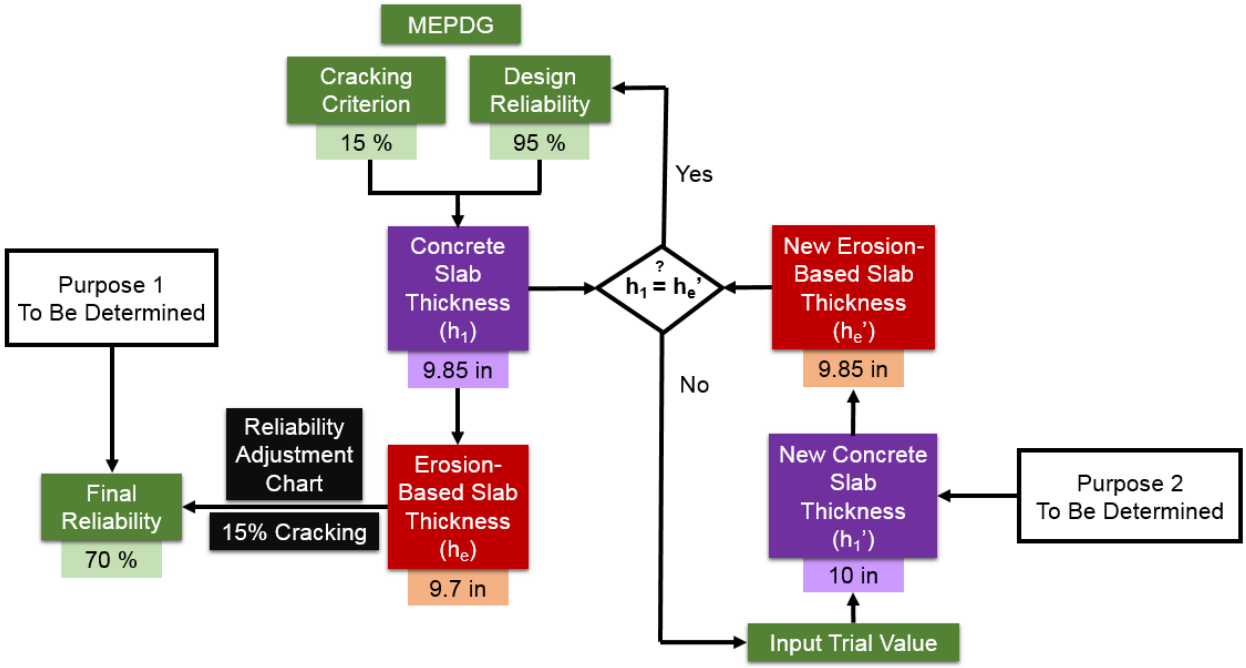

Figure 3-23 Flowchart of the reliability analysis

Design output

As shown in Figure 3-23, the design output for this section can be either one of the following two options depending on the purpose of the practitioner:

1. If the purpose is to evaluate the reduction in the design reliability due to the consideration of erosion damage, an adjusted design reliability (i.e. 70%) which is determined using the erosion-based slab thickness will be the output;
2. If the purpose is to achieve the original design reliability (i.e. 95%) and performance criterion (15% slab cracking), then selecting a new design of

concrete slab thickness (h_1') to meet the 95% design reliability will be the design purpose.

DESIGN EXAMPLE FOR JPrCP

The design for JPrCP should follow the design procedure of MEPDG; however, the design inputs and design criteria need to be adjusted to reflect the effects of using precast concrete panels. The detailed user guideline for the MEPDG design software is not further elaborated since that exceeds the scope of this guideline. The following shows an example of using the MEPDG procedure to design JPrCP [10].

Step 1

1. Determine the input values as if designing a conventional CIP JCP;
2. Select trial design inputs (i.e. the thicknesses of precast concrete panel and underlying base layers) for JPrCP;
3. Modify the following inputs for designing a JPrCP;
    - Use a concrete modulus of rupture of 750 psi;
    - Use 50% of the actual ultimate concrete drying shrinkage (needs to be calculated using Equation (3-10)). For simplicity, this example assumes the actual ultimate concrete drying shrinkage to be 600 με.

The design inputs of the example are shown in Table 3-8.

Table 3-8 Design inputs of the design example of JPrCP [10]

Site Conditions	Project site	Oklahoma City
	Traffic ESALs, million	100
Design limits	Design reliability	90%
	Design service life, years	40
Design Criteria	Cracking, %	25
	Faulting, in	0.15
	Smoothness (IRI), in/mi	180
Precast Concrete Panel	Thickness, in	10
	Lane width, ft	12
	Transverse joint spacing, ft	6
	Dowel bar diameter, in	1.5
	Dowel bar spacing, in	12
	Modulus of rupture at 28-day, psi	750

	Concrete CTE, millionth in/in/˚F	5.5
	Permanent curl/warp effective temperature difference, ˚F	-10
	Concrete ultimate drying shrinkage, 10^{-6} in	300
Permeable Granular Base	Thickness, in	6
	Modulus of elasticity, psi	15000
	Base erodibility index	erosion resistant (level 3)
	Loss of full friction, months	480
Subgrade	Modulus of elasticity, psi	8000

Step 2

1. Establish design criteria for JPrCP. The recommended design criteria for a JPrCP with an initial service life of 40 years is shown in Table 3-9;
2. Perform trial design analysis using the design inputs and criteria of JPrCP with the assistance of MEPDG design software;
3. The design software predicts the following performance results as shown in Table 3-9, where all the design criteria are met; therefore, the design alternative is valid. Otherwise, the inputs in ***Step 1*** (i.e. the thickness of precast concrete panel or underlying base layers) need to be modified to meet the design criteria.

Table 3-9 Comparison of design criteria and predicted performance prediction results of JPrCP and CIP JCP, after [10]

	Design criteria	**Predicted performance criteria**
Cracking, %	25	5.3
Faulting, in	0.15	0.12
Smoothness (IRI), in/mi	180	159

Step 3

1. Evaluate design alternatives by utilizing engineering judgment and considering life-cycle cost analysis. Table 3-10 provides a comparison of various design alternatives with respect to the thickness design of JPrCP at different levels of traffic and base support conditions by using the same design criteria shown in Table 3-9.

Table 3-10 Comparison of design alternatives for JPrCP at various levels of traffic and base support conditions, after [10]

	Traffic level (estimated million ESALs)	Thickness of JPrCP, in
Poor Support Condition (base modulus = 15 ksi)	50	8.5
	100	9.5
	200	11.5
Granular Base (base modulus = 30 ksi)	50	8.5
	100	9.5
	200	11.5
Cement-treated Base (base modulus = 2000 ksi)	50	8.5
	100	9.5
	200	11.5

DESIGN EXAMPLE FOR PPCP

The overall design procedure for PPCP can be illustrated as shown in Figure 3-13. The design procedure for PPCP relies on the use of finite-element based software (e.g. ISLAB2000) and MEPDG design software, however, the detailed user guidelines for using the software are not further elaborated since that exceeds the scope of this guideline. The following shows a step-by-step example for designing PPCP [10].

Step 1

Provides a baseline design for a conventional CIP JCP following the MEPDG design procedure using default design inputs (concrete modulus of rupture of 650 psi and actual ultimate concrete shrinkage) and criteria; output a design alternative that meets the design criteria;

Design output

1. Thickness of concrete slab = 13 in.;
2. Thickness of base = 6 in.;

Step 2

The determination of PPCP panel thickness and required effective prestress can be achieved by applying two different criteria, the stress equivalent criterion and the strength equivalent criterion.

Criterion 1. Stress equivalent criterion

1. Perform tensile stresses analysis by using a finite-element based software (e.g. ISLAB2000) and obtain the relations between slab thickness and critical tensile stress at the bottom of the slab at different loading conditions, which requires the following inputs:
    a. Loading magnitude: Single axel load – 9000 lb.;
    b. Loading position: edge condition (single lane) or interior condition (multiple lanes);

c. Width of the concrete slab: 12 ft. for edge condition and 14 ft. for interior condition;
d. Length of the concrete slab: 6 ft.
e. Thickness of the concrete slab: 8 – 14 in.
f. Modulus of subgrade reaction – assuming 300 and 50 pci.

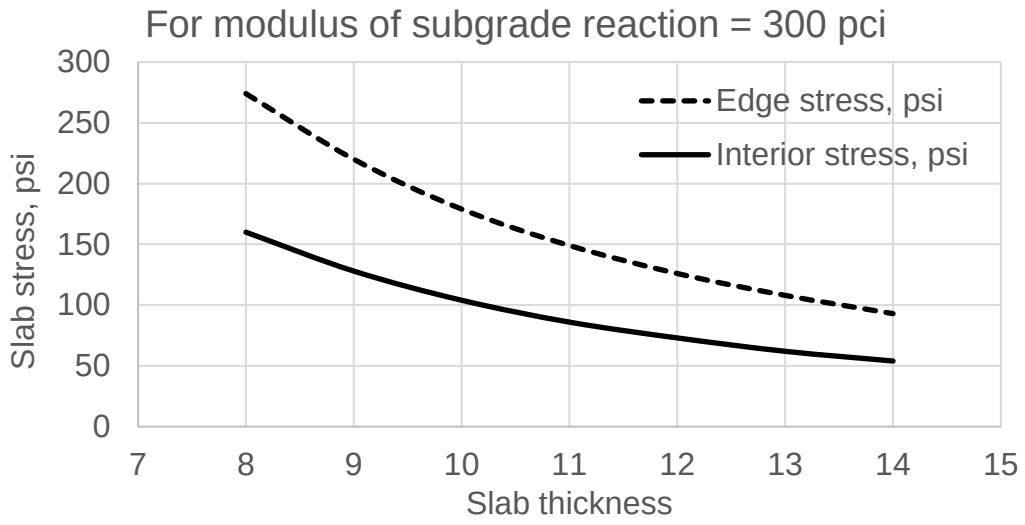

(a)

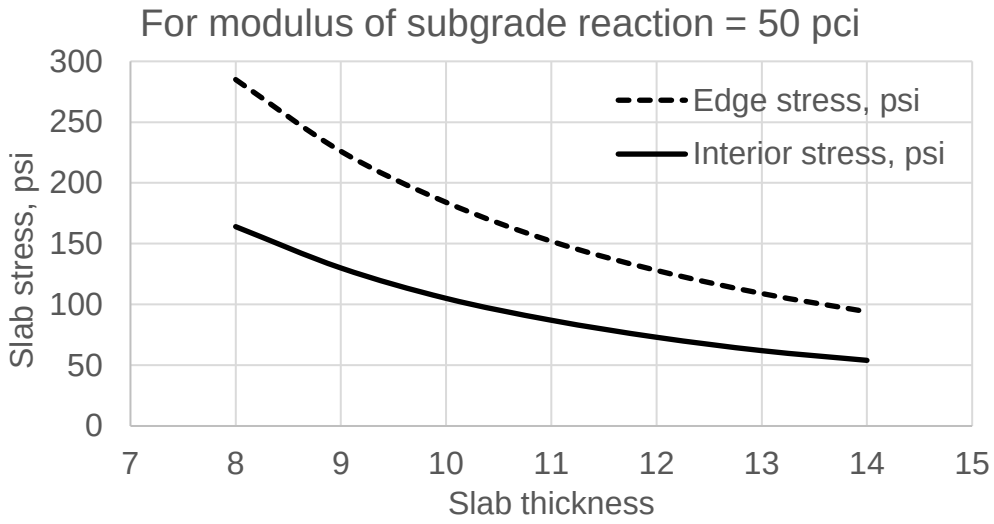

(b)

Figure 3-24 Example plots of critical panel tensile stress as a function of slab thickness for different loading conditions and modulus of subgrade reaction

2. Perform trial thickness design for PPCP and determine and the required effective prestress based on critical tensile stresses dictated by slab thickness and loading condition (single-lane PPCP – edge loading condition; multi-lane PPCP- interior loading condition).

   An example of using Figure 3-24 to design PPCP panel thickness and determine the required effective prestress is given below considering an interior loading condition and a modulus of subgrade reaction of 50 pci [10].

   a. The thickness of baseline design is determined to be 13 in. from the baseline design, the edge stress at the midway of the panel is 105 psi based on Figure 3-24;
   b. Trial design input for PPCP panel thickness is assumed to be 8 in., the interior stress is 160 psi from Figure 3-24;
   c. The required effective prestress $EP_1 = 160 - 105 = 55psi$.

Criterion 2. Strength equivalency criterion

The design for PPCP thickness and required effective prestress using the strength equivalency criterion should follow the design procedure of MEPDG or any mechanistic–empirical design method that incorporates concrete flexural strength as an input. The following shows an example of using the MEPDG procedure to design PPCP [1].

Step A

1. Determine the input values as if designing a conventional CIP JCP;
2. Select trial design inputs for PPCP;
   a. Thickness of PPCP panels: 8 in;
   b. Thickness of base layer: 6 in.;
   c. Required effective prestress: $EP_2 = 150psi$.
3. Modify the following inputs for designing a PPCP;
   a. Use a concrete modulus of rupture of 850 psi (original modulus of rupture of 700 psi + required effective prestress of 150 psi);
   b. Use 50% of the actual ultimate concrete shrinkage.

The design inputs of the example are shown Table 3-11.

Table 3-11 Design inputs of the design example of PPCP [10]

Site Conditions	Project site	Oklahoma City
	Traffic ESALs, million	100
Design limits	Design reliability	90%
	Design service life, years	40
Design Criteria	Cracking, %	50
	Faulting, in	not applicable
	Smoothness (IRI), in/mi	not applicable
Precast Concrete Panel	Thickness, in	8
	Lane width, ft	12
	Transverse joint spacing, ft	6
	Dowel bar diameter, in	1.5
	Dowel bar spacing, in	12
	Modulus of rupture at 28-day, psi	850
	Concrete CTE, millionth in/in/˚F	5.5
	Permanent curl/warp effective temperature difference, ˚F	-10
	Concrete ultimate drying shrinkage, 10^{-6} in	300
Permeable Granular Base	Thickness, in	6
	Modulus of elasticity, psi	15000
	Base erodibility index	erosion resistant (level 3)
	Loss of full friction, months	480
Subgrade	Modulus of elasticity, psi	8000

Step B

1. Establish design criteria for PPCP. The recommended design criteria for a PPCP with an initial service life of 40 years are shown in Table 3-12;
2. Perform trial design analysis using the design inputs and criteria shown in Table 3-11 with the assistance of MEPDG design software;
3. The design software predicts the following performance results as shown in Table 3-12, where all the design criteria are met; therefore, the design is valid. Otherwise, the inputs in ***Step A*** (e.g. the thickness of the precast

concrete panel or the underlying base layer or the level of required prestress) need to be modified to meet the design criteria.

Table 3-12 Comparison of design criteria and predicted performance prediction results of PPCP and CIP JCP, after [10]

	Design criteria	Predicted performance criteria
Cracking, %	50	19.4
Faulting, in	not applicable	not applicable
Smoothness (IRI), in/mi	not applicable	59

Step C

1. Evaluate design alternatives by utilizing engineering judgment and considering life-cycle cost analysis. Table 3-13 provides a comparison of various design alternatives with respect to the thickness design of PPCP at different levels of traffic and base support conditions by using the same design criteria shown in Table 3-12.

Table 3-13 Comparison of design alternatives for PPCP at various levels of traffic and base support conditions, after [10]

	Traffic level (estimated million ESALs)	Thickness of PPCP, in
Poor Support Condition (base modulus = 15 ksi)	50	<8
	100	<8
	200	8
Granular Base (base modulus = 30 ksi)	50	<8
	100	<8
	200	8
Cement-treated Base (base modulus = 2000 ksi)	50	<8
	100	<8
	200	8

Initial design output

1. The initial design of PPCP panel thickness = 8 in.;

2. The initial predicted slab cracking = 19.4%;
3. The initial design of base thickness = 6 in.;
4. The initial required effective prestress is determined as the maximum value of the results determined based on the two criteria and a minimum requirement of the effective prestress (i.e. 100 psi):

$$EP_{required} = Max(EP_1, EP_2, EP_{\min}) = Max(55,150,100) = 150psi$$

Erosion Consideration

Step A. Determination of erosion damage

1. Summarize the five key parameters:
   - the ADT at the start year = 10000;
   - the percent of trucks = 60%;
   - the number of wet days (min 0.1" rain) = 50;
   - the initial design of PPCP panel thickness = 8 in.;
   - the cohesion of the base = 5 psi.
2. Refer to the database in the tab "**Percent of erosion**" of the given Excel spreadsheet and obtain the erosion damage at the end of the design life (40 years) based on the five key parameters (interpolations may be conducted if necessary): $\%E = 0.491\%$;
3. In addition, the effective coefficient of friction μ_e of the slab-base interface at the end of the design life can be readily obtained in the Excel spreadsheet: $\mu_e = 2.121$.

Step B. Determination of Erosion-Based Slab Thickness

Refer to the procedure shown in Figure 3-21 and the procedure elaborated in the tab "**Erosion-based slab thickness**" of the given Excel spreadsheet:

1. Based on Equation (3-42) – Equation (3-47), using the Excel spreadsheet, the partially-bonded concrete layer thickness can be determined as: $h_{e-p} = 8.03\ in.$;

2. Assuming $\%E = 0$ for the new slab system and fully bonded condition for the slab-base interface;
3. Through trial and error, it is determined that the erosion-based slab thickness $h_e = 7.53\ in.$, such that $h_{e-b}{}' = h_{e-p} = 8.03\ in.$.

Step C. Reliability Analysis

Refer to the procedure shown in Figure 3-23:

Purpose 1 – Determine the final design reliability due to erosion

1. Develop a design chart to perform reliability adjustment as shown in Figure 3-25, which can be done by using the MEPGD software. The hollow points on the curves in Figure 3-25 are design outputs (i.e. predicted percent slab cracking) of MEPDG obtained by varying the slab thickness (e.g. 6.5 – 10 in.) and design reliability (e.g. 70% - 95%) while holding other inputs constant (i.e. the inputs shown in Table 3-11);
2. As shown in Table 3-12, for the initial design of concrete slab thickness = 8 in., the predicted slab cracking is 19.4%. As shown in Figure 3-25, in order to achieve the 19.4% slab cracking for the erosion-based slab thickness $h_e = 7.53\ in.$, the final design reliability has to drop from 90% to about 82%. The 8% reduction in the design reliability reflects how much the erosion damage affects the BAS performance with respect to slab cracking.

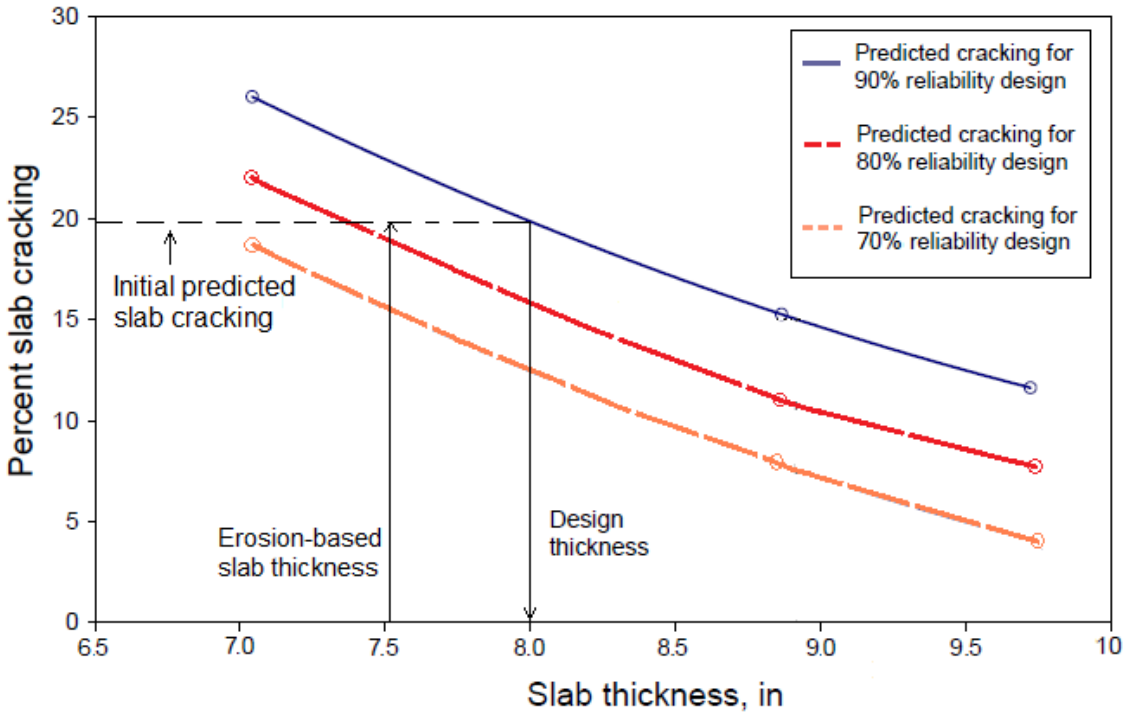

Figure 3-25 Reliability adjustment chart

Purpose 2 – Determine a new concrete slab thickness

1. If the purpose is to achieve the initial design reliability (i.e. 90%), the practitioner should determine a new concrete slab thickness $h_1{}'$ such that the new erosion-based slab thickness $h_e{}'$ is equivalent to the initial design of concrete slab thickness $h_1 = 8\ in.$; this requires a few steps of trial and error by applying the procedures described in the previous steps (i.e. applying ***Step A*** to determine the erosion damage $\%E$ and the effective coefficient of friction μ_e for a trial new concrete slab thickness $h_1{}'$ and applying ***Step B*** to determine the new erosion-based slab thickness $h_e{}'$ until $h_e{}' = h_1 = 8\ in.$);
2. It is determined that the new concrete slab thickness should be $h_1{}' = 8.45\ in.$ (this leads to $\%E = 0.482\%$ and $\mu_e = 2.40$) such that the new erosion-based slab thickness $h_e{}' = h_1 = 8\ in.$.

Final design output

Purpose 1 – Determine the final design reliability due to erosion

1. The final design of PPCP panel thickness = 8 in.;
2. The final design reliability dropped from 90% to 82% due to the consideration of erosion (for predicted slab cracking = 19.4%);
3. The final design of base thickness = 6 in.;
4. The final required effective prestress is determined as the maximum value of the results determined based on the two criteria and a minimum requirement of the effective prestress (i.e. 100 psi):

$$EP_{required} = Max(EP_1, EP_2, EP_{\min}) = Max(55,150,100) = 150psi$$

Purpose 2 – Determine a new concrete slab thickness

In order to achieve the initial design reliability (i.e. 90%), the final design PPCP panel thickness is adjusted to the new concrete slab thickness $h_1{}' = 8.45\ in.$

1. The final design of PPCP panel thickness = 8.45 in. ≈ 8.5 in.;
2. The final design reliability is maintained at 90% (for predicted slab cracking = 19.4%);
3. The final design of base thickness = 6 in.;
4. The final required effective prestress is determined as the maximum value of the results determined based on the two criteria and a minimum requirement of the effective prestress (i.e. 100 psi):

$$EP_{required} = Max(EP_1, EP_2, EP_{\min}) = Max(55,150,100) = 150psi$$

For demonstration, the following steps apply the results of Purpose 2.

Step 3

1. Selecting the size and force of prestressing tendons;
    a. Tendon size: 0.6 in diameter 7-wire tendons are used;
    b. Tendon force: 75% of the ultimate load capacity = 43000 lbf;
    c. Tendon spacing: 18 in.
2. Determining the length of a PPCP section;

Table 3-14 Inputs for PPCP length determination

Maximum concrete temperature during the summer, ˚F	120
Minimum concrete temperature during the winter, ˚F	20
Concrete modulus of elasticity, psi	4000000
Concrete CTE, millionth in/in/˚F	5
Slab–base friction coefficient	20
Concrete unit weight, pci	0.0868

$$L \geq \frac{E_c \cdot \alpha \cdot \Delta T}{\mu \cdot \gamma} = \frac{4 \times 10^6 \times 5 \times 10^{-6} \times (120 - 20)}{20 \times 0.0868} / 12 = 96ft$$

Use 96 ft. for the length of PPCP BAS. Assuming the post-tensioning can be performed segmentally in every 6 ft. (same as the length of each concrete slab) of the BAS, so $L = 6ft$

3. Determining the total applied prestress based on panel thickness and tendon spacing;
    a. The area of concrete per tendon A_c = tendon spacing x panel thickness = 18 in. x 8.5 in. = 153 in.^{2}
    b. The total applied end stress f_{pe} = Tendon force/area of concrete per tendon = 43000 lbf/153 in.^{2} = 281 psi

Table 3-15 Design inputs for prestress loss calculation

Length of a PPCP section, ft	96
Tendon (strand) diameter, in	0.6
Tendon cross-sectional area, in^2	0.217
Tendon spacing, in	18
Panel thickness, in	8.5
Concrete modulus of elasticity, psi	4000000
Steel modulus of elasticity, psi	28000000
Tendon force at 75% of yield stress, lbf	43000
Slab–base friction coefficient	20
Concrete shrinkage strain, million in/in	300

Concrete ultimate creep coefficient	2.5
Steel relaxation coefficient	0.04

4. Accounting for the prestress loss due to various factors such as the slab-base friction, concrete shrinkage and creep and etc., the required design inputs are summarized in Table 3-15;
    a. Prestress loss due to slab-base friction:

    Assuming the post-tensioning can be performed segmentally in every 6 ft. of the BAS, so $L = 6ft$

    $$\sigma_F = \frac{\mu L}{2} = 20 \cdot 6ft/2 = 60psi$$

    b. Prestress loss due to concrete shrinkage:

    For simplicity, this example assumes the actual ultimate concrete drying shrinkage to be 600 με, therefore the ultimate concrete drying shrinkage for precast slab is 300 με. However, the practitioner should calculate the actual ultimate concrete drying shrinkage using Equation (3-10) based on the properties of real concrete mixture.

    Based on Table 3-5, $A_s = 0.217\ in^2$ for 0.6 in. diameter tendons

    $$f_s = \varepsilon_s E_S(\frac{A_s}{A_c}) = 300 \text{ x } 10^{-6} \text{ x } 28000000 \text{ x } (\frac{0.217}{153}) = 11.91 \text{ psi}$$

    c. Prestress loss due to concrete creep:

    $$f_{cr} = C_u \frac{E_s}{E_c} f_{pe}(\frac{A_s}{A_c}) = 2.5 \text{ x } \frac{28000000}{4000000} \text{ x } 299 \text{ x } (\frac{0.217}{153}) = 7.42 \text{ psi}$$

    d. Prestress loss due to steel relaxation:

    $$f_r = \rho \cdot f_{pe} = 0.04 \times 281 = 11.24psi$$

    e. Total prestress loss = 60 + 11.91 + 7.42 + 11.24 = 90.57 psi
5. Determining the effective prestress by subtracting the prestress loss from the total applied prestress.
    a. $P_{effective}$= The total applied end stress – the total prestress loss = 281 – 90.57 = 190.43 psi

Design output

1. Compare the effective prestress $P_{effective}$ with the required effective prestress $EP_{required}$ determined from ***Step 2***

$$P_{effective} = 190.43psi > EP_{required} = 150psi$$

   Therefore the design is valid.
2. Otherwise, adjust the length of a PPCP section, tendon spacing or panel thickness until $P_{effective} \geq EP_{required}$

Step 4

Determine the inputs required for calculating PPCP panel movement and designing joint width. Example inputs are shown in Table 3-16.

Table 3-16 Design inputs for total movement calculation [10]

Length of a PPCP section, ft	96
Maximum concrete temperature during the summer, ˚F	120
Minimum concrete temperature during the winter, ˚F	20
Concrete temperature at install, ˚F	70
Minimum joint width, in	0.25
Concrete CTE, millionth in/in/˚F	5
Concrete ultimate creep coefficient	2.5
Total applied end stress, psi	281
Effective prestress, psi	190.43
Concrete modulus of elasticity, psi	4000000
Concrete shrinkage strain, million in/in	300

Movement calculations

1. The temperature variation induced movement:

$dL_{Temp} = (T_{c\max} - T_{c\min}) \times CTE_c \times L =$ (120-20) $\times$ 5 $\times$ 10^{-6} $\times$ (96 x 12) = 0.576 in

2. The creep induced movement:

$$dL_{creep} = C_u \times (P_{end} + P_{effective})/2 \times (1/E_c) \times L$$
$$= 2.5 \times (281 + 190.43)/2 \times (1/4000000) \times (96 \times 12)$$
$$= 0.170 \text{ in.}$$

3. The shrinkage induced movement:

$$dL_{shrinkage} = \varepsilon_s \times L = 300 \times 10^{-6} \times (96 \times 12) = 0.3456 \text{ in.}$$

4. Total movement of a PPCP section:

$$dL_{Total} = dL_{temp} + dL_{creep} + dL_{shrinkage} = 0.576 + 0.170 + 0.3456 = 1.09 \text{ in.}$$

Joint width calculations

1. Set minimum joint width $dL_{\min} = 0.25$ in.
2. Joint width at the time of installation:

$$JW_{Install} = dL_{\min} + (T_{\max} - T_{Install}) \times CTE_C \times L$$
$$= 0.25 + (120\text{-}70) \times 5 \times 10^{-6} \times (96 \times 12)$$
$$= 0.538 \text{ in.}$$

3. Long-term minimum joint width:

$$JW_{(L-T)\min} = dL_{\min} + dL_{creep} + dL_{shrinkage}$$
$$= 0.25 + 0.17 + 0.3456$$
$$= 0.766 \text{ in.}$$

4. Maximum joint width:

$$JW_{\max} = dL_{\min} + dL_{total} = 0.25 + 1.09 = 1.34 \text{ in.}$$

The long-term joint width variation is shown in Figure 3-26.

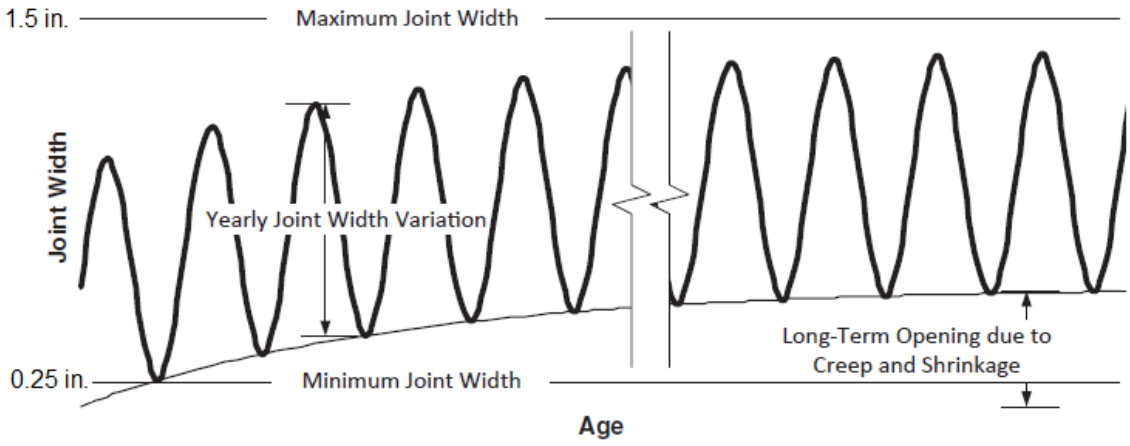

Figure 3-26 Long-term joint width variation [10]

Design output

1. The joint width at the time of installation = 0.538 in.;
2. Long-term minimum joint width = 0.766 in.;
3. Maximum joint width = 1.34 in. < 1.5 in. OK;
4. If the maximum joint width is greater than 1.5 in., then revise design inputs (i.e. length of a PPCP section and total applied end stress) and re-design starting from ***Step 3***.

CHAPTER 4

CONSTRUCTION OF BRIDGE APPROACH SLAB USING PRECAST CONCRETE PAVEMENT

This chapter provides a general guideline for the construction of BAS using precast concrete pavement (i.e. JPrCP and PPCP), including the following activities [10, 11, 43, 51, 52]:

1. Panel manufacture and storage;
2. Base preparation;
3. Panel installation;
4. Post-installation activities.

PANEL MANUFACTURE AND STORAGE

The standards for manufacture and storage of precast concrete panels have been well-established both by highway agencies and industry, including the requirements for fabrication facilities, production operations and quality control procedures; participation of highway agency or industry-managed precast plant certification program is a necessity prior to the operation of manufacturing facility.

The process of panel manufacturing starts with:

1. Setting up formwork and casting beds which should be able to maintain required tolerance for panel fabrication after repeated use;
2. Installing panel hardware (depending on specific design features), including steel reinforcement, pretensioning strands, ducts for post-tensioning (per design), lifting anchors, block-outs for load transfer (dowel bars or post-tensioning stressing pockets), dowel bars (per design), grout tubes and anchor sleeves (per design);
3. Performing pretensioning if pretensioning method is applied; the effective prestress due to pretensioning can range from 100 – 200 psi;

4. Placing concrete into the formwork; either conventional concrete (7 – 9 in. slump is required) or self-consolidated concrete may be used; performing surfacing and texturing; curing the panels using plastic sheeting;
5. Releasing pretensioning strands from anchorage (per design) and stripping formwork when the strength of concrete reaches at least 2000 psi (or 3000 – 4000 psi if pretensioned);
6. Performing finishing procedures, including cleaning block-outs, marking panel information, repairing damaged panel surface if any, rounding panel edges and checking panel dimension tolerances;
7. Once panels are manufactured, they are moved to storage locations. A layer of curing compound may be applied at the edges of panels to minimize moisture evaporation. The panels should be stacked on solid dunnage to minimize warping and should be arranged in the order for construction need. The upper panel of a stack should not be used as a storage area.

BASE PREPARATION

Prior to the placement of precast panels on site during construction, base preparation is very important to achieve satisfactory performance of new BASs; for rehabilitation of existing BASs, it often requires regrading the existing base to provide a uniform base support.

Different from the preparation for the base of pavement, special attention needs to be paid for the base preparation of BASs with respect to minimizing settlement and erosion issues. Based on the experience of previous precast BAS construction projects [11, 43, 52], the following is recommended:

1. Use base materials with higher modulus to minimize settlement; in most of the previous precast BAS projects, coarse aggregates (e.g. crushed limestone) were used as the base material;
2. Install subsurface underdrain system prior to placing new base material, if necessary;

3. If the existing embankment material is not suitable for directly being used as base, then undercut the supporting area to allow for placing satisfactory base materials; besides using a coarse aggregate base, cement-treated permeable base (CTPB) and rapid-setting lean concrete base (RSLCB) may also be viable options for new construction where lane closure time is not the major concern. Operations are not allowed on neither the base types until either their compressive strengths reach 100 psi or 2 hours after placement; otherwise, surface damage can occur at the surface of the bases during panel installation [2];
4. Place surcharge load on the embankment to expedite the occurrence of primary consolidation settlement;
5. Properly consolidate the base material to the desired elevation and use Nuclear Density test to ensure compaction quality; Figure 4-1 shows a figure showing the compaction operations and the gradation of aggregate base for the PPCP BAS demonstration project in Iowa, where a portable vibratory compactor was used to perform the base material compaction [11];

Figure 4-1 Compaction and grading of aggregate base in a PPCP BAS demonstration project in Iowa [11]

6. Place a thin layer of bedding material (fine-grained unbound or rapid setting material) to achieve smooth grade; this can be performed by using a precision grading system shown in Figure 4-2. The system uses accurate grade rails laying longitudinally along each side of the grading area, a grading screed is pushed along the rail to perform grading at the surface of the base area [52];

Figure 4-2 Precision grading of base layer [18].

7. Place a layer of bearing pads on the paving notch of the abutment (space designated for laying one end of the BAS).

PANEL INSTALLATION

Once the base preparation is finished, precast panels installation is conducted. Due to the differences in the panel connection procedure and joint load transferring devices, the panel installation procedures are different for JPrCP and PPCP.

JPrCP

Prior to the placement JPrCP panels, it is required to perform different drilling styles at the edges of existing pavement to accommodate dowel bars for joint load transferring depending on the dowel slot system used in the precast panels (i.e. either top or bottom slot system):

1. If a top slot system is used, the top of the adjacent pavement slab needs to be jackhammered to create slots, then removing debris from the slots and sandblasting the slots; four slots spaced at 12 in. are usually cut per wheel path;
2. If a modified narrow top surface slot system is used, holes that are about 7 – 8 in. long need to be drilled at the vertical face of the adjacent slab; once precast panels are placed, epoxy grouting is injected into the holes before dowel bars are slid into them;
3. If a bottom slot system is used, holes are drilled at the vertical face of the adjacent slab and filled with epoxy grouting, then dowel bars are inserted into the adjacent panels prior to placement of precast panels.

Two options are available for panel installation of JPrCP:

1. The first option is to directly place precast panels on a finished base layer which has been fine-graded and compacted to the desired elevation; this normally involves the use of a layer of fine-grained granular material as bedding material and the application of a precision grading system as shown in Figure 4-2 to perform accurate grading;
2. The second option uses threaded setting bolts to position the precast panels. As shown in Figure 4-3, a precast panel is equipped with four symmetrically positioned leveling rods with threads on top portion; accordingly, four seating plates are placed at the same locations on top of the existing base prior to installation of the panel to match the bolts. Once the panel is installed and positioned, a rapid-setting bedding material is injected into the gap between the panel bottom and the existing base through the undersealing access holes in the panel. Once the bedding material reaches a compressive strength of 50 psi, the bolts are removed and the access holes are grouted.

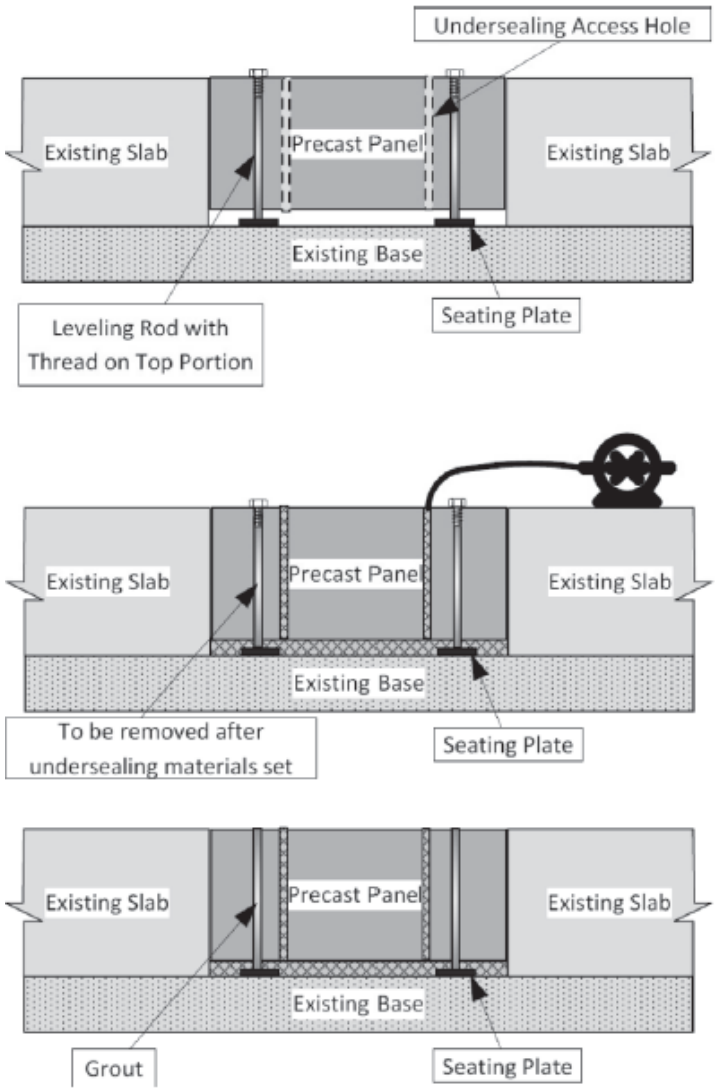

Figure 4-3 Threaded setting bolts installation option [10]

PPCP

The panel installation procedure for PPCP is different from JPrCP due to the inclusion of post-tensioning.

The procedure of PPCP panel installation starts with placing the abutment panel as shown in Figure 4-5 (a) on the paving notch of the abutment; then anchor the abutment panel to the paving notch through the pin sleeves located at the edge of the panel to prevent it from moving during post-tensioning; once the abutment panel is set

into the final position, the rest panels are installed one at a time using the following procedure:

1. Place the adjacent panel into a temporary position with a gap left between the previous panel for applying joint epoxy and installing gasket for the post-tensioning ducks;
2. Feed post-tensioning strands into the ducks from the anchor at the joint panel to the anchor at the abutment panel;
3. Apply a thin layer (1/8 in.) of epoxy at the keyway joint face as shown in Figure 4-4, to fill any unevenness or voids after panel assembling and seal the joint to prevent water from infiltrating into the underlying base layer;

Figure 4-4 Application of joint epoxy in the Iowa demonstration project [11]

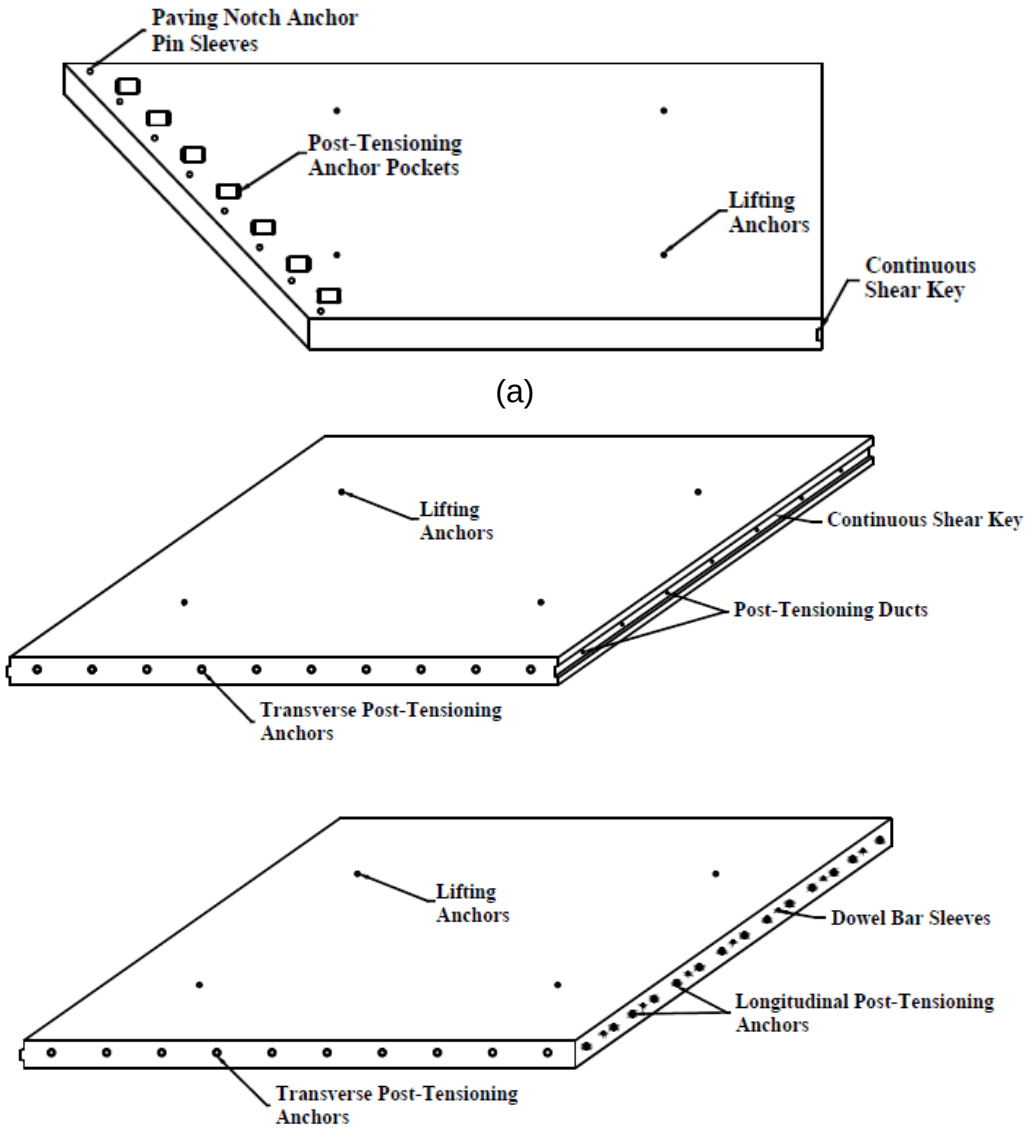

Figure 4-5 Precast penal design details of a PPCP BAS demonstration project in Iowa (a) abutment panel, (b) base panel, and (c) joint panel [11]

4. Perform temporary post-tensioning to bring two adjacent panels together using only two strands located at the quarter points (i.e. ¼ and ¾) of the panel; squeeze out the excessive epoxy and maintain the post-tensioning stress; once the epoxy reaches an initial set, release the temporary post-tensioning force and perform installation for the next panel;

5. Once all the panels are in their final positions, perform final post-tensioning where the strands are post-tensioned to 75% of their ultimate tensile strength; the final post-tensioning starts from the strands near the center of each panel and alternates out to the ones at the edges. If the panels are designed with two-way post-tensioning, longitudinal post-tensioning needs to be performed prior to the transverse post-tensioning;
6. The elongation of post-tensioning strands needs to be measured with an accuracy of 1/8 in. and compared against the theoretical value which can be computed using the following equation [53]:

$$\delta = \frac{PL}{E_S A_S + E_e A_e} \tag{4-1}$$

where δ is the theoretical elongation, P is the applied load, L is the length of the slab, E_S is the young's modulus of the steel (typically 28000000 psi), A_S is the cross-section area of the steel, E_e is the young's modulus of the epoxy (typically 3500000 psi) and A_e is the surface area of the epoxy (typically 1.56 E-4 in^2). If the difference between measured and theoretical values exceeds 7%, then post-tensioning needs to be ceased until the issue is resolved.

In addition, it should be noted that a new construction practice referred to as the incrementally connected precast concrete pavements (ICPCP) as shown in Figure 4-6 [10] is recommended for constructing BASs. This practice allows the shortly-spaced precast panels to be connected segmentally, therefore reducing the effective friction during the final post-tensioning and avoiding the necessity of using polyethylene sheeting (as a means to reduce friction during construction) underneath the concrete slab. By applying this practice, greater concrete panel-base friction resistance will develop which helps to prevent the abutment from moving.

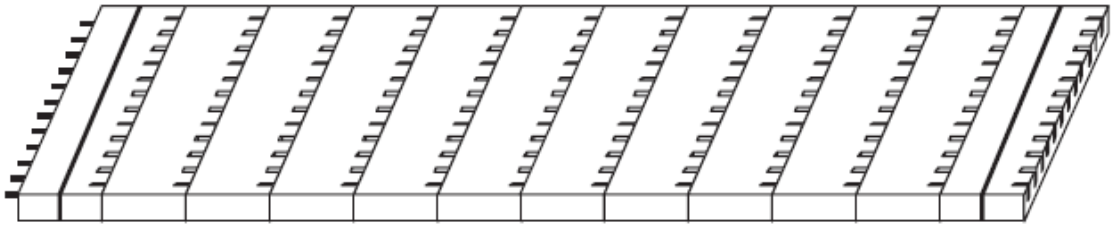

Figure 4-6 A representation of ICPCP [10]

POST-INSTALLATION ACTIVITIES

Once the panels are post-tensioned, the following activities need to be performed before the BAS can be open to traffic:

1. Pump grout into the post-tensioning ducts through grout inlets as soon as post-tensioning is finished; grouting should be finished uninterrupted within one operation and full grouting is checked when grout flow out from outlet;
2. Perform under-slab grouting to fill voids underneath the BAS to achieve full support condition by using rapid-setting cementitious materials that can provide compressive strength of 500 psi once hardened. The grout pressure needs to be controlled to lower than 30 psi to avoid the risk of panel lifting;
3. Perform joint sealing at the longitudinal joints according to the agency's practice; For two-way post-tensioning system, if an open keyway is used (in order to overcome the issue of joint mismatch if the pavement is crowned at the centerline of roadway) at the longitudinal joint as shown in Figure 4-7, it needs to be filled with gavel concrete mixture prior to performing transverse post-tensioning; in this case, perform initial transverse post-tensioning (10% of ultimate tensile strength) 3 – 4 hours after filling the joint and then final transverse post-tensioning (75% of ultimate tensile strength) after 24 hours. Wet burlap method may be used to cure the concrete after placement.

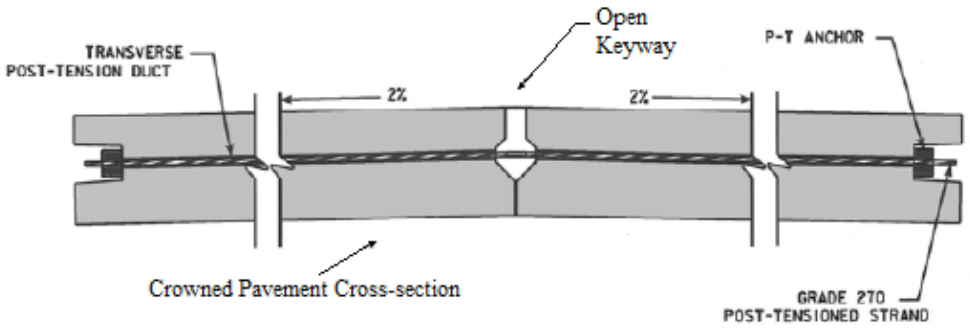

Figure 4-7 Design details of the transverse post-tensioning and longitudinal open keyway in the Iowa demonstration project [11]

4. Fill the post-tensioning anchor pockets using the same concrete mixture and at the same time when longitudinal joints are filled;
5. Install epoxy coated dowel bars at the joint panel; if the adjacent pavement is cast-in-place, then dowel bars are enclosed by concrete; if the adjacent pavement is existing, dowel bar slots need to be cut and filled with grout once dowel bars are placed;
6. Perform surface grinding to achieve satisfactory surface smoothness for high-speed traffic. A layer of asphalt overlay may be placed on top of the precast panels as the riding surface.

MAINTENANCE

A routine monitoring/maintenance program may be established by the practitioner as a means to consistently provide satisfying BAS performance to the public transportation over its entire design life. The approaches (i.e. performing visual distress inspections, FWD and DCP testing) elaborated in Chapter 2 may be applied to decide whether maintenance measures are required.

To address the Level 1 and 2 severity distress (where a BAS replacement or reconstruction is not necessary) defined as shown in Table 1-1, a conceptual design detail which is to provide re-openable undersealing access holes in the BASs can be used to facilitate performing maintenance measures [19]. When maintenance is needed,

grout or expansive polymer can be injected underneath the BAS through those re-openable access holes to fill the voids that may have developed in the base layer or the embankment backfill. When significant settlement has developed, the practitioner may use the leveling the system (shown in Figure 4-3) that is built in the precast panel to lift the BAS back to a proper elevation before grouting.

CHAPTER 5

DESIGN OF KEY ELEMENTS IN A BRIDGE APPROACH SLAB SYSTEM

Once the type of the precast bridge approach slab (BAS) is selected and designed following the information elaborated in Chapter 3, it is also necessary to select the design details or construction measures for the key elements (subsequently described) within the BAS system. A well-performed BAS is not only a result of well-designed precast BASs, but also relies on the effective interactions between the BAS and the key elements within that system. Appropriately selecting the design details for these elements helps to create a favorable environment for achieving successful performance of the BAS and preventing the potential bump issues from occurring. Without properly addressing these elements, the failure of either one of them can be a weakness within the system leading to the development of the bump issues. In this chapter, 10 key elements have been identified and the design details for these elements are evaluated regarding their applicability to precast technologies and the effectiveness to prevent the occurrence of the potential bump condition. Specific criteria are also provided for selecting the design details for each element.

KEY ELEMENTS IDENTIFICATION

10 key elements as shown in Figure 5-1 are identified within a BAS system, including:

1) BAS base layer;
2) Bridge deck-BAS joint;
3) BAS-pavement joint;
4) BAS drainage;
5) Abutment details;
6) Wing wall details;
7) Subsurface drainage;
8) Backfill wedge;
9) Embankment; and

10) Foundation support.

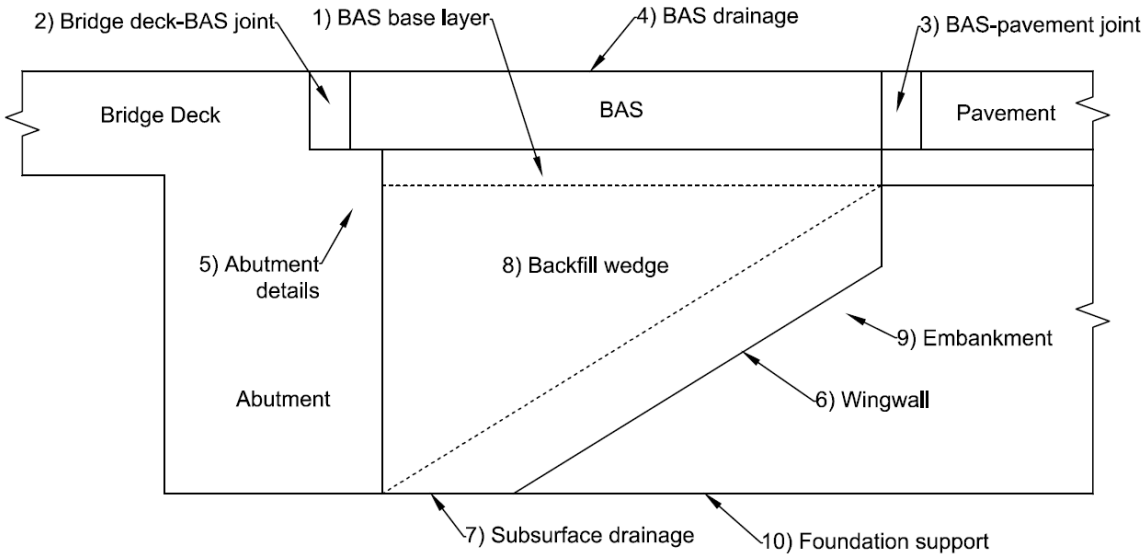

Figure 5-1 Key elements within a BAS system

In order to appropriately select the design details or construction measures for each element, the practitioner should establish selection criteria (subsequent example selection criteria for each element is provided) which clearly define the boundaries/conditions for which specific design details should apply. For instance, if the construction area is subjected to a potential for heavy rainfall (i.e. a selection criterion), an open graded aggregate is recommended as the BAS base layer (**Element 1**) to provide drainage.

Reliability Considerations

With respect to each of the 10 elements, the practitioner can evaluate and select the appropriate design detail that meets the selection criteria (e.g. need a drainable base in **Element 1** in areas with heavy rainfall potential) at a given level of reliability.

In order to better help practitioners make design decisions with respect to these elements at various levels of design assurance/reliability, the aforementioned 10 elements are classified into three categories with respect their design purposes or utility in the system.

Table 5-1 Categories for BAS system elements as per design objective

Design Objective	Performance/Reliability Indicator	Pertinent Element
BAS Thickness Design	Slab cracking	1, 8
BAS Erosion Prevention	Slab cracking	1, 2, 3, 4, 5, 6, 7, 8
	Transition smoothness	
Settlement Potential	Slab cracking	8, 9, 10
	Transition smoothness	

Element 1 and 8 are direct factors affecting the BAS thickness design in which the cracking performance of the BAS is the main design criteria/concern; the reliability of the design is directly accounted for and can be quantified in the design procedure (elaborated in Chapter 3) as well. In general, a greater level of design assurance (i.e. a high possibility of reaching the design life) can be achieved if a stiff, uniform and less erodible base layer (**Element 1**) and a strong, less compressible backfill wedge (**Element 8**) are used.

Element 1 – 8 are factors affecting the erosion performance of the BAS which is one of the most significant considerations in the BAS thickness design and directly affects the cracking performance of the BAS. Adequately addressing either one of the elements will help to improve the chances of achieving the expected design life of the BAS; in other words, if either one of them fail to perform in the way it is designed for, erosion failure with the concomitant slab cracking can be the result. In general, erosion at the BAS can be minimized if a less erodible base layer (**Element 1**) is used, the bridge deck-BAS joint (**Element 2**) and the BAS-pavement joint (**Element 3**) are well designed to maintain the transitions smooth and the joints tight, the BAS drainage (**Element 4**) is properly designed both at the surface and underneath the BAS to prevent the accumulation of runoff water, the abutment details (**Element 5**) are appropriately designed and constructed to prevent issues from occurring at the

connections between the abutment and the adjacent structures (i.e. BAS and backfill wedge), the wing wall (**Element 6**) is adequately designed to prevent widening of the wing wall-BAS joint, the subsurface drainage (**Element 7**) is well designed to avoid wetting induced soil collapse or erosion and a less erodible backfill wedge (**Element 8**) is constructed.

Construction of **Elements 8 – 10** are key to providing support for the BAS; any settlement or loss of support in any of these elements directly affect the smoothness at the bridge deck-BAS and the BAS-pavement joints as well as the BAS cracking performance (partial support condition induces more slab cracking). Therefore, appropriate construction practices and/or design details for these elements is the key to minimizing the potential of a bump at the transitional joints associated with the BAS. This approach allows for a fully supported pavement to be maintained such that the probability of achieving the expected design life and performance (i.e. less slab cracking and smooth transition) of the BAS is greatly enhanced. In general, settlement potential can be minimized if the backfill wedge (**Element 8**) is constructed using non-erodible and non-compressible materials, the embankment (**Element 9**) is compacted or treated with sufficient stability to support the backfill wedge and the BAS structure, and the foundation soil (**Element 10**) is adequately treated to minimize the primary consolidation settlement.

Achieving the expected design life and performance of a BAS relies on appropriately selecting the assurance level of the design detail or construction practice for a specific key element. For instance, for **Element 1**, using a stabilized aggregate base provides a greater level of assurance in terms of facilitating drainage and preventing erosion (i.e. the 2nd design objective shown in Table 5-1) compared to using a typical dense graded granular base; for **Element 10**, the use of stone columns in the foundation materials provides a greater level of assurance for limiting the foundation settlement (i.e. the 3rd design objective shown in Table 5-1). However, it should be noted that increasing the assurance level of the design usually induces higher cost. Therefore, the practitioner should appropriately select the design details based on the funding availability.

Finally, in order to obtain satisfactory design outcome (i.e. achieving the expected design life of the BAS) at a certain assurance/reliability level, the practitioners need to apply a table like Table 5-2 to help select the appropriate design details for each element.

The main benefit of using such table is that it will help practitioners to better take into account reliability considerations into the design, especially for the 2nd and the 3rd design objectives (this is because the reliability consideration is automatically accounted for in the design process for the 1st design objective, which is elaborated in Chapter 3).

Table 5-2 is created as an example of the design for **Elements 8 – 10** with respect to the 3rd design objective (i.e. settlement potential). The table consists of various design combinations (6 combinations are shown in Table 5-2) as a result of selecting different design details for each element. The various design combinations are categorized into three levels of overall assurance (i.e. low, medium and high); the rule for determining the overall assurance level of a specific design combination can be described as: the majority of the individual assurance level of the design detail selected for each single key element within that design combination dictates the overall assurance level. For instance, the majority of the individual assurance level in design combination #4 is “High” (design details of high individual assurance levels are selected for **Elements 8 and 10**), so the overall assurance level of design combination #4 is categorized into “High”. A similar table can also be created in the same fashion to help with designing the elements pertinent to the 2nd design objective.

Table 5-2 Establishment of assurance levels for the 3rd design objective

Design Objective	**Overall Assurance Level**	**Design Combination No.**	**Element No.**						
			8		**9**			**10**	
			Low	High	Low	Medium	High	Low	High
			Granular backfill	CLSM	Natural soils	Natural soils with geogrid reinforcement	Concrete piles	Untreated natural ground	Stone column treated ground
Settlement Potential	Low	1	√		√			√	
	Medium	2	√			√			√
		3		√		√		√	
	High	4		√	√				√

		5		√		√			√
		6		√			√	√	

The following provides an example to use the table for designing **Elements 8 – 10** with respect to the 3rd design objective (i.e. settlement potential):

1. Choose one of three levels of overall assurance as the target (shown in Table 5-2 (i.e. low, medium and high). For instance, the practitioner expects that settlement may potentially cause some problems based the local experience, then a “High” overall assurance level should be selected;
2. Select the specific design detail for each element based on the design criteria (which are subsequently elaborated for each element in the pertinent subsection). For instance, if the project area consists of soft compressible foundation soils, then the selection criterion leads to choosing stone columns for **Element 10** or choosing concrete piles for **Element 9**);
3. Check if the viable design combinations meet the target overall assurance level and select the appropriate one based on funding availability. In this example, design combinations #4, #5 and #6 are viable options since they all meet the “High” overall assurance level; the practitioner may choose either design combination #4 for the lowest cost or design combination #6 for the lowest settlement potential.

Sometime, to achieve a certain level of overall assurance for a specific design objective, selecting the design detail with a lower level of individual assurance for a specific key element can be compensated by increasing the individual assurance level of another key element under the same design objective. For instance, if **Element 9** is designed with concrete piles supporting the backfill wedge (which provides a higher level of individual assurance) to address the potential of foundation settlement, it would be unnecessary to use stone columns for **Element 10** (which also provides a higher level of individual assurance)**,** because the design combination already provides satisfactory level of overall assurance.

ELEMENT 1. BASE TYPE SELECTION

The selection of the base material is one of the most important aspects in the design considerations of BASs. The base should be designed in order to not only provide sufficient structural capacity in terms of modulus, thickness and bondability (which are design considerations incorporated into the procedure for designing the thickness of BAS as elaborated in Chapter 3), but also to have good resistance to erosion damage and settlement or proper drainability to avoid the accumulation of runoff water. In addition, considerations related to the construction/preparation of base are also important concerns when it comes to selecting appropriate design details for the base.

Base Design Considerations

Currently, the standard in Oklahoma is to place the BAS directly on top of the CLSM wedge; with regard to the inclusion of an additional base layer (i.e. **Element 1** as shown in Figure 5-1) between the BAS and the embankment backfill wedge, the following criterion can be applied:

1. If a greater level of design reliability is needed with respect to the erosion prevention in BASs (i.e. by assuming that the joint sealant will eventually fail to prevent moisture infiltration and the CLSM is designed impermeable and erodible), an additional drainable and less erodible base layer should be placed in between the BAS and the CLSM.

Base Type Selection

A few base layer options can potentially be used for precast BASs:

1. Untreated crushed stone aggregate base as was used in Iowa [11] and Missouri [43] projects (shown in Figure 5-2). This type of aggregate is usually made of pure granite or limestone which is crushed to create a range of particle sizes in order to make it easier for compaction as well as providing better load bearing capacity. A typical gradation of the crushed stone aggregate base can be found in Table 5-3. The main advantage of using the

crushed stone aggregate base is to facilitate drainage beneath the BAS through connecting the aggregate base to the drains installed along the longitudinal edges of the pavement slabs.

Table 5-3 The gradation requirement of the crushed stone aggregate base [54]

Sieve	Percent by weight
Passing 1 in	100
Passing ½ in	60 - 90
Passing No. 4	35 - 60
Passing No. 30	10 - 35

Figure 5-2 Compaction of crushed stone aggregate base in Missouri [43]

Note that due to the nature of the crushed stone aggregate base (i.e. open-graded), large voids may still be prevalent at the surface of the base even after compaction is finished, which makes it very difficult to precisely perform grading. In this case, a finer type of aggregates (not passing No. 200 sieve) may be placed at the surface of the crushed stone aggregate base as a bedding layer to facilitate precise grading [11]. However, it should be noted

that if the size of the finer aggregates is not well designed, there is a risk that the drainage may be restricted which will defeat the purpose of facilitating drainage and induce the potential of erosion. To overcome the potential of erosion, the elements associated with drainage concerns may be specifically addressed (such as placing drainage pipes directly underneath the transverse joints to collect runoff water and direct them to the edge drains). In addition, high quality geotextile is recommended to be installed at the interface between the base and the CLSM wedge, which is expected to provide additional stability to the base structure as well as preventing coarse and angular aggregates from puncturing into the subgrade under the influence of heavy truck traffic;

2. Cement-treated or asphalt treated open-graded (stabilized permeable) bases are also viable options when the duration of lane-closure is not a concern during construction [10, 55]. For this type of base, the upper portion of the open-graded aggregates are stabilized using either cement or asphalt. The permeability of the open-graded base is recommended to be designed in the range of 300 – 500 ft./day and it should be noted that the stability of the open-graded based should not be affected for achieving a greater level of permeability [10]. Comparing to untreated aggregate base, the advantages of using the treated bases are 1). Increased smoothness and less voided area at the surface of the base; 2). Better controlled grade and increased stability; 3). Greater durability and resistance to rutting in the base layer; 4) Greater bonding at the slab-base interface which increases the effective slab thickness and provides greater restraint to prevent the movement of integral abutment bridges; 5) Drainage is also addressed attributed to the use of open-graded aggregates. Again, longitudinal edge drains can be used to facilitate drainage.
3. In the case where CLSM is designed to meet the requirements for both drainage and erosion resistance, precast BASs may be directly placed over the CLSM as long as the base grade is well-controlled. For rehabilitation projects where damage exist on the surface of the existing CLSM, a layer of

bedding material such as fast-setting CLSM or fast-setting cementitious grout may be placed to restore the grade.

Selection criteria

The criteria to select the base type can be found in Table 5-4.

Table 5-4 Base type selection criteria

	Untreated aggregate base	**Treated aggregate base**
Criteria	Constrained construction time	Need for greater slab-base bonding (i.e. Integral abutment bridge)
	Constrained budget	Need for greater reliability

ELEMENT 2. BRIDGE DECK – BAS JOINT DESIGN

For integral abutment bridges, in order to reduce the movement of the bridge structure due to the thermal and load effects, BASs are usually tied or anchored to the bridge structure through the use of reinforcing bars. In that case, the bridge deck – BAS joint, being a construction joint, is usually designed to also function as a contraction joint which is formed in the fresh concrete at the location of the joint for CIP BASs. Once the joint is formed, it should be sealed with joint sealing materials such as hot pour, silicon and preformed compression seals with/ without the use of filler materials (such as bituminous material, polystyrene foam or neoprene pad) underneath the joint sealant [56] (similar to the joint sealant design detail in Oklahoma as shown in Figure 5-3).

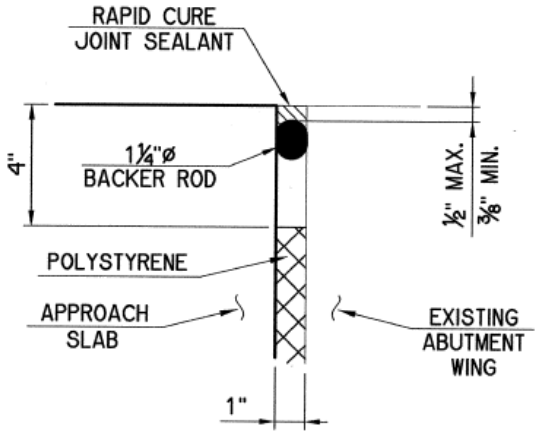

Figure 5-3 Sealed contraction joint detail [2]

Due to the nature of the construction of precast BAS, the bridge deck – BAS joint may be addressed differently relative to the CIP BAS. In some instances, if a good match is not achieved at the precast BAS and the bridge deck joint, a large and nonuniform opening at the bridge deck – BAS joint (such as the ones shown in Figure 5-4) may be the result. The imperfectly matched junction may also create difficulties when installing the joint filler and sealant, which could lead to poor performance such as greater rates of water infiltration at the bridge deck – BAS joint.

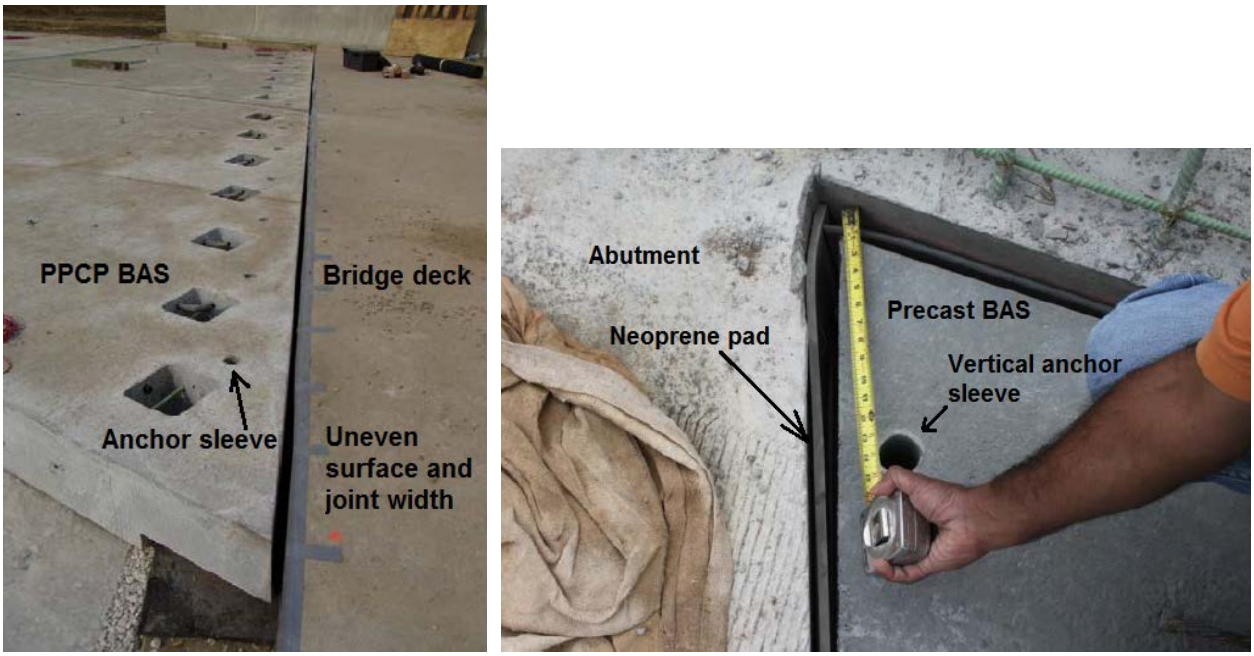

(a) (b)

Figure 5-4 the construction of the bridge deck – BAS joint for (a) a PPCP BAS project and (b) a JPrCP BAS project [11, 43]

For precast BASs that are anchored to the abutment using vertical reinforcement connections (through the vertical anchor sleeves such as the ones shown in Figure 5-4), based on the previous experience [11, 43], a layer of 0.5 in. thick neoprene pad can be used to fill the bridge deck – BAS joint and bituminous or fast-setting cementitious materials can be used as a means for sealing any gaps in the joint due to imperfect matching. In order to provide a smooth transition at the joint, the unevenness can be addressed by diamond grinding; alternatively, according to some previous projects, an asphalt overlay over the precast BAS can be used to correct an irregular surface, particularly if the BAS leads to an asphalt pavement surface [43, 52].

For precast BASs that are tied to the abutment using horizontal deformed steel bar connections (such as the one shown in Figure 5-5), high strength grout is used to fill the bottom slots (as a means to accommodate the horizontal connection bars) in the precast BAS as well as the space in between the precast BAS and abutment (i.e. the bridge deck – BAS joint). This design results in a tight (non-working) connection between the BAS and the abutment such that the expansion joint (for accommodating

the movement of the bridge structure) can be moved to the BAS – pavement junction, which minimizes the potential for bump issues to occur at the bridge deck – BAS joint.

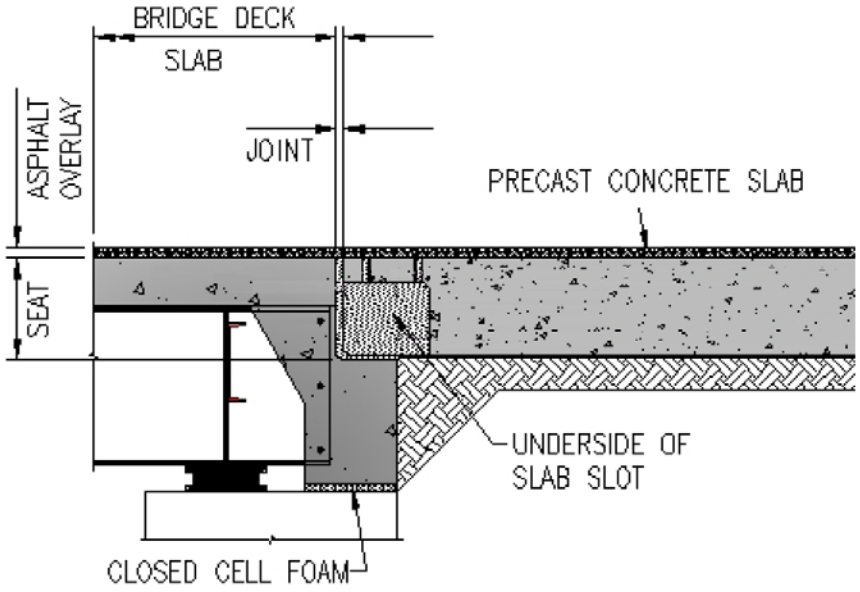

Figure 5-5 JPrCP BAS using horizontal deformed steel bars for connecting to the abutment [52]

Drainage Considerations

Although the bridge deck – BAS joint is to be filled with filler materials as a means to prevent water infiltration as was discussed earlier, however, as the joint filler material ages and deteriorates, due to the effects of traffic loads and temperature variations, it is not likely that water tightness can be maintained at this joint over the entire service life of the BAS. Therefore, drainage needs to be addressed at this joint to minimize the erosion potential for the base material underneath the BAS, as a means to provide a higher level of design assurance.

A possible design solution to provide drainage at the bridge deck – BAS joint will be similar to the design detail of an expansion joint found in Colorado [57] as shown in Figure 5-6, where the bridge deck – BAS joint uses a strip seal joint and a trimmed plastic pipe in the joint slot to direct water to the outside face of the wing wall. For precast BASs that are anchored to the abutment, instead of using the strip seal joint which can be difficult and time-consuming to build during construction, the bridge deck –

BAS joint may be filled with permeable materials (cement or asphalt-treated) such that runoff water can be directly drained through the permeable material and the trimmed plastic pipe. This design detail intends to provide a higher level of design reliability with respect to minimizing the embankment erosion possibilities, therefore, it is recommended for the construction of precast BASs that are anchored to the abutment, especially for districts with high-intensity of precipitation.

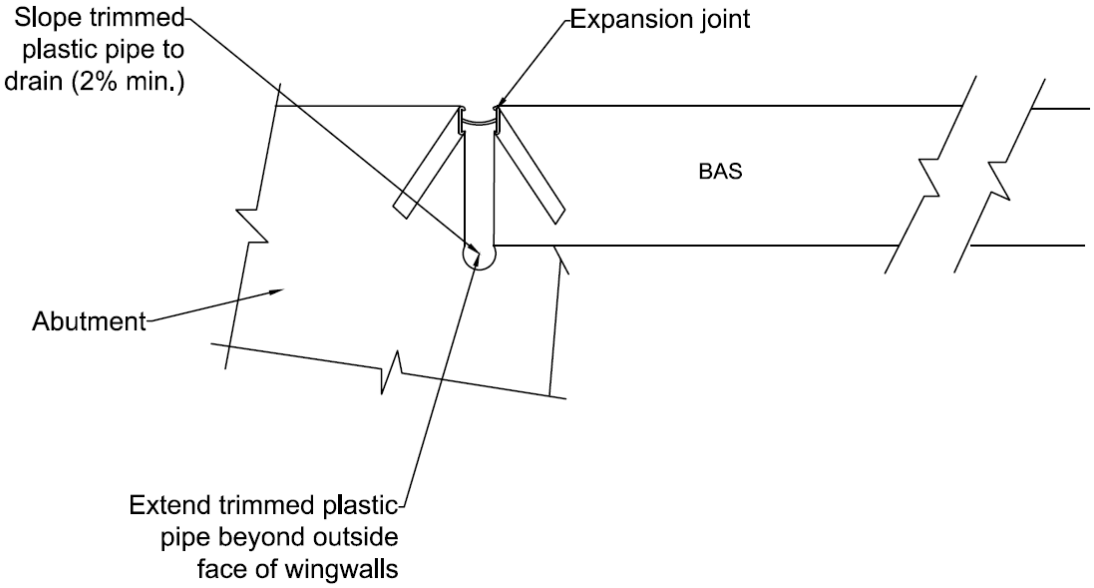

Figure 5-6 A detail of expansion joint in CDOT , after [57]

Besides this option, there are other alternatives to address the water infiltration at the abutment joint, such as using permeable materials as the base and edge drains to direct any infiltrated water away from the embankment (i.e. designing **Element 1**) or placing a layer of composite drainage fabric (shown in Figure 5-17) at the face of the abutment back wall to direct any water leaking from the joint into the subsurface drainage system underneath the embankment (i.e. designing **Element 7**).

ELEMENT 3. BAS – PAVEMENT JOINT DESIGN

Since the BAS are usually tied or anchored to the abutment for integral abutment bridges, the BAS becomes an extension of the bridge structure which may move as the

bridge structure expands or contracts due to the effects of temperature and moisture variations. If a wide joint spacing (e.g. 15 ft.) is used for the BASs, an expansion joint needs to be placed at the BAS-pavement connection to accommodate the large thermal movement of the BAS. However, if a narrow joint spacing (6 – 8 ft.) is used (as a means to limit thermal-induced expansive or contractive movement of the BAS), the movement of the BAS will be distributed and manifest discretely at the intermediate joints in between the individual slabs rather than concentrating excessively at the end of the BAS. Therefore, if the length of the BAS – pavement joint can be significantly reduced, it helps to maintain the tightness of the joint sealing and prevent moisture infiltration.

Concrete Pavement Joint

For precast BASs directly connecting to concrete pavements, the most widely applied practice [11, 52, 58] has been the epoxy-coated dowelled expansion joint as shown in Figure 5-7. This practice is actually very similar to the expansion joint design for the CIP concrete pavement in Oklahoma as shown in Figure 5-8. Different from the construction for CIP BASs, the dowel sleeves (1 5/8 in. in diameter) are cast in the precast BASs during panel fabrication; during the construction, one side of the epoxy-coated dowel bars (1 ½ in. in diameter) are inserted into the sleeves in the precast BASs and the other end of them are encased by the CIP concrete pavement or inserted into the holes drilled in the vertical face of the existing concrete pavement; then the expansion joint is formed by placing a flexible foam (as a joint filler material) over the dowel bars, topped with a waterproof sealant material to prevent the moisture from infiltrating into the expansion joint.

Figure 5-7 Epoxy-coated dowels to be installed at the BAS – pavement joint [11]

The joint seal should be capable of accommodating the movement of the expansion joint (which can be determined based on the calculation elaborated in Chapter 3). In Oklahoma, poured silicone seals are usually used as the sealing material. This type of sealant was considered to be not only long-lasting (typically 10 – 15 years) [59], but also easier and faster for installation [60] compared with other types of sealants. The poured silicone seal can be used for joints up to 3 in. wide and accommodate movement up to 0.25 in. (depending on the types of products) [61].

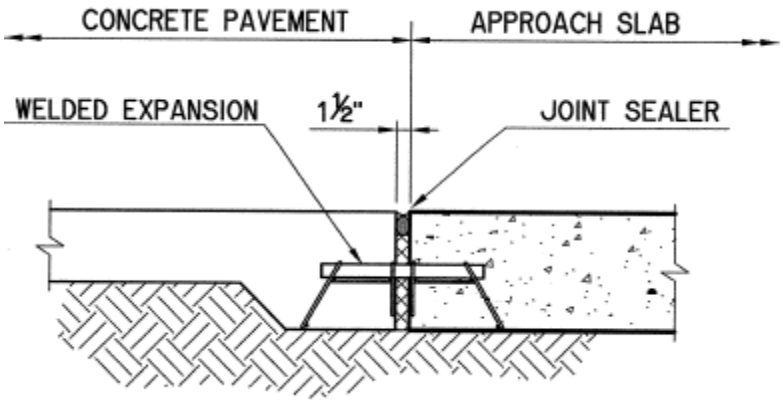

Figure 5-8 BAS – pavement expansion joint detail in Oklahoma [2]

Another detail often used in Oklahoma for sealing concrete joints is the use of an open cell foam compression sealer as shown in Figure 5-9. This type of sealer which consists of the silicone facing and the foam body is installed and glued into concrete joints by applying epoxy on the concrete joint faces and field-injected silicone sealant at

the edge of the silicone facing. The sealer allows movement ranging from 0.5” – 4”. The greatest advantage of this sealer is that it is free of compression or tension failures [62].

Regardless of what the joint sealing material is used, the practitioner should obtain the key specifications from the manufacturer such that the joint sealing material is able to accommodate the movement the joint.

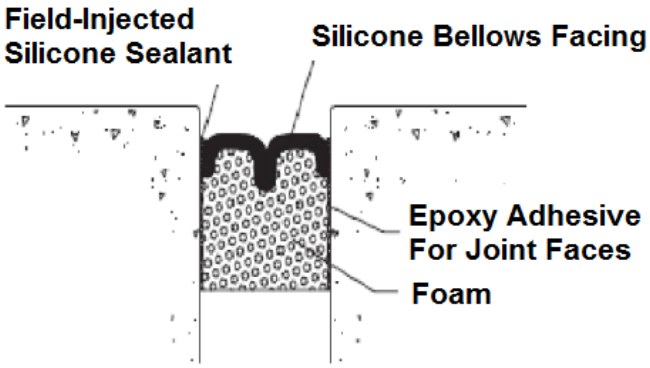

Figure 5-9 Open cell foam compression seal [62]

Asphalt Pavement Joint

For precast BASs connecting to asphalt pavements, special attention should be paid to the design of the BAS – pavement transition. In this case, a transition concrete slab may be placed (as a buffer) in between the precast BAS and the asphalt pavement as shown in Figure 5-10 [63]. The objective of applying the transition slab is to 1) provide an expansion joint to facilitate the movement of the BAS; 2) reduce the free edge deflection at the edge of the BAS and 3) provide a continuous and smooth transition between the concrete BAS and the asphalt pavement (i.e. at both the joint with BAS and the joint with asphalt pavement).

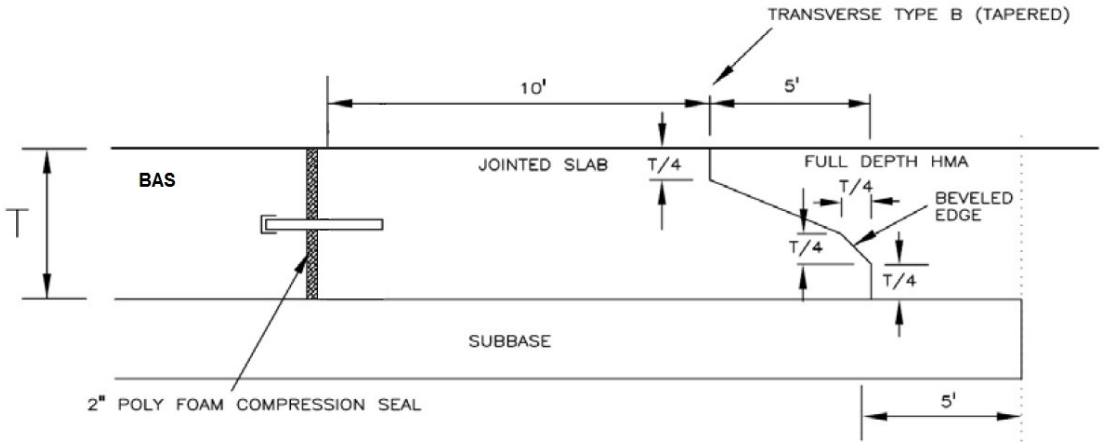

(a)

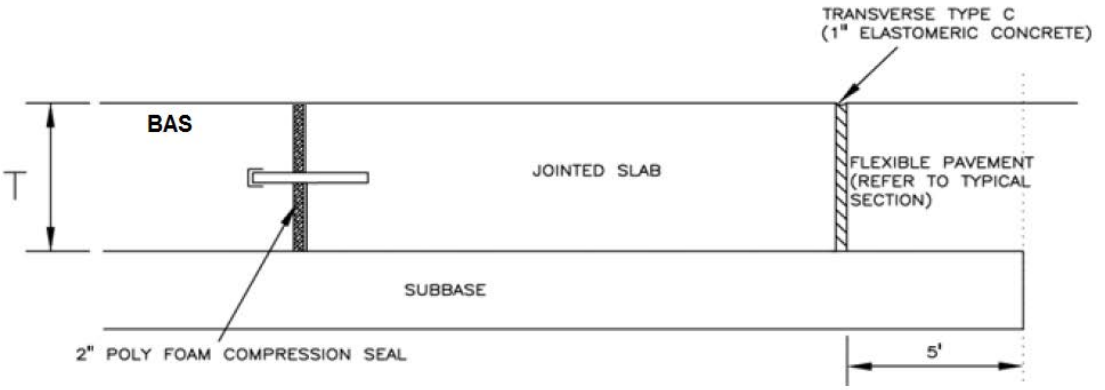

(b)

Figure 5-10 BAS – pavement transition design using (a) transition-tapered slab and (b) transition-elastomeric slab, after [63]

As shown in Figure 5-10 (a), the first option is to use a tapered transition slab between the BAS and the asphalt pavement. The pavement end of the transition slab is designed with a beveled edge as a means to minimize crack reflection in the asphalt pavement. Alternatively, an elastomeric concrete joint (as shown in Figure 5-10 (b)) may be applied to accommodate the movement between the transition slab and the asphalt pavement. Note that the elastomeric concrete joint should be installed by cutting a slot at the transition slab after all the pavement slabs are placed. In addition, the base of the BAS should extend into the asphalt pavement section for at least 5 ft. if it is different from the base of the asphalt pavement for both the two options.

Drainage Considerations

For BASs connecting to either concrete or asphalt pavements, a greater level of design assurance with respect to reducing the potential of base erosion is to include drainage features at these joints. Although the joint sealing materials are designed to perform well for many years, however, they may eventually deteriorate and break down under the effects of environmental factors and traffic repetitions. Therefore, transversely placing a perforated underdrain pipe underneath the BAS – pavement joint can be an effective practice to facilitate drainage. The selection criteria for the underdrain practice are:

1. For districts with heavy rainfall potential; and
2. When the base layer material is not drainable, such as the lime or cement stabilized bases.

ELEMENT 4. BAS DRAINAGE DESIGN CONSIDERATION

One drainage condition previously observed shown in Figure 5-11 (a) concerned water infiltration at the widened joint (due to load induced movement of wing wall or settlement of BAS) between the wing wall and the BAS. This situation can be avoided by building the concrete barrier parapet directly over the edge of the BAS as shown in Figure 5-11 (b); this configuration prevents runoff water from directly infiltrating into the joint between the wing wall and the BAS [64, 65]. For precast BASs, the reinforcement for the concrete barrier parapet should be cast in the BAS like that shown in Figure 5-12 (a), which facilitates the construction of the parapet on a job site and eliminates the joint between the parapet and the BAS.

(a)

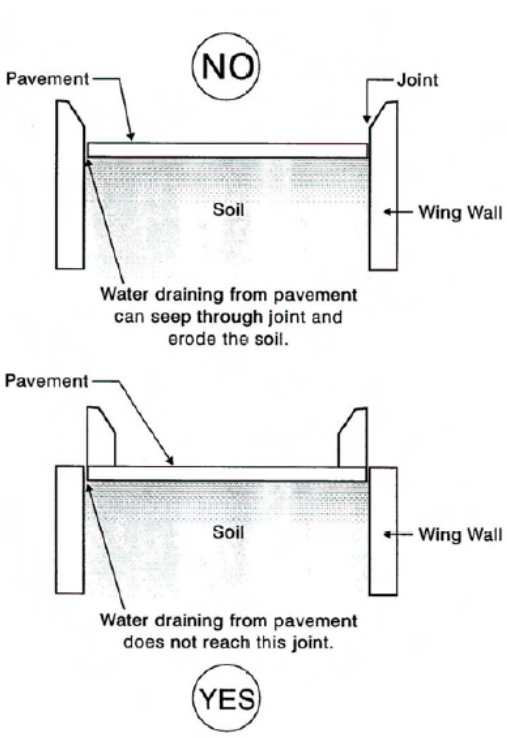

(b)

Figure 5-11 (a) Separation between wing wall and BAS [66], (b) poor and good practices of wing wall and BAS details [64, 65]

(a)

(b)

Figure 5-12 Concrete barrier parapet on precast BASs (a) during construction, (b) after construction [67]

Currently, the Oklahoma DOT standard design for BAS surface drainage relies on the use of mounted concrete curb to direct surface runoff water to a gutter system at the shoulder of the embankment area as shown in Figure 5-13. With appropriately designed slope at the surface of BASs, this design allows the runoff water to be directed away from the main pavement area to the guardrail/parapet widening area, which

appears to effectively protect the base from erosion. Therefore, this design detail is recommended for future projects. For precast BAS constructions, the reinforcement of the mounted curbs should also be cast in the precast BAS to avoid any unnecessary joints.

(a) (b)

Figure 5-13 Drainage system at the Hereford Lane site (a) location of the gutter system at the curb and (b) the gutter system at the side of the embankment

For the area subjected to heavy rainfall potential, a surface drainage inlet may be cast at the shoulder of the BAS or at the end of a bridge deck to prevent runoff water from getting into expansion joints. This type of drainage design was used at the shoulder of a BAS in Iowa as shown in Figure 5-14; White et al. [8] pointed out that the use of this large-diameter surface drainage system and the gutter system in the shoulder appeared to be effective since no soil erosion was observed underneath the BAS. A similar design was found in New Mexico at the end of a bridge deck, where a drop-inlet was used; Lenke [68] commented that this type of design functioned very well since the BASs that used this drainage design had very minimal bump issues. Note that routine maintenance may be carried out to check the drainage inlet/outlet for blockage.

(a)

(b)

Figure 5-14 Surface drainage inlets (a) at a BAS in Iowa [8] and (b) at a BAS in New Mexico [68]

ELEMENT 5. ABUTMENT DETAILS

As the supporting structure at one end of BASs, the design details selected for the abutment can play a very important role in the performance of BASs. The primary concerns for the design of abutments are the abutment back wall, the paving notch connection and the paving notch reinforcement.

Abutment Back Wall

The design details for the abutment back wall should be selected mainly based on the type of the abutment. The following provides discussions on the effects of the abutment type on the formation of the bump issue and the potential construction measures or design details that can be applied at the abutment back wall to address that issue.

Previous research studies [69, 70] have discovered that the type of the abutment (either non-integral or integral) has a clear correlation with the level of distress at BASs. Although the trend has been moving toward building more integral abutment bridges, field observations indicated [69, 71] that non-integral abutment bridges were associated with less voiding occurring underneath the BASs next to the back wall. This was probably because most of the non-integral abutment bridges were built with an expansion joint (shown in Figure 5-15) at the connection between the bridge deck and the abutment, which was able to accommodate some of the expansion and contraction of the bridge deck due to the effects of thermal variations. Although the bump issue may not be the leading distress appeared at the BASs of non-integral abutment bridges, however, the repair of the damaged expansion joints and eroded bridge bearing system can be a major cost for these bridges, which is the major reason leading to building more integral abutment bridges. If non-integral abutment bridges were built, routine maintenance has to be conducted for the expansion joints to avoid leaking, clogging and accumulation of debris.

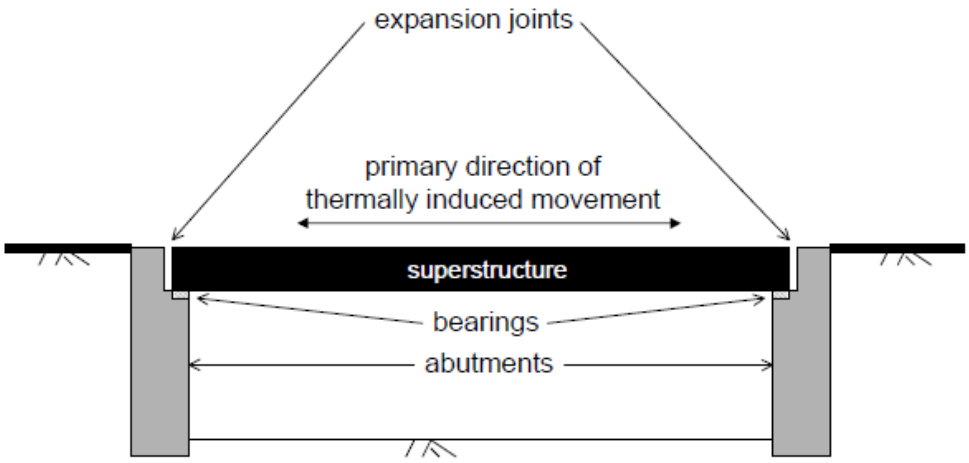

Figure 5-15 Conventional non-integral abutment bridges [72]

Integral abutment bridges have now become more preferred than the conventional non-integral abutment bridges due to the lower construction and maintenance costs as a result of eliminating expansion joints [70]. However, field investigations [73] indicated that voids tended to occur underneath the BAS (especially behind the back wall of the abutment) for integral abutment bridges and the magnitude of the voids generally increased with the increase of the bridge length. This is probably due to the mechanism shown in Figure 5-16 [70]: the daily and seasonal changes in the temperature and moisture lead to the expansion and contraction of the bridge structure, which forces the abutment to translate or rotate back and forth relative to the embankment backfill; the cyclic movement (especially when the abutment moves away from the backfill during winter as the bridge structure contracts) will mobilize active earth pressure on the abutment when the backfill soil tends to move downward and toward the abutment. The movement of the backfill soil can be one of the major reasons to account for the formation of the voids underneath the BASs, especially the ones localized near the back wall of the abutment as shown in Figure 5-16.

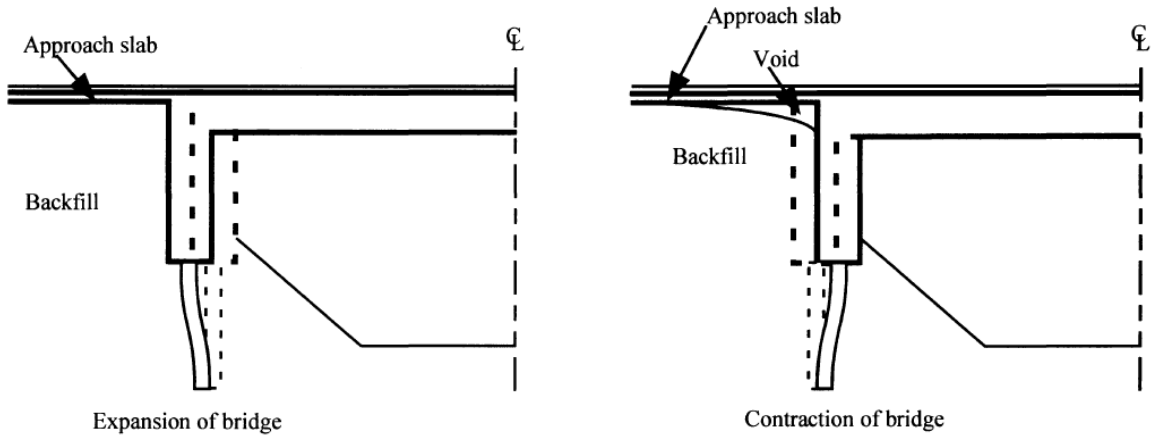

Figure 5-16 A potential mechanism leading to the formation of voids underneath BASs [70]

In addition to designing sufficient length of PPCP BASs (as a means to limit the movement of the abutment as was elaborated in Chapter 3), previous research [72] suggested that attaching a layer of compressible inclusion on the face of the abutment back wall might be able to absorb portion of the cyclic thermal movement of the integral abutment and therefore avoiding the occurrence of the voiding underneath the BAS. Field implementations conducted by the Virginia Transportation Research Council [74-76] made the first few attempts to use expanded polystyrene (EPS) geofoam at the abutment back wall of integral abutment bridges, such as the one shown in Figure 5-17. In this field implementation of a 110 ft. long semi-integral bridge [76], a densely compacted aggregate material (well-graded crushed stone type) was used as the base for the roadway pavement in conjunction with the use of a 15 in. EPS geofoam which was covered by a layer of composite drainage fabric as a means to facilitate drainage at the abutment back wall. The compressible inclusion material has been selected to be able to remain elastic within the range of the thermal induced movement and to have minimal long-term creep. Elasticized EPS was identified as the appropriate material since it exhibits linear elastic behavior up to about 10% strain (whereas regular EPS only reaches to 1% strain). A formula was developed to calculate the thickness of the EPS geofoam [76]:

$$EPS_t = 10 \times (0.01 \times h + 0.67 \times \Delta L) \quad (5\text{-}1)$$

where EPS_t is the required thickness of the EPS in inches (should be greater than 10 in.), h is the height of the abutment (in inches) and ΔL is the total thermal induced movement at the abutment (in inches).The field monitoring lasted 5 years and the collected results indicated that the use of the elasticized EPS has significantly reduced the earth pressure on the abutment, which led to negligible settlement issue near the abutment back wall and even the elimination of the need for using reinforcement in BASs. Therefore, the elasticized EPS geofoam is recommended to be used for integral abutment bridges.

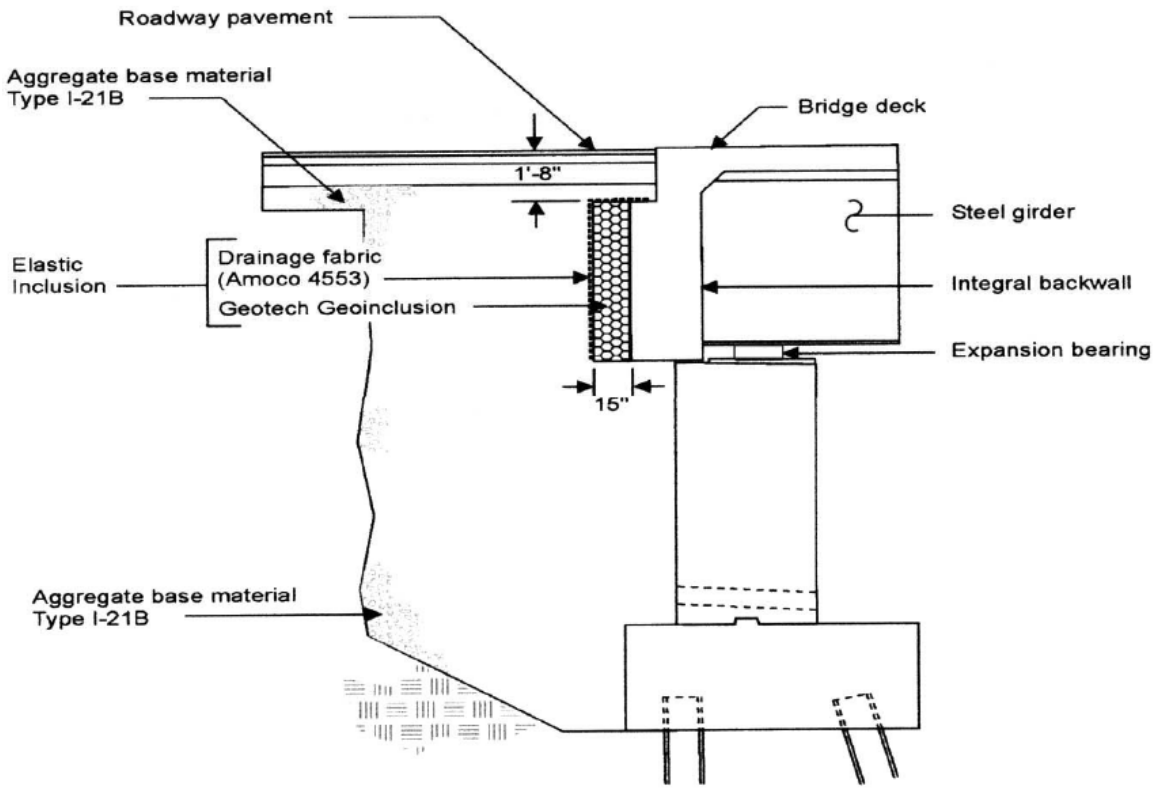

Figure 5-17 Use of elastic inclusion at the abutment back wall [76]

Experience of Virginia Transportation Research Council [74-76] also indicated that the combination of using EPS geofoam and well-compacted granular backfill yields a cost-effective option to minimize voiding.

Selection criteria

The criteria for using the EPS geofoam design detail:

- For integral abutment bridges;
- For achieving higher level of design assurance.

Currently, using CLSM at the back wall of the abutment is a standard practice in Oklahoma, however, the compatibility and applicability of using EPS geofoam in between the CLSM and the abutment back wall has not been validated under field conditions. Due to lack of field implementations and experience in Oklahoma, this design detail is only a recommendation.

Paving Notch Connection

The paving notch connection refers to the reinforcement used at the connection between the BAS and abutment. The connection is installed mainly due to the concerns regarding the opening of the joint between the BAS and the abutment. Without using reinforcements at this connection, the width of the joint may gradually become wider when the bridge structure starts to contract during the winter while the friction at the BAS-base interface restrains the BAS from moving with the bridge. When the joint becomes wide enough, water can infiltrate into the joint easily leading to erosion if subsurface drainage is not provided.

Previous research [9] indicated that two types of paving notch connections were widely used in the states as shown in Figure 5-19. The first option is to horizontally connect the BAS to the bridge deck through the extension of the bridge deck reinforcement or the use of deformed steel bars. However, in some cases it was reported that this type of connection may lead to transverse cracking near the BAS-bridge deck connection, especially if the horizontal reinforcement connection is placed at a shallow depth in the concrete. It was suggested [57] that the cause of the transverse cracking was likely due to the fact that the horizontal reinforcement connection was not able to sustain the bending moment induced by the rotation of the BAS (upon traffic loading) as a result of loss of base support underneath the BAS.

South Dakota DOT's experience [57] indicated that if this option is used, the horizontal reinforcement connection should be placed deeper in the slab to avoid transverse cracking that may occur at the surface of the BAS. The current standard design detail for this connection in Oklahoma as shown in Figure 5-18 also addresses the position of the reinforcement; in this detail, a mechanical splice is used to connect the reinforcement extended from the bridge deck to that in the BAS and the position of the reinforcement in the BAS is about the same depth as the bottom reinforcement.

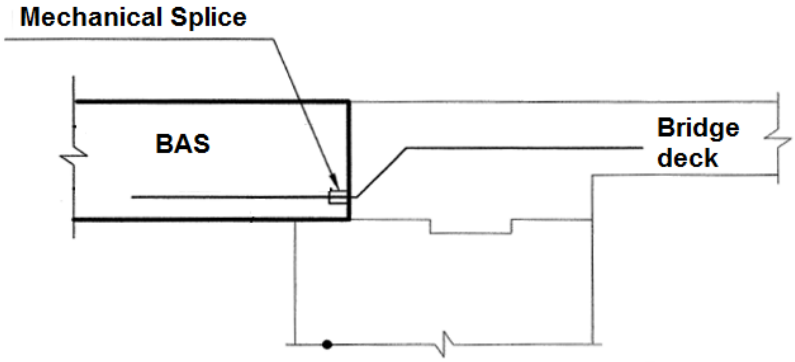

Figure 5-18 Standard design detail for the paving notch connection in Oklahoma [2]

The second option is to extend a reinforcement bar diagonally from the paving notch of the abutment to the BAS as shown in Figure 5-19 (b). It was reported by Minnesota DOT [57] that the use of this configuration in lieu of the first option (i.e. the horizontal reinforcement connection) has effectively reduced the rotational resistance caused by the horizontal reinforcement connection in the first option and no more transverse cracking was observed afterwards.

Note that if the BAS is connected to the bridge deck using either one of the two options for integral abutment bridges, the BAS should be considered as an extension of the bridge deck which moves as the bridge structure expands or contracts due to the effects of temperature and moisture variations. In this case, an expansion joint should be placed at the BAS-pavement connection to accommodate the movement of the bridge structure. In fact, it was reported by some DOTs that the bump-at-the-end-of-the-bridge problem can be transferred to the BAS-pavement connection as a result of connecting the BAS to the bridge deck for integral abutment bridges; this however may

be beneficial for the maintenance team because it is much easier and cost-effective to deal with issues of pavements than issues of bridge structures.

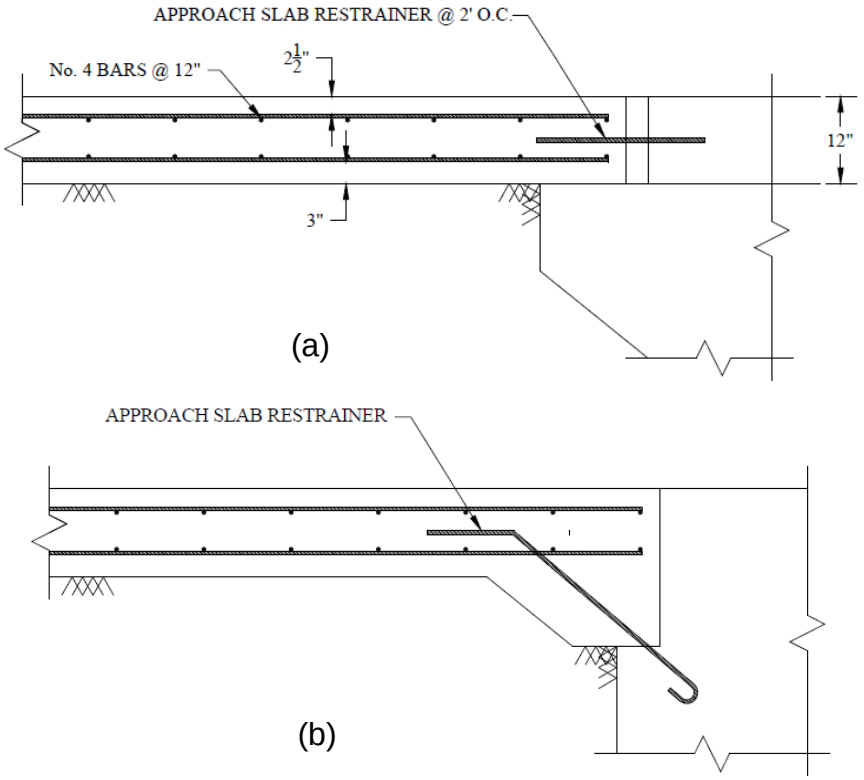

Figure 5-19 Two types of paving notch connections (a) bridge deck extension connection (b) abutment connection [9]

Selection criteria

Although both the two options yielded satisfying performance in the application of CIP BASs based on the past field experience [9], details may need to be modified for the construction of precast BASs.

For the construction of JPrCP BAS, the horizontal reinforcement connection can be applied based on the past experience [66] where #8 epoxy-coated deformed steel bars are cast in the bridge deck as shown in Figure 5-20. For a project in which the deformed steel bar connections are not cast in the bridge deck, the contractor needs to saw cut on the edge of the bridge deck or drill holes to accommodate the placement of steel bars and the opened slots will be filled with grout once the placement is finished. Although no record was found in the literature with respect to the use of the diagonal

reinforcement bar as the connection for precast BAS and abutment, it may also be applied similarly by drilling holes in the paving notch of the abutment as a means to install the diagonal bars. It should be noted that, if either the horizontal or diagonal reinforcement bars are used as the connection, the BAS has to contain a slot system (such as the one shown in Figure 3-4) to help with enclosing the connection bars installed on the abutment during the panel installation. These slot systems should be filled with rapid-setting materials once the BAS is placed on the paving notch.

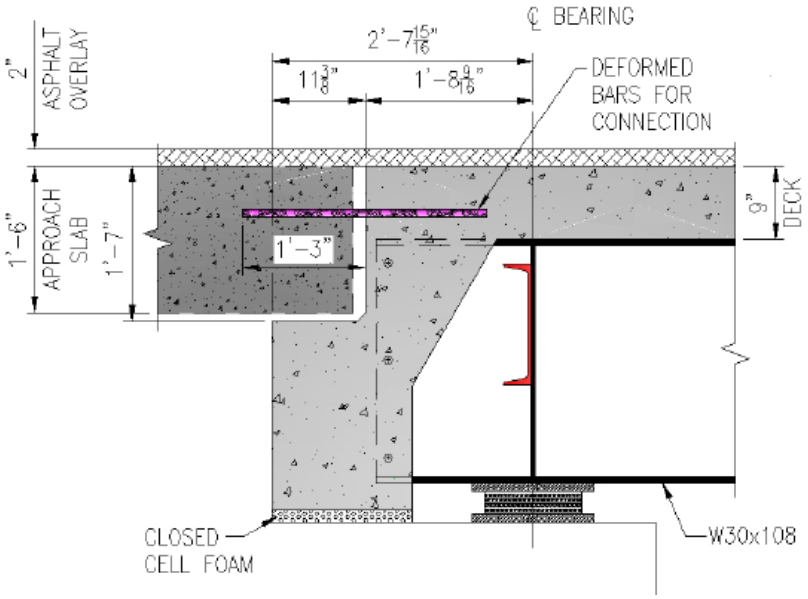

Figure 5-20 Design details of JPrCP BAS – bridge deck connection [66]

For the construction of PPCP BAS, the preferred solution is the application of vertical anchor bars as shown in Figure 5-21 which may be considered as a modification of the diagonal reinforcement connection. After pouring non-shrink grout into the anchor hole, the vertical anchor bars will be inserted into the anchor sleeves (cast into panel) during the construction (before performing final longitudinal post-tensioning [11]) as a mean to connect the BAS and the abutment. The installation of the vertical anchor bars for PPCP BAS will help to prevent movement of the BAS relative to the abutment when performing post-tensioning longitudinally along the BAS during the construction, which is the reason that this design detail is recommended for connecting the PPCP BAS with the abutment.

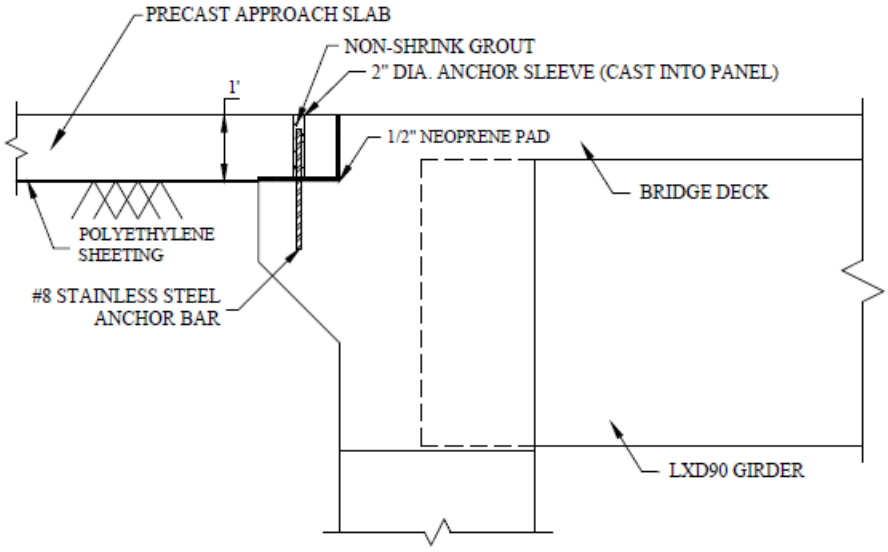

Figure 5-21 Vertical reinforcement connection between the BAS and abutment [9]

Paving Notch Reinforcement

Although not normally drawing much attention from engineers in regard to the performance of BASs, shear failure at the edge of the abutment paving notch can be one of the sources leading to the bump at BASs. It was suggested that, as shown in Figure 5-22, unreinforced concrete segments at the edge of the abutment paving notch may potentially fail due to direct shear mechanism; therefore, the practitioner may need to employ a structural engineer to appropriately design the location and size of the reinforcement in the abutment in order to prevent those shear failures.

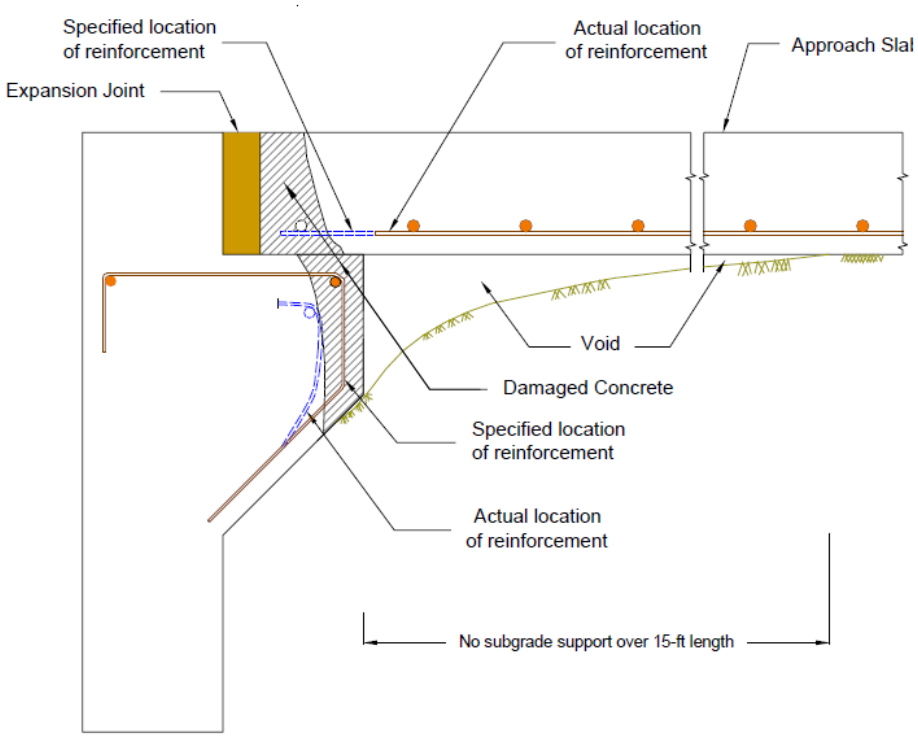

Figure 5-22 Inappropriate placement of reinforcement in the paving notch and BAS [8]

White et al. [8] conducted both field investigations and analytical analyses on the performance of paving notches. Based on the field investigations, poor construction quality including sloping paving notch surface and inadequate consolidation of the concrete were the potential issues for newly constructed paving notches; for existing BASs, shear failure at the edge of the paving notches was suspected to account for some of the settlements underneath the BASs. In order to better understand the failure mechanism of the paving notches, White et al. [8] also performed FEM and strut-and-tie model analyses (shown in Figure 5-23) to evaluate the design capacity of the paving notch reinforcement by considering the worst case scenario where the BAS was assumed to be simply supported with no soil contact in between the two supporting ends. Results indicated that shear failure of reinforced section of the paving notch was not likely to happen because the reinforcement design was sufficient; however, it was suggested that the vertical tension reinforcement (such as BA and AA' shown in Figure 5-23) should be increased to at least #7 bars @12 inches to avoid tension failure. In the

end, it was concluded that the shear failure at the unreinforced edge segments (i.e. the concrete cover for reinforcement CD) of the paving notch might have occurred mainly due to the dynamic traffic load effects and poor construction quality.

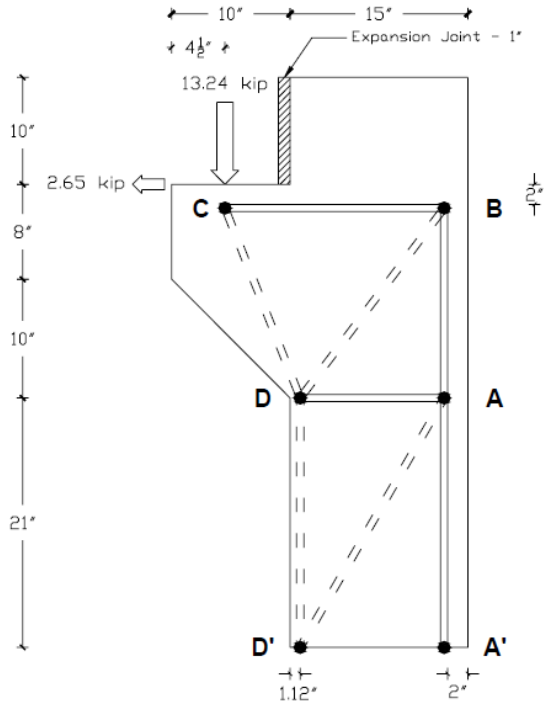

Figure 5-23 Strut-and-tie model developed based on finite element analysis results [8]

Although the failure of paving notch was not identified as a source leading to the bump issue at the BASs in Oklahoma based on the past field investigations (probably due to the difficulty in evaluating the paving notch condition unless the BAS is demolished), the following are recommended for the future BAS construction before a precast BAS is placed:

1. The construction quality control of the paving notch should be better conducted during the construction with respect to:
    - The levelness and smoothness of the paving notch;
    - The uniformity of the concrete mixture in the paving notch;
    - The quality of the concrete consolidation.
2. A 0.5 in. neoprene pad may be placed on the paving notch to provide a more uniform support for precast BASs [11];

3. Include drainage design details in the paving notch to help with draining infiltrated water and prevent deterioration of the concrete.

ELEMENT 6. WING WALL DETAILS

Wing walls are routinely used for integral abutment bridges, not designed to directly carry any traffic loads, but as a means to retain and provide additional stability for the embankment backfill material. Although not deemed as important as the abutment with respect to sustaining traffic loads, the configuration (i.e. size, capacity and geometry) of the wing walls may have some impact on the performance of the BAS [77]. Some literature suggested that the use of wing walls can reduce the erosion and settlement possibilities underneath the BAS [64, 68]. In general, the wing walls can be divided into two categories, integral and non-integral, which are elaborated in the following section.

Integral Wing Wall

An integral wing wall is the one built integrally with the stem of the abutment; as a result, the wing wall and the abutment move together. In terms of the geometry, wing walls can be classified into three different types, which are in-line wing walls, flared wing walls and U-wing walls [77] as shown in Figure 5-24. The figure also shows the directions of the rotation and translation of the abutment-wing wall structure.

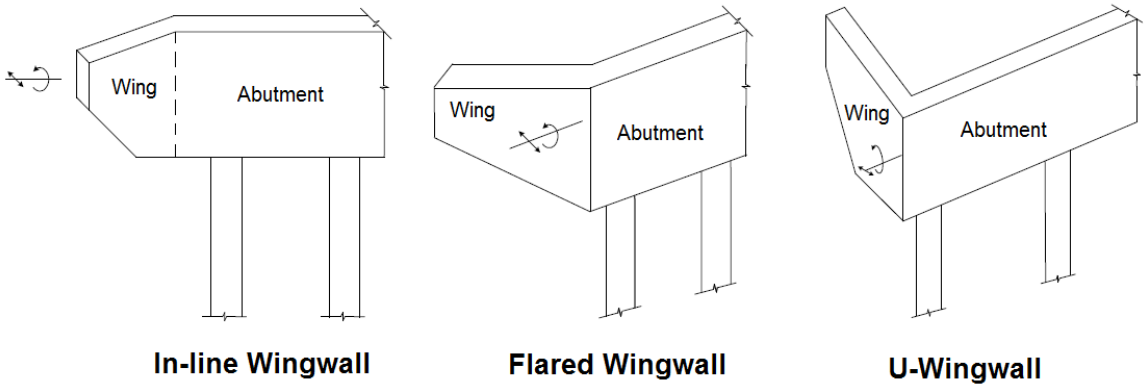

Figure 5-24 Wing wall types in terms of geometry [77]

Type selection

Based on a survey [77] conducted to study the integral wing wall designs in 34 U.S. transportation agencies, it was found that 64.5% permit the use of in-line wing walls, 32.3% for flared wing walls and 80.6% for U-wing walls. Although it appears that the U-wing walls are the most prevalent type, in fact, very limited consensus was achieved among the agencies with respect to the selection of wing wall geometry. For instance, some agencies (such as NYSDOT [78]) consider the in-line wing walls to be the first option and U-wing walls are not allowed to be used unless neither the in-line nor the flared wing walls can be used due to right-of-way or wetlands encroachment; other agencies (such as NDOT [79]) consistently use U-wing walls as the first option and only use flared wing walls in combination with box culverts; in fact, very few state agencies offer thorough design considerations for the wing wall with respect to its effect on the overall performance of the bridge structure (including BASs) [77].

A previous research [80] indicated that the orientation of the wing wall can affect the distribution of the earth pressure of the embankment backfill soils. A later field investigation conducted by Thompson [81] indicated that the wing wall geometry has a confinement effect on the embankment backfill soil where the U-wing wall provides the greatest confinement and the in-line wing wall has the least confinement effect. Greater confinement leads to greater octahedral stress developed in the embankment backfill soil when the abutment translates or rotates horizontally (i.e. parallel to the direction of roadway centerline) into the backfill soil. Under that stress induced by the movement of the abutment, the embankment backfill soil tends to expand in the lateral direction (i.e. perpendicular to the direction of roadway centerline). However, because the integral wing walls are not able to rotate in the lateral direction (being physically attached to the abutment), the lateral confinement stress will build up which generates restraint against the further rotation of the abutment. This mechanism has been also verified by FEM investigations conducted by other researchers [82]. Because the U-wing wall can theoretically provide the greatest benefits with respect to restraining the movement of the abutment (as one of the major reasons leading to the settlement issue underneath the BAS) comparing to other wing wall types, it should be the most effective type to prevent settlement and bump issues at BASs.

A drawback of using the U-wing wall is that it can be difficult to conduct compaction for the backfill soil near the abutment back wall due to the confined space. Usually, the compaction near the faces of the abutment and wing walls are conducted using small vibratory rollers or handhold vibratory plates to avoid damaging or inducing movement of the structures [83]. Some state agencies reported that larger BAS settlement was discovered for bridges with wing walls comparing to bridges without wing walls due to the inadequate compaction of the backfill soils [57].

In order to avoid the difficulties encountered during the compaction of the backfill material, state agencies started to use CLSM and similar technologies in lieu of the conventional granular backfill material. In this case, the U-wing wall functions as a retaining structure to facilitate the placement of CLSM, which is the practice that Oklahoma DOT has consistently applied in recent years. Different from that of the conventional granular backfill soils, the pattern of the pressure distribution in the CLSM can be much different since a CLSM does not behave like soils. In fact, when the CLSM is in the flowable stage, it behaves much like water which exerts hydrostatic pressure on the retaining structure; when the CLSM gets hardened, it behaves much like a concrete which does not produce any active or passive pressure on the retaining structure. Therefore, the wing wall – abutment connection should be designed with adequate capacity to sustain the lateral bending moment induced by the flowable CLSM, which is usually not a major design concern for integral wing walls with limited length and height.

Distress mechanism and treatment

Field investigations conducted in Ohio [57] found that horizontal separation between BASs and wing walls may sometimes occur which led to drainage and erosion possibilities. A representation of this issue is shown in Figure 5-25 where a 20 in. deep void was discovered at the gap between the wing wall and the BAS. An effective method to alleviate this issue was addressed earlier as shown in Figure 5-11 where concrete guard rails should be constructed at the edge of the BAS to prevent surface runoff water from directly flowing into the joint between the BAS and the wing wall.

Figure 5-25 Separation between the wing wall and the BAS in Ohio [57]

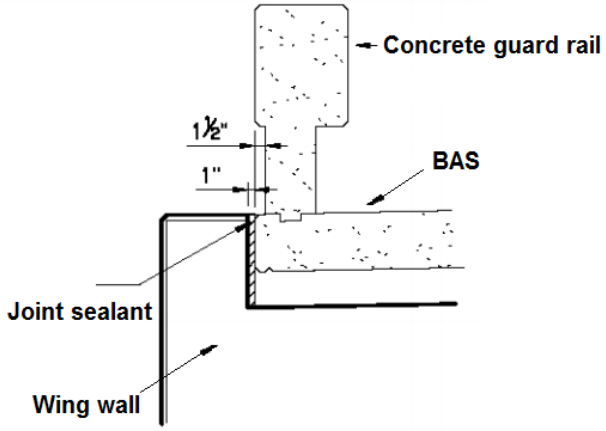

Figure 5-26 Design details of the concrete guard rail by Oklahoma DOT [2]

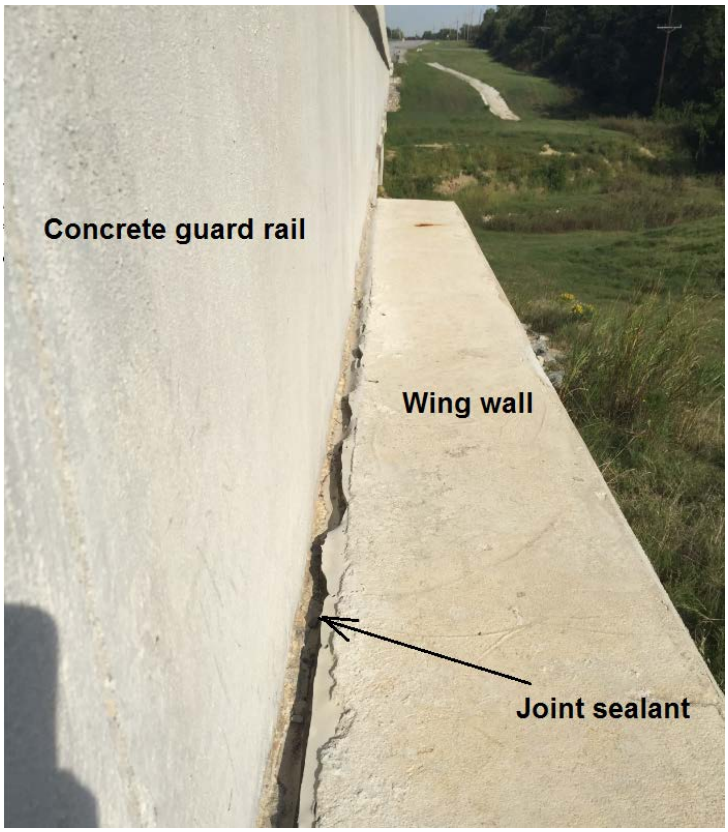

Figure 5-27 Separation between wing wall and BAS in Oklahoma

Although having adopted the concrete guard rail practice as shown in Figure 5-26, similar phenomenon (i.e. separation between wing wall and BAS as shown in Figure 5-27) was still extensively observed during the field investigations conducted in Oklahoma [35]. It was found that the joint sealant at the connection between the BAS and the wing wall was deteriorating and falling apart; when the opening becomes large enough, rainwater may infiltrate into the opening causing potential erosion possibilities in the embankment, which could eventually lead to even worse issues such as settlement of the embankment and bump issues at the BAS.

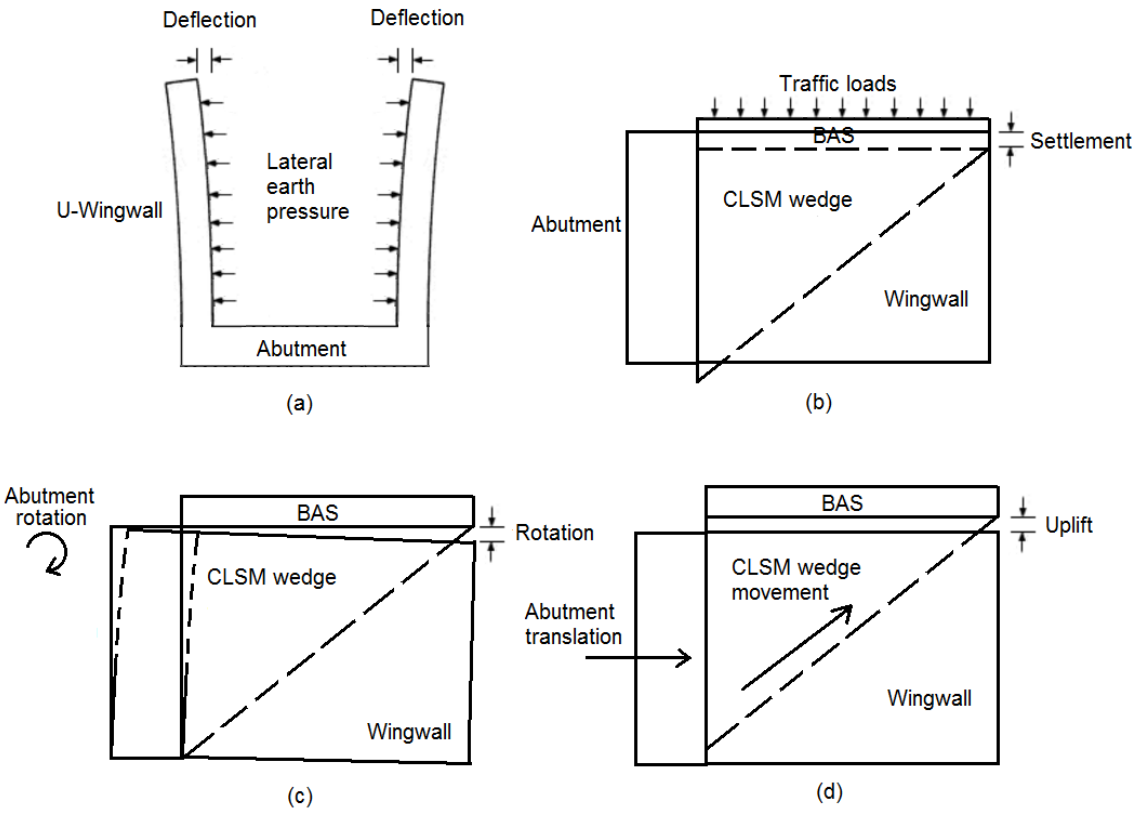

Figure 5-28 Potential mechanisms leading to the wing wall-BAS separation (a) wing wall deflection (b) foundation settlement (c) abutment rotation and (d) abutment translation

This phenomenon was probably due to the combined effect of a few different mechanisms illustrated as shown in Figure 5-28. The first possible mechanism, although not applied to the case when CLSM is used, may be related to the lateral earth pressures induced by the embankment backfill soils which creates large bending moment and causes the wing wall to deflect away from the BAS structure. Therefore, the practitioner should employ a structural engineer to design the length and height of the wing wall in order to avoid the problem, or to appropriately design the reinforcement at the junction between the wing wall and the abutment to prevent the junction from cracking. The second possible mechanism could be the settling of the BAS structure due to the settlement of the foundation soil or the consolidation of the embankment backfill material (if it is a compressible type) under the effect of traffic loads; this issue

can be alleviated by applying ground improvement techniques such as the use of stone columns in the foundation soil and the use of CLSM or EPS geofoam wedge as the embankment backfill material to avoid the potential consolidation induced settlement. The third potential mechanism could be related to the rotational movement (either clockwise or counter-clockwise) of the abutment-wing wall structure as a result of the expansion or contraction of the bridge deck due to the effects of daily and seasonal temperature and moisture variations as shown in Figure 5-28 (c). The last potential mechanism may be due to the translational movement of the abutment-wing wall structure (also a result of the thermal and moisture movement of the bridge structure) which forces the CLSM wedge to climb up the slope of the embankment.

There are a few practices can potentially be applied to alleviate the issues caused by the third and fourth mechanisms. First, applying PPCP as the BAS for integral abutment bridges and appropriately design the length of it can help to restrain the movement of the integral abutment as was discussed in Chapter 3. Second, a compressible inclusion may be installed in between the abutment and the backfill to absorb the movement of the abutment as shown in Figure 5-17. Third, piles may be placed underneath the wing walls to prevent rotational movement of the wing wall as shown in Figure 5-29. Note that, in this case, the rotational movement of the abutment is restricted, which can lead to greater end bending moment for the bridge beams and bending and shear forces for the wing wall [77]. Due to these concerns, the previous survey [77] indicates that, out of the agencies that permit the use of U-wing walls, 80% of them prohibit the application of this option such as NYSDOT [78]; the other 20% agencies indicate that their bridge and wing wall designs are capable of handling those additional stresses induced due to restraining the rotational movement of wing wall based on field observations on the structure performance in their states. Third, another potential solution is to build non-integral wing walls such that they do not move when the abutment moves, which is elaborated in the following section.

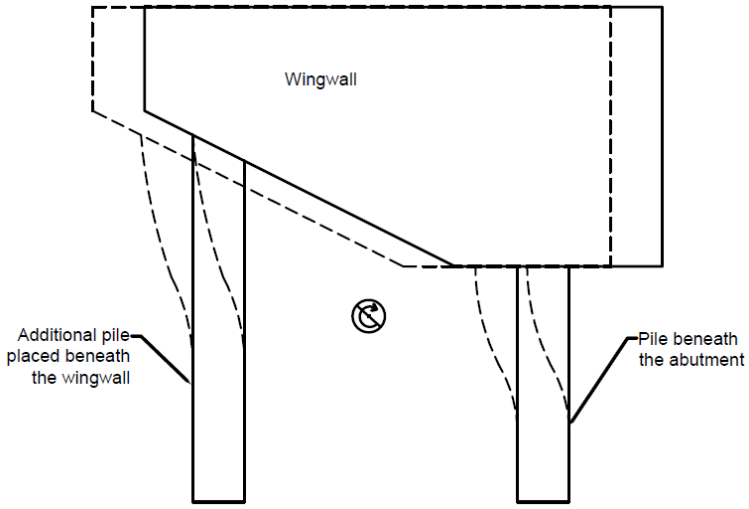

Figure 5-29 Pile supported U-wing wall [77]

Note that one type of wing wall design should be avoided based on the experience in Texas, which is to construct the BASs directly on top of the wing walls. In that case, indicated by TxDOT [31], the BAS may eventually become a slab only supported on the three edges (i.e. the paving notch on the abutment and the two wing walls on each side) if the embankment backfill settles over time, which are not the boundary conditions that BASs and wing walls are designed for (the wing walls are not designed to sustain traffic loads) and will lead to damage of the structures.

Non-Integral Wing wall

Non-integral wing walls are also built by some agencies in the U.S. based on the survey conducted by White [77]. Out of the 34 agencies, 35.5% permit the use of non-integral in-line wing walls, 58.1% permit U-wing walls and 41.9% for flared wing walls. These wing walls are built independently without directly connecting to the abutment; therefore, they are normally designed like a retaining wall with their own foundations to avoid rotation, which however may not yield the most economical solution due to the extra cost on the foundation. Non-integral wing walls are usually used when the wing wall is too long or too high to be designed like an integral wing wall; however, states like

Michigan and Nebraska regulate that only non-integral wing walls can be used for integral abutment bridges regardless of the length of the wing wall [77].

As indicated previously, one notable feature of non-integral wing walls is that they do not move as the abutment moves, which is important for keeping the tightness of the wing wall-BAS joint and prevent drainage and erosion issues. Because the non-integral wing walls are not attached to the abutment, the construction joint between them requires special design considerations. This joint should allow for the movement of the abutment without causing too much interfacial friction as well as maintaining appropriate degree of tightness over the life of the bridge. Generally, an expansion joint or a mortar joint is used at this junction [79, 84] along with some kind of waterproofing membranes to prevent water infiltration. In addition, a layer of geocomposite vertical drain system may be installed to facilitate drainage at this location. A typical design (by Pennsylvania DOT [85]) of the wing wall-abutment joint is shown in Figure 5-30.

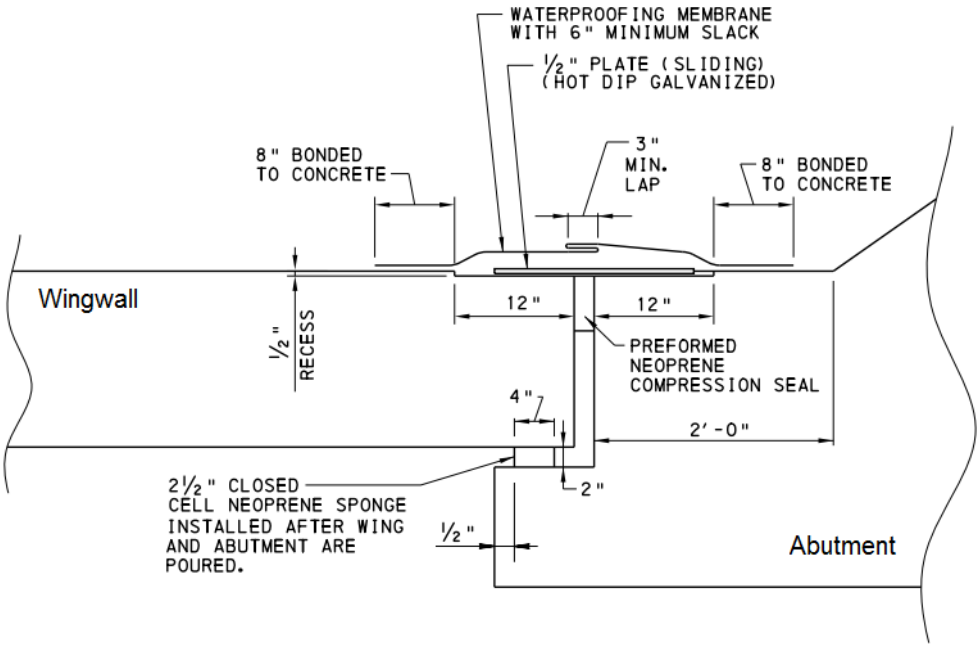

Figure 5-30 Design details of wing wall-abutment joint [85]

Although using non-integral wing wall may potentially be a viable option to prevent the separation at the wing wall-BAS joint which is one of the most prevalent distress types found in Oklahoma, however, it is still debatable with respect to the benefits of using non-integral wing wall. First, the introduction of non-integral wing walls

can incur new issues at the wing wall-abutment joint which may be even worse than those at the wing wall-BAS joint. Second, an integral abutment with non-integral wing walls may have greater thermal induced movement comparing to an abutment with integral wing walls due to the fact that integral wing walls can provide greater restraint against that type of movement as was discussed earlier; the greater movement of the abutment may lead to greater movement at the BAS, thus still resulting in tearing of the joint sealant and separation at the wing wall-BAS joint regardless if non-integral wing walls are used.

Selection Criteria

In terms of selecting the shape of the wing wall, it appears that U-wing walls are the most widely accepted type in the U.S. regardless if it is integral or non-integral wing wall based on the survey conducted in the 34 transportation agencies. In addition, the U-wing wall was determined to theoretically provide the greatest benefits with respect to restraining the movement of the abutment (thus preventing bump issues at the BAS) comparing to other wing wall types. Therefore, the U-wing wall is recommended to be consistently constructed whenever an integral abutment bridge is built.

In terms of selecting the type of the wing wall (either integral or non-integral), the practitioner should be aware that both the two types of wing walls can potentially experience issues at the junction with the adjoining structures, such as at the wing wall-BAS joint (for integral) or at the abutment-wing wall joint (for non-integral). In most cases, the occurrence of the separation between the wing wall and the adjoining structure is not dictated by the type of the wing wall; rather, the very essential reasons are usually related to the movement of the adjoining structure, such as the thermal induced movement of the integral abutment or the settlement of the BAS due to the settlement of its supporting structure. Therefore, in order to prevent the separation between the wing wall and its adjoining structure, the design engineers should focus on selecting the practices that will limit the movement of the adjoining structures, such as:

- Use a layer of compressible inclusion to absorb the translational movement of the integral abutment;

- Place piles underneath the integral wing walls to prevent the rotational movement of the integral abutment;
- Use stone columns in the foundation soil to reduce foundation settlement;
- Use a CLSM or EPS geofoam wedge as the embankment backfill to reduce the settlement of the embankment.

ELEMENT 7. SUBSURFACE DRAINAGE SYSTEM

With many efforts made to direct runoff water away from the surface of BASs, properly designed subsurface drainage system also plays a significant role in preventing the erosion of subsurface foundation materials.

Subsurface drainage in Oklahoma involves the use of a perforated pipe underdrain right underneath the CLSM wedge behind abutment, which is enclosed by filter sand, coarse underdrain cover material with filter fabric wrapping around. However, this standard design sometimes does not appear to prevent water from flowing underneath the abutment which creates substantial soil erosion problems such as the ones shown in Figure 5-31.

The research conducted by Miller et al. [66] investigated the erosion problem underneath the abutment and pointed out that the problem was probably due to a hydraulic short circuit (shown in Figure 5-32) developed underneath the abutment, which allowed water to bypass the drainage pipe and flow through the gap underneath the abutment leading to substantial erosion over time.

(a) (b)

Figure 5-31 Examples of erosion underneath abutment problem in Oklahoma [66]

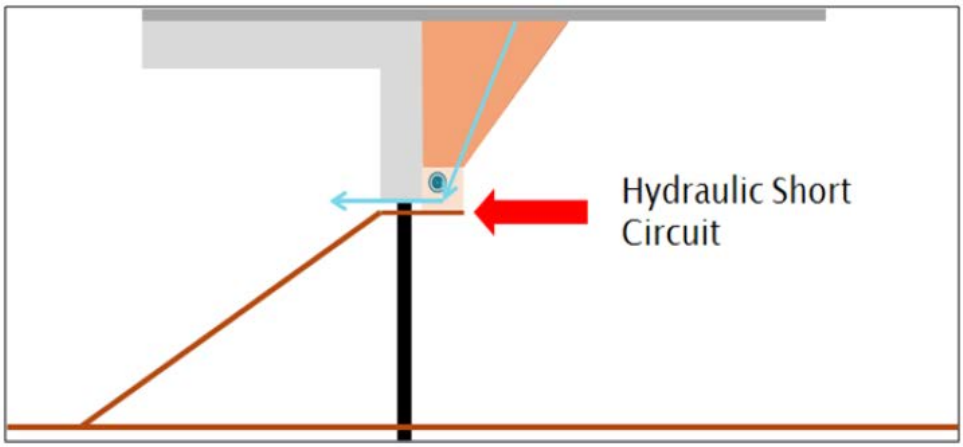

Figure 5-32 Hydraulic short circuit developing mechanism underneath the abutment drainage system [66]

Based on a previous field investigation where it was found that the use of water stop in the subsurface drainage system appeared to have good performance, Miller et al. [66] modified the standard details by introducing a geomembrane as a water stop at the interface between the abutment and the underdrain cover material to prevent the erosion problem of the backfill material (mainly granular material) due to the developed hydraulic short circuit. A detail of such system is shown in Figure 5-33. This detail seems reasonable to solve the problem, although special attention needs to be paid to the vertical movement of the geomembrane relative to the abutment; geomembrane with high elongation potential may be used to address the issue [66].

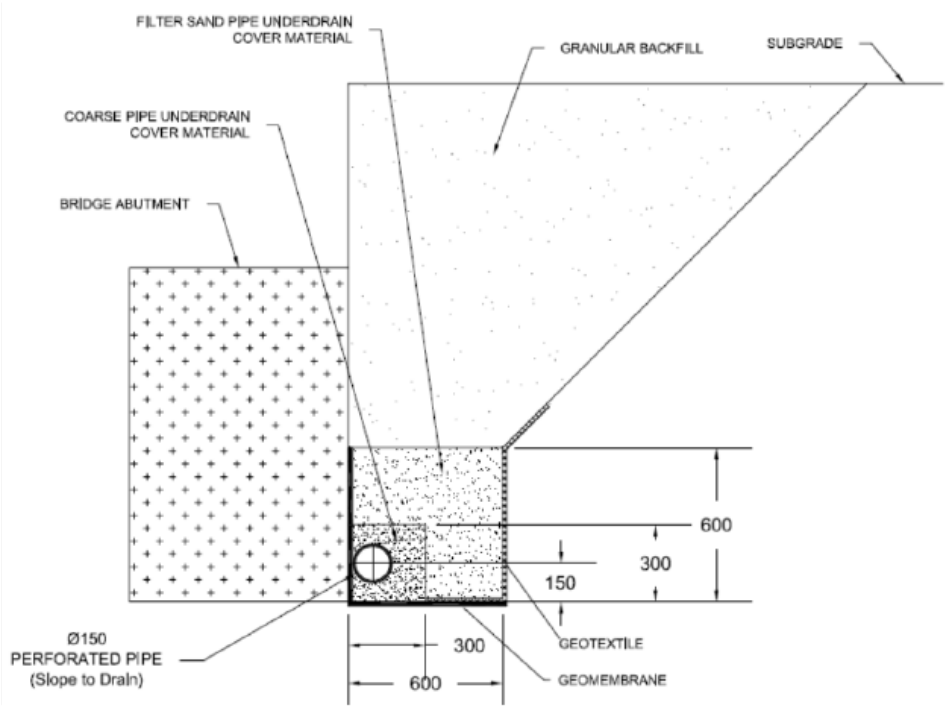

Figure 5-33 Abutment backfill drainage system with geomembrane proposed by Miller et al. [66]

Details from other state DOTs may also be adopted to address the subsurface drainage issue. White et al. [8] conducted laboratory testing and found that the use of a geocomposite vertical drain system as shown in Figure 5-34 significantly increased the capacity of drainage behind abutment. These geocomposite are made from different types of polymeric drainage cores which are covered by geo-textile filters. Once the geocomposite vertical drain system is installed at the face of the abutment, it behaves like an open channel to facilitate drainage [86]. It appears that this approach may be integrated into the design details of the subsurface drainage design in Oklahoma to better transport water into the subsurface underdrain.

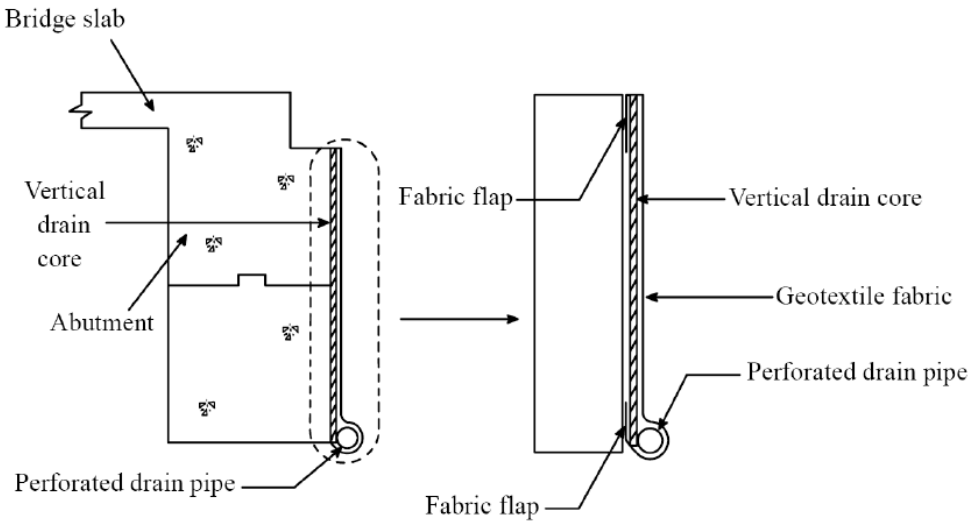

Figure 5-34 Schematic diagram of the use of vertical drain behind abutment [8]

Another practice which was proposed by the Colorado Department of Transportation (CDOT) to improve the subsurface drainage can be illustrated as shown in Figure 5-35. In this practice, the subsurface drainage pipe is placed at the bottom of a "V" shape groove made behind the abutment wall; it appears that this practice can effectively prevent the hydraulic short circuit (which causes erosion at the bottom of the abutment) from occurring if the configuration of the groove and the capacity of the drainage pipe are well-designed. In addition to the drainage pipe placed at the bottom of the backfill, CDOT also placed another one at the shallow depth of the backfill behind the abutment, which helps to collect any water leaking into the expansion joint at the bridge deck - BAS connection. Also, a layer of polystyrene vertical drain is placed at the face of the abutment wall to direct any leaking water to the subsurface underdrain. This subsurface drainage scheme seems to be very effective since it provides a double-insurance to prevent erosion from taking place underneath the abutment wall.

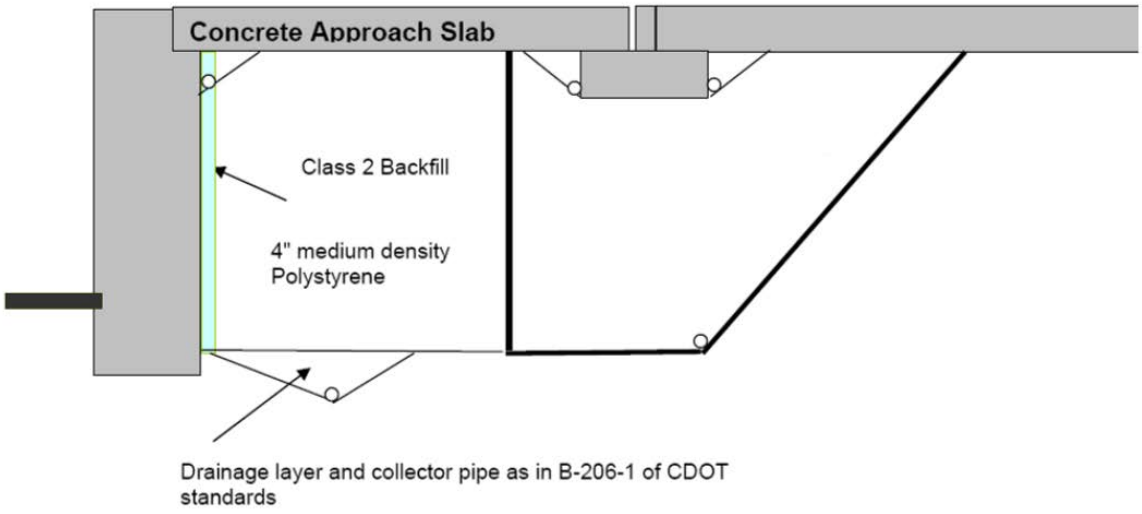

Figure 5-35 the subsurface drainage system provided by CDOT [87]

Selection Criteria

Since it is a standard practice in Oklahoma, the subsurface drainage system should be consistently applied in the embankment construction. This research recommends that the standard detail should be modified to include the features of the geomembrane water stop and the “V” shape groove as shown in Figure 5-33 and Figure 5-35, respectively.

The geocomposite vertical drain system may also be used if:

- The construction area is subjected to heavy rainfall potential;
- The practitioner wants to further increase the design reliability with respect to minimizing the erosion in the embankment.

ELEMENT 8. EMBANKMENT BACKFILL WEDGE

The selection of the embankment backfill wedge material behind the abutment can significantly influence the performance of BASs considering its effect on the erosion or settlement related problems occurring underneath BASs.

The embankment backfill material should be selected based on the following considerations:

- Less compressibility to avoid settlement issues;
- Less erodibility to prevent erosion issues (Figure 5-36 shows the range of most erodible soils);
- Greater modulus to provide a strong support for the BAS; and
- Better drainability to facilitate subsurface drainage.

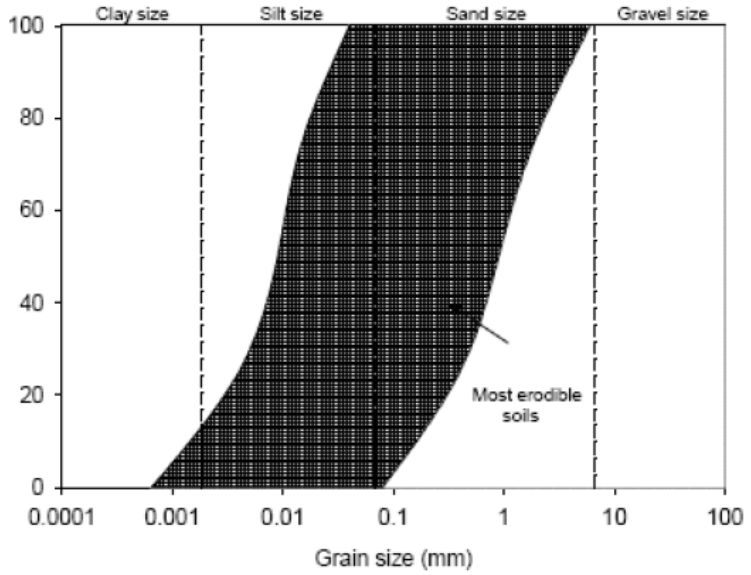

Figure 5-36 Grain size range of most erodible soils [68]

In the past, Oklahoma has been using granular materials as the backfill; however, due to the fact that the granular materials undergo significant amount of settlement upon wetting, now they have been gradually replaced by the controlled low strength material (CLSM) which is also referred to as the flowable fill. A detailed illustration of the CLSM underneath a BAS is shown in Figure 5-37. The CLSM has a couple of notable advantages comparing to granular backfill materials; first, it has

negligible consolidation settlement attributed to its low compressibility; second, it does not require compaction that can be very difficult to conduct especially near the abutment wall; third, it has much less erodibility comparing to granular soils; fourth, it can provide adequate strength equivalent to or greater than well compacted granular soils. In addition, the permeability of CLSM can be designed with huge flexibility; it is recommended that the permeability of the CLSM should be designed at least greater than that of the surrounding soil to facilitate subsurface drainage [88].

In this regard, it appears that the use of CLSM as the backfill behind abutment is a viable option to provide satisfying performance with respect to preventing consolidation induced settlement problems as well as facilitating drainage. In the case where CLSM is designed with drainage capability (i.e. by appropriately designing its permeability) in combination with the use of well-designed subsurface drainage system underneath it, accumulation of infiltrated runoff water at the bottom of a BAS (which may lead to erosion of the CLSM and exacerbation of the distress at the BAS) can be prevented. If the CLSM is designed impermeable, a drainable base layer and edge drains should be used to prevent infiltrated runoff water from accumulating underneath the BAS. Although the initial cost may be high, the application of CLSM is highly recommended considering all the aforementioned benefits.

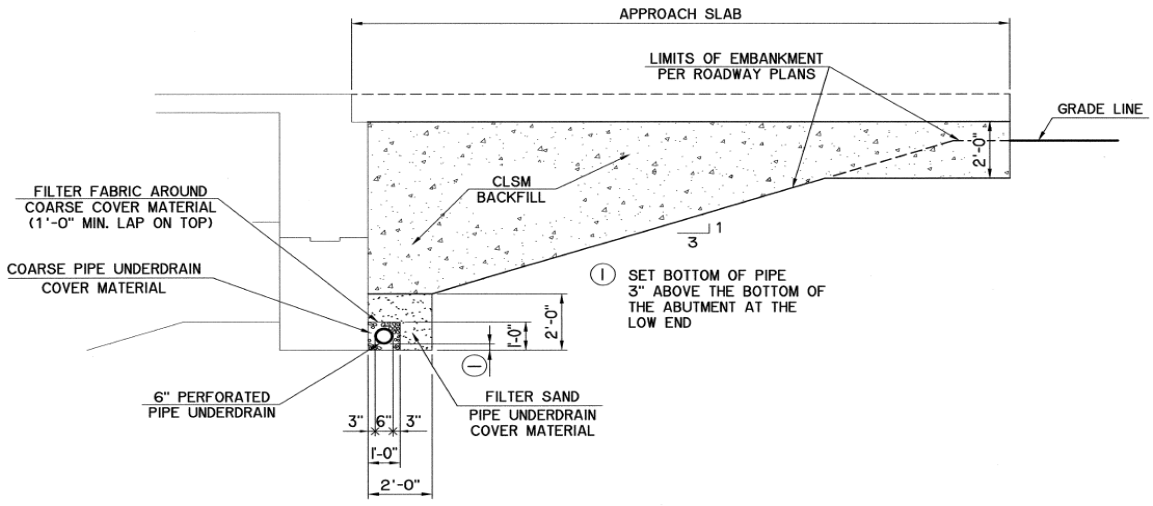

Figure 5-37 The CLSM and subsurface drainage system used in Oklahoma [2]

In addition to the CLMS, there are many other options that can potentially be used as the backfill material. Similarly to the use of CLMS, TxDOT promotes the use of cement stabilized sand (CSS) wedge as the backfill material. This type of material is less susceptible to moisture change and less erodible comparing to traditional granular materials. It was reported that this technique has been adopted by many districts in Texas as the standard practice [89].

One another viable option mentioned in literatures [68, 86, 90] is the use of the expanded polystyrene (EPS) geofoam (shown in Figure 5-38) which also provided excellent performance based on the past experience. This technique has been applied to geotechnical engineering for a few decades and the major advantages provided by this technique are reduced lateral earth pressure on the abutment, reduced vertical pressure on the foundation soil and associated settlement issues, greater resistance to temperature and moisture changes, ease of construction and cost-effective. Attributed to the nature of lightweight, the application of EPS geofoam in the embankment can create zero net loading on the underlying foundation; this can be achieved by removing a specific amount of foundation soil and replacing them with EPS geofoam if design calculation is properly conducted. This can be extremely helpful and cost-effective for construction projects with highly compressible soil layers in the foundation that can be very expensive and time-consuming to address.

Special attention needs to be paid to the drainage issue where a layer of granular materials should be placed between the EPS geofoam and the inclined embankment slope on which the geofoam structure is stepped; otherwise, the buoyancy effect caused by standing water can have negative influence on the performance of the EPS geofoam structure.

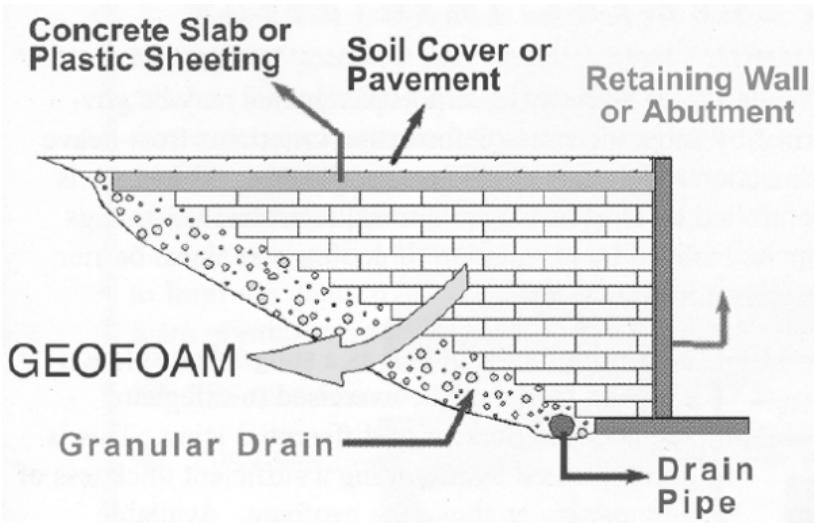

Figure 5-38 Details of EPS geofoam backfill [91]

In a research by White et al. [8], a Water Management Bridge Approach Model (WMBAM) was built under a laboratory condition and a series of laboratory testing was conducted for different backfill materials and practices using the WMBAM to simulate settlement and erosion conditions underneath the BAS when water was allowed to flow through the expansion joint between the BAS and the abutment. This research found that the use of porous backfill materials (poorly graded gravel) yielded very ideal results (zero settlement and voids) comparing to the use of other materials and practices (such as using granular backfill materials with/without the inclusion of geotextile reinforcement). The model that used the porous backfill material is shown in Figure 5-39 and the grain size distribution of the porous material is shown in Figure 5-40. Although lacking an evaluation of the BAS performance under wheel load stress during the model testing (only the self-weight of the approach slab was applied to the backfill materials), this research still provided valuable information with respect to the potential utility for applying porous materials as the backfill material behind the abutment. Future field implementations should be made to further validate the utility of this practice under field conditions.

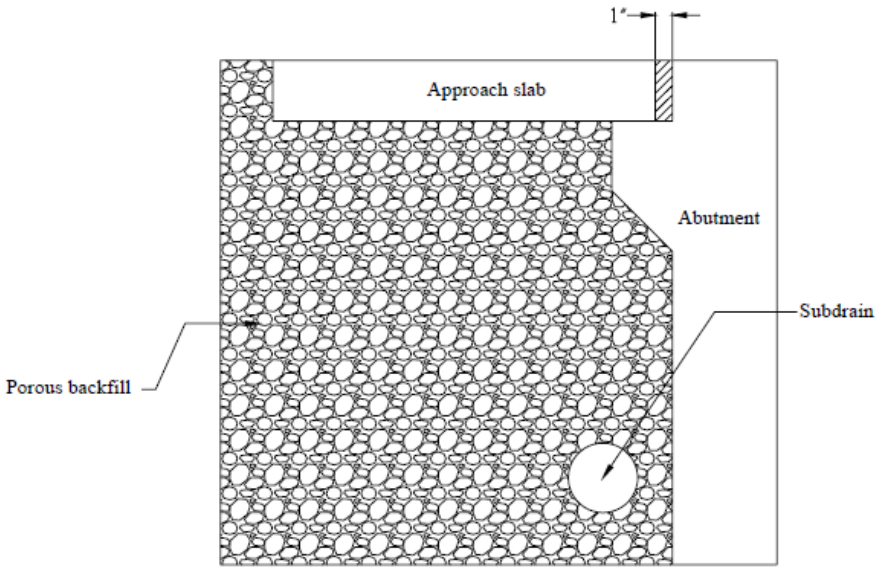

Figure 5-39 Porous backfill materials placed behind the abutment [8]

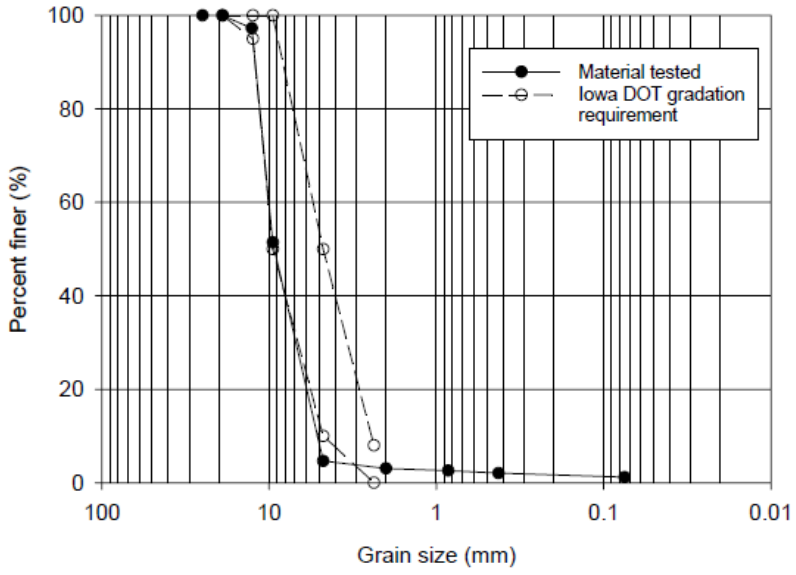

Figure 5-40 Grain size distribution for the porous backfill material [8]

Selection Criteria

Since the CLSM has become a standard practice in Oklahoma, it should be selected as the material for constructing embankment backfill wedge considering all the aforementioned benefits.

The practitioner may also consider using the EPS geofoam as an alternative especially for the following conditions:

- If the foundation of the embankment consists of extremely soft soil layers (e.g. peat) and it becomes too costly to address the settlement problem;
- If a higher level of design assurance is needed to address the erosion of the backfill wedge especially for the areas with heavy rainfall potential, since the EPS geofoam has much greater erosion resistance to water than CLSM.

ELEMENT 9. EMBANKMENT TREATMENT

The prevention of differential settlement issues which helps to maintain smooth transition and minimize slab cracking at the BAS is not only affected by the design of the embankment backfill wedge, but also depends on the performance of the embankment material on which the backfill wedge is stepped.

The most fundamental and efficient way to prevent consolidation induced settlement in the embankment area is to strictly ensure that the compaction effort is well achieved during the construction of the embankment. According to a survey conducted by Hoppe which summarized the specifications of various DOTs [28]:

- At least 95% of standard proctor should be achieved when constructing the embankment;
- The compaction should be conducted with a lift thickness of 6 – 8 inches and the thinner the lift thickness, the less settlement potential.

To further increase the design reliability of embankment, especially for embankments that are more than 10 ft. in height [34], the use geosynthetic materials in the embankment will add additional confinement and stiffness to the embankment structure which will increase the stability of the embankment slope as well as providing erosion resistance [8]. Successful experience was reported in Wyoming [92] where it was found that none of the ninety BASs which were constructed on geosynthetic reinforced embankments require any maintenance within 5 years of construction. In addition, research by Maddison et al. [93] indicated that, if columns (either stone

columns or concrete columns) were used in the foundation to address compressible soil layers, placing a layer of geosynthetic material (such as geocell elements) at the base of the embankment (i.e. the interface between the embankment and the foundation) can significantly increase the stability and reduce settlement of the embankment structure. In addition to being used at each lift of the embankment, the geosynthetic materials are also frequently used as the slope protection layer to control erosion on the embankment slopes as shown in Figure 5-41.

Figure 5-41 Geocells used as slope protection layer [94]

In order to address the settlement issues in soft compressible foundation layers and ensure uniform transition at the BASs, concrete columns have been used in the embankment to support BASs as shown in Figure 5-42, which were mostly seen Louisiana [95, 96]. The design concept anticipates that a smooth transition will form between the bridge deck end and the pavement end, assuming that the long-term consolidation settlement of the concrete piles increases as the length of the piles decreases. Theoretically, the pile near the bridge end will develop the smallest amount of settlement (negligible) comparable to the settlement underneath the abutment; the pile near the pavement end will develop the greatest amount of settlement which is close to the settlement underneath the pavement.

However, field performance [96] indicated that inconsistent performance was observed for the pile-supported BASs in Louisiana due to the variations in the subsoil conditions. In fact, the design of pile-supported BASs can be very tricky and unreliable attributed to the difficulties in predicting the settlement of the piles due to the downdrag effect, which can vary significantly not only from one site to another, but also from one location to another for a single site. Even Louisiana has been considering replacing the pile-supported BAS solution due to the high cost (BAS usually ranges from 80 – 120 ft. in length) and the low predictability with respect to its performance [95]. Therefore, this option is not recommended.

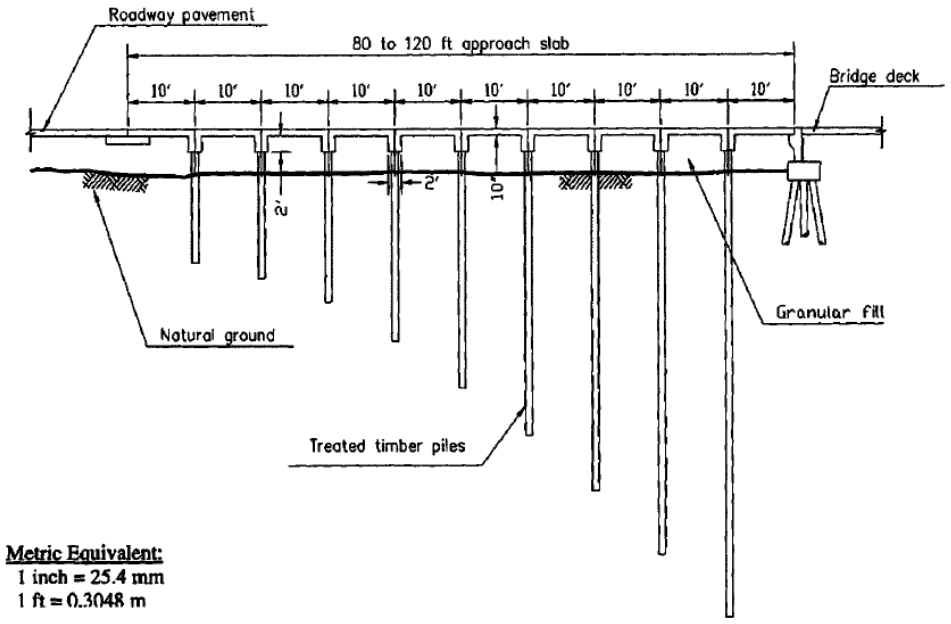

Figure 5-42 Column-supported BASs [96]

Another pile-supported BAS detail was found in Illinois as shown in Figure 5-43. In this design detail, one end of the BAS is supported by the abutment and the other sits on a pile cap supported by a concrete column. Essentially, this BAS is designed to behave like a simply supported one-way slab [97] due to the use of the deep foundations at the two supporting ends (with negligible settlement), which indicates that the function of the supporting medium in between the two ends (i.e. the embankment) is actually insignificant. Although the supporting medium may eventually settle over time if attention is not paid to minimize consolidation settlement or erosion issues, it may be

still way too conservative to design a BAS like a simply supported bridge deck (e.g. being 15 in. in thickness and highly doubly reinforced). In addition, without providing adequate support in between the two ends, the thick and highly reinforced BAS can still crack in the tension zone near the bridge deck-BAS joint (due to the negative bending moment), which eventually leads to badly spalled transverse cracking band near the joint as was repetitively observed in many field investigations.

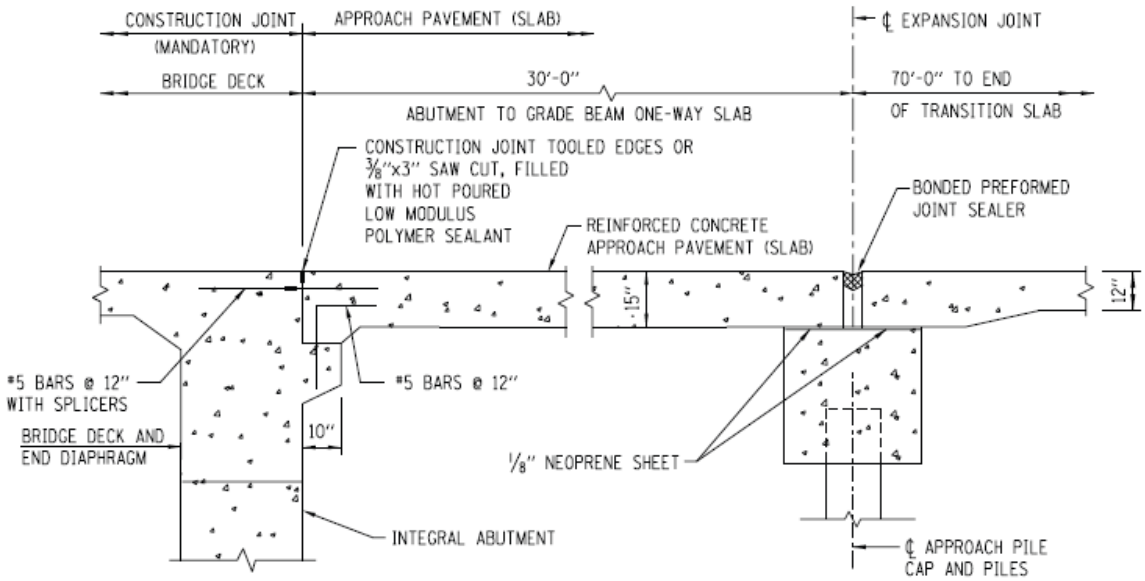

Figure 5-43 Illinois approach slab design details [97]

In order to provide a greater level of design assurance with respect to maintaining smooth transition at the BAS, this research also proposes a new design option to treat the embankment, which is the pile-supported backfill wedge option as shown in Figure 5-44. The aim of this design detail is to prevent differential settlement at the BAS by introducing the same deep foundation detail to support both the abutment and the BAS such that they have identical settlement behavior. The concrete columns supporting the CLSM wedge should be designed with the same diameter and placed at the same depth in the bearing stratum of the foundation as the concrete column supporting underneath the abutment. In addition, if concrete columns are used in the embankment to support CLSM and BAS, it is not necessary to apply any ground improvement technique (e.g. stone columns) at least in the area where concrete

columns are placed. The effectiveness of this new concept may be evaluated in the future research studies.

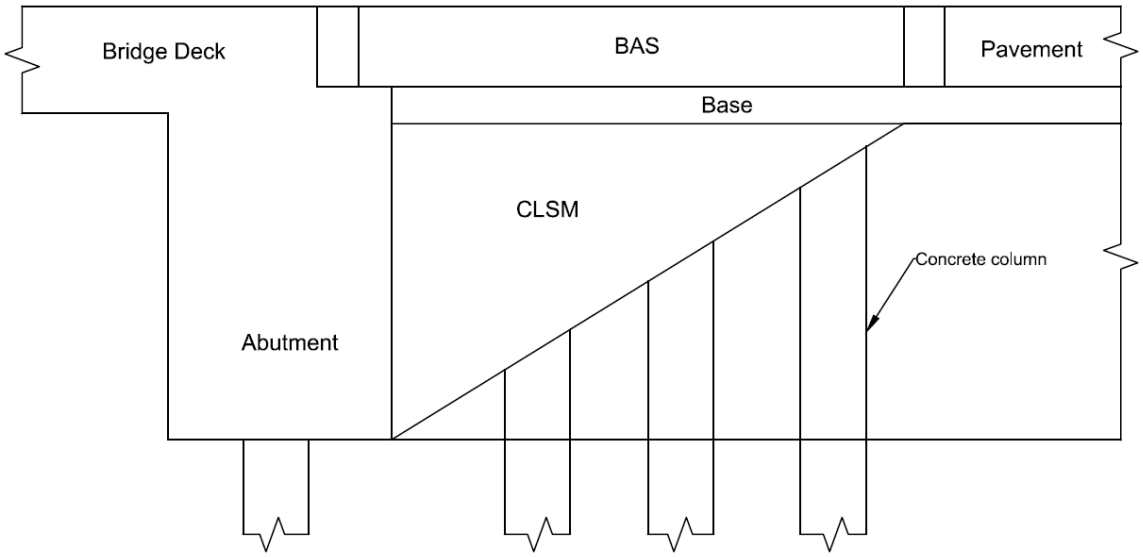

Figure 5-44 Concept of pile-supported backfill wedge option

Selection Criteria

The geosynthetic materials should be selected as an alternative for the embankment construction if:

- It is needed to increase the design reliability (for stability, settlement and erosion prevention) for embankments that are higher than 10 ft.;
- If the foundation is supported by columns, a layer of geosynthetic material should be placed at the interface between the foundation and the embankment.

The pile-supported backfill wedge option should be selected as an alternative for the embankment construction if:

- Weak and compressible layers are present in the foundation;
- The construction schedule cannot accommodate the long construction period associated with applying ground improvement techniques to address the weak and compressible layers;

- It is needed to increase the design reliability with respect to minimizing the embankment and foundation settlement (this option is expected to provide the greatest reliability to maintain smooth transition at the BAS).

CHAPTER 6

DESIGN OF STONE COLUMN

As a means to address the potential excessive settlement issues that may occur in the foundation underneath bridge embankments (i.e. **Element 10** shown in Figure 5-1), this chapter intends to provide a detailed design guideline for the stone column technique as well as the associated background information through conducting an extensive literature review. Design examples are also provided to facilitate better understanding of the design procedures.

BACKGROUND

The stone column technique is one of the ground improvement methods used worldwide since the 1950's. This technique which was originally implemented by Keller in Europe in 1937 [98] involves replacing 10% – 35% of weak soil with coarse granular material which is then placed and compacted into deep cylindrical holes made in the foundation soils to improve the shear strength, reduce the foundation settlement and provide a stable base for embankments or structures. Although stiffer than the surrounding soil, the stone column is essentially a soil improvement method rather than a foundation element (e.g. concrete pile deep foundations); therefore, it generally does not apply for heavy loading conditions (e.g. high-rise buildings) since stone columns do not behave like concrete piles which can transfer much greater portion of the loading to deeper strata [98-100].

General Applications

The stone column technique can be used under various circumstances, including [101-104]:

- Stabilizing the foundation soils of highway embankments or bridge approach fills;
- Providing foundation support for bridge abutments, bridge bents, mechanically stabilized earth retaining walls and other retaining structures;

- Stabilizing landslides; and
- Reducing liquefaction potential of clean sand.

Material Compatibility

The stone column technique is suitable for a wide range of soil types regarding the grain size distribution as shown in Figure 6-1. In terms of the undrained shear strength of soils, this technique works best for soils having undrained shear strengths of 2.2 – 7.3 psi (15 - 50 kPa); for soils with shear strength lower than 1.2 psi (8 kPa), stone columns may not have sufficient lateral support; for soils with shear strength greater than 7.3 psi (50 kPa), the equipment may encounter difficulty while opening bore holes [105].

Although general compatibility limits were established as aforementioned (mainly based on experience in the U.S.), experience from both Europe and Asia has shown that the stone column technique can also be used for soils with undrained shear strength as low as 0.7 psi (5 kPa) where the soils are not used in structural engineering but for pavement applications; specific soil conditions are indicated as follows, including [104, 106]:

- Loose Silty Sands: foundation soils with loose sands or silts are prone to liquefaction during an earthquake, the use of stone columns are a proven technique to reduce the occurrence of liquefaction, especially for petrochemical related structures such as LNG tanks;
- Soft and ultra-soft silts (slimes): foundation soil layers with the low shear strength (generally from 0.7 – 1.5 psi (5 – 10 kPa)) slimes can often lead to stability problems and low bearing capacity, previous experience indicated that stone columns can be used to support embankments with such layers without placing surcharge [107];
- Soft and ultra-soft marine clays: this type of soil is usually found in coastal areas and has low shear strength (generally from 0.9 – 1.7 psi (6 – 12 kPa));

- Garbage fills: structures are sometimes built over garbage landfills due to the shortage of land; stone columns were used to address the high compressibility of this type of material which often leads to large settlement.

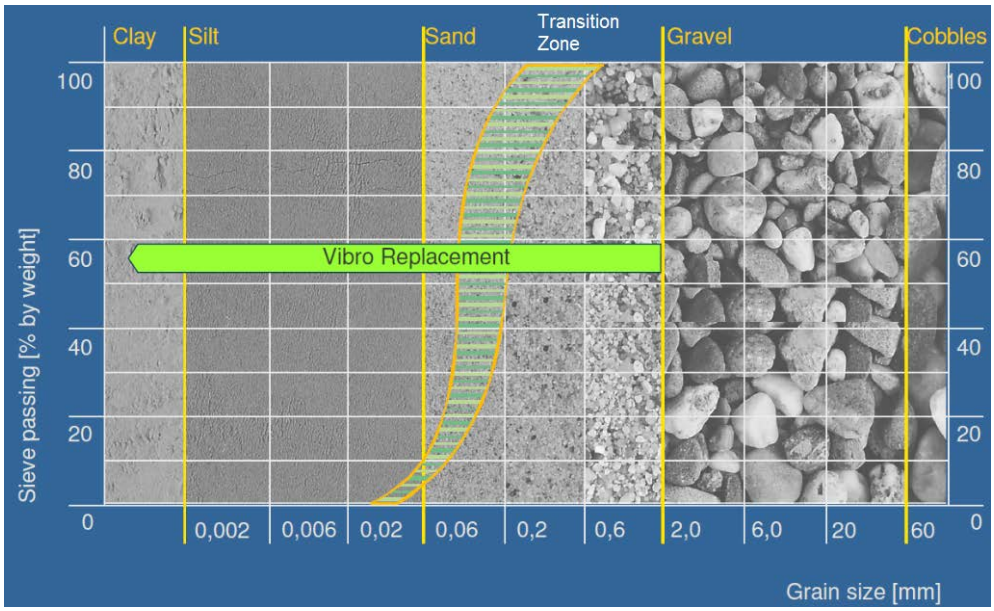

Figure 6-1 Material limits for application [108]

Construction Methods

In the U.S., stone columns can be installed using two different methods, the vibro-replacement (wet top feed) and the vibro-displacement (dry top and bottom feed) methods [101, 109]. In Europe, the name of the techniques are different where both the dry top and bottom feed methods are referred to as the vibro-replacement technique [108, 110]. Detailed equipment and techniques pertaining to each are discussed subsequently.

The original stone column construction method is referred to as the vibro-replacement, which involves the use of a high-pressure water jetting method to penetrate a vibratory probe into the ground; the stones are fed into the hole incrementally as the probe retracts, during which both the stones and surrounding soils are compacted and densified. The method is suitable for sites with high groundwater table and soft to firm soils that have undrained shear strengths of 2.2 – 7.3 psi (15 - 50

kPa) [105]. The diameter of the holes made using this method ranges from 2.6 – 3.9 ft. (0.8 – 1.2 m.) [111]. Note that attention needs to be paid to the management of runoff water (i.e. water from rainfall) induced during application of this method which may cause environmental problems. A schematic diagram of this method is shown in Figure 6-2.

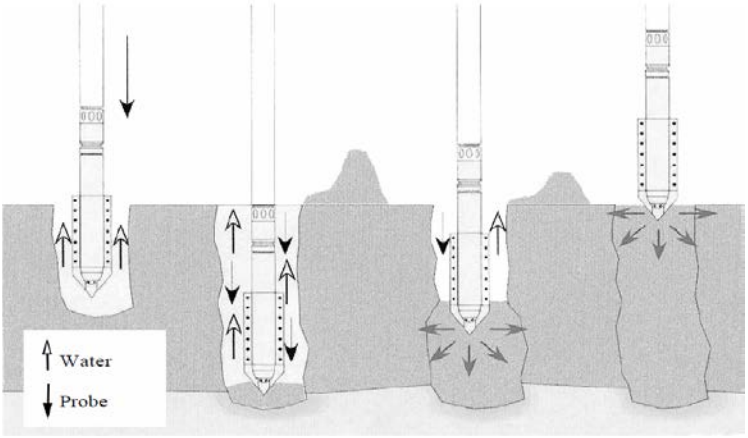

Figure 6-2 A schematic diagram of vibro-replacement method [109]

The second method, vibro-displacement (dry top and bottom feed) was introduced to solve the environmental issues that may occur after using the vibro-replacement method. This method mainly focuses on soils with undrained shear strength of 4.4 – 7.3 psi (30 - 50 kPa) [111]. The diameter of the holes which ranges from 1.6 – 2.6 ft. (0.5 – 0.8 m.) is usually smaller than that of the holes made using the vibro-replacement method [98]. In this method, air jetting and/or pre-augering techniques are used associated with a vibrator probe to open holes in the ground. Unlike the wet top feed method where soils are removed from the bore holes, the soils are displaced laterally by the probe inside the holes for the vibro-displacement method; as a result, the soils around the inside surface of the bore holes are densified, which leads to greater strength [112]. However, this method may cause smear damage at the column-soil interface due to the restructuring of the compacted soils, leading to blocked drainage and delaying the consolidation process [98, 111].

Two different procedures are available to feed stones using the vibro-displacement method, one is named as the top feed procedure and the other is the bottom feed procedure. The difference between the two is that for a top feed procedure

as shown in Figure 6-3 (a), stones (range from 0.47 – 2.95 in. in size) are fed into the holes from the ground surface after the probe is either fully or partially removed from the holes; whereas for a bottom feed procedure as shown in Figure 6-3 (b), the stones (with smaller sizes ranging from 0.08 – 1.77 in.) are fed through an auxiliary tube to the bottom of the holes without taking the probe out [113]. The top feed procedure is suitable for making shallow and shorter stone columns; the bottom feed procedure is mainly used to prevent the holes from collapsing when opening deep holes and to address high water table or unstable soil conditions [110, 113].

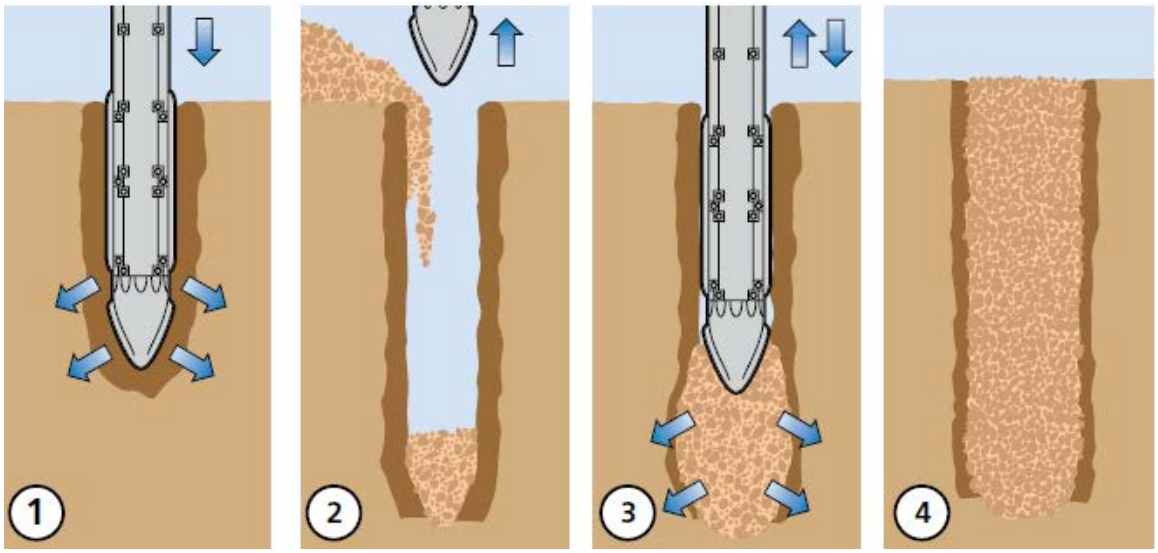

(a)

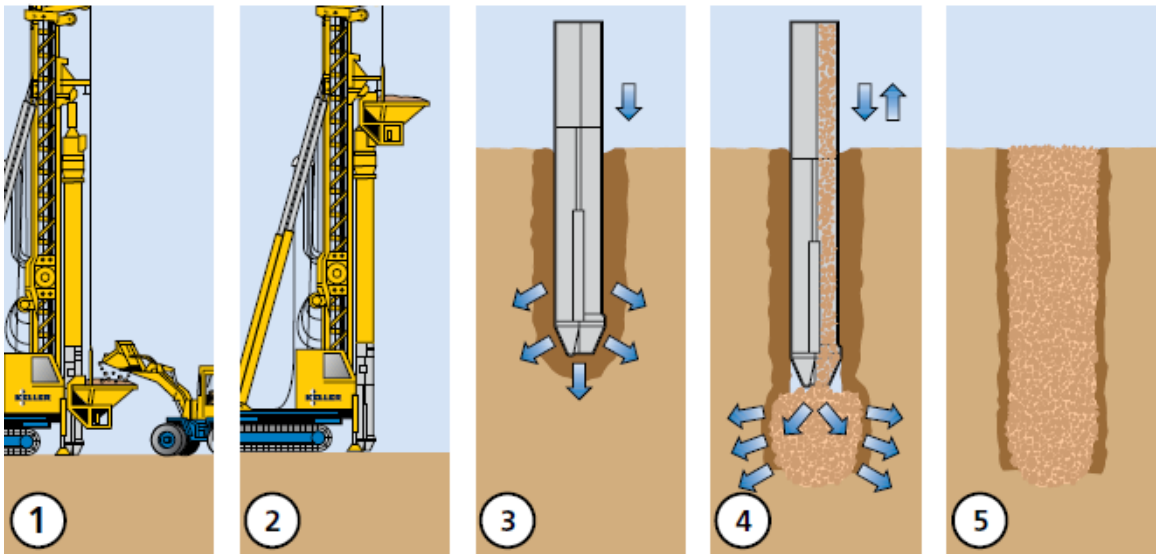

(b)

Figure 6-3 Schematic diagrams of (a) dry top feed procedure and (b) dry bottom feed procedure [110]

In addition to those two main construction methods, an alternative construction method worth noting is the bottom rammed columns or rammed aggregate piers (RAP) [114, 115]. A schematic diagram of the RAP method is shown in Figure 6-4. As seen in the figure, after drilling, poorly graded crushed gravel is placed into the “bulb” formed at the bottom of the cavity and are compacted by a beveled ram which also displaces the

crushed stone radially into the surrounding soil [115, 116]. This compaction pattern often leads to aggregate pier with high angle of friction and radial stress developed in the surrounding soil [117]. As a result, previous research indicated that the stiffness of RAPs is usually 5 – 10 times greater than that of stone columns placed in the same soil [116], however this method leads to higher construction cost [114].

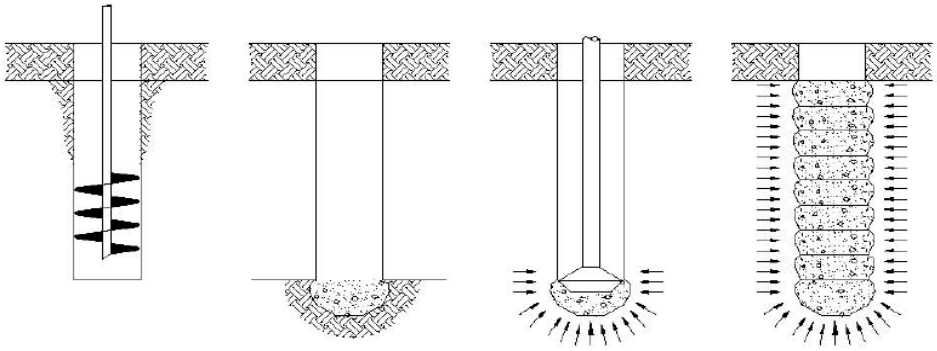

Figure 6-4 A schematic diagram of rammed aggregate pier method [103]

Construction Provisions

The following summarizes the factors that affecting the feasibility of using stone columns as a ground improvement method [100, 101]:

- The loading condition should be relatively uniform and magnitude of the loading should be limited to a maximum of 112000 lbf (500 kN) per column; the bearing capacity of a single column is usually designed 45000 – 67000 lbf (200 – 300 kN);
- Improvements are most significant for compressible silts and clay within 3.3 ft. below the ground surface and shear strength ranging from 2.2 to 7.3 psi (15 – 50 kPa);
- Soil layers containing organics and peat that have undrained shear strength lower than 1.5 psi (10 kPa) should be specially treated; the diameter (or half the diameter at least) of the stone column should be greater than the thickness of the layers with those materials;

- The undrained shear strength of the applicable soils has an upper limit of 7.3 – 14.5 psi (50 – 100 kPa); those soils will be strong enough without the installation of stone columns;
- The diameter of the stone columns may vary over their length depending on the shear strength of different layers; the diameter of most stone columns (dry feed method) ranges from 1.6 – 2.6 ft.;
- A load transfer platform may be introduced at the interface between a structure element (e.g. strip footing, raft foundation or concrete slab) and the stone column-soil foundation, if the structure does not homogeneously distribute load bearing on the column grid in the foundation.

Benefits and Limitations

The benefits of using stone columns are summarized as follows [98, 101, 108, 116]:

- Providing greater shear strength and stiffness for the overall soil-column system;
- Densifying the soil in between stone columns depending on the soil condition;
- Mitigating soil liquefaction during earthquake;
- Providing greater bearing capacity;
- Reducing settlement;
- Expediting the dissipation of excess pore water pressure in soil by providing a vertical drain through the column, which results in shorter time for primary consolidation settlement to occur;
- Behaving differently from concrete piles: cannot break, no buckling and no downdrag effect;
- Cost saving comparing to many other ground improvement techniques;
- Applicable for a wide range of soil conditions; and
- Proven successful worldwide.

Some of the limitations of using stone columns are [101, 116]:

- Requiring adequate lateral support from the surrounding soil, not applicable for soft soil conditions, such as peat, mulch and other organic materials;
- Not suitable if the thickness of the undesirable soil layer is greater than the diameter of the stone column;
- For soils containing more than 15% - 25% fines or greater than 2% clay, the density of the soil in between stone columns is not improved significantly;
- Disposal of spoil water is required for the wet feed method and the dry feed method can cause soil heave that may influence the surrounding construction activities; and
- Expansive pre and post construction testing is needed to confirm.

Selection Criteria

To facilitate decision making process for the practitioners, the stone column technique can be selected as a construction practice to better support the bridge embankment if one of the following conditions is present:

- The permeability of the foundation soil layer is too low to allow for the dissipation of excess pore water pressure in the foundation;
- The construction schedule cannot accommodate the long waiting period for the primary consolidation settlement to be complete (usually through preloading the foundation) before constructing the BAS;
- The budget of the project is limited to allow for the application of deep foundations; and
- The construction area is within an earthquake zone.

PRELIMINARY DESIGN CONSIDERATIONS AND CONCEPTS

Prior to designing a stone column, it is necessary to obtain preliminary knowledge to support the design process, the following information is considered important [100]:

- Limit of the treatment area;
- The nature of the soil to be treated: laboratory or in-site testing needs to be conducted to obtain the key soil properties;
- The characteristics and behavior of the structure to be built on top of the stone column-soil matrix;
- Stress level to be exerted on the foundation.

The preliminary design of stone columns consists of the following steps [109]:

1. Estimate the settlement of the unimproved ground using conventional settlement calculation procedures;
2. Determine the required reduction of settlement to meet the design criteria. A reduction factor named as “settlement ratio” or “improvement factor” (by Priebe’s method subsequently discussed) needs to be calculated by the ratio of the settlement of the unimproved soil to the settlement of stone column treated soil;
3. Determine if the stone columns can achieve the required reduction of settlement based on previous experience and published empirical data; generally, the improvement factor of stone columns ranges from 2 to 3;
4. Determine the area replacement ratio, which is expressed as the stone column area divided by the tributary area of the stone columns (subsequently explained), in order to achieve the required reduction of settlement;
5. Determine the length, diameter and spacing of the stone column; the length is determined based on the settlement calculation; the diameter and spacing are determined by experience;
6. Evaluate the load bearing capacity of the stone columns.

The basic relationship and design concepts relative to the design of stone columns are elaborated in the following, which is mainly based on the original work made by Barksdale and Bachus (1983) [118] and Elias et al. (1998) [101].

Unit Cell Concept

Although a square pattern (shown in Figure 6-5 (a)) is used sometimes, stone columns are usually constructed in an equilateral triangular pattern (shown in Figure 6-5 (b)) since it gives the densest packing of stone columns within a given area [118].

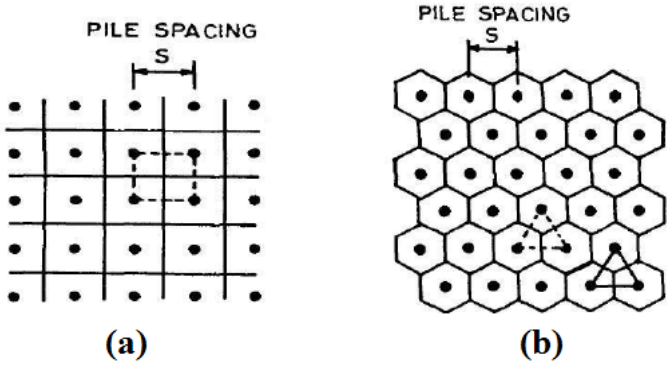

Figure 6-5 Pattern of stone column arrangement (a) square pattern (b) equilateral triangular pattern [113]

In order to perform bearing capacity and settlement analysis, the unit cell concept shown in Figure 6-6 takes into account the tributary area of the soil surrounding each stone column. For an equilateral triangular pattern, the hexagonal tributary area is usually approximated by an equivalent circular-shaped tributary area and the effective diameter, D_e of the circle is:

$$D_e = 1.05s \tag{6-1}$$

and for a square pattern, the effective diameter is:

$$D_e = 1.13s \tag{6-2}$$

where s is the spacing of the stone columns. In consequence, a unit cell with a diameter of D_e is formed considering the stone column and the surrounding tributary soil [118].

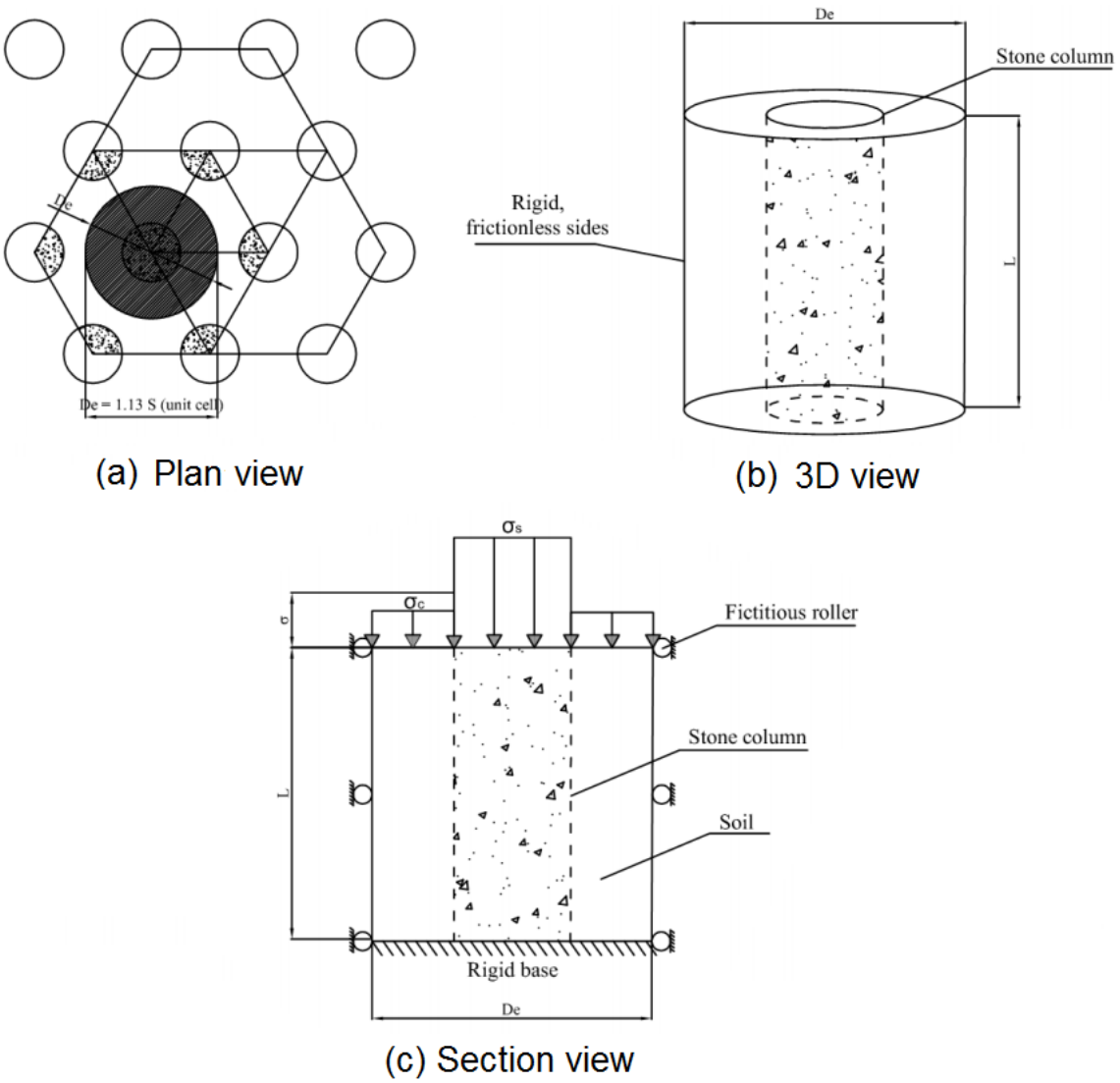

Figure 6-6 the unit cell concept (a) plan view (b) 3D view and (c) section view [119]

Spacing, Diameter and Area Replacement Ratio

The center to center spacing of the stone columns is usually 4.9 – 11.5 ft. for triangular, square or rectangular patterns of installation [101].

The diameter of stone columns ranges from 1.5 – 3.9 ft.; typically, the stone column placed using the dry feed method has a diameter ranging from 3.0 – 3.6 ft. and larger if a wet feed method is used [101].

A term named as the “area replacement ratio”, a_s is introduced to quantify the amount of soil replaced by the stone column, which is expressed as:

$$a_s = A_s/A \tag{6-3}$$

$$a_c = A_c/A = 1 - a_s \tag{6-4}$$

where A_s is the area of the stone column, A_c is the area of the surrounding soil, A is the total area within a unit cell and a_c is the ratio of the area of the surrounding soil to the total area.

Further, the area replacement ratio can be expressed in terms of the diameter and spacing of the stone columns as:

$$a_s = C_1(\frac{D}{s})^2 \tag{6-5}$$

where D is the diameter of the stone column, s is the center to center spacing and C_1 is a constant depending on the pattern of arrangement where $C_1 = \pi/4$ for a square pattern and $C_1 = \pi/(2\sqrt{3})$ for an equilateral triangular pattern [118].

It was reported that an area replacement ratio less than 10% would lead to insignificant ground improvement, whereas a ratio greater than 35% would be difficult to achieve due to the limitation of the construction technology [120].

Stress Concentration Ratio

An equal strain assumption is usually made for the case in which the vertical settlement of the stone columns and the surrounding soil is almost the same upon a uniform loading over the stone column treated ground [101, 118]. This assumption has been validated both in the field and through finite element analysis [101]. As a result, stress concentration usually occurs in the stone columns because stone columns are stiffer than the surrounding soils.

The distribution of vertical stress within a unit cell can be expressed using a stress concentration ratio, SCR which is defined as [121]:

$$SCR = \sigma_s/\sigma_c \tag{6-6}$$

where σ_s is the stress in stone columns and σ_c is the stress in the surrounding soils. Note that many others in the literature use n to represent the stress concentration ratio,

however, a different parameter is used to avoid confusion since the Priebe's method (subsequently explained) uses n to represent the settlement improvement ratio [121].

The average stress σ over the area of a unit cell can be determined based on the equilibrium of vertical forces within the unit cell:

$$\sigma = \sigma_s \cdot a_s + \sigma_c(1 - a_s) \tag{6-7}$$

where σ is the stress applied on the unit cell and other terms are defined as aforementioned. Using the stress concentration ratio, σ_s and σ_c can be determined as:

$$\sigma_c = \frac{\sigma}{1+(SCR-1)\cdot a_s} = \mu_c \sigma \tag{6-8}$$

$$\sigma_s = \frac{SCR\cdot\sigma}{1+(SCR-1)\cdot a_s} = \mu_s \sigma \tag{6-9}$$

where μ_c and μ_s are the ratio of stresses in the surrounding soil and stone column, respectively, to the stress σ over the unit cell. If the stress concentration ratio is obtained, the stress in the soil and stone columns can be easily determined, which are both useful in the calculation of settlement and bearing capacity analyses [118].

The SCR is the key in the design of stone columns, however, the determination of this parameter is mostly based on experience, although theoretical solutions exist [101].

Many factors can influence the SCR, including the relative stiffness between stones and the surrounding soil, the length of the stone column, the area ratio (diameter and spacing of stone columns), the loading platform placed over the stone columns and the rate of loading [101, 121].

In general, the measured SCR ranges between 2 to 5, and the value increases with time considering the fact that the secondary settlement in the surrounding soil is greater than that in the stone column. For stronger soil and large column spacing conditions, SCR usually ranges between 2 to 2.5; whereas for weak soil and tight column spacing condition, SCR can be from 3 to 4. Usually, a SCR of 2.5 is used as a conservative assumption for preliminary design purpose [101]. A SCR can also be determined using a design chart developed by Barksdale and Bachus [118] based on the area replacement ratio and the settlement ratio; although it gives slightly unconservative estimations.

SETTLEMENT

One of the major benefits of using stone columns is to reduce settlement of a foundation upon loading. Numerous research studies have been conducted to develop methods for predicting settlement behavior of stone column reinforced soil [118, 122-126]. In general, most of these methods were assuming equal strain, using the unit cell concept and either based on pseudo-elastic or elasto-plastic theory. In many of the methods, the settlement of the untreated ground needs to be determined first using those conventional settlement analyses [101].

Several design methods were evaluated in the report by Barksdale and Bachus [118], such as the equilibrium, Priebe, Greenwood, incremental and the finite element methods. Specifically, the report [118] suggested that the equilibrium method can be used to provide an upper bound estimation of the settlement of reinforced ground; whereas the nonlinear finite element method can be used to determine a lower bound estimation. The best estimation should be the average of the two estimates.

In the FHWA report by Elias et al. [101], it was suggested that the equilibrium method gives an average or upper bound estimation and the Priebe's method can be used to provide a lower bound estimation for the settlement of stone column treated ground.

Therefore, in order to have a comprehensive idea which requires the knowledge of both upper and lower bound settlement estimations of stone column treated ground, the following of the section mainly focuses on elaborating the three methods introduced in the literature, which are the equilibrium, the finite element and the Priebe's methods.

Note that the compression index C_c of the foundation soils, as the key soil property to be used in the settlement analysis, can either be determined by performing the conventional oedometer test or by applying the new procedure proposed in Chapter 7.

Equilibrium Method

The equilibrium method provides a very simple and realistic approach for determining the reduction in settlement of stone column treated soil. This method is

based on the following assumption: (1) the unit cell idealization, (2) force equilibrium in the unit cell, (3) equal strain (vertical settlement) assumption, and (4) a uniform vertical stress exits throughout the length of the stone column [118].

The vertical stress in the surrounding soil σ_c due to applied stress σ at the ground surface can be determined as:

$$\sigma_c = \mu_c \sigma \tag{6-10}$$

where these terms are already defined in Equation (6-8).

The change in the vertical stress $\Delta\sigma_c$ at the center of each soil layer can be estimated by the Boussinesq stress distribution theory as shown in Figure 6-7.

$$\Delta\sigma_c = I_z \sigma_c \tag{6-11}$$

where I_z is the influence factor determined using the Boussinesq stress distribution as shown in Figure 6-7. Besides using the Boussinesq stress distribution theory, there are other options such as the Newmark's chart method, Osterberg's Influence Chart method and Griffiths' influence factor method to determine the stress increase in soils. For simplicity, this report uses the Boussinesq solution.

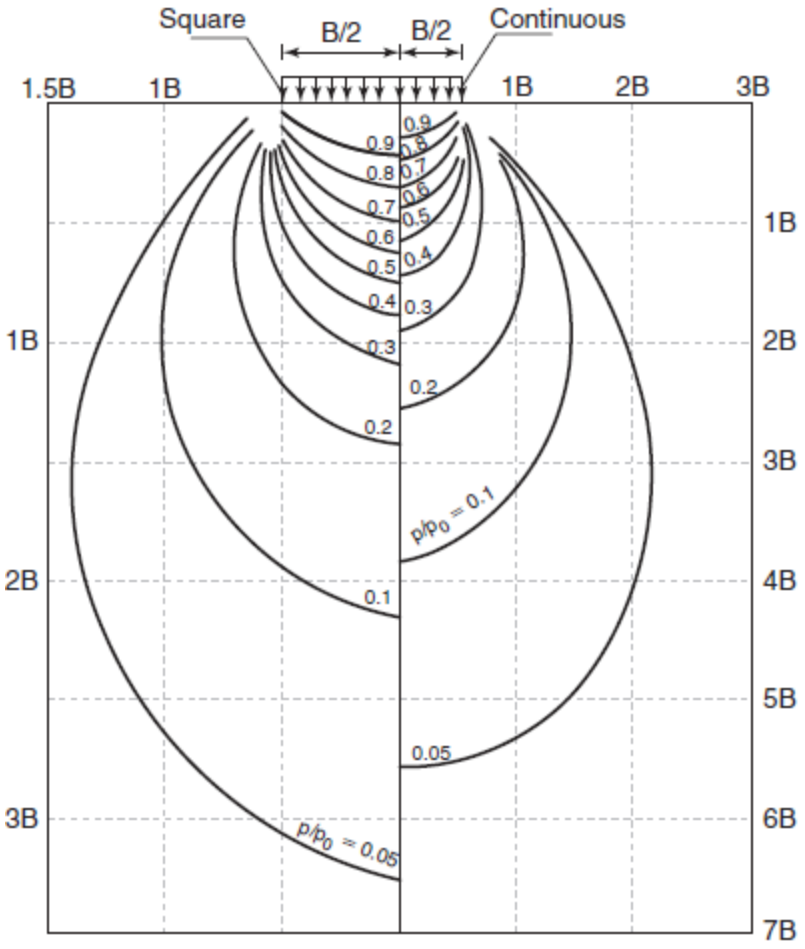

Figure 6-7 Stress distribution based on the Boussinesq elastic theory for a flexible foundation [127]

The conventional 1-d consolidation theory is expressed as:

$$S_t = \left(\frac{C_c}{1+e_0}\right)\log_{10}\left(\frac{\bar{\sigma}_0+\Delta\sigma_c}{\bar{\sigma}_0}\right)\cdot H \tag{6-12}$$

where S_t is the primary consolidation settlement within a depth H of the stone column treated ground, H is the height of the stone column treated ground, $\bar{\sigma}_0$ is the average initial effective vertical stress in the soil layer, C_c is the compression index from a 1-d consolidation test and e_0 is the initial void ratio.

The ratio of settlement in the stone column treated ground to that in the untreated ground, S_t/S can be determined as:

$$\frac{S_t}{S} = \frac{\log_{10}\left(\frac{\bar{\sigma}_0+\mu_c\Delta\sigma}{\bar{\sigma}_0}\right)}{\log_{10}\left(\frac{\bar{\sigma}_0+\Delta\sigma}{\bar{\sigma}_0}\right)} \tag{6-13}$$

This equation essentially indicates that the level of improvement of settlement depends on: (1) the stress concentration ratio, SCR which is reflected through μ_c, (2) the average initial effective vertical stress in the soil (or the length of the stone column since $\bar{\sigma}_0$ increases with the increase of length of the stone column), (3) the applied stress σ.

For very large $\bar{\sigma}_0$ and small applied stress σ, the ratio of settlement rapidly approaches:

$$\frac{S_t}{S} = \frac{1}{[1+(SCR-1)\cdot a_s]} = \mu_c = \frac{1}{n} \quad (6\text{-}14)$$

where n is the settlement improvement ratio and all the terms are previously defined. The equation is shown graphically in Figure 6-8 which provides a slightly unconservative estimation of the settlement improvement and can be used for preliminary estimations. For the equilibrium method, a SCR of 4 – 5 is recommended based on the comparison between the calculated and measured settlement in field studies [118].

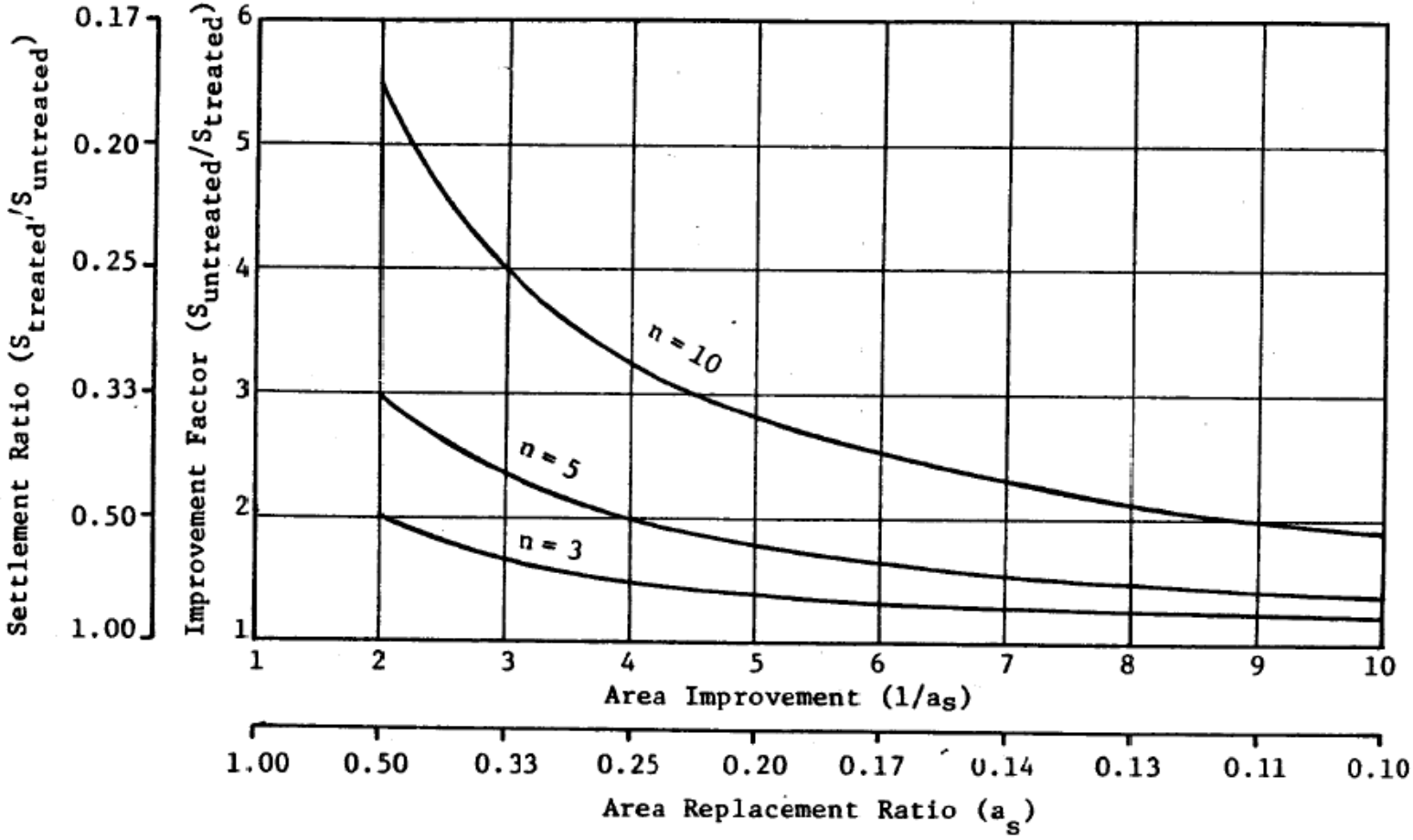

Figure 6-8 Maximum reduction in settlement that can be obtained using the equilibrium method [118]

Finite Element Method

The finite element method provides the most theoretical approach to model the stone column treated ground, in which nonlinear material properties, interface slip and suitable boundary conditions can all be modeled [118]. Barksdale and Bachus [118] conducted finite element modeling on the behavior of stone column treated ground to extend the early work into design chart for predicting primary consolidation settlement.

In this finite element study, computations of incremental and total stresses were conducted by solving a system of linear, incremental equilibrium equations. Eight node isoparametric material elements were used in the modeling; only one unit cell was modeled since the stress condition was uniform in the stone columns and soils. The interface element was set to be capable of modeling no slip, slip and separation by using the Mohr-coulomb failure theory, in order to define the maximum allowable shear at the interface between stone and soil particles. The stiffness of the system was allowed to vary after each load increment and iteration.

The finite element analyses which led to the development of design charts were divided into two sections: the first section dealt with low compressibility soils and the other focused on compressible cohesive soils. A low compressibility soil is defined as the soils that have a modulus ratio $E_s/E_c \leq 10$, where E_s and E_c are the average modulus of elasticity of the stone column and soil, respectively. A compressible cohesive soils is defined as the soils that have a modulus ratio $E_s/E_c > 10$.

Low compressibility soil

For low compressibility soil, such as stone column treated sand, silty sand and some silts, a linear elastic theory was used in the finite element modeling. The Poisson's ratio is assumed to be 0.30 for soil and 0.35 for stone. The finite element model based on the unit cell idealization is shown in Figure 6-9. Settlement prediction curves were developed for area replacement ratio of 0.1, 0.15 and 0.25; an example of the curve is shown in Figure 6-10 for an area replacement ratio of 0.1. Other curves that use different area replacement ratios can be found from Figure A-1 to Figure A-3 in the

Appendix A [118]. The curves are applicable for stone column length to diameter ratios L/D of 5, 10, 15 and 20.

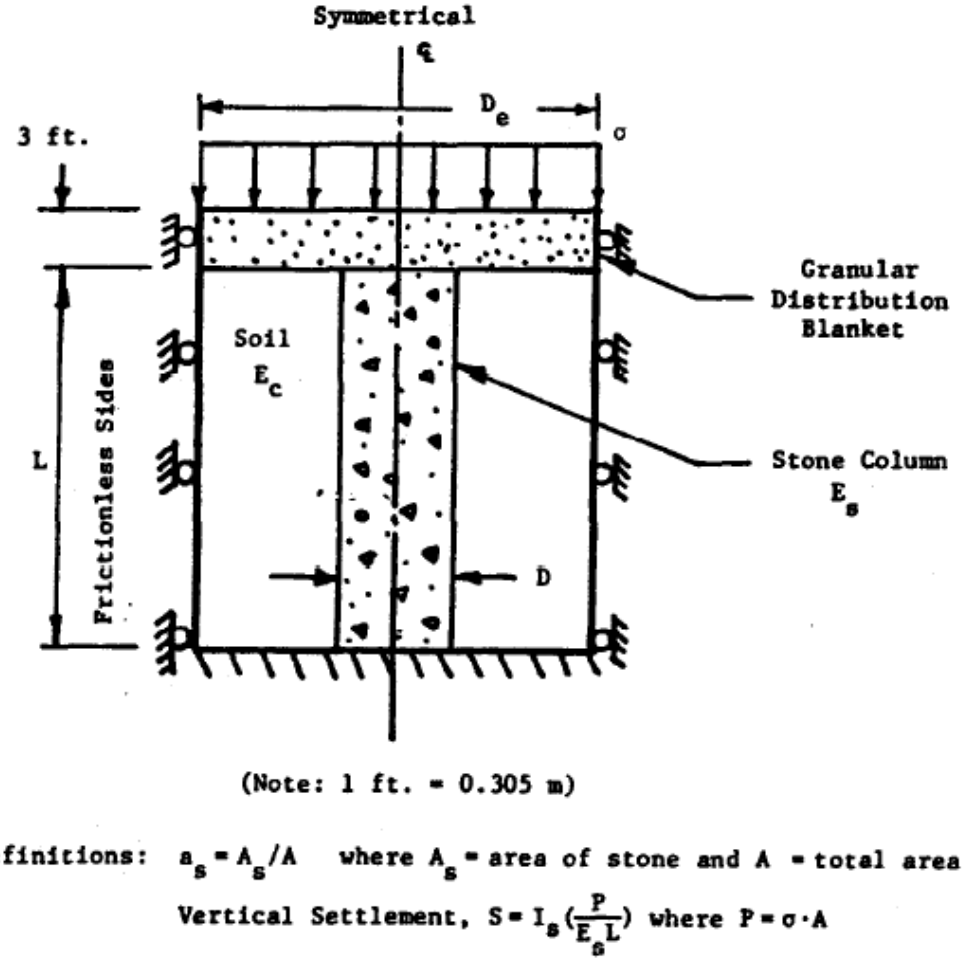

Figure 6-9 Unit cell model for low compressibility soil [118]

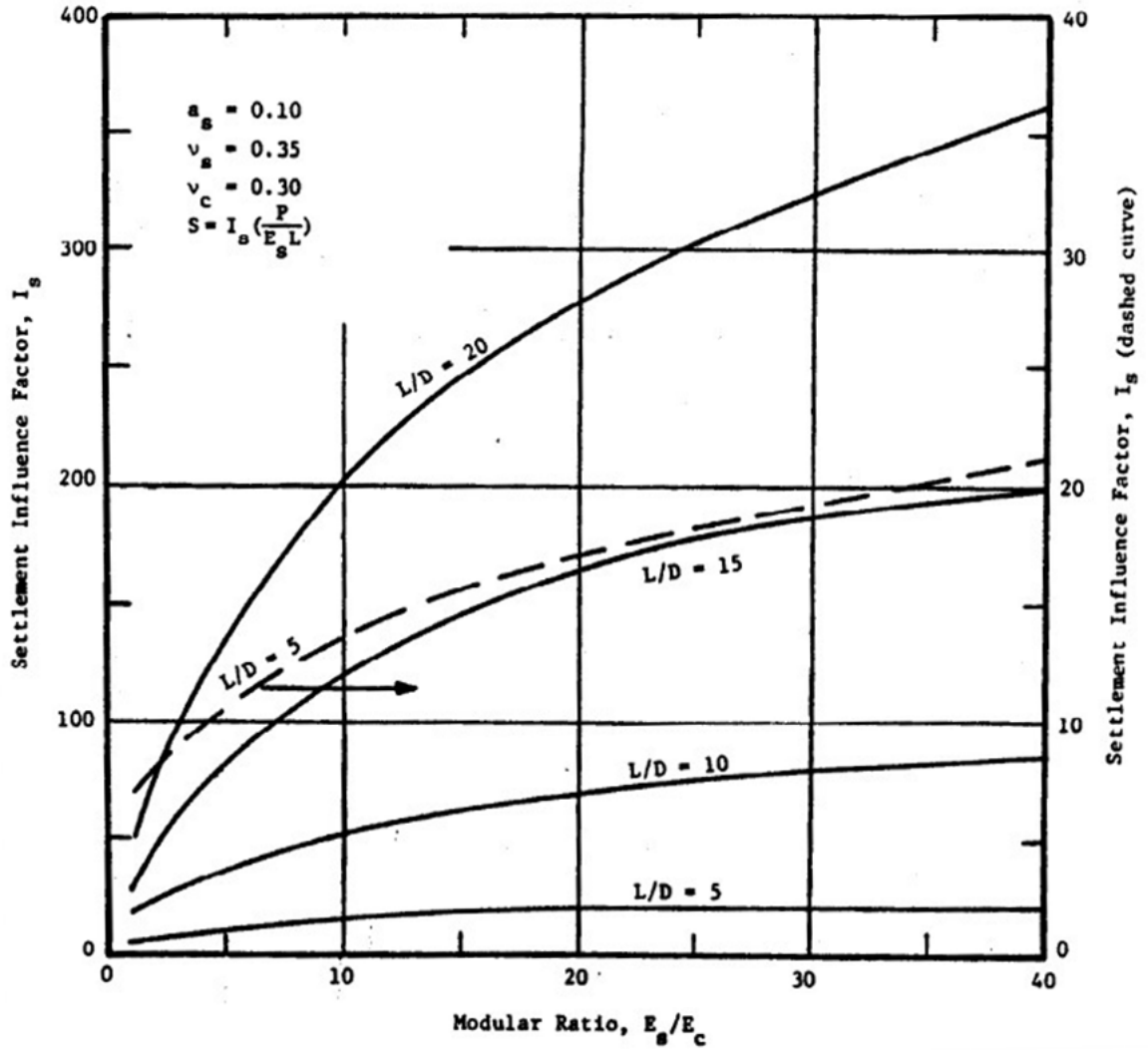

Figure 6-10 Settlement prediction curve for low compressibility soil with an area replacement ratio of 0.1 [118]

To predict the long-term primary consolidation settlement of the low compressibility soil, the drained modulus of elasticity of the cohesive soil needs to be used, which can be estimated using the following function if a drained triaxial test is not performed [118]:

$$E_c = \frac{(1+\nu)(1-2\nu)(1+e_0)\sigma_{va}}{0.435(1-\nu)C_c} \tag{6-15}$$

where E_c is the drained modulus of elasticity of the soil, e_0 is the initial void ratio, C_c is the compression index, ν is the Poisson's ratio (drained) and σ_{va} is the average of initial

and final stress state applied in the field (vertical stress). The selection of drained Poisson's ratio can be found in Figure 6-11.

Soil Consistency	Poisson's Ratio[1]
Very Soft to Soft[2,3]	0.35 - 0.45
Firm to Stiff[2]	0.30 - 0.35
Stiff Overconsolidated Clays	0.1 - 0.30

Notes: 1. For undrained loading use 0.45.
2. For normally consolidated clays.
3. For very soft to soft clays a value of 0.40-0.45 is recommended for calculating E_c for nonlinear finite element settlement analyses of stone column improved ground; for firm to stiff use at least $\nu_c = 0.35$.

Figure 6-11 Typical Poisson's ratio of clay under drained loading [118]

The stress dependent modulus of elasticity of stone column E_s is also required in the calculation, which is expressed as:

$$E_s = (\sigma_1 - \sigma_3)/\varepsilon_a \tag{6-16}$$

where $(\sigma_1 - \sigma_3)$ is the deviator stress under the applied load, σ_1 is the vertical stress in the column and σ_3 is the lateral stress in the column. It should be noted that both the at-rest stress and the change in stress due to loading should be accounted for when calculating σ_1 and σ_3. The axial strain ε_a can be obtained from the stress-strain curve of a triaxial shear test on the stone column.

If a triaxial shear test or a field loading test is not available, the modulus of elasticity of stone column E_s can be determined using a hyperbolic expression developed by Duncan and Chang [128]:

$$E_s = K \cdot \sigma_\theta^n \cdot [1 - \frac{(\sigma_1-\sigma_3)R_f}{(\frac{2(c\cdot\cos\varphi_s+\sigma_3\sin\varphi_s)}{1-\sin\varphi_s})}] \tag{6-17}$$

where E_s is the stress-dependent secant modulus of the stone (psi.), K, n are constants defining the initial modulus of the stone under low deviator stress, c is the cohesion of the stone which is often assumed as zero, φ_s is the friction angle of the stone, R_f is the failure ratio and $\sigma_\theta = \sigma_1 + \sigma_2 + \sigma_3$ (psi.). Without having specific test data, the following

parameters can be assumed where $K = 88.6$, $n = 1.14$, $R_f = 0.86$, $c = 0$ and $\varphi_s = 42° - 45°$. The settlement curves developed in this study were based on these values [118].

Compressible cohesive soil

For compressible cohesive soil, such as soft to firm clays, the soil was assumed to be elasto-plastic and the stones are stress dependent. The finite element model based on the unit cell idealization is shown in Figure 6-12. As shown in the figure, a soft boundary is placed around the unit cell in addition to the stone column and cohesive soil elements; this soft boundary is introduced to account for the effect of later bulging which induces lateral deformation at the support contributed by the sides of the unit cell. By trial and error using the finite element analysis, it was found that the use of a boundary of 1 in. thick with elastic modulus of 12 psi could successfully model the maximum lateral deformation induced by lateral spreading occurred in a unit cell; to obtain variation in the boundary stiffness, a rigid boundary with a modulus of 1000 psi was also used. The model shown in Figure 6-12 was developed by also considering a representative friction angle of $42°$ for the stone and $0°$ for the soil, a coefficient of at-rest earth pressure of 0.75 and a Poisson's ratio of 0.35 for both stones and soil. The modulus of elasticity and shear strength of the soil were assumed to be equal or less than 160 psi and 400 psf, respectively [118].

One example of the settlement prediction curves for compressible cohesive soil is shown in Figure 6-13. Other curves that use different area replacement ratios (ranging from 0.1 to 0.35) and column length to diameter ratios (ranging from 5 to 20) can be found from Figure A-4 to Figure A-12 in Appendix A [118]. As seen in the figure, settlement is a function of the average applied stress σ over the unit cell, modulus of elasticity of the soil E_c, area replacement ratio a_s, column length to diameter ratio $L/D$and boundary rigidity E_b. The modulus of elasticity of the soil can be determined again using Equation (6-15); also knowing the values of other parameters, the settlement of stone column improved ground can be determined using these prediction curves.

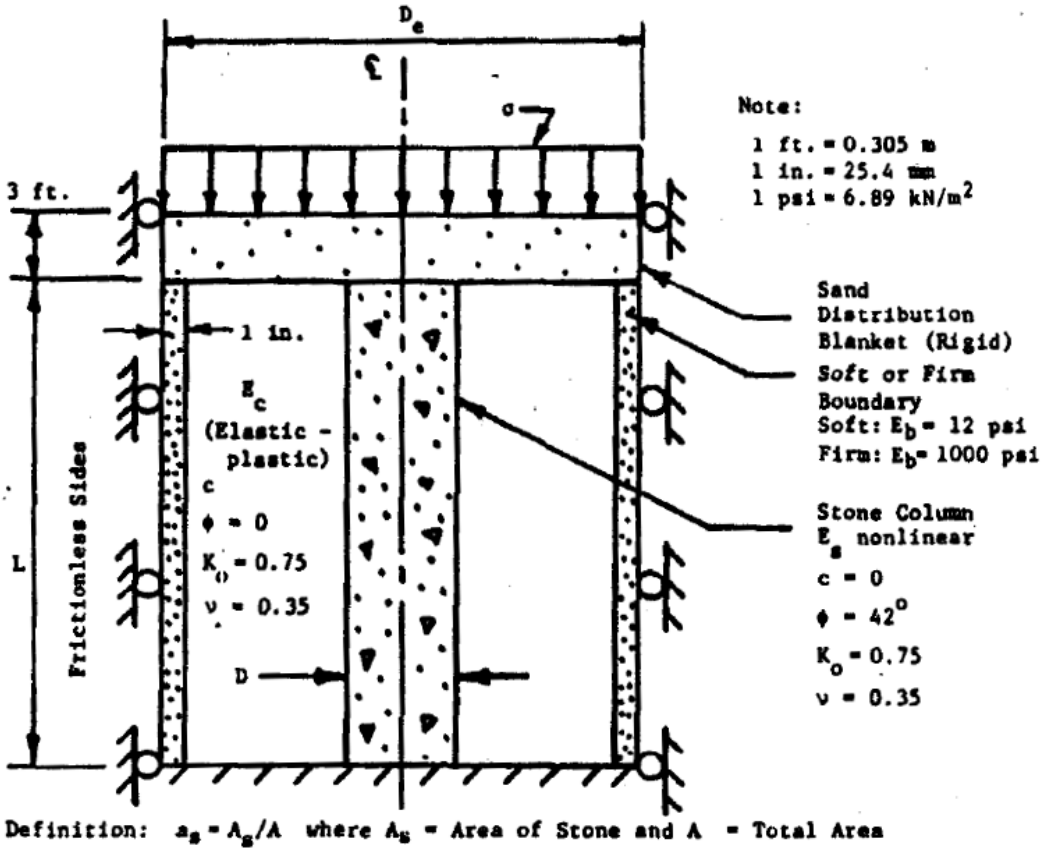

Figure 6-12 Unit cell model for compressible cohesive soil [118]

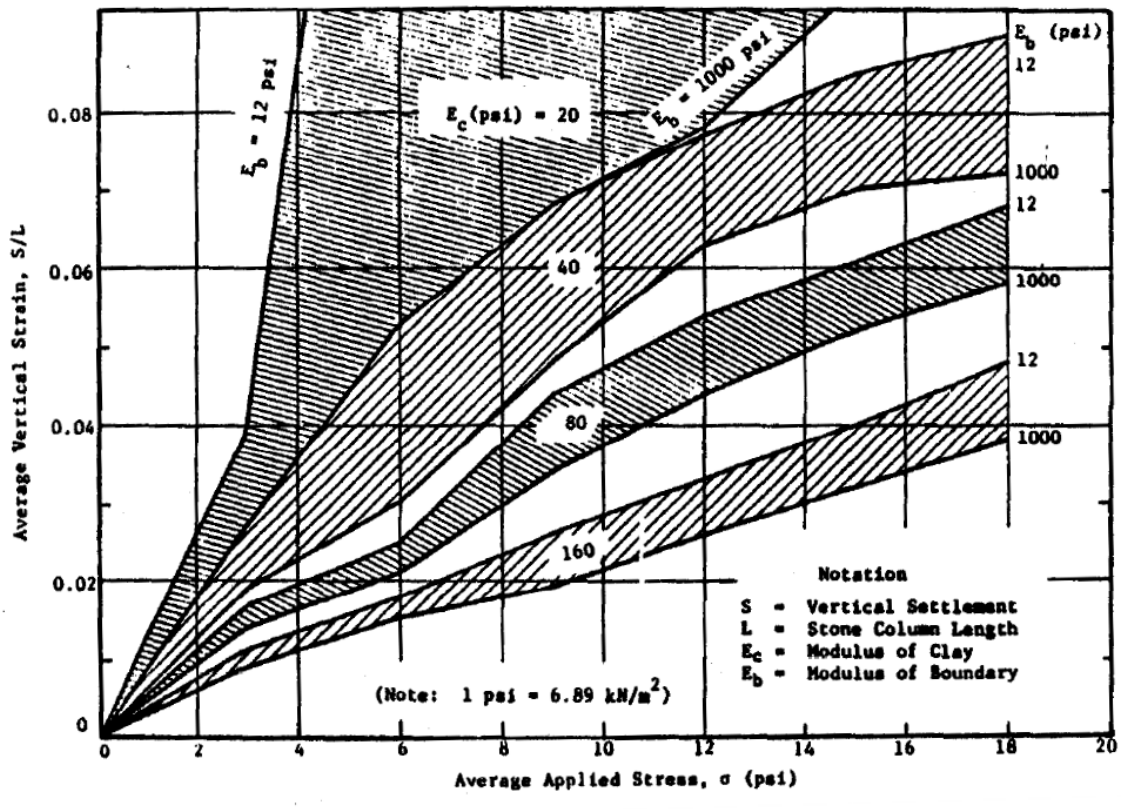

Figure 6-13 Settlement prediction curve for compressible cohesive soil with an area replacement ratio of 0.1 and *L/D* of 5 [118]

Priebe's Method

The Priebe's method is a semi-empirical method commonly used for predicting settlement design of stone columns and has been widely used in the industry, especially in Europe, by corporations such as Chambosse & Dobson (undated-a) with GKN Keller and the Vibroflotation Group [121, 129].

The Priebe's method has made a few assumptions for the analyses; the aggregates in a stone column are assumed to be plastic and incompressible; the soil in a unit cell is assumed to have elastic behavior; any change in the volume within the soil is due to the bulging of the column; the radial deformation in the soil is calculated using an infinitely long, elastic hollow cylinder solution; the bulk densities of both the stone column and the soil are neglected; the surrounding soil is assumed to be already displaced due to the inclusion of stone column which therefore results in a liquid state

(the coefficient of earth pressure $K = 1$) [118, 121, 129]. In addition, equal vertical strain (settlement) assumption and unit cell idealization are used. Based on the conservation of load and equal strain assumption, deformation and stresses in the elastic soil can be calculated systematically [130].

The following equations provide the derivation of the basic settlement improvement factor based on the aforementioned assumptions:

$$n_0 = 1 + \frac{A_s}{A}\left[\frac{1/2 + f(\nu, A_s/A)}{K_{aC} \cdot f(\nu, A_s/A)} - 1\right] \tag{6-18}$$

Where n_0 is the basic settlement improvement factor, A_s is the area of the stone column, A is the total area within a unit cell, K_{aC} is the Rankine's active earth pressure, which is a function of:

$$K_{aC} = \tan^2(45° - \varphi_s/2) \tag{6-19}$$

and $f(\nu, A_s/A)$can be expressed as:

$$f(\nu, A_s/A) = \frac{(1-\nu)\cdot(1-A_s/A)}{1-2\nu+A_s/A} \tag{6-20}$$

where ν is the Poisson's ratio of the surrounding soil and φ_s is the friction angle of the stone column.

If a Poisson's ratio of $\nu = 1/3$ is used, Equation (6-18) becomes:

$$n_0 = 1 + \frac{A_s}{A}\left[\frac{5 - A_s/A}{4 \cdot K_{aC} \cdot (1 - A_s/A)} - 1\right] \tag{6-21}$$

The relationship between the basic settlement improvement factor n_0, the friction angle of the stone column material φ_s and the reciprocal area ratio A/A_s can be illustrated in the widely-known diagram as shown in Figure 6-14. In the end, the settlement of stone column improved ground can be calculated by using the improvement factor as:

$$S_t = S/n_0 \tag{6-22}$$

Where S_t is the settlement of the stone column treated ground and S is the settlement of the untreated ground which can be determined using conventional settlement analysis methods.

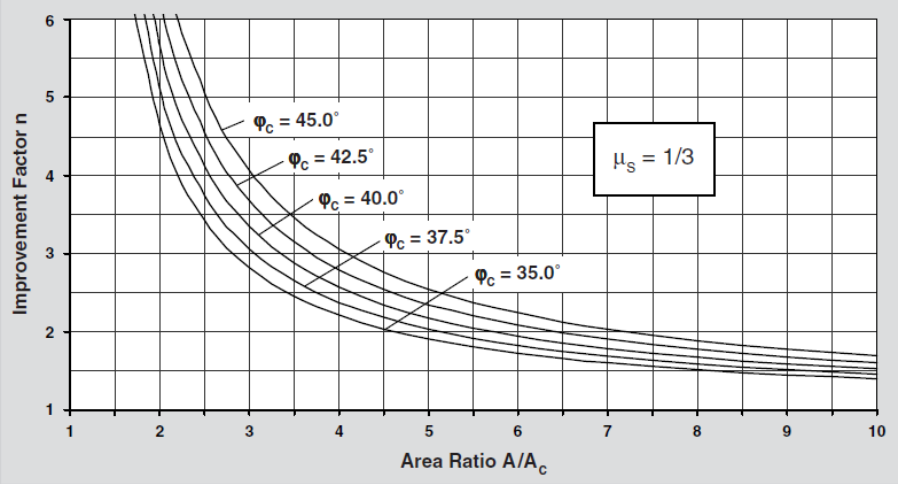

Figure 6-14 Design chart for stone column using Priebe's Method [129]

It should be noted that the above method is the original one published in 1976; there have been a few adaptions, extensions and supplements made in the 1995 version [129] which justify a more comprehensive application of this method, such as the consideration of the compressibility of stone column (resulting in slightly increased value of predicted settlement) , overburden (leading to a reduced value of predicted settlement) and compatibility control (prevents the compressibility of the stone column from being greater than the settlement of the composite structure). Overall, the consideration of these factors results in smaller values of predicted settlement (especially when the overburden is included) which may provide unconservative settlement predictions; therefore, it is considered that the calculation of the basic improvement factor n_0 is adequate for a lower bound settlement estimation.

Time Rate of Settlement

The inclusion of stone columns may significantly accelerate the process of the primary consolidation since the stone columns act like drainage paths. The report by Barksdale and Bachus [118] showed that the time rate of primary consolidation settlement of stone column treated ground could be estimated by using the sand drain consolidation theory, in which the primary consolidation settlement of a cohesive soil layer reinforced by stone column at time t can be expressed as:

$$S'_t = U \cdot S_t \tag{6-23}$$

where S'_t is the primary consolidation settlement at time t, S_t is the ultimate primary consolidation settlement and U is the average degree of consolidation considering both radial and vertical drainage, which is expressed as:

$$U = 1 - (1 - U_z)(1 - U_r) \tag{6-24}$$

where U_z is the degree of consolidation considering only vertical drainage and U_r is the degree of consolidation considering only radial drainage.

U_z can be determined by using Figure 6-15 and the vertical time factor T_z which is expressed by the following function:

$$T_z = \frac{C_v \cdot t}{(\frac{H}{N})^2} \tag{6-25}$$

where C_v is the coefficient of consolidation in the vertical direction, t is the elapsed time, H is the thickness of the soil layer and N is the number of permeable drainage surface at the top and/or the bottom of the layer ($N = 1$ for one-way draining and $N = 2$ for two-way draining).

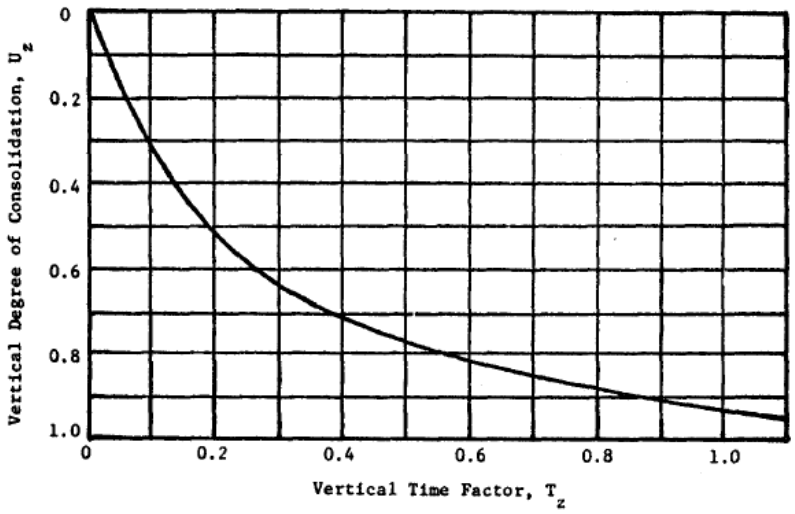

Figure 6-15 Determination of the degree of consolidation considering only vertical drainage [118]

U_r can be determined by using Figure 6-16 and the radial time factor T_r which is expressed by the following function:

$$T_r = \frac{C_{vr} \cdot t}{(D_e)^2} \tag{6-26}$$

where C_{v_r} is the coefficient of consolidation in the radial direction (which is usually 3 – 5 times greater than the coefficient of consolidation in the vertical direction), t is the elapsed time and D_e is the equivalent diameter of the unit cell. In Figure 6-16, the determination of U_r requires the calculation of n^* which can be expressed as:

$$n^* = D_e/D' \tag{6-27}$$

where D' is the reduced drain diameter which accounts for the "smear effects" in the surrounding soil (a reduction effect in the horizontal permeability of the soil around stone columns due to the remolding, disturbance and smear of the surrounding soil caused by the installation of stone columns). Literature [118] indicated that the research regarding the smear effects on the stone column was very limited; if not having enough information about the smear effect, it was tentatively recommended that the reduced drain diameter could be taken as from 1/2 to 1/15 of the original diameter of the stone column [118].

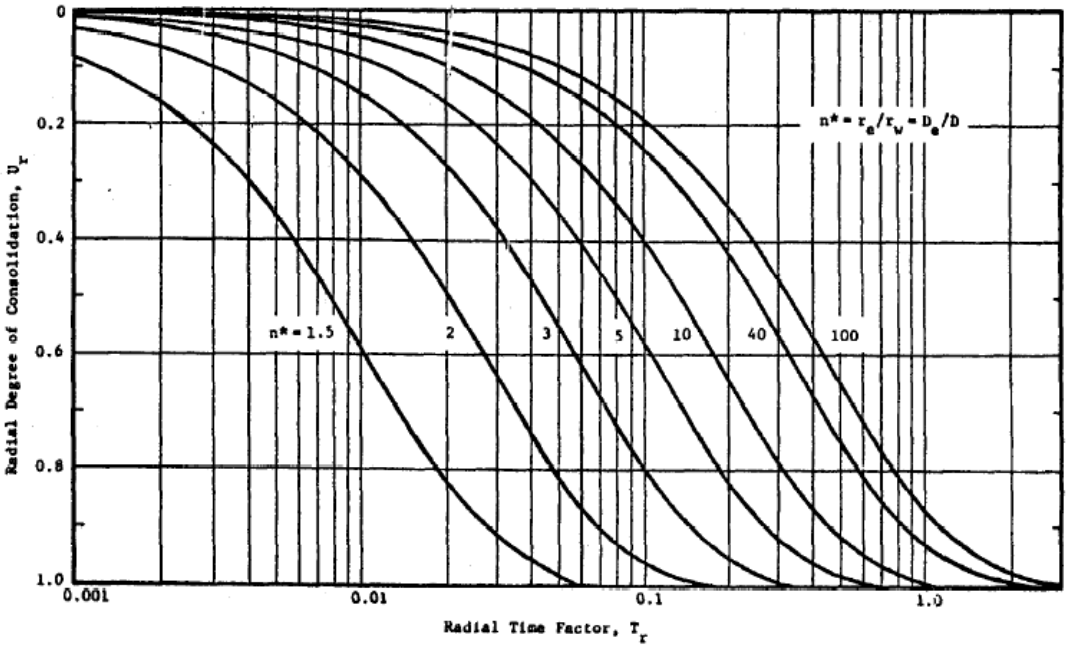

Figure 6-16 Determination of the degree of consolidation considering only radial drainage [118]

Secondary Compression Settlement

Once excess pore water pressure has dissipated at the end of the primary consolidation stage, the volume of soil body continues to decrease under loading due to the plastic deformation of the soil particles. The settlement of ground associated with this volume decrease is referred to as the secondary compression settlement. In the report by Barksdale and Bachus [118], a crude method was proposed to determine the secondary compression settlement based on a linear relationship between the secondary compression settlement and the logarithm of time by using the following function:

$$\Delta S = C_\alpha H \log_{10} \frac{t_2}{t_1} \tag{6-28}$$

where ΔS is the secondary compression settlement of the soil layer, C_α is the secondary compression index which is a physical constant evaluated by keeping the 1-d consolidation test beyond the primary consolidation stage, H is the thickness of the soil layer, t_1 is the time when the secondary compression stage starts (usually taken as the time when 90% of the primary consolidation settlement is achieved) and t_2 is the time of interest during the secondary compression stage.

Different from the primary consolidation settlement, the installation of stone columns does not accelerate the rate of secondary compression settlement. In the case where very soft clay and highly organic soils are present, the secondary compression settlement should be specially addressed since it can be even equal to or greater than the primary consolidation settlement [118]. Research [131] also found that the surcharge loading method can be used to effectively control the secondary compression settlement; sometimes, the applied surcharge loading should be greater than the ultimate service load in order to achieve greatest effectiveness.

DESIGN EXAMPLE FOR SETTLEMENT

This section provides an example to determine the settlement of the stone column treated ground.

The background information of the example project is shown Table 6-1and Table 6-2.

Table 6-1 Treatment area and loading condition

Embankment length, ft	50
Embankment width, ft	20
Embankment height, ft	8
Saturated unit weight of embankment material, pcf	125
Unit weight of concrete pavement, pcf	150
Thickness of concrete pavement, in	12
Wing wall and other structures, kips	50
Traffic loading, kips	150

Table 6-2 Soil properties for bearing capacity calculation

Layer	Type	Depth	Thickness, ft	Undrained shear strength, psf	PI	Saturated unit weight, pcf
1	Soft clay	0 - 20 ft	20	500	20	100
2	Very soft clay	20 - 30 ft	10	250	40	100
3	Soft clay	30 - 35 ft	5	500	20	100
4	Firm bearing layer	> 35 ft	\	\	\	\

The friction angle of the stone column is assumed to be 40 degree.

Step 1

1. Prepare preliminary information, including the treatment area, loading condition, soil properties for each soil layer and the stone column information.

   In addition to the data shown in Table 6-2, additional soil property information shown in Table 6-3 is need to perform the settlement calculation.

Table 6-3 Additional soil properties for settlement calculation

Layer	Type	Depth	Thickness, ft	Compression index	Initial void ratio	Drained Poisson's ratio
1	Soft clay	0 - 20 ft	20	0.25	1.5	0.42
2	Very soft clay	20 - 30 ft	10	0.8	3.5	0.45
3	Soft clay	30 - 35 ft	5	0.25	1.5	0.42
4	Firm bearing layer	> 35 ft	\	\	\	\

2. Calculate the total factored stress Q_f on the treatment area.

   The total dead load (DL) can be calculated as:

Embankment weight + Pavement weight + Wing wall and other structures

= (125*50*20*8)/1000 + (150*50*20*12/12)/1000 +50 = 1000+150+50

= 1200 kips.

   The total live load (LL) is:

Traffic loading = 150 kips

   The total factored load P_f can be calculated as:

$$P_f = 1.2\ (\text{DL} + 1.67\ \text{LL}) = 1.2 \times (1200 + 1.67 \times 150) = 1741\ \text{kips}$$

   The total factored stress Q_f can be calculated as:

$$Q_f = P_f / A_{total} = 1741\ \text{kips}/(50\ \text{ft} \times 20\ \text{ft}) = 1741\ \text{kips}/1000\ \text{ft}^2 = 1741 psf$$

Step 2

1. Determine the trial spacing, diameter and installation pattern for the stone columns.

   Trial column spacing $s = 6$ ft

Trial column diameter $D = 3.5$ ft

Trial installation pattern: equilateral triangular pattern ($C_1 = \pi/4$ for a square pattern and $C_1 = \pi/2\sqrt{3}$ for an equilateral triangular pattern).

2. Calculate area replacement ratio, area of each stone column and area of each unit cell.

   Area replacement ratio: $a_s = C_1(\frac{D}{s})^2 = \frac{\pi}{2\sqrt{3}}(\frac{3.5}{6})^2 = 0.308$

   Area of each stone column, ft^2: $A_s = \pi(\frac{D}{2})^2 = 9.62$ ft^2

   Area of each unit cell, ft^2: $A = A_s/a_s = 31.23$ ft^2

   Area of soil in each unit cell, ft^2: $A_c = A - A_s = 21.61$ ft^2

3. Estimate stress concentration ratio SCR and calculate ratio of stress in the stone column and the surrounding soil.

   Assume $SCR = 3$

   Ratio of stress in the stone column:

$$\mu_s = \frac{SCR}{1 + (SCR - 1) \cdot a_s} = \frac{3}{1 + 2 \cdot 0.308} = 1.856$$

   Ratio of stress in the surrounding soil:

$$\mu_c = \frac{1}{1 + (SCR - 1) \cdot a_s} = 0.619$$

Step 3

1. Determine the primary consolidation settlement of the stone column treated ground using the Equilibrium Method:

   a. Calculate the initial effective vertical stress $\bar{\sigma}_0$ in the center of each soil layer (assuming water table is at the ground surface):

      Layer 1: $\bar{\sigma}_{0-1} = (100 \text{ pcf-}62.4 \text{ pcf}) \times 10 \text{ ft} = 376$ psf

      Layer 2:

      $\bar{\sigma}_{0-2} = 100 \text{ pcf} \times 20 \text{ ft} + 100 \text{ pcf} \times 5 \text{ ft-}62.4 \text{ pcf} \times 25 \text{ ft} = 940$ psf

      Layer 3: $\bar{\sigma}_{0-3} = (100 \text{ pcf-}62.4 \text{ pcf}) \times (20 \text{ ft} + 10 \text{ ft} + 2.5 \text{ ft}) = 1222$ psf

b. Estimate the change in the vertical stress $\Delta\sigma_c$ in the surrounding soil due to the embankment loading at the center of each soil layer by using the Boussinesq stress distribution theory:

The vertical stress in the surrounding soil σ_c at the ground Surface:

$\sigma_c = \mu_c\sigma = \mu_c Q_f = 0.619 \times 1741$ psf $= 1078$ psf

Layer 1: $z/B = 10$ ft/50 ft $= 0.2$B

From the Boussinesq solution shown in Figure 6-7, $I_{z-1} = 0.91$

$$\Delta\sigma_{c-1} = I_{z-1}\sigma_c = 0.91 \times 1078 = 981 \text{ psf}$$

Layer 2: $z/B = 25$ ft/50 ft $= 0.5$B $\quad I_{z-2} = 0.7$

$$\Delta\sigma_{c-2} = I_{z-2}\sigma_c = 0.7 \times 1078 = 755 \text{ psf}$$

Layer 3: $z/B = 32.5$ ft/50 ft $= 0.65$B $\quad I_{z-3} = 0.55$

$$\Delta\sigma_{c-3} = I_{z-3}\sigma_c = 0.55 \times 1078 = 593 \text{ psf}$$

c. Determine the primary consolidation settlement S_t of stone column treated ground for each layer

Layer 1:

$$S_{t-1} = \left(\frac{C_c}{1+e_0}\right)\log_{10}\left(\frac{\bar{\sigma}_0 + \Delta\sigma_c}{\bar{\sigma}_0}\right) \cdot H$$

$$= \left(\frac{0.25}{1+1.5}\right)\log_{10}\left(\frac{376+981}{376}\right) \times 20 \times \frac{12 \text{ in}}{1 \text{ ft}} = 13.37$$

Layer 2:

$$S_{t-2} = \left(\frac{C_c}{1+e_0}\right)\log_{10}\left(\frac{\bar{\sigma}_0+\Delta\sigma_c}{\bar{\sigma}_0}\right) \cdot H = \left(\frac{0.8}{1+3.5}\right)\log_{10}\left(\frac{940+755}{940}\right) \times 10 \times \frac{12 \text{ in}}{1 \text{ ft}} = 5.46$$

Layer 3:

$$S_{t-3} = \left(\frac{C_c}{1+e_0}\right)\log_{10}\left(\frac{\bar{\sigma}_0 + \Delta\sigma_c}{\bar{\sigma}_0}\right) \cdot H$$

$$= \left(\frac{0.25}{1+1.5}\right)\log_{10}\left(\frac{1222+593}{1222}\right) \times 5 \times \frac{12 \text{ in}}{1 \text{ ft}} = 1.03$$

d. Determine the total primary consolidation settlement S_t of stone column treated ground:

$$S_t = S_{t-1} + S_{t-2} + S_{t-3} = 19.86 \text{ in}$$

e. Calculate the primary consolidation settlement S of untreated ground:

Layer 1: $\Delta\sigma_1 = I_{z-1}\sigma = 0.91 \times 1741 = 1584$ psf

$$S_1 = (\frac{C_c}{1+e_0})\log_{10}(\frac{\bar{\sigma}_0 + \Delta\sigma}{\bar{\sigma}_0}) \cdot H$$

$$= (\frac{0.25}{1+1.5})\log_{10}(\frac{376+1584}{376}) \times 20 \times \frac{12 \text{ in}}{1 \text{ ft}} = 17.21$$

Layer 2: $\Delta\sigma_2 = I_{z-2}\sigma = 0.7 \times 1741 = 1219$ psf

$$S_2 = (\frac{C_c}{1+e_0})\log_{10}(\frac{\bar{\sigma}_0 + \Delta\sigma}{\bar{\sigma}_0}) \cdot H$$

$$= (\frac{0.8}{1+3.5})\log_{10}(\frac{940+1219}{940}) \times 10 \times \frac{12 \text{ in}}{1 \text{ ft}} = 7.71$$

Layer 3: $\Delta\sigma_3 = I_{z-3}\sigma = 0.55 \times 1741 = 958$ psf

$$S_3 = (\frac{C_c}{1+e_0})\log_{10}(\frac{\bar{\sigma}_0 + \Delta\sigma}{\bar{\sigma}_0}) \cdot H$$

$$= (\frac{0.25}{1+1.5})\log_{10}(\frac{1222+958}{1222}) \times 5 \times \frac{12 \text{ in}}{1 \text{ ft}} = 1.51S$$

$$= S_1 + S_2 + S_3 = 26.43 \text{ in}$$

f. Calculate the improvement factor S/S_t (ratio of settlement in the untreated ground to that in the stone column treated ground):

$$S/S_t = \frac{26.43}{19.86} = 1.33$$

2. Determine the primary consolidation settlement of the stone column treated ground using the Finite Element Method:

   a. Calculate the drained modulus of elasticity of the soil:

      Layer 1:

      The Poisson's ratio (drained) ν can be estimated based on Figure 6-11; for this layer, $\nu = 0.42$ is adopted.

      Based on the calculation of the Equilibrium method, the initial average effective vertical stress is $\bar{\sigma}_{0-1} = 376$ psf and the change in the vertical stress in the surrounding soil due to embankment loading is $\Delta\sigma_{c-1} = 981$ psf, therefore the average of initial and final stress state applied in the field (vertical stress) σ_{va} is:

$$\sigma_{va} = \frac{\bar{\sigma}_0 + \Delta\sigma_c}{2} = 679 \text{ psf}$$

Using Equation (6-15), the drained modulus of elasticity of the soil can be calculated as:

$$E_c = \frac{(1+\nu)(1-2\nu)(1+e_0)\sigma_{va}}{0.435(1-\nu)C_c} = \frac{(1+0.42)(1-2\times 0.42)(1+1.5)679}{0.435(1-0.42)0.25}$$
$$= 6115 \text{ psf} = 42.47 \text{ psi}$$

Layer 2: $\nu = 0.45$ $\bar{\sigma}_{0-2} = 940$ psf $\Delta\sigma_{c-2} = 755$ psf

$$\sigma_{va} = \frac{\bar{\sigma}_0 + \Delta\sigma_c}{2} = 848 \text{ psf}$$

$$E_c = \frac{(1+\nu)(1-2\nu)(1+e_0)\sigma_{va}}{0.435(1-\nu)C_c} = \frac{(1+0.45)(1-2\times 0.45)(1+3.5)848}{0.435(1-0.45)0.8}$$
$$= 2891 \text{ psf} = 20.07\text{psi}$$

Layer 3: $\nu = 0.42$ $\bar{\sigma}_{0-3} = 1222$ psf $\Delta\sigma_{c-3} = 593$ psf

$$\sigma_{va} = \frac{\bar{\sigma}_0 + \Delta\sigma_c}{2} = 908 \text{ psf}$$

$$E_c = \frac{(1+\nu)(1-2\nu)(1+e_0)\sigma_{va}}{0.435(1-\nu)C_c} = \frac{(1+0.42)(1-2\times 0.42)(1+1.5)908}{0.435(1-0.42)0.25}$$
$$= 8177 \text{ psf} = 56.78psi$$

b. Estimate the modulus of elasticity of the stone column using Equation (6-17):

Without having specific test data, the following parameters can be assumed:

$K = 88.6$, $n = 1.14$, $R_f = 0.86$, $c = 0$ and $\varphi_s = 40°$.

Based on the example design for bearing capacity shown previously, for the most critical failure mode:

$\sigma_1 = 7015$ psf $\sigma_2 = \sigma_3 = 1525$ psf

$$\sigma_\theta = \sigma_1 + \sigma_2 + \sigma_3 = 7015 + 1525 \times 2 = 10065 \text{ psf}$$

Therefore:

$$E_s = K \cdot \sigma_\theta^n \cdot [1 - \frac{(\sigma_1 - \sigma_3)R_f}{(\frac{2(c \cdot \cos\varphi_s + \sigma_3 \sin\varphi_s)}{1 - \sin\varphi_s})}]$$

$$= 88.6 \cdot 10065^{1.14} \cdot [1 - \frac{(7015 - 1525) \times 0.86}{(\frac{2(0 + 1525 \times \sin 40°)}{1 - \sin 40°})}] = 452857 \text{ psf} = 3145 \text{ psi}$$

c. Decide the compressibility of the soil:

If $E_s/E_c \leq 10$, it is low compressibility cohesive soil;

If $E_s/E_c > 10$, it is compressible cohesive soil.

Based on this rule, all the three layers are compressible cohesive soil.

d. Determine the average vertical strain using the design charts shown in Appendix A:

For this design example: $a_s = 0.308$ and $L/D = 10$; therefore, interpolate results by using Figure A-8 and Figure A-11 is needed.

The average applied stress: $\sigma = Q_f = 1741$ psf $= 12.09$ psi

Layer 1: $E_c =$ 42.47 psi $\quad \Delta\sigma_1 = 1584$ psf $= 11.00$ psi

Layer 2: $E_c =$ 20.07 psi $\quad \Delta\sigma_2 = 1219$ psf = 8.47 psi

Layer 3: $E_c =$ 56.78 psi $\quad \Delta\sigma_3 = 958$ psf = 6.65 psi

To be conservative, $E_b = 12$ psi is used as the modulus of the soft boundary for all the layers.

The average vertical strain S/L and settlement S can be estimated:

Layer 1: From Figure A-8 $S/L =$ 0.049 where $a_s = 0.25$

From Figure A-11 $S/L =$ 0.022 where $a_s = 0.35$

Therefore, $S/L =$ 0.0333 for $a_s = 0.308$

$S_1 = L_1 \times$ 0.0333 = 20 × 0.0333 × (12 in/1ft) = 7.99 in

Layer 2: From Figure A-8 $S/L =$ 0.062 where $a_s = 0.25$

From Figure A-11 $S/L =$ 0.03 where $a_s = 0.35$

Therefore, $S/L =$ 0.0434 for $a_s = 0.308$

$S_2 = L_2 \times$ 0.0434 = 10 ft × 0.0434 × (12 in/1ft) = 5.21 in

Layer 3: From Figure A-8 $S/L =$ 0.023 where $a_s = 0.25$

From Figure A-11 $S/L =$ 0.01 where $a_s = 0.35$

Therefore, $S/L =$ 0.0155 for $a_s = 0.308$

$S_3 = L_3 \times$ 0.0155 = 5 ft × 0.0155 × (12 in/1ft) = 0.93 in

e. Calculate the total settlement of the stone column treated ground:

$$S_t = S_1 + S_2 + S_3 = 14.13 \text{ in}$$

f. Calculate the improvement factor S/S_t (ratio of settlement in the untreated ground to that in the stone column treated ground):

$$S/S_t = \frac{26.43}{14.13} = 1.87$$

3. Determine the primary consolidation settlement of the stone column treated ground using the Priebe's Method:

a. Calculate the improvement factor n_0:

The friction angle of the stone column is assumed to be 40°. The Rankine's active earth pressure:

$$K_{aC} = \tan^2(45° - \varphi_s/2) = \tan^2(45° - 40°/2) = 0.217$$

For Layer 1 & 3, the Poisson's ratio $\nu = 0.42$:

$$f(\nu, A_s/A) = \frac{(1-\nu)\cdot(1-A_s/A)}{1-2\nu+A_s/A} = \frac{(1-0.42)\cdot(1-0.308)}{1-2\times0.42+0.308} = 0.858$$

$$n_0 = 1 + \frac{A_s}{A}\left[\frac{1/2+f(\nu,A_s/A)}{K_{aC}\cdot f(\nu,A_s/A)} - 1\right] = 1 + 0.308\left[\frac{1/2+0.858}{0.217\cdot0.858} - 1\right] = 2.938$$

For Layer 2, the Poisson's ratio $\nu = 0.45$:

$$f(\nu, A_s/A) = \frac{(1-\nu)\cdot(1-A_s/A)}{1-2\nu+A_s/A} = \frac{(1-0.45)\cdot(1-0.308)}{1-2\times0.45+0.308} = 0.933$$

$$n_0 = 1 + \frac{A_s}{A}\left[\frac{1/2+f(\nu,A_s/A)}{K_{aC}\cdot f(\nu,A_s/A)} - 1\right] = 1 + 0.308\left[\frac{1/2+0.933}{0.217\cdot0.933} - 1\right] = 2.872$$

b. Calculate the primary consolidation settlement of untreated ground:

This has been previously determined by using the conventional 1-d consolidation theory:

$$S_1 = 17.21 \text{ in}$$

$$S_2 = 7.71 \text{ in}$$

$$S_3 = 1.51 \text{ in}$$

c. Calculate the primary consolidation settlement of stone column treated ground:

Layer 1: $S_{t-1} = S_1/n_0 = 17.21/2.938 = 5.86$ in

Layer 2: $S_{t-2} = S_2/n_0 = 7.71/2.872 = 2.68$ in

Layer 3: $S_{t-3} = S_3/n_0 = 1.51/2.938 = 0.51$ in

Total: $S_t = S_{t-1} + S_{t-2} + S_{t-3} = 9.05$ in

d. Calculate the overall improvement factor S/S_t (ratio of settlement in the untreated ground to that in the stone column treated ground):

$$S/S_t = \frac{26.43}{9.05} = 2.92$$

4. Determine the lower and upper bounds of predicted primary consolidation settlements of stone column treated ground:

The upper bound settlement (by the Equilibrium Method):

$$S_t = 19.86 \text{ in}$$

The lower bound settlement (by the Priebe's Method):

$$S_t = 9.05 \text{ in}$$

The average of the settlements (for the lower and upper bounds):

$$S_t = \frac{19.86 + 9.05}{2} = 14.46 \text{ in}$$

The average of the settlements (for the three methods):

$$S_t = \frac{19.86 + 14.13 + 9.05}{3} = 14.35 \text{ in}$$

Therefore, it appears that the Finite Element Method provides settlement estimations that are reasonably close to the average of the three methods.

Step 4

1. Determine the time rate of settlement. Assuming t is at 100 day. Additional soil property information that is required for the calculation is shown in Table 6-4.

Table 6-4 Additional soil properties for time rate of settlement calculation

Layer	Type	Depth	Thickness, ft	Coefficient of consolidation in the vertical direction, ft^2/day	Coefficient of consolidation in the radial direction, ft^2/day
1	Soft clay	0 - 20 ft	20	0.04	0.12
2	Very soft clay	20 - 30 ft	10	0.08	0.24
3	Soft clay	30 - 35 ft	5	0.04	0.12
4	Firm bearing layer	> 35 ft	\	\	\

a. Determine the degree of consolidation U_z considering only vertical drainage by using Figure 6-15:

Layer 1: $T_z = \frac{C_v \cdot t}{(\frac{H}{N})^2} = \frac{0.04 ft^2/day \cdot 100 day}{(\frac{20}{2})^2} = 0.04$ $U_z = 0.15$

Layer 2: $T_z = \frac{C_v \cdot t}{(\frac{H}{N})^2} = \frac{0.08 ft^2/day \cdot 100 day}{(\frac{10}{2})^2} = 0.32$ $U_z = 0.65$

Layer 3: $T_z = \frac{C_v \cdot t}{(\frac{H}{N})^2} = \frac{0.04 ft^2/day \cdot 100 day}{(\frac{5}{2})^2} = 0.64$ $U_z = 0.83$

b. Determine the degree of consolidation U_r considering only radial drainage by using Figure 6-16:

The equivalent diameter D_e of a unit cell can be determined by using Equation (6-1) for an equilateral triangular pattern:

$$D_e = 1.05s = 1.05 \times 6 = 6.3 \text{ ft}$$

The reduced drain diameter D' is assumed to be 1/5 of the diameter of the stone columns:

$$D' = \frac{1}{5} D = \frac{1}{5} \times 3.5 = 0.7 \text{ ft}$$

$$n^* = D_e / D' = 6.3/0.7 = 9$$

Layer 1: $T_r = \frac{C_{vr} \cdot t}{(D_e)^2} = \frac{0.12 ft^2/day \cdot 100 day}{(6.3)^2} = 0.302$ $U_r = 0.82$

Layer 2: $T_r = \frac{C_{vr} \cdot t}{(D_e)^2} = \frac{0.24 ft^2/day \cdot 100 day}{(6.3)^2} = 0.605$ $U_r = 0.97$

Layer 3: $T_r = \frac{C_{vr} \cdot t}{(D_e)^2} = \frac{0.12 ft^2/day \cdot 100 day}{(6.3)^2} = 0.302$ $U_r = 0.82$

c. Determine the average degree of consolidation considering both radial and vertical drainage U:

Layer 1: $U = 1 - (1 - U_z)(1 - U_r) = 1 - (1 - 0.15)(1 - 0.82) = 0.847$

Layer 2: $U = 1 - (1 - U_z)(1 - U_r) = 1 - (1 - 0.65)(1 - 0.97) = 0.99$

Layer 3: $U = 1 - (1 - U_z)(1 - U_r) = 1 - (1 - 0.83)(1 - 0.82) = 0.969$

d. Determine the primary consolidation settlement of a cohesive soil layer reinforced by stone column at the time $t = 100 day$:

As an example, the settlement of each layer calculated using the Finite Element Method is used to determine the time rate of settlement.

For the Finite Element Method:

$S_1 = 7.99$ in $\quad S_2 = 5.21$ in $\quad S_3 = 0.93$ in

$$S_t = S_1 + S_2 + S_3 = 14.13 \text{ in}$$

Layer 1: $S'_{t1} = U \cdot S_1 = 0.847 \times 7.99 = 6.77$ in

Layer 2: $S'_{t2} = U \cdot S_2 = 0.99 \times 5.21 = 5.16$ in

Layer 3: $S'_{t3} = U \cdot S_3 = 0.969 \times 0.93 = 0.90$ in

Total: $S'_t = S'_{t1} + S'_{t2} + S'_{t3} = 6.77 + 5.16 + 0.9 = 12.83$ in

Step 5

1. Determine the secondary compression settlement ΔS that would occur $t_2 = 5$ year after construction.

   Additional soil property information that is required for the calculation is the secondary compression index for each layer:

   Layer 1: $C_\alpha = 0.005$

   Layer 2: $C_\alpha = 0.01$

   Layer 3: $C_\alpha = 0.005$

   a. Determine t_1 which is the time when 90% of the primary consolidation settlement is achieved for each layer:

      In order to achieve an average degree of consolidation $U = 0.9$considering both radial and vertical drainage for each layer, it is necessary to determine both U_r and U_z for each layer that would lead to $U = 0.9$; following the procedure showed in **Step 4,** it can be determined:

      Layer 1: when $t = 130day$

      $T_r = \frac{C_{vr} \cdot t}{(D_e)^2} = \frac{0.12ft^2/day \cdot 130day}{(6.3)^2} = 0.393 \qquad U_r = 0.88$

      $T_z = \frac{C_v \cdot t}{(\frac{H}{N})^2} = \frac{0.04ft^2/day \cdot 130day}{(\frac{20}{2})^2} = 0.052 \; U_z = 0.2$

$$U = 1 - (1 - U_z)(1 - U_r) = 1 - (1 - 0.2)(1 - 0.88) = 0.904$$

Therefore, $t_1 = 130$ day for Layer 1.

Layer 2: when $t = 50day$

$$T_r = \frac{C_{v_r} \cdot t}{(D_e)^2} = \frac{0.24ft^2/day \cdot 50day}{(6.3)^2} = 0.302 \quad U_r = 0.82$$

$$T_z = \frac{C_v \cdot t}{(\frac{H}{N})^2} = \frac{0.08ft^2/day \cdot 50day}{(\frac{10}{2})^2} = 0.16 \quad U_z = 0.47$$

$$U = 1 - (1 - U_z)(1 - U_r) = 1 - (1 - 0.47)(1 - 0.82) = 0.905$$

Therefore: $t_1 = 50$ day for Layer 2.

Layer 3: when $t = 65day$

$$T_r = \frac{C_{v_r} \cdot t}{(D_e)^2} = \frac{0.12ft^2/day \cdot 65day}{(6.3)^2} = 0.197 \quad U_r = 0.64$$

$$T_z = \frac{C_v \cdot t}{(\frac{H}{N})^2} = \frac{0.04ft^2/day \cdot 65day}{(\frac{5}{2})^2} = 0.416 \quad U_z = 0.72$$

$$U = 1 - (1 - U_z)(1 - U_r) = 1 - (1 - 0.72)(1 - 0.64) = 0.899$$

Therefore: $t_1 = 65$ day for Layer 3.

b. Determine the secondary compression settlement ΔS that would occur $t_2 = 5$ year after construction for each layer:

Layer 1: $\Delta S_1 = C_\alpha H \log_{10} \frac{t_2}{t_1} = 0.005 \times 20 \text{ ft} \times \log \frac{5 \times 365 \text{ day}}{130 \text{ day}} = 0.115$

Layer 2: $\Delta S_2 = C_\alpha H \log_{10} \frac{t_2}{t_1} = 0.01 \times 10 \text{ ft} \times \log \frac{5 \times 365 \text{ day}}{50 \text{ day}} = 0.156$

Layer 3: $\Delta S_3 = C_\alpha H \log_{10} \frac{t_2}{t_1} = 0.005 \times 5 \text{ ft} \times \log \frac{5 \times 365 \text{ day}}{65 \text{ day}} = 0.036$

Total secondary settlement 5 years after construction:

$$\Delta S = \Delta S_1 + \Delta S_2 + \Delta S_3 = 0.115 + 0.156 + 0.036 = 0.307 \text{ ft} = 3.68 \text{ in}$$

BEARING CAPACITY

The possible modes of failure to be considered in the ultimate bearing capacity calculation of a single or a group of stone columns are illustrated in Figure 6-17, Figure 6-18 and Figure 6-19. As shown in the figure, the failure modes of a single stone column consist of global or local bulging failure, shear failure and punching failure; the failure modes of stone column groups consist of lateral spreading failure, general circular failure, bulging failure and punching failure [101].

Special attention needs to be paid to avoiding the bulging failure due to the presence of weak or organic layers; this type of failure has influences on both the time rate and magnitude of settlement; the use of bulging failure analysis for a single column to predict the group behavior yields a conservative solution [101].

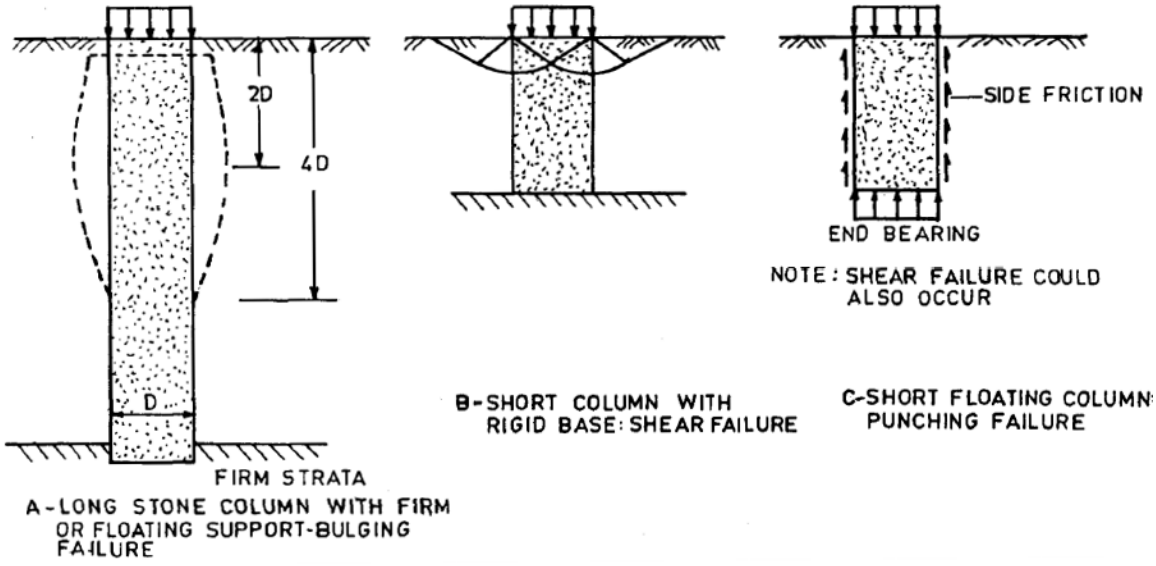

Figure 6-17 Failure modes of a single stone column in a homogeneous soft layer a) bulging failure, b) shear failure and c) punching failure [118]

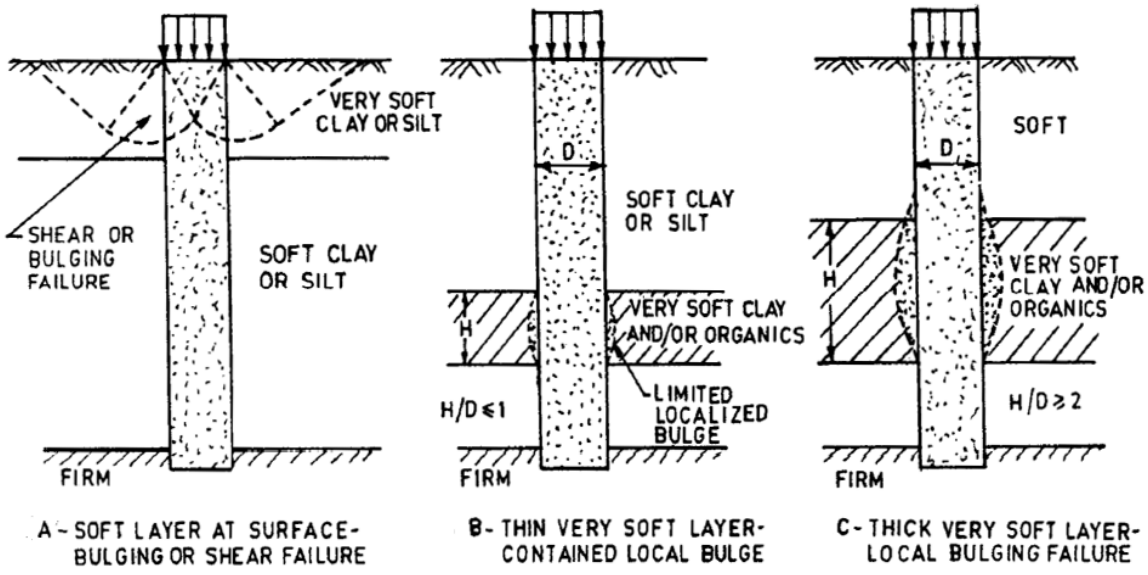

Figure 6-18 Failure modes of a single stone column in a nonhomogeneous cohesive soil a) surface bulging or shear failure, b) local bulge at thin very soft layer and c) local bulge at thick very soft layer [118]

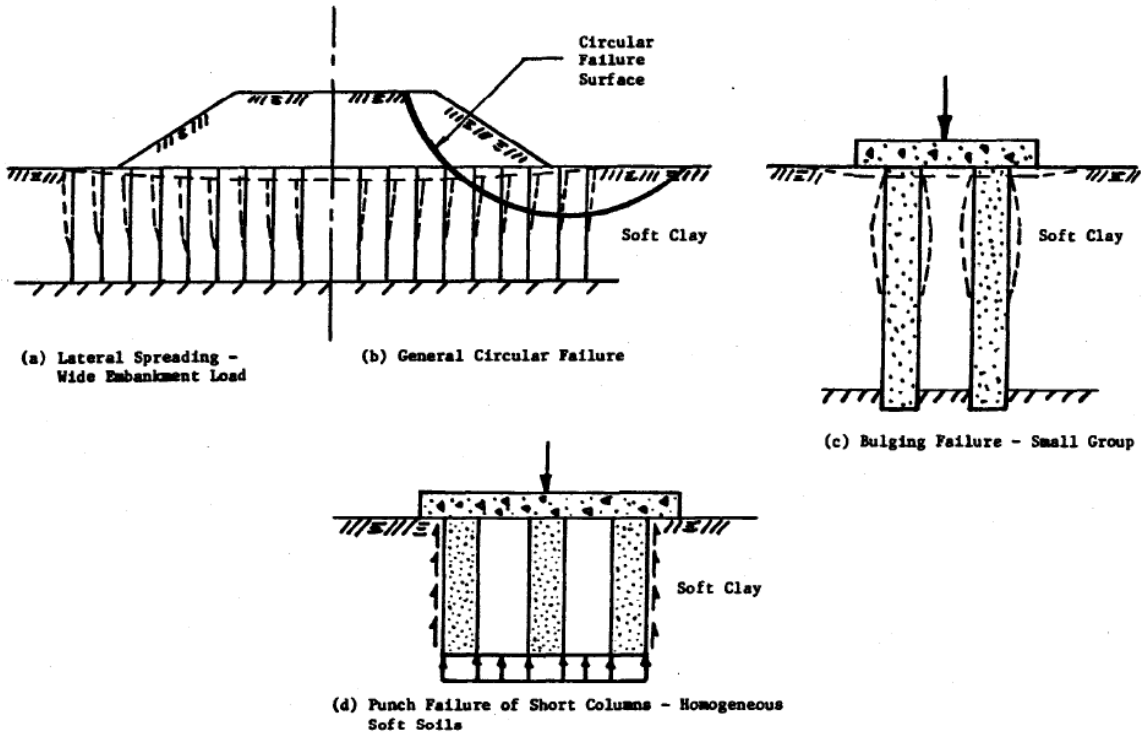

Figure 6-19 Failure modes of stone column groups [118]

Many theories are available to determine the ultimate bearing capacity of a single column surrounded by soft soils and most of them assume a triaxial stress state in the stone columns and failure occurs both in stone columns and the surrounding soil, whereas other methods uses empirical relationships [118]. Regarding the design of stone column groups, some design methods focus on the behavior of an isolated (single) stone column where the bearing capacity of a stone column group is controlled by the behavior of each individual stone column (behavior of individual stone columns are identical in a group of columns) and the number of the stone columns in the group; whereas other methods consider the overall behavior of an infinite grid of stone columns [111]. The following section introduces these methods considering different failure modes and group effects.

Note that the undrained shear strength c_u of the foundation soil, as the key soil property to be used in the bearing capacity analysis, can either be determined by applying the conventional unconsolidated undrained (UU) shear test or by applying the new procedure proposed in Chapter 7.

Failure Mode 1. General Bulging Failure for Single Long Column

The bulging failure shown in Figure 6-17 (a) usually occurs in the most generally constructed long stone columns (with length to diameter ratio equal or greater than 4 – 6) within the depth of the upper 3-diameters of the stone column. Either the cavity expansion theory [132] or the bearing capacity factor method [118] can be used to calculate the bearing capacity of stone column treated ground considering the general bulging failure.

Cavity expansion theory

A very conservative way to determine the bearing capacity of stone columns in homogenous soil considering general bulging failure is by applying classic plasticity theory, in which the failure of a stone column occurs when the lateral confining pressure σ_3 reaches the ultimate passive resistance mobilized by the surrounding soil as the stone column bulges against the soil [118]. In this case, the ratio of the ultimate vertical

stress q_{ult} (i.e. σ_1) to the ultimate lateral stress σ_3 is equal to the coefficient of passive earth pressure K_p which is a function of the internal friction angle of the stone column φ_s:

$$\sigma_1/\sigma_3 = K_p = \frac{1+\sin\varphi_s}{1-\sin\varphi_s} \tag{6-29}$$

$$q_{ult} = \sigma_3 \cdot \frac{1+\sin\varphi_s}{1-\sin\varphi_s} \tag{6-30}$$

where q_{ult} is the ultimate bearing stress that the stone column can sustain and the other parameters are previously defined.

Hughes and Withers [133] proposed a cavity expansion theory in which the bulging failure of a stone column is modeled as an infinitely long expanding cylindrical cavity (similar to the cavity in a pressure-meter test) [118] using elastic-plastic theory for frictionless material; Vesic [132] also proposed a cavity expansion theory taking into account both the friction and cohesion of soils. The ultimate lateral stress σ_3 of Vesic's cavity expansion theory is expressed as:

$$\sigma_3 = cF_c' + qF_q' \tag{6-31}$$

with

$$q = \frac{(1+2\cdot K_0)\cdot\sigma_v}{3} \tag{6-32}$$

$$\sigma_v = \gamma_c \cdot h \tag{6-33}$$

$$h = d_f + \frac{1}{2}D\tan(45^\circ + \frac{\varphi_s}{2}) \tag{6-34}$$

where c is the cohesion of the surrounding cohesive soil (equivalent to undrained shear strength), q is the mean stress at the failure depth, K_0 is the coefficient of earth pressure at rest ($K_0 = 1 - \sin\varphi_c$), φ_c is the friction angle of the surrounding soil (for clay under undrained condition $\varphi_c = 0$), σ_v is the overburden pressure, γ_c is the saturated or wet unit weight of the soil, h which is the depth where the bulging failure occurs can be estimated as a function of [134] the depth of the foundation structure (if any) below ground surface d_f, the diameter of the stone column D and the friction angle of the stone column φ_s as shown in Equation (6-34), F_c' and F_q' are cavity expansion factors determined using Figure 6-20 or Equation (6-35) and (3-12).

$$F_c' = \ln I_r + 1 \tag{6-35}$$

$$F_q' = (1+\sin\varphi_c)(I_r\sec\varphi_c)^{\frac{\sin\varphi_c}{1+\sin\varphi_c}} \tag{6-36}$$

The Rigidity Index shown in Figure 6-20 is determined as follows:

$$I_r = \frac{E}{2(1+\nu)(c+q\tan\varphi_c)} \tag{6-37}$$

where E is the modulus of elasticity of the surrounding soils in which the failure occurs (use an upper bound limit $E = 11c_u$ for soft to stiff non-organic soils; use an lower bound limit $E = 5c_u$ for very soft or organic soil with Plasticity Index greater than 30), ν is the Poisson's ratio (0.5 for undrained clay) and other parameters are previously defined.

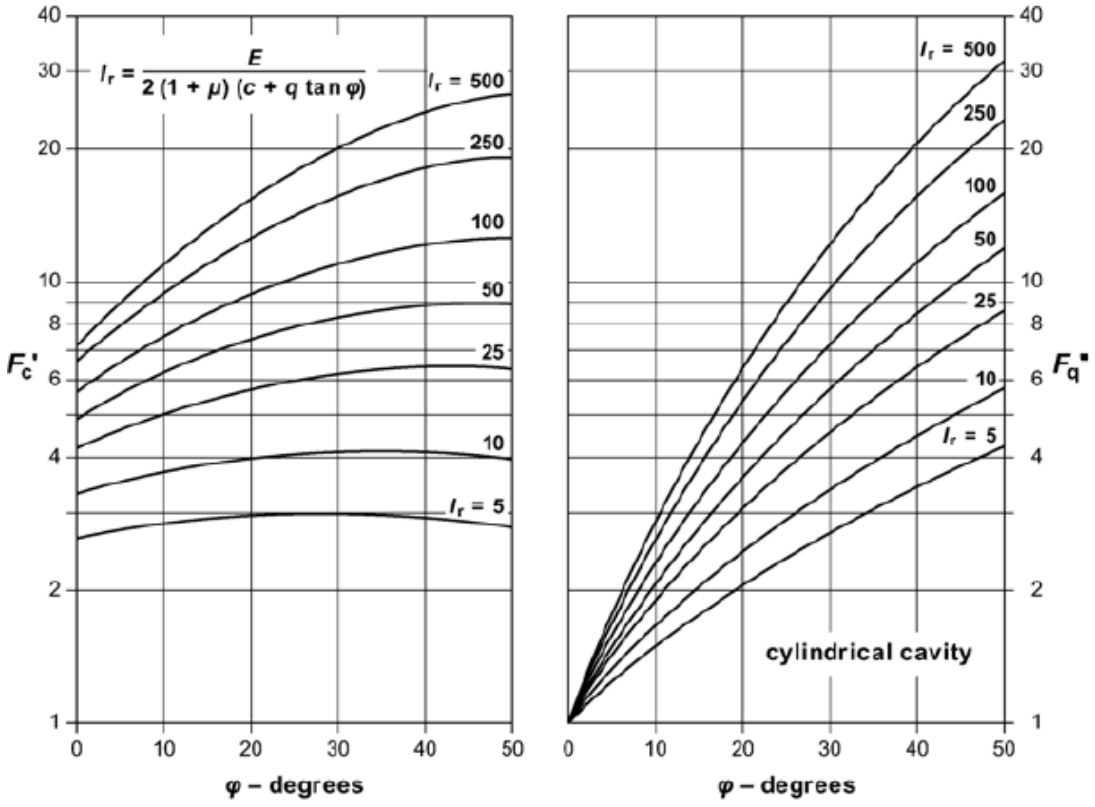

Figure 6-20 Cylindrical cavity expansion factors [111]

Bearing capacity factor method

Barksdale and Bachus [118] proposed a simple bearing capacity factor method on the basis of the Vesic's method to determine the bearing capacity of a single long column. In this method, the bearing capacity of a single column (either isolated or located within a group) is expressed as:

$$q_{ult} = c_u N_c \tag{6-38}$$

where q_{ult} is the ultimate stress that the stone column can carry, c_u is the undrained shear strength of the surrounding soil and N_c is the bearing capacity factor for the stone column determined based on back-calculation of field testing results [105]. Mitchell [135] provided a recommended value of $N_c = 25$ for stone columns constructed using the vibro-replacement method, whereas Datye et al. [136] suggested to use 25 to 30 for stone columns; however these analyses do not consider the strength of the surrounding soil which are more applicable in the case of foundations where settlement is the greatest concern rather than stability [118].

Barksdale and Bachus [118] indicated that N_c ranges from 18 to 22 depending on the stiffness of the surrounding soil. For soils with low stiffness, such as peats, organic cohesive soils and soft clays with Plasticity Index greater than 30, N_c of 18 is recommended; for soils with high stiffness, such as inorganic soft to stiff clays and silts, N_c of 22 is recommended. It should be noted that the strength of both soil and stone columns is considered in this analysis. In addition, a factor of safety equal to 3 is recommended for design [101].

For routine design, the ultimate bearing capacity of stone column groups can be estimated by multiplying the ultimate bearing capacity of a single stone column by the number of the columns in the group. In the case of the analysis for embankments or heavy tanks where bearing capacity is critical, a circular arc analysis should be performed to analyze the overall group effects on the stability of the structure and a minimum safety factor of 1.5 to 2 is recommended [118].

Failure Mode 2. Column Head Shear Failure for Single Long Column

Brauns [137] proposed a method which considered the passive earth pressure theory to determine the ultimate bearing stress of stone columns for shear failure that may occur at the near surface area similar to that shown in Figure 6-18 (a).

Brauns' Method

This failure mechanism of the Brauns' method as shown in Figure 6-21 assumed zero skin shear within the fracture surface and zero stress due to volume change

(conservation of volume). The ultimate vertical stress determined using this theory is expressed as:

$$q_{ult} = \sigma_{1,\max} = (q_s + \frac{2 \cdot c_u}{\sin(2 \cdot \delta)}) \cdot (1 + \frac{\tan(\frac{\pi}{4} + \frac{\varphi_s}{2})}{\tan\delta}) \cdot \tan^2(\frac{\pi}{4} + \frac{\varphi_s}{2}) \quad (6\text{-}39)$$

Where q_{ult} is the ultimate vertical stress, q_s is the surcharge load at the ground surface, c_u is the undrained shear strength of the surrounding soil where failure occurs, φ_s is the friction angle of the stone column and δ is the angle of the shear failure cone which can be determined based on Figure 6-22.

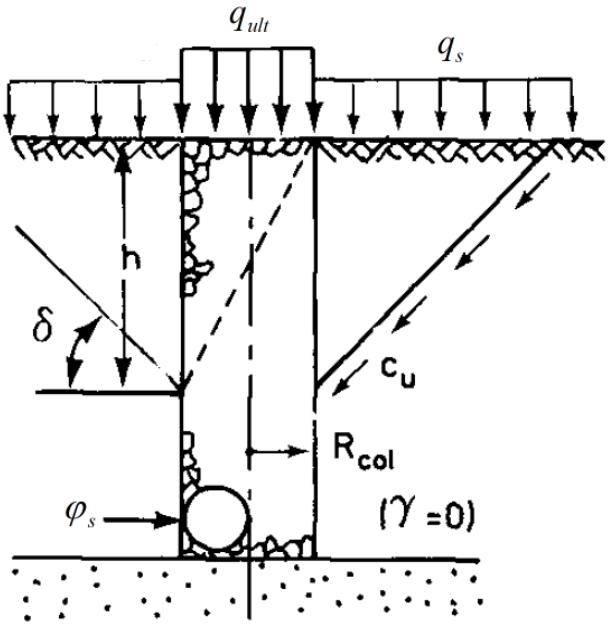

Figure 6-21 Shear failure of a single stone column near the column head [138]

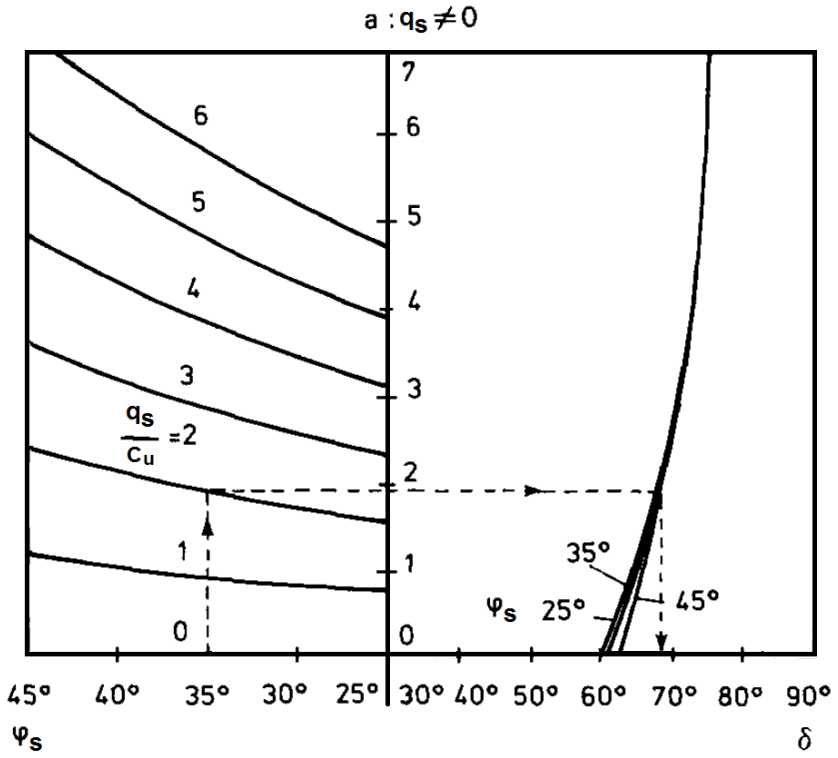

(a)

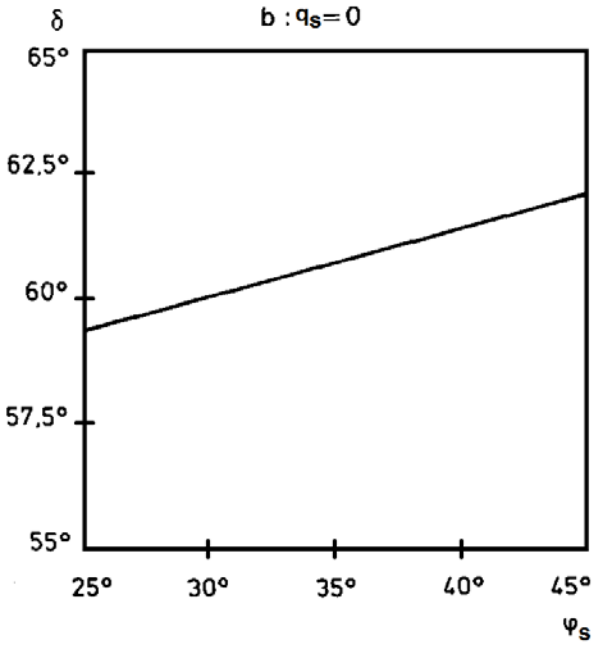

(b)

Figure 6-22 Determination of failure angle δ [137]

Failure Mode 3. Local Bulge Failure for Single Long Column

The local bulge failure mode occurs in long stone columns placed in nonhomogeneous cohesive soil when a very soft soil layer is present either at the surface or deep depth as shown in Figure 6-18. The ultimate bearing capacity of stone columns under these circumstances can be determined by using a semi-empirical method proposed by Barksdale and Bachus [118].

Barksdale and Bachus' Method

Barksdale and Bachus [118] proposed an empirical procedure to determine the ultimate lateral stress σ_3, and used the theory shown in Equation (6-30) to determine the ultimate vertical bearing stress q_{ult}.

For local bulge failure occurs at the surface layer, the ultimate lateral stress σ_3 can be estimated by:

$$\sigma_3 = 2c_u \tag{6-40}$$

where c_u is the undrained shear strength of the surrounding soil.

For local bulge failure occurs below a depth of 3-diameter of the stone column, the ultimate lateral stress σ_3 can be estimated by:

$$\sigma_3 = 9c_u \tag{6-41}$$

For the local bulge failure that occurs at a given depth below the surface and within the depth of 3-diameter of the stone column, the ultimate lateral stress σ_3 can be estimated by:

$$\sigma_3 = (2 + \frac{7h}{3D})c_u \tag{6-42}$$

where D is the diameter of the stone column and h is the depth where the stone column failure occurs [118].

Failure Mode 4. Shear and Punching Failure for Single Short Column

The failure of a short stone column may occur in the form of either general local shear failure at the near surface area as shown in Figure 6-17 (b) or punching failure as shown in Figure 6-17 (c).

The general local shear failure of a stone column treated ground under the surcharge load is shown in Figure 6-23; the bearing capacity of this case can be calculated based on the theorems of Drucker and Prager for the plane strain loading condition [118]:

$$q_{ult} = \frac{\gamma_c B}{2} N_r + cN_c + D_f \gamma_c N_q \tag{6-43}$$

where q_{ult} is the ultimate bearing stress, γ_c is the saturated or wet unit weight of the cohesive soil, B is the width of the loading area, c is the cohesion of the surrounding soil (equivalent to undrained shear strength), D_f is the depth of embedment and N_r, N_c and N_q are the bearing capacity factors given in Figure 6-24.

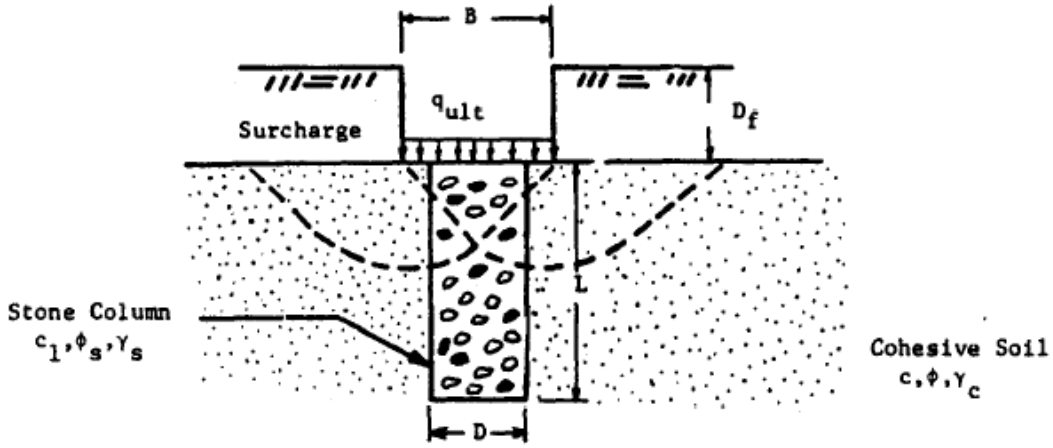

Figure 6-23 General local shear failure of a stone column treated ground [118]

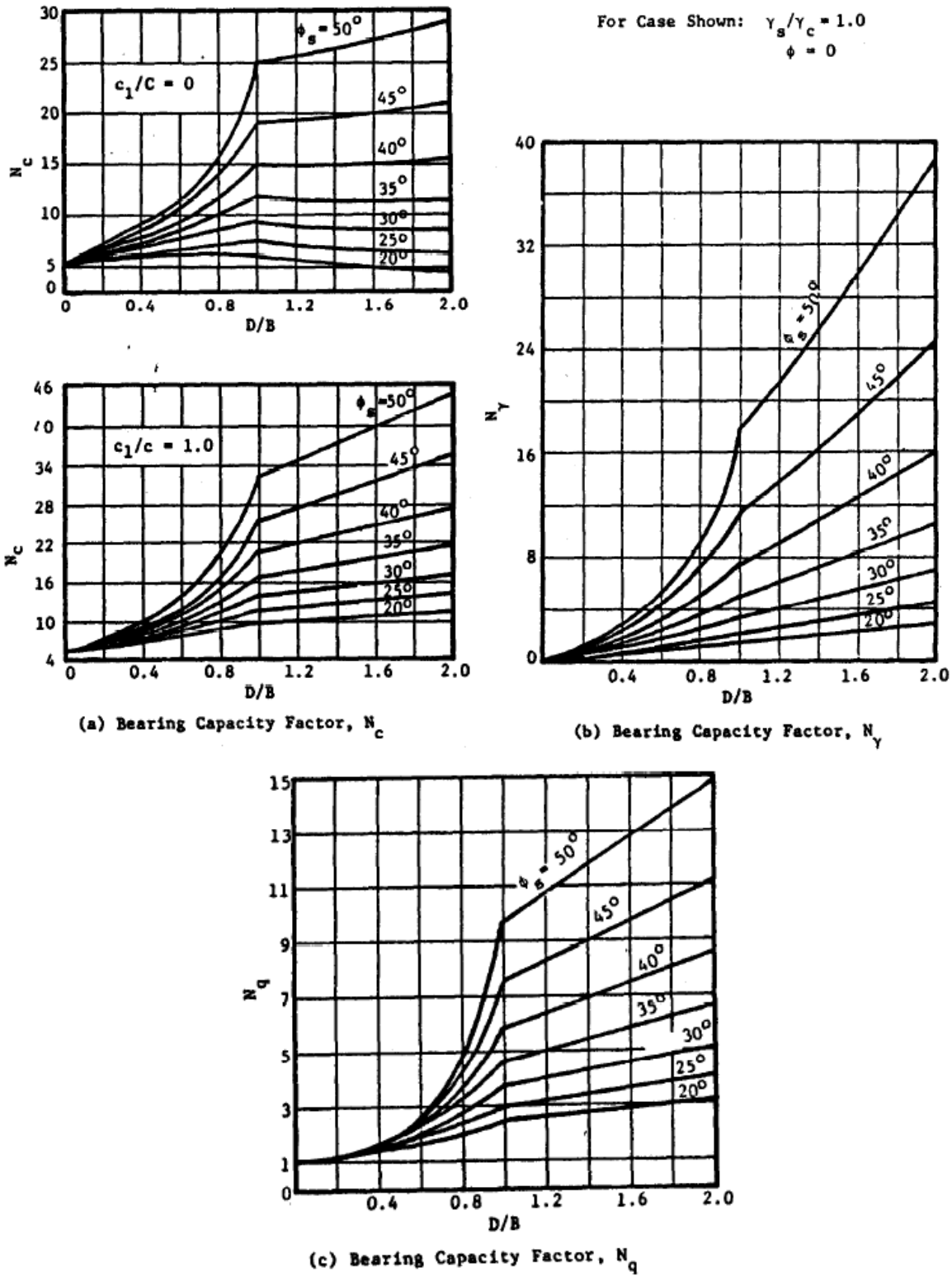

(a) Bearing Capacity Factor, N_c

(b) Bearing Capacity Factor, N_γ

(c) Bearing Capacity Factor, N_q

Figure 6-24 Bearing capacity factors for stone column treated soil [118]

The ultimate bearing capacity for punching failure can be calculated using the conventional bearing capacity theories considering the end bearing capacity of a stone column plus the skin friction along the side of the column [118].

Failure Mode 5. Shear Failure of Stone Column Groups

The method is applicable for small stone column groups placed in firm to strong cohesive type of soils with undrained shear strength greater than 600 – 800 psf under either a square or infinitely long rigid concrete footing as shown in Figure 6-25. Shear type failure which usually occurs in the form of a composite soil-stone column triangular failure wedge underneath the footing area is assumed for this type of stone column groups [118].

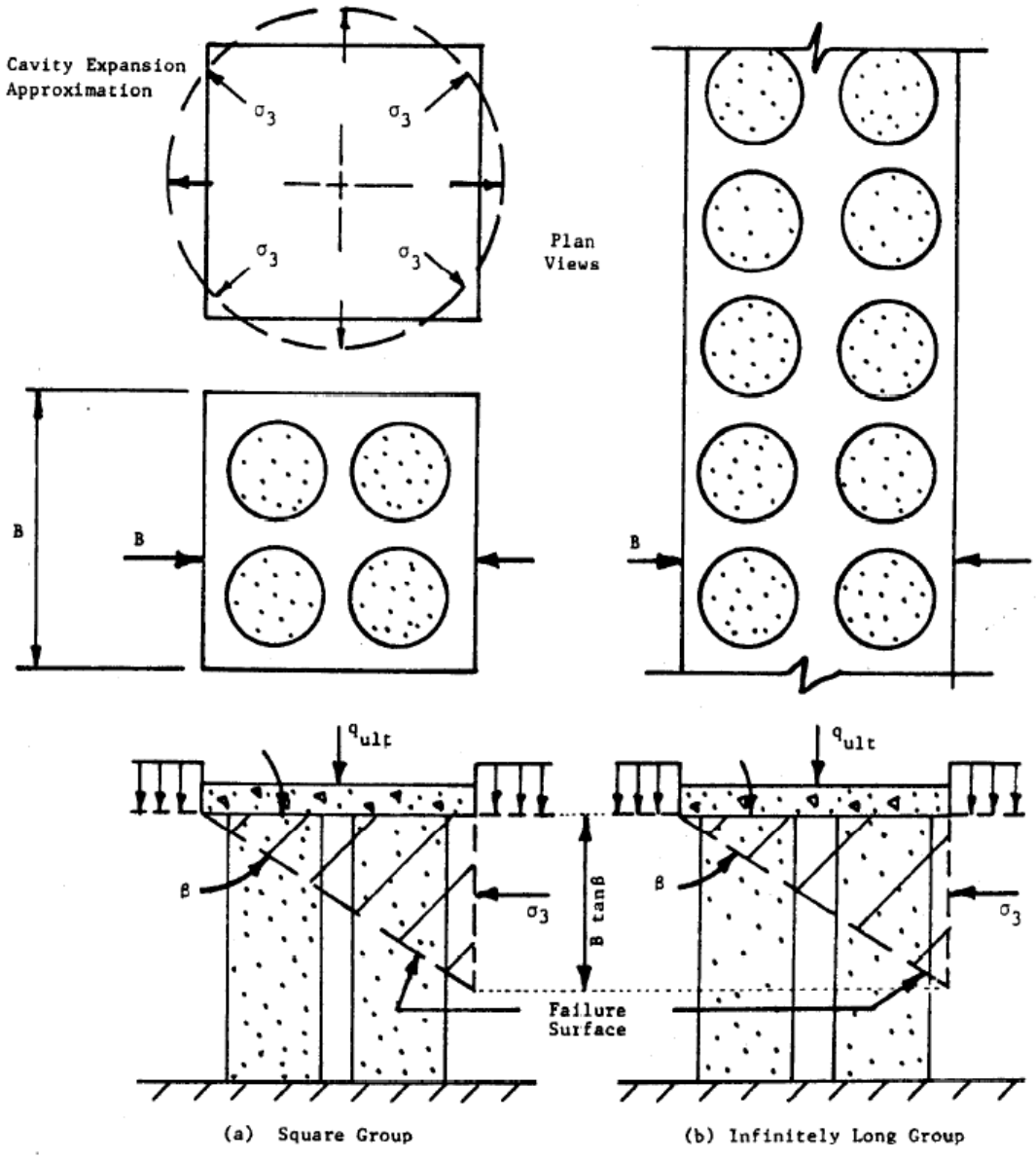

Figure 6-25 Shear failure of (a) square and (b) infinitely long stone column groups [118]

The ultimate vertical stress q_{ult} of the failure wedge depends on the shear strength of the composite soil-stone column wedge and the ultimate lateral resistance of the wedge σ_3. The parameters relative to the shear strength of the composite wedge are defined as:

$$\tan\varphi_{avg} = \mu_s a_s \tan\varphi_s \tag{6-44}$$

$$c_{avg} = (1 - a_s)c \tag{6-45}$$

where $\tan\varphi_{avg}$ is the tangent of the composite internal friction angle on the failure plane, μ_s is the ratio of stresses in the stone column to the stress over the unit cell as defined in Equation (6-9), a_s is the area replacement ratio defined in Equation (6-3), $\tan\varphi_s$ is the tangent of the stone column internal friction angle on the failure plane, c_{avg} is the composite cohesion on the failure plane and c is the cohesion (equivalent to undrained shear strength) of the surrounding cohesive soil. The angle of the failure surface β can be determined as:

$$\beta = 45° + \frac{\varphi_{avg}}{2} \tag{6-46}$$

$$\varphi_{avg} = \tan^{-1}(\mu_s a_s \tan\varphi_s) \tag{6-47}$$

The ultimate lateral pressure σ_3 for a square foundation can be determined using the Vesic [132] cavity expansion theory as shown from Equation (6-31) to (6-37), where Equation (6-34) can be modified to:

$$h = d_f + D\tan\beta \tag{6-48}$$

with

$$D = \sqrt{4A/\pi} \tag{6-49}$$

$$A = B^2 \text{ or } A = BL \tag{6-50}$$

where h is the depth of the failing wedge, D is the diameter of the failing cavity (i.e. width of the failing wedge), d_f is the depth of the foundation structure (if any) below ground surface, B is the length of a side of a square foundation structure or the width of a rectangular foundation structure and L is the length of the rectangular foundation structure.

The ultimate lateral pressure σ_3 for an infinitely long footing can be expressed as Equation (6-51) which is derived based on classical earth pressure theory [118]:

$$\sigma_3 = \frac{\gamma_c D\tan\beta}{2} + 2c_u \tag{6-51}$$

where γ_c is the saturated or wet unit weight of the cohesive soil, and the other parameters are previously defined.

Therefore, the ultimate vertical stress q_{ult} for a stone column group considering shear failure can be determined as:

$$q_{ult} = \sigma_3\tan^2\beta + 2c_{avg}\tan\beta \tag{6-52}$$

where σ_3 is calculated using either Equation (6-31) or (6-51) depending on the type of the footing (i.e. foundation structure) and all the other terms are previously defined. Note that the weight of the soil within the failure wedge is neglected which yields conservative results.

DESIGN EXAMPLE FOR BEARING CAPACITY

Following the same example for demonstrating the procedure for determining the settlement of stone column treated ground, the objective of this section is to determine the number of stone columns needed that will provide sufficient ultimate bearing capacity for the given level of stress.

Step 1

1. Prepare preliminary information, including the treatment area, loading condition, soil properties for each soil layer and the stone column information.

   The preliminary information is shown Table 6-1 and Table 6-2.

2. Calculate the total factored stress Q_f on the treatment area.

   Using the same loading condition shown in the settlement calculation example, the total factored stress Q_f can be calculated as:

$$Q_f = P_f/A_{total} = 1741 \text{ kips}/(50 \text{ ft} \times 20 \text{ ft}) = 1741 \text{ kips}/1000 \text{ ft}^2 = 1741 psf$$

Step 2

1. Determine the trial spacing, diameter and installation pattern for the stone columns.

   Trial column spacing $s = 6$ ft

   Trial column diameter $D = 3.5$ ft

   Trial installation pattern: equilateral triangular pattern ($C_1 = \pi/4$ for a square pattern and $C_1 = \pi/2\sqrt{3}$ for an equilateral triangular pattern).

2. Calculate area replacement ratio, area of each stone column and area of each unit cell.

   Area replacement ratio: $a_s = C_1(\frac{D}{s})^2 = \frac{\pi}{2\sqrt{3}}(\frac{3.5}{6})^2 = 0.308$

   Area of each stone column, ft^2: $A_s = \pi(\frac{D}{2})^2 = 9.62$ ft^2

   Area of each unit cell, ft^2: $A = A_s/a_s = 31.23$ ft^2

   Area of soil in each unit cell, ft^2: $A_c = A - A_s = 21.61$ ft^2

3. Estimate stress concentration ratio SCR and calculate ratio of stress in the stone column and the surrounding soil.

   Assume $SCR = 3$

   Ratio of stress in the stone column:

$$\mu_s = \frac{SCR}{1 + (SCR - 1) \cdot a_s} = \frac{3}{1 + 2 \cdot 0.308} = 1.856$$

   Ratio of stress in the surrounding soil:

$$\mu_c = \frac{1}{1 + (SCR - 1) \cdot a_s} = 0.619$$

Step 3

1. Identify the type of stone column (long or short stone column).

   Assuming the stone column is placed on top of the firm bearing layer and the length of the stone column is 35 ft. The length to diameter ratio L/D for the stone column is:

$$L/D = 10 > 4$$

   Therefore, it is a long stone column.

2. Identify the possible failure mode.

   The possible failure mode for a long stone column:

   - General bulging failure
   - Column head shear failure
   - Local bulge failure occurs at very soft soil layer

Step 4

1. Determine the ultimate bearing stress for general bulging failure

   Cavity expansion theory:

   a. Determine the depth where bulge occurs, ft.:

   $$h = d_f + \frac{1}{2}D\tan(45^\circ + \frac{\varphi_s}{2}) = 0 + \frac{1}{2} \times 3.5 \times \tan(45^\circ + \frac{40^\circ}{2}) = 3.75 \text{ ft}$$

   b. Determine the overburden pressure σ_v:

   $$\sigma_v = \gamma_c \cdot h = 100 * 3.75 = 375 \text{ psf}$$

   c. Determine the mean stress at the failure depth q:

   $$q = \frac{(1 + 2 \cdot K_0) \cdot \sigma_v}{3} = \frac{(1 + 2 \cdot 1) \cdot 375}{3} = 375 \text{ psf}$$

   d. Determine the Rigidity Index I_r:

   $$I_r = \frac{E}{2(1 + \nu)(c + q\tan\varphi_c)} = \frac{11 \times 500}{2(1 + 0.5)(500 + 0)} = 3.67$$

   e. Determine cavity expansion factors F_c' and F_q' using determined Rigidity Index and Equation (6-35) and (6-36) :

   $$F_c' = \ln I_r + 1 = 2.3$$

   $$F_q' = (1 + \sin\varphi_c)(I_r \sec\varphi_c)^{\frac{\sin\varphi_c}{1+\sin\varphi_c}} = 1$$

   f. Determine the ultimate lateral stress σ_3

   $$\sigma_3 = cF_c' + qF_q' = 500 \times 2.3 + 375 \times 1 = 1525 \text{ psf}$$

   g. Determine the ultimate bearing stress $q_{ult} = \sigma_3 \cdot \frac{1+\sin\varphi_s}{1-\sin\varphi_s}$

   $$q_{ult} = \sigma_3 \cdot \frac{1 + \sin\varphi_s}{1 - \sin\varphi_s} = 1525 \times \frac{1 + 0.643}{1 - 0.643} = 1525 \times 4.6 = 7015 \text{ psf}$$

   Bearing capacity factor method:

   a. Select bearing capacity factor N_c for bulging failure occurs within the depth of the upper 3-diameter of the stone column, where a soft clay soil is present; based on the previous experience

   $$N_c = 20$$

   b. Determine the ultimate bearing stress $q_{ult} = \sigma_3 \cdot \frac{1+\sin\varphi_s}{1-\sin\varphi_s}$

   $$q_{ult} = c_u N_c = 500 * 20 = 10000 \text{ psf}$$

2. Determine the ultimate bearing stress for column head shear failure

   Brauns' Method:

   a. Determine angle of the shear failure cone based on Figure 6-22 for the case of surcharge load = 0

$$\delta = 61.5^{\circ}$$

   b. Determine the ultimate bearing stress $q_{ult} = \sigma_3 \cdot \frac{1+\sin\varphi_s}{1-\sin\varphi_s}$

$$q_{ult} = \sigma_{1,\max} = (q_s + \frac{2 \cdot c_u}{\sin(2 \cdot \delta)}) \cdot (1 + \frac{\tan(\frac{\pi}{4} + \frac{\varphi_s}{2})}{\tan\delta}) \cdot \tan^2(\frac{\pi}{4} + \frac{\varphi_s}{2})$$

$$= (0 + \frac{2 \cdot 500}{\sin(2 \cdot 61.5^{\circ})}) \cdot (1 + \frac{\tan(\frac{\pi}{4} + \frac{40^{\circ}}{2})}{\tan 61.5^{\circ}}) \cdot \tan^2(\frac{\pi}{4} + \frac{40^{\circ}}{2})$$

$$= 11843 \text{ psf}$$

3. Determine the ultimate bearing stress for local bulge failure to occur at very soft soil layer

   Barksdale and Bachus' Method:

   a. Determine the depth of very soft soil layer:

$$h = 20 > 3 \cdot D = 10.5 \text{ ft}$$

   b. Determine the ultimate lateral stress σ_3, since the local bulge failure occurs below a depth of 3-diameter of the stone column, the ultimate lateral stress σ_3 can be estimated by applying Equation (6-41):

$$\sigma_3 = 9c_u = 9 \times 250 = 2250 \text{ psf}$$

   c. Determine the ultimate bearing stress $q_{ult} = \sigma_3 \cdot \frac{1+\sin\varphi_s}{1-\sin\varphi_s}$

$$q_{ult} = \sigma_3 \cdot \frac{1+\sin\varphi_s}{1-\sin\varphi_s} = 2250 \times \frac{1+0.643}{1-0.643} = 2250 \times 4.6 = 10350 \text{ psf}$$

Step 5

1. Identify the most critical failure mode and the associated ultimate bearing stress in the stone column

   The stone column is most likely to fail due to general bulging failure.

$$\sigma_s = q_{ult} = 7015psf$$

2. Determine the ultimate allowable bearing stress for the tributary soils σ_{c-ult} which can be estimated by:

$$\sigma_{c-ult} = 5c_u = 5 \times 500 = 2500\text{psf}$$

3. Determine the stress for the tributary soils σ_c when the ultimate bearing stress in the stone column is achieved:

$$\sigma_c = \mu_c \sigma = \mu_c \frac{\sigma_s}{\mu_s} = \mu_c \frac{q_{ult}}{\mu_s} = 0.619 \frac{7015}{1.856} = 2340 \text{ psf} < \sigma_{c-ult}$$

Therefore, the stress level in the tributary soil is satisfactory. If the condition is not satisfied, start over the design from **Step 2**.

Step 6

1. Calculate the ultimate load P_{ult} for each unit cell, with a factor of safety of 2:

$$P_{ult} = \frac{\sigma_s A_s + \sigma_c A_c}{FS} = \frac{7015 \times 9.62 + 2340 \times 21.61}{2} = 59026 \text{ lb.}$$

2. Calculate the ultimate allowable stress Q_{ult} for each unit cell:

$$Q_{ult} = \frac{P_{ult}}{A} = \frac{59026}{31.23} = 1890 \text{ psf}$$

3. Check the ultimate allowable stress Q_{ult} with the total factored stress Q_f

$$Q_f = 1741 \text{ psf} \leq Q_{ult} = 1890 \text{ psf}$$

Therefore, the design is valid.

CHAPTER 7

CHARACTERIZATION OF SOIL PROPERTIES

Foundation settlement is one of the main problems leading to the bump-at-the-end-of-the-bridge. Ground improvement techniques such as the use of stone columns have been proven to reduce settlement and improve the bearing capacity of the ground. In order to achieve satisfactory design outcomes, it is always significant to carry out field investigations and laboratory experiments in order to characterize foundation soils and obtain key soil properties for design purposes.

In order to conduct laboratory testing and obtain strength and compressibility related soil properties for the stone column design, it is often required to obtain undisturbed soil samples from bore holes which can be very complex and expensive; in addition, the traditional laboratory testing is difficult to conduct under field conditions.

This chapter considers the use of alternative methods as a means to expedite the testing process. The main objective is to develop non-destructive testing (NDT) technology that can be used under field conditions to determine the key soil properties.

BACKGROUND

Sahin [139] made important advancements in the use of NDT technology to determine key material properties of unbound aggregate materials which are usually used as base and subbase layers beneath pavements. In his research, Sahin [139] was able to use only two NDT measurements, such as Methylene Blue Value (MBV) and dielectric constant (DC) to estimate a variety of properties of unbound aggregate materials under a field condition, including the percent fine content (pfc), volumetric water content (θ), soil matric suction (h_m), dry unit weight (γ_d), resilient modulus and permanent deformation. The MBV and DC can be measured by performing the Methylene Blue Test (MBT) and percometer test, respectively. Both of the tests are considered with the following benefits, rapid (no complicated procedures involved), portable (all testing equipment can fit into a small toolbox), comprehensive (applicable to a wide range of soils), simple (no advanced training required) and accurate with good

repeatability. The core of this technology is the use of laboratory empirical relationships which must be established under laboratory conditions prior to the application under field conditions.

Although the aforementioned NDT technologies were conducted for predicting properties of unbound aggregate materials, it appears that there is great potential that the technologies can be applicable for other types of soil materials, such as clay and silts which are often found in the foundation underneath bridge embankments. The use of NDT technologies to estimate the strength and compressibility characteristics of foundation soils will be useful for the design of ground improvement techniques such as the use of stone columns.

PROPOSED PROCEDURE FOR ESTIMATING SOIL STRENGTH

As elaborated in the previous chapters, the undrained shear strength of foundation soils is one of the main properties to be used for the design of the bearing capacity of stone column treated ground. The undrained shear strength of a soil can be determined from the analysis of a Mohr circle as illustrated in Figure 7-1:

$$\sin\phi' = \frac{c_u}{c_u - \theta f h_m} \tag{7-1}$$

$$c_u = -h_m \theta f \frac{\sin\phi'}{1-\sin\phi'} \tag{7-2}$$

where c_u is the undrained shear strength of the soil, ϕ' is the effective internal friction angle of the soil, h_m is the matric suction of the soil, θ is the volumetric water content and f is the unsaturated shear strength factor which can be expressed as:

$$f = 1 + (\frac{S_r - 0.85}{0.15})(\frac{0.01}{\theta} - 1) \tag{7-3}$$

and

$$S_r = \frac{wG_s}{e_0} \tag{7-4}$$

$$w = \frac{\theta\gamma_w}{\gamma_d} \tag{7-5}$$

$$e_0 = \frac{G_s\gamma_w}{\gamma_d} - 1 \tag{7-6}$$

where S_r is the degree of saturation, θ is the volumetric water content, w is the gravimetric moisture content, e_0 is the void ratio of the soil, G_s is the specific gravity of the soil, γ_w is the unit weight of water (62.4 lb/ft^3) and γ_d is the dry unit weight of the soil.

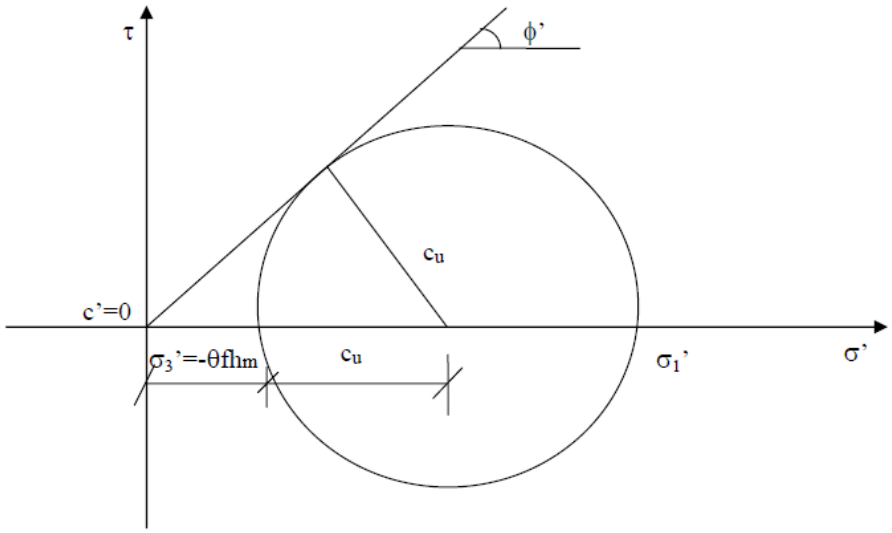

Figure 7-1 Mohr circle for the shear strength of unsaturated soils [140]

Therefore, it appears that the undrained shear strength c_u can be estimated if the following five parameters are known (shown in Figure 7-2):

- the effective internal friction angle ϕ';
- the specific gravity G_s;
- the matric suction h_m;
- the volumetric water content θ; and
- the dry unit weight of the soil γ_d.

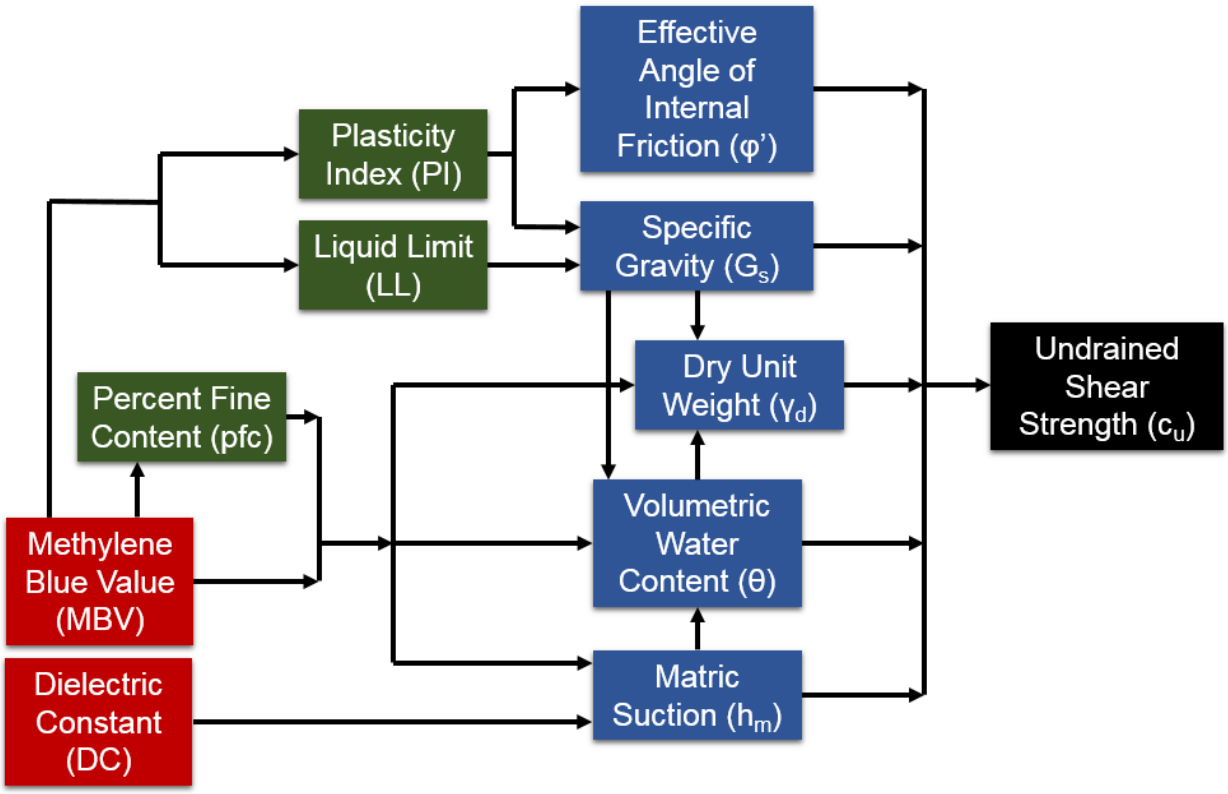

Figure 7-2 Flowchart of proposed field testing protocol for estimating c_u

As shown in Figure 7-2, the proposed field testing protocol considers the use of only two field measurements (i.e. MBV and DC) to estimate all of the five required parameters in order to predict the undrained shear strength c_u under a field condition, which can be achieved by using empirical relationships between the measurable parameters (i.e. MBV and DC) and the five required parameters established under laboratory conditions. The detailed procedures for establishing those empirical relationships under laboratory conditions are elaborated in Appendix B.

PROPOSED PROCEDURE FOR ESTIMATING SOIL COMPRESSIBILITY

In addition to predicting the undrained shear strength c_u under a field condition for calculating the bearing capacity of stone column treated ground, this chapter also provides a procedure to estimate the compression index C_c of cohesive foundation soils which is used for calculating the settlement of stone column treated ground. Conventionally, the compression index of a cohesive soil is determined by performing

an oedometer test under a laboratory condition which can be very time-consuming. If reliable empirical correlations can be established between the compression index and other soil properties, the process of determining compression index can be much faster and more cost-effective.

Previous Experience

Over the last few decades, researchers have proposed a number of empirical relationships to relate the compression index to different soil properties, such as the one by Koppula (1981) [141]:

$$C_c = 0.009w + 0.005LL \tag{7-7}$$

the one by Yoon and Kim (2006) [142]:

$$C_c = -0.404 + 0.341e_0 + 0.006w + 0.004LL \tag{7-8}$$

and the one by Ozer et al. (2008)

$$C_c = 0.151 + 0.001225w + 0.193e_0 - 0.000258LL - 0.0699\gamma_d \tag{7-9}$$

where C_c is the compression index, w is the gravimetric moisture content, LL is the liquid limit, γ_d is the dry unit weight and e_0 is the initial void ratio of the soil which can be calculated as:

$$e_0 = \frac{n}{1-n} = \frac{\theta_{ws}}{1-\theta_{ws}} = \frac{G_s\gamma_w}{\gamma_d} - 1 \tag{7-10}$$

where n is the porosity and θ_{ws} is the volumetric water content at saturation which is defined in Equation (B-18).

These empirical relationships can be easily applied under a field condition to estimate the compression index since all the required parameters (i.e. w, LL, γ_d, G_s, e_0 and θ_{ws}) are predictable with only the measurements of MBV and DC following the procedures elaborated in Appendix B.

New Protocol

Besides using the pure empirical relationships (such as the ones shown in Equation (7-7) – (7-9)) previously proposed by other researchers, this research proposed a new protocol based on mechanistic-empirical relationships, in which the

compression index can be calculated in terms of a constrained modulus D based on the stress-strain relationship of a soil under a confined (1-D) compression test [143]:

$$D = \frac{\partial \bar{\sigma}_{axial}}{\partial \varepsilon_{axial}} = \frac{(1+e_0)\ln 10 \sigma_{va}}{C_c} = \frac{2.3(1+e_0)\sigma_{va}}{C_c} \tag{7-11}$$

and the relationship between constrained modulus D and Young's modulus E of the soil is:

$$D = \frac{E(1-\nu)}{(1+\nu)(1-2\nu)} \tag{7-12}$$

where e_0 is the initial void ratio, σ_{va} is the average of initial and final stress state applied in the field (vertical stress) and ν is the Poisson's ratio of the soil. The Young's modulus E of the soil can be calculated by using a nonlinear elastic model proposed by Lytton et al. (2005) [144]:

$$E = \frac{\sigma_{va}(1+\frac{0.4343}{Sw})}{0.435\gamma_h} \frac{(1+\nu)(1-2\nu)}{(1-\nu)} \tag{7-13}$$

therefore, the compression index can be expressed as:

$$C_c = \frac{(1+e_0)\gamma_h}{1+\frac{0.4343}{|S|w}} \tag{7-14}$$

where e_0 is the initial void ratio of the soil and can be determined using Equation (7-10) (which requires the knowledge of both the dry unit weight γ_d and the specific gravity G_s of the soil), γ_h is the suction compression index (related to the percent fine content pfc, plasticity index PI and liquid limit LL) and can be determined following the procedure elaborated in Appendix B, S is related to the slope of the SWCC and w is the gravimetric water content. As shown in Figure 7-3, the relation between volumetric water content θ and soil matric suction h_m can be expressed as [144]:

$$\frac{\theta}{1} = \frac{h_{m-\mathrm{intercept}} - h_m}{|S|\frac{\gamma_w}{\gamma_d}} \tag{7-15}$$

rearranging Equation (7-15):

$$|S|\theta\frac{\gamma_w}{\gamma_d} = h_{m-\mathrm{intercept}} - h_m \tag{7-16}$$

since $w = \theta\frac{\gamma_w}{\gamma_d}$, Equation (7-16) becomes:

$$|S|w = h_{m-\mathrm{intercept}} - h_m \tag{7-17}$$

where $h_{m-\mathrm{intercept}}$ is the matric suction at the intersection with the vertical axis and it is a function of the percent fine content pfc:

$$h_{m-\mathrm{intercept}} = 5.622 + 0.0041(pfc) \quad (7\text{-}18)$$

and h_m is the soil matric suction which can be estimated under a field condition as elaborated in Appendix B.

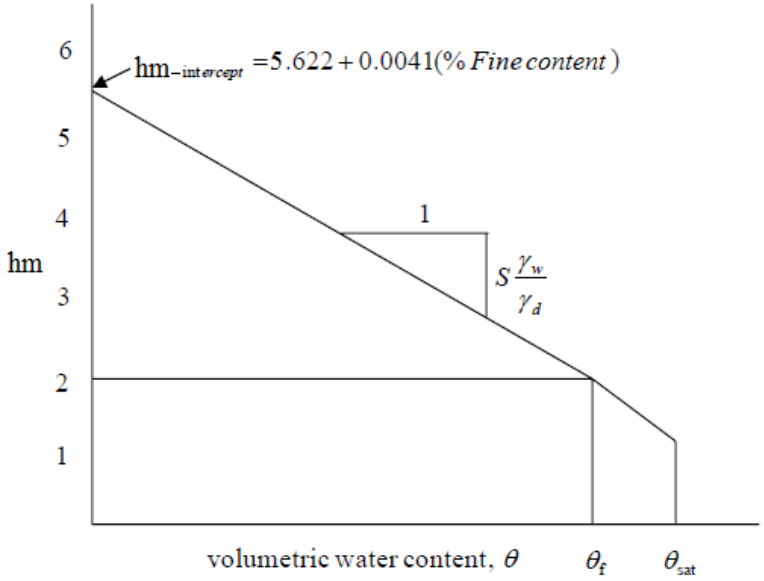

Figure 7-3 The SWCC of a clay soil [144]

To sum up, the compression index C_c can be estimated using Equation (7-14) if the following parameters are known:

- the matric suction h_m;
- the specific gravity G_s;
- the volumetric water content θ;
- the dry unit weight of the soil γ_d;
- the matric suction at intersection $h_{m-\mathrm{intercept}}$; and
- the suction compression index γ_h.

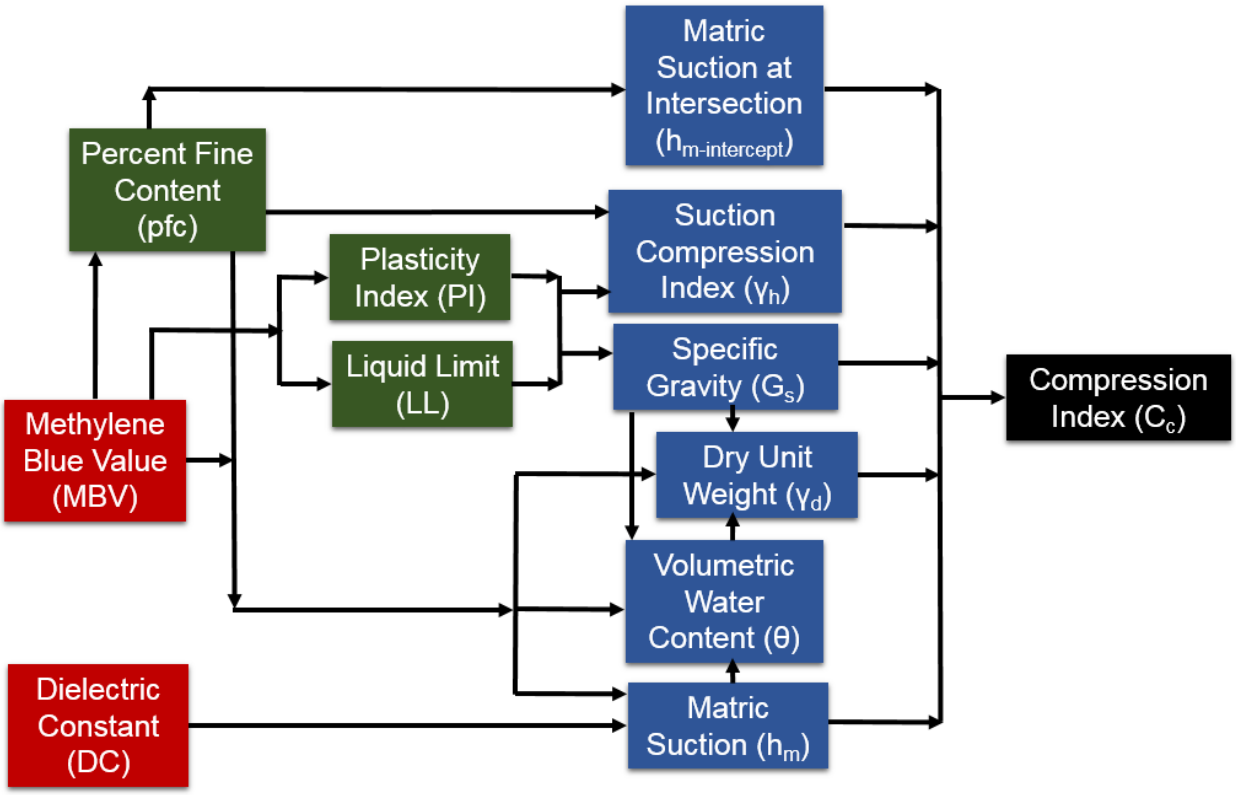

Figure 7-4 Flowchart of proposed field testing protocol for estimating C_c

As shown in Figure 7-4, the proposed field testing protocol considers the use of only two field measurements (i.e. MBV and DC) to estimate all the six required parameters in order to determine the compression index C_c under a field condition.

The empirical relationship shown in Equation (7-18) to determine the matric suction at intersection $h_{m-\mathrm{intercept}}$ is valid for clay soils as indicated in the report by Lytton et al. (2005) [144]. The charts shown from Figure B-12 – Figure B-20 to determine the suction compression index γ_h can also be directly used for natural clay soils since they are generated based on a large database of the Soil Survey Laboratory (SSL) of the Natural Resources Conservation Service of the U.S. Department of Agriculture. The procedures and empirical relationships to estimate the specific gravity G_s, the dry unit weight γ_d, the volumetric water content θ and the soil matric suction h_m under a field condition are elaborated in Appendix B. Again, it is important to note that those empirical relationships will have greater utilities under a field condition if they are established based on a wide range of soil types tested under laboratory conditions.

DEMONSTRATION OF PROPOSED PROCEDURES

This section consists of three major objectives:

1. Provide the results of the laboratory experiments;
2. Briefly demonstrate how to use the results to establish empirical relationships; and
3. Briefly demonstrate how the empirical relationships can be used to facilitate the estimation/characterization of soil properties using the NDT technologies.

Note that an Excel spreadsheet which contains all the laboratory experiment results and detailed information for establishing those empirical relationships will be provided to the practitioner (i.e. OKDOT engineers) to facilitate better understanding regarding how the empirical relationships are established using laboratory experiment results.

Laboratory Experiment Results

Three soil samples (Port, Kirkland and Osage) obtained from Oklahoma were used in the study to facilitate the development of the laboratory empirical relationships. In order to develop the empirical relationships that can be used under field conditions to estimate key soil properties, the following laboratory tests were performed:

1. the Atterberg limits test
2. the Methylene Blue Test
3. the specific gravity test
4. the percent fine content test
5. the percometer test
6. the filter paper test
7. the standard laboratory compaction test

Atterberg limits

Table 7-1 shows the Atterberg limits of the three soil samples obtained in Oklahoma.

Table 7-1 Atterberg limits

	Liquid limit	Plastic limit	Plasticity Index
Port	43.5	18.64	24.86
Kirkland	47	16.61	30.39
Osage	66.5	28.55	37.95

Methylene Blue Value

Table 7-2 shows the MBV of the three soil samples.

Table 7-2 MBV of the soil samples

	Sample	MBV	Average of MBV
Port	1	60.4	59.58
	2	59.2	
	3	58.7	
	4	60	
Kirkland	1	61.9	65.15
	2	65.4	
	3	66.1	
	4	67.2	
Osage	1	80.4	78.67
	2	77.6	
	3	78	

Specific gravity

Table 7-3 shows the specific gravity of the three soil samples.

Table 7-3 Specific gravity of the soil samples

	Port	Kirkland	Osage
Specific Gravity (G_s)	2.62	2.75	2.66

Percent fine content

Table 7-4 shows the pfc of the three soil samples.

Table 7-4 pfc of the soil samples

	Sample	Percent fine content, %	Average, %
Port	1	77.43	82.90
	2	87.14	
	3	82.54	
	4	78.04	
	5	89.37	
Kirkland	1	78.36	83.72
	2	80.37	
	3	82.88	
	4	89.22	
	5	87.78	
Osage	1	99.4	99.19
	2	97.25	
	3	99.59	
	4	100	
	5	99.72	

Dielectric constant and suction

Six 4-in diameter and 1.5-in height cylindrical soil samples were made for each soil to conduct percometer test and filter paper test (each test requires two soil samples). Dielectric constant and suction of the samples are shown in Table 7-5 and Table 7-6.

Table 7-5 Dielectric constant of the samples

	Sample	Total	Average
Port	1	27.2	28.48
	2	26.9	
	3	27.6	
	4	34.16	
	5	29.44	
	6	25.6	
Kirkland	1	35.18	33.29
	2	35.32	
	3	33.98	
	4	35.24	

	5	29.88	
	6	30.14	
Osage	1	37.68	33.96
	2	33.5	
	3	31.42	
	4	32.04	
	5	34.64	
	6	34.48	

Table 7-6 Matric suction of the samples

	Sample	Matric suction, pF	Average matric suction, pF
Port	1	3.56	3.49
	2	3.63	
	3	3.27	
Kirkland	1	3.73	3.71
	2	3.81	
	3	3.58	
Osage	1	3.61	3.42
	2	3.51	
	3	3.13	

Optimum water content and maximum dry unit weight

Figure 7-5 shows the compaction curves from which the optimum moisture content and maximum dry unit weight of the three soil samples are determined as shown in Table 7-7.

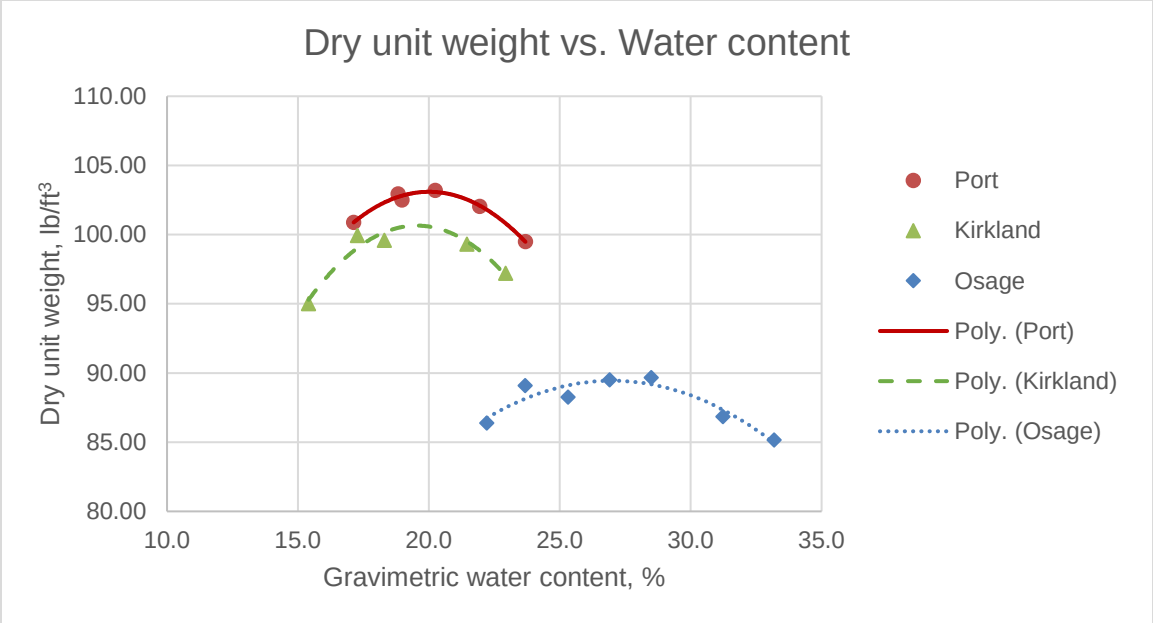

Figure 7-5 Compaction curves of the soil samples

Table 7-7 Optimum water content and maximum dry unit weight of the soil samples

	Optimum Water Content, %	Maximum Dry Unit Weight, lb./ft^3
Port	20.01	103.03
Kirkland	19.54	100.06
Osage	27.02	89.48

Establishment of Empirical Relationships

By using the results of the laboratory experiments for the three representative soils taken from Oklahoma, this section demonstrates examples of how to establish the empirical relationships that will be used to perform estimations of the strength and compressibility related soil properties under a field condition. Note that the empirical relationships developed within this section only have limited utilities due to the small sample database which is constrained by the scope of the research; therefore, they are developed for demonstration purposes only and greater utilities can be achieved if a

large number of soils samples are tested to cover a wide range of soil types in the interested local area.

Empirical relationships between Atterberg limits and MBV

As shown in Figure 7-6, the relationship between MBV and PI can be described by a linear relationship for the three samples:

$$PI = 0.6622MBV - 13.828 \quad (7\text{-}19)$$

and the relationship between MBV and LL shown in Figure 7-7 can also be described by a linear function:

$$LL = 1.2489MBV - 32.338 \quad (7\text{-}20)$$

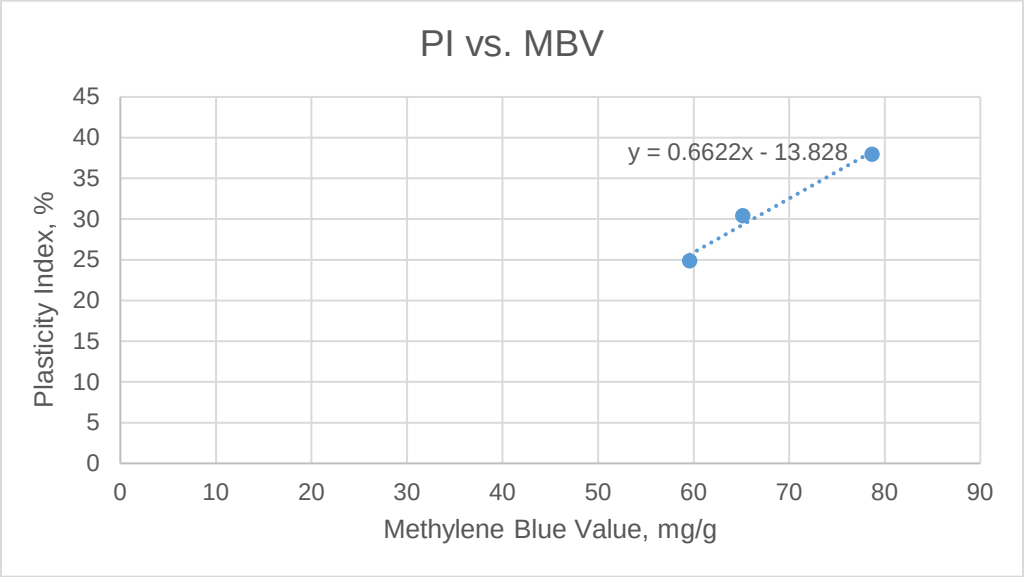

Figure 7-6 the correlation between MBV and PI for the three soil samples

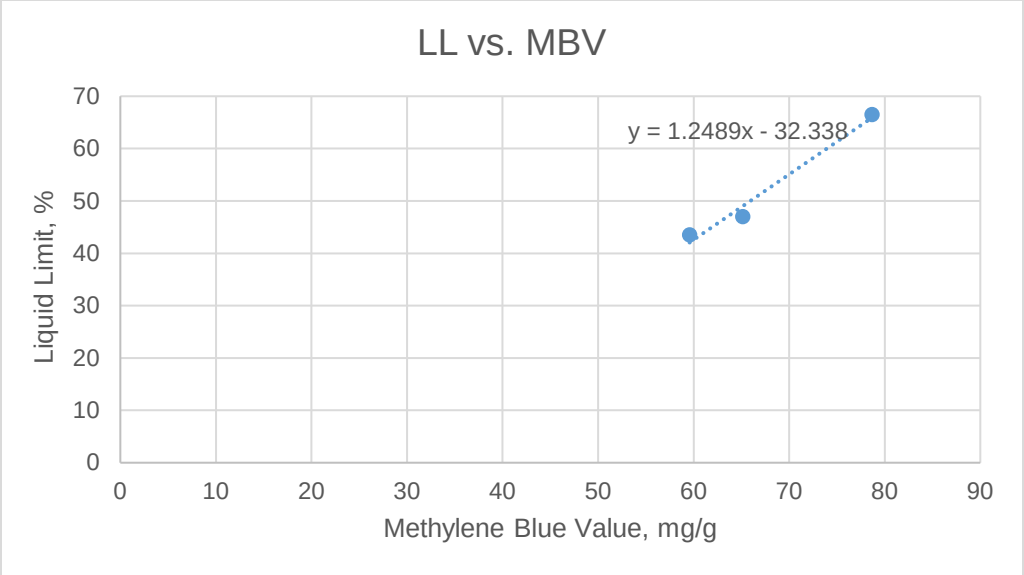

Figure 7-7 the correlation between MBV and LL for the three soil samples

Empirical relationship for predicting specific gravity

Laboratory experiment results of the specific gravity and Atterberg limits are summarized as shown in Table 7-8. These results are fitted to the mathematical function as shown in Equation (B-5), from which the fitting parameters β, γ and δ are determined as shown in Table 7-9.

Table 7-8 Specific gravity and Atterberg limits

	Port	Kirkland	Osage
Specific Gravity (G_s)	2.62	2.75	2.66
Liquid Limit (LL)	43.5	47	66.5
Plasticity Index (PI)	24.86	30.39	37.95
Approximate minimum liquid limit (L_0)	40		
Approximate maximum liquid limit (L_m)	70		
Approximate minimum plasticity index (P_0)	20		
Approximate maximum plasticity index (P_m)	40		

Table 7-9 Fitting parameters determined using the experiment results

Beta (β)	Gamma (γ)	Delta (δ)
0.057	3.24	-2.45

Once the fitting parameters are determined, the empirical function to calculate specific gravity of a soil can be formulated as:

$$G_s = \frac{2.55+2.91(0.057)\left(\frac{PI-20}{40-PI}\right)^{3.24}\left(\frac{LL-40}{70-LL}\right)^{-2.45}}{1+0.057\left(\frac{PI-20}{40-PI}\right)^{3.24}\left(\frac{LL-40}{70-LL}\right)^{-2.45}} \quad (7\text{-}21)$$

Empirical relationship for predicting pfc using MBV

As shown in Figure 7-8, the correlation between MBV and pfc can be described by the following function for the three samples:

$$pfc = 62.221\ln(MBV) - 173.33 \quad (7\text{-}22)$$

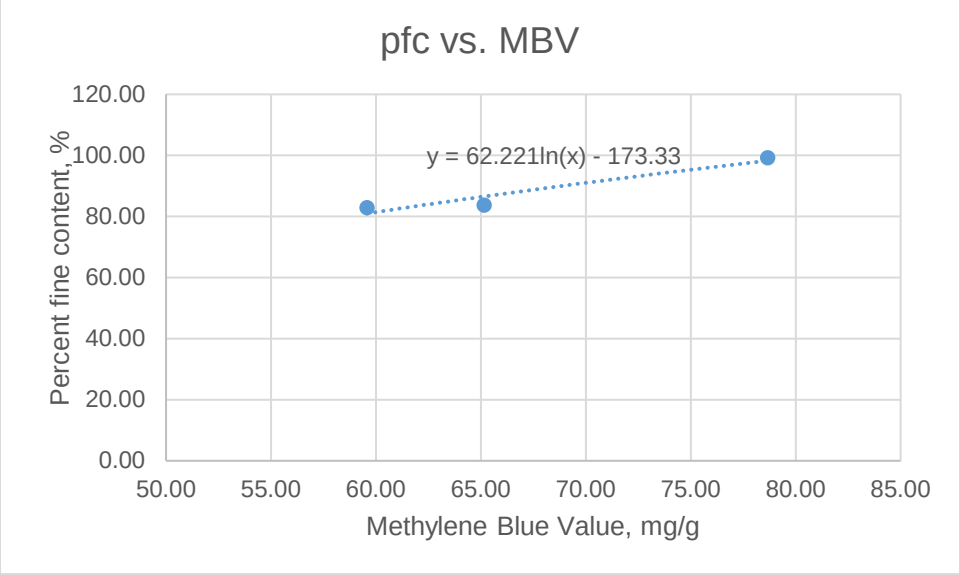

Figure 7-8 the correlation between MBV and pfc for the three soil samples

Empirical relationships for predicting ε_{sat} and ε_{min} to define SDCC

In order to establish the empirical relationships, it is necessary to determine $\varepsilon_{\min}$ and ε_{sat}, which can be calculated by applying the complex refraction index model (CRIM) (elaborated in Appendix B) based on the DC measurements of the soil samples.

Table 7-10 shows the results of the minimum and saturated DC calculated following the procedure elaborated previously. Figure 7-9 and Figure 7-10 show the correlations of $\varepsilon_{\min}$ vs. MBV and ε_{sat} vs. MBV, respectively. Both the empirical relationships can be represented by the quadratic functions shown in the figures. The relationship between $\varepsilon_{\min}$ and MBV is expressed as:

$$\varepsilon_{\min} = -0.0178MBV^2 + 2.414MBV - 71.026 \quad (7\text{-}23)$$

and the relationship between ε_{sat} and MBV is expressed as:

$$\varepsilon_{sat} = -0.0582MBV^2 + 8.4438MBV - 259.51 \quad (7\text{-}24)$$

Table 7-10 Determination of $\varepsilon_{\min}$ and ε_{sat}

	Measured DC of the soil (ε_r)	Specific Gravity (G_s)	Water content (w)	Dry unit weight (γ_d)	Volumetric solid content (θ_s)	Volumetric water content (θ)	Volumetric water content at saturation (θ_{ws})	DC of the solid (ε_s)	Minimum DC (ε_{min})	Saturated DC (ε_{sat})
Port	28.48	2.62	0.169	103.03	0.630	0.279	0.370	18.88	9.66	36.81
Kirkland	33.29	2.75	0.193	100.66	0.587	0.311	0.413	23.87	10.75	43.38
Osage	33.96	2.66	0.249	89.48	0.539	0.357	0.461	21.62	8.81	44.29

Sample calculation (take “Port” as an example):

Based on Equation (B-16) shown in Appendix B

The volumetric solid content θ_s:

$$\theta_s = \frac{\gamma_d}{G_s\gamma_w} = \frac{103.03}{2.62 \times 62.4} = 0.63$$

The volumetric water content θ:

$$\theta = \frac{w\gamma_d}{\gamma_w} = \frac{0.169 \times 103.03}{62.4} = 0.279$$

The DC of the solid ε_s:

$$\varepsilon_s = \left(\frac{\sqrt{\varepsilon_r} - 1 - (\sqrt{\varepsilon_w} - 1)\theta}{\theta_s} + 1\right)^2 = \left(\frac{\sqrt{28.48} - 1 - (\sqrt{81} - 1)0.279}{0.63} + 1\right)^2 = 18.88$$

Based on Equation (B-17) shown in Appendix B

The minimum DC $\varepsilon_{\min}$:

$$\varepsilon_{\min} = (1 + \theta_s(\sqrt{\varepsilon_s} - 1))^2 = (1 + 0.63(\sqrt{18.88} - 1))^2 = 9.66$$

Based on Equation (B-18) shown in Appendix B

The volumetric water content at saturation θ_{ws}:

$$\theta_{ws} = 1 - \theta_s = 1 - 0.63 = 0.37$$

The saturated DC ε_{sat}:

$$\varepsilon_{sat} = [(\sqrt{\varepsilon_s} - 1)\theta_s + (\sqrt{\varepsilon_w} - 1)\theta_{ws} + 1]^2 = [(\sqrt{18.88} - 1)0.63 + (\sqrt{81} - 1)0.37 + 1]^2$$
$$= 36.81$$

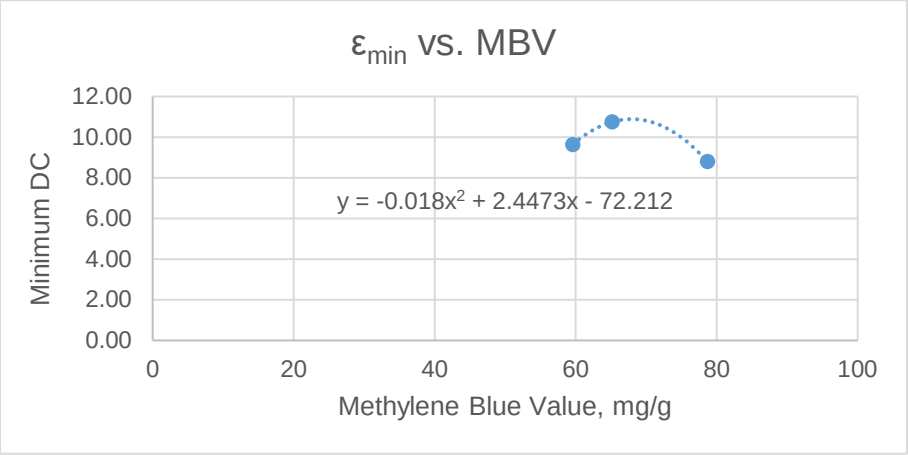

Figure 7-9 the correlation between MBV and ε_{min} for the three soil samples

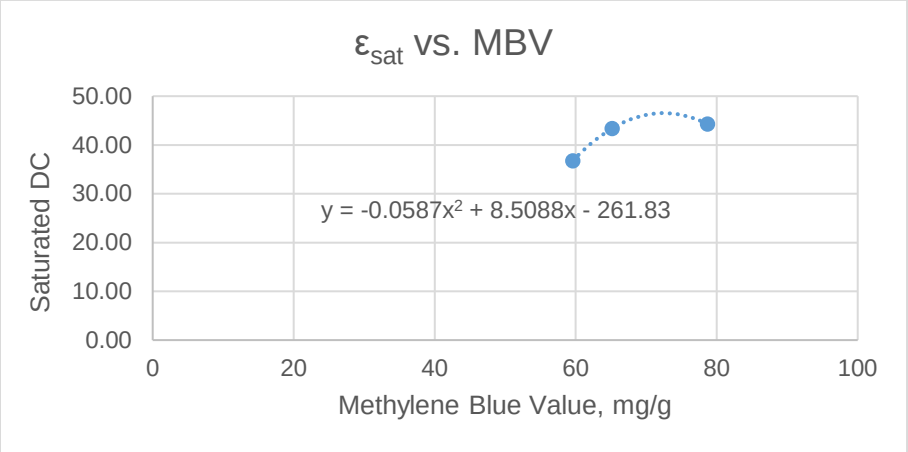

Figure 7-10 the correlation between MBV and ε_{sat} for the three soil samples

Empirical relationships for predicting fitting parameters to define SDCC

Once the three points of a SDCC (i.e. Point A, B and C as shown in Figure B-4) are determined by conducting laboratory experiments as aforementioned, they are fitted

to the general mathematical form as shown in Equation (B-6), from which the fitting parameters α and γ can be determined. Table 7-11 provides a summary of the three points of the SDCCs and Table 7-12 shows the fitting parameters α and γ determined for the three soil samples.

Table 7-11 the three points of the SDCCs for the soil samples

	Point A		Point B		Point C	
	Minimum DC (ε_{min})	**Maximum Suction (h_{max}), pF**	**Measured DC (ε_r)**	**Measured Matric Suction(h_m), pF**	**Saturated DC (ε_{sat})**	**Minimum Suction (h_{min}), pF**
Port	9.66	7	28.48	3.49	36.81	0
Kirkland	10.75	7	33.29	3.71	43.38	0
Osage	8.81	7	33.96	3.42	44.29	0

Table 7-12 the fitting parameters of the SDCCs of the soil samples

	α	γ	**MBV**	pfc**, %**
Port	0.449	2.868	59.58	82.90
Kirkland	0.177	7.741	65.15	83.72
Osage	0.448	1.930	78.67	99.19

Empirical relationships are established between the two fitting parameters and MBV and pfc using the neural network function in the statistical software JMP (detailed user guide is elaborated in Appendix C). The empirical prediction functions for α and γ are:

$$H_1 = TANH(0.5(a_1(MBV) + b_1(pfc) + c_1)) \quad (7\text{-}25)$$

$$\alpha, \gamma = m(H_1) + n \quad (7\text{-}26)$$

where H_1 is the hidden layer function and the coefficients in the prediction functions are shown in Table 7-13.

Table 7-13 coefficients in the empirical prediction functions

	α	γ
$\mathbf{a_1}$	0.22795851	-0.069916606

b_1	-0.266616429	0.085548558
c_1	9.551699184	-3.284691246
m	-0.900976768	-32.73418563
n	0.878226792	-2.935133574

Finally, using Equation (B-6), complete SDCCs can be plotted for the soil samples if α, γ, ε_{sat} and $\varepsilon_{\min}$ are predicted with only the measurements of MBV under a field condition as shown in Figure 7-11 (the three points of each sample are shown in the figure as well). As elaborated earlier, with also the measurements of DC, the SDCCs can be used to predict the matric suction h_m which is one of the required parameters to estimate the undrained shear strength and compression index of the soils.

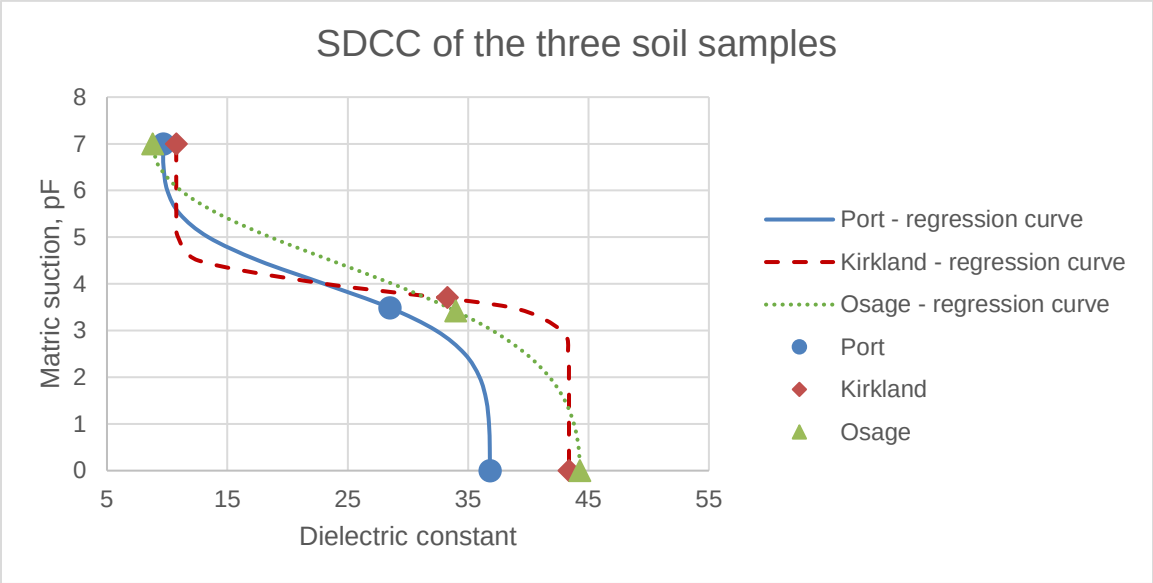

Figure 7-11 the SDCCs of the three soil samples

Empirical relationships for predicting required parameters to define SWCC

Once the three points of a SWCC (i.e. Point A, B and C as shown in Figure B-10) are determined by conducting laboratory experiments as aforementioned, they are fitted to the Fredlund and Xing model as shown in Equation (B-21) and (B-22), from which the fitting parameters a_f, b_f, c_f and h_r can be determined. Table 7-14 provides a summary

of the three points of the SWCCs and Table 7-15 shows the fitting parameters determined for the three soil samples.

Table 7-14 the three points of the SWCCs for the soil samples

	Point A		Point B		Point C	
	Minimum Volumetric Water Content	**Maximum Suction (h_{max}), pF**	**Measured Volumetric Water Content (θ)**	**Measured Matric Suction (h_m), pF**	**Saturated Volumetric Water Content (θ_{sat})**	**Minimum Suction (h_{min}), pF**
Port	0	7	0.279	3.49	0.370	0
Kirkland	0	7	0.311	3.71	0.413	0
Osage	0	7	0.357	3.42	0.461	0

Table 7-15 the fitting parameters of the SWCCs of the soil samples

	a_f	b_f	c_f	h_r	**MBV**
Port	11.250	1.050	-8.240	2.290	59.58
Kirkland	7.950	1.060	-7.000	1.500	65.15
Osage	6.950	1.070	-5.110	2.890	78.67

The four fitting parameters of each soil sample are plotted against their MBV as shown in Figure 7-12. The empirical correlations of a_f vs. MBV and c_f vs. MBV can be represented by linear functions as shown in Figure 7-12 (a) and (c), respectively; the correlations of b_f vs. MBV and h_r vs. MBV can be represented by quadratic functions as shown in Figure 7-12 (b) and (d), respectively. The empirical relationship between a_f and MBV is expressed as:

$$a_f = -0.1972MBV + 22.083 \quad (7\text{-}27)$$

The empirical relationship between b_f and MBV is expressed as:

$$b_f = -6 \times 10^{-5}MBV^2 + 0.0087MBV + 0.7289 \quad (7\text{-}28)$$

The empirical relationship between c_f and MBV is expressed as:

$$c_f = 0.1595MBV - 17.595 \quad (7\text{-}29)$$

The empirical relationship between h_r and MBV is expressed as:

$$h_r = 0.0128MBV^2 - 1.7393MBV + 60.447 \quad (7\text{-}30)$$

Once MBV is measured under a field condition, all the fitting parameters can be predicted using the empirical relationships.

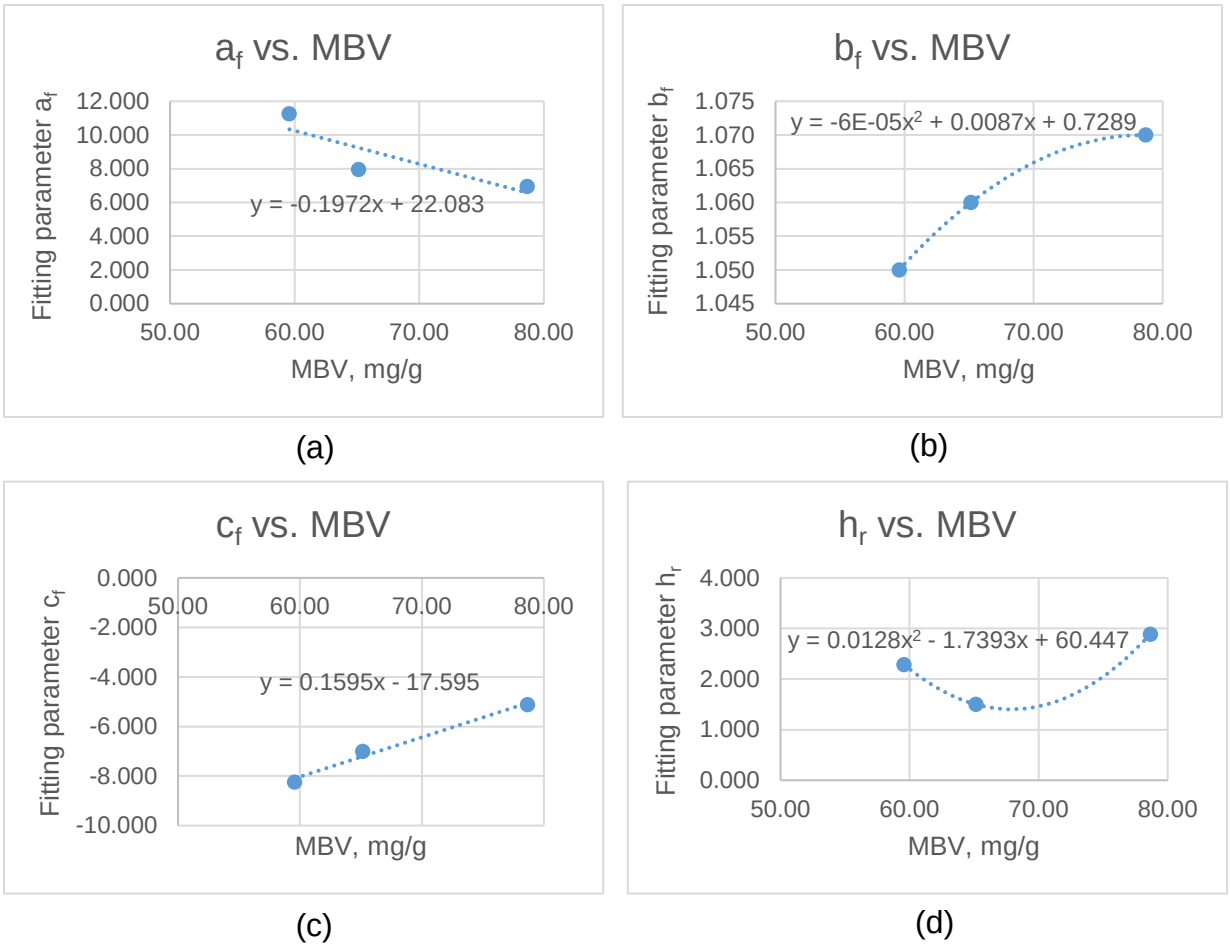

Figure 7-12 the empirical relationships between the four fitting parameters and MBV

In addition to the four fitting parameters, the saturated volumetric water content θ_{sat} is also required to define the SWCC of a soil. In order to obtain the required empirical relationships, the saturated volumetric water content θ_{sat} is correlated to the MBV, pfc and specific gravity G_s of the soil samples. The saturated volumetric water content for the three soil samples are calculated using Equation (B-31) as shown in Table 7-16.

Table 7-16 the saturated volumetric water content of the three soil samples

	Maximum dry unit weight, lb/ft^3	Specific Gravity (G_s)	Saturated volumetric water content (θ_{sat})	MBV	pfc, %
Port	103.03	2.62	0.370	59.58	82.90
Kirkland	100.66	2.75	0.413	65.15	83.72
Osage	89.48	2.66	0.461	78.67	99.19

Sample calculation (take “Port” as an example):

Based on Equation (B-31)

The saturated volumetric water content θ_{sat}:

$$\theta_{sat} = [1 - \frac{\gamma_{d-\max}}{(G_s\gamma_w)}] = [1 - \frac{103.03}{(2.62 \times 62.4)}] = 0.37$$

Empirical relationships are established between θ_{sat} and MBV, pfc and specific gravity G_s using the neural network function in the statistical software JMP as aforementioned. The empirical prediction functions for θ_{sat} are:

$$H_1 = TANH(0.5(a_1(MBV) + b_1(pfc) + c_1(G_s) + d_1)) \quad (7\text{-}31)$$

$$\theta_{sat} = m(H_1) + n \quad (7\text{-}32)$$

where H_1 is the hidden layer function and the coefficients in the prediction functions are shown in Table 7-17.

Table 7-17 coefficients in the empirical prediction functions

	θ_{sat}
a_1	0.1816298
b_1	-0.09726
c_1	1.6012614
d_1	-9.078068
m	0.130049
n	0.4722762

Finally, using Equation (B-21) and (B-22), complete SWCCs can be plotted for the soil samples once the four fitting parameters a_f, b_f, c_f, h_r and the saturated volumetric water content θ_{sat} are predicted with only the measurements of MBV (both pfc and specific gravity G_s can be estimated by MBV) under a field condition as shown in Figure 7-13 (the three points of each sample are shown in the figure as well). As elaborated earlier, once the SWCCs of the soil samples are obtained, with also the assist of the SDCCs from which the matric suction h_m of the soils are predicted, one is able to estimate the volumetric water content θ which is another required parameter used to estimate the undrained shear strength and compression index of the soils.

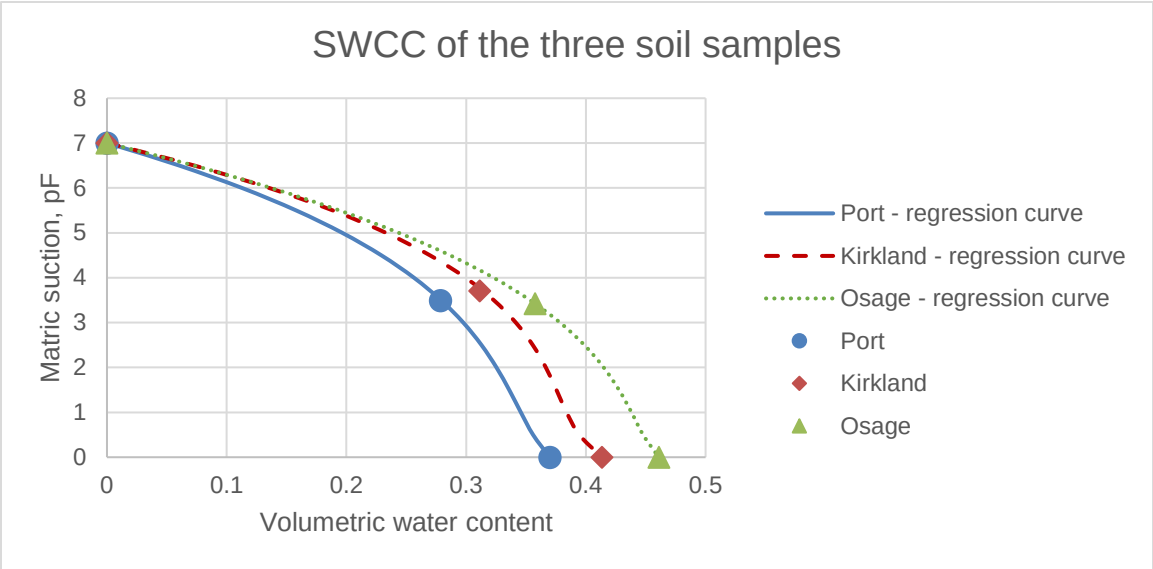

Figure 7-13 the SWCCs of the three soil samples

Empirical relationships for predicting dry unit weight

Once the standard laboratory compaction tests are performed for the three soil samples, the data points are fitted to the CCM shown in Equation (B-32), from which the fitting parameters a_d, b_d and n_d can be determined. The required laboratory experiment results to perform curve fitting are shown in Table 7-18. The fitted regression curves and the fitting parameters are shown in Figure 7-14 and Table 7-19, respectively.

Table 7-18 the required data points for compaction curve fitting

	Data point #	Water content, %	Dry unit weight, lb/ft^3	Volumetric water content	Saturated volumetric water content
Port	Point 1	17.13	100.89	0.28	0.37
	Point 2	18.82	102.94	0.31	0.37
	Point 3	18.97	102.51	0.31	0.37
	Point 4	20.24	103.21	0.33	0.37
	Point 5	21.94	102.04	0.36	0.37
	Point 6	23.69	99.50	0.38	0.37
Kirkland	Point 1	15.41	95.01	0.23	0.41
	Point 2	17.27	99.93	0.28	0.41
	Point 3	18.30	99.59	0.29	0.41
	Point 4	21.45	99.31	0.34	0.41
	Point 5	22.94	97.20	0.36	0.41
Osage	Point 1	22.22	86.37	0.31	0.46
	Point 2	23.68	89.09	0.34	0.46
	Point 3	25.31	88.26	0.36	0.46
	Point 4	26.91	89.50	0.39	0.46
	Point 5	28.50	89.67	0.41	0.46
	Point 6	31.23	86.85	0.43	0.46
	Point 7	33.19	85.17	0.45	0.46

Table 7-19 the fitting parameters of the CCMs of the soil samples

	a_d	b_d	n_d
Port	1.686771073	0.035955963	0.0088836
Kirkland	1.658890903	0.090392904	0.1091659
Osage	1.440218177	0.017872965	0.0062712

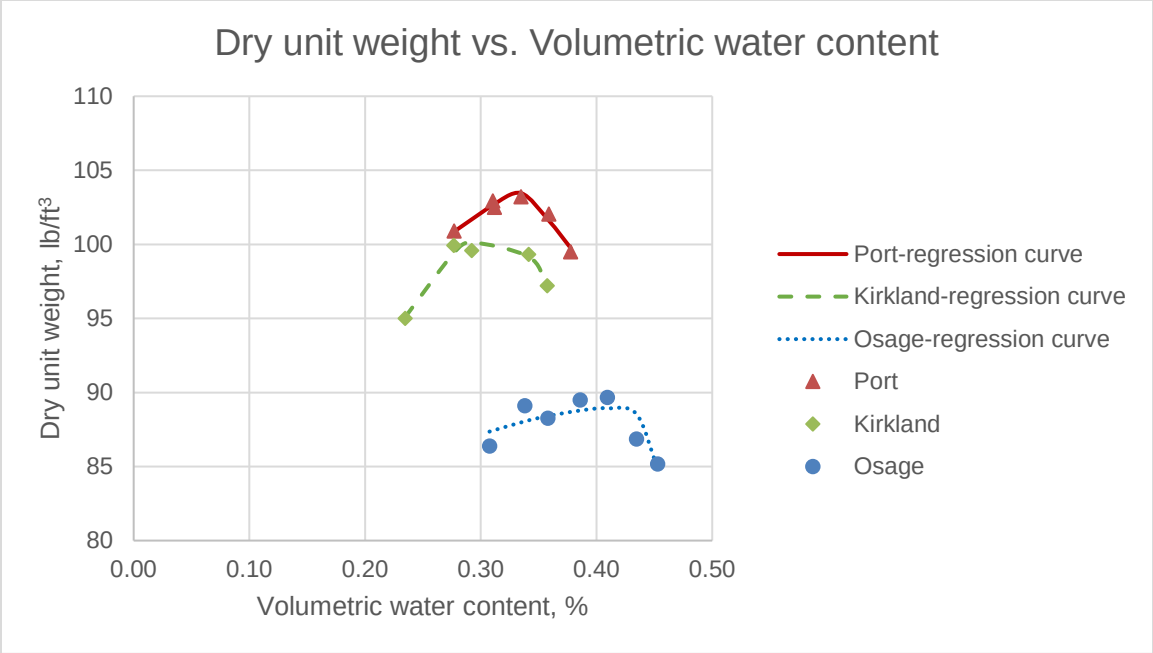

Figure 7-14 Regressed curves for the CCMs of the soil samples

In order to obtain the required empirical relationships for predicting the CCMs, the fitting parameters are correlated to the MBV, pfc and specific gravity G_s of the soil samples using the neural network function in the statistical software JMP as aforementioned. The empirical prediction functions for a_d, b_d and n_d are:

$$H_1 = TANH(0.5(a_1(MBV) + b_1(pfc) + c_1(G_s) + d_1)) \quad (7\text{-}33)$$

$$a_d, b_d, n_d = m(H_1) + n \quad (7\text{-}34)$$

where H_1 is the hidden layer function and the coefficients in the prediction functions are shown in Table 7-20.

Table 7-20 the fitting parameters of the CCMs of the soil samples

	a_d	b_d	n_d
a_1	0.099185396	-0.039174583	0.057947024
b_1	0.083715306	0.144640778	0.063143883
c_1	-1.824986435	-19.44194219	-50.73109753
d_1	-9.14215919	41.71321966	125.2064624
m	-0.195976385	-0.053774475	-0.069498463
n	1.593813729	0.047394686	0.040398477

Under a field condition, one is able to estimate the required fitting parameters to define the CCM using the empirical relationships shown in Equation (7-33) and (7-34) with only the measurements of MBV. The procedures to predict the saturated volumetric water content θ_{sat} and volumetric water content θ have been elaborated as aforementioned. Finally, one is able to obtain the dry unit weight γ_d of the soil using the CCM shown in Equation (B-32), which is one of the required parameters to estimate the undrained shear strength and compression index of the soils.

Estimation of Soil Properties

Once the empirical relationships are established, the following provides a brief demonstration of how to estimate the two key soil properties (i.e. the undrained shear strength c_u and the compression index C_c) using those relationships. The parameters required to conduct the estimations are (also illustrated in Figure 7-2 and Figure 7-4):

- the effective internal friction angle ϕ';
- the specific gravity G_s;
- the matric suction h_m;
- the volumetric water content θ; and
- the dry unit weight of the soil γ_d.
- the matric suction at intersection $h_{m-\mathrm{int}ercept}$; and
- the suction compression index γ_h.

For the purpose of demonstration, assuming that the MBV and DC are measured under a field condition for an unknown cohesive foundation soil which has properties similar to those of the three soil samples obtained from Oklahoma:

- MBV = 70 mg/g;
- DC = 25;

Task 1. Estimation of Effective Internal Friction Angle

Based on Equation (7-19):

$$PI = 0.6622MBV - 13.828 = 32.57$$

Based on Equation (7-20):

$$LL = 1.2489MBV - 32.338 = 55.09$$

Based on Equation (B-1):

$$\phi' = 0.0016PI^2 - 0.302PI + 36.208 = 28.07$$

Task 2. Estimation of Specific Gravity

Based on Equation (3-12):

$$G_s = \frac{2.55 + 2.91(0.057)(\frac{PI-20}{40-PI})^{3.24}(\frac{LL-40}{70-LL})^{-2.45}}{1 + 0.057(\frac{PI-20}{40-PI})^{3.24}(\frac{LL-40}{70-LL})^{-2.45}}$$

$$= \frac{2.55 + 2.91(0.057)(\frac{32.57-20}{40-32.57})^{3.24}(\frac{55.09-40}{70-55.09})^{-2.45}}{1 + 0.057(\frac{32.57-20}{40-32.57})^{3.24}(\frac{55.09-40}{70-55.09})^{-2.45}}$$

$$= 2.63$$

Task 3. Estimation of Matric Suction

1. Determine pfc using Equation (7-22)

$$pfc = 62.221\ln(MBV) - 173.33 = 62.221 \times \ln(70) - 173.33 = 91.02$$

2. Determine $\varepsilon_{\min}$ using Equation (7-23)

$$\varepsilon_{\min} = -0.0178MBV^2 + 2.414MBV - 71.026$$
$$= -0.0178 \times 70^2 + 2.414 \times 70 - 71.026$$
$$= 10.73$$

3. Determine ε_{sat} using Equation (7-24)

$$\varepsilon_{sat} = -0.0582MBV^2 + 8.4438MBV - 259.51$$
$$= -0.0582 \times 70^2 + 8.4438 \times 70 - 259.51$$
$$= 46.38$$

4. Determine fitting parameters α and γ for SDCC using Equation (7-25) and (7-26) and Table 7-13

$$H_1, \alpha = TANH(0.5(a_1(MBV) + b_1(pfc) + c_1))$$
$$= TANH(0.5(0.22795851(70) - 0.266616429(91.02) + 9.551699184))$$
$$= 0.5516$$

$$H_1, \gamma = TANH(0.5(a_1(MBV) + b_1(pfc) + c_1))$$
$$= TANH(0.5(-0.069916606(70) + 0.085548558(91.02) - 3.284691246))$$
$$= -0.1936$$

$$\alpha = m(H_1, \alpha) + n = -0.900976768 \times 0.5516 + 0.878226792 = 0.3812$$

$$\gamma = m(H_1, \gamma) + n = -32.73418563 \times (-0.1936) - 2.935133574 = 3.4034$$

5. Determine the matric suction using Equation (B-6)

$$\varepsilon_r = [\frac{\varepsilon_{sat}+\varepsilon_{\min}\alpha[\frac{h_m}{h_{\max}-h_m}]^{\gamma}}{1+\alpha(\frac{h_m}{h_{\max}-h_m})^{\gamma}}] \Rightarrow 25 = [\frac{46.38+10.73\times0.3812[\frac{h_m}{7-h_m}]^{3.4034}}{1+0.3812(\frac{h_m}{7-h_m})^{3.4034}}]$$

Solve for the only unknown in the function and found that

$$h_m = 4.1945\ pF$$

Task 4. Estimation of Volumetric Water Content

1. Determine the fitting parameters a_f, b_f, c_f and h_r using Equation (7-27) – (7-30)

$$a_f = -0.1972MBV + 22.083 = -0.1972 \times 70 + 22.083 = 8.279$$

$$b_f = -6 \times 10^{-5}MBV^2 + 0.0087MBV + 0.7289 = 1.0439$$

$$c_f = 0.1595MBV - 17.595 = 0.1595 \times 70 - 17.595 = -6.43$$

$$h_r = 0.0128MBV^2 - 1.7393MBV + 60.447$$
$$= 0.0128 \times 70^2 - 1.7393 \times 70 + 60.447 = 1.416$$

2. Determine saturated volumetric water content using Equation (7-31) and (7-32) and Table 7-17

$$H_1 = TANH(0.5(a_1(MBV) + b_1(pfc) + c_1(G_s) + d_1))$$
$$= TANH(0.5(0.1816298(70) - 0.09726(91.02) + 1.6012614(2.63) - 9.078068))$$
$$= -0.4642$$

3. Determine the volumetric water content using Equation (B-21) and (B-22)

$$\theta = C(h) \times [\frac{\theta_{sat}}{[\ln[\exp(1) + (\frac{h_m}{a_f})^{b_f}]]^{c_f}}]$$

$$= [1 - \frac{\ln(1 + \frac{4.1945}{1.416})}{\ln(1 + \frac{7}{1.416})}] \times [\frac{0.4119}{[\ln[\exp(1) + (\frac{4.1945}{8.279})^{1.0439}]]^{-6.43}}]$$
$$= 0.252$$

Task 5. Estimation of Dry Unit Weight

1. Determine the fitting parameters a_d, b_d and n_d using Equation (7-33) and (7-34) and Table 7-20

$$H_1, a_d = TANH(0.5(a_1(MBV) + b_1(pfc) + c_1(G_s) + d_1))$$
$$= TANH(0.5(0.099185396(70) + 0.083715306(91.02) - 1.824986435(2.63) - 9.14215919))$$
$$= 0.30083$$

$$H_1, b_d = TANH(0.5(a_1(MBV) + b_1(pfc) + c_1(G_s) + d_1))$$
$$= TANH(0.5(-0.039174583(70) + 0.144640778(91.02) - 19.44194219(2.63) + 41.71321996))$$
$$= 0.46365$$

$$H_1, n_d = TANH(0.5(a_1(MBV) + b_1(pfc) + c_1(G_s) + d_1))$$
$$= TANH(0.5(0.057947(70) + 0.0631439(91.02) - 50.7311(2.63) + 125.20646))$$
$$= 0.66048$$

$$a_d = m(H_1, a_d) + n = -0.195976 \times 0.30083 + 1.5938137 = 1.53486$$

$$b_d = m(H_1, b_d) + n = -0.053774 \times 0.46365 + 0.0473947 = 0.02246$$

$$n_d = m(H_1, n_d) + n = -0.069498 \times 0.66048 + 0.0403985 = -0.0055$$

2. Determine the dry unit weight using Equation (B-32)

$$\gamma_d = (a_d[\text{csch}(\frac{\theta\theta_{sat}}{G_s(|\theta_{sat} - \theta|)})]^{n_d} - b_d[\text{csch}(\frac{\theta\theta_{sat}}{G_s(|\theta_{sat} - \theta|)})]) \times \gamma_w$$

$$= \left(\begin{matrix} 1.53486[\text{csch}(\frac{0.252 \times 0.4119}{2.63(|0.4119 - 0.252|)})]^{-0.0055} \\ -0.02246[\text{csch}(\frac{0.252 \times 0.4119}{2.63(|0.4119 - 0.252|)})] \end{matrix}\right) \times 62.4$$

$$= 89.43\ lb/ft^3$$

Task 6. Estimation of Matric Suction at Intersection

Based on Equation (7-18)

$$h_{m-\text{int}ercept} = 5.622 + 0.0041(pfc) = 5.622 + 0.0041(91.02) = 5.995\ pF$$

Task 7. Estimation of Suction Compression Index

1. Determine the mineralogical zone using Figure B-12.

$$PI = 32.57$$

$$LL = 55.09$$

Based on Figure B-12, the mineralogical zone is Zone II.

2. Determine $\frac{LL}{pfc}$, $Ac = \frac{PI}{pfc}$ and the volume change guide number γ_0 using Figure B-14

$$\frac{LL}{pfc} = \frac{55.09}{91.02} = 0.605$$

$$Ac = \frac{PI}{pfc} = \frac{32.57}{91.02} = 0.358$$

$$\gamma_0 = 0.05$$

3. Determine suction compression index using Equation (B-46)

$$\gamma_h = \gamma_0 \times \frac{pfc}{100} = 0.05 \times 0.9102 = 0.0455$$

Estimation of undrained shear strength

The undrained shear strength of a soil can be estimated using Equation (7-2) – (7-6):

$$e_0 = \frac{G_s\gamma_w}{\gamma_d} - 1 = \frac{2.63 \times 62.4}{89.43} - 1 = 0.835$$

$$w = \frac{\theta\gamma_w}{\gamma_d} = \frac{0.252 \times 62.4}{89.43} = 0.1758$$

$$S_r = \frac{wG_s}{e_0} = \frac{0.1758 \times 2.63}{0.835} = 0.5537$$

$$f = 1 + (\frac{S_r - 0.85}{0.15})(\frac{0.01}{\theta} - 1) = 1 + (\frac{0.5537 - 0.85}{0.15})(\frac{0.01}{0.252} - 1) = 2.897$$

$$h_m = 4.1945\ pF$$
$$= 10^{4.1945}\ cm\ of\ water\ column$$
$$=\ 6161\ inch\ of\ water\ column$$
$$= -222.36psi$$

$$c_u = -h_m\theta f\frac{\sin\phi'}{1 - \sin\phi'}$$

$$= (222.36) \times 0.252 \times (2.897) \times \frac{\sin 28.07'}{1 - \sin 28.07'}$$
$$= 144.27\ psi$$

Therefore, the undrained shear strength of the soil is 144.27 psi.

Estimation of compression index

The compression index of a soil can be estimated using Equation (7-14) and (7-17):

$$|S|w = h_{m-\mathrm{int}ercept} - h_m = 5.995 - 4.1945 = 1.8005$$

$$C_c = \frac{(1+e_0)\gamma_h}{1+\frac{0.4343}{|S|w}} = \frac{(1+0.835)0.0455}{1+\frac{0.4343}{1.8005}} = 0.0673$$

Therefore, the compression index of the soil is 0.0673.

CHAPTER 8

SUMMARY AND CONCLUSION

Oklahoma has experienced the well-known bump-at-the-end-of-the-bridge condition for many years and the state highway agency is seeking for an innovative approach that allows for practitioners to rapidly and radically address the bump condition as opposed to simply placing an asphalt overlay. The main objective of this research was to introduce a method of using precast concrete pavement technologies for repairing distressed BASs. Besides elaborating the design and construction procedures for precast BASs, this research also identified 10 key elements within a BAS system and provided design considerations for these elements regarding the prevention of erosion damage that may occur underneath the BAS. In addition, this research also provided a detailed design procedure for the stone column technique as a means to address the potential for the occurrence of large settlement in the foundation of bridge embankments and proposed a procedure that utilized non-destructive testing methods to rapidly characterize soil properties which are key inputs for designing stone columns. The following summarizes the key findings and conclusions made in each section of the research.

I. Field Investigation

- The field investigations conducted at the four sites indicated that poor drainage conditions appeared to be the leading factor causing excessive moisture infiltration that created conditions for pumping and erosion to occur underneath joints with failed sealants, which eventually led to extensive slab cracking and bump conditions;
- As a standard practice that Oklahoma DOT has been promoting, using a CLSM wedge to support the BAS in combination with tying the BAS to the bridge deck appeared to significantly reduce the potential for bump to take place at the bridge deck – BAS joint;

- There was evidence showing that the bump issue was more prone to occurring at the BAS – pavement joint (as opposed to at the bridge deck – BAS joint) in Oklahoma due to the base erosion underneath that joint caused by excessive moisture infiltration combining with repetitive traffic loads;
- It appeared that a more well-considered BAS – pavement transition design (including both load transferring and drainage considerations) is needed to insure proper functioning of the joints in order to minimize the potential for moisture infiltration and the development of erosion damage.

II. Design and Construction of Precast BAS

- It is recommended that the thickness of precast BASs be designed using a mechanistic-empirical procedure that takes in account the various factors influencing the performance of BASs, as opposed to simply applying any empirical equation that is usually only a function of the unsupported span length. The design procedures established in the study by Tayabji et.al [10] were adopted in this study and certain modifications were made by incorporating a method which took into account the determination of the erosion damage that could potentially develop underneath precast BASs;
- A more realistic scheme was proposed to characterize the development of the erosion damage that could take place underneath the BAS – pavement joint based on the observations of the field investigation, where the amount of erosion damage should gradually increase from zero (representing a fully bonded condition at the slab-base interface) at the beginning of the design life to the maximum level (representing a fully unbonded condition) after a certain number of years depending on the design reliability;
- A design procedure was proposed to adjust the initial BAS design thickness to an “erosion-based slab thickness” taking into account the degree of slab-base bonding which is a function of the erosion damage. More importantly, the procedure facilitated an adjustment of the design reliability to quantitatively reflect the effects of various construction practices or design details on the performance of the BAS with respect to their utilities in preventing erosion damage underneath

the BAS and maintaining a satisfactory structural capacity to minimize the potential for bump issues;

- The construction procedure for precast BASs was briefly explained, including the panel fabrication and storage, base preparation, panel installation, post-installation activities and maintenance.

III. Key Element Design and Material Property Characterization

- 10 key elements within a BAS system were identified as a means to facilitate designing and creating a favorable environment for achieving successful performance of the BAS and preventing bump conditions from occurring; the design details for these elements were evaluated regarding their applicability to precast technologies and the effectiveness to prevent the occurrence of the potential bump condition; in addition, reliability considerations were established to better help practitioners make design decisions for various levels of design assurance;
- Detailed procedures (including the determinations of both settlement and bearing capacity) for designing the stone column technique were provided as a means to address any excessive settlement that may potential take place in the foundation underneath the bridge embankment;
- Three methods (including the equilibrium method, the finite element method and the Priebe's method) were elaborated for determining the settlement of a stone column treated ground, where it was found that the Priebe's method tended to provide a lower bound estimation and the equilibrium method generally provided the upper bound solution. Five failure modes were summarized that facilitated the determination of the bearing capacity of stone column treated grounds;
- To facilitate the determination of key soil properties (i.e. undrained shear strength and compression index) used for the stone column design, detailed procedures were proposed that used NDT technologies (i.e. methylene blue test and percometer test) to expedite the testing process.

APPENDIX A

STONE COLUMN SETTLEMENT – FINITE ELEMENT METHOD DESIGN CHART

LOW COMPRESSIBILITY SOIL

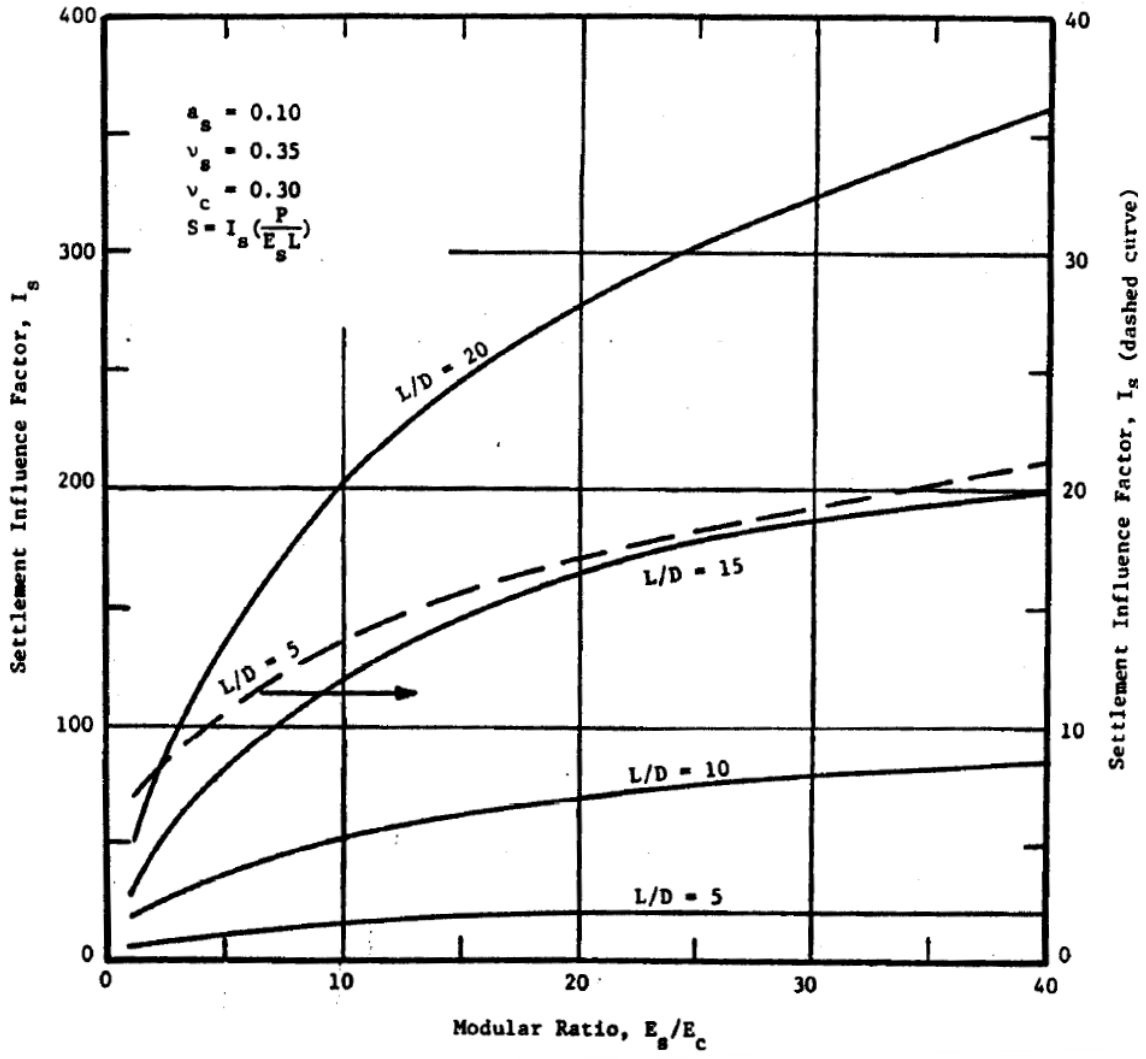

Figure A-1 Settlement prediction curve for low compressibility soil with an area replacement ratio a_s = 0.1 [118]

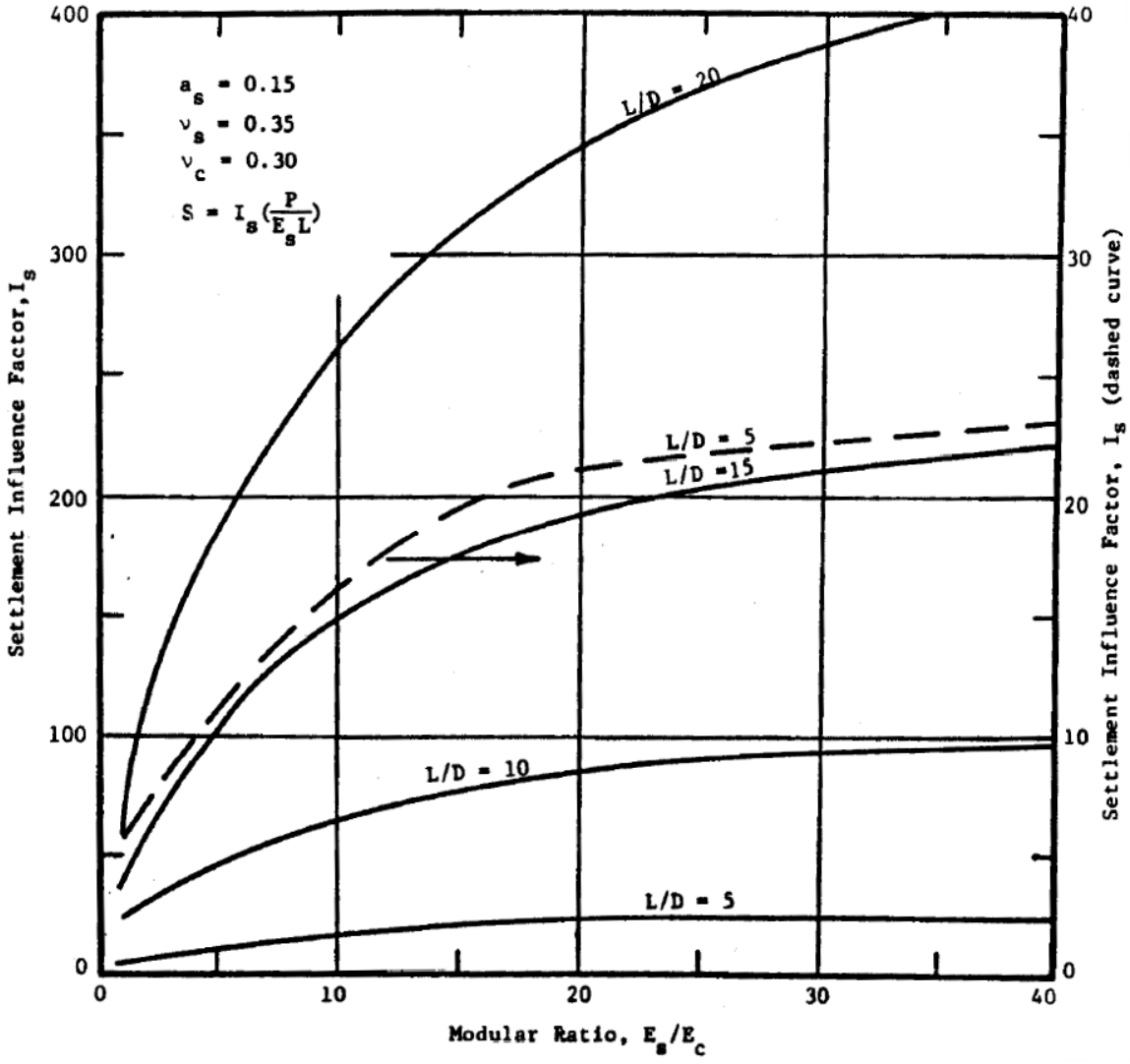

Figure A-2 Settlement prediction curve for low compressibility soil with an area replacement ratio a_s = 0.15 [118]

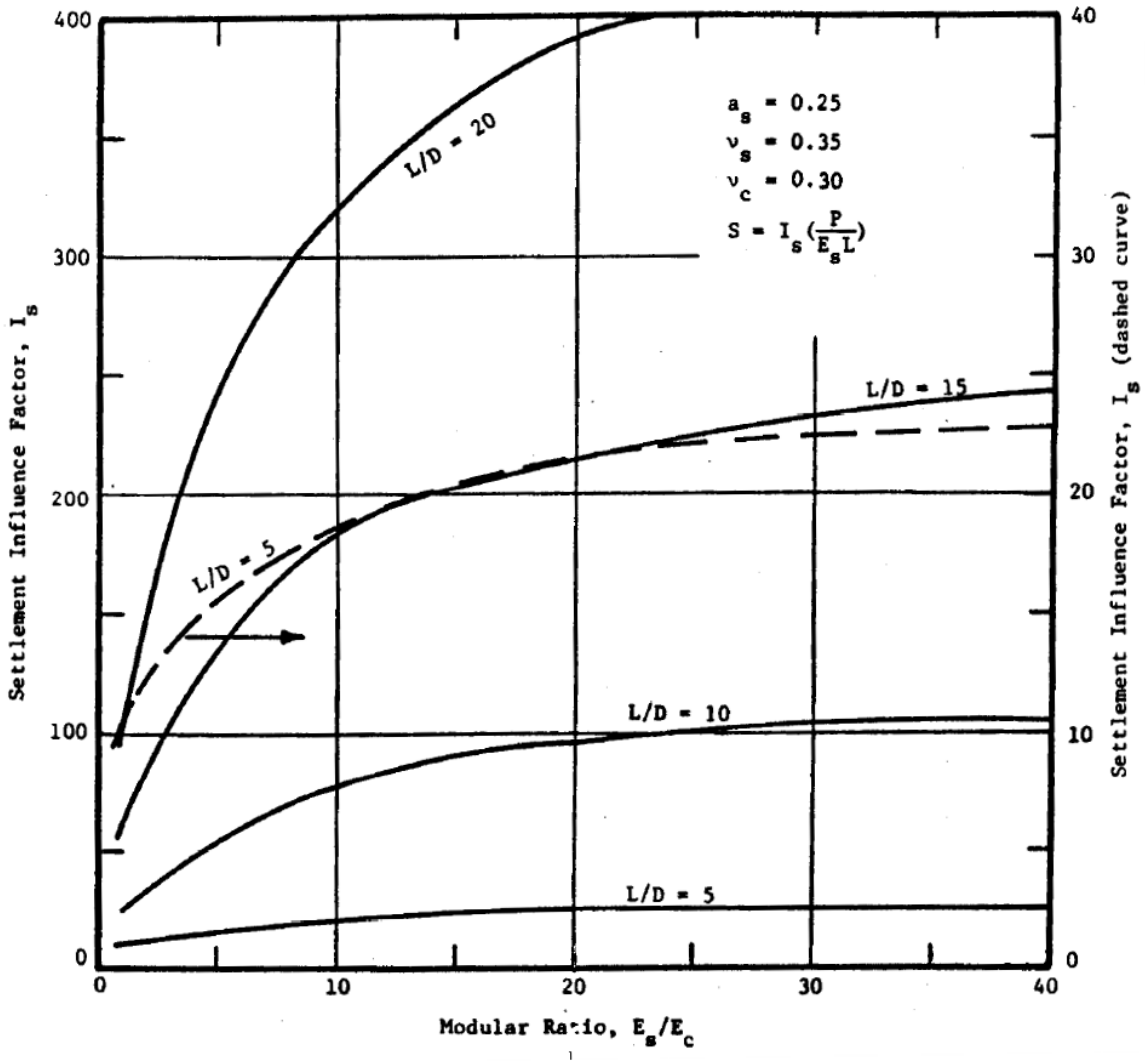

Figure A-3 Settlement prediction curve for low compressibility soil with an area replacement ratio a_s = 0.25 [118]

COMPRESSIBLE COHESIVE SOIL

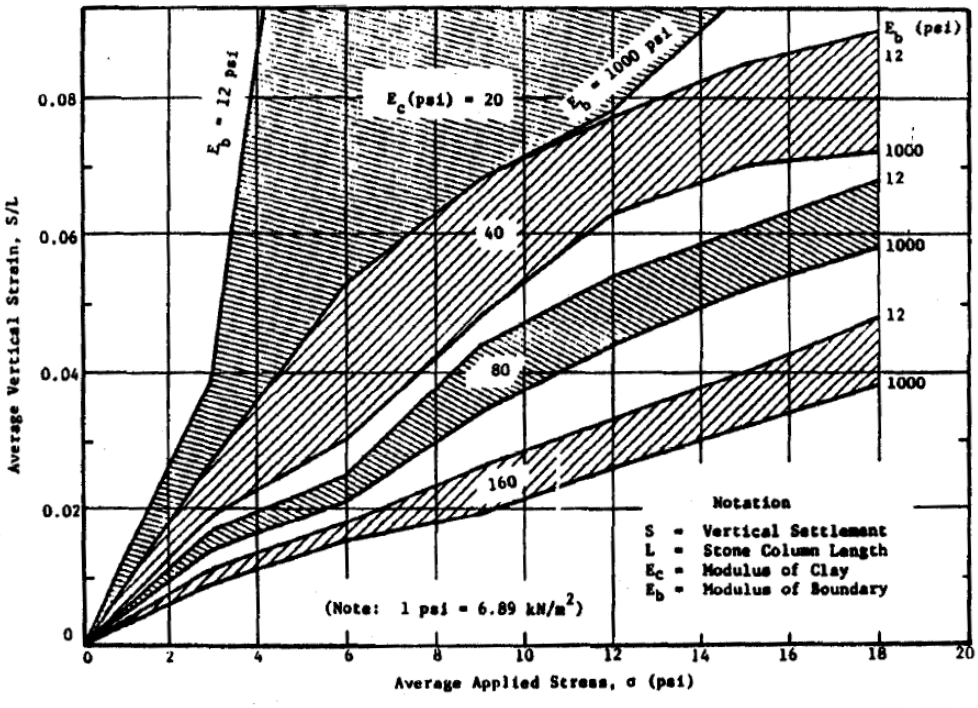

Figure A-4 Settlement prediction curve for compressible cohesive soil with an area replacement ratio a_s = 0.1 and L/D = 5 [118]

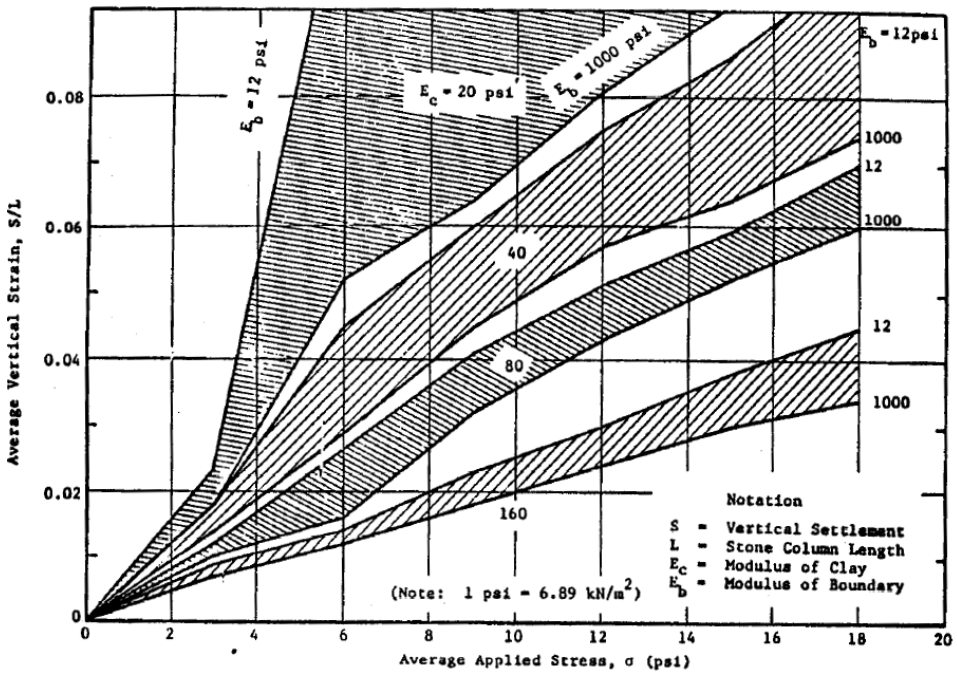

Figure A-5 Settlement prediction curve for compressible cohesive soil with an area replacement ratio a_s = 0.1 and L/D = 10 [118]

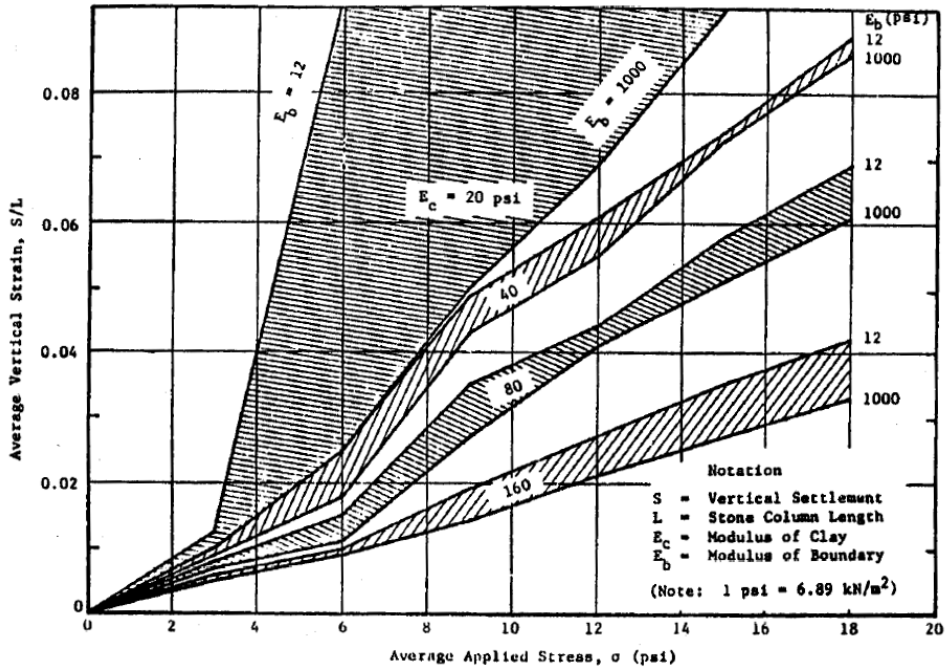

Figure A-6 Settlement prediction curve for compressible cohesive soil with an area replacement ratio a_s = 0.1 and L/D = 20 [118]

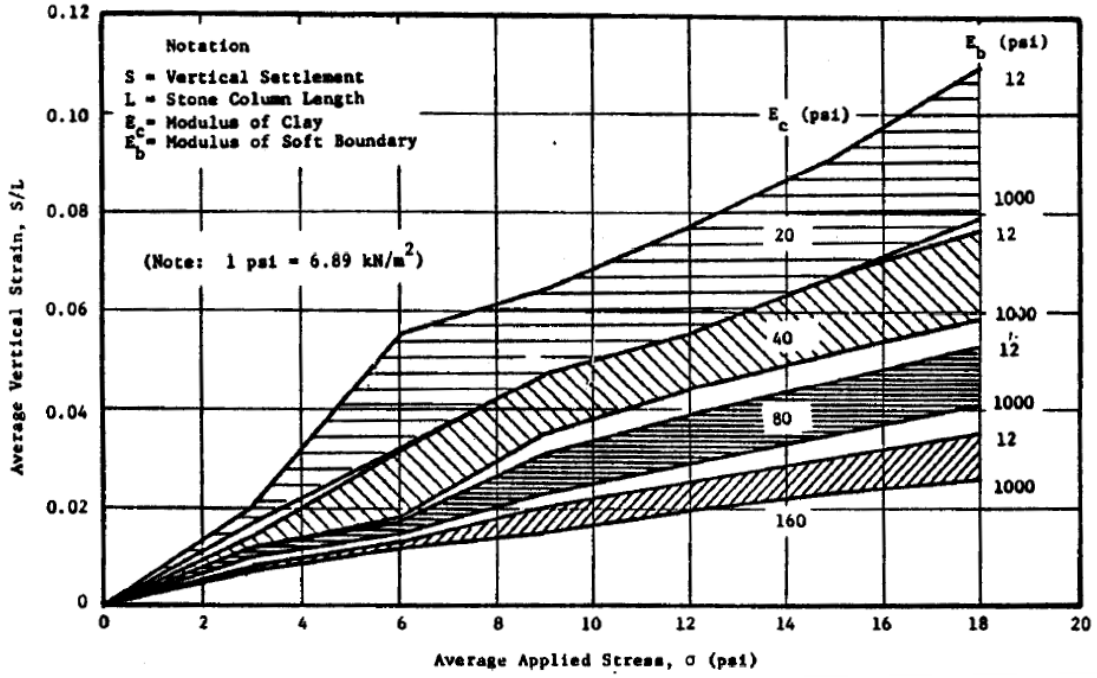

Figure A-7 Settlement prediction curve for compressible cohesive soil with an area replacement ratio a_s = 0.25 and L/D = 5 [118]

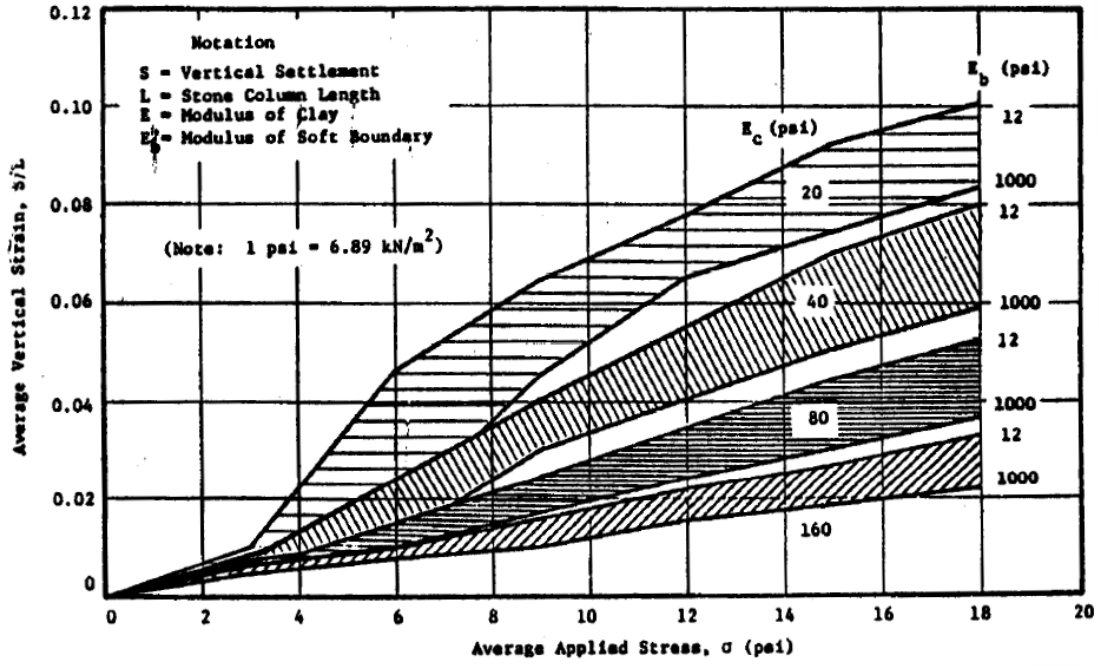

Figure A-8 Settlement prediction curve for compressible cohesive soil with an area replacement ratio a_s = 0.25 and L/D = 10 [118]

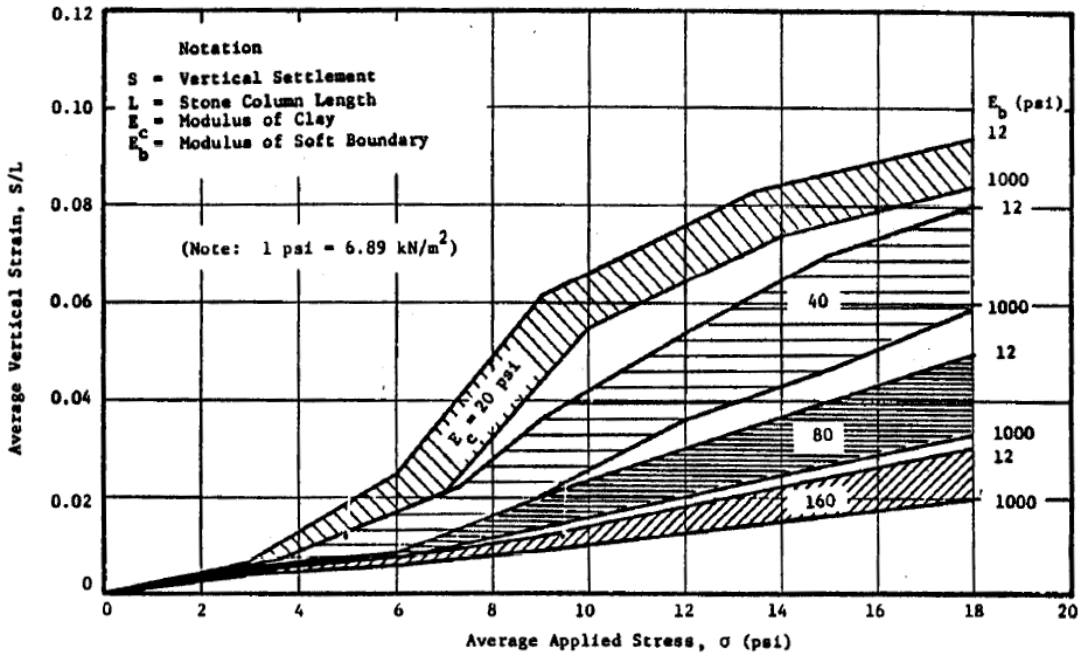

Figure A-9 Settlement prediction curve for compressible cohesive soil with an area replacement ratio a_s = 0.25 and L/D = 15 [118]

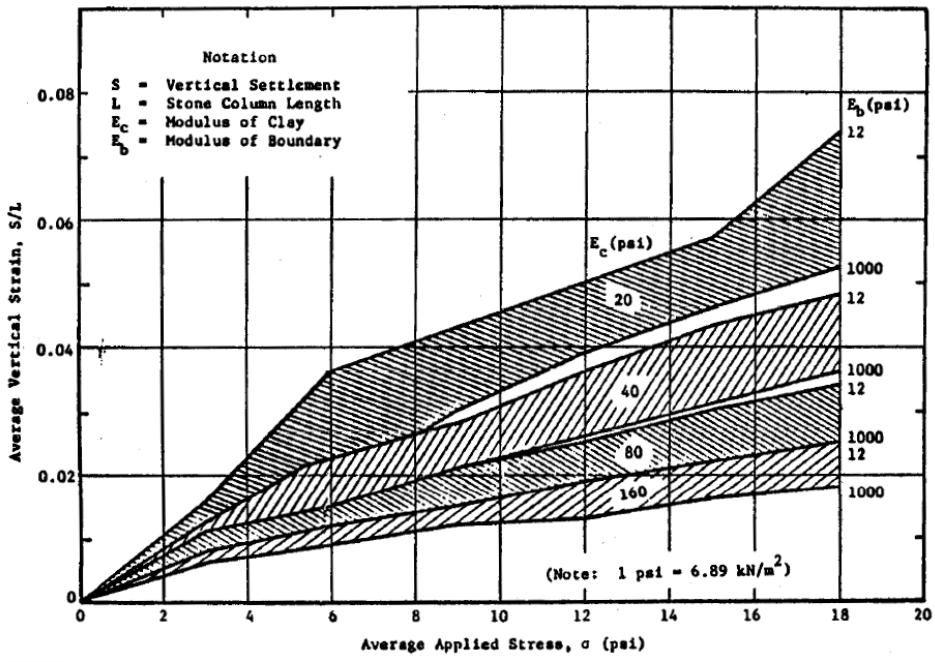

Figure A-10 Settlement prediction curve for compressible cohesive soil with an area replacement ratio a_s = 0.35 and L/D = 5 [118]

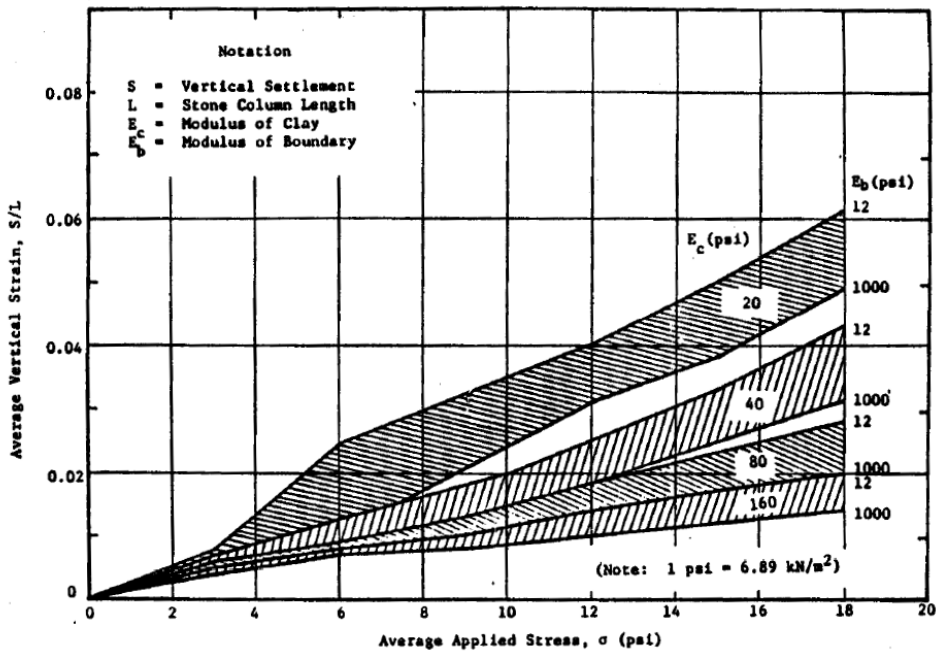

Figure A-11 Settlement prediction curve for compressible cohesive soil with an area replacement ratio a_s = 0.35 and L/D = 10 [118]

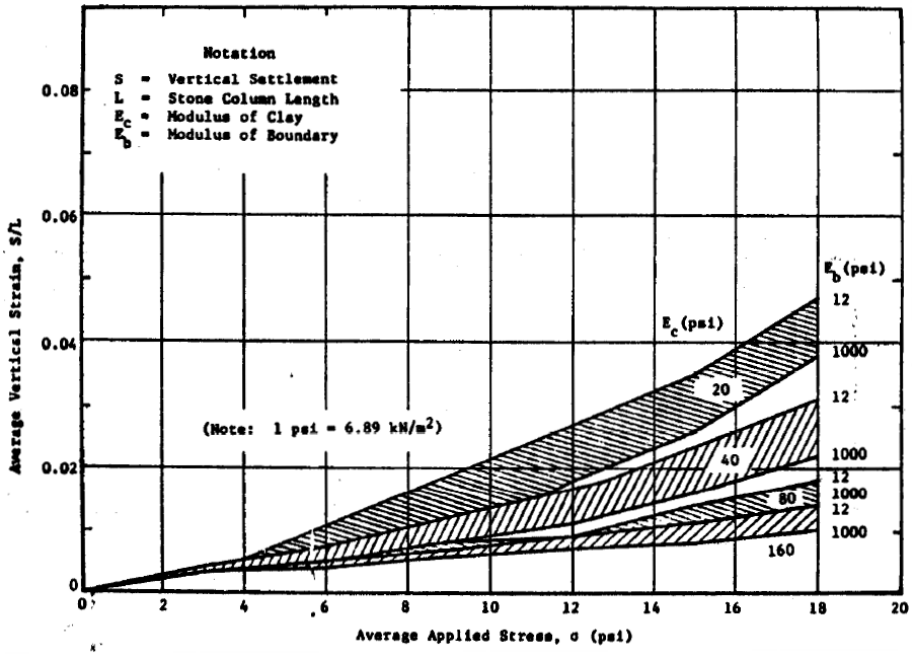

Figure A-12 Settlement prediction curve for compressible cohesive soil with an area replacement ratio a_s = 0.35 and L/D = 20 [118]

APPENDIX B

DETAILED PROCEDURES FOR CHARACTERIZATION OF SOIL PROPERTIES

This chapter provides detailed procedures for establishing empirical relationships under laboratory conditions and elaborates how the empirical relationships can be used to characterize soil properties using NDT technologies under field conditions.

Prediction of Effective Internal Friction Angle by Methylene Blue Test

The effective internal friction angle ϕ' of a soil can be determined under a laboratory condition by performing either consolidated-drained or consolidated-undrained triaxial shear test with the measurements of pore water pressure. Alternatively, ϕ' can also be estimated by applying empirical relationship based on the plasticity index (PI) of the soil, which can be expressed as [145]:

$$\phi' = 0.0016PI^2 - 0.302PI + 36.208 \quad \text{(B-1)}$$

where PI is the plasticity index and ϕ' is the effective internal friction angle of the soil. The PI of a soil can be determined under laboratory conditions by conducting standard Atterberg limits tests; alternatively, it can also be predicted by performing Methylene Blue Test (MBT) following Sahin's work [139].

A Methylene Blue Value (MBV) which provides an indication of the amount of fine content in a soil sample can be obtained by performing MBT. Experience indicates that it is the amount and characteristics of the fine content that govern the engineering properties (such as PI and ϕ') of a soil [139]; therefore, it is possible to estimate PI and calculate the effective internal friction angle ϕ' based on only the measurement of the MBV of a soil.

In contrast to the standard laboratory tests to determine PI and ϕ', the MBT can be performed under either a field or a laboratory condition within less than 10 min by using the testing apparatus shown in Figure B-1 which all can fit together into a portable kit. The testing apparatus kit consists of a colorimeter, a timer, two 45 mL plastic tube, a

micropipette, a 1.4 mL plastic tube, a plastic syringe, a 0.20 micrometers size filter, a 7.50 mL eyedropper, a bottle of methylene blue solution, a bottle of double distilled water and a high precision portable scale with 0.01 gram sensitivity [139].

Figure B-1 Methylene Blue Test apparatus [139]

A brief MBT testing procedure is shown in Figure B-2. The procedure consists of mixing the soil sample with methylene blue solution, diluting an aliquot of the mixed solution and measuring the MBV of the solution by using a colorimeter. The MBV provides a measurement of the color change of the methylene blue solution, which is affected by the amount and characteristics of the fine content in that soil sample. The test is not only rapid and simple, but also provides accurate and repeatable results [146]. The step-by-step MBT testing procedure can be found elsewhere [139].

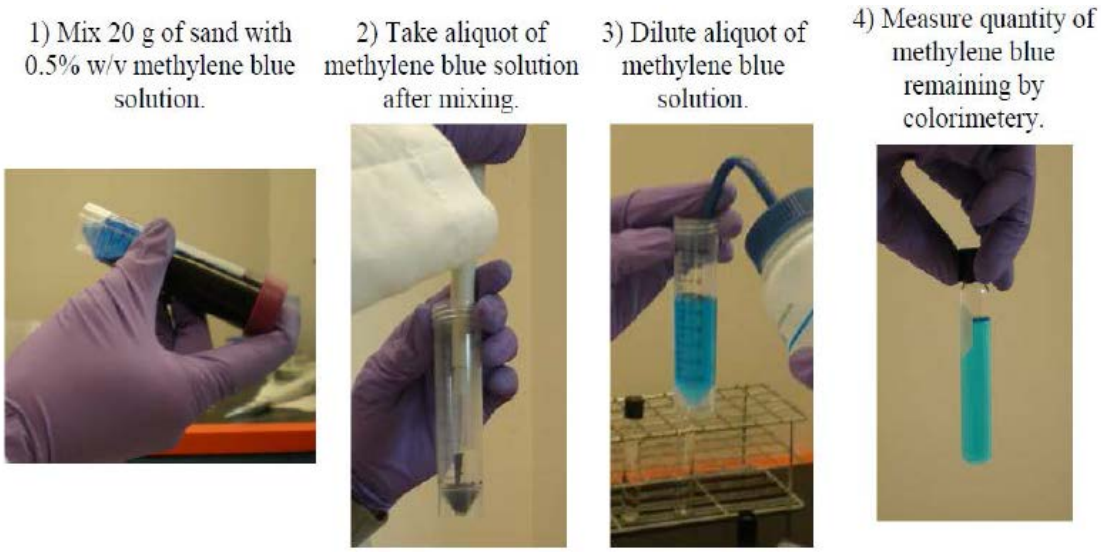

Figure B-2 Methylene Blue Test procedure [146]

Establishment of empirical relationships under laboratory conditions

In order to achieve the objective (using measured MBV to estimate PI and ϕ' under a field condition), an empirical relationship between MBV and PI must be established under a laboratory condition prior to the application of this technology under a field condition. Sahin [139] performed both MBT and Atterberg limits tests for a variety of base course aggregate materials under laboratory conditions and obtained the relationship between MBV and PI of the materials, which is shown in Figure B-3 with 90% confidence level boundaries.

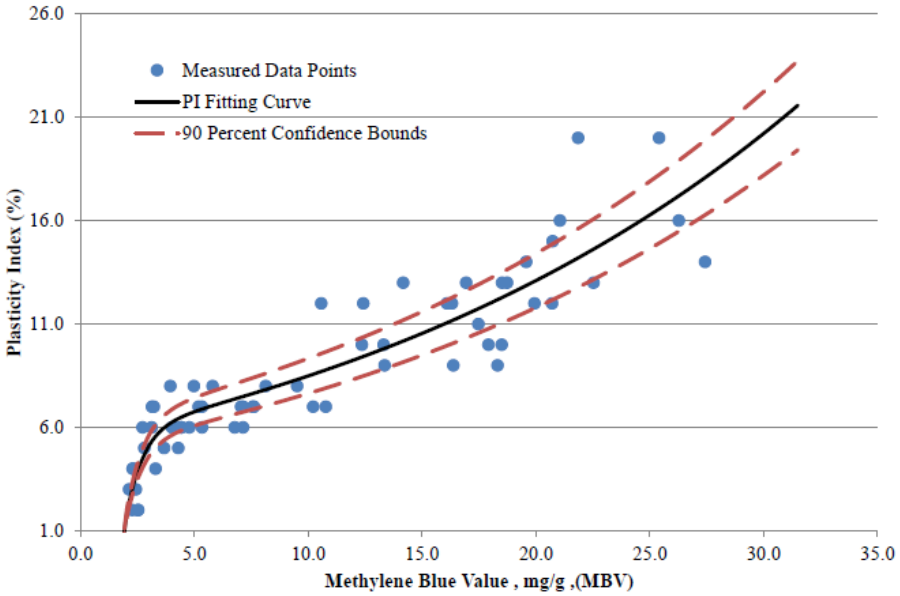

Figure B-3 The correlation between MBV and PI for base course materials [139]

Sahin [139] proposed an equation to characterize the relationship between MBV and PI of the base course materials, which is expressed as:

$$PI = 5.503e^{(0.04337MBV)} - 62.37 \cdot 10^{-5}e^{(-1.331MBV)} \quad \text{(B-2)}$$

where all the parameters are previously defined. Once the MBV is measured under a field condition, PI and ϕ' can be estimated by applying Equation (B-2) and Equation (B-1), respectively. Note that the relationship shown in Figure B-3 and the empirical function Equation (B-2) are only valid for the base course materials. In order to establish the specific empirical relationship for foundation soils, it is necessary to conduct laboratory experiments (i.e. MBT and Atterberg limits tests) on a large variety of foundation soils that cover the range of the typical soils found in the area of interest.

Prediction of Specific Gravity by Methylene Blue Test

The specific gravity of the most commonly found soil minerals ranges from 2.6 – 2.9 depending on the soil mineralogy and grain size [147]. Sahin [139] proposed a mathematical formulation to estimate the specific gravity of soils:

$$G_s = \frac{2.55+2.91(2.43)(\frac{PI-1}{22-PI})^{0.3076}(\frac{LL-1}{40-LL})^{-0.3525}}{1+(2.43)(\frac{PI-1}{22-PI})^{0.3076}(\frac{LL-1}{40-LL})^{-0.3525}} \quad \text{(B-3)}$$

where G_s is the specific gravity, PI is the plasticity index and LL is the liquid limit of the soil.

Sahin [139] also found the following relationship between MBV and LL of the tested base course materials:

$$LL = 14.64e^{(0.03371MBV)} - 24.99e^{(-1.149MBV)} \quad \text{(B-4)}$$

where all the parameters are previously defined. Similar to the empirical relationship between MBV and PI, the empirical relationship between MBV and LL shown in Equation (B-4) is only valid for the unbound base course materials, MBT and Atterberg limits tests should be performed under a laboratory condition on a large variety of foundation soils to find the empirical relationship between MBV and LL for foundation soils.

Establishment of empirical relationships under laboratory conditions

The specific gravity of a soil G_s can be easily estimated under a field condition by applying empirical relationship such as the one shown in Equation (B-3) once the PI and LL are estimated first (based on the measurements of MBV applying the empirical relationships such as the ones shown in Equation (B-2) and (B-4)). The empirical relationship shown in Equation (B-3) can be established based on the equation developed by Juárez-Badillo:

$$G_s = \frac{G_0 + G_m(\beta)(\frac{PI-P_0}{P_m-PI})^{\gamma}(\frac{LL-L_0}{L_m-LL})^{\delta}}{1+\beta(\frac{PI-P_0}{P_m-PI})^{\gamma}(\frac{LL-L_0}{L_m-LL})^{\delta}} \quad \text{(B-5)}$$

where G_0 is the minimum specific gravity (taken as 2.55), G_0 is the maximum specific gravity (taken as 2.91), P_0 is the approximate minimum plasticity index, P_m is the approximate maximum plasticity index, L_0 is the approximate minimum liquid limit, L_m is the approximate maximum liquid limit, β, γ and δ are fitting parameters. Note that P_0, P_m, L_0 and L_m are the approximate values of the true minimum or maximum values within the database of the laboratory experiment results. The approximate minimum values are determined by rounding down the true minimum values to 2 significant digits and the approximate maximum values are determined by rounding up the true maximum values to 2 significant digits. For instance, if the true minimum plasticity index in the database is 44, then the approximate minimum plasticity index should be $P_0 = 40$;

if the true maximum plasticity index in the database is 79, then the approximate maximum plasticity index should be $P_m = 80$.

Prediction of Matric Suction by Soil Dielectric Characteristic Curve

The determination of soil matric suction h_m under a field condition relies on the use of the soil dielectric characteristic curve (SDCC) which is an S-shape curve that describes the correlation between the soil matric suction h_m and dielectric constant (DC) ε_r as shown in Figure B-4. Each soil material corresponds to a unique shape of SDCC curve due to the differences in soil properties. The general form of a SDCC can be expressed as [139]:

$$\varepsilon_r = \left[\frac{\varepsilon_{sat}+\varepsilon_{\min}\alpha\left[\frac{h_m}{h_{\max}-h_m}\right]^{\gamma}}{1+\alpha\left(\frac{h_m}{h_{\max}-h_m}\right)^{\gamma}}\right] \quad \text{(B-6)}$$

where ε_r is the DC of the soil, ε_{sat} is the saturated DC of the soil which is also the maximum DC and relates to the minimum potential of soil suction, $\varepsilon_{\min}$ is the minimum soil DC and relates to the maximum potential of soil suction, h_m is the soil matric suction, $h_{\max}$ is the maximum soil suction (equals to 1.45 x 10^5 psi or 10^6 kPa or 7 pF), α and γ are fitting parameters depending on the type of the soil.

If the SDCC of a soil is known (i.e. the fitting parameters α and γ are known), the matric suction h_m of the soil can be easily determined by a DC measurement using the known SDCC relationship. The DC of a soil can be measured by using a percometer as shown in Figure B-5. The percometer is a NDT instrument specifically designed for measuring the DC of a material. It can provide highly accurate and reliable DC measurements within 5 seconds once a good contact is achieved between the material and the measuring probe. The percometer with a surface probe is useful to make DC measurements for materials with smooth surfaces and the percometer with a tube probe is applicable for inserting into soft materials (e.g. foundation soils) which requires a minimum 3.94 in (10 cm) of penetration depth [139].

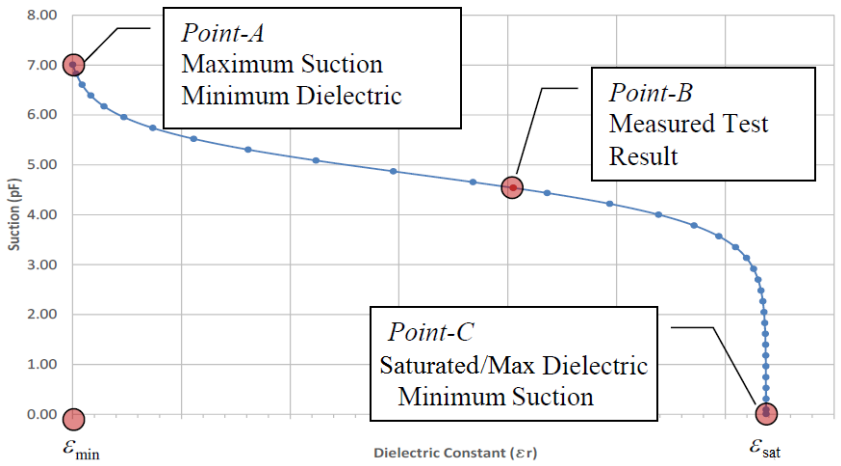

Figure B-4 A schematic illustration of the SDCC of a soil [139]

Figure B-5 Standard Adek Percometer™ with a surface probe and a tube probe [139]

However, very often, the SDCC of a soil is unknown under a field condition; in that case, it is necessary to determine all the unknown parameters (i.e. ε_{sat}, $\varepsilon_{\min}$, α and γ) in order to plot the SDCC of the soil. Sahin [139] has proposed empirical relationships to estimate the unknowns with only the measurements of MBV.

By conducting laboratory experiments (subsequently described) on a variety of base course materials, Sahin [139] found the following empirical relationship (shown in Figure B-6) between MBV and the saturated DC ε_{sat}:

$$\varepsilon_{sat} = 0.0334(MBV^2) - 0.1086(MBV) + 12.569 \quad \text{(B-7)}$$

where all the parameters are previously defined.

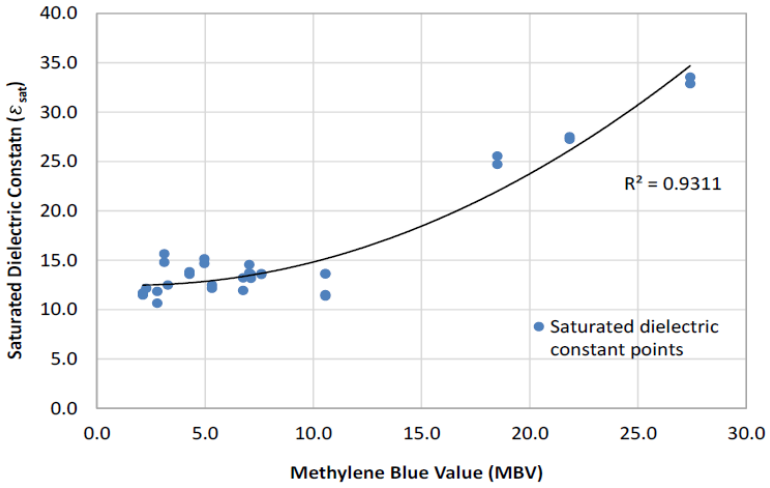

Figure B-6 Empirical relationship between MBV and ε_{sat} [139]

Similarly, the empirical relationship (shown in Figure B-7) between MBV and the minimum soil DC $\varepsilon_{\min}$ can be expressed as:

$$\varepsilon_{\min} = 0.1243\log(MBV) + 1.0668 \quad \text{(B-8)}$$

where all the parameters are previously defined.

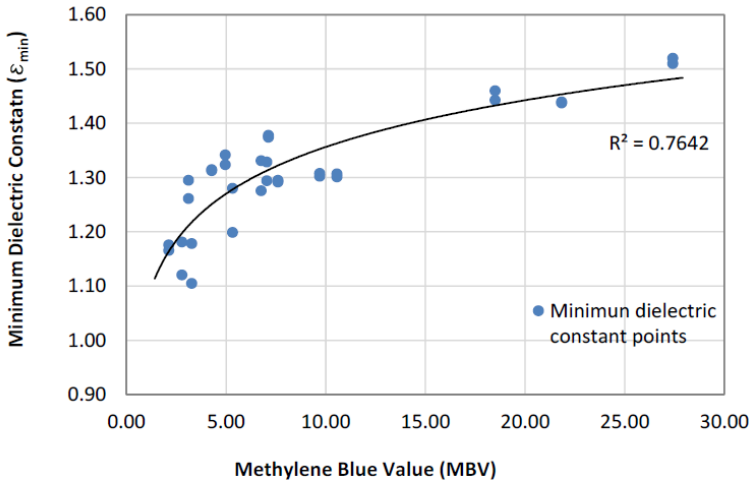

Figure B-7 Empirical relationship between MBV and $\varepsilon_{\min}$ [139]

The fitting parameters α and γ can also be estimated by using their empirical relationships with MBV and pfc (a parameter that can also be predicted by MBV). To estimate α, the following equations were proposed by Sahin [139]:

$$H_{1\alpha} = TANH(0.5(-0.478027(MBV) - 0.034582(pfc) + 8.923868)) \quad \text{(B-9)}$$

$$H_{2\alpha} = TANH(0.5(-0.207206(MBV) + 0.334387(pfc) - 8.088245)) \quad \text{(B-10)}$$

$$\alpha = 6.3772003(H_{1\alpha}) - 46.1404624(H_{2\alpha}) + 53.363999 \quad \text{(B-11)}$$

where $H_{1\alpha}$ and $H_{2\alpha}$ are hidden layer functions used to determine α and all the other parameters are previously defined. To estimate γ, the following equations were proposed [139]:

$$H_{1\gamma} = TANH(0.5(0.0897001(MBV) - 0.1597119(pfc) + 0.69592558)) \quad \text{(B-12)}$$

$$H_{2\gamma} = TANH(0.5(-0.0968849(MBV) - 0.020036(pfc) + 1.1379340)) \quad \text{(B-13)}$$

$$H_{3\gamma} = TANH(0.5(0.0668142(MBV) + 0.2112468(pfc) - 4.4814587)) \quad \text{(B-14)}$$

$$\gamma = 3.0066674(H_{1\gamma}) + 4.212358(H_{2\gamma}) + 3.211806(H_{3\gamma}) + 3.045290 \quad \text{(B-15)}$$

where $H_{1\gamma}$, $H_{2\gamma}$ and $H_{3\gamma}$ are hidden layer functions used to determine γ and all the other parameters are previously defined.

Establishment of empirical relationships under laboratory conditions

As noted previously, the core of this method is to establish empirical relationships (such as the ones shown in Equation (B-7) – (B-15)) under a laboratory condition in the first place and then use these relationships to expedite the process of characterizing soil properties under a field condition. This section provides the procedures for establishing the empirical relationships.

In order to establish the empirical relationships, a series of laboratory experiments should be performed, including:

1. the percometer test (to obtain the soil DC ε_r);
2. the filter paper test (to obtain the soil matric suction h_m);
3. the Methylene Blue Test (to obtain MBV of the soil);
4. the percent fine content test (to obtain pfc of the soil);
5. the standard laboratory compaction test (to obtain the dry unit weight γ_d and water content w); and
6. the specific gravity test (to obtain the specific gravity of the soil G_s).

Empirical relationships of ε_{sat} vs. MBV and ε_{min} vs. MBV

The percometer test is performed under a laboratory condition by using a surface probe percometer to obtain the DC ε_r of the soil samples. The detailed sample preparation and test procedures can be found elsewhere [139]. The main objective to

perform a percometer test is to determine the three main points (ε_r, ε_{sat} and $\varepsilon_{\min}$) of a SDCC as shown in Figure B-4, which are used to fit the general mathematical form of a SDCC (shown in Equation (B-6)) and perform regression analysis to obtain the two fitting parameters (i.e. α and γ).

ε_r is directly measured from a percometer test, based on which ε_{sat} and $\varepsilon_{\min}$ can be calculated by using a complex refraction index model (CRIM) following a two step-procedure. In the first step where an unsaturated condition is considered, the CRIM model can be expressed as:

$$\sqrt{\varepsilon_r} = [(\sqrt{\varepsilon_s} - 1)\theta_s + (\sqrt{\varepsilon_w} - 1)\theta + 1] \quad \text{(B-16)}$$

where ε_r is the measured composite DC, ε_s is the DC of the solid within the soil material, ε_w is the DC of water (which is a constant that equals to 81), $\theta_s = \frac{\gamma_d}{G_s\gamma_w}$ is the volumetric solid content of the soil, $\theta = \frac{w\gamma_d}{\gamma_w}$ is the volumetric water content and all the other parameters are previously defined. The goal of the first step which is to calculate the DC of the solid ε_s can be easily achieved once the volumetric solid content θ_s and volumetric water content θ are determined (unknown parameters γ_d, G_s, w can be determined under laboratory conditions). Once ε_s is determined, $\varepsilon_{\min}$ can be calculated using the following function:

$$\sqrt{\varepsilon_{\min}} = 1 + \theta_s(\sqrt{\varepsilon_s} - 1) \quad \text{(B-17)}$$

where all the parameters are previously defined.

In the second step where a saturated condition is considered, the CRIM model can be expressed as:

$$(\sqrt{\varepsilon_{sat}}) = [(\sqrt{\varepsilon_s} - 1)\theta_s + (\sqrt{\varepsilon_w} - 1)\theta_{ws} + 1] \quad \text{(B-18)}$$

where ε_{sat} is the saturated DC, $\theta_{ws} = 1 - \theta_s$ is the volumetric water content corresponds to the saturated condition and all the other parameters are previously defined.

The MBT is also performed under a laboratory condition, from which the MBV is obtained for each soil sample and is plotted against ε_{sat} and $\varepsilon_{\min}$ of the same soil sample as shown in Figure B-6 and Figure B-7, respectively. In this way, empirical relationships can be established for ε_{sat} vs. MBV and $\varepsilon_{\min}$ vs. MBV (such as the ones

shown in Equation (B-7) and (B-8)). As a result, ε_{sat} and $\varepsilon_{\min}$ can be easily estimated with only the measurements of MBV under a field condition.

Empirical relationships of α vs. (MBV & pfc) and γ vs. (MBV & pfc)

In order to establish the SDCC for a soil and determine the fitting parameters (i.e. α and γ) under a laboratory condition, it is also required to determine soil matric suction h_m by performing filter paper tests. The filter paper test is immediately conducted on the same samples after the completion of percometer tests under a laboratory condition. The detailed sample preparation and test procedures can be found elsewhere [139, 148]. Once all the required parameters are determined (ε_{sat}, $\varepsilon_{\min}$, ε_r and h_m) under a laboratory condition, the SDCC of the soil can be plotted and fitted to the general mathematical form as shown in Equation (B-6), from which the fitting parameters α and γ can be determined.

To facilitate the establishment of empirical relationships of α vs. (MBV & pfc) and γ vs. (MBV & pfc) (such as the ones shown in Equation (B-9) – (B-15) which can be used under a field condition to estimate α and γ), pfc test is also performed in addition to the MBT.

The pfc of a soil is defined as the ratio of the percent passing No.2 microns size to the percent passing No.200 sieve as shown in the following equation [139]:

$$pfc = \frac{\%-No.2 \text{ micron}}{\%-No.200 \text{ sieve}} \times 100 \quad \text{(B-19)}$$

The pfc of a soil is measured by using a Horiba Laser Scattering Particle Size Distribution Analyzer (shown in Figure B-8) under a laboratory condition. The equipment is able to provide test results within 10 minutes with reasonable accuracy and repeatability. The detailed test procedure is elaborated elsewhere [139].

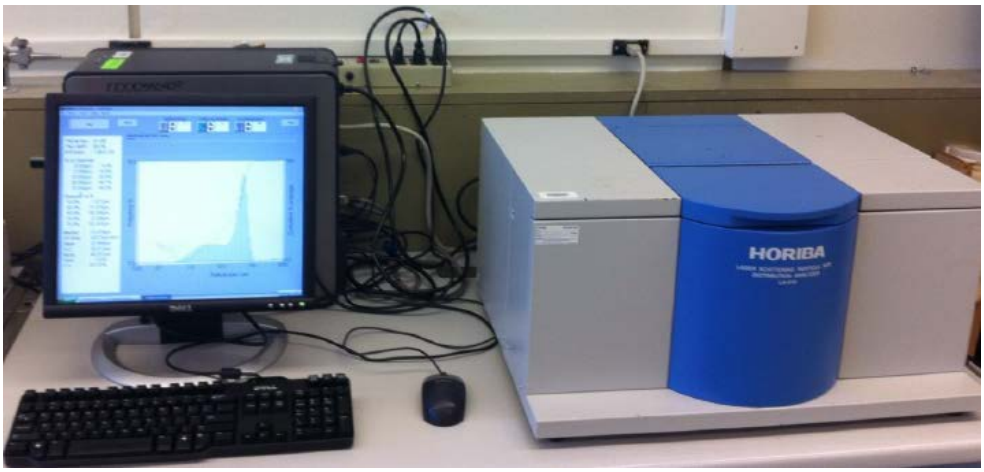

Figure B-8 Configuration of the Horiba LA-910 Particle Size Distribution Analyzer [139]

Once all of the required parameters are determined (i.e. α, γ, MBV and pfc) under the laboratory condition, neural network analyses are performed to obtain the empirical relationships by using a statistical software named as JMP which provides the most realistic mathematical relationship between the inputs and the empirical estimation models. Sahin [139] used JMP and successfully developed empirical relationships to estimate α and γ by inputting MBV and pfc as aforementioned. By using these empirical relationships, the fitting parameters α and γ of a soil can be easily estimated with only the measurements of MBV under a field condition (pfc can also be estimated with the measurement of MBV).

Empirical relationships between MBV and pfc

The equipment to measure pfc is not available under a field condition; therefore, it is necessary to establish empirical relationship between MBV and pfc under a laboratory condition as well in order to estimate pfc under a field condition with only the measurements of MBV.

Sahin [139] performed both MBT and pfc test for a variety of base course aggregate materials (same materials as aforementioned) and found a “C” shape correlation between the measured MBV and pfc as shown in Figure B-9.

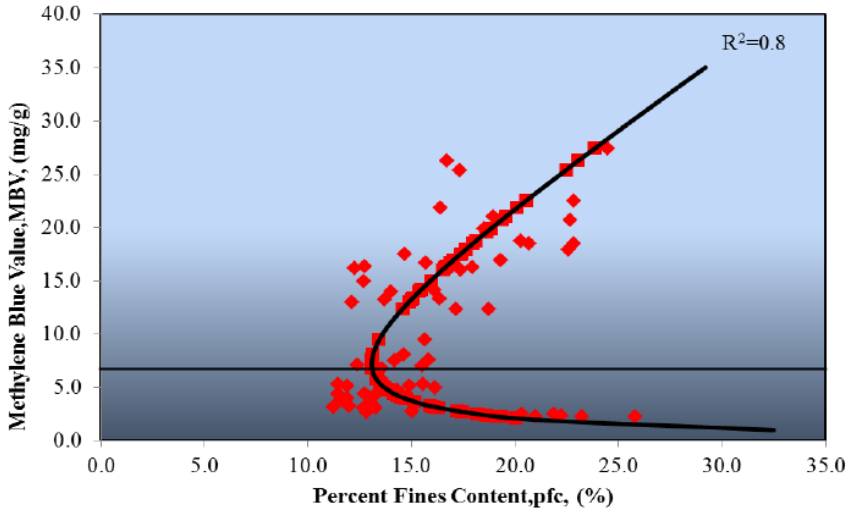

Figure B-9 the relationship between Methylene Blue Value and percent fines content [139]

Sahin [139] found that the "C" shape relationship can be best described by the following mathematical equation:

$$pfc = \frac{a_m}{(MBV)^{n_m}} + b_m(MBV) \quad \text{(B-20)}$$

where a_m, b_m and n_m are fitting parameters depending on the clay mineralogy, characteristics and fraction [139]. Although each type of aggregates corresponds to a unique set of fitting parameters, a single set of fitting parameters in which $a_m = 27.6$, $b_m = 1.55$ and $n_m = 0.92$ was obtained when all the data points (which corresponded to all the tested unbound aggregate materials) are fitted to Equation (B-20). In order to obtain the best empirical relationship, ideally, this single set of fitting parameters should be obtained through testing a large variety of soils that cover the typical range of the soil types found in the area of interest. Once the empirical relationship is obtained, pfc can be predicted using MBV measurements made under a field condition; the predicted pfc is used in the prediction of α and γ which are parameters required to form the SDCC of the soil (that is used to predict the soil matric suction h_m) under a field condition.

Prediction of Volumetric Water Content by Soil Water Characteristic Curve

The determination of volumetric water content θ under a field condition relies on the use of the soil water characteristic curve (SWCC) which is also an S-shape curve that describes the relation between the soil matric suction h_m and soil volumetric water content θ as shown in Figure B-10. Each soil material corresponds to a unique shape of SWCC curve due to the differences in soil properties. The Fredlund and Xing model [149] is one of the most commonly used models to characterize a SWCC, which is expressed as [139]:

$$\theta = C(h) \times \left[\frac{\theta_{sat}}{\left[\ln\left[\exp(1)+\left(\frac{h_m}{a_f}\right)^{b_f}\right]\right]^{c_f}}\right] \quad \text{(B-21)}$$

$$C(h) = \left[1 - \frac{\ln\left(1+\frac{h_m}{h_r}\right)}{\ln\left(1+\frac{7}{h_r}\right)}\right] \quad \text{(B-22)}$$

where θ is the volumetric water content, θ_{sat} is the saturated volumetric water content, h_m is the soil matric suction, a_f, b_f, c_f and h_r are all fitting parameters where a_f is related to the air entry value of the soil, b_f is a function of the rate of moisture extracted from the soil when the air entry value is exceeded, c_f is a function of the residual moisture content, h_r is related to the suction at the residual moisture content.

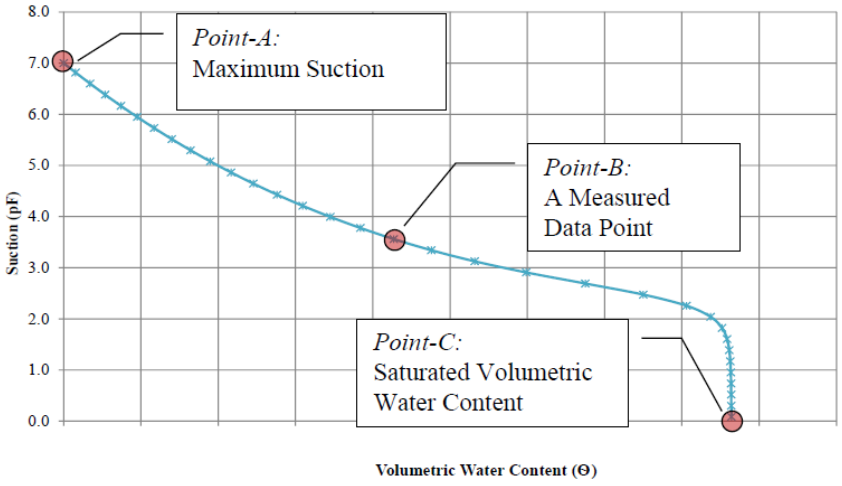

Figure B-10 A schematic illustration of the SWCC of a soil [139]

In order to determine the volumetric water content θ under a field condition, it is necessary to determine all the unknown parameters (i.e. h_m, a_f, b_f, c_f, h_r and θ_{sat}). The

last section already explained the detailed procedure to estimate the soil matric suction h_m by only performing MBT and percometer test under a field condition; the rest of the unknowns can also be predicted using the empirical relationships described as follows.

By conducting laboratory experiments on a variety of base course materials, Sahin [139] found the following empirical relationships between MBV and the fitting parameters:

$$a_f = 3.4994MBV^{0.0002} \tag{B-23}$$

$$b_f = 2.0044MBV^{-0.003} \tag{B-24}$$

$$c_f = 0.4956MBV^{-0.415} \tag{B-25}$$

$$h_r = 20MBV^{9.5E-06} \tag{B-26}$$

where all the other parameters are previously defined.

Sahin [139] also found that the saturated volumetric water content θ_{sat} has the following empirical relationship with the MBV, pfc and specific gravity G_s of the base course materials:

$$H_{1\theta_{sat}} = \tanh[\begin{matrix}0.5(0.1353107MBV + 0.14124964pfc \\ -2.67159193G_s + 4.689449)\end{matrix}] \tag{B-27}$$

$$H_{2\theta_{sat}} = \tanh[\begin{matrix}0.5(0.42673905MBV + 0.4791957pfc \\ -14.5836317G_s + 28.3844308)\end{matrix}] \tag{B-28}$$

$$H_{3\theta_{sat}} = \tanh[\begin{matrix}0.5(0.65761429MBV + 1.56633384pfc \\ -39.54978185G_s + 79.178564)\end{matrix}] \tag{B-29}$$

$$\begin{matrix}\theta_{sat} = 0.214926485H_{1\theta_{sat}} + 0.27640261H_{2\theta_{sat}} \\ -0.12511932H_{3\theta_{sat}} + 0.30045553\end{matrix} \tag{B-30}$$

where $H_{1\theta_{sat}}$, $H_{2\theta_{sat}}$ and $H_{3\theta_{sat}}$ are hidden layer functions used to determine θ_{sat} and all the other parameters are previously defined.

Establishment of empirical relationships under laboratory conditions

In order to establish the empirical relationships (such as the ones shown in Equation (B-23) – (B-30)) for foundation soil materials, a series of laboratory experiments should be performed, including:

1. the filter paper test (to obtain the soil matric suction h_m and the volumetric water content θ);
2. the Methylene Blue Test (to obtain MBV of the soil);

3. the percent fine content test (to obtain pfc of the soil);
4. the standard laboratory compaction test (to obtain the maximum dry unit weight $\gamma_{d-\max}$); and
5. the specific gravity test (to obtain the specific gravity of the soil G_s).

In order to perform curve fitting and obtain the four fitting parameters of the SWCC for a soil, at least three points are required as shown in Figure B-10. Point A which is a known point corresponds to the maximum level of suction (where h_m equals to 1.45 x 10^5 psi or 10^6 kPa or 7 pF) and the minimum level of volumetric water content (where θ equals to 0). Point B is obtained by performing the filter paper test, from which both the matric suction and volumetric water content are measured once the test is finished. Point C corresponds to the minimum level of suction (where h_m equals to 0) and the maximum level of volumetric water content which is defined as the saturated volumetric water content θ_{sat}; the saturated volumetric water content can be calculated as:

$$\theta_{sat} = [1 - \frac{\gamma_{d-\max}}{(G_s \gamma_w)}] \quad \text{(B-31)}$$

where $\gamma_{d-\max}$ is the maximum dry unit weight of the soil and all the parameters are previously defined. Again, the statistical software JMP is used to construct the empirical relationship between θ_{sat} and MBV, pfc and G_s (such as the ones shown in Equation (B-27) – (B-30)).

Once the three points are determined, they are fitted to Equation (B-21) and (B-22) to obtain the four fitting parameters (i.e. a_f, b_f, c_f and h_r) for a soil. After testing a variety of soil materials, the empirical relationships (such as the ones shown in Equation (B-23) – (B-26)) between the fitting parameters and MBV then can be established which are useful under a field condition to determine the SWCC and the volumetric water content of the soil.

Prediction of Dry Unit Weight by Compaction Curve Model

The determination of dry unit weight γ_d under a field condition relies on the use of the compaction curve model (CCM) which is a C-shape curve that describes the relation

between the dry unit weight γ_d and soil volumetric water content θ as shown in Figure B-11. Each soil material corresponds to a unique shape of CCM curve due to the differences in soil properties. The general mathematical form of a CCM is expressed as [139]:

$$(\frac{\gamma_d}{\gamma_w}) = a_d[\mathrm{csch}(\frac{\theta\theta_{sat}}{G_s(|\theta_{sat}-\theta|)})]^{n_d} - b_d[\mathrm{csch}(\frac{\theta\theta_{sat}}{G_s(|\theta_{sat}-\theta|)})] \quad \text{(B-32)}$$

where a_d, b_d and n_d are fitting parameters depending on the soil type and all the other parameters are previously defined.

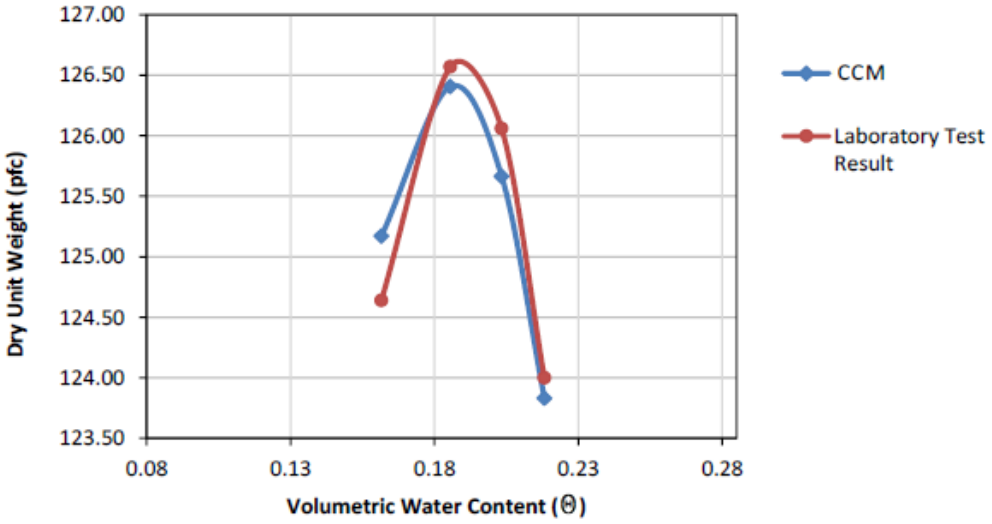

Figure B-11 A schematic illustration of the CCM of a soil in comparison with laboratory test results [139]

In order to estimate the dry unit weight γ_d under a field condition, it is necessary to determine all the unknown parameters (i.e. θ, θ_{sat}, a_d, b_d and n_d). The last section already explained the detailed procedures to estimate the volumetric water content θ (by using the SWCC) and saturated volumetric water content θ_{sat} (Equation (B-27) – (B-30)) under a field condition; the rest of the unknowns a_d, b_d and n_d can be estimated using the empirical relationships described as follows.

Sahin [139] found that the three fitting parameters can be estimated by the following functions:

$$H_{1a_d} = \tanh[^{0.5(0.40877300MBV + 0.21113984pfc}_{-8.72963215G_s + 16.336761)}] \quad \text{(B-33)}$$

$$H_{2a_d} = \tanh\left[\begin{matrix}0.5(-0.27242731MBV + 0.38117451pfc \\ +4.81581562G_s - 15.246911)\end{matrix}\right] \quad \text{(B-34)}$$

$$H_{3a_d} = \tanh\left[\begin{matrix}0.5(0.65761429MBV + 1.56633384pfc \\ -39.54978184G_s + 79.17856)\end{matrix}\right] \quad \text{(B-35)}$$

$$a_d = -0.7255499645H_{1a_d} + 0.2397642438H_{2a_d} + 0.8786388739H_{3a_d} + 1.88831833 \quad \text{(B-36)}$$

$$H_{1b_d} = \tanh\left[\begin{matrix}0.5(0.30481277MBV + 0.4712751pfc \\ -23.51993211G_s + 52.840434)\end{matrix}\right] \quad \text{(B-37)}$$

$$H_{2b_d} = \tanh\left[\begin{matrix}0.5(-0.05056449MBV - 0.11228127pfc \\ +27.55907692G_s - 71.931755)\end{matrix}\right] \quad \text{(B-38)}$$

$$H_{3b_d} = \tanh\left[\begin{matrix}0.5(-0.13331382MBV - 0.36012434pfc \\ +29.23482354G_s - 72.562443)\end{matrix}\right] \quad \text{(B-39)}$$

$$b_d = 0.10805394H_{1b_d} - 0.166763132H_{2b_d} + 0.160133497H_{3b_d} + 1.22496083 \quad \text{(B-40)}$$

$$H_{1n_d} = \tanh\left[\begin{matrix}0.5(-0.26235498MBV + 0.47405037pfc \\ -71.58187117G_s + 189.223422)\end{matrix}\right] \quad \text{(B-41)}$$

$$H_{2n_d} = \tanh\left[\begin{matrix}0.5(-0.78480185MBV - 0.75914733pfc \\ +56.24092591G_s - 133.107727)\end{matrix}\right] \quad \text{(B-42)}$$

$$H_{3n_d} = \tanh\left[\begin{matrix}0.5(-0.23889927MBV - 0.87246044pfc \\ -84.01782691G_s + 246.667662)\end{matrix}\right] \quad \text{(B-43)}$$

$$n_d = -0.013073056H_{1n_d} - 0.045526936H_{2n_d} + 0.013674419H_{3n_d} + 0.058352963 \quad \text{(B-44)}$$

where H_{1a_d}, H_{2a_d} and H_{3a_d} are hidden layer functions used to determine a_d, H_{1b_d}, H_{2b_d} and H_{3b_d} are hidden layer functions used to determine b_d, H_{1n_d}, H_{2n_d} and H_{3n_d} are hidden layer functions used to determine n_d and all the other parameters are previously defined.

Establishment of empirical relationships under laboratory conditions

In order to establish the empirical relationships shown in Equation (B-33) – (B-44), a series of laboratory experiments should be performed, including:

1. the standard laboratory compaction test (to obtain the dry unit weight γ_d and the volumetric water content θ);
2. the Methylene Blue Test (to obtain MBV of the soil);
3. the percent fine content test (to obtain pfc of the soil); and

4. the specific gravity test (to obtain the specific gravity of the soil G_s).

In order to perform curve fitting and obtain the three fitting parameters, the standard laboratory compaction test should be performed according to ASTM D698 the Standard Test Methods for Laboratory Compaction Characteristics of Soil Using Standard Effort (12400 ft-lbf/ft^3) [150]. At least four data points are required for each soil type to obtain a well-defined dry unit weight vs. volumetric water content curve. Again, the volumetric water content θ can be calculated as:

$$\theta = \frac{w\gamma_d}{\gamma_w} \tag{B-45}$$

where w is the gravimetric moisture content, γ_d is the dry unit weight of the soil and γ_w is the unit weight of water (62.4 lb/ft^3). The saturated volumetric water content θ_{sat} can be calculated using Equation (B-31). Once the dry unit weight vs. volumetric water content curve is plotted for laboratory results, the data points on the curve are fitted to the mathematical form of a CCM (shown in Equation (B-32)) to obtain the three fitting parameters a_d, b_d and n_d. Again, the statistical software JMP is used to construct the empirical relationships between the three fitting parameters and MBV, pfc and G_s.

Prediction of Suction Compression Index

The suction compression index γ_h equals to:

$$\gamma_h = \gamma_0 \times \frac{pfc}{100} \tag{B-46}$$

where γ_0 is the volume change guide number and pfc is the percent fine content. The determination of the volume change guide number is based on the procedure proposed by Lytton et al. (2005) [144]. The first step is to determine the mineralogical zone with the plasticity index PI and liquid limit LL of the soil by using Figure B-12. The next step is to determine the volume change guide number γ_0 using a series of charts (shown from Figure B-13 – Figure B-20), which requires the inputs of $\frac{LL}{pfc}$ and $Ac = \frac{PI}{pfc}$.

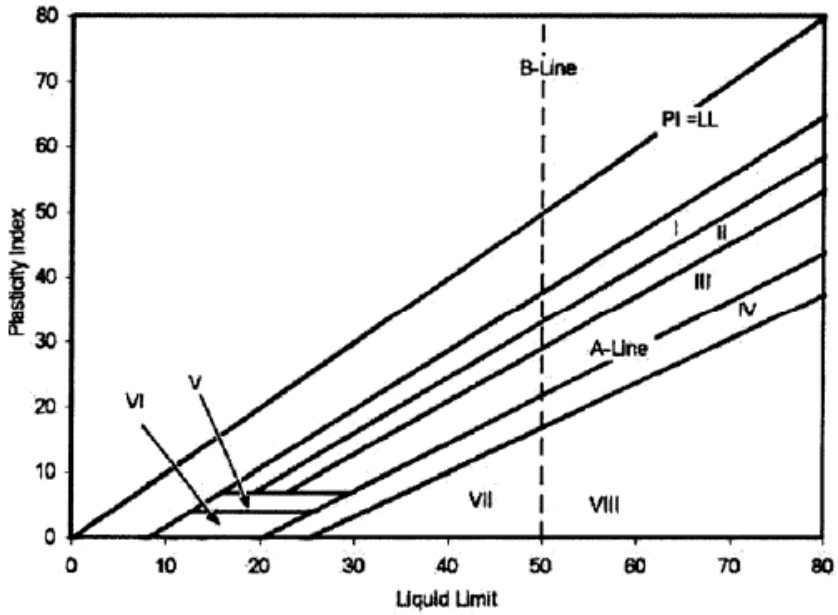

Figure B-12 Partitioning database on mineralogical types [144]

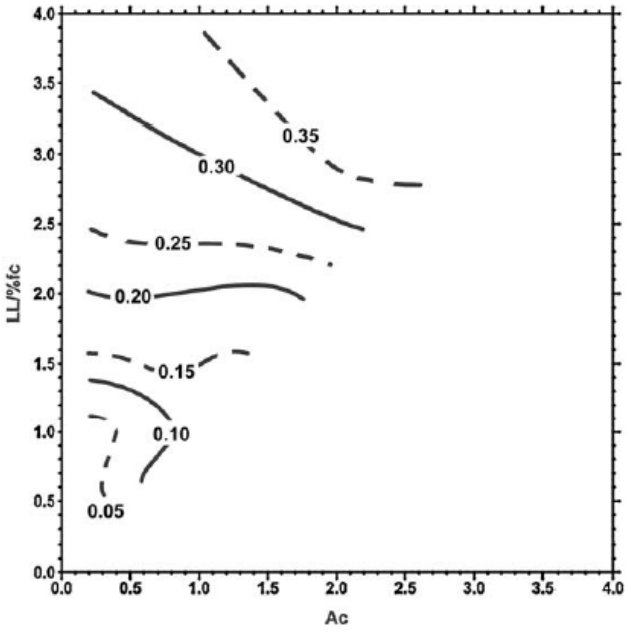

Figure B-13 Zone I Chart for Determining γ_0 [151]

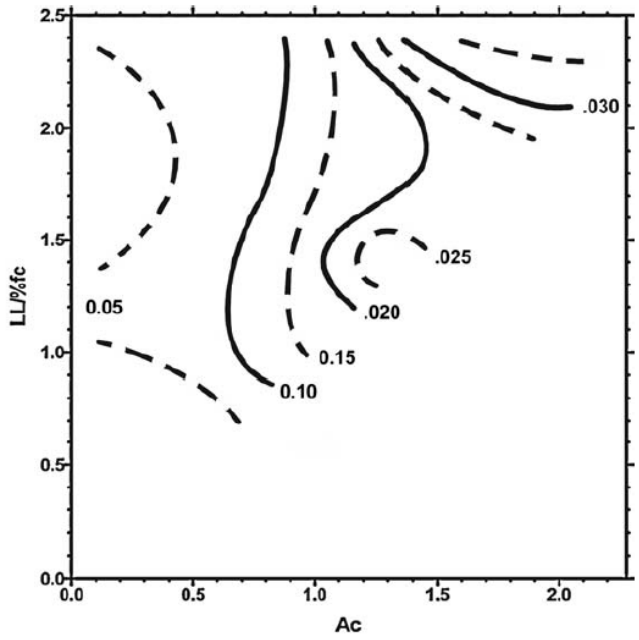

Figure B-14 Zone II Chart for Determining γ_0 [151]

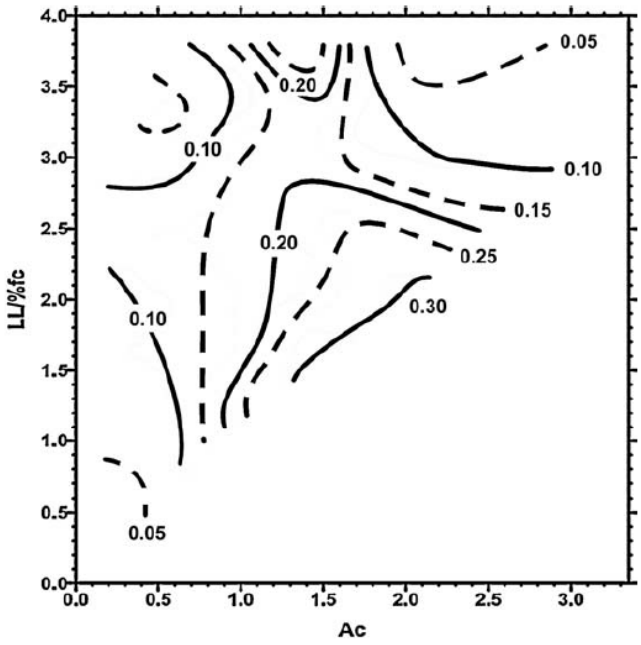

Figure B-15 Zone III Chart for Determining γ_0 [151]

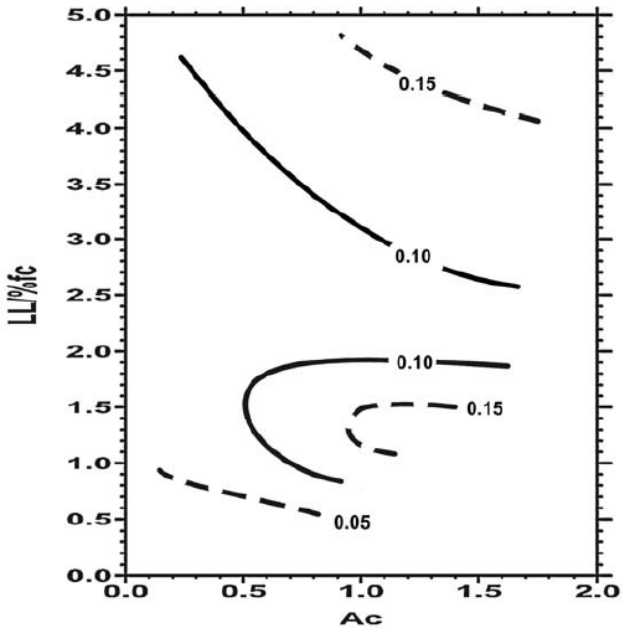

Figure B-16 Zone IV Chart for Determining γ_0 [151]

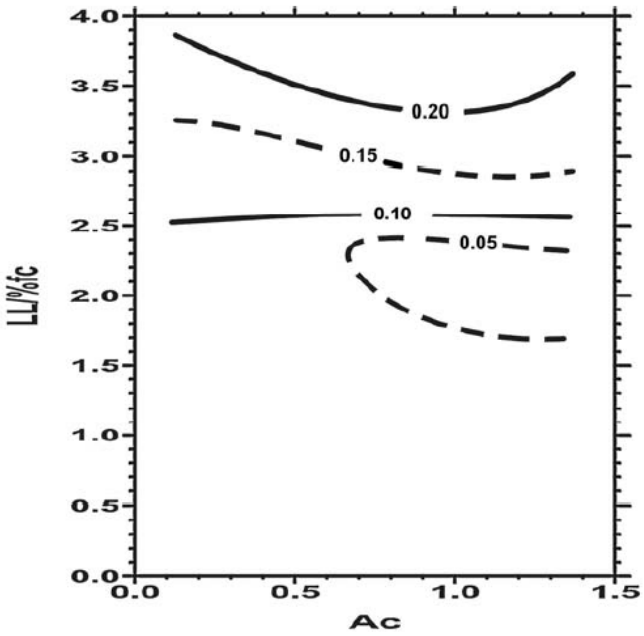

Figure B-17 Zone V Chart for Determining γ_0 [151]

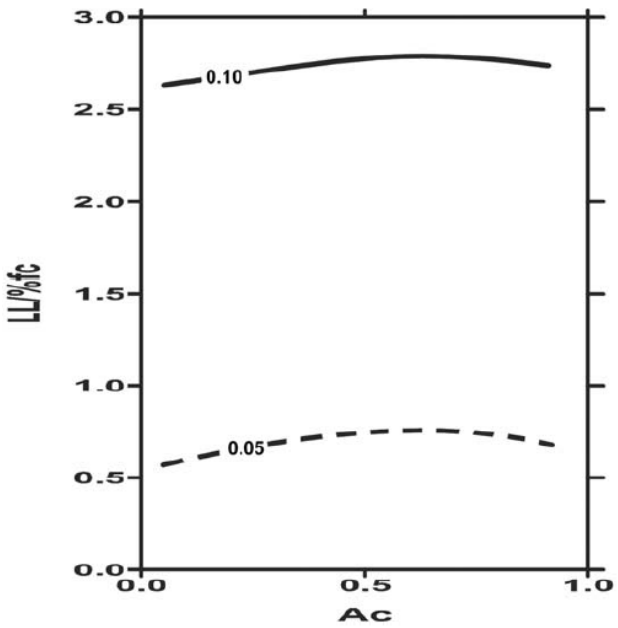

Figure B-18 Zone VI Chart for Determining γ_0 [151]

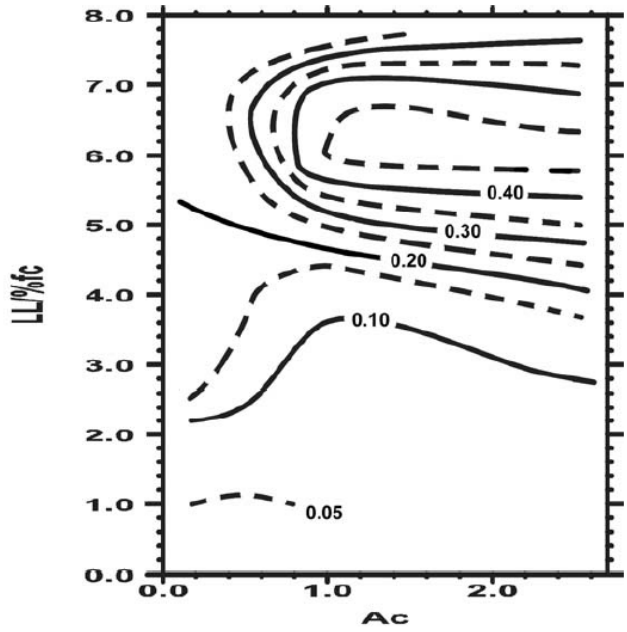

Figure B-19 Zone VII Chart for Determining γ_0 [151]

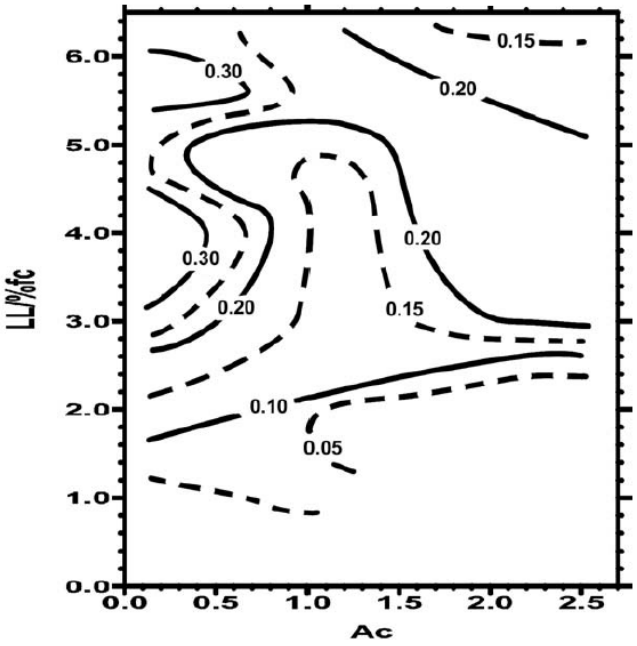

Figure B-20 Zone VIII Chart for Determining γ_0 [151]

APPENDIX C

JMP USER GUIDE AND EXAMPLE DEMONSTRATION

This section provides a demonstration of how to use the neural network function in the statistical software JMP to construct empirical functions. The user may need to purchase JMP in order to get full access to all the functions in the software. Alternatively, the practitioner can apply the procedure elaborated in Appendix D to determine the regression coefficients by executing Matlab codes.

Example: Referring to the given Excel spreadsheet tab "**Task 3C**", then read "**Step 3**" and "**Step 4**" of the instruction.

Inputs: MBV and pfc as shown in "**Table 3**" in tab "**Task 3C**" of the Excel spreadsheet.

Targets: α and γ as shown in "**Table 3**" in tab "**Task 3C**" of the Excel spreadsheet.

Objective: Use the neural network function in the "JMP" software and the information summarized in "**Table 3**" to construct empirical relationships for "α vs. MBV & pfc" and "γ vs. MBV & pfc", such that one can use MBV and pfc to estimate either α or γ.

Procedure:

1. Launch the "JMP" software;
2. Select File > New > Data Table to create a new table;
3. Copy the data from "**Table 3**" and paste them into the table just created as shown in Figure C-1;

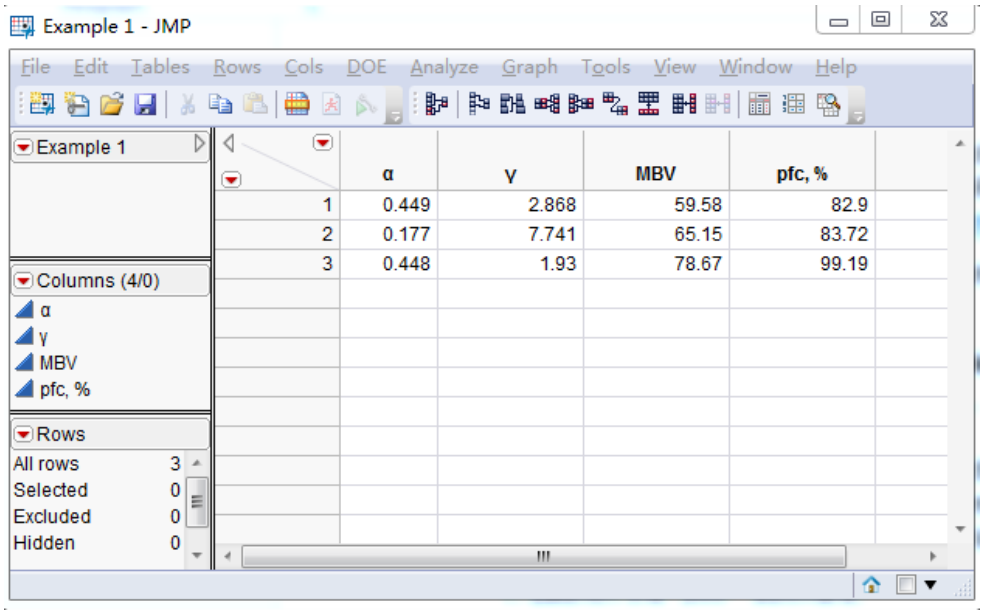

Figure C-1 Copy and paste the required information into JMP

4. Select **Analyze** > **Modeling** > **Neural**;
5. Assign α (target) to the **Y, Response** role and assign MBV and pfc (inputs) to the **X, Factor** role as shown in Figure C-2, then click **OK;** (The empirical relationship of γ vs. MBV & pfc can be established in the same way by setting γ to the **Y, Response** role and assign MBV and pfc (inputs) to the **X, Factor** role);

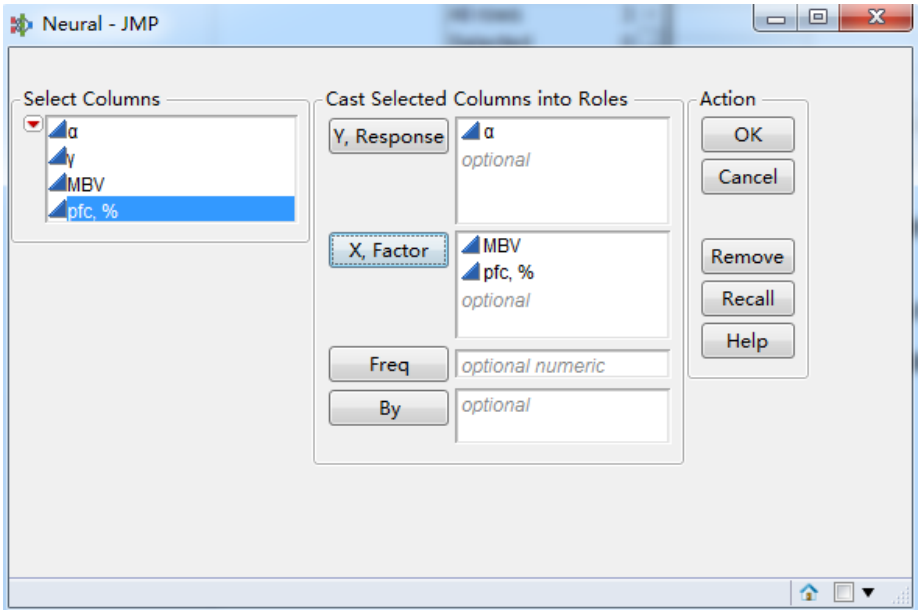

Figure C-2 Select target and inputs for the neural network function

6. Once the window as shown in Figure C-3 pops out, edit the **Hidden Nodes** to 1 (can be modified to different values if 1 does not generate a good empirical model) , then click **Go;**

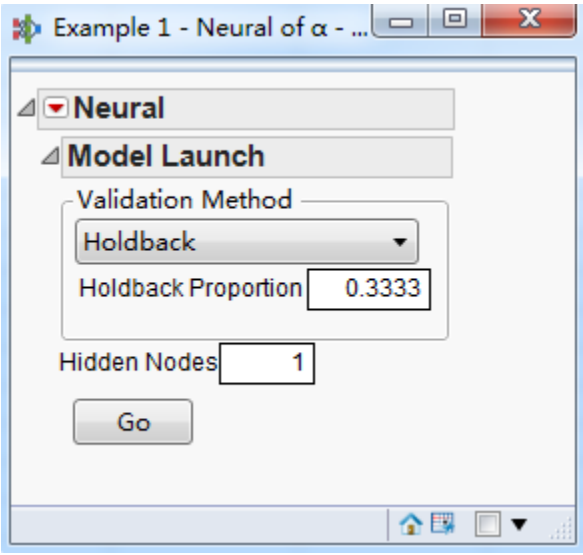

Figure C-3 Model launch

7. The neural network training results will pop out as shown in Figure C-4;

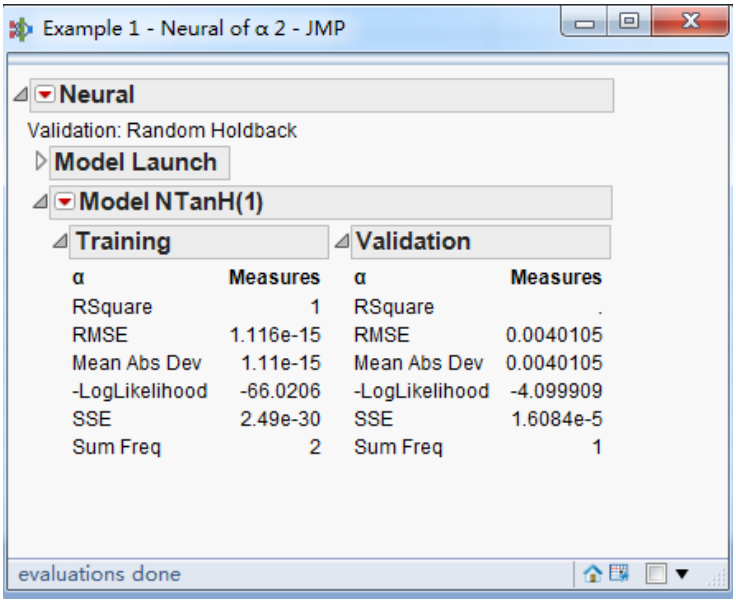

Figure C-4 Result of neural network training

8. Left click on **Model NTanH (1),** select **Save Fast Formulas**, a new column will be created in the table previously formed as shown in Figure C-5;

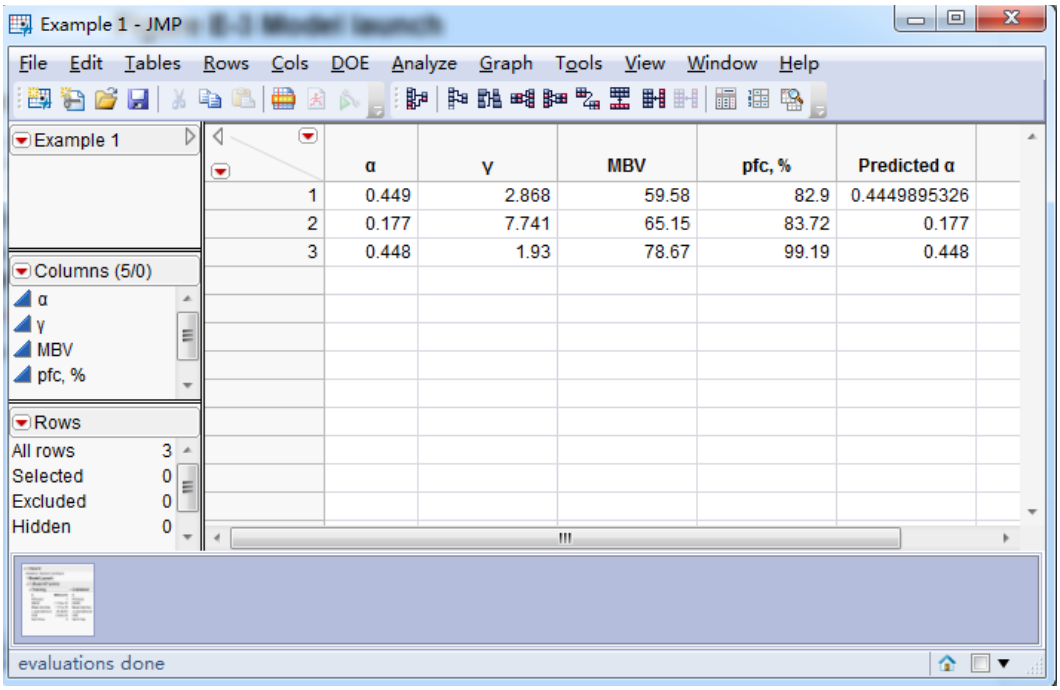

Figure C-5 Predicted target values

9. Check the values in the new column "**Predicted** α", if the predicted α values in this column are reasonably closed to the target α values in the first column, then, Left click again on **Model NTanH (1),** select **Make SAS DATA Step,** the following will pop out as shown Figure C-6;

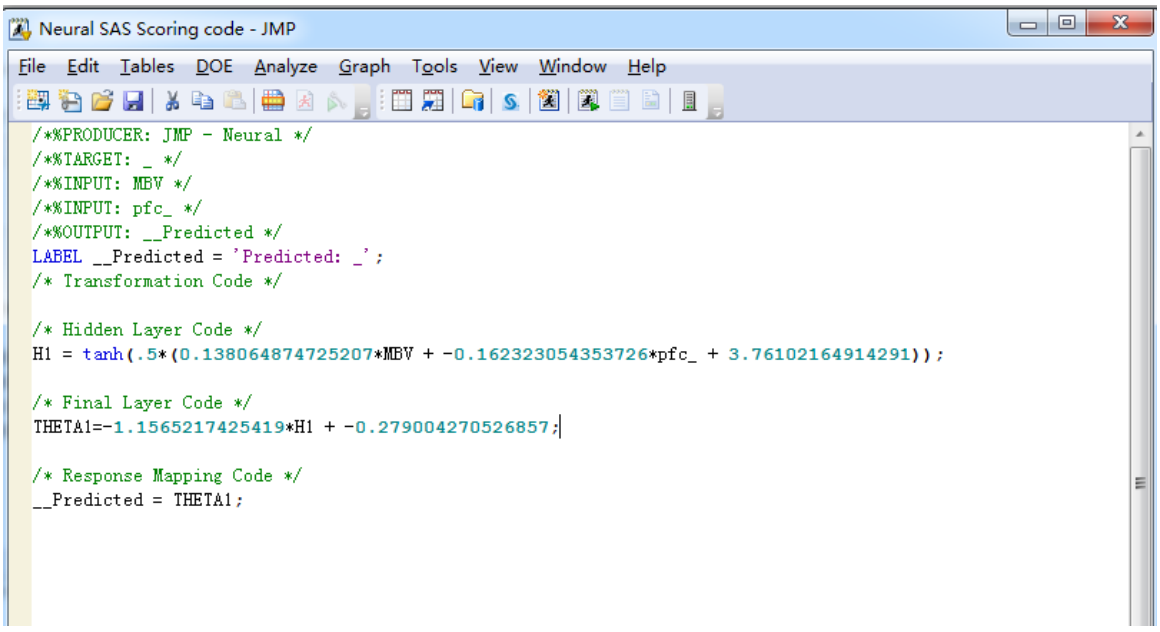

Figure C-6 Make SAS DATA Step

10. Identify the coefficients in the hidden layer functions as shown in Figure C-7 and copy these coefficients into "**Table 4**" in tab "**Task 3C**" of the given Excel spreadsheet;

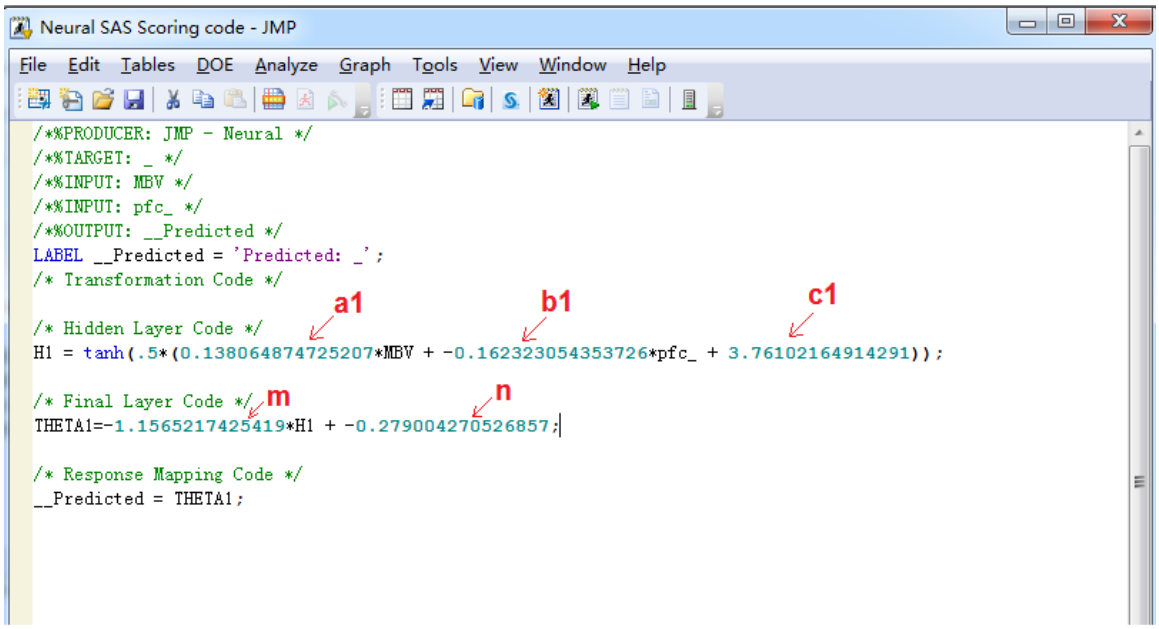

Figure C-7 Identification of regression coefficients

11. Check "**Table 5**" in tab "**Task 3C**" of the given Excel spreadsheet, the total tolerance for predicting α should be less than 0.001; otherwise, repeat the neural network analysis by left clicking on **Neural**, select **Script** and then **Redo Analysis** as shown in Figure C-8 until the tolerance is satisfactory.

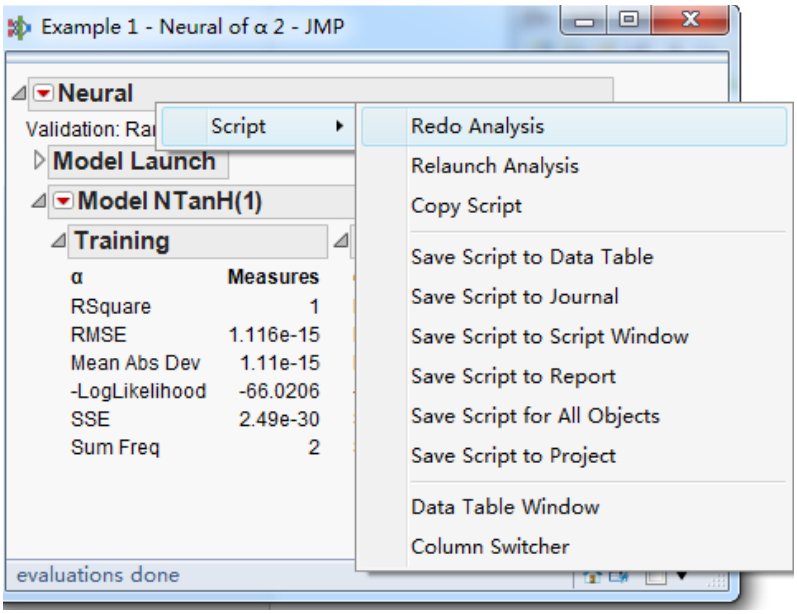

Figure C-8 Redo Analysis

APPENDIX D

MATLAB CODE USER GUIDE AND EXAMPLE DEMONSTRATION

This chapter provides guidelines and demonstrates an example of how to use the Matlab code (as an alternative method to the JMP software) to determine the unknown coefficients in the empirical relationships using laboratory experiment results. This Matlab code is written such that it is applicable for all the tasks elaborated in the Excel spreadsheet (i.e. **Task 3C**, **Task 4** and **Task 5**).

Example: Referring to the given Excel spreadsheet tab "**Task 3C**", the Matlab code should be performed once all the required information are summarized in Table 3 as elaborated in "**Step 3**" of the instruction in the spreadsheet.

Prerequisite: In Table 4 of the Excel spreadsheet tab "**Task 3C**", the user needs to input initial guess of the coefficients.

Procedure:

1. Launch the "Matlab" software and open the Matlab code;
2. Click "Run" to run the Matlab code, the following window will pop out;

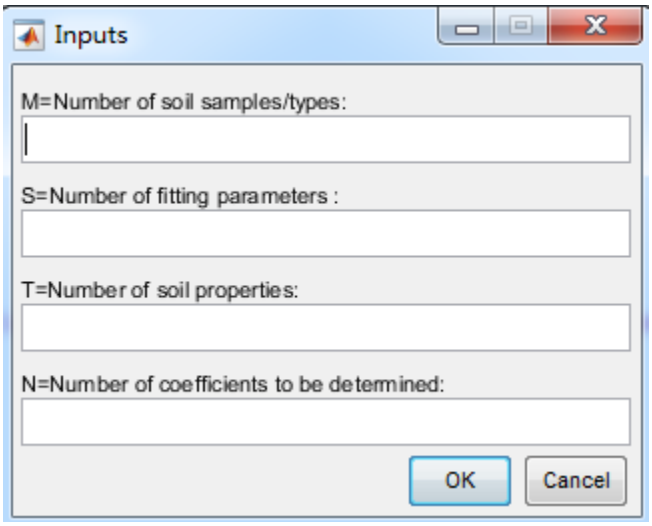

Figure D-1 Inputs window 1

3. Referring to the Table 3 in the Excel spreadsheet, input the number of soil samples/types which is 3 in this example (i.e. Port, Kirkland and Osage), the number of fitting parameters which is 2 in this example (i.e. α and γ), the number of soil properties which is 2 in this example (i.e. MBV and pfc) and the number of coefficients to be determined which is 5 in this example (i.e. a_1, b_1, c_1, m, n);
4. Click “OK”, the following window will pop out as shown in Figure D-2 (tables are blank initially). Copy the soil properties, fitting parameters (found in Table 3 in the Excel spreadsheet) and the initial guess of coefficients (found in Table 4 in the Excel spreadsheet) and paste them into “Soil Property Matrix”, “Fitting Parameter Matrix” and “Initial Guess of Coefficient Matrix”, respectively as shown in Figure D-2;

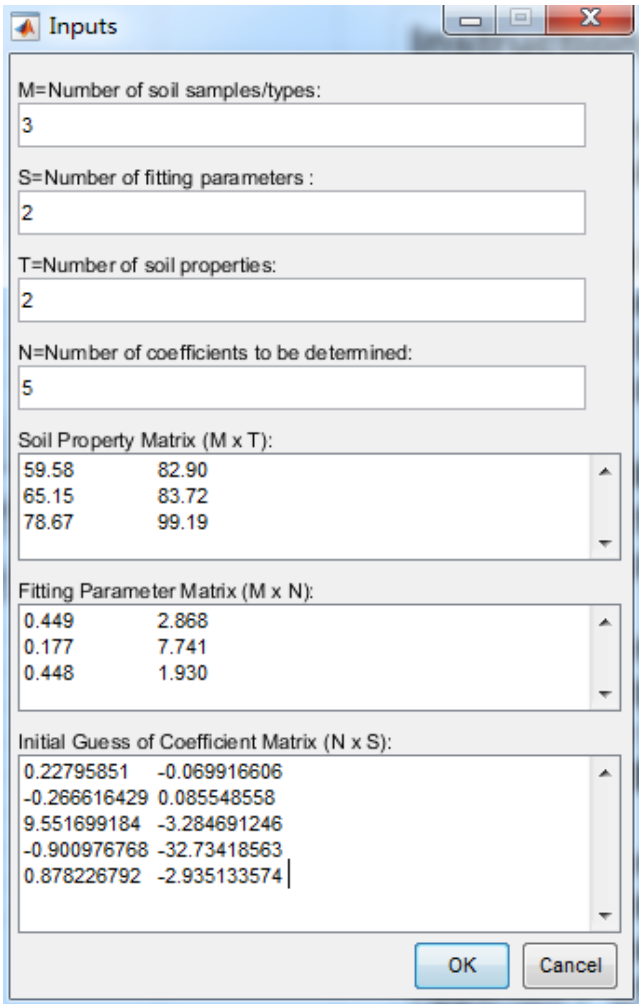

Figure D-2 Inputs window 2

5. Click “OK”, the Matlab will perform calculations automatically and the final results of the coefficients will pop out as shown in Figure D-3;

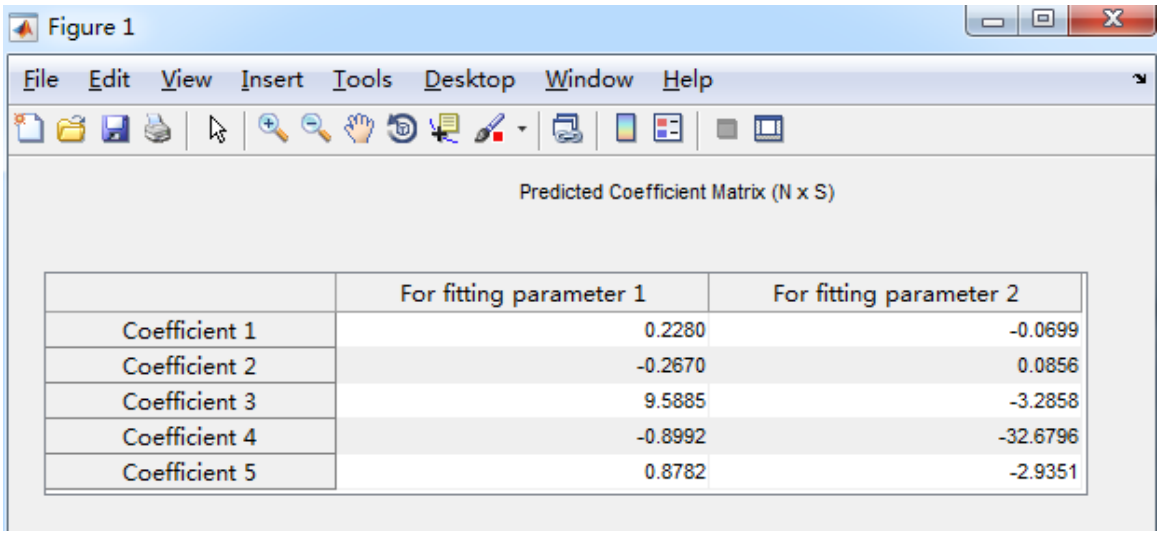

	For fitting parameter 1	For fitting parameter 2
Coefficient 1	0.2280	-0.0699
Coefficient 2	-0.2670	0.0856
Coefficient 3	9.5885	-3.2858
Coefficient 4	-0.8992	-32.6796
Coefficient 5	0.8782	-2.9351

Figure D-3 Predicted Coefficient Matrix

6. Copy the final results shown in the Figure D-3 and paste them into Table 4 of the Excel spreadsheet;
7. Referring to “**Step 4**” of the instruction, the total tolerances for predicting the two fitting parameters (i.e. α and γ) found in Table 5 of the Excel spreadsheet should be less than 0.001; otherwise, the user needs to modify the initial guess of the coefficients and repeat the procedure elaborated in this chapter until the tolerances are met.

REFERENCES

1. Nevels, J.B., *Final Report of the Approach Embankment Settlement Investigation for Federal Aid Project No. NHY-013N(014)*, 2011.
2. Oklahoma, D., *Standard specifications for highway construction*, 2009, Oklahoma City.
3. Brown, R.W. and S.S. Reed, *Evaluation of the Uretek Deep Injection (UDI) Process for Improving Performance of Cardinal Drive (US 69 North Frontage Road) Beaumont, TX*, in *Pilot Project Report*2011, Texas Department of Transportation and Ureteck USA, inc.
4. Schmalzer, P., *LTPP Manual for Falling Weight Deflectometer Measurements*, 2006, FHWA-HRT-06-132.
5. Zollinger, C.J., et al. *Innovative approach to pavement rehabilitation analysis and design of runway (R/W) 15L-33R at George Bush Intercontinental Airport (IAH) in Houston, TX*. in *Eighth International Conference on Concrete Pavement*s. 2005.
6. Miller, G.A., et al., *APPLIED APPROACH SLAB SETTLEMENT RESEARCH, DESIGN/CONSTRUCTION.* 2013.
7. Dupont, B. and D.L. Allen, *Movements and Settlements of Highway Bridge Approaches.* 2002.
8. White, D., et al., *Identification of the best practices for design, construction, and repair of bridge approaches*, 2005.
9. Greimann, L.F., et al., *Integral Bridge Abutment-to-Approach Slab Connection*, 2008.
10. Tayabji, S.D., D. Ye, and N. Buch, *Precast concrete pavement technology*2013: Transportation Research Board.
11. Merritt, D.K., et al., *Construction of the Iowa Highway 60 Precast Prestressed Concrete Pavement Bridge Approach Slab Demonstration Project*, 2007.
12. Merritt, D.K., B.F. McCullough, and N.H. Burns, *Construction and Preliminary Monitoring of the Georgetown, Texas Precast Prestressed Concrete Pavement*, 2002, Citeseer.
13. Merritt, D., B. Frank McCullough, and N. Burns, *Precast prestressed concrete pavement pilot project near Georgetown, Texas.* Transportation Research Record: Journal of the Transportation Research Board, 2003(1823): p. 11-17.
14. Larrazabal, E., *Precast Concrete (PC) Pavement Tests on Taxiway DD at Laguardia Airport.* 2004.
15. Switzer, W., et al. *Overnight Pavement Replacement Using Precast Panels and Conventional Subgrade Material - Washington Dulles International Airport Case Study in Airfield Pavements. Challenges and New Technologies*. in *Airfield Pavements. Challenges and New Technologies*. 2004.
16. Farrington, R., et al. *Overnight Concrete Pavement Replacement Using a Precast Panel and Expanding Polymer Positioning Technique - Washington Dulles International Airport Case Study in Airfield Pavements. Challenges and New Technologies*. in *Airfield Pavements. Challenges and New Technologies*. 2004.

17. Tayabji, S. and K. Hall, *Precast Concrete Panels for Repair and Rehabilitation of Jointed Concrete Pavements.* CPTP TechBrief, 2008.
18. Association, N.P.C., *Jointed precast concrete pavement (JPrCP)*, 2011, National Precast Concrete Association: http://precast.org/wp-content/uploads/2011/11/PCPSbrochure.pdf.
19. Ye, D., *Personal communication*, 2016.
20. Merritt, D.K., et al., *The Feasibility of Using Precast Concrete Panels to Expedite Highway Pavement Construction*2000: Center for Transportation Research, University of Texas at Austin.
21. Merritt, D.K. and S. Tayabji, *Precast Prestressed Concrete Pavement for Reconstruction and Rehabilitation of Existing Pavements*, 2009.
22. Merritt, D., R. Rogers, and R. Rasmussen, *Construction of a Precast Prestressed Concrete Pavement Demonstration Project on Interstate 57 near Sikeston, Missouri*, 2008, FHWA-HIF-08-009. Washington, DC: Federal Highway Administration.
23. Merritt, D.K., P. MCCULLOUGH, and N.H. Burns, *Design-construction of a precast, prestressed concrete pavement for interstate 10, El Monte, California.* PCI journal, 2005. **50**(2): p. 18-27.
24. Tayabji, S., *Precast Concrete Pavement Technology ~ Rapidly Evolving*, in *International Society for concrete pavements*2011.
25. Sun, P., *A new protocol for evaluating concrete curing effectiveness*, 2013, Texas A&M University.
26. Sun, P. and D.G. Zollinger, *Concepts to Enhance Specification and Inspection of Curing Effectiveness in Concrete Pavement Design and Construction.* Transportation Research Record: Journal of the Transportation Research Board, 2015(2504): p. 124-132.
27. Ma, S., *Bridge approach slab analysis and design incorporating elastic soil support*, 2011, University of Missouri--Columbia.
28. Hoppe, E.J., *Guidelines for the use, design, and construction of bridge approach slabs*, 1999.
29. Shi, X., et al., *Finite element analysis of concrete approach slab on soil embankment*, 2004.
30. Cai, C., et al., *Structural performance of bridge approach slabs under given embankment settlement.* Journal of Bridge Engineering, 2005. **10**(4): p. 482-489.
31. Puppala, A.J., et al., *Recommendations for design, construction, and maintenance of bridge approach slabs: Synthesis report*, 2009, University of Texas at Arlington.
32. Dunn, K.H.A., G.H. Rodes, T.H., and Zieher, J.J., *Performance Evaluation of Bridge Approaches.* Wisconsin Department of Transportation, 1983.
33. Thiagarajan, G., et al., *Bridge Approach Slabs for Missouri DOT: Looking at Alternative and Cost Efficient Approaches*, 2010.
34. Luna, R., *Evaluation of Bridge Approach Slabs, Performance and Design*, 2004.
35. Northeast, P., *Guideline for Accelerated Bridge Construction Using Precast/Prestressed Concrete Elements Including Guideline Details*, 2014, Report No. PCINE-14-ABC. Precast/Prestressed Concrete Institute, Chicago, IL.

36. Schmitz, M.E., et al., *Use of controlled low-strength material as abutment backfill*, 2004, Kansas Department of Transportation.
37. Guide, M.E.P.D., *A Manual of Practice.* American Association of State Highway and Transportation Officials, 2008.
38. Pierce, L.M. and G. McGovern, *Implementation of the AASHTO Mechanistic-Empirical Pavement Design Guide and Software*2014.
39. su Jung, Y., et al., *Subbase and subgrade performance investigation and design guidelines for concrete pavement.* 2010.
40. Tayabji, S., D. Ye, and F. Motamed, *Final Report, Proposed Process for Design of Precast Concrete Pavements Sacramento, California*, 2012, Fugro Consultants, Inc.
41. Jang, S.H., *Automated crack control analysis for concrete pavement construction*, 2005, Texas A&M University.
42. Jung, Y. and D. Zollinger, *New laboratory-based mechanistic-empirical model for faulting in jointed concrete pavement.* Transportation Research Record: Journal of the Transportation Research Board, 2011(2226): p. 60-70.
43. su Jung, Y., D. Zollinger, and A. Wimsatt, *Test method and model development of subbase erosion for concrete pavement design.* Transportation Research Record: Journal of the Transportation Research Board, 2010(2154): p. 22-31.
44. Bari, M.E. and D.G. Zollinger, *New concepts for the assessment of concrete slab interfacial effects in pavement design and analysis.* International Journal of Pavement Engineering, 2016. **17**(3): p. 233-244.
45. Bakhsh, K.N. and D. Zollinger. *Faulting Prediction Model for Design of Concrete Pavement Structures*. in *Geo-Shanghai 2014*. 2014.
46. Jung, Y., D. Zollinger, and B. Ehsanul, *Improved mechanistic-empirical continuously reinforced concrete pavement design approach with modified punchout model.* Transportation Research Record: Journal of the Transportation Research Board, 2012(2305): p. 32-42.
47. Darter, M., *Design of zero-maintenance plain jointed pavements.* Federal Highway Administration, Washington DC, 1977.
48. Ioannides, A.M., L. Khazanovich, and J.L. Becque, *Structural evaluation of base layers in concrete pavement systems.* Transportation Research Record, 1992(1370).
49. Buch, N., *Precast Concrete Panel Systems for Full-Depth Pavement Repairs. Field Trials*, 2007.
50. Smith, P.J., *Replacement of Bridge Approach Slabs and Super-Structure In Two Consecutive Weekends, Rt. 46 Over Broad St., Clifton, NJ*, 2011, The Fort Miller Co. Inc: New Jersey.
51. Thiagarajan, G., J. Myers, and C. Halmen, *Field Evaluation of Alternative and Cost-Efficient Bridge Approach Slabs*, 2013.
52. Mishra, T., P. French, and Z. Sakkal, *Engineering a better road: Use of two-way prestressed, precast concrete pavement for rapid rehabilitation.* PCI journal, 2013. **58**(1): p. 129-141.
53. Highways, M. and T. Commission, *Missouri Standard Specifications for Highway Construction, 2004*2016: Missouri Highways and Transportation Commission.

54. Dailey, C.L., *Instrumentation and early performance of an innovative prestressed precast pavement system*, 2006, University of Missouri--Columbia.
55. LLC, C.A., *Concrete bridge approach pavements: a survey of state practices*, 2010, Wisconsin Highway Research Program Rigid Pavements Technical Oversight Committee.
56. Phares, B.M., et al., *Identification and evaluation of pavement-bridge interface ride quality improvement and corrective strategies.* Rep. No. Federal Highway Administration (FHWA)/Ohio (OH)-2011/1, Washington, DC, 2011.
57. Nadermann, A., L. Greimann, and B. Phares, *Instrumentation and Monitoring of Precast Bridge Approach Tied to an Integral Abutment Bridge in Bremer County.* 2010.
58. Bautista, F.E. and I. Basheer, *Jointed Plain Concrete Pavement (JPCP) Preservation and Rehabilitation Design Guide*, in *Office of Pavement Design Pavement Design & Analysis Branch*2008.
59. Corporation, D.C., *Rapid cure sealant demonstrates remarkable success*, 1999: Available from Internet:<http://www.dowcorning.com/content/publishedlit/62283A01.pdf>.
60. Purvis, R.L. and M.P. Burke, *Bridge deck joint performance: A synthesis of highway practice*. Vol. 319. 2003: Transportation Research Board.
61. Milner, M.H. and H.W. Shenton III, *Survey of Past Experience and State-of-the-Practice in the Design and Maintenance of Small Movement Expansion Joints in the Northeast.* AASHTO Transportation System Preservation Technical Services Program (TSP2) Report, 2014. **242**.
62. su Jung, Y., D.G. Zollinger, and S.D. Tayabji, *Best Practices for Concrete Pavement Transition Design and Construction*2007: Texas Transportation Institute, Texas A&M University System.
63. Seo, J., H. Ha, and J.-L. Briaud, *Investigation of settlement at bridge approach slab expansion joint: Numerical simulations and model tests*, 2002.
64. Briaud, J., R. JAMES, and S. Hoffman, *SETTLEMENT OF BRIDGE APPROACHES (THE BUMP AT THE END OF THE BRIDGE)*, 1997.
65. Miller, G.A., et al., *APPLIED APPROACH SLAB SETTLEMENT RESEARCH, DESIGN/CONSTRUCTION.* 2011.
66. Ziehl, P., M. EIBatanouny, and M.K. Jones, *In-Situ Monitoring of Precast Concrete Approach Slab Systems*, 2015, South Carolina Department of Transportation Federal Highway Administration.
67. Lenke, L.R., *Settlement Issues--Bridge Approach Slabs*, 2006.
68. Hopkins, T.C., *Settlement of highway bridge approaches and embankment foundations*, 1969, University of Kentucky.
69. Arsoy, S., R.M. Barker, and J.M. Duncan, *The behavior of integral abutment bridges*. Vol. 3. 1999: Virginia Transportation Research Council Charlottesville, VA.
70. Mahmood, I.U., *Evaluation of causes of bridge approach settlement and development of settlement prediction models*1990.
71. Horvath, J.S., *Integral-abutment bridges: problems and innovative solutions using EPS geofoam and other geosynthetics.* Res. Rpt. No. CE/GE-00, 2000. **2**.

72. Schaefer, V.R., J.C. Koch, and S. Dakota, *Void development under bridge approaches*1992: South Dakota Department of Transportation, Office of Research.
73. Kerokoski, O., *Soil-structure interaction of long jointless bridges with integral abutments*2006.
74. Hoppe, E.J., *Field study of integral backwall with elastic inclusion*, 2005.
75. Hoppe, E.J. and S.L. Eichenthal, *Thermal response of a highly skewed integral bridge*, 2012.
76. White, H., *Wingwall type selection for integral abutment bridges: Survey of current practice in the United States of America*2008: Transportation Research and Development Bureau, New York State Department of Transportation.
77. Manual, N.B., *New York State Department of Transportation*, 2014.
78. DOT, N., *STRUCTURES MANUAL* in *Substructures*2008: https://www.nevadadot.com/uploadedFiles/NDOT/About_NDOT/NDOT_Divisions/Engineering/Structures/Chapter18.pdf.
79. Jones, C. and F. Sims, *Earth pressure against the abutments and wing walls of standard motorway bridges.* Geotechnique, 1975. **25**(4): p. 731-742.
80. Thompson, T.A., *Passive earth pressures behind integral bridge abutments.* 1999.
81. Kalayci, E., S.A. Civjan, and S.F. Breña, *Parametric study on the thermal response of curved integral abutment bridges.* Engineering Structures, 2012. **43**: p. 129-138.
82. Wahls, H.E., *Design and construction of bridge approaches*. Vol. 159. 1990: Transportation Research Board.
83. Miller, G.A., et al., *Applied approach slab settlement research, design/construction*, 2013, University of Oklahoma: Oklahoma Department of Transportation.
84. ODOT, C., *Material Specifications.* Ohio Department of Transportation, Office of Contracts, Columbus, OH, 2008.
85. Transportation, P.D.o., *Bridge Design Standards*, 2014: Pennsylvania.
86. Jayawickrama, P., et al., *Water Intrusion in Base/Subgrade Materials at Bridge Ends.* 2005.
87. Abu-Hejleh, N., et al., *Flowfill and MSE Bridge Approaches: Performance, Coast, and Recommendations for Improvements*, 2006, Colorado Department of Transportation, Research Branch.
88. Association, N.R.M.C., *Guide Specification for Controlled Low Strength Materials (CLSM).* Specification Guide, 2006.
89. Seo, J.B., *The bump at the end of the bridge: an investigation*, 2005, Texas A&M University.
90. Yeh, S.-T. and C. Su, *EPS, FLOW FILL AND STRUCTURE FILL FOR BRIDGEABUTMENTBACKnLL.* 1995.
91. Lutenegger, A.J. and M. Ciufetti, *Full-Scale Pilot Study to Reduce Lateral Stresses in Retaining Structures Using GeoFoam.* Final report, project No. RSCH010-983 Vermont DOT, University of Massachusetts, Amherst, MA, 2009.

92. Edgar, T.V., J.A. Puckett, and B. Rodney, *Effects of geotextiles on lateral pressure and deformation in highway embankments.* Geotextiles and Geomembranes, 1989. **8**(4): p. 275-292.
93. Maddison, J., et al., *Design and performance of an embankment supported using low strength geogrids and vibro concrete columns.* Geosynthetics: Applications, design and construction, De Groot, Den Hoedt, and Termaat, eds, 1996: p. 325-332.
94. Polska, G.G., *Everything tailor-made Slope protection*.
95. Shi, X., et al., *Design of ribbed concrete approach slab based on interaction with the embankment.* Transportation Research Record: Journal of the Transportation Research Board, 2005(1936): p. 181-191.
96. Bakeer, R.M., et al., *Performance of pile-supported bridge approach slabs.* Journal of Bridge Engineering, 2005. **10**(2): p. 228-237.
97. Authority, I.S.T.H., *Design Manual for Tollway Transportation Structures and Facilities*, I.S.T.H. Authority, Editor 2008.
98. Hu, W., *Physical modelling of group behaviour of stone column foundations*, 1995, University of Glasgow.
99. Ayadat, T., *Collapse of stone column foundations due to inundation.* 1990.
100. Aguado, P., et al., *Recommendations for the design, calculation, construction and quality control of stone columns*, 2011, the French geotechnical union association: http://www.cfms-sols.org/sites/default/files/recommandations/Recommandations-CB-ENGLISH.pdf.
101. Elias, V., et al., *Ground Improvement Technical Summaries, Volume II, Demonstration Project 116.* US Department of Transportation, Federal Highway Administration, Publication No. FHWA-SA-98-086, 1998.
102. Niroumand, H., *From Research to Practice in Stone Columns and Reinforced Stone Columns as Soil Improvement Techniques* 2012: LAP Lambert Academic Publishing.
103. Pitt, J.M., et al., *Highway applications for rammed aggregate piers in Iowa soils*, 2003.
104. Raju, V., R. Hari Krishna, and R. Wegner. *Ground improvement using vibro replacement in Asia 1994 to 2004-a 10 year review*. in *5th International Conference on Ground Improvement Techniques, Kuala Lumpur*. 2004.
105. Townsend, F.C. and J.B. Anderson, *A compendium of ground modification techniques*, 2004.
106. Priebe, H.J., *The application of Priebe's method to extremely soft soils,"floating "foundations and proof against slope or embankment failure.* Ground engineering, 2005.
107. Raju, V., et al. *Vibro replacement for the construction of a 15 m high highway embankment over a mining pond*. in *Malaysian Geotechnical Conference*. 2004.
108. Wehr, J., *Keller Workshop*, 2013, www.kellerholding.com: http://kellerbrasil.com.br/pdf/Brazil%20Workshop%20Keller%20Wehr%202013.pdf.
109. Taube, M.G. and J.R. Herridge, *Stone Columns for Industrial Fills*, 2002: Cuddy, Pennsylvania.

110. Foundation, K., *Keller Foundation Brochure*, in *http://www.keller-uk.com/contentfiles/files/Keller%20F_%20brochure%20Dec2010.pdf*2010.
111. Kirsch, K. and F. Kirsch, *Ground improvement by deep vibratory methods*2010: CRC Press.
112. Egan, D., W. Scott, and B. McCabe. *Installation effects of vibro replacement stone columns in soft clay*. in *Proceedings of the 2nd International Workshop on the Geotechnics of Soft Soils, Glasgow*. 2008.
113. Mani, K. and N. K, *A study on ground improvement using stone column technique.* International Journal of Innovative Research in Science, Engineering and Technology, 2013. **2**(11).
114. McCabe, B.A., et al. *A review of the settlement of stone columns in compressible soils*. in *Ground improvement and geosynthetics. Proceedings of sessions of GeoShanghai 2010, Shanghai, China, 3-5 June, 2010.* 2010. American Society of Civil Engineers (ASCE).
115. Farrell, T. and A. Taylor. *Rammed aggregate pier design and construction in California-performance, constructability, and economics*. in *Structural Engineers Association of California Convention Proceedings. Placerville, CA. and liquefied behavior, Journal Geotech. Geoenviron. Engineering*. 2004.
116. Bilgin, Ö., K. Arens, and M. Salveter, *Analysis of Aggregate Pier Systems for Stabilization of Subgrade Settlement*, 2014.
117. Handy, R., D. White, and K. Wissmann, *Concentric stress zones near rammed aggregate piers.* Manuscript in preparation–draft to be provided upon request, 2002.
118. Barksdale, R.D. and R.C. Bachus, *Design and Construction of Stone Columns Volume I*, 1983.
119. YILDIZ, M., *DETERMINATION OF STRESS CONCENTRATION FACTOR IN STONE COLUMNS BY NUMERICAL MODELLING*, 2013, MIDDLE EAST TECHNICAL UNIVERSITY.
120. Hu, W., D. Wood, and W. Stewart. *Ground improvement using stone column foundation: results of model tests*. in *International Conference on ground Improvement Techniques*. 1997.
121. Douglas, S.C.P., *A web-based information system for geoconstruction technologies and performance of stone column reinforced ground*, 2012.
122. Hughes, J., N. Withers, and D. Greenwood, *A field trial of the reinforcing effect of a stone column in soil.* Geotechnique, 1975. **25**(1): p. 31-44.
123. Goughnour, R. and A. Bayuk, *Analysis of stone column-soil matrix interaction under vertical load.* Coll. Int. Renforcements des Sols, 1979: p. 279-285.
124. Balaam, N. and J. Booker, *Effect of stone column yield on settlement of rigid foundations in stabilized clay.* International journal for numerical and analytical methods in geomechanics, 1985. **9**(4): p. 331-351.
125. Balaam, N. and H.G. Poulos. *The behaviour of foundations supported by clay stabilised by stone columns*. in *European Conference on Soil Mechanics and Foundation Engineering, 8th, 1983, Helsinki, Finland*. 1983.
126. Greenwood, D. and G. Thomson, *Ground Stabilisation: Deep compaction and grouting*1983: Telford.

127. Briaud, J.-L., *Geotechnical engineering: unsaturated and saturated soils*2013: John Wiley & Sons.
128. Duncan, J.M. and C.-Y. Chang, *Nonlinear analysis of stress and strain in soils.* Journal of the soil mechanics and foundations division, 1970. **96**(5): p. 1629-1653.
129. Priebe, H.J., *The design of vibro replacement.* Ground engineering, 1995. **28**(10): p. 31.
130. BUSCHMEIER, B. and F. MASSE, *Discusión sobre las diferencias de la metodología de diseño entre las inclusiones granulares y las inclusiones rígidas.* 2012.
131. Rutledge, P.C. and S.J. Johnson, *Review of Uses of Vertical Sand Drains.* Highway Research Board Bulletin, 1958(173).
132. Vesic, A.S., *Expansion of cavities in infinite soil mass.* Journal of Soil Mechanics & Foundations Div, 1972. **98**(sm3).
133. Hughes, J. and N. Withers, *Reinforcing of soft cohesive soils with stone columns.* Ground engineering, 1974. **7**(3).
134. BEŞLER, O.F., *A SOIL IMPROVEMENT CASE STUDY USING RAMMED STONE COLUMN SYSTEMS*, 2013, MIDDLE EAST TECHNICAL UNIVERSITY.
135. Mitchell, J.K., *State-of-the-art Report on Soil Improvement.* 10th Int. Conf. in Soil Mechanics and Foundation Engineering, Stockholm, 1981.
136. Datye, K.R. and S. S. Nagaraju, *Behavior of Foundations on Ground Improved with Stone ColumnS.* 9th International Conference on Soil Mechanics and Foundation Engineering, Tokyo, 1977. **Proceedings**.
137. Brauns, J. *Initial bearing capacity of stone column and sand piles*. in *Proc. Symp.„Soil Reinforcing and Stabilizing Techniques in Engineering Practise", Sydney*. 1978.
138. Soyez, B., *Méthodes de dimensionnement des colonnes ballastées.* Bulletin de liaison des Laboratoires des Ponts et Chaussées, 1985. **135**(135): p. 35-51.
139. Sahin, H., *Nondestructive Test Methods for Rapid Assessment of Flexible Base Performance in Transportation Infrastructures*, 2014.
140. Long, X., *Prediction of shear strength and vertical movement due to moisture diffusion through expansive soils*, 2006, Texas A&M University.
141. Koppula, S., *Statistical estimation of compression index.* ASTM Geotechnical Testing Journal, 1981. **4**(2).
142. Yoon, G.L. and B.T. Kim, *Regression analysis of compression index for Kwangyang marine clay.* KSCE Journal of Civil Engineering, 2006. **10**(6): p. 415-418.
143. Kulhawy, F.H. and P.W. Mayne, *Manual on estimating soil properties for foundation design*, 1990, Electric Power Research Inst., Palo Alto, CA (USA); Cornell Univ., Ithaca, NY (USA). Geotechnical Engineering Group.
144. Lytton, R., C. Aubeny, and R. Bulut, *Design Procedure for Pavements on Expansive Soils: Volume 1*, 2005.
145. Holtz, R.D. and W.D. Kovacs, *An introduction to geotechnical engineering*1981.
146. Bakhsh, K.N. and D. Zollinger, *Design Methodology for Subgrades and Bases Under Concrete Roads and Parking Lots Test Methods & Results of Erosion*

Potential of Commonly Used, 2014, Ready Mixed Concrete (RMC) Research and Education Foundation: Texas Transportation Institute.
147. Das, B., *Principles of geotechnical engineering. Cengage Learning.* Stamford, CT, 2010.
148. AUBENY, C., R. BULUT, and R. LYTTON, *Design Procedure for Pavements on Expansive Soils: Volume 2.* 2006.
149. Fredlund, D.G. and A. Xing, *Equations for the soil-water characteristic curve.* Canadian geotechnical journal, 1994. **31**(4): p. 521-532.
150. Standard, A., *D698. Standard test methods for laboratory compaction characteristics of soil using standard effort 12 400 ft-lbf/ft3 600 kN-m/m3. West Conshohocken (PA): ASTM International; 2011*.
151. Covar, A.P. and R.L. Lytton, *Estimating Soil Swelling Behavior Using Soil Classification Properties.* ASCE Geotechnical Special Technical Publication No. 115, 2001.

BRIDGE APPROACH DESIGN GUIDELINE

FINAL REPORT ~ FHWA-OK-16-08

ODOT SP&R ITEM NUMBER 2265

Submitted to:
John R. Bowman, P.E.
Director of Capital Programs
Oklahoma Department of Transportation

Submitted by:
Peizhi Sun, Ph.D. Candidate
Dan G. Zollinger, Ph.D., P.Eng
Zachary Department of Civil Engineering
Texas A& M University
Texas Transportation Institute

October 2015

CHAPTER 9

PRECAST CONCRETE PAVEMENT BRIDGE APPROACH SLABS

The well-known bump-at-the-end-of-the-bridge that is often associated with concrete bridge approach slabs (BASs) have been a recurring issue in many states for several decades. DOTs have reported differential settlement and cracking issues near the joint between a bridge deck and a BAS which has significantly reduced ride quality. Numerous research studies have been conducted to investigate the mechanisms that lead to the formation of the bump associated distress as well as the development of new strategies to address it. The leading mechanisms are those associated with settlement of the foundation materials due to consolidation, poor compaction during construction or the weakening of embankment fill under saturation caused by water infiltration through unsealed joints or cracks in the pavement surface. Other mechanisms relate to voiding between the slab and the base layer due to erosion coupled with poor drainage again caused by water infiltration through joints and cracks in the approach slab particularly under contractive movements caused by seasonal temperature variations.

The practitioners (i.e. the Oklahoma DOT engineers) often have to face the choices of whether maintenance/rehabilitation or new construction is needed for an existing problematic site and selecting the associated measures, which usually depends on the severity of the distress as well as the availability of funds. Sometimes, it is less complicated but costly decision if the BAS has settled so much that leaves new construction the only option; in other situations, it can be difficult to define the level of the severity of the distress and determine what measures should be taken.

Table 9-1 attempts to provide a simple guide to help practitioners make the choice on a method of repair. As shown in the table, the severity of the distress has been categorized into four levels. One major criterion for differentiating Level 1 & 2 from Level 3 & 4 severity of distress is the location of the potential problems leading to the bump issue. For Level 1 & 2 severity, the location of the potential problems appears only at the surface of the BAS (e.g. failed joint sealing) or at the slab-base interface

(e.g. erosion underneath the BAS); for Level 3 & 4 severity, the location of the potential problems propagates into the deeper layers of the embankment (e.g. embankment settlement) or pre-exists in the foundation underneath the embankment (e.g. very compressible foundation soils). Therefore, different measures should be applied to address different levels of severity. For Level 1 and 2 severity of distress (relatively less severe conditions), maintenance/rehabilitation measures are considered adequate to correct the problematic conditions and improve the ride quality; for Level 3 and 4 severity of distress (relatively more severe conditions), where maintenance/rehabilitation measures are not sufficient or ineffective to restore the conditions, project-level rehabilitation or new construction is required to radically address the problems.

There have been a variety of maintenance or rehabilitation measures to address the potential problems associated with the Level 1 and 2 severity of distress. As shown in Table 9-1, for Level 1 severity where surface drainage issues appear, general maintenance measures such as cleaning out edge drains, resealing the joints and cracks in the BAS may effectively prevent further moisture infiltration if done on a regular basis. For Level 2 severity where noticeable bump and widening joints are present, to address the root causes of the bump distress associated with this level of severity (e.g. excessive moisture infiltration inducing erosion underneath the BAS), viable solutions consist of improving the BAS surface grading to avoid accumulation of runoff water, resealing the joints and cracks in the BAS, retrofitting widening joints with load transfer devices and injecting cementitious grout or proprietary polyurethane materials into the embankment or foundation (as a means to address the eroded and voided area in the base layer and to pressure grout a settled BAS back into position).

Table 9-1 Guidelines for evaluating severity of distress and selecting possible repair measures

	Maintenance/Rehabilitation		**Project-level Rehabilitation/Re Construction**	
Level of Severity	**Level 1**	**Level 2**	**Level 3**	**Level 4**

Settlement and Bump Condition	None	Noticeable	Apparent	Significant
Failure Stages	Blocked drainage	Standing water	Clogged drainage system	Failed drainage system
	Joint sealant debonding	Joint sealant separation	Missing joint sealant	Wide open expansion joint
	Slab cracking	Widening joints/cracks	Moving cracks	Spalled and faulted cracks
		Pumping/water on the interface	Slab staining	Base erosion
			Signs of embankment settling	Voided and saturated embankment fill
				Embankment and foundation settling
Repair Measures	Clean out edge drains	Improve grading	Reshape cross drainage	Add/clean edge or cross drainage
	Reseal the joints/cracks	Reseal the joints	Reseal the joints	Reseal the joints
		Retrofit the crack with load transfer devices	Partial/Full replacement of the approach slab	Full replacement of the BAS
		Slab undersealing/ jacking	Deep stabilization of the base layer and embankment fill	Replace the embankment fill
				Reinforce the foundation soil

In order to adequately address the Level 3 and 4 severity of distress, where the potential issues are in the deeper layers of the embankment or in the foundation soils, it may be necessary to remove at least portion of the BAS in order to repair the underlying layers applying the measures listed in Table 9-1. The reasons for partial or full slab replacement can be summarized as:

- to restore and strengthen the underlying supporting layers for the new BAS;

- to fully replace cracked segments of the BAS thus preventing further moisture infiltration;
- to fully restore the joint sealing and load transfer;
- to redesign the BAS (such as optimizing the joint spacing to avoid excessive thermal induced joint movement and redesigning the surface grading to better direct runoff away from the BAS).

However, the drawbacks of replacing BASs are the costs of lane-closure and user delays, since it requires to allow time for curing cast-in-place (CIP) concrete.

It should also be noted that the aforementioned advantages of replacing BASs do not necessarily lead to satisfying long-term BAS performance; if the causes of the bump issue are due to voids or weakened areas in the underlying supporting layers (e.g. saturated embankment or very compressible foundation soils), only replacement of the BAS will not minimize reoccurrence of the distress. Therefore comprehensive remedial measures may be needed to address all the possible root causes leading to the bump issues.

CURRENT PRACTICE IN OKLAHOMA

Currently, the most common remedial method applied by the Oklahoma DOT maintenance team is to place an asphalt overlay, considering its easiness and lower cost, at the location where bump occurs to smooth out the unevenness; however, several drawbacks are associated with this method:

- Asphalt materials are essentially prone to rutting therefore requiring frequent maintenance or replacement;
- It may become only a short-term fix and further bump issues may still occur if the root causes are not resolved;
- Without correctly identifying and addressing the real causes of the bump issue, it may be a waste of money to place asphalt overlay and can yield much higher life cycle cost.

Therefore, the first step for achieving successful BAS maintenance is to correctly identify the severity level of the bump issue (whether it is Level 1, 2, 3 or 4) and the root

causes (whether it is only caused by the surface drainage issues or by the problems deep in the foundation soils); thorough site investigations and evaluations need to be conducted by structural and geotechnical engineers to achieve those purposes rather than simply placing a layer of asphalt overlay every time a bump is observed.

If the site is identified as Level 1 or 2 severity where the root causes of the bump issue can be treated without removing the BAS, the asphalt overlay method may be a possible option, but needs to be applied in combination with other remedial practices that address the root cause of the bump issue pertinent to that level of severity (e.g. reseal the joints and improve the drainage to avoid excessive moisture infiltration). In this case, the asphalt overlay method (although slab undersealing/jacking is more preferred) may be effective in smoothing the road surface for a certain period (depending on the quality of the asphalt material) since exacerbation of the base erosion condition is minimized through addressing the root causes.

If the site is identified as Level 3 or 4 severity where very compressible soil layers pre-exist in the foundation or the BAS has badly cracked leading to excessive moisture infiltration into deeper layers of the embankment, placing an asphalt overlay may work initially, but the overlay will not be long-lasting and new bump issues will likely develop again very soon because the root causes of the bump issue cannot be treated without removing the cracked BAS.

Currently, Oklahoma DOT applies 13 in. doubly reinforced CIP concrete slabs as the standard practice for building BASs. However, requiring significant amount of time for curing which complicates lane closures has been the major obstacle preventing the reconstruction/rehabilitation of CIP BASs. In many cases where the bump issues become urgent (e.g. after a heavy rainfall event) and need to be fixed quickly to minimize the disruption of traffic (e.g. in high traffic volume areas), the asphalt overlay method remains the only quick solution for the Oklahoma DOT maintenance team to address the Level 3 or 4 severity bump issues even if acknowledging that it will not last long nor fix the root causes of the bump, which is essentially a waste of time and money. Therefore, faster and less traffic-disruptive methods are needed for constructing BASs as a means to replace the asphalt overlay method especially when addressing the Level 3 or 4 severity conditions. Fortunately, precast concrete pavement (PCP)

technologies have been developed and facilitated in recent years, which provides a quick solution for constructing BASs.

OBJECTIVES

This document mainly focuses on elaborating the specific measures pertaining to resolving/preventing the Level 3 and 4 severity distress, which are more related to project-level rehabilitations or reconstruction. Specifically, this document will provide background information on:

- a method of using precast technologies for constructing BASs;
- designing and constructing long-lasting BASs using precast concrete pavement technologies;
- applying appropriate practices to create a favorable environment (which consists of design details of drainage, expansion joint, embankment backfill, foundation improvement measures, and etc.) in order to facilitate successful performance of the BAS.

The ultimate goal of this document is to provide Oklahoma DOT with a new option/tool for addressing the bump issues in a faster, more cost effective and less traffic-disruptive manner rather than solely relying on applying the asphalt overlay method.

PRECAST BAS

Precast concrete pavement (PCP) is an emerging technology which provides durable and longer-lasting features that meet the needs for rapid construction and rehabilitation of existing pavements. Although the history of PCP in the U.S. has been more than 40 years, early applications of PCP were limited to small scale emergency repairs. Over the past 15 years, substantial effort has been made by highway agencies as well as industry organizations to facilitate the advancement and application of PCP; specific types of PCPs were developed and used for both intermittent repairs and

project-level rehabilitations/reconstructions for highway and airfield pavements as well as BASs [10-16].

The following provides an introduction to two different types of PCPs that can potentially be used for constructing BASs – one being the jointed precast concrete pavement (JPrCP) and the other precast prestressed concrete pavement (PPCP). The specific features of the two options allow engineers to tailor the design of BASs based on key site conditions and design objectives associated with the use of BASs in Oklahoma, which provides a more durable system to effectively minimize the bump-at-the-end-of-the-bridge.

Note that the main purpose of the following content is to provide a brief review of the possible characteristics/features (including some proprietary details) of the two types of precast slabs. A standardized design solution is provided in the appendix for both JPrCP and PPCP. Certain details of the standardized design solutions may be revised to better suit the needs of the project.

Jointed Precast Concrete Pavement

The introduction of JPrCP comes from the need for a more appropriate and rapid method to rehabilitate distressed concrete pavement BASs. In general, a JPrCP behaves very similarly to a conventional cast-in-place (CIP) jointed concrete pavement (JCP). [10]; however, different from the conventional CIP JCP where aggregate interlock is thought to contribute a greater portion of the load transfer capability (when the joint opening is less than 0.03 in.) at the transverse joints, the application of JPrCP heavily relies on the use of dowel bars to provide load transfer mainly because that the fabricated precast concrete slabs have smooth joint faces and lack the aggregate interlocking mechanism.

JPrCP can be made of either reinforced concrete panels or pretensioned concrete panels. With regard to the embedment of dowel bars, a slot system is fabricated in the precast panels to allow for their installation; there are currently two options available for making precast concrete panels [10]:

1. Top slot system;

2. Proprietary bottom slot system.

Top Slot System

In a top slot system, the precast panels are equipped with three 1.5 in. diameter and 18 in. long dowel bars spaced at 12 in. at the transverse joint centered on each wheel path of the pavement slab [17] as shown in Figure 9-1. To accommodate the dowels, dowel slots are either pre-formed in precast panels or made at the edges or joints of adjacent slabs through sawing, jackhammering, air cleaning and sandblasting. Once the precast panel is installed, the dowel slots are filled with high strength concrete grout that often consists of non-shrink proprietary materials [17]. Load transfer in the top slot system is achieved through the bond resistance between the grout and the sandblasted face of the slots as shown in Figure 9-2.

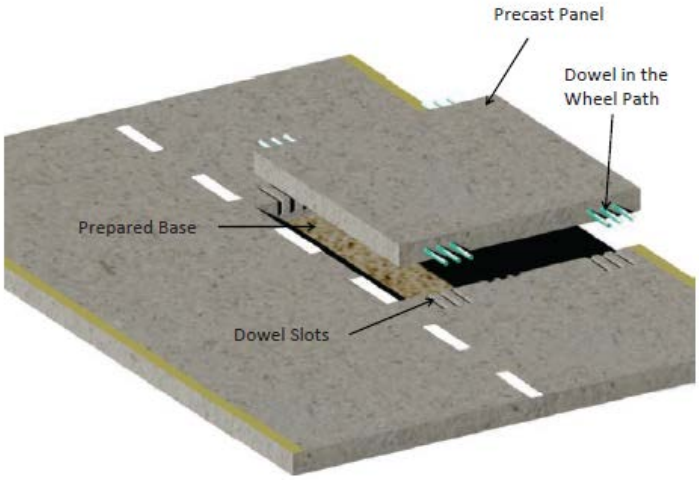

Figure 9-1 A JPrCP with top slot system [10]

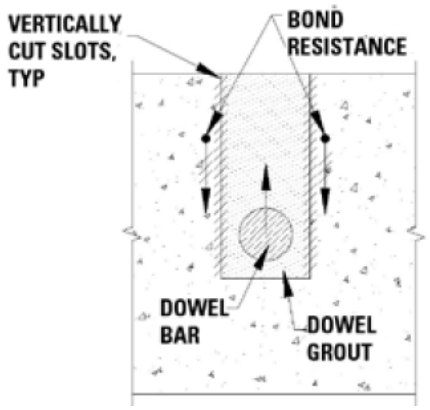

Figure 9-2 Vertical face of the joint of the top slot system [18]

A modified version of the top slot system uses only 1 in. wide narrow top surface slots as shown in Figure 9-3 (the length of the slot has been significantly reduced in a more recent version [19]) which allows for temporary traffic opening until the slots are patched. The development of this version of top slot system aims at addressing multiple lane closures that are involved during the construction, in which the original surface slots are too wide (about 2.5 – 3 in.) to be left open for traffic without being patched, which affects construction efficiency during each lane closure. In this modified version, dowel bars are inserted into the slots before the placement of the precast panels; once the panels are in place, the dowel bars are then slid into the drilled holes in the adjacent concrete panels; following that the slots are patched with rapid-setting materials [10].

Figure 9-3 A narrow-mouth top surface slot system [10]

Bottom Slot System

In a proprietary bottom slot system, the dowel slots are cast at the bottom of the precast panel along the transverse joints as shown in Figure 9-4. The dowel bars are embedded into the adjacent panels by drilling and epoxy grouting to provide load transfer [10]. Once installed, the bottom slots in the precast panel are filled with non-shrink grout through the grout holes at the surface of the panel. Similar to the top slot system, load transfer in the bottom slot system is achieved through the bond resistance; in addition, the specially designed dove-tail shape bottom slot system shown in Figure 9-5 can also provide a mechanical resistance to avoid pull-out of dowel bars [18].

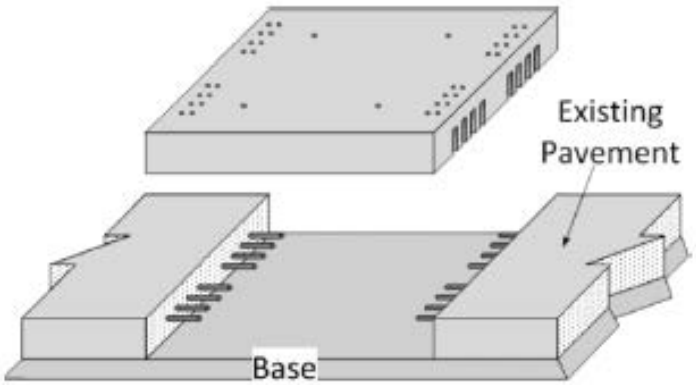

Figure 9-4 A precast concrete panel with bottom slot system [10]

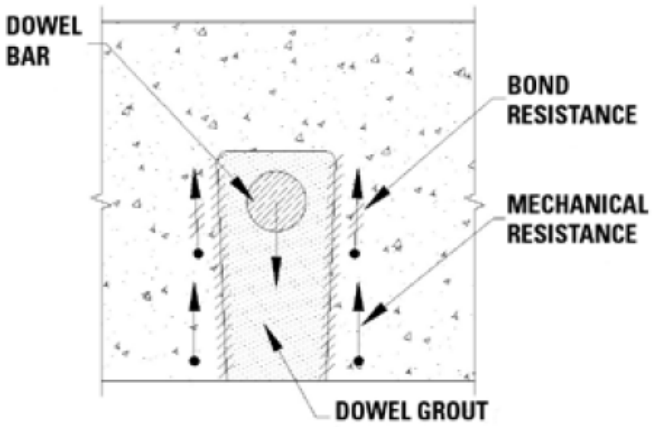

Figure 9-5 Vertical face of the joint of the bottom slot system [18]

Precast Prestressed Concrete Pavement

The concept of PPCP was developed based on the past experiences with CIP prestressed concrete pavement projects [20]. A PPCP section which usually has much longer expansion joint spacing (150 – 250 ft.) (compared with a conventional CIP JCP) is composed of a series of individual panels; each panel has a length of 8 – 10 ft. and a width of up to 38 ft. [21] (note that sometimes the width of individual panels is designed the same as the width of one lane as a means to expedite the construction [19]). The panels within a PPCP section are usually pretensioned in the transverse direction during panel fabrication stage, and are post-tensioned together in the longitudinal direction during construction stage; or they can also be post-tensioned in both the directions during the construction.

Three versions of PPCP shown in Figure 9-6 have been used in the previous projects [10, 13, 22]:

1. Central stressing system;
2. End hand hole stressing system;
3. End gap slab stressing system.

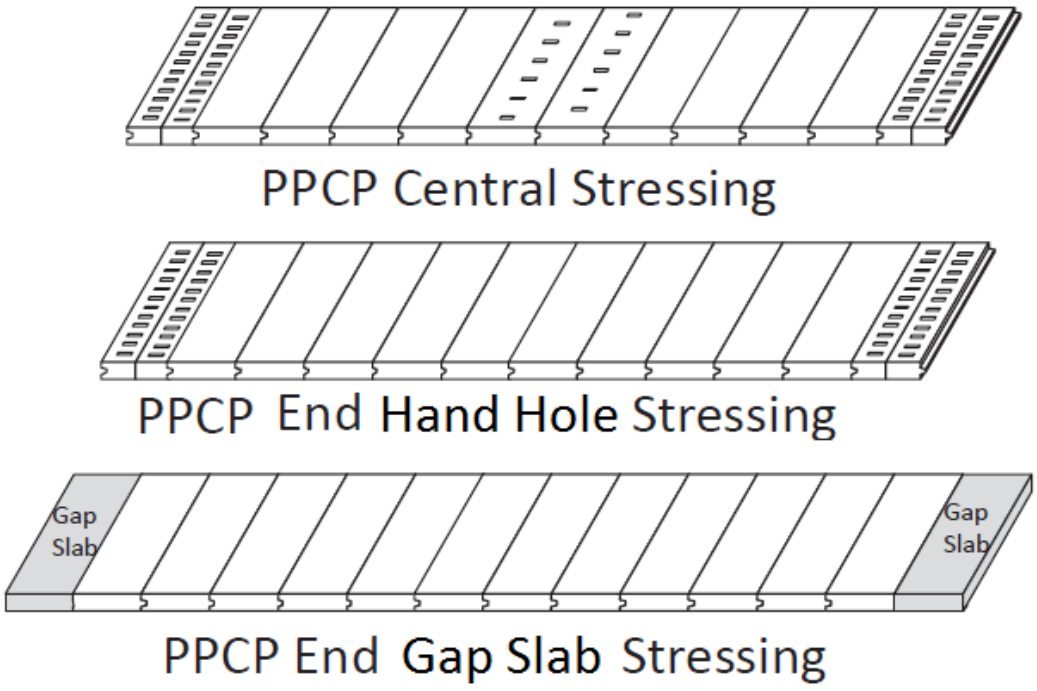

Figure 9-6 The three version of PPCP, after [10]

Central Stressing System

The original version of PPCP consists of three different types of panels, the base panels, the central stressing panel and the joint panels as shown in Figure 9-7. The three different types of panels work together to achieve successful post-tensioning throughout the entire pavement section. As indicated in the details in Figure 9-7, in addition to the pretensioning strands that transversely pre-tension the panels, each of the three different types of panels are fabricated with a continuous shear key along the joint surface to ensure a tight connection and vertical alignment of the panels, lifting anchors cast for moving and positioning the panels, and ducts mounted for post-tensioning the strands in the longitudinal direction of the PPCP [12].

Each type of panel is designed with a specific purpose in mind. A joint panel, as shown in Figure 9-7 (a), contains two half panels at the end of each PPCP segment. The expansion joint between the two half panels is designed to relieve the contraction or expansion of the pavement materials due to temperature variation. The post-tensioning (P-T) anchor access or hand holes facilitate the installation of a dead-end anchorage system which contains a wedge attached to a bearing plate to lock the strands in place while they are being post-tensioned at the central stressing panels. The grout inlet/vent is usually cast in front of the anchorage system to allow for grouting after post-tensioning is finished. A base panel, as shown in Figure 9-7 (b), is the very generic part that constitutes the majority of a PPCP system. The main purpose of the base panels (varied number) is to fill the space between the joint panels and the central stressing panel depending on the total length of a PPCP system. Meanwhile, the base panels also provide a medium for the ducts in which to pass the post-tensioning strands through. A central stressing panel, as indicated in Figure 9-7 (c), is designed similarly as the base panels, but with central stressing pockets which allow for the installation of a coupler as shown in Figure 9-8. The couplers are designed such that the post-tensioning strands extend from both ends of the panels are held together and post-tensioned using a stressing ram at the central stressing pockets during construction. Followed by that, the pockets and the post-tensioning ducts are filled with fast setting concrete to secure the strands and minimize the traffic interruption [12].

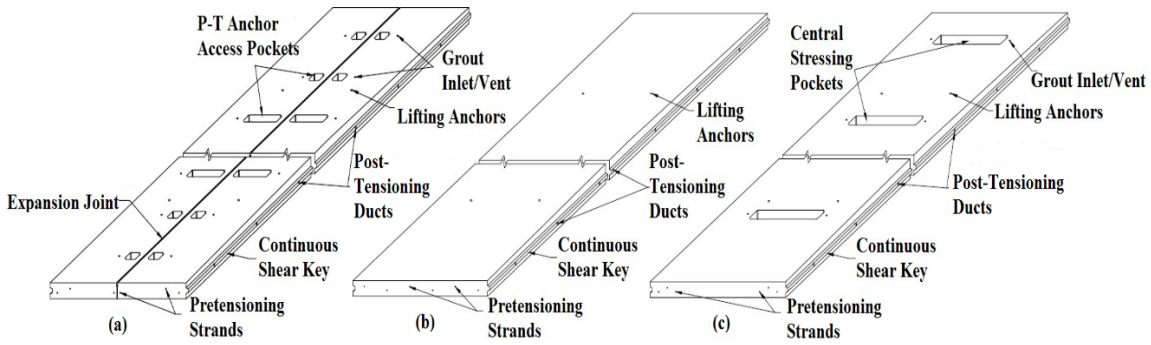

Figure 9-7 (a) Joint panel, (b) base panel and (c) central stressing panel, after [23]

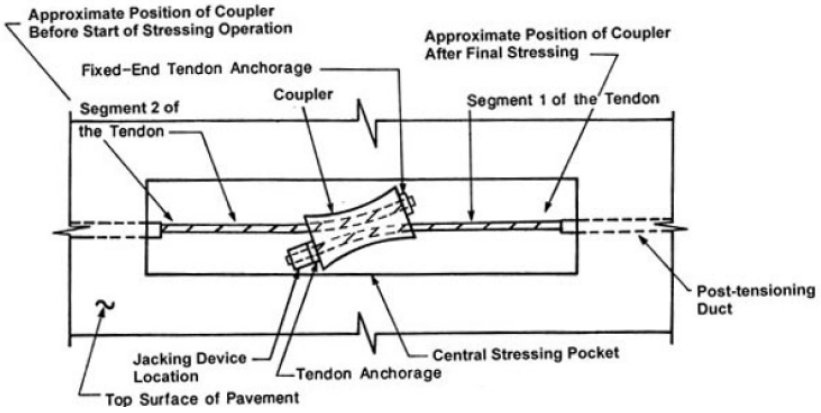

Figure 9-8 Coupler installed at the central stressing pockets [12]

End Hand Hole Stressing System

Another version of a PPCP system shown in Figure 9-9 was used in demonstration projects in Missouri in 2005 [22] and Delaware in 2009 [10].

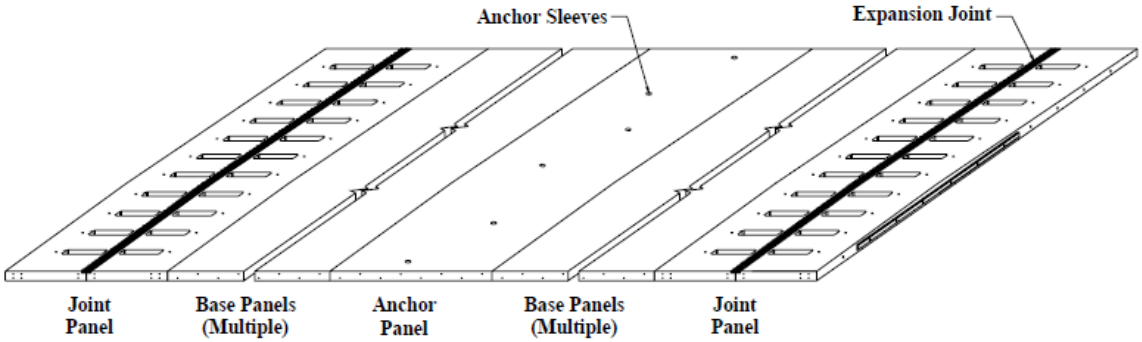

Figure 9-9 PPCP system with end stressing system at surface [22]

Different from the original version, this version of PPCP uses an anchor panel cast with anchor sleeves in place of the central stressing panel. As shown in Figure 9-10, the anchor panels will be anchored into the base and subgrade layer using anchor pins through the anchor sleeves which will be grouted afterwards. Anchoring the anchor panel into the underlying layer will be beneficial to keeping the panels from progressively moving along the direction of traffic and forcing the panels to contract towards or expand outwards from the centerline of the anchor panel, which is helpful to maintain the uniformity of the width of expansion joints.

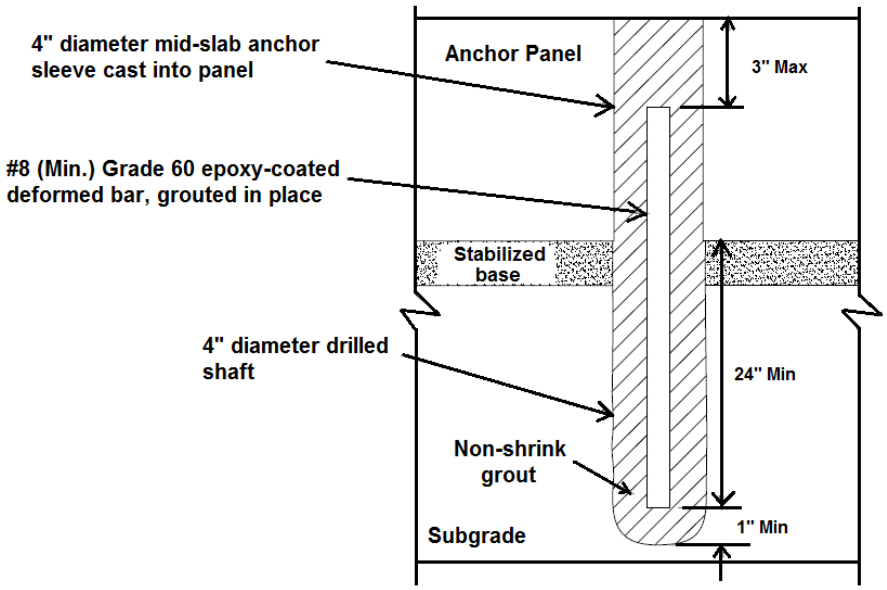

Figure 9-10 Design details of the anchor system in the anchor panels [22]

The modifications to the features at the central stressing panels are the result of the change in the post-tensioning method in later versions of this PPCP system. Instead of applying the central-stressing method at the central stressing panels, the later version uses the concept of end-stressing that allows the post-tensioning to be finished at the joint panels, which essentially eliminates the need for the stressing pockets in the central stressing panels. The size of the stressing pocket in the joint panels is also greatly reduced due to the benefit of using a “banana nose” stressing ram as shown in Figure 9-11. The nose of the special stressing ram is able to reach into the anchorage system and the post-tensioning strands from the outside without having to fit into the access pockets.

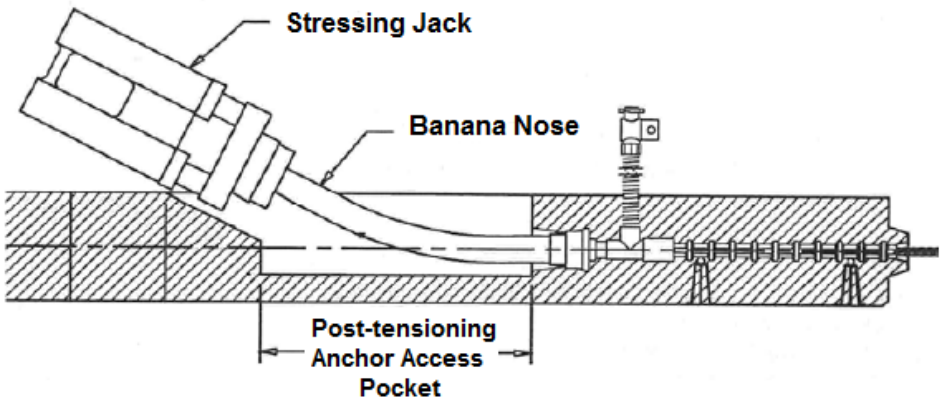

Figure 9-11 Stressing ram with a "banana nose" [22]

End Gap Slab Stressing System

The third version of PPCP was used in a project on I-680 in California in 2011 [10, 24]. Different from the previous two versions, this version, shown in Figure 9-12, consists of base panels, end joint panels and gap panels that form an expansion joint. Besides casting with dowel bars for load transfer, the end joint panels are also designed with anchorage system pockets that permit post-tensioning via the gap at each end, which avoids the need for the surface access pockets. However, the gap that is left for post-tensioning operations between two adjacent end joint panels needs to be filled with an additional panel which can be cast in place.

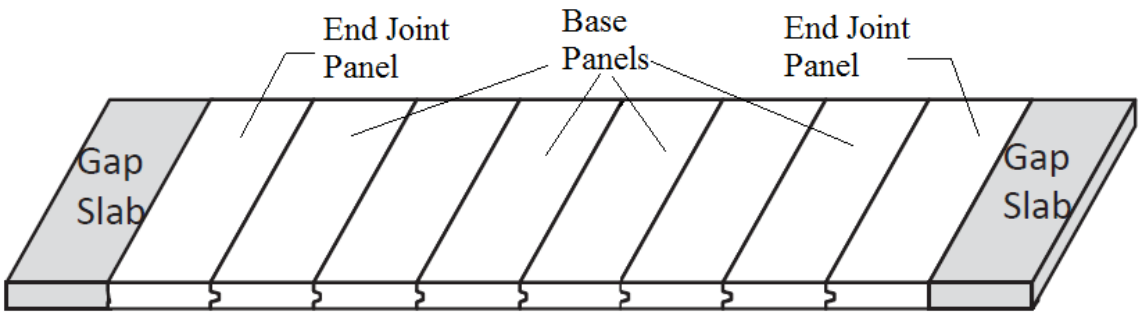

Figure 9-12 PPCP with end gap slab stressing system, after [10]

Benefits of Using Precast BAS

The benefits of using precast panels have been clearly identified as [10-12, 18, 20, 22, 23].

1. The most noticeable advantage is the short closure period. This is due to the fact that concrete panels are precast, which means that their strengths are developed off-site and panels are ready for traffic loading as soon as the panel installation is finished. This benefit allows the construction to be finished overnight or during weekends without encountering peak traffic hours, which greatly reduces the degree of traffic disruption and minimizes the user delay costs;
2. Generally speaking, the quality and performance of precast concrete panels are essentially better than the cast-in-place concrete slabs. This is because the precast panels are made at fabrication facilities in which the concrete mixture can be placed with more flexibility without accounting for curing on the job site; in addition, some other challenges associated with the placement of fresh concrete (e.g. late or shallow joint saw cutting) can be avoided;
3. More consistent quality of concrete can be assured at a fabrication facility particularly with regard to the effects of curing. Curing conditions at fabrication facilities allows the manufacture to make concrete panels with negative built-in temperature gradient, which improves the performance of concrete (up to a certain degree). This type of pavement allows construction to be carried out during very cool or hot seasons which is often restricted in the constructions of CIP concrete pavements.
4. Precast concrete panels provide extensive flexibility and applicability under various conditions, from intermittent distressed area repair to project-level rehabilitations/new constructions for both concrete and asphalt pavements, toll plazas, intersections, freeway ramps tunnels and BASs.

BAS TYPE SELECTION

For JPrCP panels, the specific advantages are:

1. A JPrCP system is simpler and easier to design, fabricate and install comparing to a PPCP system, therefore yields lower initial cost;
2. The design method of cast-in-place JPCP which has been proved successful over years, can be directly used to design JPrCP;
3. JPrCP is more versatile, because it can not only be used for continuous repairs or new constructions like PPCP, but also is more suitable for intermittent repairs comparing to PPCP;
4. JPrCP has better applicability for various site conditions, such as horizontal curves, 3-dimensional surfaces, crown line changes, utility-intensive area and heavily-skewed BASs.

For PPCP panels, the specific advantages are related to the fact that the panels are usually pretensioned during fabrication and post-tensioned during construction:

1. By prestressing concrete panels, the pretensioned/post-tensioned tendons are able to provide compressive stress once the tension force is released, which significantly increase the tensile capacity of concrete panels and reduce the occurrence of tensile cracking which improves the performance of the concrete slab; therefore, they usually last longer;
2. Prestressing concrete can also reduce the design thickness of the panels. With the method of prestressing through post-tensioning, the compressive stress induced in the concrete panels essentially allows a thinner slab to behave like a thicker slab resulting in equivalent structural capacity, which can potentially yield lower life-cycle cost;
3. Prestressing provides greater confining pressure to the intermittent (inactive) joints which increases the joint load transfer capability;
4. Prestressing is able to maintain the tightness of pavement joints which is favorable for preventing the base layer erosion in check.

For the purpose of constructing BASs, the PPCP has additional benefits in addition to the aforementioned ones.

1. Prestressing panels provides a BAS with greater structural capacity in spite of partially supported conditions that may occur due to the settlement of the embankment or material loss due to erosion;
2. The intermittent joints of PPCP are effectively sealed by the compressive force exerted by post-tensioning strands which may reduce water infiltration into the supporting layers;
3. Once tied to the integral abutment, the PPCP BAS behaves like a single piece slab which can create a sufficiently large resistant force at the slab-base interface (if designed long enough) that inhibits the load induced movement of an integral bridge abutment structure, thus keeping the joints between the abutment back wall and BAS tight protecting the sealant and preventing infiltration issues.

Selection Criteria

Based on the aforementioned advantages of the two types of PCPs, the criteria for BAS type selection can be established as shown in Table 9-2. The criteria are divided into two categories, direct and secondary criteria. For the direct criteria, meeting either one of them will lead to the selection of the specific BAS type pertinent to that criterion. For instance, if it is an integral abutment bridge, PPCP is automatically selected as the BAS type (considering the additional benefits listed above). The secondary criteria come into play if none of the direct criterion is present and therefore both the types are viable options for building the BAS; in this case, the secondary criteria provide only recommendations (rather than requirements) to the BAS type selection. Note that when both the direct criteria for choosing JPrCP and PPCP are present (e.g. only limited initial funds are available and it is an integral abutment bridge), it is recommended that the direct criteria for JPrCP governs.

Table 9-2 BAS type selection criteria

	JPrCP	**PPCP**
Direct	Limited initial funds	Integral abutment bridge

Criteria	Intermittent repairs only	Higher structure performance standards (less slab cracking)
	Complex road surface geometry	Longer service life requirements
	Heavily-skewed bridge	\
Secondary Criteria	Shorter construction time	Potential lower life cycle cost
	\	Limited space for providing lateral drainage

KEY ELEMENTS IDENTIFICATION

Once the type of the precast BAS is selected and designed following the aforementioned criteria, it is also necessary to select the design details or construction measures for the key elements (subsequently described) within the BAS system. A well-performed BAS is not only a result of well-designed precast BASs, but also relies on the effective interactions between the BAS and the key elements within that system. Appropriately selecting the design details for these elements helps to create a favorable environment for achieving successful performance of the BAS and preventing the potential bump issues from occurring. Without properly addressing these elements, the failure of either one of them can be a weakness within the system leading to the development of the bump issues. In this guideline, 10 key elements have been identified and the design details for these elements are evaluated regarding their applicability to precast technologies and effectiveness to prevent the occurrence of the potential bump issues. Specific criteria are also provided for selecting the design details for each element.

In this guideline, 10 key elements as shown in Figure 9-13 are identified within a BAS system, including:

1) BAS base layer;
2) Bridge deck-BAS joint;
3) BAS-pavement joint;

4) BAS drainage;
5) Abutment details;
6) Wing wall details;
7) Subsurface drainage;
8) Backfill wedge;
9) Embankment; and
10) Foundation support.

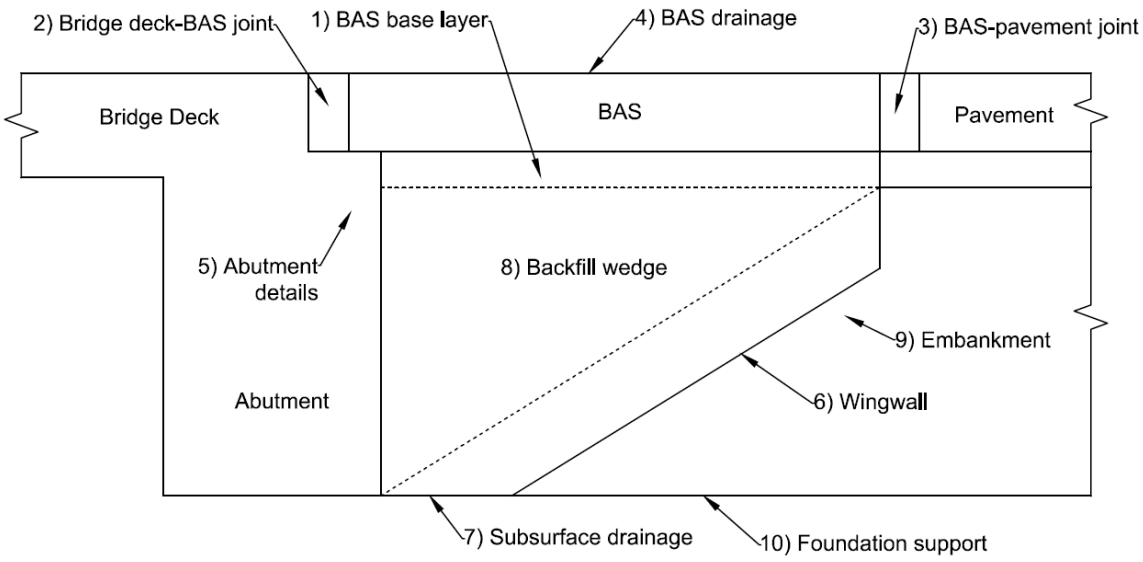

Figure 9-13 Key elements in a BAS system

In order to appropriately select the design details or construction measures for each element, the practitioner should establish selection criteria (subsequent example selection criteria for each element is provided in the pertinent chapters) which clearly define the boundaries for which specific design details should apply. For instance, if the construction area is subjected to a potential for heavy rainfall (i.e. a selection criterion), an open graded aggregate is recommended as the BAS base layer (**Element 1**) to provide drainage.

The detailed discussions of the design details and the associated selection criteria for each element are elaborated in the pertinent chapters. In this guideline, the design of **Element 1** is incorporated in both Chapter 10 and Chapter 12, **Element 2 – 4**

are addressed in Chapter 11, **Element 5 – 6** are addressed in Chapter 5; **Element 7 – 10** are addressed in the “Stone Column and Embankment Design Guideline”.

Reliability Consideration

With respect to each of the 10 elements, the practitioner can evaluate and select the appropriate design detail that meets the selection criteria (e.g. need a drainable base in **Element 1** in areas with heavy rainfall potential) at a given level of reliability.

In order to better help practitioners make design decisions with respect to these elements at various levels of design assurance/reliability, the aforementioned 10 elements are classified into three categories with respect their design purposes or utility in the system.

Table 9-3 Categories for BAS system elements as per design purposes

Design Objective	Performance/Reliability Indicator	Pertinent Element
BAS Thickness Design	Slab cracking	1, 8
BAS Erosion Prevention	Slab cracking	1, 2, 3, 4, 5, 6, 7, 8
	Transition smoothness	
Settlement Potential	Slab cracking	8, 9, 10
	Transition smoothness	

Element 1 and 8 are direct factors affecting the BAS thickness design in which the cracking performance of the BAS is the main design criteria/concern; the reliability of the design is directly accounted for and can be quantified in the design procedure (elaborated in Chapter 10) as well. In general, a greater level of design assurance (i.e. a high possibility of reaching the design life) can be achieved if a stiff, uniform and less erodible base layer (**Element 1**) and a strong, less compressible backfill wedge (**Element 8**) are used.

Element 1 – 8 are factors affecting the erosion performance of the BAS which is one of the most significant considerations in the BAS thickness design and directly affects the cracking performance of the BAS. Adequately addressing either one of the elements will help to improve the chances of achieving the expected design life of the BAS; in other words, if either one of them fail to perform in the way it is designed for, erosion failure with the concomitant slab cracking can be the result. In general, erosion at the BAS can be minimized if a less erodible base layer (**Element 1**) is used, the bridge deck-BAS joint (**Element 2**) and the BAS-pavement joint (**Element 3**) are well designed to maintain the transitions smooth and the joints tight, the BAS drainage (**Element 4**) is properly designed both at the surface and underneath the BAS to prevent the accumulation of runoff water, the abutment details (**Element 5**) are appropriately designed and constructed to prevent issues from occurring at the connections between the abutment and the adjacent structures (i.e. BAS and backfill wedge), the wing wall (**Element 6**) is adequately designed to prevent widening of the wing wall-BAS joint, the subsurface drainage (**Element 7**) is well designed to avoid wetting induced soil collapse or erosion and a less erodible backfill wedge (**Element 8**) is constructed.

Construction of **Element 8 – 10** are key to providing support for the BAS; any settlement or loss of support in any of these elements directly affect the smoothness at the bridge deck-BAS and the BAS-pavement joints as well as the BAS cracking performance (partial support condition induces more slab cracking). Therefore, appropriate construction practices and/or design details for these elements is the key to minimizing the potential of a bump at the transitional joints associated with the BAS. This approach allows for a fully supported pavement to be maintained such that the probability of achieving the expected design life and performance (i.e. less slab cracking and smooth transition) of the BAS is greatly enhanced. In general, settlement potential can be minimized if the backfill wedge (**Element 8**) is constructed using non-erodible and non-compressible materials, the embankment (**Element 9**) is compacted or treated with sufficient stability to support the backfill wedge and the BAS structure, and the foundation soil (**Element 10**) is adequately treated to minimize the primary consolidation settlement.

Achieving the expected design life and performance of a BAS relies on appropriately selecting the assurance level of the design detail or construction practice for a specific key element. For instance, for **Element 1**, using a stabilized aggregate base provides a greater level of assurance in terms of facilitating drainage and preventing erosion (i.e. the 2nd design purpose shown in Table 9-3) compared to using a typical dense graded granular base; for **Element 9**, the use of stone columns in the foundation materials provides a greater level of assurance for limiting the foundation settlement (i.e. the 3rd design purpose shown in Table 9-3). However, it should be noted that increasing the assurance level of the design usually induces higher cost. Therefore, the practitioner should appropriately select the design details based on the funding availability.

Finally, in order to obtain satisfactory design outcome (i.e. achieving the expected design life of the BAS) at a certain assurance/reliability level, the practitioners need to apply a table like Table 9-4 to help select the appropriate design details for each element.

The main benefit of using such table is that it will help practitioners to better take into account reliability considerations into the design, especially for the 2nd and the 3rd design objectives (this is because the reliability consideration is automatically accounted for in the design process for the 1st design objective, which is elaborated in Chapter 10).

Table 9-4 is created as an example of the design for **Elements 8 – 10** with respect to the 3rd design objective (i.e. settlement potential). The table consists of various design combinations (6 combinations are shown in Table 9-4) as a result of selecting different design details for each element. The various design combinations are categorized into three levels of overall assurance (i.e. low, medium and high); the rule for determining the overall assurance level of a specific design combination can be described as: the majority of the individual assurance level of the design detail selected for each single key element within that design combination dictates the overall assurance level. For instance, the majority of the individual assurance level in design combination #4 is “High” (design details of high individual assurance levels are selected for **Elements 8 and 10**), so the overall assurance level of design combination #4 is

categorized into “High”. A similar table can also be created in the same fashion to help with designing the elements pertinent to the 2nd design objective.

Table 9-4 Establishment of assurance levels for the 3rd design purpose

Design Objective	Overall Assurance Level	Design Combination No.	Element No.						
			8		9			10	
			Low	High	Low	Medium	High	Low	High
			Granular backfill	CLSM	Natural soils	Natural soils with geogrid reinforcement	Concrete piles	Untreated natural ground	Stone column treated ground
Settlement Potential	Low	1	√		√			√	
	Medium	2	√			√			√
		3		√		√		√	
	High	4		√	√				√
		5		√		√			√
		6		√			√	√	

The following provides an example to use the table for designing **Elements 8 – 10** with respect to the 3rd design objective (i.e. settlement potential):

1. Choose one of three levels of overall assurance as the target (shown in Table 9-4 (i.e. low, medium and high). For instance, the practitioner expects that settlement may potentially cause some problems based the local experience, then a “High” overall assurance level should be selected;
2. Select the specific design detail for each element based on the design criteria (which are subsequently elaborated for each element in the pertinent subsection). For instance, if the project area consists of soft compressible foundation soils, then the selection criterion leads to choosing stone columns for **Element 10** or choosing concrete piles for **Element 9**);
3. Check if the viable design combinations meet the target overall assurance level and select the appropriate one based on funding availability. In this example, design combinations #4, #5 and #6 are viable options since they all meet the “High” overall assurance level; the practitioner may choose either

design combination #4 for the lowest cost or design combination #6 for the lowest settlement potential.

Sometime, to achieve a certain level of overall assurance for a specific design objective, selecting the design detail with a lower level of individual assurance for a specific key element can be compensated by increasing the individual assurance level of another key element under the same design objective. For instance, if **Element 9** is designed with concrete piles supporting the backfill wedge (which provides a higher level of individual assurance) to address the potential of foundation settlement, it would be unnecessary to use stone columns for **Element 10** (which also provides a higher level of individual assurance), because the design combination already provides satisfactory level of overall assurance.

CHAPTER 10

DESIGN GUIDELINE FOR BRIDGE APPROACH SLAB USING PRECAST CONCRETE PAVEMENT

A report by Tayabji et.al [10] sponsored by the 2nd Strategic Highway Research Program (SHRP) provides the most recent and comprehensive information for the precast concrete pavement (PCP) technology including the design guidelines for jointed precast concrete pavement (JPrCP) and precast prestressed concrete pavement (PPCP). In this guideline, the design of precast BASs using these precast technologies are based on the procedure elaborated [10] but with certain modifications and improvements to account for the erosion damage that may take place underneath a BAS.

In order to apply these guidelines, the following prerequisites have been identified:

1. A full base support condition must be provided beneath the BAS. This requirement should be satisfied due to the fact that Oklahoma has adopted the use of a controlled low strength material (CLSM) as the backfill behind the abutment to support the BAS and which minimizes the potential for settlement of the CLSM as much as possible [37]. However, settlement can still occur in the compressible soils underneath the CLSM especially if they become saturated. Therefore, certain foundation improvement techniques (i.e. stone columns addressed in the “Stone Column and Embankment Design Guideline”) are suggested to prevent settlement from occurring beneath the CLSM.
2. Only minimal base erosion is allowed to occur over the design life of the BAS. The design should take into account the potential of base erosion in the design phase following the procedure elaborated in this chapter as well as applying certain techniques (addressed in the other chapters) to minimize water infiltration into the joints and facilitate drainage of the BAS in order to minimize the potential for erosion.

Due to the lack of direct field validation, the current design procedure for PCP was developed based on the design procedures for conventional CIP concrete pavements, i.e. the Mechanistic-Empirical Pavement Design Guide (MEPDG) by American Association for State Highway and Transportation Officials (AASHTO) [38] and the associated design software named as the AASHTOWare Pavement ME Design released in 2013 (previously known as the DARWin-ME released in 2011) [39]. The following summarizes the key steps for designing a precast BAS following the procedure established in the study by Tayabji et.al [10].

DESIGN GUIDELINE FOR JPrCP [10]

The MEPDG design procedure is recommended for the design of JPrCP, considering adjusted design inputs and design criteria subsequently discussed. In addition, other available concrete pavement design procedures may be adopted and modified to design JPrCP following this guideline as well.

The general concrete pavement design procedure of MEPDG can be structured in terms of three major steps, which are summarized as follows [38]:

Step 1. Determine the trial input values for design, including the trial type and thickness of the pavement layers, material properties, joint spacing, dowel bar size and spacing, traffic ESALs and climate;

Step 2. Establish threshold limits in terms of the design performance criteria (i.e. cracking and faulting) and the associated reliability levels for the trial design; if the performance criteria predicted by the software do not meet the design criteria, the trial design inputs need to be modified until the design performance criteria are met;

Step 3. Evaluate design alternatives by utilizing engineering judgment and considering life-cycle cost analysis (LCCA); note that this step is beyond the scope of the MEPDG design procedure, LCCA should be conducted based on project needs.

Modification of Design Inputs

In ***Step 1*** of the design procedure for JPrCP, the following design aspects/inputs must be considered/adjusted to reflect the nature of the precast concrete panels and the conditions of BASs:

1. The default value of the concrete modulus of rupture is 650 psi for CIP concrete panels. For precast concrete panels, this value usually exceeds 700 psi due to the high construction quality; the level of prestress applied to the panels can also affect this input. A concrete modulus of rupture of 750 psi is recommended for JPrCP in this guideline; if the concrete panel is prestressed (i.e. through pretensioning), the effective modulus of rupture would be 850 psi (consider an additional effective pre-stress of 200 psi);
2. The default value of the permanent curl/warp effective temperature difference for CIP JCP is -10˚F. For precast concrete panels, it is expected that much less permanent temperature difference would occur since they are fabricated in manufacturing facilities with better temperature control condition. However, surface drying service to PPCP panels may effectively also lead to some permanent temperature difference. Although an extreme assumption, a -10˚F is still used for the permanent curl/warp effective temperature difference for the design of JPrCP;
3. A 50% of the actual ultimate concrete shrinkage (somewhere between 500 – 800 με (micro-strain)) is recommended because substantial shrinkage of the PPCP panels have already taken place during the storage period prior to being installed on site;
4. The default value of the contact friction time (i.e. the time that takes for the panel to lose contact with the underlying base layer) in the MEPDG is 136-month for CIP JCP. However, because the design procedure described in this chapter will incorporate a separate analysis to account for the erosion taking place at the interface between the concrete panel and the underlying base layer; therefore, the contact friction time value should be set as the design life of the BAS (e.g. if the design life is 40 years, the contact friction time should be 480-month);

5. The contact friction coefficient is considered low since the bottom of the precast panel is not expected to strongly bond with the underlying base layer as in the case of CIP JCP (due to the smooth precast panel bottom surface). Therefore, the “sliding” friction values as shown in Table 10-1 can be used in the design of precast BASs;

Table 10-1 Recommended values of coefficient of friction [40]

Subbase/Base type	Friction Coefficient		
	Low	Mean	High
Fine grained soil	0.5	1.1	2
Sand	0.5	0.8	1
Aggregate	0.5	2.5	4
Lime-stabilized clay	3	4.1	5.3
ATB	2.5	7.5	15
CTB	3.5	8.9	13
Soil cement	6	7.9	23
LCB	3	8.5	20
LCB not cured	> 36 (higher than LCB cured)		

6. The joint spacing of the BASs should be set in the range of 6 – 8 ft. in order to minimize the concrete slab movement at the joints due to thermal effects; this will help to keep the joint width narrow and the joint sealant functional, which is beneficial to preventing moisture infiltration into the joints and the associated erosion possibilities.

Adjustment of Design Criteria

Second, design criteria needs to be established prior to the design of JPrCP. The long-term failure types of JPrCPs are considered similar to the conventional CIP JCPs, including: 1. Structural distress such as a). Slab cracking; 2. Functional distress such as a). Joint faulting; b). Joint spalling; c). Poor ride quality (i.e. transition smoothness) and d). Poor surface texture (in terms of friction and noise). Similarly, the design criteria of JPrCP can be adopted from those of conventional CIP JCP; fortunately, because of the better quality precast concrete panels, the design criteria for slab cracking can be

relaxed. Table 10-2 provides the recommended design criteria for a JPrCP with an initial service life of 40 years.

Table 10-2 Recommended design criteria for JPrCP [10]

	Distress type	Value
Structural distress	Cracked slab (%)	25 - 30
Functional distress	Faulting (in)	0.15
	Spalling (length, severity)	minimal
	Smoothness (IRI) (in/mi)	150 - 180
	Surface texture (friction)	Long lasting (FN>35)
	Surface texture (noise)	Not available, but surface should produce accepted level of pavement-tire noise

DESIGN GUIDELINE FOR PPCP [10]

The design procedure for PPCP consists of the following four key steps:

1. Design the panel thickness of baseline design for conventional CIP JCP;
2. Design the PPCP panel thickness and determine the required effective prestress;
3. Design the prestressing system to achieve the required effective prestress;
4. Design the expansion joint.

The overall design procedure for PPCP can be illustrated as shown in Figure 10-1.

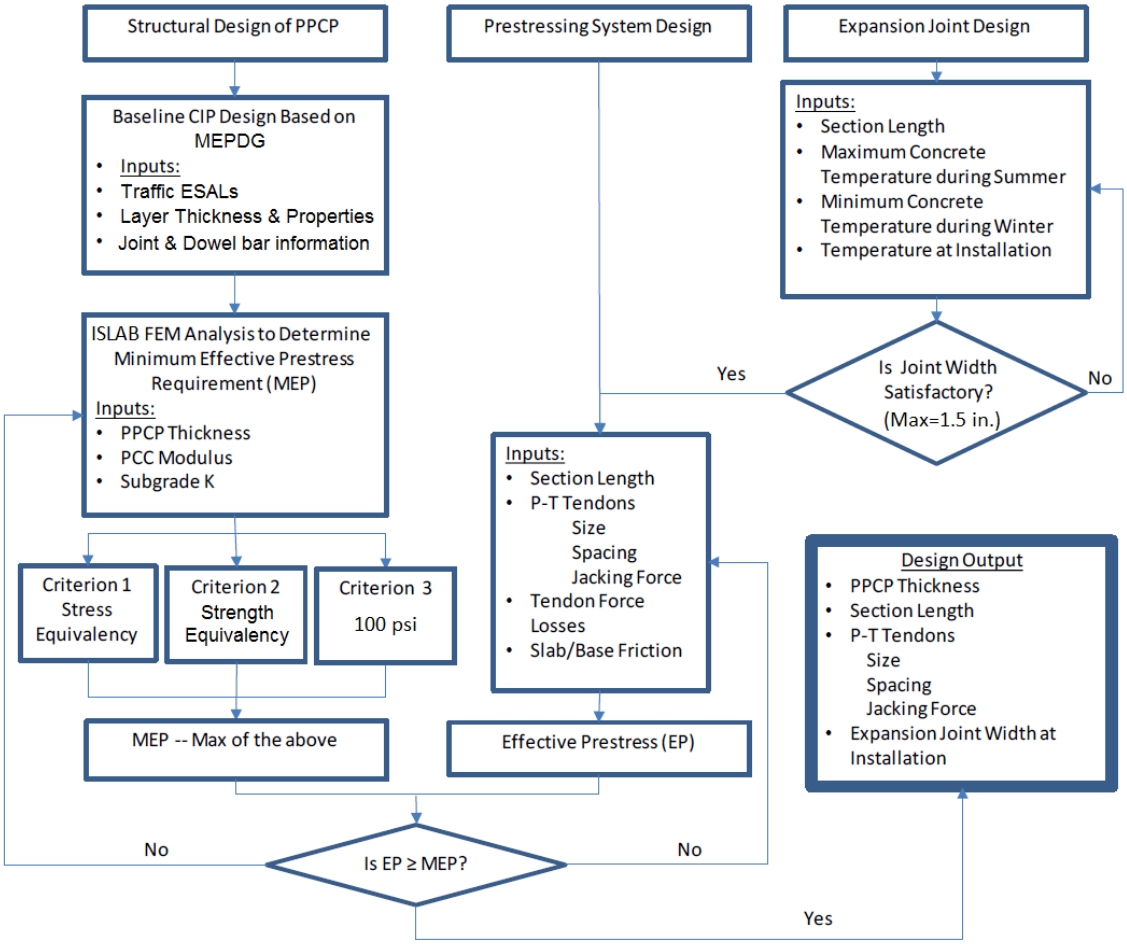

Figure 10-1 Design flow chart for PPCP, after [41]

Step 1. Baseline Panel Thickness Design

Prior to determining the required effective prestress, it is necessary to establish a baseline design for a conventional CIP JCP, which serves as a reference for the design of a PPCP BAS that is considered to have a performance equivalent to or better than the baseline design. The baseline design can be conducted using any mechanistic–empirical pavement design procedure with considering the local environmental condition, traffic loading information, subgrade type, pavement shoulder information and etc. (which are the same inputs for the design of PPCP). This guideline recommends using the MEPDG procedure and the associated design software to establish the baseline design. The design procedure for CIP JCP (i.e. baseline design) is almost

identical to the design procedure for JPrCP which has been elaborated previously, except that there is no need to modify the design inputs and criteria because the baseline design applies the default concrete material properties of the conventional CIP JCP.

Design output

It is expected that the baseline design will output the thicknesses of the JCP slab and the underlying base layers which will be used in the design of PPCP.

Step 2. PPCP Panel Thickness and Required Effective Prestress Design

This section elaborates the design of the PPCP panel thickness and the determination of the effective prestress required to provide the PPCP panel with performance equivalent to or superior than the baseline design. The concept is based on the assumption that, once installed, PPCPs will perform similarly to the CIP prestressed concrete pavements.

It is recommended that the minimum PPCP panel thickness should be at least 8 in. or enough thickness to allow for the inclusion of prestressing and reinforcing hardware (prestressing strand ducts, anchorage system, expansion sleeves for steel dowel and etc.). The thickness of the PPCP panels and the required effective prestress are designed using the criteria described in the following sections.

Criterion 1. Stress equivalency criterion

The stress equivalency criterion shown in Figure 10-2 is sometimes referred to as the thickness equivalency criterion. The main objective of this criterion is to determine the effective prestress that is sufficient to provide a compressive stress such that the critical tensile stress in a thin PPCP system is equivalent to the critical tensile stress in a thick conventional CIP JCP considering the same traffic loading condition. This criterion considers both edge and interior loading conditions to address the design for single-lane and multi-lane PPCP panels, respectively.

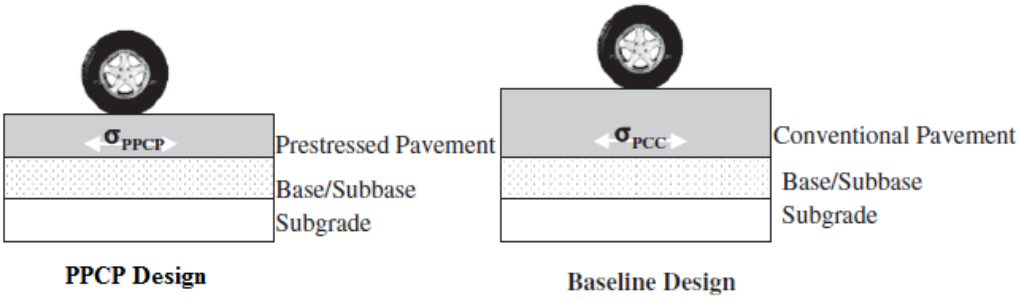

Figure 10-2 Stress equivalency criterion[10]

Depending on the specific design details of a PPCP project, the critical loading position can either be at the edge of a single-lane-wide panel (at the midway of the panel) as shown in Figure 10-3 (a) or at the interior edge of a multi-lane-wide panel (e.g. 2 ft. away from the edge) as shown in Figure 10-3 (b).

For either case, to determine the required effective prestress, the critical tensile stresses at the bottom of both the baseline design panel and the PPCP panel need to be determined using a finite-element based software (e.g. ISLAB2000), which requires design inputs such as loading magnitude, loading position, panel dimension, panel thickness and modulus of subgrade reaction.

Once the tensile stresses at the bottom of the PPCP panel and baseline design panel are determined, the effective prestress is calculated using the following equation:

$$EP_1 = \sigma_{PPCP} - \sigma_{Baseline} \quad (10\text{-}1)$$

where:

EP_1 = required effective prestress for a PPCP system considering stress equivalency criterion;

σ_{PPCP} = tensile stress at the bottom of a PPCP panel due to the design axle loading at the specified loading position (either at the edge for a single-lane-wide panel or at the interior edge for a multi-lane-wide panel); and

$\sigma_{Baseline}$ = tensile stress at the bottom of a baseline design panel due to the design axle loading at the edge loading position.

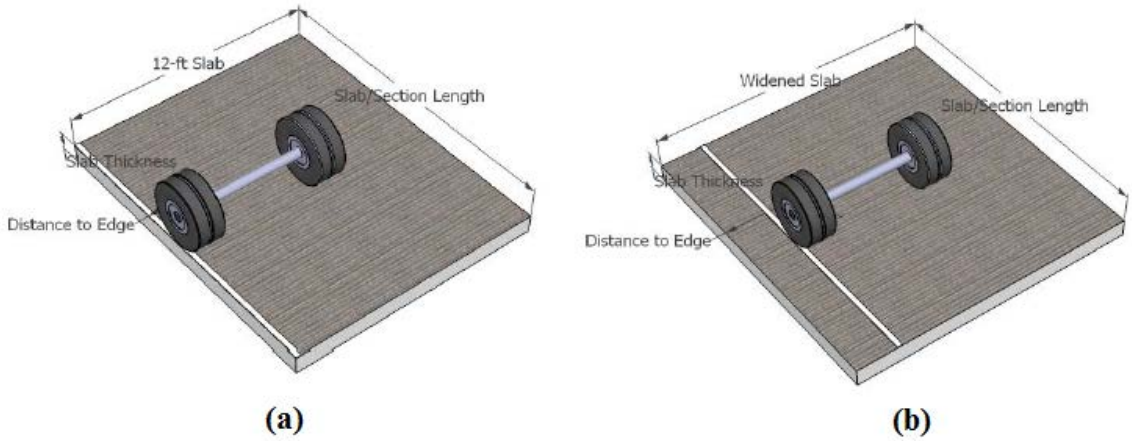

Figure 10-3 Critical loading positions for (a) a single-lane-wide panel and (b) a multi-lane-wide panel [41]

The stress equivalency criterion does have its limitations, because a strong base needs to be assumed such that deflection can be ignored in the analysis as well as the joint load transfer. Therefore, this criterion has limited utility and should only be used to generate a preliminary prestress design of a PPCP system.

Criterion 2. Strength equivalency criterion

The strength equivalency criterion assumes that the effective flexural strength (modulus of rupture) of a PPCP panel is the combination of the flexural strength of the precast concrete panel (usually 650 – 750 psi) plus the effective prestress EP_2 (typically 150 psi). The effective flexural strength can be used in any mechanistic–empirical design method that incorporates concrete flexural strength as an input to design the thickness of a concrete pavement. One example of such mechanistic–empirical design methods is the MEPDG [38].

The main purpose of the strength equivalency criterion is to design a thin PPCP system with an effective flexural strength equivalent to the flexural strength of a thick conventional JCP such that the PPCP system has a performance equivalent to or exceeds the performance criteria of the conventional JCP using the same design inputs. However, the design performance criteria of a PPCP system is somewhat different from

that of a JCP system due to the fact that the distresses do not develop in the same fashion in the two pavement systems.

Design Criteria and Inputs Adjustments

Design criteria need to be first established prior to the design of PPCP using the strength equivalent criterion.

1. Cracking criterion is the only performance criterion considered when designing a PPCP system and it was noted that even the cracking criterion for a PPCP system reaches 100%, it still yields much fewer cracks (20 – 30 cracks/mile. if assuming the length a PPCP system is about 150 – 250 ft.) than a JCP system which usually has a 15% cracking criterion (this leads to about 50 cracks/mile. if a 15-ft spacing is assumed for the JCP slabs). Therefore, the cracking criterion of a JCP system cannot be directly applied to a PPCP system.

   It is recommended to use calibrated fatigue analysis and calibrated cracking criterion (e.g. 50%) to design PPCP BAS. However, the application of this criterion can often lead to unsatisfactory design thickness (less than 8 in.) if the pavement is designed for less than 10 million ESALs traffic load repetitions with good base support. In these cases, the 8 in. minimum PPCP panel thickness requirement will govern the thickness design;
2. Deflection-based joint faulting criterion has not been established for the design of a PPCP system. Although the joint faulting criterion is applicable to a PPCP system, it is mainly set to account for the faulting of short-spaced concrete pavement (i.e. JCP which usually has a 15-ft joint spacing), whereas the expansion joint spacing for a PPCP system generally ranges from 150 – 250 ft.. Therefore, joint faulting criterion is not directly designed for, but is warranted by using a stiff base to reduce the joint deflection under heavy traffic loading as well as by providing sufficient effective level of prestress;
3. Material-related distress is also ignored in the design consideration of a PPCP system due to the fact that precast concrete panels are made in

fabrication facilities where better quality control and curing conditions are warranted comparing to the conventional cast-in-place JCP;

4. For function distress criteria, neither smoothness nor surface texture criterion were considered. However, it is expected that two cycles of diamond grinding may be performed to restore and satisfy the smoothness and texture conditions for a 40-year pavement design life. Note that it is desirable to perform a medium-heavy shot blast (i.e. meeting concrete surface profiles (CSP) 5 or 6) in order to retain adequate skid resistance.

Besides modifying design performance criteria, some of the design inputs also need to be adjusted to account for the difference between PPCP and CIP JCP. This section is similar to the modification of the inputs for design JPrCP:

1. The default value of the concrete modulus of rupture is 650 psi for CIP concrete panels. For PPCP panels, the effective flexural strength is the combination of the flexural strength of the concrete panel (usually 650 – 750 psi) plus the effective prestress (typically 150 psi);
2. A -10˚F is still used for the permanent curl/warp effective temperature difference for the design of PPCP;
3. A 50% of the actual ultimate concrete shrinkage (somewhere between 500 – 800 millionths of an inch) is recommended to design PPCP;
4. The default value of the contact friction time (i.e. the time that takes for the panel to lose contact with the underlying base layer) in the MEPDG is 136-month for CIP JCP. However, because the design procedure described in this chapter will incorporate a separate analysis to account for the erosion taking place at the interface between the concrete panel and the underlying base layer; therefore, the contact friction time value should be set as the design life of the BAS (e.g. if the design life is 40 years, the contact friction time should be 480-month; although it should be noted that the AASHTO LRFD uses a 75-year design life for BASs);
5. The contact friction coefficient is considered low since the bottom of the precast panel is not expected to strongly bond with the underlying base layer

as in the case of CIP JCP (due to the smooth precast panel bottom surface). Therefore, the “sliding” friction values as shown in Table 10-1 can be used in the design of precast BASs.

To design a PPCP following the strength equivalency criterion, the following summarizes the design criteria and inputs that are needed to be specially considered regarding their differences between PPCP and JCP as shown in Table 10-3.

Table 10-3 Design criteria and input adjustments between PPCP and JCP, after Tayabji et.al [10]

	Design Parameters	PPCP	JCP
Distress Criteria	Cracking	50%	15%
	Faulting	not applicable	0.15 in
	Smoothness	not applicable	180 in/mi
Precast Panel Inputs	Thickness	minimum 8 in	minimum 8 in
	Flexural strength	700 psi	650 psi
	Required effective prestress	150 psi	0
	Effective flexural strength	850 psi	650 psi
	ultimate drying shrinkage, 10^{-6} in	300	600

Design output

The design output of this step are the thickness of the PPCP panel and the required effective prestress. Note that the final required effective prestress can be determined based on the following function [41]:

$$EP_{required} = Max(EP_1, EP_2, EP_{\min}) \quad (10\text{-}2)$$

where $EP_{required}$ is the required effective prestress, EP_1 and EP_2 are the effective prestress determined using Criterion 1 and 2, respectively and $EP_{\min}$ is the minimum required effective prestress which has a recommended value of 100 psi [41].

Step 3. Prestressing System Design

The main purpose of designing a prestressing system for a PPCP system is to provide adequate level of effective prestress that satisfies the structural capacity requirement for the effective prestress in a PPCP system. The design procedure consists of:

1. Selecting the size, force and spacing of prestressing tendons;
2. Determining the length of a PPCP section;
3. Determining the total applied prestress based on panel thickness and tendon spacing;
4. Accounting for the prestress loss due to various factors such as the slab-base friction, concrete shrinkage and creep and etc. (these are explained in the following section);
5. Determining the effective prestress by subtracting the prestress loss from the total applied prestress.

Total applied end prestress

The total applied prestress in a PPCP system is achieved by pretensioning (usually in transverse direction) each concrete panel during fabrication and post-tensioning (usually in longitudinal direction but can also be in transverse direction) all the concrete panels within a PPCP system together during installation. In the United States, PPCP demonstration projects mainly used 0.5-in diameter, Grade 270, 7-wire strands for pretensioning and 0.6-in diameter, Grade 270, 7-wire strands for post-tensioning; strands are usually prestressed to 75% - 80% of the ultimate strength. The properties of prestressing strands (tendons) are shown in Table 10-4.

Table 10-4 Properties of prestressing strands [10]

Property	0.5-in Tendon Diameter	0.6-in Tendon Diameter
Tendon cross-sectional area (in^2)	0.153	0.217
75% of ultimate load (lbf)	31000	43000
80% of ultimate load (lbf)	33000	46900
ultimate load (lbf)	41300	58600

The spacing of prestressing strands (ranges from 18 – 36 in. based on previous experience) needs to be designed based on the length a PPCP system which usually ranges from 150 to 250 ft. (the shortest PPCP section was 110 ft. and the longest was 325 ft. from previous experience) such that the effective prestress meets the structural capacity requirement. For the construction of BAS, the length a PPCP section may be reduced and the guidance to determine the length of the BAS is subsequently elaborated. Once the spacing of prestressing strands is selected, the total applied end prestress can be determined based on the designed panel thickness as shown in Table 10-5.

Table 10-5 Total applied end prestress assuming 75% of ultimate load [10]

Panel thickness (in)	End Prestress (psi) for Strand Spacing of			
	18 in	**24 in**	**30 in**	**36 in**
8	299	224	179	149
9	265	199	159	133
10	239	179	143	119
11	217	163	130	109
12	199	149	119	100

The total applied prestress cannot be directly used in the design to meet the required level of prestress in a PPCP system, because it is also necessary to account for the prestress loss to avoid overestimation of the structural capacity of a PPCP system.

Section length determination

The length of the BASs in the U.S. generally ranges from 10 – 40 ft. [28], which are mostly determined based on empirical experience. Based on the past experience, one source that leads to the bump issue at BASs is due to the thermal induced contractive and expansive movements of the integral abutment bridge which force the BAS to also slide back and forth relative to the embankment backfill (the mechanism is elaborated in the Chapter 5). if the BAS is tied or anchored to the bridge deck. In order to restrain the BAS from sliding, the BAS should be designed with enough length (i.e. the drag length as shown in Figure 10-4) such that sufficient resisting force can be developed at the slab-base interface to resist the force induced due to the thermal changes in the integral abutment bridge.

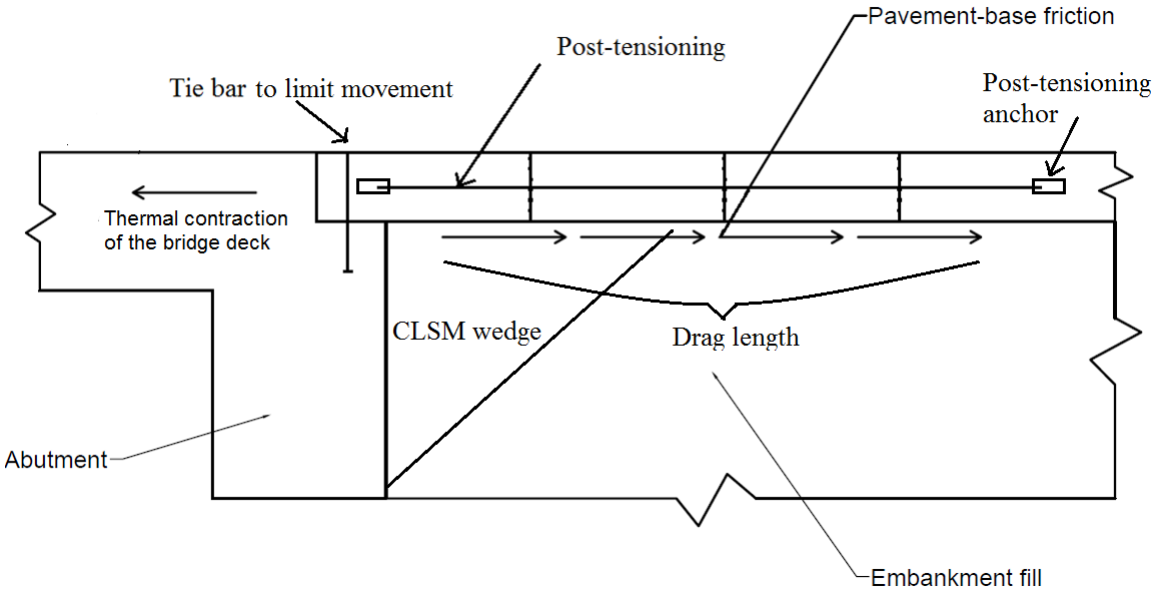

Figure 10-4 Illustration of the drag length concept

A simple analytical model as shown in Figure 10-5 is proposed to facilitate the estimation of the drag length, where Ft is the thermal force induced by the temperature change in the bridge structure, Fs is the resisting force at the slab-base interface. The BAS will not slide if the thermal force does not exceed the resisting force.

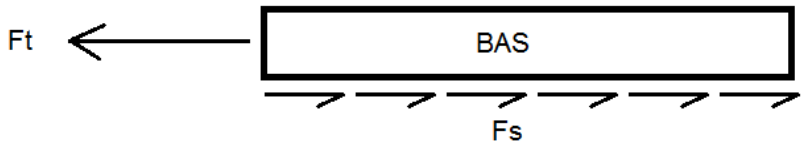

Figure 10-5 A simple analytical model for drag length determination

The thermal force Ft can be calculated by:

$$Ft = A \cdot E_c \cdot \alpha \cdot \Delta T \tag{10-3}$$

where

A = the cross section area of the BAS;

E_c = young's modulus of the concrete;

α = coefficient of thermal expansion of the concrete;

ΔT = the temperature change in the bridge deck.

The slab-base friction Fs can be calculated as:

$$Fs = \mu \cdot N = \mu \cdot \gamma \cdot h \cdot w \cdot L \tag{10-4}$$

where

μ = coefficient of friction at the slab-base interface;

γ = unit weight of concrete;

h = thickness of the BAS;

w = width of the BAS; and

L = the length of the BAS (i.e. the drag length).

Therefore, the length of the BAS can be determined as:

$$Fs \geq Ft \tag{10-5}$$

$$L \geq \frac{E_c \cdot \alpha \cdot \Delta T}{\mu \cdot \gamma} \tag{10-6}$$

where all the parameters are defined previously.

Prestress loss

Prestress losses of a PPCP system must be taken into consideration when designing the prestress provided by post-tensioning strands. It is very important that the

prestress loss is not overlooked, because it determines the level of effective prestress in a PPCP system which is not equivalent to the initial total prestress being applied to the system. Failure to consider prestress losses can result in overestimated structural capacity of a PPCP system. The factors that contribute to the prestress losses include slab-base friction, concrete shrinkage and creep, elastic shortening of concrete (often negligible), relaxation of steel tendons, slippage of steel tendons in anchorage system (extra attention being paid during post-tensioning to avoid this situation) and friction between steel tendons and ducts (often negligible for tangent pavement sections). Among these factors, the slab-base friction contributes the most to the prestress loss and can be relieved by placing a layer of polyethylene sheeting at the slab-base interface or segmentally performing post-tensioning to the system (i.e. reducing the length of post-tensioning). In general, the total prestress loss caused by the aforementioned factors can be as large as 100 psi (0.7 MPa) based on extensive testing results and experience. The following summarized the methods to predict the prestress losses due to the various factors.

Prestress loss due to slab-base friction

Prestress loss caused by the slab-base friction (σ_F) in psi is calculated as:

$$\sigma_F = \frac{\mu\gamma L}{2 \cdot 144} \tag{10-7}$$

where:

μ = coefficient of friction at the slab-base interface, which ranges from 0.5 to 1.5 for a PPCP system depending on the properties of the base layer and the bond breaker placed at the interface; a value of 1.0 is recommended;

γ = unit weight of concrete in pci; and

L = the length of the BAS (or the length of each section being segmentally post-tensioned) in ft.,

The above equation can be simplified assuming a concrete unit weight of about 142 – 146 lb/ft.^{3} as shown in the following:

$$\sigma_F = \frac{\mu L}{2} \tag{10-8}$$

Prestress loss due to concrete shrinkage

The concrete shrinkage induced prestress loss (f_s) is calculated by the following equation:

$$f_s = \varepsilon_s E_S(\frac{A_s}{A_c}) \tag{10-9}$$

where:

E_S = young's modulus of steel tendons;

A_s = area of tendons per unit width of a panel; and

A_c = area of concrete per unit width of a panel.

ε_s = concrete ultimate drying shrinkage strain which can be calculated using the following equations [42]:

$$\varepsilon_s = 1330 - 970y \tag{10-10}$$

$$y = (390z^{-4} + 1)^{-1} \tag{10-11}$$

$$z = 0.381\sqrt{f'_{c28}}[1.25\sqrt{\frac{a}{cm}} + 0.5(\frac{g}{s})^2](\frac{1+s/c}{w/cm})^{1/3} - 12 \tag{10-12}$$

where:

a/cm = aggregate-cementitious material ratio,

g/s = gravel-sand ratio,

s/c = sand-cement ratio,

w/cm = water-cementitious material ratio,

f'_{c28} = compressive strength at 28 days in ksi.

The shrinkage strain of concrete is a material property depending on the type of cement, water-to-cement ratio, type and gradation of aggregates, curing conditions and etc. For a PPCP system, concrete panel shrinkage takes place at both fabrication facilities and after being installed on site. The ultimate drying shrinkage strain for precast should be 50% of the actual value calculated from Equation (10-10).

Prestress loss due to concrete creep

The concrete creep induced prestress loss (f_{cr}) is determined by the following equation:

$$f_{cr} = C_u \frac{E_s}{E_c} f_{pe} (\frac{A_s}{A_c}) \quad (10\text{-}13)$$

where:

C_u = ultimate concrete creep coefficient which depends on many factors such as the properties and gradation of aggregates, cementitious material ratio, curing condition, concrete age at the time of stress and etc.. A value of 2.5 is recommended;

E_c = concrete modulus of elasticity; and

f_{pe} = prestress applied at the end of a PPCP system

Prestress loss due to steel relaxation

The tendon steel relaxation induced prestress loss (f_r) is determined by the following equation:

$$f_r = \rho \cdot f_{pe} \quad (10\text{-}14)$$

where:

ρ = coefficient of steel relaxation, a value of 0.04 is recommended.

Effective prestress

The long-term effective prestress at the midpoint of a PPCP system can be determined using the following equation:

$P_{effective}$=total applied end stress – prestress loss (10-15)

Design output

The main design output of this section is to finalize the design of prestressing system and obtain the effective prestress $P_{effective}$ by applying the following steps:

1. Compare the effective prestress $P_{effective}$ with the required effective prestress $EP_{required}$ determined from the last step. If $P_{effective} \geq EP_{required}$, the design is valid.
2. Otherwise, adjust the length of a PPCP section, tendon spacing and panel thickness until $P_{effective} \geq EP_{required}$

Step 4. Expansion Joint Design

An initial expansion joint width is determined at the beginning, thereafter the variation is estimated considering short-term effects due to post-tensioning and long-term effects due to temperature induced movement, creep and shrinkage of concrete. The joint width variation is determined in this step.

Panel movement calculation

This section provides procedures to determine the movement of PPCP, specifically referring to the movement at the BAS – pavement joint if the BAS is tied to the abutment.

Long-term movement of PPCP

Long term expansion joint is affected by diurnal and seasonal temperature variation as well as creep and shrinkage. The maximum seasonal temperature difference (i.e. the minimum temperature during winter subtracted from the maximum temperature during summer) is greater than the maximum daily temperature difference (i.e. daily temperature change during winter); therefore, it controls the maximum temperature difference when calculating the concrete movement due to temperature difference.

The movement (including both ends) of a PPCP section due to seasonal temperature variation is determined by the following equation:

$$dL_{Temp} = (T_{c\max} - T_{c\min}) \times CTE_c \times L \qquad (10\text{-}16)$$

where:

$T_{c\max}$ = maximum concrete temperature during summer;

$T_{c\min}$ = minimum concrete temperature during winter;

The movement of a PPCP section due to concrete creep is determined by the following equation:

$$dL_{creep} = C_u \times (P_{end} + P_{effective})/2 \times (1/E_c) \times L \qquad (10\text{-}17)$$

where:

C_u = ultimate concrete creep coefficient which depends on many factors such as the properties and gradation of aggregates, cementitious material ratio, curing condition, concrete age at the time of stress and etc.. A value of 2.5 is recommended;

P_{end} = prestress applied at the end of a PPCP system;

$P_{effective}$ = effective prestress = applied prestress – prestress loss; and

E_c = concrete modulus of elasticity.

The movement of a PPCP section due to concrete shrinkage ($dL_{shrinkage}$) is determined by the following equation:

$$dL_{shrinkage} = \varepsilon_s \times L \tag{10-18}$$

where:

ε_s = long-term concrete shrinkage strain, which can be calculated using Equation (10-10) – (3-12).

Total movement of PPCP

The total long-term movement (dL_{Total}) of a PPCP section due to the aforementioned considerations is determined as:

$$dL_{Total} = dL_{temp} + dL_{creep} + dL_{shrinkage} \tag{10-19}$$

Where all the terms are previously defined. Note that the traffic load induced movement may also be incorporated into the calculation of the total long-term movement of the BAS depending on the specific site condition, the practitioner may employ a structural engineer to perform that kind of calculation if necessary.

Joint width design

The following provides the calculations for designing joint width, including determining the joint width at placement and the maximum joint width.

Join width at placement

The design of initial joint width takes into consideration that a minimum joint width needs to be maintained during the first summer after construction based on the amount

of concrete expansion due to the temperature difference between the maximum summer temperature and the concrete temperature at the time of installation. The initial joint width ($JW_{Install}$) is determined by:

$$JW_{Install} = dL_{\min} + (T_{\max} - T_{Install}) \times CTE_C \times L \quad (10\text{-}20)$$

where:

$dL_{\min}$ = minimum joint width to be maintained during the first summer, assumed to be 0.25 in;

$T_{\max}$ = maximum temperature during summer, assumed to be 120˚F;

$T_{Install}$ = concrete temperature at the time of PPCP system installation;

CTE_C = concrete coefficient of thermal expansion; and

L = total length of a PPCP system.

Long-term minimum joint width

The long-term minimum joint width ($JW_{(L-T)\min}$) takes into account the effects of concrete creep and shrinkage and can be calculated using the following equation:

$$JW_{(L-T)\min} = dL_{\min} + dL_{creep} + dL_{shrinkage} \quad (10\text{-}21)$$

Where all the terms are previously defined.

Maximum joint width

The maximum joint width ($JW_{\max}$) can be determined as:

$$JW_{\max} = dL_{\min} + dL_{total} \quad (10\text{-}22)$$

Where all the terms are previously defined.

Joint sealant design

Joint sealant systems should be designed to accommodate for the changes in the expansion joint width which fluctuates from the minimum joint width during the first summer (assumed to be 0.25 in.) to the maximum joint width (the summation of the minimum joint width during the first summer plus the total long-term movement of a PPCP system). However, the long-term maximum joint width should not be greater than 1.5 in. in order to maintain a certain level of joint load transfer capacity. Underestimation

of minimum joint width can result in early failure of joint sealant; overestimation of maximum joint width can lead to overdesign of the joint sealing system.

Design output

The main design outputs of this step which are useful for the design of PPCP are:

1. The joint width at the time of installation;
2. Long-term minimum joint width;
3. Maximum joint width.

The main criterion is that the maximum joint width should not exceed 1.5 in, otherwise load transfer capability of expansion joints cannot be well achieved. If the criterion is not met, the design inputs need to be modified, such as changing the length of the PPCP section and the level of total applied prestress and re-design starting from ***"Step 3. Prestressing System Design"***.

DESIGN CONSIDERATION OF EROSION

It has been well-recognized that erosion underneath the BAS is one of the main issues leading to the bump-at-the-end-of-the-bridge as aforementioned. In the past, engineers have made various attempts with respect to different construction methods in order to minimize erosion, such as optimizing the surface or subsurface drainage system to better drain runoff away from the BAS and using controlled low strength material (CLSM) which provides a less erodible base support. However, erosion was not well considered in the design of BAS since most BASs were designed assuming that a certain length of the BAS is totally unsupported due to the erosion or settlement occurring at the base layer. In order to design BAS like a pavement which is considered fully supported by the embankment backfill along its entire length, the degree of bonding (affected by the erosion condition) at the slab-base interface which contributes to the structural capacity of the BAS must not be overlooked. Therefore, a design procedure to adequately consider and quantify the erosion underneath the BAS would be of great interest for the design of BAS.

This section elaborates a procedure to better model the base erosion condition for the design of BAS using the precast concrete technologies. Essentially, this section provides a means to adjust the slab thickness (calculated based on either fully bonded or unbonded condition using the concrete and base layer thicknesses which are design outputs of the MEPDG) to an “erosion-based slab thickness” (subsequently defined) which takes into account the degree of bonding as a function of the erosion damage. More importantly, the procedure facilitates an adjustment of the design reliability to quantitatively reflect the effects of various construction practices or design details on the performance of the BAS with respect to their utilities in preventing erosion damage underneath the BAS and maintaining a satisfactory structural capacity to minimize the bump issue.

The step-by-step procedure can be briefly described as:

1. Calculate the percent of erosion damage $\%E$ taken place at the end of the design period based on the following five key parameters:
    - the average daily traffic (ADT) at the start year;
    - the percent of trucks;
    - the number of wet days (min 0.1” rain);
    - the thickness of the concrete slab; and
    - the cohesion of the base.

    In order to better help the practitioner perform the design calculations, the complex design procedure has been simplified and an Excel spreadsheet was developed to facilitate the determination of the erosion damage based on the five key parameters (each has 3 levels of magnitude to help with interpolating the results).

2. Determine the “erosion-based slab thickness” based on the erosion damage which dictates the degree of bonding at the slab-base interface;
3. Adjusting the reliability for the specific performance criterion (i.e. cracking or faulting) based on the “erosion-based slab thickness”.

The procedure described in this section can be incorporated into the design procedures for both JPrCP and PPCP as described in the previous sections:

- For JPrCP: this procedure should be used after the MEPDG outputs the predicted performance (i.e. cracking or faulting) that satisfy the initial design performance criteria at the design reliability using the trial design inputs (i.e. concrete and base layer thicknesses and etc.);
- For PPCP: this procedure should be used following the ***Criterion 2*** in ***Step 2*** of the "***Design Guideline for PPCP***" once MEPDG outputs the predicted performance that satisfy the initial design performance criteria at the design reliability using the trial design inputs.

Step 1. Determination of Erosion Damage

In a recently research by Bari and Zollinger [46], the effects of both the interfacial friction and adhesion are incorporated into the design of concrete pavement regarding the erosion damage. The erosion damage model can be expressed as:

$$\%E = \frac{f_i}{f_0} = e^{-(\frac{\rho}{D_i})^{\alpha}} \quad (10\text{-}23)$$

where $\%E$ is the percent of erosion, f_i is the level of faulting for load cycle i, f_0 is the ultimate faulting, ρ and α are the local calibration coefficients and D_i is the accumulated erosion damage for load cycle i along the slab-base interface which is defined as:

$$D_i = \sum \frac{N}{N_f} \times (\%\ Wet\ Days) \quad (10\text{-}24)$$

where N is the accumulated traffic ESALs (subsequently elaborated), N_f is the ultimate load to failure (subsequently elaborated) and $\%\ Wet\ Days$ is the number of days in which the precipitation is greater than 0.5 inch over the number of days in one year (365 days) for the project area (data can be retrieved from the LTPP database).

Design output

The output of this step is the percent of erosion $\%E$ and the effective coefficient of friction μ_e.

Step 2. Determination of Erosion-Based Slab Thickness

This section proposes a new concept named as the “erosion-based slab thickness” and a procedure for calculating this parameter as shown in Figure 10-6. The necessary information for calculating the “erosion-based slab thickness” is:

- The thicknesses of the concrete slab and base layers (outputs of the MEPDG design);
- The predicted percent of erosion and the effective coefficient of friction at the slab-base interface at the end of the design life (outputs of the erosion analysis).

Before elaborating the concept of the “erosion-based slab thickness”, the “effective slab thickness” concept must be introduced to facilitate the understanding of the newly proposed concept. The “effective slab thickness” concept comes from a theoretically rigorous approach proposed by Ioannides et al. [50] focusing on transforming a multi-layered system (i.e. the concrete slab layer and the base layer) to a single composite layer system (i.e. a single effective concrete slab – base layer resting on a subgrade). In other words, the base layer is considered as a portion of the concrete slab (after transformation) rather than a portion of the subgrade. In this regard, the “effective slab thickness” refers to an effective equivalent slab thickness taking into account the structural capacities of both the concrete layer and the base layer (which can vary due to the presence of voiding as a result of base erosion).

It is considered that, due to the erosion of the supporting soil layer underneath the BAS, the slab-base interface condition varies from one extreme condition (fully bonded) to another (totally unbonded/separated) depending on the associated traffic repetitions and accumulated damage; a transitional state which exists between the two extreme conditions is referred to as the partially bonded condition and the degree of bonding is influenced by the erosion damage occurred at the slab-base interface. In general, the higher the degree of the bonding, the greater the effective slab thickness. The detailed definitions and equations for the thickness of the unbonded slab thickness, fully bonded slab thickness and their relation to the partially-bonded slab thickness are included in the Chapter 3.

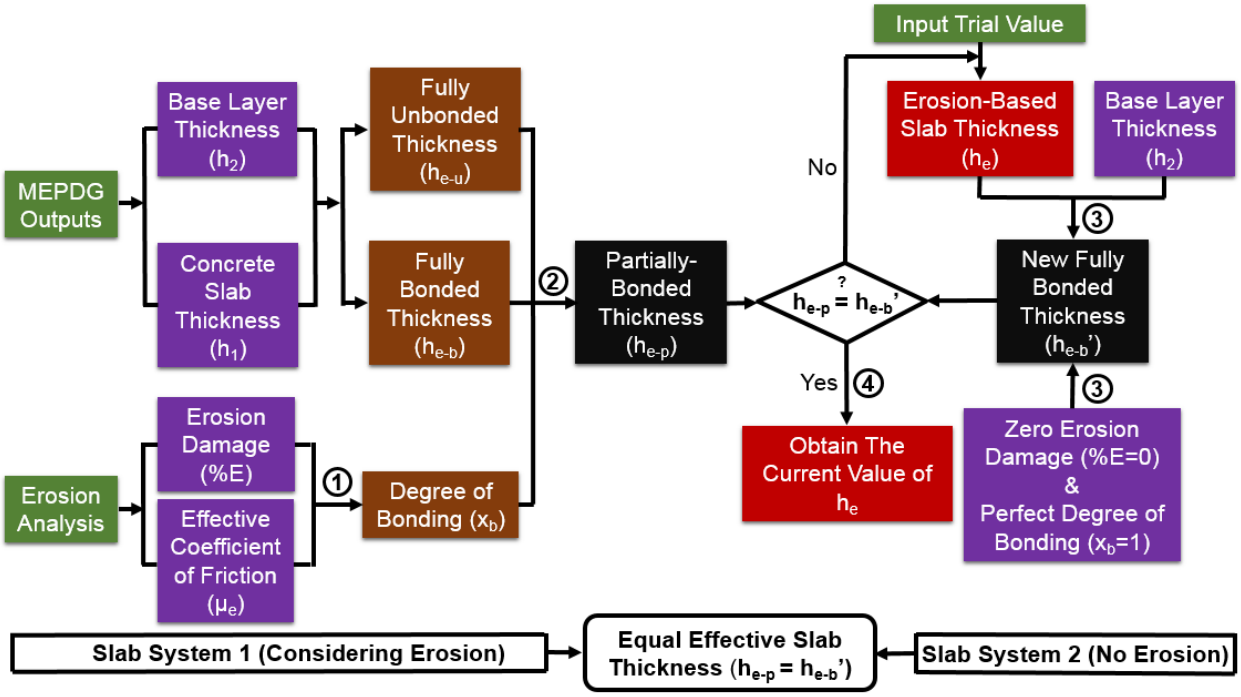

Figure 10-6 Flowchart of the procedure to determine the erosion-based slab thickness

The "erosion-based slab thickness" concept is proposed as a means to reflect how much the erosion damage could affect the structural capacity of a concrete layer only; in other words, in the single composite layer system (i.e. the effective concrete slab – base layer), the reduction in the structural capacity of the base layer due to the erosion damage is replaced by the reduction in the structural capacity of the concrete slab layer only (by reducing the concrete slab thickness and assuming zero erosion damage). The calculated erosion-based slab thickness (usually a reduced concrete slab thickness comparing to the initial design thickness) will help to facilitate determining the effect of the erosion damage on the reliability of the BAS performance, which is subsequently elaborated (see section "***Step 3. Reliability Analysis***").

As shown in Figure 10-6, where a step-by-step procedure is provided, the determination of the erosion-based slab thickness h_e relies on assuming two slab systems, which are slab system 1 (considering realistic erosion) and slab system 2 (considering zero erosion); the effective slab thicknesses of the two systems are equal to each other.

As marked in Figure 10-6, the procedure to calculate the erosion-based slab thickness h_e can be described as:

1. Calculate the degree of bonding x_b based on the percent of erosion $\%E$ and the effective coefficient of friction μ_e at the end of the BAS design life obtained by performing the erosion analysis (i.e. see section "***Step 1. Determination of Erosion Damage***");
2. Calculate the partially-bonded slab thickness h_{e-p} based on the degree of bonding x_b, fully bonded thickness h_{e-b} and fully unbonded thickness h_{e-u}; in slab system 1 where the percent of erosion $\%E$ is taken into account, the effective slab thickness is equivalent to the partially-bonded slab thickness h_{e-p};
3. In slab system 2, assume that erosion damage does not exist (i.e. $\%E = 0$) and the degree of bonding is perfect (i.e. $x_b = 1$); calculate the new fully bonded thickness $h_{e-b}{}'$; the effective slab thickness for slab system 2 is equivalent to the new fully bonded thickness $h_{e-b}{}'$;
4. The erosion-based slab thickness h_e of slab system 2 can be determined through trial and error such that the effective thicknesses of the two systems are equal to each other (i.e. $h_{e-p} = h_{e-b}{}'$).

To facilitate the calculation process, an Excel spreadsheet is made to help the practitioner determine the unknown which is the erosion-based slab thickness h_e. The inputs needed for this section are the original concrete layer and base layer thicknesses h_1, h_2, the material properties (modulus of subgrade reaction and young's modulus of each layer) and the effective coefficient of friction μ_e.

Design output

The output of this step is the erosion-based slab thickness h_e.

Step 3. Reliability Analysis

A reliability analysis is included in this procedure to account for the erosion-related factors leading to the variability in the performance of BASs. In general, increasing the design thicknesses of the pavement layers (or other design parameters such as base layer shear strength) can result in a greater level of design reliability. In this procedure, due to the consideration of erosion, a reduced concrete slab thickness (i.e. the erosion-based slab thickness) would result in a reduction in the design reliability. The following provides a method to obtain the final reliability due to the consideration of erosion and a way to adjust the BAS thickness in order to achieve the initial design reliability.

In the MEPDG, the deviations of all the factors leading to the slab cracking are assumed to be normally distributed. The predicted cracking for the design reliability can be determined as:

$$CK_p = CK_{50} + STD_{CK} \cdot Z_P \quad (10\text{-}25)$$

where CK_p is the predicted cracking at the design reliability level P (e.g. 95%), CK_{50} is the predicted cracking based on the mean inputs (corresponding to the 50% reliability), STD_{CK} is the standard deviation of the cracking and Z_P is the standardized normal deviate corresponding to the design reliability level P (one-tailed normal distribution). MEPDG finalizes the design process once the predicted cracking at the design reliability level reaches the design cracking criterion.

A design chart such as the one shown in Figure 10-7 can be developed in order to perform the reliability adjustment. The hollow points on the curves shown in Figure 10-7 represent the percentages of predicted slab cracking (a design output of MEPDG) which are obtained by varying the design concrete slab thickness (e.g. 9.5 – 10 in) at various levels of cracking reliability (e.g. 50 – 95 %) while holding the values of other design inputs constant.

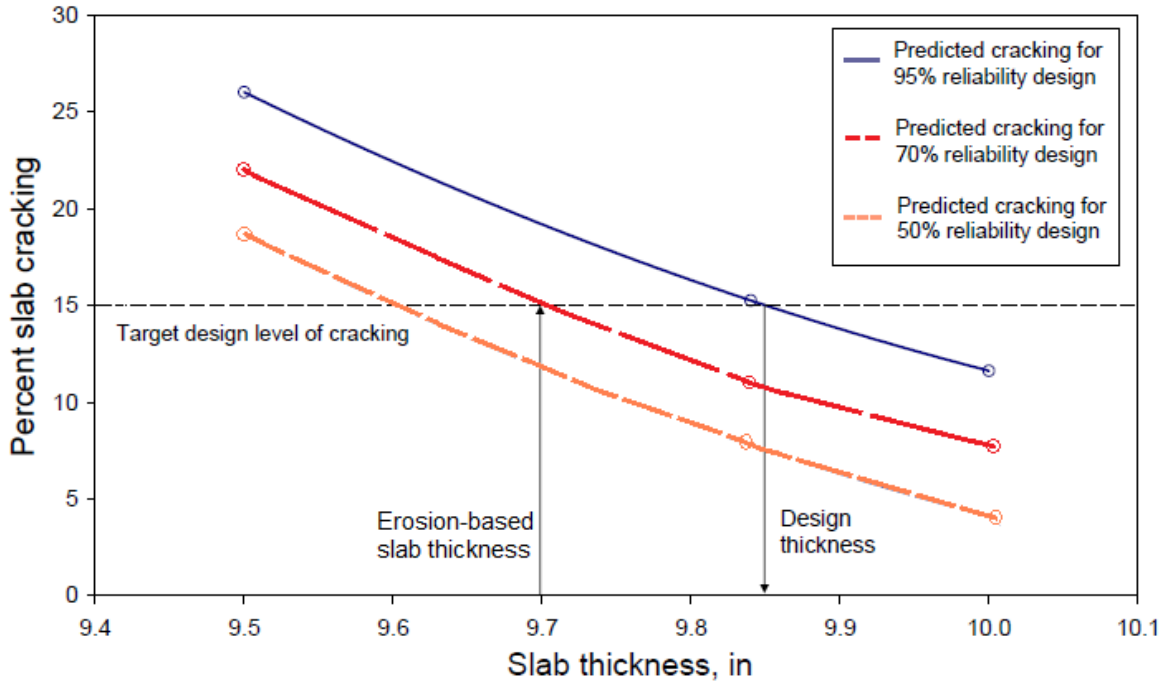

Figure 10-7 Reliability adjustment chart, modified based on [38]

Once the chart is developed, the level of reliability can be easily determined for the erosion-based slab thickness following the procedure shown in Figure 10-8. Two design purposes can be achieved by using the flowchart; Purpose 1 is to determine the final reliability due to the consideration of the erosion damage; Purpose 2 is to determine a new concrete slab thickness in order to meet the original design reliability as a result of considering erosion in the design.

For instance, if the cracking reliability is designed at 95% initially, the MEPDG outputs a design concrete slab thickness of 9.85 inches meeting the cracking criterion (e.g. 15%) as shown in Figure 10-8. Due to the consideration of the erosion damage taken place at the slab-base interface, the design thickness of the concrete slab is reduced from 9.85 to 9.7 inches (the determination of the erosion-based slab thickness was previously elaborated); accordingly, in order to meet the 15% cracking criterion (i.e. Purpose 1 as shown in Figure 10-8), the final design reliability has to be reduced from 95% to 70% (by using the reliability adjustment chart shown in Figure 10-7). The 25% reduction in the design cracking reliability is attributed to the consideration of the erosion damage.

The practitioners should also determine whether the adjusted level of reliability (i.e. 70%) will meet their design expectations; if it is determined that meeting the original 95% cracking reliability is a necessity, then a new concrete slab thickness h_1' (e.g. 10 inches) should be determined (Purpose 2 shown in Figure 10-8) through trial and error such that the new erosion-based slab thickness h_e' (e.g. 9.85 inches) is equivalent to the original design concrete slab thickness h_1 (since it is known that the original 95% reliability for 15% slab cracking can be achieved at this thickness).

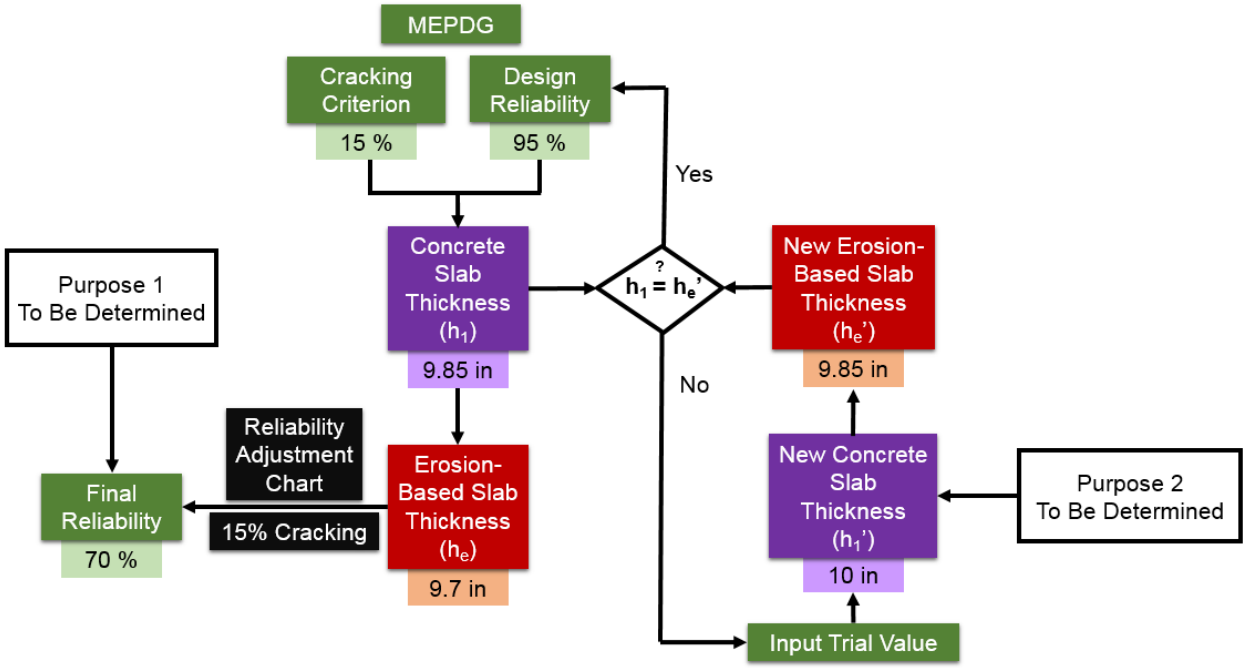

Figure 10-8 Flowchart of the reliability analysis

Design output

As shown in Figure 10-8, the design output for this section can be either one of the following two options depending on the purpose of the practitioner:

1. If the purpose is to evaluate the reduction in the design reliability due to the consideration of erosion damage, an adjusted design reliability (i.e. 70%) which is determined using the erosion-based slab thickness will be the output;
2. If the purpose is to achieve the original design reliability (i.e. 95%) and performance criterion (15% slab cracking), then selecting a new design of

concrete slab thickness (h_1') to meet the 95% design reliability will be the design purpose.

CHAPTER 11

JOINT AND DRAINAGE DESIGN

Joint and drainage designs are major factors affecting the performance of bridge approach slabs (BASs). The two primary joints in the BAS are at the bridge deck – BAS and the BAS – pavement interfaces. Appropriately designed and constructed joints can not only provide smooth transition between the two adjoining structures, but also protect the base from becoming saturated which can be one of the major reasons leading to the bump issues.

According to the field investigation conducted by Miller et al. [66] for the BASs in Oklahoma, runoff water infiltrating into joints with failed sealant was identified as one of the major sources leading to erosion damage underneath the BASs, where 84% of investigated BASs had failed joint sealant either at the joints between slabs or at the joints between BASs and wing walls. Other states also indicated that the better the joint sealing, the less chance that BASs would experience the bump issues [86]. In addition, the field observation also indicated that improperly designed or functioned drainage system also led to the accumulation of runoff water at the surface of the BASs and the base erosion. Therefore, constructing tightly sealed joint to minimize water infiltration and providing effective drainage system to direct water away from the surface of the BASs are two primary considerations with respect to preventing the base erosion issue underneath the BASs.

This chapter mainly focuses on providing design details and guidelines for the transitional joints (including both the bridge deck – BAS and the BAS – pavement joints) and the drainage systems (both at the surface and base) at the BASs.

BRIDGE DECK – BAS JOINT DESIGN

Three design aspects need to be addressed at the bridge deck – BAS joint, which are the paving notch connection, joint sealing and drainage considerations.

Paving Notch Connection

The paving notch connection refers to the reinforcement used at the connection between the BAS and abutment. The connection is installed mainly due to the concerns regarding the opening of the joint between the BAS and the abutment. Without using reinforcement in the connection, the width of the joint may gradually become wider when the bridge structure starts to contract during the winter while the friction at the BAS-base interface restrains the BAS from moving with the bridge. When the joint becomes wide enough, water can infiltrate into the joint easily leading to erosion if subsurface drainage is not provided.

Previous research [9] indicated that two types of paving notch connection were widely used in the states as shown in Figure 11-2. The first option is to horizontally connect the BAS to the bridge deck through the extension of the bridge deck reinforcement or the use of deformed steel bars. However, in some cases it was reported that this type of connection may lead to transverse cracking near the BAS-bridge deck connection, especially if the horizontal reinforcement connection is placed at a shallow depth in the concrete. It was suggested [57] that the cause of the transverse cracking was likely due to the fact that the horizontal reinforcement connection was not able to sustain the bending moment induced by the rotation of the BAS (upon traffic loading) as a result of loss of base support underneath the BAS. South Dakota DOT's experience [57] indicated that if this option is used, the horizontal reinforcement connection should be placed deeper in the slab to avoid transverse cracking that may occur at the surface of the BAS. The current standard design detail for this connection in Oklahoma as shown in Figure 11-1 also addresses the position of the reinforcement; in this detail, a mechanical splice is used to connect the reinforcement extended from the bridge deck to that in the BAS and the position of the reinforcement in the BAS is about the same depth as the bottom reinforcement.

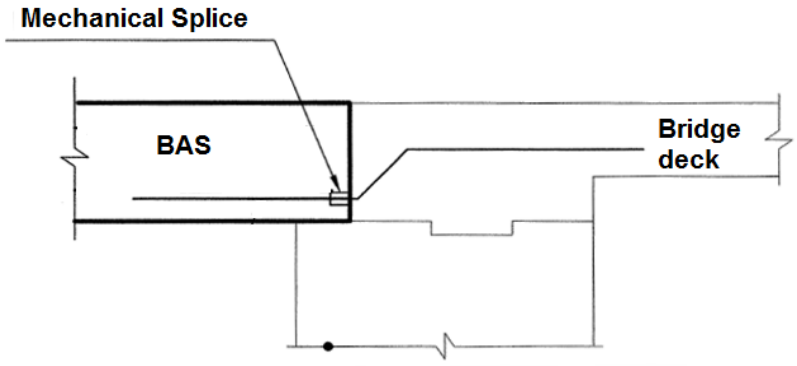

Figure 11-1 Standard design detail for the paving notch connection in Oklahoma [2]

The second option is to extend a reinforcement bar diagonally from the paving notch of the abutment to the BAS as shown in Figure 11-2 (b). It was reported by Minnesota DOT [57] that the use of this configuration in lieu of the first option (i.e. the horizontal reinforcement connection) has effectively reduced the rotational resistance caused by the horizontal reinforcement connection in the first option and no more transverse cracking was observed afterwards.

Note that if the BAS is connected to the bridge deck using either one of the two options for integral abutment bridges, the BAS should be considered as an extension of the bridge deck which moves as the bridge structure expands or contracts due to the effects of temperature and moisture variations. In this case, an expansion joint should be placed at the BAS-pavement connection to accommodate the movement of the bridge structure. In fact, it was reported by some DOTs that the bump-at-the-end-of-the-bridge problem can be transferred to the BAS-pavement connection as a result of connecting the BAS to the bridge deck for integral abutment bridges; this however may be beneficial for the maintenance team because it is much easier and cost-effective to deal with issues of pavements than issues of bridge structures.

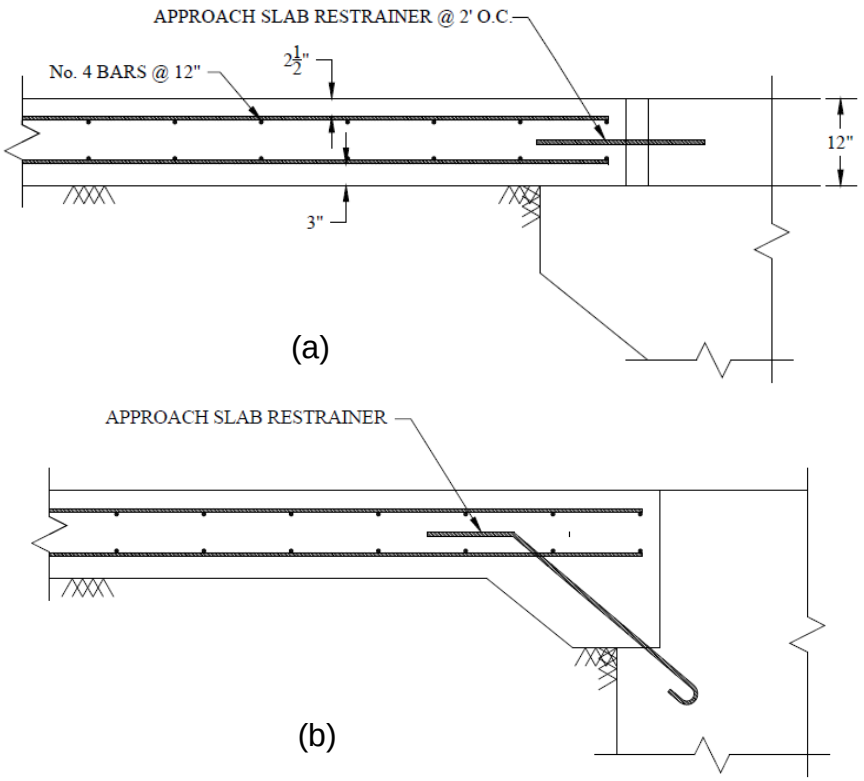

Figure 11-2 Two types of paving notch connections (a) bridge deck extension connection (b) abutment connection [9]

Selection criteria

Although both the two options yielded satisfying performance in the application for CIP BASs based on the past field experience [9], details may need to be modified for the construction of precast BASs.

For the construction of JPrCP BAS, the horizontal reinforcement connection can be applied base on the past experience [66] where #8 epoxy-coated deformed steel bars are cast in the bridge deck as shown in Figure 11-3. For a project in which the deformed steel bar connections are not cast in the bridge deck, the contractor needs to saw cut on the edge of the bridge deck or drill holes to accommodate the placement of steel bars and the opened slots will be filled with grout once the placement is finished. Although no record was found in the literature with respect to the use of the diagonal reinforcement bar as the connection for precast BAS and abutment, it may also be applied similarly by drilling holes in the paving notch of the abutment as a means to

install the diagonal bars. It should be noted that, if either the horizontal or diagonal reinforcement bars are used as the connection, the BAS has to contain a slot system (such as the one shown in Figure 9-4) to help with enclosing the connection bars installed on the abutment during the panel installation. These slot systems will be filled with rapid-setting materials once the BAS is placed on the paving notch.

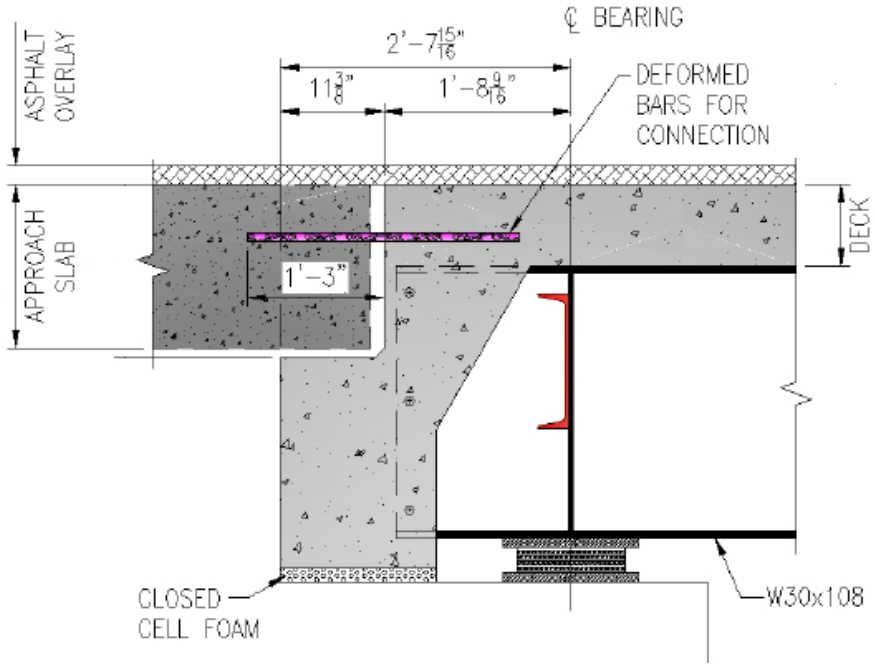

Figure 11-3 Design details of JPrCP BAS – bridge deck connection [66]

For the construction of PPCP BAS, the preferred solution is the application of vertical anchor bars as shown in Figure 11-4 which may be considered as a modification of the diagonal reinforcement connection. After pouring non-shrink grout into the anchor hole, the vertical anchor bars will be inserted into the anchor sleeves (cast into panel) during the construction (before performing final longitudinal post-tensioning [11]) as a mean to connect the BAS and the abutment. The installation of the vertical anchor bars for PPCP BAS will help to prevent movement of the BAS relative to the abutment when performing post-tensioning longitudinally along the BAS during the construction, which is the reason that this design detail is recommended for connecting the PPCP BAS and the abutment.

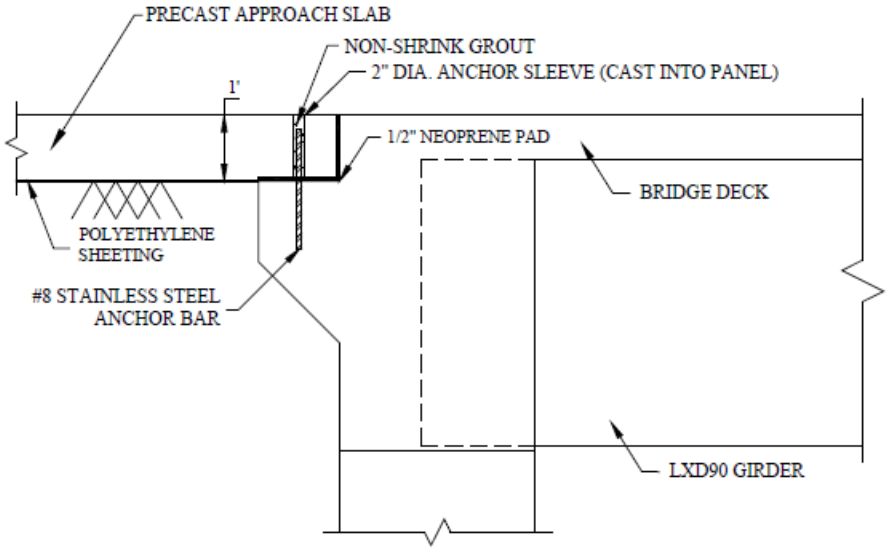

Figure 11-4 Vertical reinforcement connection between the BAS and abutment [9]

Joint Sealing

For integral abutment bridges, in order to reduce the movement of the bridge structure due to the thermal and load effects, BASs are usually tied or anchored to the bridge structure through the use of reinforcing bars as aforementioned. In that case, the bridge deck – BAS joint, being a construction joint, is usually designed to also function as a contraction joint which is formed in the fresh concrete at the location of the joint for CIP BASs. Once the joint is formed, it should be sealed with joint sealing materials such as hot pour, silicon and preformed compression seals with/ without the use of filler materials (such as bituminous material, polystyrene foam or neoprene pad) underneath the joint sealant [56] (similar to the joint sealant design detail in Oklahoma as shown in Figure 11-5).

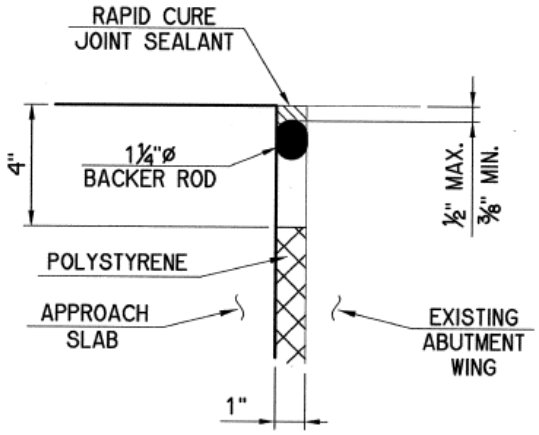

Figure 11-5 Sealed contraction joint detail [2]

Due to the nature of the construction of precast BAS, the bridge deck – BAS joint may be addressed differently relative to the CIP BAS. In some instances, if a good match is not achieved at the precast BAS and the bridge deck joint, a large and nonuniform opening at the bridge deck – BAS joint (such as the ones shown in Figure 11-6) may be the result. The imperfectly matched junction may also create difficulties when installing the joint filler and sealant, which could lead to poor performance such as greater rates of water infiltration at the bridge deck – BAS joint.

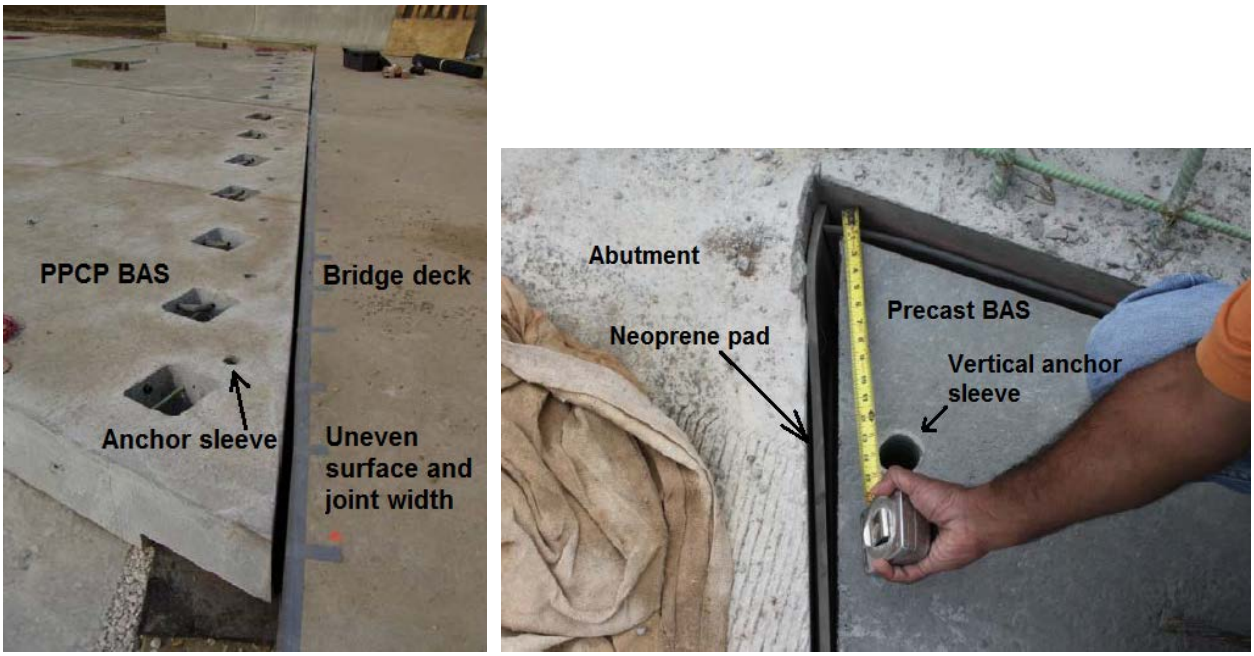

(a) (b)

Figure 11-6 The construction of the bridge deck – BAS joint for (a) a PPCP BAS project [11] and (b) a JPrCP BAS project [43]

For precast BASs that are anchored to the abutment using vertical reinforcement connections (through the vertical anchor sleeves such as the ones shown in Figure 11-6), based on the previous experience [11, 43], a layer of 0.5 in. thick neoprene pad can be used to fill the bridge deck – BAS joint and bituminous or cementitious materials can be used as a means for sealing any gaps in the joint due to imperfect matching. In order to provide a smooth transition at the joint, the unevenness can be addressed by diamond grinding; alternatively, according to some previous projects, an asphalt overlay over the precast BAS can be used to even out the irregular surface, particularly if the BAS leads to an asphalt pavement surface [43, 52].

For precast BASs that are tied to the abutment using horizontal deformed steel bar connections (such as the one shown in Figure 11-7), high strength grout is used to fill the bottom slots (as a means to accommodate the horizontal connection bars) in the precast BAS as well as the space in between the precast BAS and abutment (i.e. the bridge deck – BAS joint). This design results in a tight (non-working) connection between the BAS and the abutment such that the expansion joint (for accommodating

the movement of the bridge structure) can be moved to the BAS – pavement junction, which minimizes the potential for bump issues to occur at the bridge deck – BAS joint.

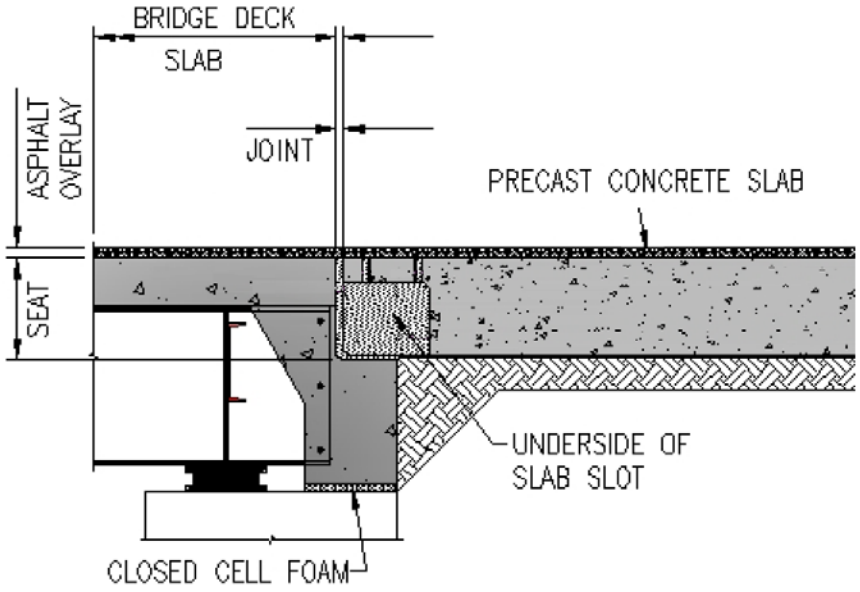

Figure 11-7 JPrCP BAS using horizontal deformed steel bars for connecting to the abutment [52]

Drainage Considerations

Although the bridge deck – BAS joint is to be filled with filler materials as a means to prevent water infiltration as aforementioned, however, as the joint filler material ages and deteriorates, due to the effects of traffic loads and temperature variations, it is not likely that water tightness can be maintained at this joint over the entire service life of the BAS. Therefore, drainage needs to be addressed at this joint to minimize the erosion potential for the base material underneath the BAS, as a means to provide a higher level of design assurance.

A possible design solution to provide drainage at the bridge deck – BAS joint will be similar to the design detail of an expansion joint found in Colorado [57] as shown in Figure 11-8, where the bridge deck – BAS joint uses a strip seal joint and a trimmed plastic pipe in the joint slot to direct water to the outside face of the wing wall. For precast BASs that are anchored to the abutment, instead of using the strip seal joint which can be difficult and time-consuming to build during construction, the bridge deck –

BAS joint may be filled with permeable materials (cement or asphalt-treated) such that runoff water can be directly drained through the permeable material and the trimmed plastic pipe. This design detail intends to provide a higher level of design reliability with respect to minimizing the embankment erosion possibilities, therefore, it is recommended for the construction of precast BASs that are anchored to the abutment, especially for districts with potentials for heavy rainfall.

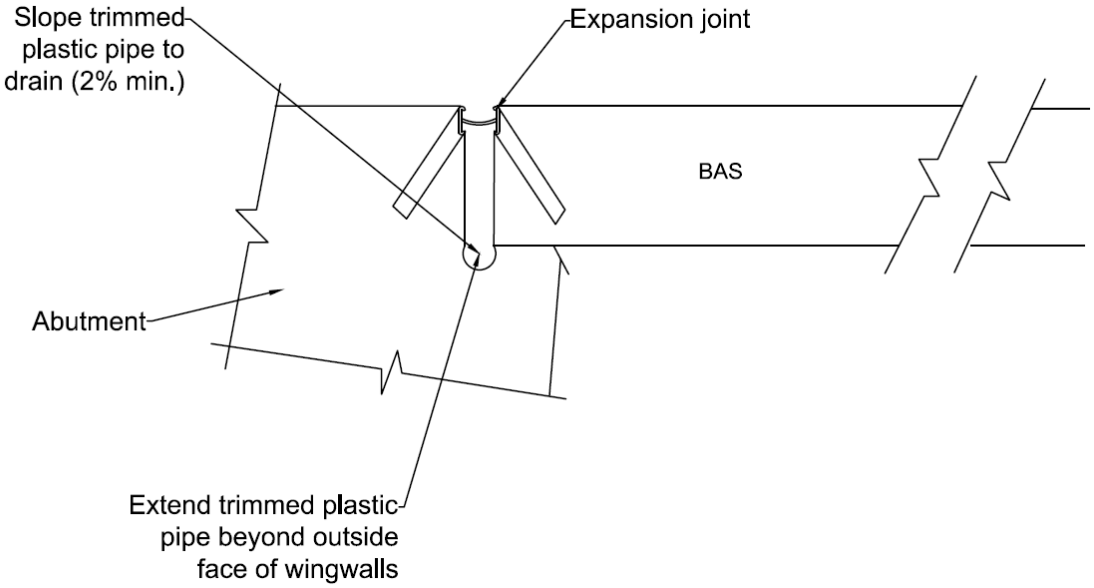

Figure 11-8 A detail of expansion joint in CDOT, after [57]

Besides this option, there are other alternatives to address the water infiltration at the abutment joint, such as using permeable materials as the base and edge drains to direct any infiltrated water away from the embankment (i.e. designing **Element 1** shown in Figure 9-13, which is addressed in Chapter 12) or placing a layer of composite drainage fabric at the face of the abutment back wall to direct any water leaking from the joint into the subsurface drainage system underneath the embankment (i.e. designing **Element 7** shown in Figure 9-13, which is addressed in the “Stone Column and Embankment Design Guideline”).

BAS – PAVEMENT JOINT DESIGN

Since the BAS are usually tied or anchored to the abutment for integral abutment bridges, the BAS becomes an extension of the bridge structure which may move as the bridge structure expands or contracts due to the effects of temperature and moisture variations. If a wide joint spacing (e.g. 15 ft.) is used for the BASs, an expansion joint needs to be placed at the BAS-pavement connection to accommodate the large thermal movement of the BAS.

However, if a narrow joint spacing (6 – 8 ft.) is used (as a means to limit thermal-induced expansive or contractive movement of the BAS), the movement of the BAS will be distributed and manifest discretely at the intermediate joints in between the individual slabs rather than concentrating excessively at the end of the BAS. Therefore, if the length of the BAS – pavement joint can be significantly reduced, it helps to maintain the tightness of the joint sealing and prevent moisture infiltration.

Concrete Pavement Joint

For precast BASs directly connecting to concrete pavements, the most widely applied practice [11, 52, 58] has been the epoxy-coated dowelled expansion joint as shown in Figure 11-9. This practice is actually very similar to the expansion joint design for the CIP concrete pavement in Oklahoma as shown in Figure 11-10. Different from the construction for CIP BASs, the dowel sleeves (1 5/8 in. in diameter) are cast in the precast BASs during panel fabrication; during the construction, one side of the epoxy-coated dowel bars (1 ½ in. in diameter) are inserted into the sleeves in the precast BASs and the other end of them are encased by the CIP concrete pavement or inserted into the holes drilled in the vertical face of the existing concrete pavement; then the expansion joint is formed by placing a flexible foam (as a joint filler material) over the dowel bars, topped with a waterproof sealant material to prevent the moisture from infiltrating into the expansion joint.

Figure 11-9 Epoxy-coated dowels to be installed at the BAS – pavement joint [11]

The joint seal should be capable of accommodating the movement of the expansion joint (which can be determined based on the calculation elaborated in Chapter 10). In Oklahoma, poured silicone seals are usually used as the sealing material. This type of sealant was considered to be not only long-lasting (typically 10 – 15 years) [59], but also easier and faster for installation [60] compared with other types of sealants. The poured silicone seal can be used for joints up to 3 in. wide and accommodate movement up to 0.25 in. (depending on the types of products) [61].

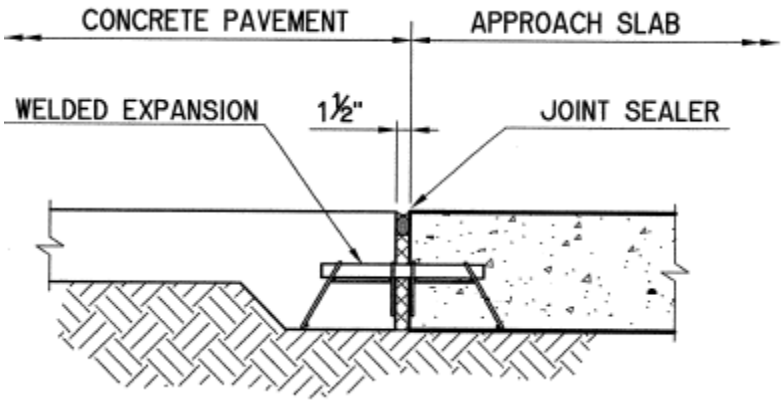

Figure 11-10 BAS – pavement expansion joint detail in Oklahoma [2]

Another detail often used in Oklahoma for sealing concrete joints is the use of an open cell foam compression sealer as shown in Figure 11-11. This type of sealer which consists of the silicone facing and the foam body is installed and glued into concrete joints by applying epoxy on the concrete joint faces and field-injected silicone sealant at

the edge of the silicone facing. The sealer allows movement ranging from 0.5” – 4”. The greatest advantage of this sealer is that it is free of compression or tension failures [62].

Regardless of what the joint sealing material is used, the practitioner should obtain the key specifications from the manufacturer such that the joint sealing material is able to accommodate the movement the joint.

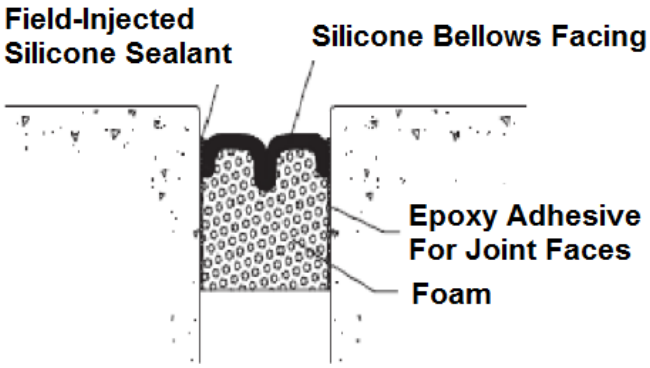

Figure 11-11 Open cell foam compression seal [62]

Asphalt Pavement Joint

For precast BASs connecting to asphalt pavements, special attention should be paid to the design of the BAS – pavement transition. In this case, a transition concrete slab may be placed (as a buffer) in between the precast BAS and the asphalt pavement as shown in Figure 11-12 [63]. The objective of applying the transition slab is to 1) provide an expansion joint to facilitate the movement of the BAS; 2) reduce the free edge deflection at the edge of the BAS and 3) provide a continuous and smooth transition between the concrete BAS and the asphalt pavement (i.e. at both the joint with BAS and the joint with asphalt pavement).

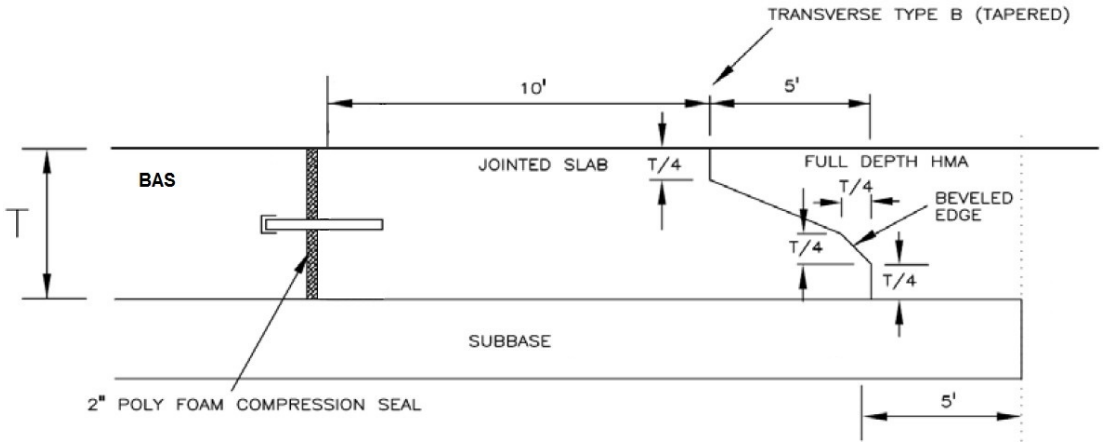

(a)

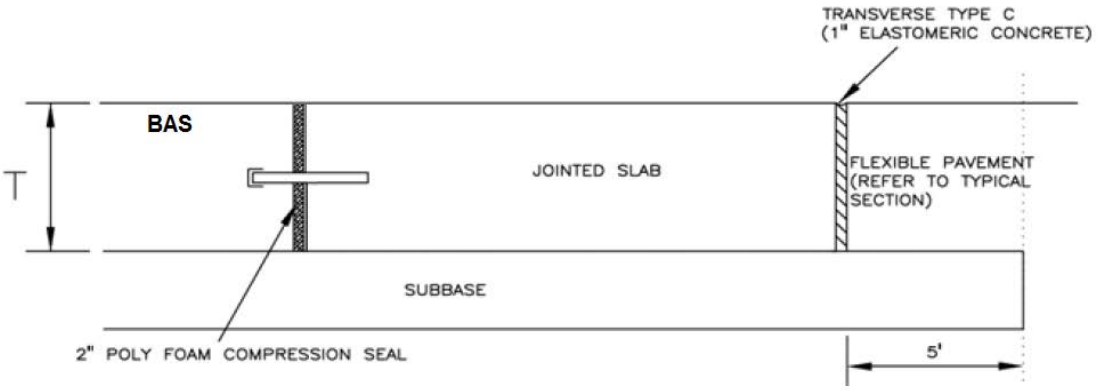

(b)

Figure 11-12 BAS – pavement transition design using (a) transition-tapered slab and (b) transition-elastomeric slab, after [63]

As shown in Figure 11-12 (a), the first option is to use a tapered transition slab between the BAS and the asphalt pavement. The pavement end of the transition slab is designed with a beveled edge as a means to minimize crack reflection in the asphalt pavement. Alternatively, an elastomeric concrete joint (as shown in Figure 11-12 (b)) may be applied to accommodate the movement between the transition slab and the asphalt pavement. Note that the elastomeric concrete joint should be installed by cutting a slot at the transition slab after all the pavement slabs are placed. In addition, the base of the BAS should extend into the asphalt pavement section for at least 5 ft. if it is different from the base of the asphalt pavement for both the two options.

Drainage Considerations

For BASs connecting to either concrete or asphalt pavements, a greater level of design assurance with respect to reducing the potential of base erosion is to include drainage considerations at these joints. Although the joint sealing materials are designed to perform well for many years, however, they may eventually deteriorate and break down under the effects of environmental factors and traffic repetitions. Therefore, transversely placing a perforated underdrain pipe underneath the BAS – pavement joint can be an effective practice to facilitate drainage. The selection criteria for the underdrain practice are:

1. For districts with heavy rainfall potential; and
2. When the base layer material is not drainable, such as the lime or cement stabilized bases.

BAS DRAINAGE DESIGN CONSIDERATION

One drainage condition previously observed shown in Figure 11-13 (a) concerned water infiltration at the widened joint (due to load induced movement of wing wall or settlement of BAS) between the wing wall and the BAS. This situation can be avoided by building the concrete barrier parapet directly over the edge of the BAS as shown in Figure 11-13 (b); this configuration prevents runoff water from directly infiltrating into the joint between the wing wall and the BAS [64, 65]. For precast BASs, the reinforcement for the concrete barrier parapet should be cast in the BAS such as that shown in Figure 11-14 (a), which facilitates the construction of the parapet on the job site and eliminates the joint between the parapet and the BAS.

(a)

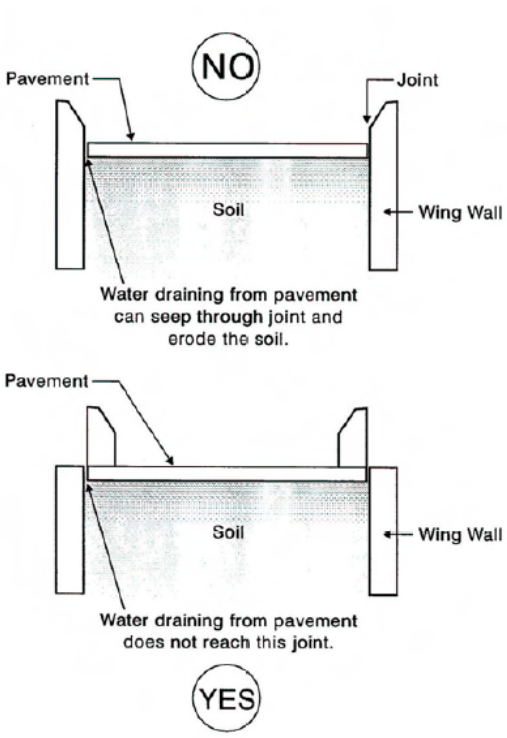

(b)

Figure 11-13 (a) Separation between wing wall and BAS [66], (b) poor and good practices of wing wall and BAS details [64, 65]

(a)

(b)

Figure 11-14 Concrete barrier parapet on precast BASs (a) during construction, (b) after construction [67]

Currently, the Oklahoma DOT standard design for BAS surface drainage relies on the use of mounted concrete curb to direct surface runoff water to a gutter system at the shoulder of the embankment area as shown in Figure 11-15. With appropriately designed slope at the surface of BASs, this design allows the runoff water to be directed away from the main pavement area to the guardrail/parapet widening area, which

appears to effectively protect the base from erosion. Therefore, this design detail is recommended for future projects. For precast BAS constructions, the reinforcement of the mounted curbs should also be cast in the precast BAS to avoid any unnecessary joints.

(a) (b)

Figure 11-15 Drainage system at the Hereford Lane site (a) location of the gutter system at the curb and (b) the gutter system at the side of the embankment

For the area subjected to heavy rainfall potential, a surface drainage inlet may be cast at the shoulder of the BAS or at the end of a bridge deck to prevent runoff water from getting into expansion joints. This type of drainage design was used at the shoulder of a BAS in Iowa as shown in Figure 11-16; White et al. [8] pointed out that the use of this large-diameter surface drainage system and the gutter system in the shoulder appeared to be effective since no soil erosion was observed underneath the BAS. A similar design was found in New Mexico at the end of a bridge deck, where a drop-inlet was used; Lenke [68] commented that this type of design functioned very well since the BASs that used this drainage design had very minimal bump issues. Note that routine maintenance may be carried out to check the drainage inlet/outlet for blockage.

(a)

(b)

Figure 11-16 Surface drainage inlets (a) at a BAS in Iowa [8] and (b) at a BAS in New Mexico [68]

CHAPTER 12

CONSTRUCTION OF PRECAST CONCRETE

This chapter provides a general guideline for the construction of BAS using precast concrete pavement (i.e. JPrCP and PPCP), including the following activities [10, 11, 43, 51, 52]:

1. Panel manufacture and storage;
2. Base type selection and preparation;
3. Panel installation;
4. Post-installation activities.

PANEL MANUFACTURE AND STORAGE

The standards for manufacture and storage of precast concrete panels have been well-established both by highway agencies and industry, including the requirements for fabrication facilities, production operations and quality control procedures; participation of highway agency or industry-managed precast plant certification program is a necessity prior to the operation of manufacturing facility.

The process of panel manufacturing starts with:

1. Setting up formwork and casting beds which should be able to maintain required tolerance for panel fabrication after repeated use;
2. Installing panel hardware (depending on specific design features), including steel reinforcement, pretensioning strands, ducts for post-tensioning (per design), lifting anchors, block-outs for load transfer (dowel bars or post-tensioning stressing pockets), dowel bars (per design), grout tubes and anchor sleeves (per design);
3. Performing pretensioning if pretensioning method is applied; the effective prestress due to pretensioning can range from 100 – 200 psi;
4. Placing concrete into the formwork; either conventional concrete (7 – 9 in. slump is required) or self-consolidated concrete may be used; performing surfacing and texturing; curing the panels using plastic sheeting;

5. Releasing pretensioning strands from anchorage (per design) and stripping formwork when the strength of concrete reaches at least 2000 psi (or 3000 – 4000 psi if pretensioned);
6. Performing finishing procedures, including cleaning block-outs, marking panel information, repairing damaged panel surface if any, rounding panel edges and checking panel dimension tolerances.
7. Once panels are manufactured, they are moved to storage locations. A layer of curing compound may be applied at the edges of panels to minimize moisture evaporation. The panels should be stacked on solid dunnage to minimize warping and should be arranged in the order for construction need. The upper panel of a stack should not be used as a storage area.

BASE TYPE SELECTION AND PREPARATION

The selection of the base material is one of the most important aspects in the design considerations of BASs. The base should be designed in order to not only provide sufficient structural capacity in terms of modulus, thickness and bondability (which are design considerations incorporated into the procedure for designing the thickness of BAS as elaborated in Chapter 10), but also to have good resistance to erosion damage and settlement or proper drainability to avoid the accumulation of runoff water. In addition, considerations related to the construction/preparation of base are also important concerns when it comes to selecting appropriate design details for the base.

Base Type Selection

Currently, the standard in Oklahoma is to place the BAS directly on top of the CLSM wedge; with regard to the inclusion of an additional base layer (i.e. **Element 1** as shown in Figure 9-13) between the BAS and the embankment backfill wedge, the following criterion can be applied: If a greater level of design reliability is needed with respect to the erosion prevention in BASs (i.e. by assuming that the joint sealant will eventually fail to prevent moisture infiltration and the CLSM is designed impermeable

and erodible), an additional drainable and less erodible base layer should be placed in between the BAS and the CLSM.

A few base layer options can potentially be used for precast BASs:

1. Untreated crushed stone aggregate base as was used in Iowa [11] and Missouri [43] projects (shown in Figure 12-1). This type of aggregate is usually made of pure granite or limestone which is crushed to create a range of particle sizes in order to make it easier for compaction as well as providing better load bearing capacity. A typical gradation of the crushed stone aggregate base can be found in Table 12-1. The main advantage of using the crushed stone aggregate base is to facilitate drainage beneath the BAS through connecting the aggregate base to the drains installed along the longitudinal edges of the pavement slabs.

Table 12-1 The gradation requirement of the crushed stone aggregate base [54]

Sieve	Percent by weight
Passing 1 in	100
Passing ½ in	60 - 90
Passing No. 4	35 - 60
Passing No. 30	10 - 35

Figure 12-1 Compaction of crushed stone aggregate base in Missouri [43]

Note that due to the nature of the crushed stone aggregate base (i.e. open-graded), large voids may still be prevalent at the surface of the base even after compaction is finished, which makes it very difficult to precisely perform grading. In this case, a finer type of aggregates (not passing No. 200 sieve) may be placed at the surface of the crushed stone aggregate base as a bedding layer to facilitate precise grading [11]. However, it should be noted that if the size of the finer aggregates is not well designed, there is a risk that the drainage may be restricted which will defeat the purpose of facilitating drainage and induce the potential of erosion. To overcome the potential of erosion, the elements associated with drainage concerns (elaborated in Chapter 10) may be specifically addressed (such as placing drainage pipes directly underneath the transverse joints to collect runoff water and direct them to the edge drains). In addition, high quality geotextile is recommended to be installed at the interface between the base and the CLSM wedge, which is expected to provide additional stability to the base structure as well as preventing coarse and angular aggregates from puncturing into the subgrade under the influence of heavy truck traffic;

2. Cement-treated or asphalt treated open-graded (stabilized permeable) bases are also viable options when the duration of lane-closure is not a concern during construction [10, 55]. For this type of base, the upper portion of the open-graded aggregates are stabilized using either cement or asphalt. The permeability of the open-graded base is recommended to be designed in the range of 300 – 500 ft./day and it should be noted that the stability of the open-graded based should not be affected for achieving a greater level of permeability [10]. Comparing to untreated aggregate base, the advantages of using the treated bases are 1). Increased smoothness and less voided area at the surface of the base; 2). Better controlled grade and increased stability; 3). Greater durability and resistance to rutting in the base layer; 4) Greater bonding at the slab-base interface which increases the effective slab thickness and provides greater restraint to prevent the movement of integral abutment bridges; 5) Drainage is also addressed attributed to the use of open-graded aggregates. Again, longitudinal edge drains can be used to facilitate drainage;
3. In the case where CLSM is designed to meet the requirements for both drainage and erosion resistance, precast BASs may be directly placed over the CLSM as long as the base grade is well-controlled. For rehabilitation projects where damage exist on the surface of the existing CLSM, a layer of bedding material such as fast-setting CLSM or fast-setting cementitious grout may be placed to restore the grade.

Selection criteria

The criteria to select the base type can be found in Table 12-2.

Table 12-2 Base type selection criteria

	Untreated aggregate base	**Treated aggregate base**

Criteria	Constrained construction time	Need for greater slab-base bonding (i.e. Integral abutment bridge)
	Constrained budget	Need for greater reliability

Base Preparation

Prior to the placement of precast panels on site during construction, base preparation is very important to achieve satisfactory performance of new BASs; for rehabilitation of existing BASs, it often requires regrading the existing base to provide a uniform base support.

Different from the preparation for the base of pavement, special attention needs to be paid for the base preparation of BASs with respect to minimizing settlement and erosion issues. Based on the experience of previous precast BAS construction projects [11, 43, 52], the following is recommended:

1. Use base materials with higher modulus to minimize settlement; in most of the previous precast BAS projects, coarse aggregates (e.g. crushed limestone) were used as the base material;
2. Install subsurface underdrain system prior to placing new base material, if necessary;
3. If the existing embankment material is not suitable for directly being used as base, then undercut the supporting area to allow for placing satisfactory base materials; besides using a coarse aggregate base, cement-treated permeable base (CTPB) and rapid-setting lean concrete base (RSLCB) may also be viable options for new construction where lane closure time is not the major concern. Operations are not allowed on neither the base types until either their compressive strengths reach 100 psi or 2 hours after placement; otherwise, surface damage can occur at the surface of the bases during panel installation [2].

4. Place surcharge load on the embankment to expedite the occurrence of primary consolidation settlement;
5. Properly consolidate the base material to the desired elevation and use Nuclear Density test to ensure compaction quality; Figure 12-2 shows a figure of the compaction operations and the gradation the aggregate base for a PPCP BAS demonstration project in Iowa, where a portable vibratory compactor was used to perform the base material compaction [11].

Figure 12-2 Compaction and grading of aggregate base in a PPCP BAS demonstration project in Iowa [11]

6. Place a thin layer of bedding material (fine-grained unbound or rapid setting material) to achieve smooth grade; this can be performed by using a precision grading system shown in Figure 12-3. The system uses accurate grade rails laying longitudinally along each side of the grading area, a grading screed is pushed along the rail to perform grading at the surface of the base area [52].

Figure 12-3 Precision grading of base layer [18].

7. Place a layer of bearing pads on the paving notch of the abutment (space designated for laying one end of the BAS).

PANEL INSTALLATION

Once the base preparation is finished, precast panels installation is conducted. Due to the differences in the panel connection procedure and joint load transferring devices, the panel installation procedures are different for JPrCP and PPCP.

JPrCP

Prior to the placement JPrCP panels, it is required to perform different drilling styles at the edges of existing pavement to accommodate dowel bars for joint load transferring depending on the dowel slot system used in the precast panels (i.e. either top or bottom slot system):

1. If a top slot system is used, the top of the adjacent pavement slab needs to be jackhammered to create slots, then removing debris from the slots and sandblasting the slots; four slots spaced at 12 in. are usually cut per wheel path;

2. If a modified narrow top surface slot system is used, holes that are about 7 – 8 in. long need to be drilled at the vertical face of the adjacent slab; once precast panels are placed, epoxy grouting is injected into the holes before dowel bars are slid into them;
3. If a bottom slot system is used, holes are drilled at the vertical face of the adjacent slab and filled with epoxy grouting, then dowel bars are inserted into the adjacent panels prior to placement of precast panels.

Two options are available for panel installation of JPrCP:

1. The first option is to directly place precast panels on a finished base layer which has been fine-graded and compacted to the desired elevation; this normally involves the use of a layer of fine-grained granular material as bedding material and the application of a precision grading system as shown in Figure 12-3 to perform accurate grading;
2. The second option uses threaded setting bolts to position the precast panels. As shown in Figure 12-4, a precast panel is equipped with four symmetrically positioned leveling rods with threads on top portion; accordingly, four seating plates are placed at the same locations on top of the existing base prior to installation of the panel to match the bolts. Once the panel is installed and positioned, a rapid-setting bedding material is injected into the gap between the panel bottom and the existing base through the undersealing access holes in the panel. Once the bedding material reaches a compressive strength of 50 psi, the bolts are removed and the access holes are grouted.

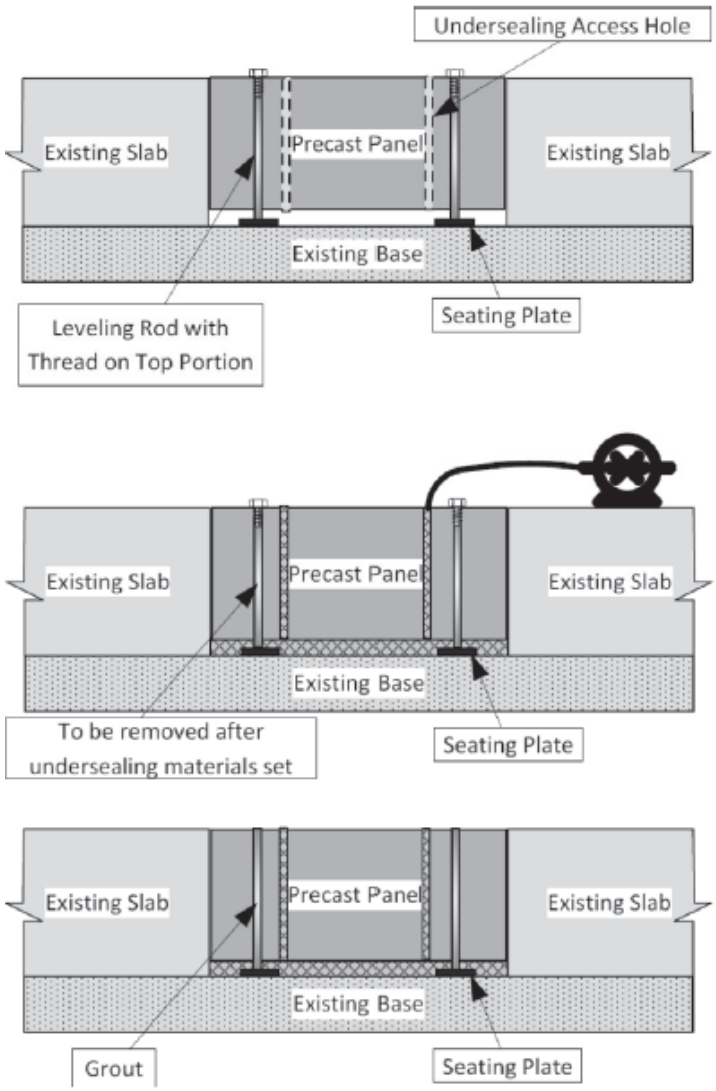

Figure 12-4 Threaded setting bolts installation option [10]

PPCP

The panel installation procedure for PPCP is different from JPrCP due to the inclusion of post-tensioning.

The procedure of PPCP panel installation starts with placing the abutment panel as shown in Figure 12-6 (a) on the paving notch of the abutment; then anchor the abutment panel to the paving notch through the pin sleeves located at the edge of the panel to prevent it from moving during post-tensioning; once the abutment panel is set

into the final position, the rest panels are installed one at a time using the following procedure:

1. Place the adjacent panel into a temporary position with a gap left between the previous panel for applying joint epoxy and installing gasket for the post-tensioning ducks;
2. Feed post-tensioning strands into the ducks from the anchor at the joint panel to the anchor at the abutment panel;
3. Apply a thin layer (1/8 in.) of epoxy at the keyway joint face as shown in Figure 12-5, to fill any unevenness or voids after panel assembling and seal the joint to prevent water from infiltrating into the underlying base layer;

Figure 12-5 Application of joint epoxy in the Iowa demonstration project [11]

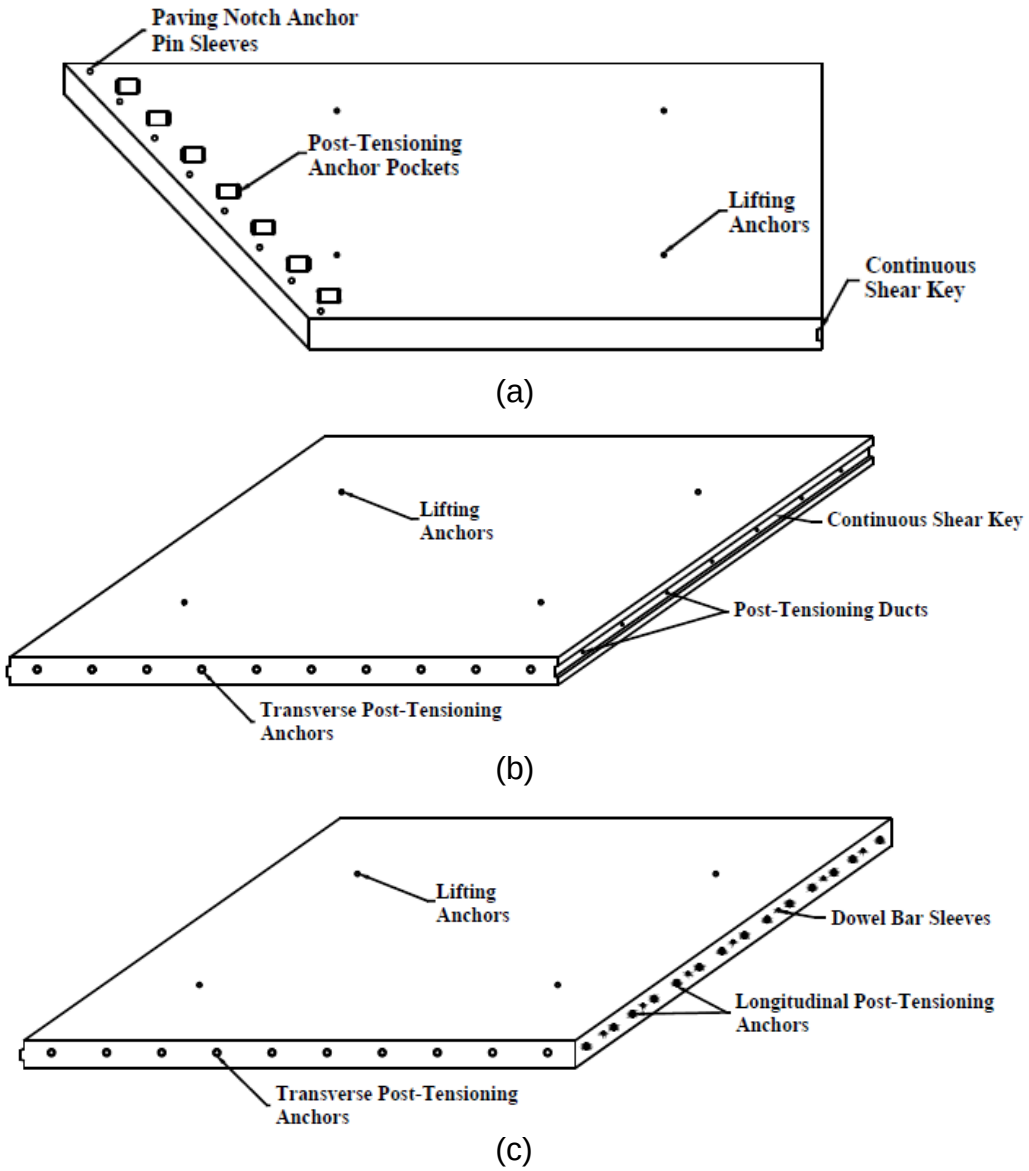

Figure 12-6 Precast penal design details of a PPCP BAS demonstration project in Iowa (a) abutment panel, (b) base panel, and (c) joint panel [11]

4. Perform temporary post-tensioning to bring two adjacent panels together using only two strands located at the quarter points (i.e. ¼ and ¾) of the panel; squeeze out the excessive epoxy and maintain the post-tensioning stress; once the epoxy reaches an initial set, release the temporary post-tensioning force and perform installation for the next panel;

5. Once all the panels are in their final positions, perform final post-tensioning where the strands are post-tensioned to 75% of their ultimate tensile strength; the final post-tensioning starts from the strands near the center of each panel and alternates out to the ones at the edges. If the panels are designed with two-way post-tensioning, longitudinal post-tensioning needs to be performed prior to the transverse post-tensioning;
6. The elongation of post-tensioning strands needs to be measured with an accuracy of 1/8 in. and compared against the theoretical value which can be computed using the following equation [53]:

$$\delta = \frac{PL}{E_S A_S + E_e A_e} \quad (12\text{-}1)$$

where δ is the theoretical elongation, P is the applied load, L is the length of the slab, E_S is the young's modulus of the steel (typically 28000000 psi), A_S is the cross-section area of the steel, E_e is the young's modulus of the epoxy (typically 3500000 psi) and A_e is the surface area of the epoxy (typically 1.56 E-4 in^2). If the difference between measured and theoretical values exceeds 7%, then post-tensioning needs to be ceased until the issue is resolved.

In addition, it should be noted that a new construction practice referred to as the incrementally connected precast concrete pavements (ICPCP) as shown in Figure 12-7 is recommended for constructing BASs. This practice allows the shortly-spaced precast panels to be connected segmentally, therefore reducing the effective friction during the final post-tensioning and avoiding the necessity of using polyethylene sheeting (as a means to reduce friction during construction) underneath the concrete slab. By applying this practice, greater concrete panel-base friction resistance will develop which helps to prevent the abutment from moving.

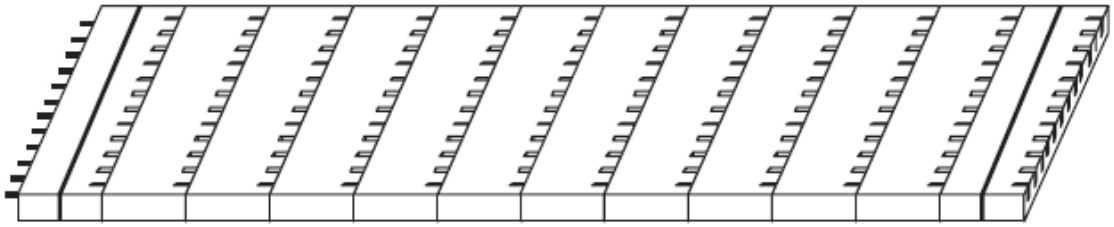

Figure 12-7 A representation of ICPCP [10]

POST-INSTALLATION ACTIVITIES

Once the panels are post-tensioned, the following activities need to be performed before the BAS can be open to traffic:

1. Pump grout into the post-tensioning ducts through grout inlets as soon as post-tensioning is finished; grouting should be finished uninterrupted within one operation and full grouting is checked when grout flow out from outlet;
2. Perform under-slab grouting to fill voids underneath the BAS to achieve full support condition by using rapid-setting cementitious materials that can provide compressive strength of 500 psi once hardened. The grout pressure needs to be controlled to lower than 30 psi to avoid the risk of panel lifting;
3. Perform joint sealing at the longitudinal joints according to the agency's practice; For two-way post-tensioning system, if an open keyway is used (in order to overcome the issue of joint mismatch if the pavement is crowned at the centerline of roadway) at the longitudinal joint as shown in Figure 12-8, it needs to be filled with gavel concrete mixture prior to performing transverse post-tensioning; in this case, perform initial transverse post-tensioning (10% of ultimate tensile strength) 3 – 4 hours after filling the joint and then final transverse post-tensioning (75% of ultimate tensile strength) after 24 hours. Wet burlap method may be used to cure the concrete after placement.

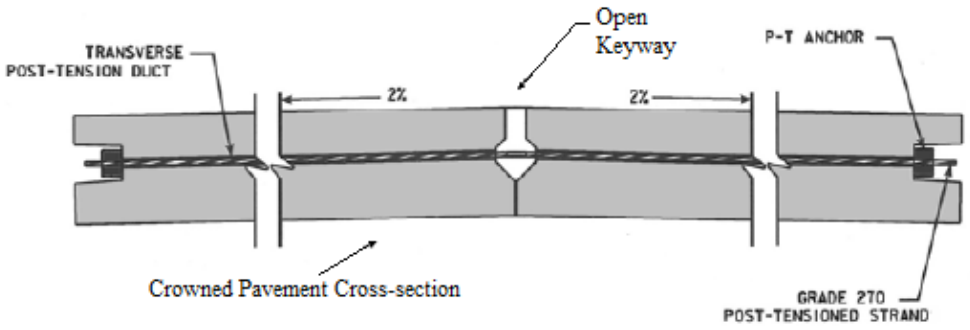

Figure 12-8 Design details of the transverse post-tensioning and longitudinal open keyway in the Iowa demonstration project [11]

4. Fill the post-tensioning anchor pockets using the same concrete mixture and at the same time when longitudinal joints are filled;
5. Install epoxy coated dowel bars at the joint panel; if the adjacent pavement is cast-in-place, then dowel bars are enclosed by concrete; if the adjacent pavement is existing, dowel bar slots need to be cut and filled with grout once dowel bars are placed;
6. Perform surface grinding to achieve satisfactory surface smoothness for high-speed traffic. A layer of asphalt overlay may be placed on top of the precast panels as the riding surface.

CHAPTER 13

DESIGN EXAMPLES AND TOOLS

This chapter provides examples and tools for designing JPrCP and PPCP.

EXAMPLE DESIGN FOR JPrCP

The design for JPrCP should follow the design procedure of MEPDG; however, the design inputs and design criteria need to be adjusted to reflect the effects of using precast concrete panels. The detailed user guideline for the MEPDG design software is not further elaborated since that exceeds the scope of this guideline. The following shows an example of using the MEPDG procedure to design JPrCP [10].

Step 1

1. Determine the input values as if designing a conventional CIP JCP;
2. Select trial design inputs (i.e. the thicknesses of precast concrete panel and underlying base layers) for JPrCP;
3. Modify the following inputs for designing a JPrCP;
    - Use a concrete modulus of rupture of 750 psi;
    - Use 50% of the actual ultimate concrete drying shrinkage (needs to be calculated using Equation (10-10)). For simplicity, this example assumes the actual ultimate concrete drying shrinkage to be 600 με.

The design inputs of the example are shown in Table 13-1.

Table 13-1 Design inputs of the design example of JPrCP [10]

Site Conditions	Project site	Oklahoma City
	Traffic ESALs, million	100
Design limits	Design reliability	90%
	Design service life, years	40
Design Criteria	Cracking, %	25
	Faulting, in	0.15

	Smoothness (IRI), in/mi	180
Precast Concrete Panel	Thickness, in	10
	Lane width, ft	12
	Transverse joint spacing, ft	6
	Dowel bar diameter, in	1.5
	Dowel bar spacing, in	12
	Modulus of rupture at 28-day, psi	750
	Concrete CTE, millionth in/in/˚F	5.5
	Permanent curl/warp effective temperature difference, ˚F	-10
	Concrete ultimate drying shrinkage, 10^{-6} in	300
Permeable Granular Base	Thickness, in	6
	Modulus of elasticity, psi	15000
	Base erodibility index	erosion resistant (level 3)
	Loss of full friction, months	480
Subgrade	Modulus of elasticity, psi	8000

Step 2

1. Establish design criteria for JPrCP. The recommended design criteria for a JPrCP with an initial service life of 40 years is shown in Table 13-2;
2. Perform trial design analysis using the design inputs and criteria of JPrCP with the assistance of MEPDG design software;
3. The design software predicts the following performance results as shown in Table 13-2, where all the design criteria are met; therefore, the design alternative is valid. Otherwise, the inputs in ***Step 1*** (i.e. the thickness of precast concrete panel or underlying base layers) need to be modified to meet the design criteria.

Table 13-2 Comparison of design criteria and predicted performance prediction results of JPrCP and CIP JCP, after [10]

	Design criteria	Predicted performance criteria
Cracking, %	25	5.3
Faulting, in	0.15	0.12
Smoothness (IRI), in/mi	180	159

Step 3

1. Evaluate design alternatives by utilizing engineering judgment and considering life-cycle cost analysis. Table 13-3 provides a comparison of various design alternatives with respect to the thickness design of JPrCP at different levels of traffic and base support conditions by using the same design criteria shown in Table 13-2.

Table 13-3 Comparison of design alternatives for JPrCP at various levels of traffic and base support conditions, after [10]

	Traffic level (estimated million ESALs)	Thickness of JPrCP, in
Poor Support Condition (base modulus = 15 ksi)	50	8.5
	100	9.5
	200	11.5
Granular Base (base modulus = 30 ksi)	50	8.5
	100	9.5
	200	11.5
Cement-treated Base (base modulus = 2000 ksi)	50	8.5
	100	9.5
	200	11.5

EXAMPLE DESIGN FOR PPCP

The overall design procedure for PPCP can be illustrated as shown in Figure 10-1. The design procedure for PPCP relies on the use of finite-element based software (e.g. ISLAB2000) and MEPDG design software, however, the detailed user guidelines for using the software are not further elaborated since that exceeds the scope of this guideline. The following shows a step-by-step example for designing PPCP [10].

Step 1

Provides a baseline design for a conventional CIP JCP following the MEPDG design procedure using default design inputs (concrete modulus of rupture of 650 psi and actual ultimate concrete shrinkage) and criteria; output a design alternative that meets the design criteria;

Design output

1. Thickness of concrete slab = 13 in.;
2. Thickness of base = 6 in.;

Step 2

The determination of PPCP panel thickness and required effective prestress can be achieved by applying two different criteria, the stress equivalent criterion and the strength equivalent criterion.

Criterion 1. Stress equivalent criterion

1. Perform tensile stresses analysis by using a finite-element based software (e.g. ISLAB2000) and obtain the relations between slab thickness and critical tensile stress at the bottom of the slab at different loading conditions, which requires the following inputs:
    a. Loading magnitude: Single axel load – 9000 lb.;
    b. Loading position: edge condition (single lane) or interior condition (multiple lanes);

c. Width of the concrete slab: 12 ft. for edge condition and 14 ft. for interior condition;
d. Length of the concrete slab: 6 ft.
e. Thickness of the concrete slab: 8 – 14 in.
f. Modulus of subgrade reaction – assuming 300 and 50 pci.

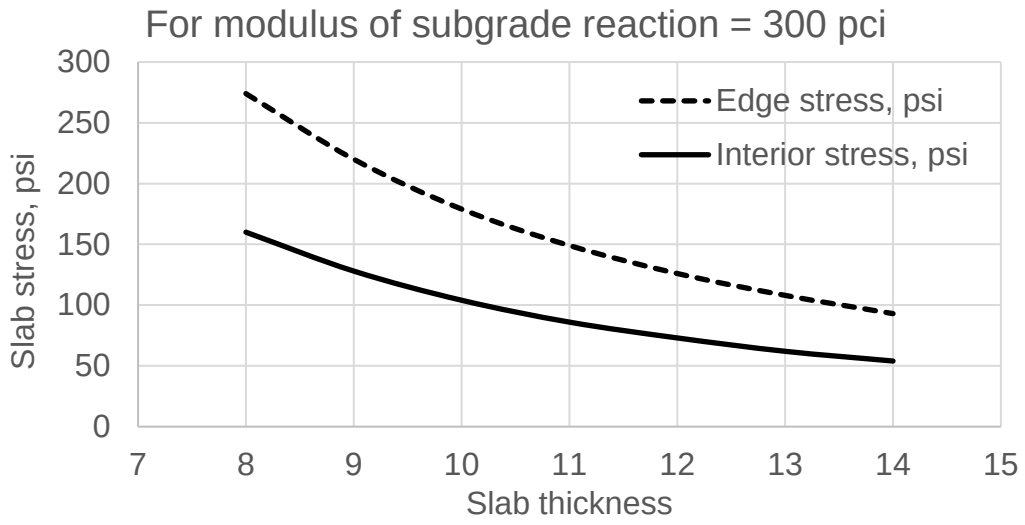

(a)

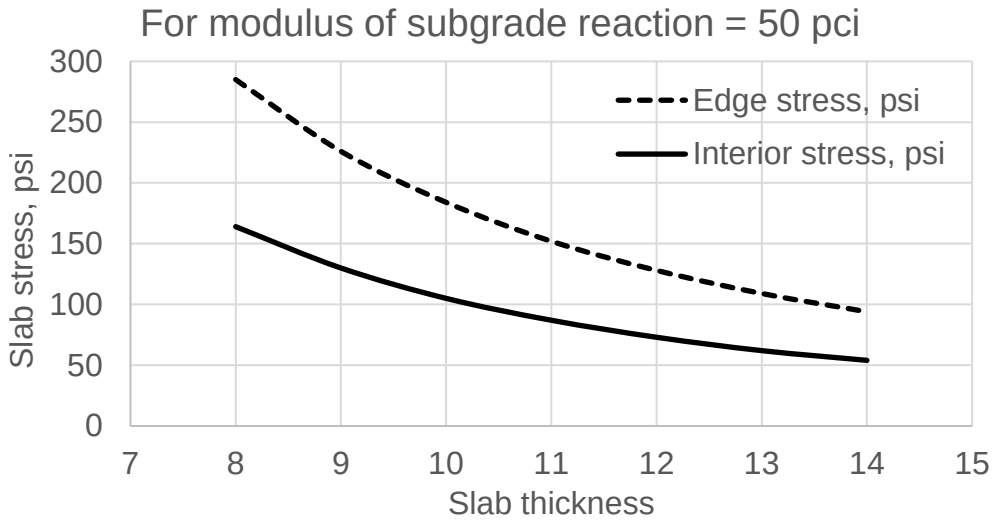

(b)

Figure 13-1 Example plots of critical panel tensile stress as a function of slab thickness for different loading conditions and modulus of subgrade reaction [10]

2. Perform trial thickness design for PPCP and determine and the required effective prestress based on critical tensile stresses dictated by slab thickness and loading condition (single-lane PPCP – edge loading condition; multi-lane PPCP- interior loading condition).

   An example of using Figure 13-1 to design PPCP panel thickness and determine the required effective prestress is given below considering an interior loading condition and a modulus of subgrade reaction of 50 pci [10].

   a. The thickness of baseline design is determined to be 13 in. from the baseline design, the edge stress at the midway of the panel is 105 psi based on Figure 13-1;
   b. Trial design input for PPCP panel thickness is assumed to be 8 in., the interior stress is 160 psi from Figure 13-1;
   c. The required effective prestress $EP_1 = 160 - 105 = 55psi$.

Criterion 2. Strength equivalency criterion

The design for PPCP thickness and required effective prestress using the strength equivalency criterion should follow the design procedure of MEPDG or any mechanistic–empirical design method that incorporates concrete flexural strength as an input. The following shows an example of using the MEPDG procedure to design PPCP [1].

Step A

1. Determine the input values as if designing a conventional CIP JCP;
2. Select trial design inputs for PPCP;
   a. Thickness of PPCP panels: 8 in;
   b. Thickness of base layer: 6 in.;
   c. Required effective prestress: $EP_2 = 150psi$.
3. Modify the following inputs for designing a PPCP;
   a. Use a concrete modulus of rupture of 850 psi (original modulus of rupture of 700 psi + required effective prestress of 150 psi);
   b. Use 50% of the actual ultimate concrete shrinkage.

The design inputs of the example are shown Table 13-4.

Table 13-4 Design inputs of the design example of PPCP [10]

Site Conditions	Project site	Oklahoma City
	Traffic ESALs, million	100
Design limits	Design reliability	90%
	Design service life, years	40
Design Criteria	Cracking, %	50
	Faulting, in	not applicable
	Smoothness (IRI), in/mi	not applicable
Precast Concrete Panel	Thickness, in	8
	Lane width, ft	12
	Transverse joint spacing, ft	6
	Dowel bar diameter, in	1.5
	Dowel bar spacing, in	12
	Modulus of rupture at 28-day, psi	850
	Concrete CTE, millionth in/in/˚F	5.5
	Permanent curl/warp effective temperature difference, ˚F	-10
	Concrete ultimate drying shrinkage, 10^{-6} in	300
Permeable Granular Base	Thickness, in	6
	Modulus of elasticity, psi	15000
	Base erodibility index	erosion resistant (level 3)
	Loss of full friction, months	480
Subgrade	Modulus of elasticity, psi	8000

Step B

1. Establish design criteria for PPCP. The recommended design criteria for a PPCP with an initial service life of 40 years are shown in Table 13-5;
2. Perform trial design analysis using the design inputs and criteria shown in Table 13-4 with the assistance of MEPDG design software;
3. The design software predicts the following performance results as shown in Table 13-5, where all the design criteria are met; therefore, the design is valid. Otherwise, the inputs in ***Step A*** (e.g. the thickness of the precast

concrete panel or the underlying base layer or the level of required prestress) need to be modified to meet the design criteria.

Table 13-5 Comparison of design criteria and predicted performance prediction results of PPCP and CIP JCP, after [10]

	Design criteria	Predicted performance criteria
Cracking, %	50	19.4
Faulting, in	not applicable	not applicable
Smoothness (IRI), in/mi	not applicable	59

Step C

1. Evaluate design alternatives by utilizing engineering judgment and considering life-cycle cost analysis. Table 13-6 provides a comparison of various design alternatives with respect to the thickness design of PPCP at different levels of traffic and base support conditions by using the same design criteria shown in Table 13-5.

Table 13-6 Comparison of design alternatives for PPCP at various levels of traffic and base support conditions, after [10]

	Traffic level (estimated million ESALs)	Thickness of PPCP, in
Poor Support Condition (base modulus = 15 ksi)	50	<8
	100	<8
	200	8
Granular Base (base modulus = 30 ksi)	50	<8
	100	<8
	200	8
Cement-treated Base (base modulus = 2000 ksi)	50	<8
	100	<8
	200	8

Initial design output

1. The initial design of PPCP panel thickness = 8 in.;

2. The initial predicted slab cracking = 19.4%;
3. The initial design of base thickness = 6 in.;
4. The initial required effective prestress is determined as the maximum value of the results determined based on the two criteria and a minimum requirement of the effective prestress (i.e. 100 psi):

$$EP_{required} = Max(EP_1, EP_2, EP_{\min}) = Max(55,150,100) = 150psi$$

Erosion Consideration

Step A. Determination of erosion damage

1. Summarize the five key parameters:
   - the ADT at the start year = 10000;
   - the percent of trucks = 60%;
   - the number of wet days (min 0.1" rain) = 50;
   - the initial design of PPCP panel thickness = 8 in.;
   - the cohesion of the base = 5 psi.
2. Refer to the database in the tab "**Percent of erosion**" of the given Excel spreadsheet and obtain the erosion damage at the end of the design life (40 years) based on the five key parameters (interpolations may be conducted if necessary): $\%E = 0.491\%$;
3. In addition, the effective coefficient of friction μ_e of the slab-base interface at the end of the design life can be readily obtained in the Excel spreadsheet: $\mu_e = 2.121$.

Step B. Determination of Erosion-Based Slab Thickness

Refer to the procedure shown in Figure 10-6 and the procedure elaborated in the tab "**Erosion-based slab thickness**" of the given Excel spreadsheet:

1. Using the Excel spreadsheet, the partially-bonded concrete layer thickness can be determined as: $h_{e-p} = 8.03\ in.$;
2. Assuming $\%E = 0$ for the new slab system and fully bonded condition for the slab-base interface;

3. Through trial and error, it is determined that the erosion-based slab thickness $h_e = 7.53\ in.$, such that $h_{e-b}{}' = h_{e-p} = 8.03\ in.$.

Step C. Reliability Analysis

Refer to the procedure shown in Figure 10-8:

Purpose 1 – Determine the final design reliability due to erosion

1. Develop a design chart to perform reliability adjustment as shown in Figure 13-2, which can be done by using the MEPGD software. The hollow points on the curves in Figure 13-2 are design outputs (i.e. predicted percent slab cracking) of MEPDG obtained by varying the slab thickness (e.g. 6.5 – 10 in.) and design reliability (e.g. 70% - 95%) while holding other inputs constant (i.e. the inputs shown in Table 13-4);
2. As shown in Table 13-5, for the initial design of concrete slab thickness = 8 in., the predicted slab cracking is 19.4%. As shown in Figure 13-2, in order to achieve the 19.4% slab cracking for the erosion-based slab thickness $h_e = 7.53\ in.$, the final design reliability has to drop from 90% to about 82%. The 8% reduction in the design reliability reflects how much the erosion damage affects the BAS performance with respect to slab cracking.

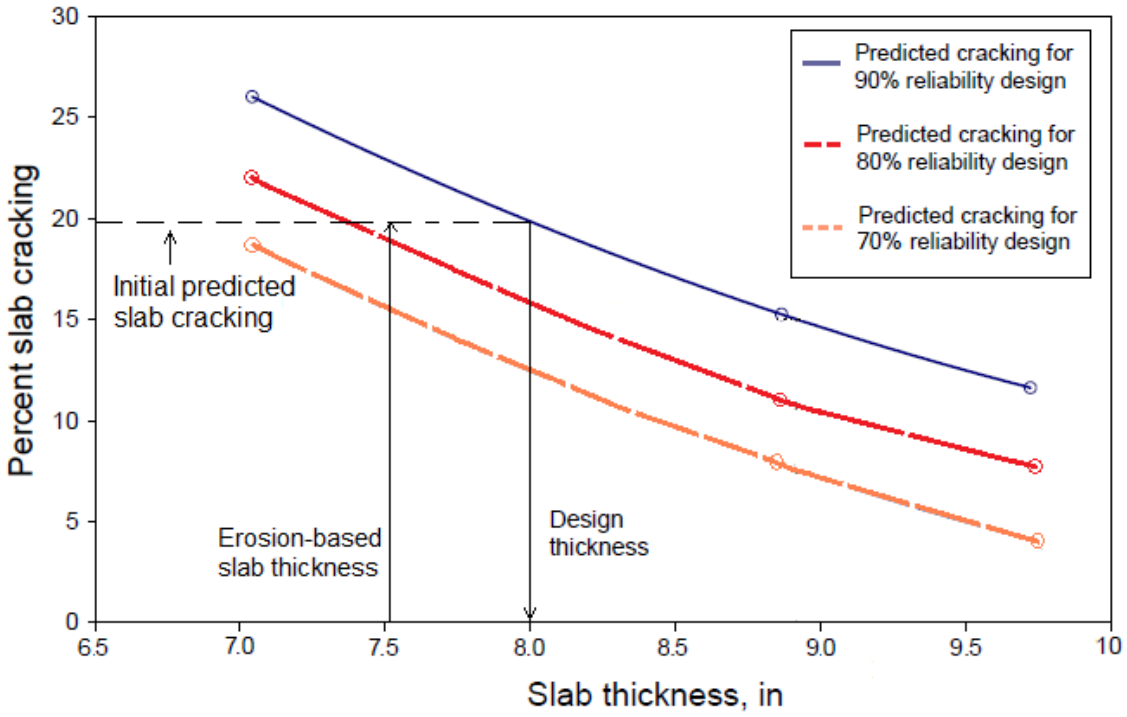

Figure 13-2 Reliability adjustment chart

Purpose 2 – Determine a new concrete slab thickness

1. If the purpose is to achieve the initial design reliability (i.e 90%), the practitioner should determine a new concrete slab thickness $h_1{}'$ such that the new erosion-based slab thickness $h_e{}'$ is equivalent to the initial design of concrete slab thickness $h_1 = 8\ in.$; this requires a few steps of trial and error by applying the procedures described in the previous steps (i.e. applying ***Step A*** to determine the erosion damage $\%E$ and the effective coefficient of friction μ_e for a trial new concrete slab thickness $h_1{}'$ and applying ***Step B*** to determine the new erosion-based slab thickness $h_e{}'$ until $h_e{}' = h_1 = 8\ in.$);
2. It is determined that the new concrete slab thickness should be $h_1{}' = 8.45\ in.$ (this leads to $\%E = 0.482\%$ and $\mu_e = 2.40$) such that the new erosion-based slab thickness $h_e{}' = h_1 = 8\ in.$.

Final design output

Purpose 1 – Determine the final design reliability due to erosion

1. The final design of PPCP panel thickness = 8 in.;
2. The final design reliability dropped from 90% to 82% due to the consideration of erosion (for predicted slab cracking = 19.4%);
3. The final design of base thickness = 6 in.;
4. The final required effective prestress is determined as the maximum value of the results determined based on the two criteria and a minimum requirement of the effective prestress (i.e. 100 psi):

$$EP_{required} = Max(EP_1, EP_2, EP_{\min}) = Max(55,150,100) = 150psi$$

Purpose 2 – Determine a new concrete slab thickness

In order to achieve the initial design reliability (i.e. 90%), the final design PPCP panel thickness is adjusted to the new concrete slab thickness $h_1{}' = 8.45\ in.$

1. The final design of PPCP panel thickness = 8.45 in. ≈ 8.5 in.;
2. The final design reliability is maintained at 90% (for predicted slab cracking = 19.4%);
3. The final design of base thickness = 6 in.;
4. The final required effective prestress is determined as the maximum value of the results determined based on the two criteria and a minimum requirement of the effective prestress (i.e. 100 psi):

$$EP_{required} = Max(EP_1, EP_2, EP_{\min}) = Max(55,150,100) = 150psi$$

For demonstration, the following steps apply the results of Purpose 2.

Step 3

1. Selecting the size and force of prestressing tendons;
    a. Tendon size: 0.6 in diameter 7-wire tendons are used;
    b. Tendon force: 75% of the ultimate load capacity = 43000 lbf;
    c. Tendon spacing: 18 in.
2. Determining the length of a PPCP section;

Table 13-7 Inputs for PPCP length determination

Maximum concrete temperature during the summer, ˚F	120
Minimum concrete temperature during the winter, ˚F	20
Concrete modulus of elasticity, psi	4000000
Concrete CTE, millionth in/in/˚F	5
Slab–base friction coefficient	20
Concrete unit weight, pci	0.0868

$$L \geq \frac{E_c \cdot \alpha \cdot \Delta T}{\mu \cdot \gamma} = \frac{4 \times 10^6 \times 5 \times 10^{-6} \times (120 - 20)}{20 \times 0.0868} / 12 = 96ft$$

Use 96 ft. for the length of PPCP BAS. Assuming the post-tensioning can be performed segmentally in every 6 ft. (same as the length of each concrete slab) of the BAS, so $L = 6ft$

3. Determining the total applied prestress based on panel thickness and tendon spacing;
    a. The area of concrete per tendon A_c = tendon spacing x panel thickness = 18 in. x 8.5 in. = 153 in.^{2}
    b. The total applied end stress f_{pe} = Tendon force/area of concrete per tendon = 43000 lbf/153 in.^{2} = 281 psi

Table 13-8 Design inputs for prestress loss calculation

Length of a PPCP section, ft	96
Tendon (strand) diameter, in	0.6
Tendon cross-sectional area, in^2	0.217
Tendon spacing, in	18
Panel thickness, in	8.5
Concrete modulus of elasticity, psi	4000000
Steel modulus of elasticity, psi	28000000
Tendon force at 75% of yield stress, lbf	43000
Slab–base friction coefficient	20
Concrete shrinkage strain, million in/in	300

Concrete ultimate creep coefficient	2.5
Steel relaxation coefficient	0.04

4. Accounting for the prestress loss due to various factors such as the slab-base friction, concrete shrinkage and creep and etc., the required design inputs are summarized in Table 13-8;
    a. Prestress loss due to slab-base friction:

    Assuming the post-tensioning can be performed segmentally in every 6 ft. of the BAS, so $L = 6ft$

    $$\sigma_F = \frac{\mu L}{2} = 20 \cdot 6ft/2 = 60psi$$

    b. Prestress loss due to concrete shrinkage:

    For simplicity, this example assumes the actual ultimate concrete drying shrinkage to be 600 με, therefore the ultimate concrete drying shrinkage for precast slab is 300 με. However, the practitioner should calculate the actual ultimate concrete drying shrinkage using Equation (10-10) based on the properties of real concrete mixture.

    Based on Table 10-4, $A_s = 0.217\ in^2$ for 0.6 in. diameter tendons

    $$f_s = \varepsilon_s E_S(\frac{A_s}{A_c}) = 300 \text{ x } 10^{-6} \text{ x } 28000000 \text{ x } (\frac{0.217}{153}) = 11.91 \text{ psi}$$

    c. Prestress loss due to concrete creep:

    $$f_{cr} = C_u \frac{E_s}{E_c} f_{pe}(\frac{A_s}{A_c}) = 2.5 \text{ x } \frac{28000000}{4000000} \text{ x } 299 \text{ x } (\frac{0.217}{153}) = 7.42 \text{ psi}$$

    d. Prestress loss due to steel relaxation:

    $$f_r = \rho \cdot f_{pe} = 0.04 \times 281 = 11.24psi$$

    e. Total prestress loss = 60 + 11.91 + 7.42 + 11.24 = 90.57 psi
5. Determining the effective prestress by subtracting the prestress loss from the total applied prestress.
    a. $P_{effective}$= The total applied end stress – the total prestress loss = 281 – 90.57 = 190.43 psi

Design output

1. Compare the effective prestress $P_{effective}$ with the required effective prestress $EP_{required}$ determined from ***Step 2***

$$P_{effective} = 190.43psi > EP_{required} = 150psi$$

   Therefore the design is valid.
2. Otherwise, adjust the length of a PPCP section, tendon spacing or panel thickness until $P_{effective} \geq EP_{required}$

Step 4

Determine the inputs required for calculating PPCP panel movement and designing joint width. Example inputs are shown in Table 13-9.

Table 13-9 Design inputs for total movement calculation [10]

Length of a PPCP section, ft	96
Maximum concrete temperature during the summer, ˚F	120
Minimum concrete temperature during the winter, ˚F	20
Concrete temperature at install, ˚F	70
Minimum joint width, in	0.25
Concrete CTE, millionth in/in/˚F	5
Concrete ultimate creep coefficient	2.5
Total applied end stress, psi	281
Effective prestress, psi	190.43
Concrete modulus of elasticity, psi	4000000
Concrete shrinkage strain, million in/in	300

Movement calculations

1. The temperature variation induced movement:

$dL_{Temp} = (T_{c\max} - T_{c\min}) \times CTE_c \times L =$ (120-20) $\times$ 5 $\times$ 10^{-6} $\times$ (96 x 12) = 0.576 in

2. The creep induced movement:

$$dL_{creep} = C_u \times (P_{end} + P_{effective})/2 \times (1/E_c) \times L$$
$$= 2.5 \times (281 + 190.43)/2 \times (1/4000000) \times (96 \times 12)$$
$$= 0.170 \text{ in.}$$

3. The shrinkage induced movement:

$$dL_{shrinkage} = \varepsilon_s \times L = 300 \times 10^{-6} \times (96 \times 12) = 0.3456 \text{ in.}$$

4. Total movement of a PPCP section:

$$dL_{Total} = dL_{temp} + dL_{creep} + dL_{shrinkage} = 0.576 + 0.170 + 0.3456 = 1.09 \text{ in.}$$

Joint width calculations

1. Set minimum joint width $dL_{\min} = 0.25$ in.
2. Joint width at the time of installation:

$$JW_{Install} = dL_{\min} + (T_{\max} - T_{Install}) \times CTE_C \times L$$
$$= 0.25 + (120\text{-}70) \times 5 \times 10^{-6} \times (96 \times 12)$$
$$= 0.538 \text{ in.}$$

3. Long-term minimum joint width:

$$JW_{(L-T)\min} = dL_{\min} + dL_{creep} + dL_{shrinkage}$$
$$= 0.25 + 0.17 + 0.3456$$
$$= 0.766 \text{ in.}$$

4. Maximum joint width:

$$JW_{\max} = dL_{\min} + dL_{total} = 0.25 + 1.09 = 1.34 \text{ in.}$$

The long-term joint width variation is shown in Table 13-3.

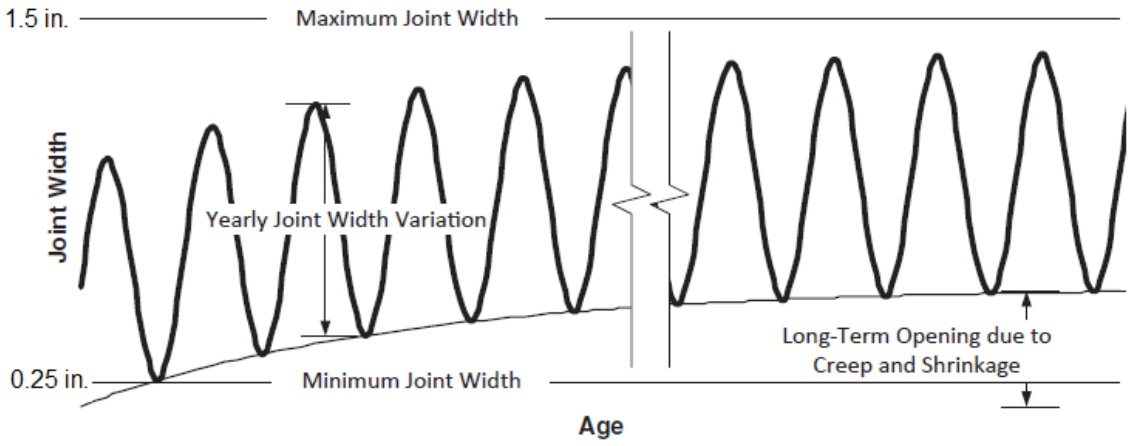

Figure 13-3 Long-term joint width variation [10]

Design output

1. The joint width at the time of installation = 0.538 in.;
2. Long-term minimum joint width = 0.766 in.;
3. Maximum joint width = 1.34 in. < 1.5 in. OK;
4. If the maximum joint width is greater than 1.5 in., then revise design inputs (i.e. length of a PPCP section and total applied end stress) and re-design starting from ***Step 3***.

JPrCP DESIGN WORKSHEET

Site Conditions

Project site: Oklahoma City Traffic ESALs, million: 100

Design limits

Design reliability: 90% Design service life, years: 40

Design Criteria

Cracking, %: 25 Faulting, in: 0.15 Smoothness (IRI), in./mi.: 180

Precast Concrete Panel

Thickness, in.: 10 Lane width, ft.: 12

Transverse joint spacing, ft.: 6

Dowel bar diameter, in: 1.5 Dowel bar spacing, in: 12

Modulus of rupture at 28-day, psi: 750

Concrete CTE, millionth in/in/˚F: 5.5

Permanent curl/warp effective temperature difference, ˚F: -10

Concrete ultimate drying shrinkage, 10^{-6} in.: 300

Permeable Granular Base

Thickness, in.: 6 Modulus of elasticity, psi: 15000

Base erodibility index: erosion resistant (level 3)

Loss of full friction, months: 480

Subgrade

Modulus of elasticity, psi: 8000

PPCP DESIGN WORKSHEET

Step 1

Baseline design

Baseline thickness of the concrete slab, in.: 13

Thickness of base, in.: 6

Step 2

Criterion 1. Stress equivalent criterion

Perform analysis using ISLAB2000

Loading magnitude, lb: 9000

Loading position (edge or interior): interior

Width of the concrete slab, ft.: 12

Length of the concrete slab, ft.: 6

Modulus of subgrade reaction: pci: 300

Baseline thickness of the concrete slab, in: 13

Trial PPCP panel thickness design, in: 8

Determine effective prestress using output of ISLAB2000

Refer to Table 13-1

Edge stress for baseline thickness design, psi: 105

Stress at loading position (edge or interior): interior for the trial PPCP panel thickness design, psi: 160

Required effective prestress, EP_1, psi: 160 - 105 = 55

Criterion 2. Strength equivalency criterion

Site Conditions

Project site: Oklahoma City Traffic ESALs, million: 100

Design limits

Design reliability: 90% Design service life, years: 40

Design Criteria

Cracking, %: 50 Faulting, in: N/A Smoothness (IRI), in./mi.: N/A

Precast Concrete Panel

Thickness, in.: 8 Lane width, ft.: 12

Transverse joint spacing, ft.: 6

Dowel bar diameter, in: 1.5 Dowel bar spacing, in: 12

Required effective prestress, EP_2, psi: 150

Modulus of rupture at 28-day, psi: 700+150 = 850

Concrete CTE, millionth in/in/˚F: 5.5

Permanent curl/warp effective temperature difference, ˚F: -10

Concrete ultimate drying shrinkage, 10^{-6} in.: 300

Permeable Granular Base

Thickness, in.: 6 Modulus of elasticity, psi: 15000

Base erodibility index: erosion resistant (level 3)

Loss of full friction, months: 480

Subgrade

Modulus of elasticity, psi: 8000

Initial Design output

Initial PPCP panel thickness, in. 8

Initial predicted slab cracking: 19.4%

Initial base thickness, in. 6

Initial required effective prestress, $EP_{required} = Max(EP_1, EP_2, EP_{\min})$, psi: 150

Erosion Consideration

Step A. Determination of erosion damage

ADT at the start year: 10000

Percent of trucks: 60%

Number of wet days (min 0.1" rain): 50

Initial design of PPCP panel thickness, in.: 8

Cohesion of the base, psi: 5

Refer to the database in given the Excel spreadsheet and obtain the:

Percent of erosion, $\%E$: 0.491%

Effective coefficient of friction, μ_e: 2.121

Step B. Determination of erosion-based slab thickness

Perform calculations in the Excel spreadsheet to obtain:

Partially-bonded concrete layer thickness, h_{e-p}: 8.03 in.

Through performing trial and error in the Excel spreadsheet, determine:

Erosion-based slab thickness, h_e: 7.53 in., such that the effective slab thickness of the two systems are equivalent (i.e. $h_{e-b}{}' = h_{e-p}$).

Step C. Reliability analysis

Perform design using MEPDG software by varying the slab thickness and design reliability while holding other inputs constant (i.e. the inputs shown in Table 13-4):

The range of slab thicknesses: 6.5 – 10 in.

The range of design reliability: 70 – 90%

Summarize the predicted cracking at various levels of slab thickness and design reliability and plot a reliability adjustment chart similar to that shown in Figure 13-2.

For Purpose 1, using the reliability adjustment chart to determine:

The final design reliability: 82% for the erosion-based slab thickness h_e to match the initial predicted slab cracking.

For Purpose 2, using the procedure described in ***Step A*** and ***Step B*** to determine:

The new concrete slab thickness, h_1': 8.45 in. such that the new erosion-based slab thickness equals to the initial design of PPCP panel thickness $h_e' = h_1$ ($h_1 = 8\ in.$).

Final Design Output

Purpose 1 – Determine the final design reliability due to erosion

Final PPCP panel thickness, in. 8

Final design reliability: 86%

Final base thickness, in. 6

Final required effective prestress, $EP_{required} = Max(EP_1, EP_2, EP_{\min})$, psi: 150

Purpose 2 – Determine a new concrete slab thickness

Final PPCP panel thickness, in. 8.5

Final design reliability: 90%

Final base thickness, in. 6

Final required effective prestress, $EP_{required} = Max(EP_1, EP_2, EP_{\min})$, psi: 150

Step 3

Inputs

Tendon (strand) diameter, in.: 0.6

Tendon cross-sectional area, in^2: 0.217

Tendon spacing, in.: 18

Panel thickness, in.: 8.5

Concrete modulus of elasticity, psi: 4000000

Steel modulus of elasticity, psi: 28000000

Tendon force at 75% of yield stress, lbf: 43000

Slab–base friction coefficient: 20

Concrete shrinkage strain, million in/in: 300

Concrete ultimate creep coefficient: 2.5

Steel relaxation coefficient: 0.04

Maximum concrete temperature during the summer, ˚F: 120

Minimum concrete temperature during the winter, ˚F: 20

Concrete CTE, millionth in/in/˚F: 5

Concrete unit weight, pci: 0.0868

Outputs

Area of concrete per tendon = tendon spacing x panel thickness

= 18 in. x 8.5 in. = 153 in.^{2}

Total applied end stress = Tendon force/area of concrete per tendon

= 43000 lbf/153 in.^{2} = 281 psi

Length of a PPCP BAS, ft.:

$$L \geq \frac{E_c \cdot \alpha \cdot \Delta T}{\mu \cdot \gamma} = \frac{4 \times 10^6 \times 5 \times 10^{-6} \times 100}{20 \times 0.0868} / 12 = 96ft$$

Use 96 ft. for the total length of the BAS and $L = 6ft$ for length of post-tensioning assuming the BAS is post-tensioned in every 6 ft..

Prestress loss due to slab-base friction, psi:

$$\sigma_F = \frac{\mu L}{2} = 20 * 6ft/2 = 60psi$$

Prestress loss due to concrete shrinkage, psi:

$$f_s = \varepsilon_s E_S (\frac{A_s}{A_c}) = 300 \text{ x } 10^{-6} \text{ x } 28000000 \text{ x } (\frac{0.217}{153}) = 11.91 \text{ psi}$$

Prestress loss due to concrete creep, psi:

$$f_{cr} = C_u \frac{E_s}{E_c} f_{pe} (\frac{A_s}{A_c}) = 2.5 \text{ x } \frac{28000000}{4000000} \text{ x } 299 \text{ x } (\frac{0.217}{153}) = 7.42 \text{ psi}$$

Prestress loss due to steel relaxation, psi:

$$f_r = \rho \cdot f_{pe} = 0.04 \times 281 = 11.24 \ psi$$

Total prestress loss, psi: $\sigma_F + f_s + f_{cr} + f_r$ = 60 + 11.91 + 7.42 + 11.24 = 90.57 psi

$P_{effective}$= The total applied end stress – the total prestress loss

= 281 – 90.57 = 190.43 psi

$P_{effective} = 190.43psi > EP_{required} = 150psi$, OK

Step 4

Inputs

Length of a PPCP BAS, ft.: 96

Maximum concrete temperature during the summer, ˚F: 120

Minimum concrete temperature during the winter, ˚F: 20

Concrete temperature at install, ˚F: 70

Minimum joint width, in: 0.25

Concrete CTE, millionth in/in/˚F: 5

Concrete ultimate creep coefficient: 2.5

Total applied end stress, psi: 281

Effective prestress, psi: 190.43

Concrete modulus of elasticity, psi: 4000000

Concrete shrinkage strain, million in/in: 300

Outputs

Movement calculations

The temperature variation induced movement:

$$dL_{Temp} = (T_{c\max} - T_{c\min}) \times CTE_c \times L = (120\text{-}20) \times 5 \times 10^{-6} \times (96 \text{x } 12) = 0.576 \text{ in}$$

The creep induced movement:

$$dL_{creep} = C_u \times (P_{end} + P_{effective})/2 \times (1/E_c) \times L$$
$$= 2.5 \times (281 + 190.43)/2 \text{ x } (1/4000000) \times (96 \times 12)$$
$$= 0.170 \text{ in.}$$

The shrinkage induced movement:

$$dL_{shrinkage} = \varepsilon_s \times L = 300 \text{ x } 10^6 \times (96 \times 12) = 0.3456 \text{ in.}$$

Total movement of a PPCP section:

$$dL_{Total} = dL_{temp} + dL_{creep} + dL_{shrinkage} = 0.576 + 0.170 + 0.3456 = 1.09 \text{ in.}$$

Joint width calculations

Joint width at the time of installation:

$$JW_{Install} = dL_{\min} + (T_{\max} - T_{Install}) \times CTE_C \times L$$

$$= 0.25 + (120\text{-}70) \times 5 \times 10^{-6} \times (96 \times 12)$$

$$= 0.538 \text{ in.}$$

Long-term minimum joint width:

$$JW_{(L-T)\min} = dL_{\min} + dL_{creep} + dL_{shrinkage}$$

$$= 0.25 + 0.17 + 0.3456$$

$$= 0.766 \text{ in.}$$

Maximum joint width:

$$JW_{\max} = dL_{\min} + dL_{total} = 0.25 + 1.09 = 1.34 \text{ in.}$$

$JW_{\max} < 1.5$ in, OK

Otherwise, revise the design inputs (i.e. length of a PPCP section and total applied end stress) and re-design starting from ***Step 3***.

APPENDIX E

STANDARDIZED DESIGN DETAILS OF JPRCP BAS

This chapter provides standardized design details for bridge approach slabs (BASs) built using jointed precast concrete pavement (JPrCP). The example design details are provided by the Fort Miller Co., Inc.

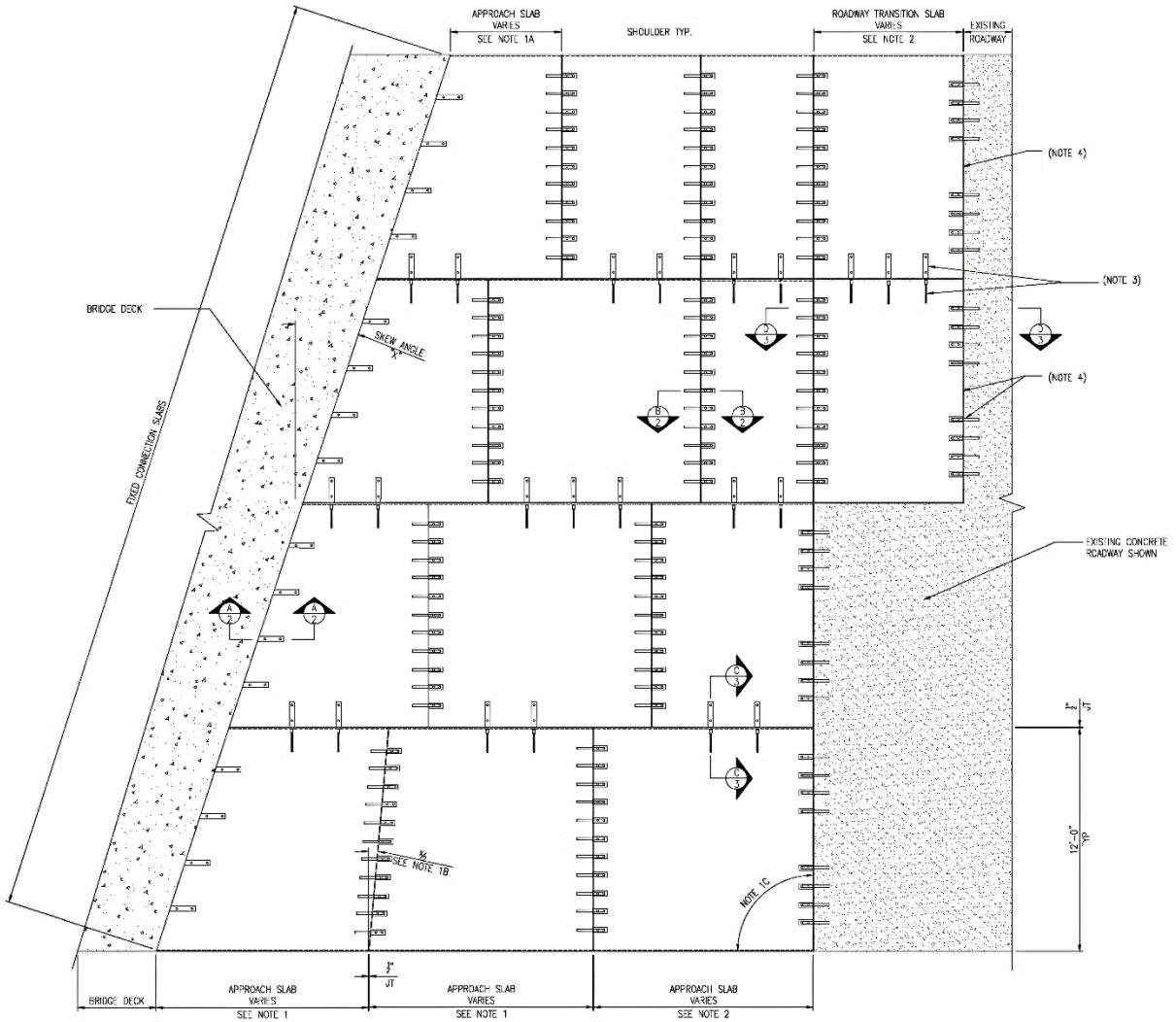

PLAN VIEW

PLAN NOTES:

1. USE SLAB LENGTH SHOWN ON THE CONTRACT DRAWINGS WHERE POSSIBLE.
1A. USE 6' MIN. SLAB LENGTH
1B. USE SKEW ANG. F/2 FOR BRIDGES WITH HEAVY SKEWS TO AVOID HEAVILY-TRAPAZOIDAL SLABS TO OPTIMIZE OVERALL JOINT LAYOUT.
1C. USE SQUARE JOINTS AT ENDS OF APPROACH SLABS WHENEVER POSSIBLE TO FACILITATE INSTALLATION OF EXPANSION JOINT MATERIAL AND DOWELS IN EXISTING PAVEMENT
2. USE ROADWAY SLAB LENGTH SHOWN ON CONTRACT DRAWINGS. DO NOT EXCEED 16' LONG ROADWAY SLAB LENGTHS
3. ORIENTATION OF SLOTS AND EMBEDDED TIES DEPENDS UPON TRAFFIC STAGING PLAN AND WHICH SLABS ARE TO BE PLACED FIRST.
4. IF EXISTING ROADWAY IS ASPHALT, USE PRECAST/ASPHALT JOINT DETAIL SHOWN ON THE CONTRACT DRAWINGS.

NOTICE

STATE DEPARTMENT OF TRANSPORTATION

SUPER-SLAB® BRIDGE APPROACH SLAB STANDARD DETAILS

CONTRACTOR:
CONTRACTOR ADDRESS:

THE FORT MILLER Co., INC.
P.O. BOX 68
SCHUYLERVILLE, NEW YORK 12871
PH: (518) 695-5000
FX: (518) 695-4910
WWW.FORTMILLER.COM

FM #: XXXXX
DATE: 7/15/11
DWN BY: DJC
CHKD BY: TDS

REVISION	BY	CK'D	DATE

September 9, 2011

SUPER-SLAB® PRECAST PAVEMENT

SHEET No. 1

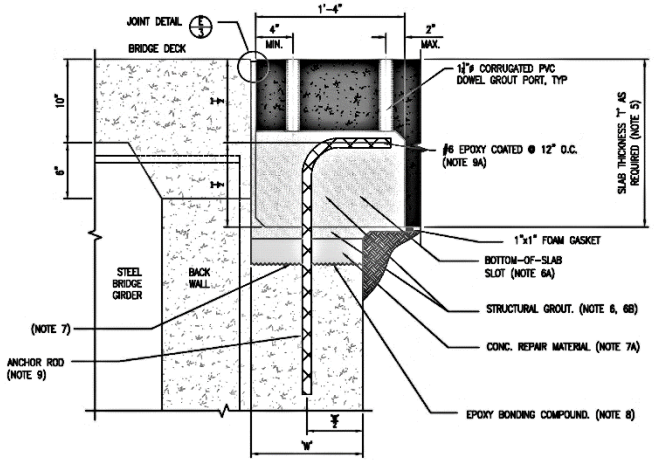

SECTION A-A
FIXED CONNECTION TO EXISTING ABUTMENT SEAT

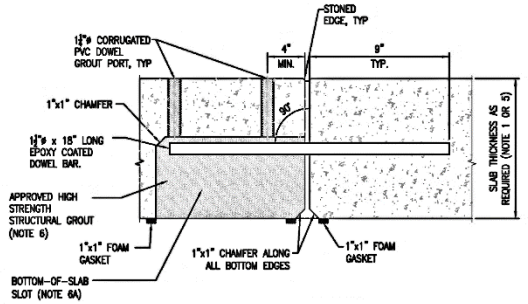

SECTION B-B
STANDARD PRECAST TO PRECAST TRANSVERSE TIE

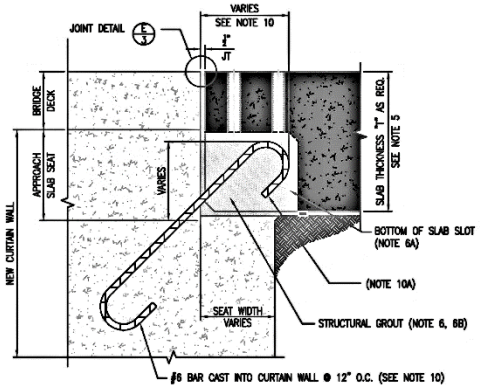

SECTION A-A
FIXED CONNECTION TO NEW CURTAIN WALL

APPROACH SLAB NOTES:

5. USE APPROACH SLAB THICKNESS AND REINFORCING SHOWN ON CONTRACT DRAWINGS.
6. USE PAVEMENT HARDWARE GROUT, AS SHOWN ON SUPER-SLAB ® STANDARD SHEET IN1, NOTE 10, FOR STRUCTURAL GROUT. INSTALL AS DIRECTED ON IN1, IN2, AND IN3. INSTALL GROUT THROUGH GROUT PORTS AFTER SLAB IS IN PLACE.
6A. BOTTOM-OF-SLAB SLOT DETAIL IS PROPRIETARY TO THE FORT MILLER CO., INC.
6B. INSTALL PAVEMENT HARDWARE GROUT UNDER APPROACH SLABS PRIOR TO OPENING THEM TO TRAFFIC.
7. REMOVE BACK WALL AS REQUIRED AND REPLACE IT WITH FAST SETTING CONCRETE REPAIR MATERIAL, APPROVED BY THE DOT, TO CREATE A NEW APPROACH SLAB SEAT. KEEP TOP OF SEAT 1" MIN. BELOW TO BOTTOM OF THE APPROACH SLAB.
7A. INSTALL NEW APPROACH SLAB SEAT USING FAST-SETTING CONCRETE REPAIR MATERIAL, APPROVED BY THE DOT. KEEP TOP OF NEW SEAT 1" MIN. BELOW BOTTOM OF APPROACH SLAB.
8. EPOXY BOND NEW APPROACH SLAB SEAT TO EXISTING CONCRETE WITH EPOXY BONDING COMPOUND AS APPROVED BY THE DOT.
9. DRILL AND EPOXY ANCHOR #6 EPOXY COATED BAR AT LOCATIONS INDICATED ON THE CONTRACT DRAWINGS PRIOR TO PLACING THE NEW APPROACH SLABS. ORIENT HORIZONTAL LEG OF ANCHOR PARALLEL TO SLOT.
9A. USE VERTICAL AND HORIZONTAL ANCHOR ROD LENGTHS SHOWN ON THE CONTRACT DRAWINGS. SIZE SLAB SLOTS ACCORDINGLY.
10. ANCHOR RODS EMBEDDED IN NEW CURTAIN WALL OR DECK.
10A. ORIENT AND SIZE SLOTS TO ALIGNMENT OF EMBEDDED ANCHOR RODS.

STATE DEPARTMENT OF TRANSPORTATION

SUPER-SLAB® BRIDGE APPROACH SLAB STANDARD DETAILS

CONTRACTOR:
CONTRACTOR ADDRESS:

THE FORT MILLER Co., INC.
PO BOX 99
SCHUYLERVILLE, NEW YORK 12871
PH: (518) 695-5000
FX: (518) 695-5670
WWW.FORTMILLER.COM

FM #:	XXXXX				
DATE:	6/8/11				
DWN BY:	DJG				
CHKD BY:	TDS	REVISION	BY	CK'D	DATE

September 9, 2011

SUPER-SLAB® PRECAST PAVEMENT

SHEET No. 2

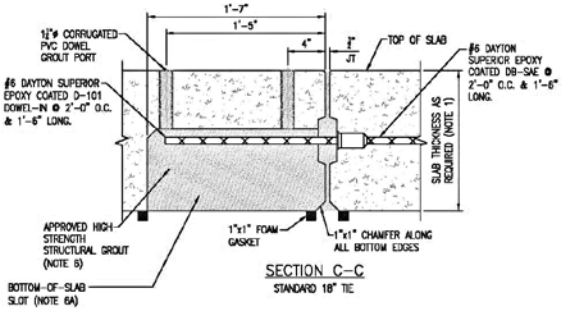

SECTION C–C
STANDARD 18" TIE

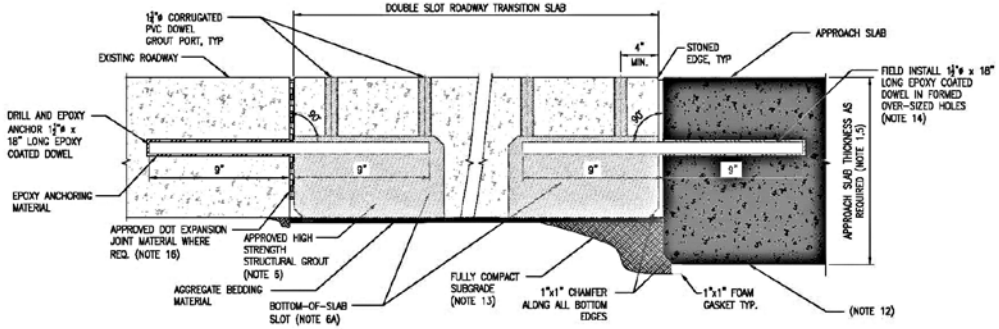

SECTION D–D
STANDARD ROADWAY TRANSITION SLAB BETWEEN APPROACH SLAB AND EXISTING ROADWAY

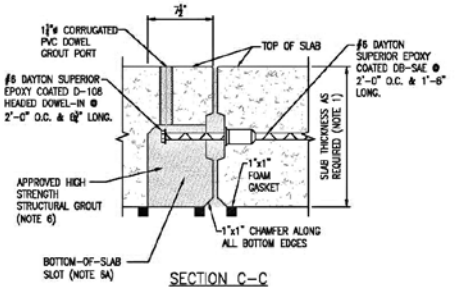

SECTION C–C
ALTERNATE HEADED TIE BAR (NOTE 11)

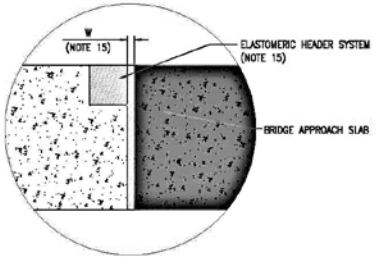

JOINT DETAIL E/3
ELASTOMERIC CONCRETE HEADER

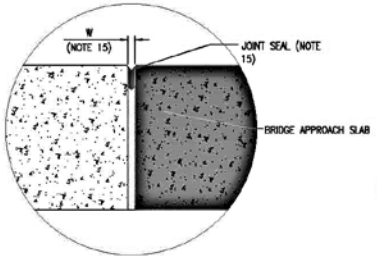

JOINT DETAIL E/3
COMPRESSION OR FOAM SEAL

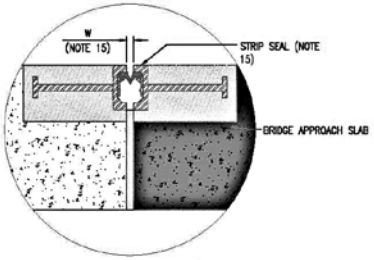

JOINT DETAIL E/3
STRIP SEAL

MISCELLANEOUS NOTES

11. USE HEADED TIE BAR DETAIL TO MINIMIZE LENGTH OF SLOT.
12. PLACE THICKER APPROACH SLAB BEFORE PLACING ADJACENT THINNER ROADWAY TRANSITION SLAB.
13. FULLY COMPACT SUBGRADE NEXT TO APPROACH SLAB BEFORE INSTALLING ROADWAY SLAB.
14. EPOXY ANCHOR DOWEL IN FORMED OVER-SIZED HOLE AFTER COMPACTION IS COMPLETE.
15. USE JOINT SEAL SYSTEM AND JOINT WIDTH SHOWN ON THE CONTRACT DRAWINGS. PROVIDE BLOCKOUT IN BRIDGE DECK OR APPROACH SLAB AS NECESSARY TO ACCOMMODATE FULL-LENGTH SEAL SYSTEM SHOWN ON THE CONTRACT DRAWINGS. USE REMOVABLE TEMPORARY BLOCKOUT FILLERS TO MAINTAIN TRAFFIC UNTIL JOINT SEAL SYSTEM IS INSTALLED.
16. USE WIDTH AND TYPE OF EXPANSION MATERIAL SHOWN ON THE CONTRACT DRAWINGS. PLACE EXPANSION MATERIAL IN ONE OR BOTH ROADWAY TRANSITION SLABS AS SHOWN ON THE CONTRACT DRAWINGS. SEAL TOP OF JOINT AS SHOWN ON THE CONTRACT DRAWINGS.

STATE DEPARTMENT OF TRANSPORTATION

SUPER-SLAB® BRIDGE APPROACH SLAB STANDARD DETAILS

CONTRACTOR:
CONTRACTOR ADDRESS:

THE FORT MILLER Co., INC.
P.O. BOX 96
SCHUYLERVILLE, NEW YORK 12871
PH: (518) 695-5000
FX: (518) 695-4570
WWW.FORTMILLER.COM

F.M. #:	XXXXX				
DATE:	6/8/11				
DWN BY:	DJG				
CHKD BY:	TDS	REVISION	BY	CKD	DATE

September 9, 2011

SUPER-SLAB® PRECAST PAVEMENT

SHEET No. 3

APPENDIX F

STANDARDIZED DESIGN DETAILS OF PPCP BAS

This chapter provides standardized design details for bridge approach slabs (BASs) built using precast prestressed concrete pavement (PPCP). The example design details are taken from the Iowa project. To obtain more detailed and complete design details for the Iowa project, please refer to the report by Merritt [11].

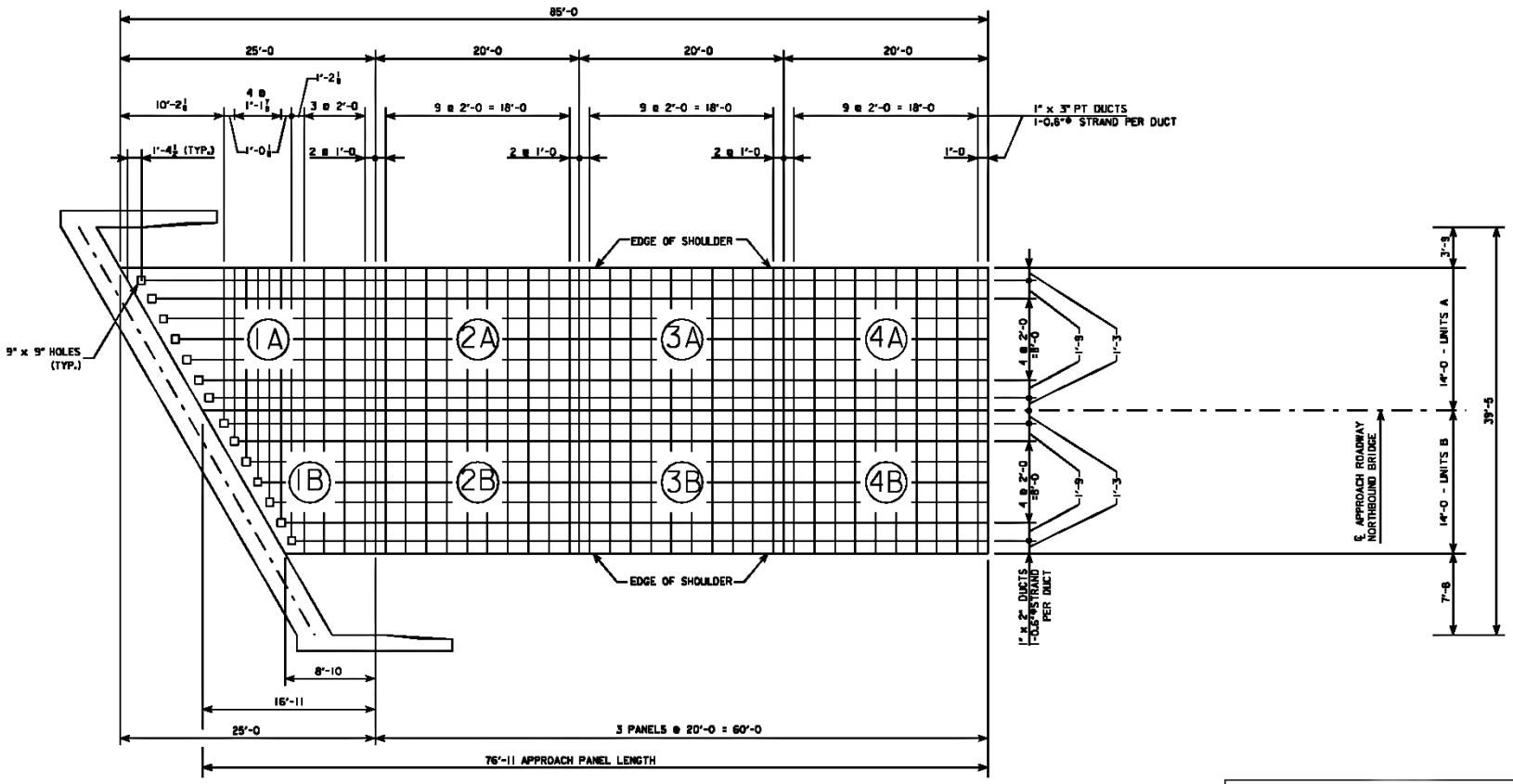

DESIGN FOR

PRECAST REINFORCED CONCRETE APPROACH PANELS

POST-TENSIONING LAYOUT

STATION: 1429+16.67 (℄ SURVEY RELOC. IA. 60) FEBRUARY, 2006

O'BRIEN COUNTY

IOWA DEPARTMENT OF TRANSPORTATION - HIGHWAY DIVISION

DESIGN SHEET NO. 5 OF 20 FILE NO. ________ DESIGN NO. ________

DESIGN TEAM	O'BRIEN COUNTY	PROJECT NUMBER	SHEET NUMBER

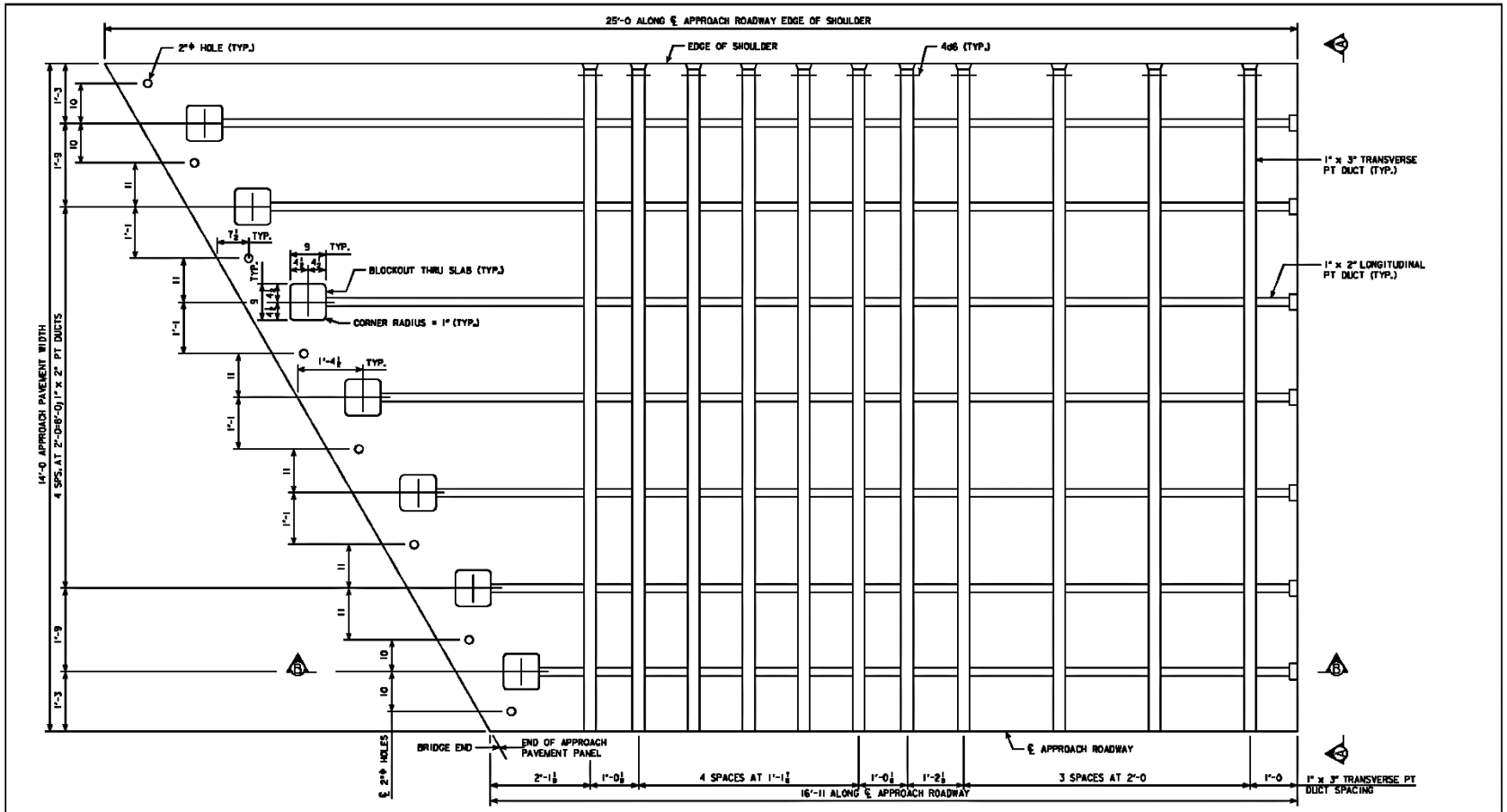

PLAN VIEW OF UNIT 1A
(SHOWING PT DUCT SPACING AND BLOCKOUTS)

DESIGN FOR
PRECAST REINFORCED CONCRETE
APPROACH PANELS
UNIT 1A PANEL PT DUCT SPACING
STATION: 1429+16.67 (℄ SURVEY RELOC. IA. 60) FEBRUARY, 2006
O'BRIEN COUNTY
IOWA DEPARTMENT OF TRANSPORTATION - HIGHWAY DIVISION
DESIGN SHEET NO. 6 OF 20 FILE NO. ________ DESIGN NO. ________

DESIGN TEAM O'BRIEN COUNTY PROJECT NUMBER SHEET NUMBER

XXXXXXXXXXSYSTEMTIME XXXXXXXUSERNAME XXXXXXXXXXXXXXXXXXXXXXXXXXXXXXXXXXXXXXXXXXXXXXXXXXXXXXXXXXXXXDGNSPEC

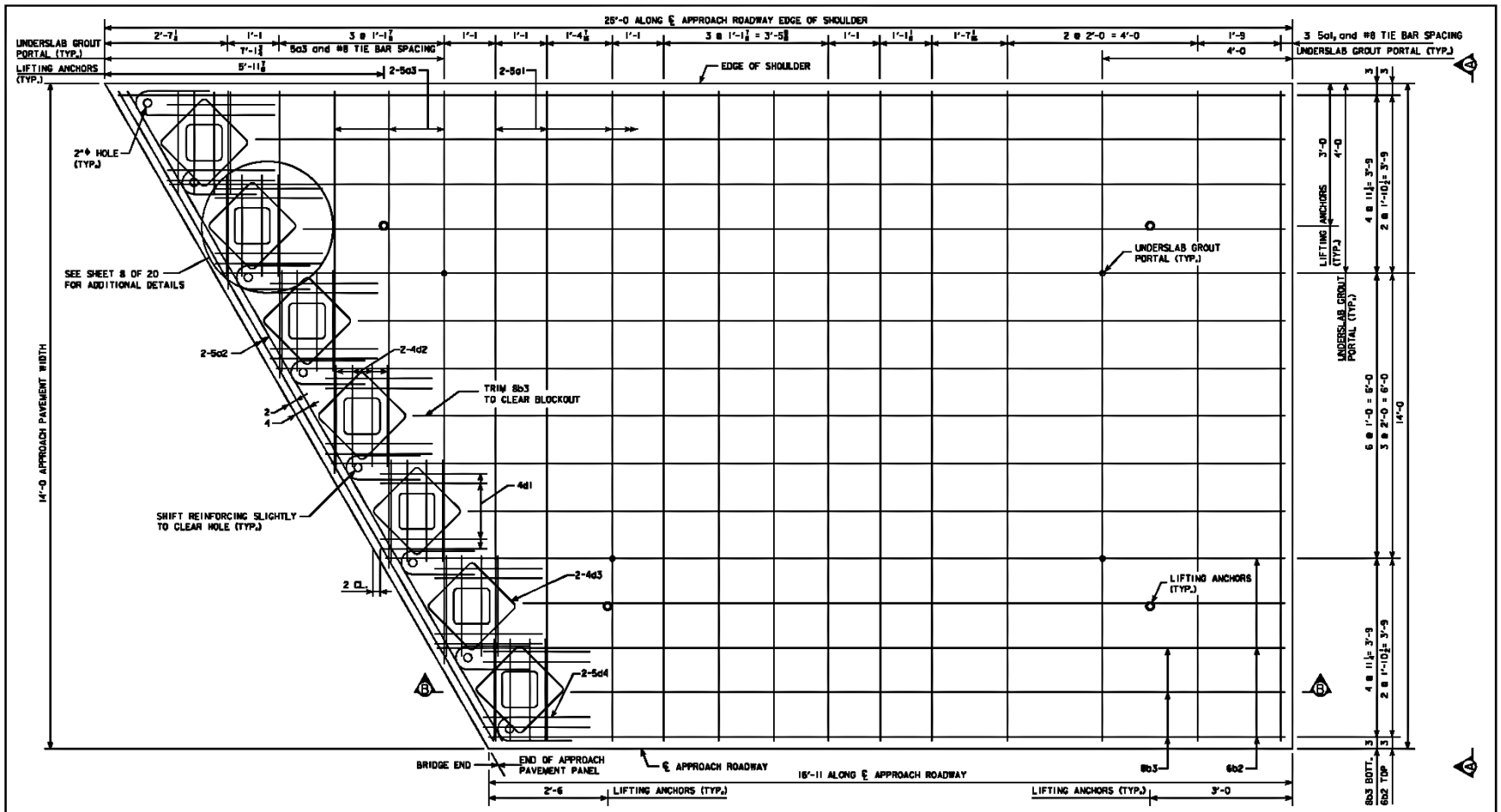

NOTE: SEE SHEET 19 OF 20
FOR REINFORCING BAR
LIST.

PLAN VIEW OF UNIT 1A

(SHOWING SLAB REINFORCING)

DESIGN FOR

PRECAST REINFORCED CONCRETE
APPROACH PANELS

UNIT 1A PANEL REIN. SPACING

STATION: 1429+16.67 (℄ SURVEY RELOC. IA. 60) FEBRUARY, 2006

O'BRIEN COUNTY

IOWA DEPARTMENT OF TRANSPORTATION - HIGHWAY DIVISION

DESIGN SHEET NO. 7 OF 20 FILE NO. ________ DESIGN NO. ________

DESIGN TEAM	O'BRIEN COUNTY	PROJECT NUMBER	SHEET NUMBER

XXXXXXXXXXSYSTEMTIME XXXXXXXUSERNAME XXXXXXXXXXXXXXXXXXXXXXXXXXXXXXXXXXXXXXXXXXXXXXXXXXXXXXXXXXXXXXXXXDGNSPEC

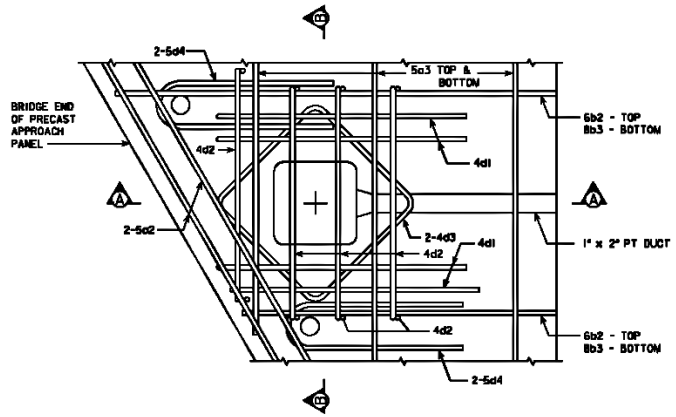

PART PLAN VIEW - UNIT 1A

(SHOWING TYPICAL BLOCKOUTS AT BRIDGE APPROACH END)

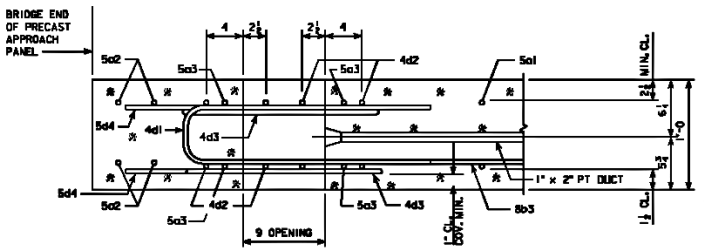

SECTION A-A

(SECTION ALONG ℄ 1" x 2" PT DUCT)

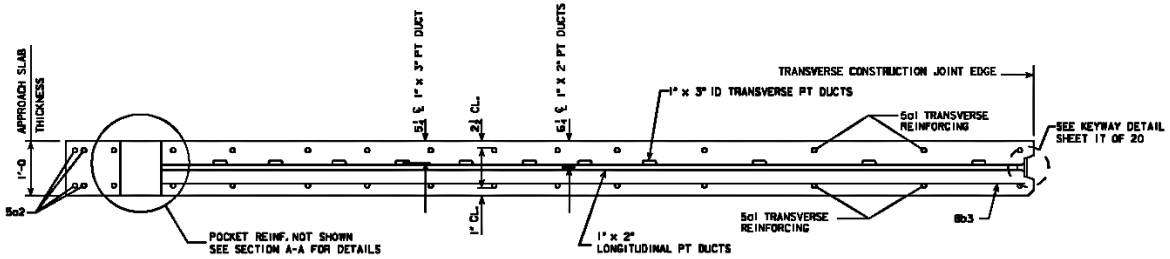

VIEW B-B ALONG ℄ PT DUCTS

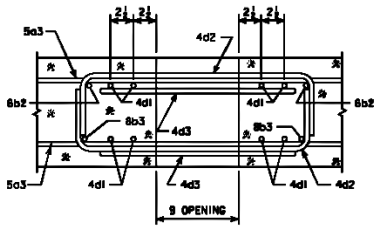

SECTION B-B

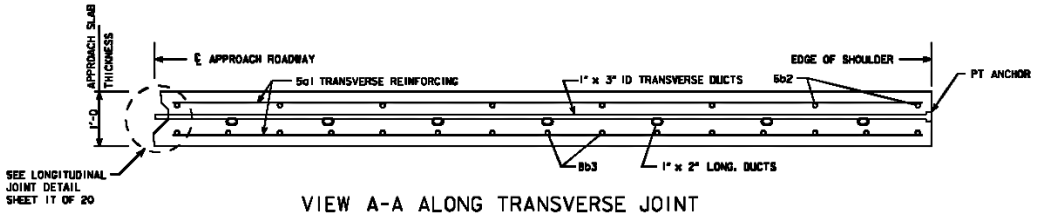

VIEW A-A ALONG TRANSVERSE JOINT

DESIGN FOR

PRECAST REINFORCED CONCRETE
APPROACH PANELS

SECTION UNIT 1A ADD. DETAILS

STATION: 1429+16.67 (℄ SURVEY RELOC. IA. 60) FEBRUARY, 2006

O'BRIEN COUNTY

IOWA DEPARTMENT OF TRANSPORTATION - HIGHWAY DIVISION

DESIGN SHEET NO. 8 OF 20 FILE NO. ________ DESIGN NO. ________

DESIGN TEAM	O'BRIEN COUNTY	PROJECT NUMBER	SHEET NUMBER

XXXXXXXXXXSYSTEMTIME XXXXXXXUSERNAME XXXXXXXXXXXXXXXXXXXXXXXXXXXXXXXXXXXXXXXXXXXXXXXXXXXXXXXXXXXXXXXDGNSPEC

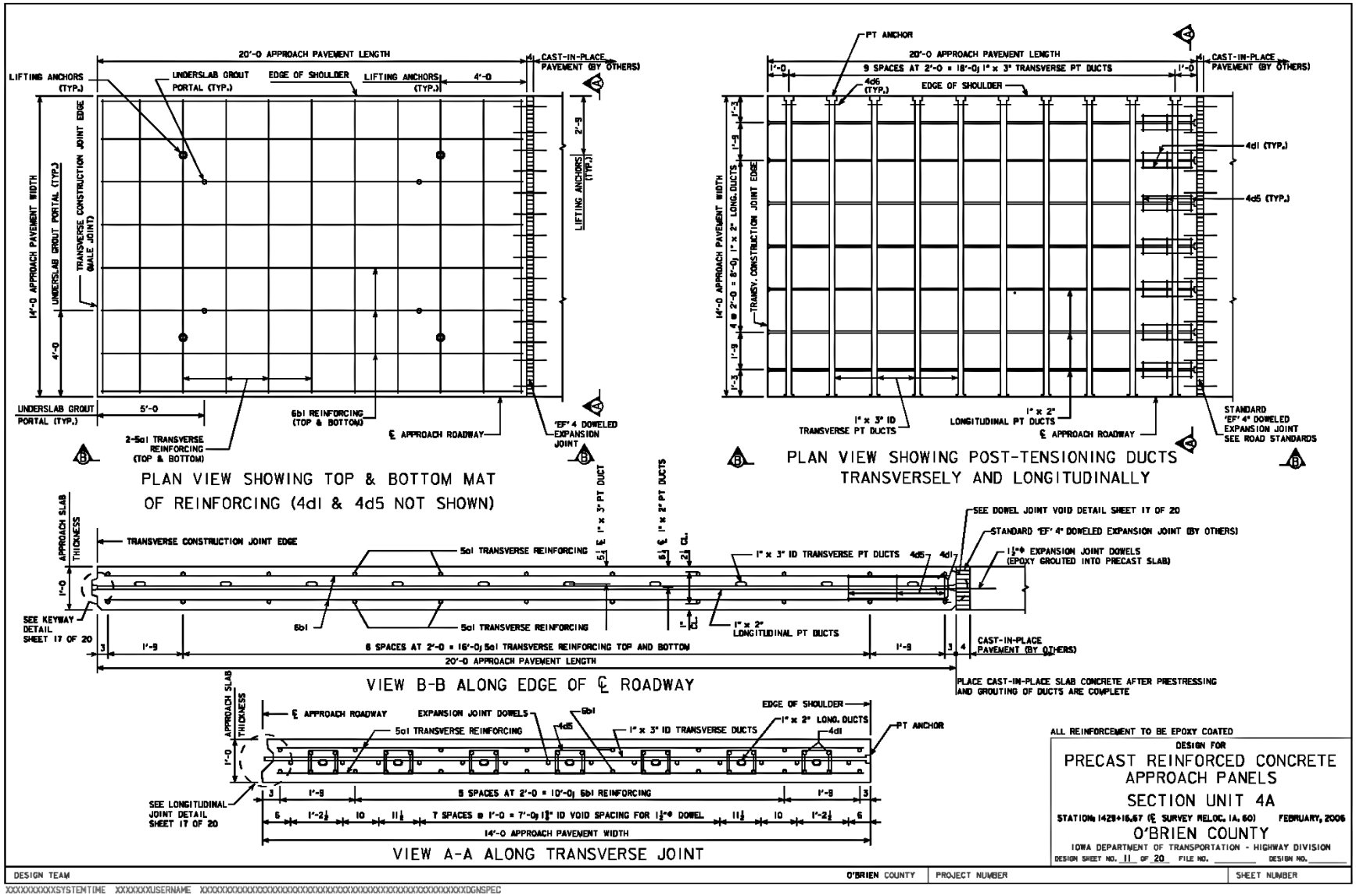
20'-0 APPROACH PAVEMENT LENGTH
CAST-IN-PLACE PAVEMENT (BY OTHERS)
LIFTING ANCHORS (TYP.)
UNDERSLAB GROUT PORTAL (TYP.)
EDGE OF SHOULDER
4'-0
14'-0 APPROACH PAVEMENT WIDTH
TRANSVERSE CONSTRUCTION JOINT EDGE (MALE JOINT)
UNDERSLAB GROUT PORTAL (TYP.)
5'-0
6bl REINFORCING (TOP & BOTTOM)
℄ APPROACH ROADWAY
'EF' 4 DOWELED EXPANSION JOINT
2-5al TRANSVERSE REINFORCING (TOP & BOTTOM)
PLAN VIEW SHOWING TOP & BOTTOM MAT OF REINFORCING (4dl & 4d5 NOT SHOWN)
PT ANCHOR
9 SPACES AT 2'-0 = 18'-0; 1" x 3" TRANSVERSE PT DUCTS
4d6 (TYP.)
4dl (TYP.)
4d5 (TYP.)
TRANSV. CONSTRUCTION JOINT EDGE
4 @ 2'-0 = 8'-0; 1" x 2" LONG. DUCTS
1" x 3" ID TRANSVERSE PT DUCTS
1" x 2" LONGITUDINAL PT DUCTS
STANDARD 'EF' 4" DOWELED EXPANSION JOINT SEE ROAD STANDARDS
PLAN VIEW SHOWING POST-TENSIONING DUCTS TRANSVERSELY AND LONGITUDINALLY
APPROACH SLAB THICKNESS
TRANSVERSE CONSTRUCTION JOINT EDGE
5al TRANSVERSE REINFORCING
5.1 ℄ 1" x 3" PT DUCT
5.1 ℄ 1" x 2" PT DUCTS
2.1 CL.
1" x 3" ID TRANSVERSE PT DUCTS
SEE DOWEL JOINT VOID DETAIL SHEET 17 OF 20
STANDARD 'EF' 4" DOWELED EXPANSION JOINT (BY OTHERS)
1½"Φ EXPANSION JOINT DOWELS (EPOXY GROUTED INTO PRECAST SLAB)
SEE KEYWAY DETAIL SHEET 17 OF 20
6bl
5al TRANSVERSE REINFORCING
1" x 2" LONGITUDINAL PT DUCTS
8 SPACES AT 2'-0 = 16'-0; 5al TRANSVERSE REINFORCING TOP AND BOTTOM
20'-0 APPROACH PAVEMENT LENGTH
CAST-IN-PLACE PAVEMENT (BY OTHERS)
PLACE CAST-IN-PLACE SLAB CONCRETE AFTER PRESTRESSING AND GROUTING OF DUCTS ARE COMPLETE
VIEW B-B ALONG EDGE OF ℄ ROADWAY
℄ APPROACH ROADWAY
EXPANSION JOINT DOWELS
5al TRANSVERSE REINFORCING
4d5
1" x 3" ID TRANSVERSE DUCTS
EDGE OF SHOULDER
1" x 2" LONG. DUCTS
4dl
PT ANCHOR
SEE LONGITUDINAL JOINT DETAIL SHEET 17 OF 20
8 SPACES AT 2'-0 = 10'-0; 6bl REINFORCING
7 SPACES @ 1'-0 = 7'-0; 1⅜" ID VOID SPACING FOR 1½"Φ DOWEL
14'-0 APPROACH PAVEMENT WIDTH
VIEW A-A ALONG TRANSVERSE JOINT
ALL REINFORCEMENT TO BE EPOXY COATED
DESIGN FOR
PRECAST REINFORCED CONCRETE APPROACH PANELS
SECTION UNIT 4A
STATION: 1428+16.67 (℄ SURVEY RELOC. 1A, 60) FEBRUARY, 2006
O'BRIEN COUNTY
IOWA DEPARTMENT OF TRANSPORTATION - HIGHWAY DIVISION
DESIGN SHEET NO. 11 OF 20 FILE NO. DESIGN NO.
DESIGN TEAM
O'BRIEN COUNTY
PROJECT NUMBER
SHEET NUMBER
XXXXXXXXXXSYSTEMTIME XXXXXXXUSERNAME XXXXXXXXXXXXXXXXXXXXXXXXXXXXXXXXXXXXXXXXXXXXXXXXXXXXXXXXXXXXXXDGNSPEC

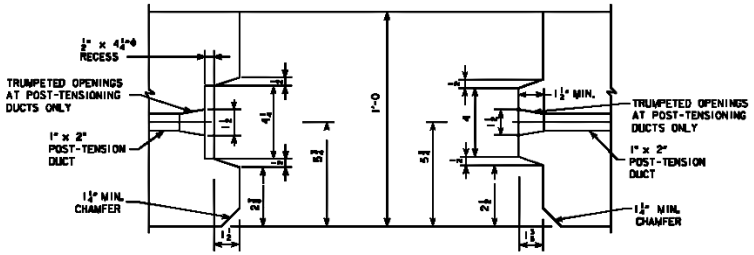

KEYWAY DIMENSIONS FOR TRANSVERSE JOINTS

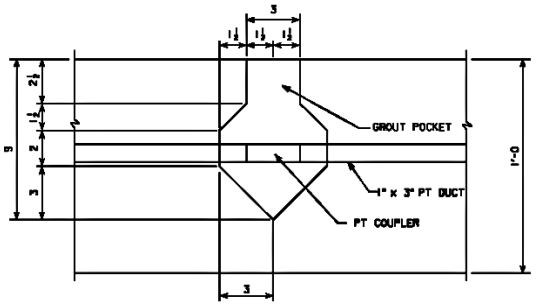

DETAIL A

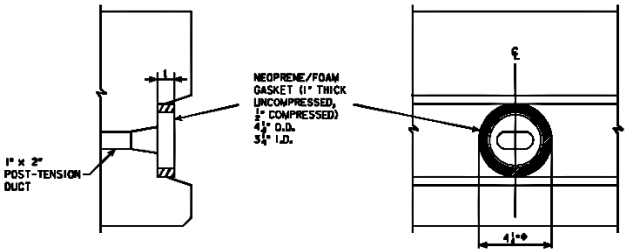

SIDE VIEW

FRONT VIEW

TENDON GASKET DETAIL FOR TRANSVERSE JOINTS

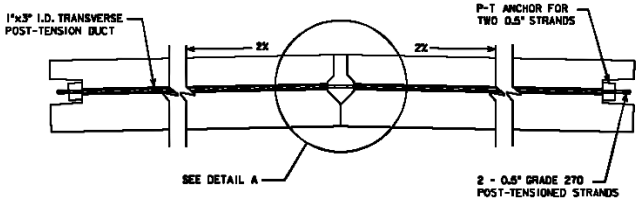

TYPICAL LONGITUDINAL JOINT

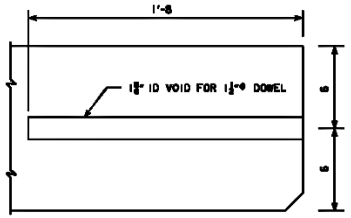

EXPANSION JOINT DOWEL VOIDS
UNITS 4A & 4B

DESIGN FOR
PRECAST REINFORCED CONCRETE
APPROACH PANELS
MISC. JOINT DETAILS
STATION: 1429+16.67 (℄ SURVEY RELOC. IA. 60) FEBRUARY, 2006
O'BRIEN COUNTY
IOWA DEPARTMENT OF TRANSPORTATION - HIGHWAY DIVISION
DESIGN SHEET NO. 17 OF 20 FILE NO. ________ DESIGN NO. ________

DESIGN TEAM	O'BRIEN COUNTY	PROJECT NUMBER	SHEET NUMBER

XXXXXXXXXXSYSTEMTIME XXXXXXXUSERNAME XXXXXXXXXXXXXXXXXXXXXXXXXXXXXXXXXXXXXXXXXXXXXXXXXXXXXXXXXXXXXXDGNSPEC

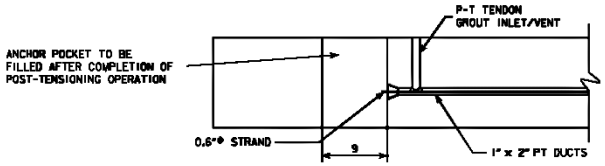

POST-TENSION ANCHORAGE DETAIL FOR
DEAD END OF STRANDS

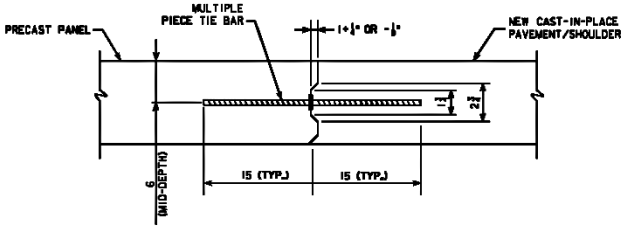

KEYWAY DIMENSIONS LONGITUDINAL JOINTS
AT ENDS OF PRECAST PANELS

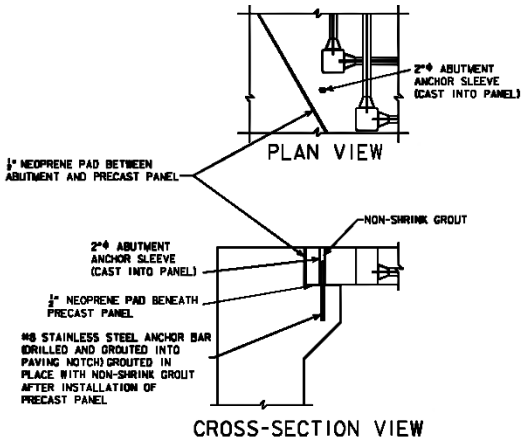

PLAN VIEW

CROSS-SECTION VIEW

DESIGN FOR
PRECAST REINFORCED CONCRETE
APPROACH PANELS

MISC. DETAILS UNIT 1A & 1B
STATION: 1429+16.67 (℄ SURVEY RELOC. IA. 60) FEBRUARY, 2006
O'BRIEN COUNTY
IOWA DEPARTMENT OF TRANSPORTATION - HIGHWAY DIVISION
DESIGN SHEET NO. 18 OF 20 FILE NO. ________ DESIGN NO. ________

DESIGN TEAM | O'BRIEN COUNTY | PROJECT NUMBER | SHEET NUMBER

XXXXXXXXXXSYSTEMTIME XXXXXXXUSERNAME XXXXXXXXXXXXXXXXXXXXXXXXXXXXXXXXXXXXXXXXXXXXXXXXXXXXXXXXXXXXXDGNSPEC

REINFORCING BAR LIST - UNIT 1A

BAR	LOCATION	SHAPE	NO.	LENGTH	WEIGHT
5a1	SLAB TRANSV. TOP & BOTT.	—	26	13'-8	371
5a3	SLAB TRANSV. TOP & BOTT.	—	10	4'0 TO 11'-11	83
6b2	SLAB LONGIT. TOP	—	8	16'-9 TO 24'-6	248
8b3	SLAB LONGIT. BOTT.	—	15	16'-9 TO 24'-6	826
4d1	BLOCKOUT	⊐	28	4'-10	90
4d2	BLOCKOUT	⊔	56	3'-2	118
4d3	BLOCKOUT	▭	14	6'-1	57
5d4	2"ϕHOLE	⊃	16	3'-8	62
4d6	TRANSVERSE PT ANCHOR	▭	11	3'-5	25
5a2	SLAB TRANSV. TOP & BOTT. AT BRIDGE END	—	4	15'-9	66
REINFORCING STEEL EPOXY COATED - TOTAL (LBS.)					1946

REINFORCING BAR LIST - UNIT 2A OR 3A

BAR	LOCATION	SHAPE	NO.	LENGTH	WEIGHT
5a1	SLAB TRANSV. TOP & BOTT.	—	22	13'-8	314
6b1	SLAB LONGIT. TOP & BOTT	—	16	19'-8	473
4d6	TRANSVERSE PT ANCHOR	▭	10	3'-5	23
REINFORCING STEEL EPOXY COATED - TOTAL (LBS.)					810

REINFORCING BAR LIST - UNIT 4A

BAR	LOCATION	SHAPE	NO.	LENGTH	WEIGHT
5a1	SLAB TRANSV. TOP & BOTT.	—	22	13'-8	314
6b1	SLAB LONGIT. TOP & BOTT.	—	16	19'-8	473
4d1	LONGITUDINAL PT ANCHOR	⊐	14	4'-10	45
4d5	LONGITUDINAL PT ANCHOR	▭	21	3'-4	47
4d6	TRANSVERSE PT ANCHOR	▭	10	3'-5	23
REINFORCING STEEL EPOXY COATED - TOTAL (LBS.)					902

BENT BAR DETAILS

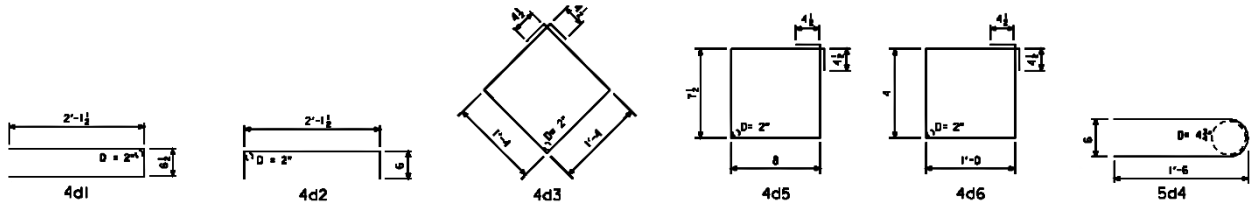

NOTE: ALL DIMENSIONS ARE OUT TO OUT. D = PIN DIAMETER.

DESIGN FOR
PRECAST REINFORCED CONCRETE
APPROACH PANELS

UNIT QUANTITIES 1A, 2A, 3A, 4A
STATION: 1429+16.67 (℄ SURVEY RELOC. IA. 60) FEBRUARY, 2006
O'BRIEN COUNTY
IOWA DEPARTMENT OF TRANSPORTATION - HIGHWAY DIVISION
DESIGN SHEET NO. 19 OF 20 FILE NO. ________ DESIGN NO. ________

DESIGN TEAM | O'BRIEN COUNTY | PROJECT NUMBER | SHEET NUMBER

XXXXXXXXXXSYSTEMTIME XXXXXXXUSERNAME XXXXXXXXXXXXXXXXXXXXXXXXXXXXXXXXXXXXXXXXXXXXXXXXXXXXXXXDGNSPEC

APPENDIX G

JPRCP DESIGN WORKSHEET

Site Conditions

Project site:_____ Traffic ESALs, million:_____

Design limits

Design reliability:_____ Design service life, years:_____

Design Criteria

Cracking, %:_____ Faulting, in:_____ Smoothness (IRI), in/mi.:_____

Precast Concrete Panel

Thickness, in.:_____ Lane width, ft.:_____

Transverse joint spacing, ft.:_____

Dowel bar diameter, in:_____ Dowel bar spacing, in:_____

Modulus of rupture at 28-day, psi:_____

Concrete CTE, millionth in/in/˚F:_____

Permanent curl/warp effective temperature difference, ˚F:_____

Concrete ultimate drying shrinkage, 10^{-6} in.:_____

Permeable Granular Base

Thickness, in.:_____ Modulus of elasticity, psi:_____

Base erodibility index:_____ Loss of full friction, months:_____

Subgrade

Modulus of elasticity, psi:_____

APPENDIX H

PPCP DESIGN WORKSHEET

Step 1

Baseline design

Thickness of concrete slab, in.:_____

Thickness of base, in.:_____

Step 2

Criterion 1. Stress equivalent criterion

Perform analysis using ISLAB2000

Loading magnitude, lb:_____

Loading position (edge or interior):_____

Width of the concrete slab, ft.:_____

Length of the concrete slab, ft.:_____

Modulus of subgrade reaction: pci:_____

Baseline thickness of the concrete slab, in:_____

Trial PPCP panel thickness design, in:_____

Determine effective prestress using output of ISLAB2000

Refer to Figure 13-1

Edge stress for baseline thickness design, psi:_____

Stress at loading position (edge or interior):_____ for the trial PPCP panel thickness design, psi:_____

Required effective prestress, EP_1, psi:_____

Criterion 2. Strength equivalency criterion

Site Conditions

Project site:_____ Traffic ESALs, million:_____

Design limits

Design reliability:_____ Design service life, years:_____

Design Criteria

Cracking, %:_____ Faulting, in:_____ Smoothness (IRI), in./mi.:_____

Precast Concrete Panel

Thickness, in.:_____ Lane width, ft.:_____

Transverse joint spacing, ft.:_____

Dowel bar diameter, in:_____ Dowel bar spacing, in:_____

Required effective prestress, EP_2, psi:_____

Modulus of rupture at 28-day, psi:_____

Concrete CTE, millionth in/in/˚F:_____

Permanent curl/warp effective temperature difference, ˚F:_____

Concrete ultimate drying shrinkage, 10^{-6} in.:_____

Permeable Granular Base

Thickness, in.:_____ Modulus of elasticity, psi:_____

Base erodibility index:_____ Loss of full friction, months:_____

Subgrade

Modulus of elasticity, psi:_____

Initial Design output

Initial PPCP panel thickness, in._____

Initial predicted slab cracking:_____

Initial base thickness, in._____

Initial required effective prestress, $EP_{required} = Max(EP_1, EP_2, EP_{\min})$, psi:_____

Erosion Consideration

Step A. Determination of erosion damage

ADT at the start year:_____

Percent of trucks:_____

Number of wet days (min 0.1" rain):_____

Initial design of PPCP panel thickness, in.:_____

Cohesion of the base, psi:_____

Check the database in given the Excel spreadsheet and obtain the:

Percent of erosion, $\%E$:_____

Effective coefficient of friction, μ_e:_____

Step B. Determination of erosion-based slab thickness

Perform calculations in the Excel spreadsheet to obtain:

Partially-bonded concrete layer thickness, h_{e-p}:_____

Through performing trial and error in the Excel spreadsheet, determine:

Erosion-based slab thickness, h_e:_____, such that the effective slab thickness of the two systems are equivalent (i.e. $h_{e-b}{}' = h_{e-p}$).

Step C. Reliability analysis

Perform design using MEPDG software by varying the slab thickness and design reliability while holding other inputs constant (i.e. the inputs shown in Table 13-4):

The range of slab thicknesses:_____

The range of design reliability:_____

Summarize the predicted cracking at various levels of slab thickness and design reliability and plot a reliability adjustment chart similar to that shown in Figure 13-2.

For Purpose 1, using the reliability adjustment chart to determine:

The final design reliability:_____ for the erosion-based slab thickness h_e to match the initial predicted slab cracking.

For Purpose 2, using the procedure described in ***Step A*** and ***Step B*** to determine:

The new concrete slab thickness, h_1':_____such that the new erosion-based slab thickness equals to the initial design of PPCP panel thickness $h_e' = h_1$.

Final Design Output

Purpose 1 – Determine the final design reliability due to erosion

Final PPCP panel thickness, in._____

Final design reliability:_____

Final base thickness, in._____

Final required effective prestress, $EP_{required} = Max(EP_1, EP_2, EP_{\min})$, psi:_____

Purpose 2 – Determine a new concrete slab thickness

Final PPCP panel thickness, in._____

Final design reliability:_____

Final base thickness, in._____

Final required effective prestress, $EP_{required} = Max(EP_1, EP_2, EP_{\min})$, psi:_____

Step 3

Inputs

Tendon (strand) diameter, in.:_____

Tendon cross-sectional area, in^2:_____

Tendon spacing, in.:_____

Panel thickness, in.:_____

Concrete modulus of elasticity, psi:_____

Steel modulus of elasticity, psi:_____

Tendon force at 75% of yield stress, lbf:_____

Slab–base friction coefficient:_____

Concrete shrinkage strain, million in/in:_____

Concrete ultimate creep coefficient:_____

Steel relaxation coefficient:_____

Maximum concrete temperature during the summer, ˚F:_____

Minimum concrete temperature during the winter, ˚F:_____

Concrete CTE, millionth in/in/˚F:_____

Concrete unit weight, pci:_____

Outputs

Area of concrete per tendon = tendon spacing x panel thickness

= _____

Total applied end stress = Tendon force/area of concrete per tendon

=_____

Length of a PPCP BAS, ft.:

$$L \geq \frac{E_c \cdot \alpha \cdot \Delta T}{\mu \cdot \gamma} =$$

Prestress loss due to slab-base friction, psi:

$\sigma_F = \frac{\mu L}{2} =$_____

Prestress loss due to concrete shrinkage, psi:

$f_s = \varepsilon_s E_S (\frac{A_s}{A_c}) =$_____

Prestress loss due to concrete creep, psi:

$f_{cr} = C_u \frac{E_s}{E_c} f_{pe} (\frac{A_s}{A_c})$=_____

Prestress loss due to steel relaxation, psi:

$f_r = \rho \cdot f_{pe} =$_____

Total prestress loss, psi: $\sigma_F + f_s + f_{cr} + f_r =$_____

$P_{effective}$= The total applied end stress – the total prestress loss

= _____

$P_{effective} \geq EP_{required}$, otherwise, modify design inputs and start over this step.

Step 4

Inputs

Length of a PPCP section, ft.:_____

Maximum concrete temperature during the summer, ˚F:_____

Minimum concrete temperature during the winter, ˚F:_____

Concrete temperature at install, ˚F:_____

Minimum joint width, in:_____

Concrete CTE, millionth in/in/˚F:_____

Concrete ultimate creep coefficient:_____

Total applied end stress, psi:_____

Effective prestress, psi:_____

Concrete modulus of elasticity, psi:_____

Concrete shrinkage strain, million in/in:_____

Outputs

Movement calculations

The temperature variation induced movement:

$$dL_{Temp} = (T_{c\max} - T_{c\min}) \times CTE_c \times L =$$_____

The creep induced movement:

$$dL_{creep} = C_u \times (P_{end} + P_{effective})/2 \times (1/E_c) \times L =$$_____

The shrinkage induced movement:

$$dL_{shrinkage} = \varepsilon_s \times L =$$_____

Total movement of a PPCP section:

$$dL_{Total} = dL_{temp} + dL_{creep} + dL_{shrinkage} =$$_____

Joint width calculations

Joint width at the time of installation:

$$JW_{Install} = dL_{\min} + (T_{\max} - T_{Install}) \times CTE_C \times L =$$_____

Long-term minimum joint width:

$$JW_{(L-T)\min} = dL_{\min} + dL_{creep} + dL_{shrinkage} =$$_____

Maximum joint width:

$$JW_{\max} = dL_{\min} + dL_{total} =$$_____

$JW_{\max}$ < 1.5 in, otherwise, revise the design inputs (i.e. length of a PPCP section and total applied end stress) and re-design starting from ***Step 3.***

REFERENCES

1. Tayabji, S.D., D. Ye, and N. Buch, *Precast concrete pavement technology*2013: Transportation Research Board.
2. Merritt, D.K., et al., *Construction of the Iowa Highway 60 Precast Prestressed Concrete Pavement Bridge Approach Slab Demonstration Project*, 2007.
3. Merritt, D.K., B.F. McCullough, and N.H. Burns, *Construction and Preliminary Monitoring of the Georgetown, Texas Precast Prestressed Concrete Pavement*, 2002, Citeseer.
4. Merritt, D., B. Frank McCullough, and N. Burns, *Precast prestressed concrete pavement pilot project near Georgetown, Texas.* Transportation Research Record: Journal of the Transportation Research Board, 2003(1823): p. 11-17.
5. Larrazabal, E., *Precast Concrete (PC) Pavement Tests on Taxiway DD at Laguardia Airport.* 2004.
6. Switzer, W., et al. *Overnight Pavement Replacement Using Precast Panels and Conventional Subgrade Material - Washington Dulles International Airport Case Study in Airfield Pavements. Challenges and New Technologies*. in *Airfield Pavements. Challenges and New Technologies*. 2004.
7. Farrington, R., et al. *Overnight Concrete Pavement Replacement Using a Precast Panel and Expanding Polymer Positioning Technique - Washington Dulles International Airport Case Study in Airfield Pavements. Challenges and New Technologies*. in *Airfield Pavements. Challenges and New Technologies*. 2004.
8. Tayabji, S. and K. Hall, *Precast Concrete Panels for Repair and Rehabilitation of Jointed Concrete Pavements.* CPTP TechBrief, 2008.
9. Association, N.P.C., *Jointed precast concrete pavement (JPrCP)*, 2011, National Precast Concrete Association: http://precast.org/wp-content/uploads/2011/11/PCPSbrochure.pdf.
10. Ye, D., *Personal communication*, 2016.
11. Merritt, D.K., et al., *The Feasibility of Using Precast Concrete Panels to Expedite Highway Pavement Construction*2000: Center for Transportation Research, University of Texas at Austin.
12. Merritt, D.K. and S. Tayabji, *Precast Prestressed Concrete Pavement for Reconstruction and Rehabilitation of Existing Pavements*, 2009.
13. Merritt, D., R. Rogers, and R. Rasmussen, *Construction of a Precast Prestressed Concrete Pavement Demonstration Project on Interstate 57 near Sikeston, Missouri*, 2008, FHWA-HIF-08-009. Washington, DC: Federal Highway Administration.
14. Merritt, D.K., P. MCCULLOUGH, and N.H. Burns, *Design-construction of a precast, prestressed concrete pavement for interstate 10, El Monte, California.* PCI journal, 2005. **50**(2): p. 18-27.
15. Tayabji, S., *Precast Concrete Pavement Technology ~ Rapidly Evolving*, in *International Society for concrete pavements*2011.
16. Schmitz, M.E., et al., *Use of controlled low-strength material as abutment backfill*, 2004, Kansas Department of Transportation.

17. Guide, M.E.P.D., *A Manual of Practice.* American Association of State Highway and Transportation Officials, 2008.
18. Pierce, L.M. and G. McGovern, *Implementation of the AASHTO Mechanistic-Empirical Pavement Design Guide and Software*2014.
19. su Jung, Y., et al., *Subbase and subgrade performance investigation and design guidelines for concrete pavement.* 2010.
20. Tayabji, S., D. Ye, and F. Motamed, *Final Report, Proposed Process for Design of Precast Concrete Pavements Sacramento, California*, 2012, Fugro Consultants, Inc.
21. Hoppe, E.J., *Guidelines for the use, design, and construction of bridge approach slabs*, 1999.
22. Jang, S.H., *Automated crack control analysis for concrete pavement construction*, 2005, Texas A&M University.
23. Bari, M.E. and D.G. Zollinger, *New concepts for the assessment of concrete slab interfacial effects in pavement design and analysis.* International Journal of Pavement Engineering, 2016. **17**(3): p. 233-244.
24. Ioannides, A.M., L. Khazanovich, and J.L. Becque, *Structural evaluation of base layers in concrete pavement systems.* Transportation Research Record, 1992(1370).
25. Miller, G.A., et al., *APPLIED APPROACH SLAB SETTLEMENT RESEARCH, DESIGN/CONSTRUCTION.* 2011.
26. Jayawickrama, P., et al., *Water Intrusion in Base/Subgrade Materials at Bridge Ends.* 2005.
27. Greimann, L.F., et al., *Integral Bridge Abutment-to-Approach Slab Connection*, 2008.
28. Phares, B.M., et al., *Identification and evaluation of pavement-bridge interface ride quality improvement and corrective strategies.* Rep. No. Federal Highway Administration (FHWA)/Ohio (OH)-2011/1, Washington, DC, 2011.
29. Oklahoma, D., *Standard specifications for highway construction*, 2009, Oklahoma City.
30. LLC, C.A., *Concrete bridge approach pavements: a survey of state practices*, 2010, Wisconsin Highway Research Program

Rigid Pavements Technical Oversight Committee.

31. Thiagarajan, G., J. Myers, and C. Halmen, *Field Evaluation of Alternative and Cost-Efficient Bridge Approach Slabs*, 2013.
32. Smith, P.J., *Replacement of Bridge Approach Slabs and Super-Structure In Two Consecutive Weekends, Rt. 46 Over Broad St., Clifton, NJ*, 2011, The Fort Miller Co. Inc: New Jersey.
33. Nadermann, A., L. Greimann, and B. Phares, *Instrumentation and Monitoring of Precast Bridge Approach Tied to an Integral Abutment Bridge in Bremer County.* 2010.
34. Bautista, F.E. and I. Basheer, *Jointed Plain Concrete Pavement (JPCP) Preservation and Rehabilitation Design Guide*, in *Office of Pavement Design Pavement Design & Analysis Branch*2008.

35. Corporation, D.C., *Rapid cure sealant demonstrates remarkable success*, 1999: Available from Internet:<http://www.dowcorning.com/content/publishedlit/62283A01.pdf>.
36. Purvis, R.L. and M.P. Burke, *Bridge deck joint performance: A synthesis of highway practice*. Vol. 319. 2003: Transportation Research Board.
37. Milner, M.H. and H.W. Shenton III, *Survey of Past Experience and State-of-the-Practice in the Design and Maintenance of Small Movement Expansion Joints in the Northeast.* AASHTO Transportation System Preservation Technical Services Program (TSP2) Report, 2014. **242**.
38. su Jung, Y., D.G. Zollinger, and S.D. Tayabji, *Best Practices for Concrete Pavement Transition Design and Construction*2007: Texas Transportation Institute, Texas A&M University System.
39. Seo, J., H. Ha, and J.-L. Briaud, *Investigation of settlement at bridge approach slab expansion joint: Numerical simulations and model tests*, 2002.
40. Briaud, J., R. JAMES, and S. Hoffman, *SETTLEMENT OF BRIDGE APPROACHES (THE BUMP AT THE END OF THE BRIDGE)*, 1997.
41. Ziehl, P., M. EIBatanouny, and M.K. Jones, *In-Situ Monitoring of Precast Concrete Approach Slab Systems*, 2015, South Carolina Department of Transportation

Federal Highway Administration.

42. White, D., et al., *Identification of the best practices for design, construction, and repair of bridge approaches*, 2005.
43. Lenke, L.R., *Settlement Issues--Bridge Approach Slabs*, 2006.
44. Buch, N., *Precast Concrete Panel Systems for Full-Depth Pavement Repairs. Field Trials*, 2007.
45. Highways, M. and T. Commission, *Missouri Standard Specifications for Highway Construction, 2004*2016: Missouri Highways and Transportation Commission.
46. Dailey, C.L., *Instrumentation and early performance of an innovative prestressed precast pavement system*, 2006, University of Missouri--Columbia.
47. Mishra, T., P. French, and Z. Sakkal, *Engineering a better road: Use of two-way prestressed, precast concrete pavement for rapid rehabilitation.* PCI journal, 2013. **58**(1): p. 129-141.

STONE COLUMN AND EMBANKMENT DESIGN GUIDELINE

FINAL REPORT ~ FHWA-OK-16-08

ODOT SP&R ITEM NUMBER 2265

Submitted to:
John R. Bowman, P.E.
Director of Capital Programs
Oklahoma Department of Transportation

Submitted by:
Peizhi Sun, Research Assistant
Dan G. Zollinger, Ph.D., P.Eng
Robert Lytton, Ph.D., P.Eng
Zachary Department of Civil Engineering
Texas A& M University
Texas Transportation Institute

October 2015

CHAPTER 14

INTRODUCTION OF STONE COLUMN

The stone column technique is one of the ground improvement methods used worldwide since the 1950's. This technique which was originally implemented by Keller in Europe in 1937 [98] involves replacing 10% – 35% of weak soil with coarse granular material which is then placed and compacted into deep cylindrical holes made in the foundation soils to improve the shear strength, reduce the foundation settlement and provide a stable base for embankments or structures. Although stiffer than the surrounding soil, the stone column is essentially a soil improvement method rather than a foundation element (e.g. rigid piles); therefore, it generally does not apply for heavy loading conditions since stone columns do not behave like rigid piles which can transfer load to deeper soil strata [98-100].

General Applications

The stone column technique can be used under various circumstances, including [101-104]:

- Stabilizing the foundation soils of highway embankments or bridge approach fills;
- Providing foundation support for bridge abutments, bridge bents, mechanically stabilized earth retaining walls and other retaining structures;
- Stabilizing landslides; and
- Reducing liquefaction potential of clean sand.

Material Compatibility

The stone column technique is suitable for a wide range of soil types regarding the grain size distribution as shown in Figure 14-1. In terms of the undrained shear strength of soils, this technique works best for soils having undrained shear strengths of 2.2 – 7.3 psi (15 - 50 kPa); for soils with shear strength lower than 1.2 psi (8 kPa), stone columns may not have sufficient lateral support; for soils with shear strength greater

than 7.3 psi (50 kPa), the equipment may encounter difficulty while opening bore holes [105].

Although general compatibility limits were established as aforementioned (mainly based on experience in the U.S.), experience from both Europe and Asia has shown that the stone column technique can also be used for soils with undrained shear strength as low as 0.7 psi (5 kPa) where the soils are not used in structural engineering but for pavement applications; specific soil conditions are indicated as follows, including [104, 106]:

- Loose Silty Sands: foundation soils with loose sands or silts are prone to liquefaction during an earthquake, the use of stone columns are a proven technique to reduce the occurrence of liquefaction, especially for petrochemical related structures such as LNG tanks;
- Soft and ultra-soft silts (slimes): foundation soil layers with the low shear strength (generally from 0.7 – 1.5 psi (5 – 10 kPa)) slimes can often lead to stability problems and low bearing capacity, previous experience indicated that stone columns can be used to support embankments with such layers without placing surcharge [107];
- Soft and ultra-soft marine clays: this type of soil is usually found in coastal areas and has low shear strength (generally from 0.9 – 1.7 psi (6 – 12 kPa));
- Garbage fills: structures are sometimes built over garbage landfills due to the shortage of land; stone columns were used to address the high compressibility of this type of material which often leads to large settlement.

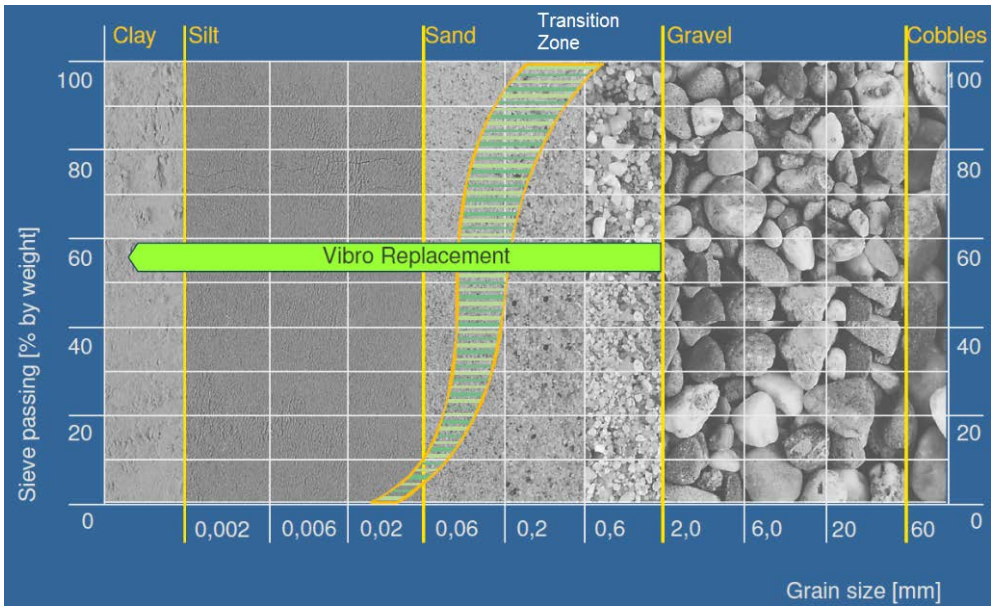

Figure 14-1 Material limits for application [108]

Construction Methods

In the U.S., stone columns can be installed using two different methods, the vibro-replacement (wet top feed) and the vibro-displacement (dry top and bottom feed) methods [101, 109]. In Europe, the name of the techniques are different where both the dry top and bottom feed methods are referred to as the vibro-replacement technique [108, 110]. Detailed equipment and techniques pertaining to each are discussed subsequently.

The original stone column construction method is referred to as the vibro-replacement, which involves the use of a high-pressure water jetting method to penetrate a vibratory probe into the ground; the stones are fed into the hole incrementally as the probe retracts, during which both the stones and surrounding soils are compacted and densified. The method is suitable for sites with high groundwater table and soft to firm soils that have undrained shear strengths of 2.2 – 7.3 psi (15 - 50 kPa) [105]. The diameter of the holes made using this method ranges from 2.6 – 3.9 ft. (0.8 – 1.2 m.) [111]. Note that attention needs to be paid to the management of runoff water (i.e. water from rainfall) induced during application of this method which may

cause environmental problems. A schematic diagram of this method is shown in Figure 14-2.

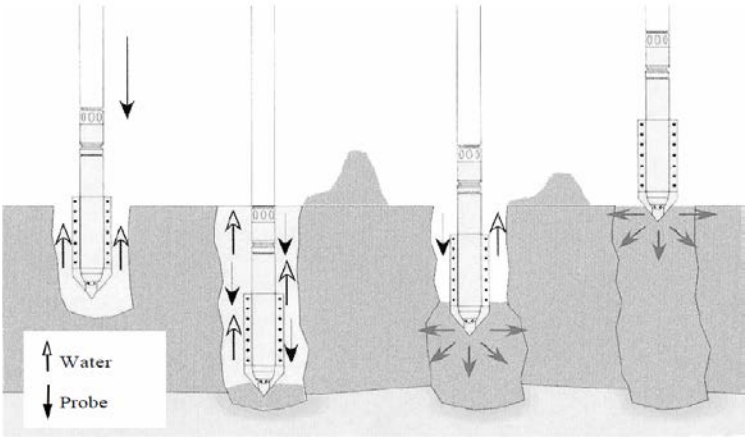

Figure 14-2 A schematic diagram of vibro-replacement method [109]

The second method, vibro-displacement (dry top and bottom feed) was introduced to solve the environmental issues that may occur after using the vibro-replacement method. This method mainly focuses on soils with undrained shear strength of 4.4 – 7.3 psi (30 - 50 kPa) [111]. The diameter of the holes which ranges from 1.6 – 2.6 ft. (0.5 – 0.8 m.) is usually smaller than that of the holes made using the vibro-replacement method [98]. In this method, air jetting and/or pre-augering techniques are used associated with a vibrator probe to open holes in the ground. Unlike the wet top feed method where soils are removed from the bore holes, the soils are displaced laterally by the probe inside the holes for the vibro-displacement method; as a result, the soils around the inside surface of the bore holes are densified, which leads to greater strength [112]. However, this method may cause smear damage at the column-soil interface due to the restructuring of the compacted soils, leading to blocked drainage and delaying the consolidation process [98, 111].

Two different procedures are available to feed stones using the vibro-displacement method, one is named as the top feed procedure and the other is the bottom feed procedure. The difference between the two is that for a top feed procedure as shown in Figure 14-3 (a), stones (range from 0.47 – 2.95 in. in size) are fed into the holes from the ground surface after the probe is either fully or partially removed from the holes; whereas for a bottom feed procedure as shown in Figure 14-3 (b), the stones

(with smaller sizes ranging from 0.08 – 1.77 in.) are fed through an auxiliary tube to the bottom of the holes without taking the probe out [113]. The top feed procedure is suitable for making shallow and shorter stone columns; the bottom feed procedure is mainly used to prevent the holes from collapsing when opening deep holes and to address high water table or unstable soil conditions [110, 113].

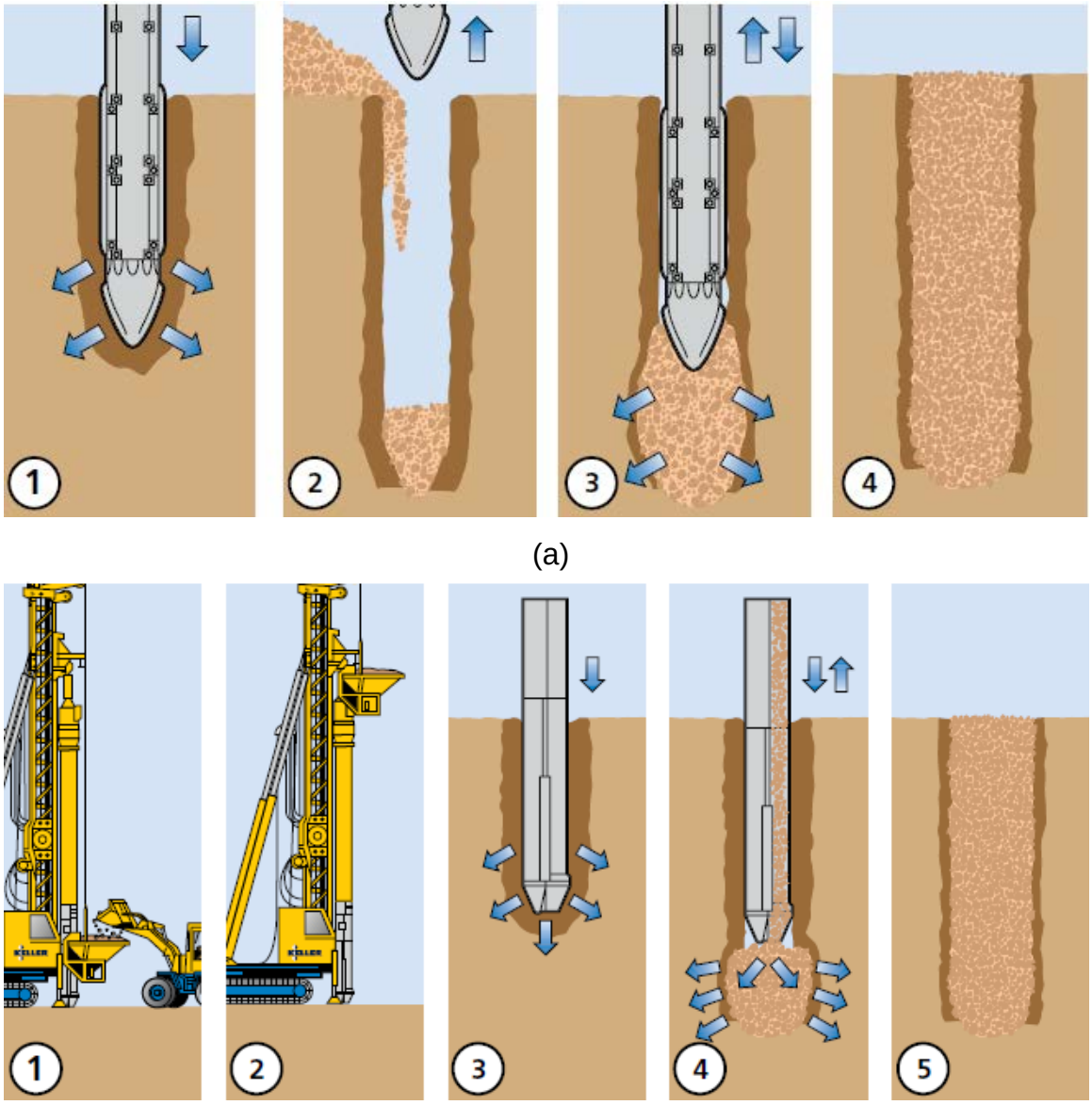

Figure 14-3 Schematic diagrams of (a) dry top feed procedure and (b) dry bottom feed procedure [110]

In addition to those two main construction methods, an alternative construction method worth noting is the bottom rammed columns or rammed aggregate piers (RAP) [114, 115]. A schematic diagram of the RAP method is shown in Figure 14-4. As seen in the figure, after drilling, poorly graded crushed gravel is placed into the “bulb” formed at the bottom of the cavity and are compacted by a beveled ram which also displaces the crushed stone radially into the surrounding soil [115, 116]. This compaction pattern often leads to aggregate pier with high angle of friction and radial stress developed in the surrounding soil [117]. As a result, previous research indicated that the stiffness of RAPs is usually 5 – 10 times greater than that of stone columns placed in the same soil [116], however this method leads to higher construction cost [114].

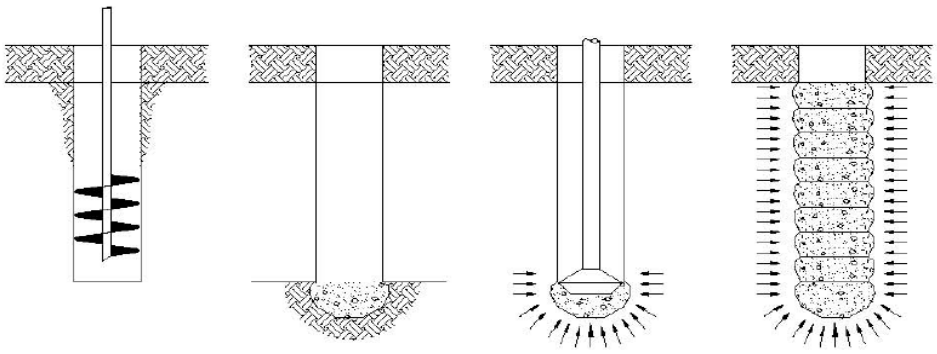

Figure 14-4 A schematic diagram of rammed aggregate pier method [103]

Construction Provisions

The following summarizes the factors that affecting the feasibility of using stone columns as a ground improvement method [100, 101]:

- The loading condition should be relatively uniform and magnitude of the loading should be limited to a maximum of 112000 lbf (500 kN) per column; the bearing capacity of a single column is usually designed 45000 – 67000 lbf (200 – 300 kN);
- Improvements are most significant for compressible silts and clay within 3.3 ft. below the ground surface and shear strength ranging from 2.2 to 7.3 psi (15 – 50 kPa);

- Soil layers containing organics and peat that have undrained shear strength lower than 1.5 psi (10 kPa) should be specially treated; the diameter (or half the diameter at least) of the stone column should be greater than the thickness of the layers with those materials;
- The undrained shear strength of the applicable soils has an upper limit of 7.3 – 14.5 psi (50 – 100 kPa); those soils will be strong enough without the installation of stone columns;
- The diameter of the stone columns may vary over their length depending on the shear strength of different layers; the diameter of most stone columns (dry feed method) ranges from 1.6 – 2.6 ft.;
- A load transfer platform may be introduced at the interface between a structure element (e.g. strip footing, raft foundation or concrete slab) and the stone column-soil foundation, if the structure does not homogeneously distribute load bearing on the column grid in the foundation.

Benefits and Limitations

The benefits of using stone columns are summarized as follows [98, 101, 108, 116]:

- Providing greater shear strength and stiffness for the overall soil-column system;
- Densifying the soil in between stone columns depending on the soil condition;
- Mitigating soil liquefaction during earthquake;
- Providing greater bearing capacity;
- Reducing settlement;
- Expediting the dissipation of excess pore water pressure in soil by providing a vertical drain through the column, which results in shorter time for primary consolidation settlement to occur;
- Behaving differently from concrete piles: cannot break, no buckling and no downdrag effect;
- Cost saving comparing to many other ground improvement techniques;
- Applicable for a wide range of soil conditions;

- Proven successful worldwide;

Some of the limitations of using stone columns are [101, 116]:

- Requiring adequate lateral support from the surrounding soil, not applicable for soft soil conditions, such as peat, mulch and other organic materials;
- Not suitable if the thickness of the undesirable soil layer is greater than the diameter of the stone column;
- For soils containing more than 15% - 25% fines or greater than 2% clay, the density of the soil in between stone columns is not improved significantly;
- Disposal of spoil water is required for the wet feed method and the dry feed method can cause soil heave that may influence the surrounding construction activities;
- Expansive pre and post construction testing is needed to confirm.

Selection Criteria

To facilitate decision making process for the practitioners, the stone column technique can be selected as a construction practice to better support the bridge embankment if one of the following conditions is present:

- The permeability of the foundation soil layer is too low to allow for the dissipation of excess pore water pressure in the foundation;
- The construction schedule cannot accommodate the long waiting period for the primary consolidation settlement to be complete (usually through preloading the foundation) before constructing the BAS;
- The budget of the project is limited to allow for the application of deep foundations;
- The construction area is within an earthquake zone.

CHAPTER 15

DESIGN OF STONE COLUMN

This chapter provides detailed design guidelines for the stone column technique.

PRELIMINARY DESIGN CONSIDERATIONS

Prior to designing a stone column, it is necessary to obtain preliminary knowledge to support the design process, the following information is considered important [100]:

- Limit of the treatment area;
- The nature of the soil to be treated: laboratory or in-site testing needs to be conducted to obtain the key soil properties;
- The characteristics and behavior of the structure to be built on top of the stone column-soil matrix;
- Stress level to be exerted on the foundation.

The preliminary design of stone columns consists of the following steps [109]:

1. Estimate the settlement of the unimproved ground using conventional settlement calculation procedures;
2. Determine the required reduction of settlement to meet the design criteria. A reduction factor named as “settlement ratio” or “improvement factor” (by Priebe’s method subsequently discussed) needs to be calculated by the ratio of the settlement of the unimproved soil to the settlement of stone column treated soil;
3. Determine if the stone columns can achieve the required reduction of settlement based on previous experience and published empirical data; generally, the improvement factor of stone columns ranges from 2 to 3;
4. Determine the area replacement ratio, which is expressed as the stone column area divided by the tributary area of the stone columns (subsequently explained), in order to achieve the required reduction of settlement;

5. Determine the length, diameter and spacing of the stone column; the length is determined based on the settlement calculation; the diameter and spacing are determined by experience;
6. Evaluate the load bearing capacity of the stone columns.

BASIC RELATIONSHIP AND DESIGN CONCEPTS

The basic relationship and design concepts relative to the design of stone columns are elaborated in this section. The information of this section is mainly based on the work from Barksdale and Bachus (1983) [118] and Elias et al. (1998) [101].

Unit Cell Concept

Although a square pattern (shown in Figure 15-1 (a)) is used sometimes, stone columns are usually constructed in an equilateral triangular pattern (shown in Figure 15-1 (b)) since it gives the densest packing of stone columns within a given area [118].

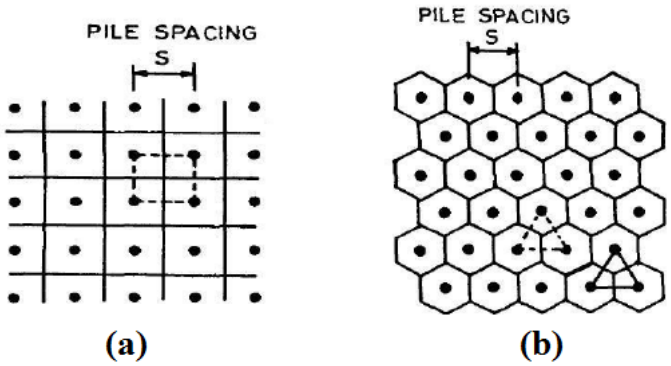

Figure 15-1 Pattern of stone column arrangement (a) square pattern (b) equilateral triangular pattern [113]

In order to perform bearing capacity and settlement analysis, the unit cell concept shown in Figure 15-2 takes into account the tributary area of the soil surrounding each stone column. For an equilateral triangular pattern, the hexagonal tributary area is usually approximated by an equivalent circular-shaped tributary area and the effective diameter, D_e of the circle is:

$$D_e = 1.05s \tag{15-1}$$

and for a square pattern, the effective diameter is:

$$D_e = 1.13s \tag{15-2}$$

where s is the spacing of the stone columns. In consequence, a unit cell with a diameter of D_e is formed considering the stone column and the surrounding tributary soil [118].

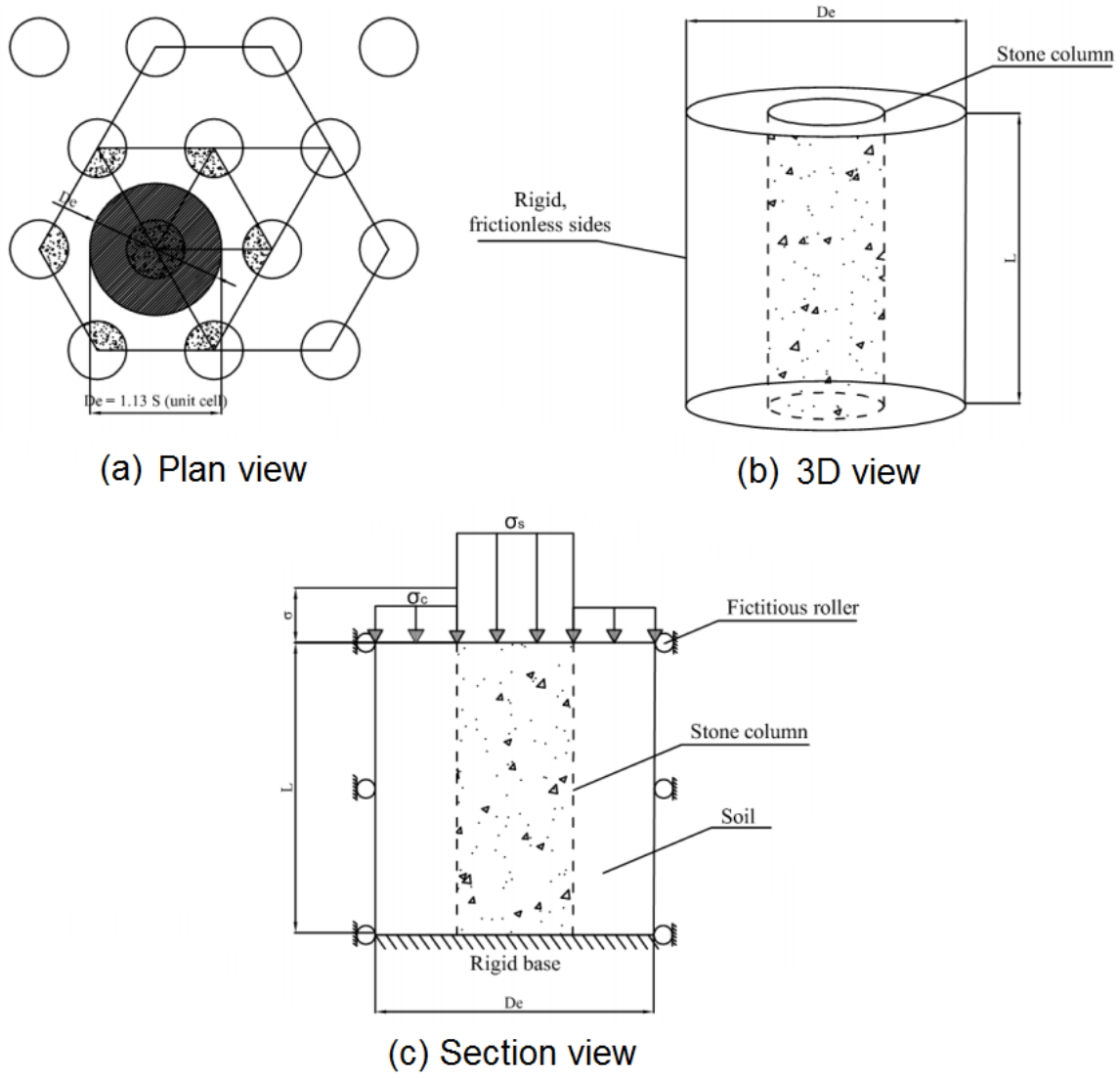

Figure 15-2 the unit cell concept (a) plan view (b) 3D view and (c) section view [119]

Spacing, Diameter and Area Replacement Ratio

The center to center spacing of the stone columns is usually 4.9 – 11.5 ft. for triangular, square or rectangular patterns of installation [101].

The diameter of stone columns ranges from 1.5 – 3.9 ft.; typically, the stone column placed using the dry feed method has a diameter ranging from 3.0 – 3.6 ft. and larger if a wet feed method is used [101].

A term named as the “area replacement ratio”, a_s is introduced to quantify the amount of soil replaced by the stone column, which is expressed as:

$$a_s = A_s/A \tag{15-3}$$

$$a_c = A_c/A = 1 - a_s \tag{15-4}$$

where A_s is the area of the stone column, A_c is the area of the surrounding soil, A is the total area within a unit cell and a_c is the ratio of the area of the surrounding soil to the total area.

Further, the area replacement ratio can be expressed in terms of the diameter and spacing of the stone columns as:

$$a_s = C_1(\frac{D}{s})^2 \tag{15-5}$$

where D is the diameter of the stone column, s is the center to center spacing and C_1 is a constant depending on the pattern of arrangement where $C_1 = \pi/4$ for a square pattern and $C_1 = \pi/(2\sqrt{3})$ for an equilateral triangular pattern [118].

It was reported that an area replacement ratio less than 10% would lead to insignificant ground improvement, whereas a ratio greater than 35% would be difficult to achieve due to the limitation of the construction technology [120].

Stress Concentration Ratio

An equal strain assumption is usually made for the case in which the vertical settlement of the stone columns and the surrounding soil is almost the same upon a uniform loading over the stone column treated ground [101, 118]. This assumption has been validated both in the field and through finite element analysis [101]. As a result, stress concentration usually occurs in the stone columns because stone columns are stiffer than the surrounding soils.

The distribution of vertical stress within a unit cell can be expressed using a stress concentration ratio, SCR which is defined as [121]:

$$SCR = \sigma_s/\sigma_c \tag{15-6}$$

where σ_s is the stress in stone columns and σ_c is the stress in the surrounding soils. Note that many others in the literature use n to represent the stress concentration ratio, however, a different parameter is used to avoid confusion since the Priebe's method (subsequently explained) uses n to represent the settlement improvement ratio [121].

The average stress σ over the area of a unit cell can be determined based on the equilibrium of vertical forces within the unit cell:

$$\sigma = \sigma_s \cdot a_s + \sigma_c(1 - a_s) \tag{15-7}$$

where σ is the stress applied on the unit cell and other terms are defined as aforementioned. Using the stress concentration ratio, σ_s and σ_c can be determined as:

$$\sigma_c = \frac{\sigma}{1+(SCR-1)\cdot a_s} = \mu_c \sigma \tag{15-8}$$

$$\sigma_s = \frac{SCR\cdot\sigma}{1+(SCR-1)\cdot a_s} = \mu_s \sigma \tag{15-9}$$

where μ_c and μ_s are the ratio of stresses in the surrounding soil and stone column, respectively, to the stress σ over the unit cell. If the stress concentration ratio is obtained, the stress in the soil and stone columns can be easily determined, which are both useful in the calculation of settlement and bearing capacity analyses [118].

The SCR is the key in the design of stone columns, however, the determination of this parameter is mostly based on experience, although theoretical solutions exist [101].

Many factors can influence the SCR, including the relative stiffness between stones and the surrounding soil, the length of the stone column, the area ratio (diameter and spacing of stone columns), the loading platform placed over the stone columns and the rate of loading [101, 121].

In general, the measured SCR ranges between 2 to 5, and the value increases with time considering the fact that the secondary settlement in the surrounding soil is greater than that in the stone column. For stronger soil and large column spacing conditions, SCR usually ranges between 2 to 2.5; whereas for weak soil and tight column spacing condition, SCR can be from 3 to 4. Usually, a SCR of 2.5 is used as a conservative assumption for preliminary design purpose [101]. A SCR can also be determined using a design chart developed by Barksdale and Bachus [118] based on the area replacement ratio and the settlement ratio; although it gives slightly unconservative estimations.

BEARING CAPACITY

The possible modes of failure to be considered in the ultimate bearing capacity calculation of a single or a group of stone columns are illustrated in Figure 15-3, Figure 15-4 and Figure 15-5. As shown in the figure, the failure modes of a single stone column consist of global or local bulging failure, shear failure and punching failure; the failure modes of stone column groups consist of lateral spreading failure, general circular failure, bulging failure and punching failure [101].

Special attention needs to be paid to avoiding the bulging failure due to the presence of weak or organic layers; this type of failure has influences on both the time rate and magnitude of settlement; the use of bulging failure analysis for a single column to predict the group behavior yields a conservative solution [101].

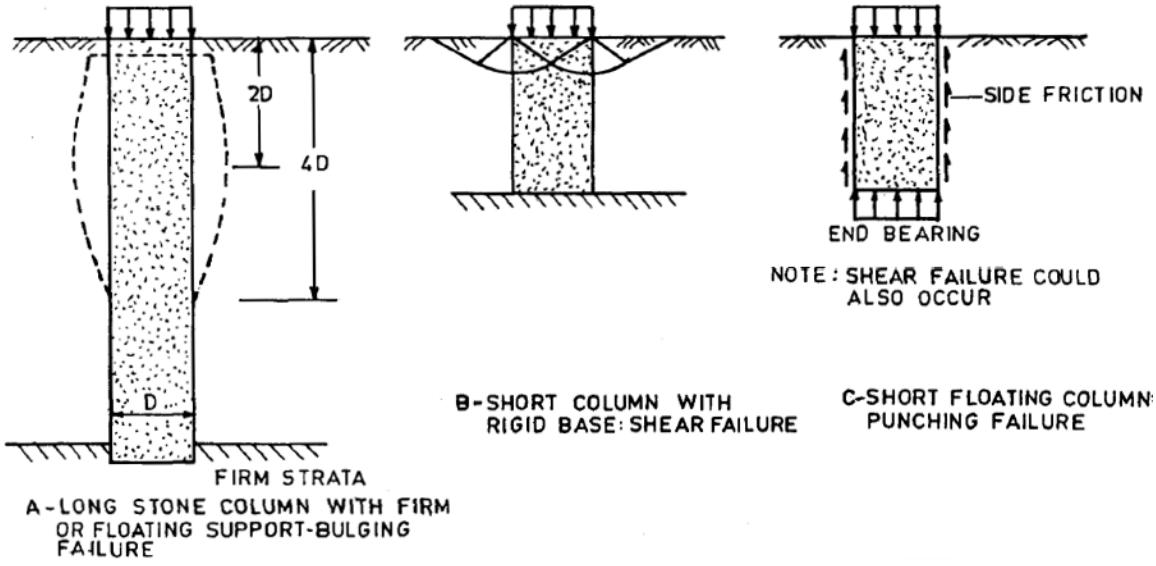

Figure 15-3 Failure modes of a single stone column in a homogeneous soft layer a) bulging failure, b) shear failure and c) punching failure [118]

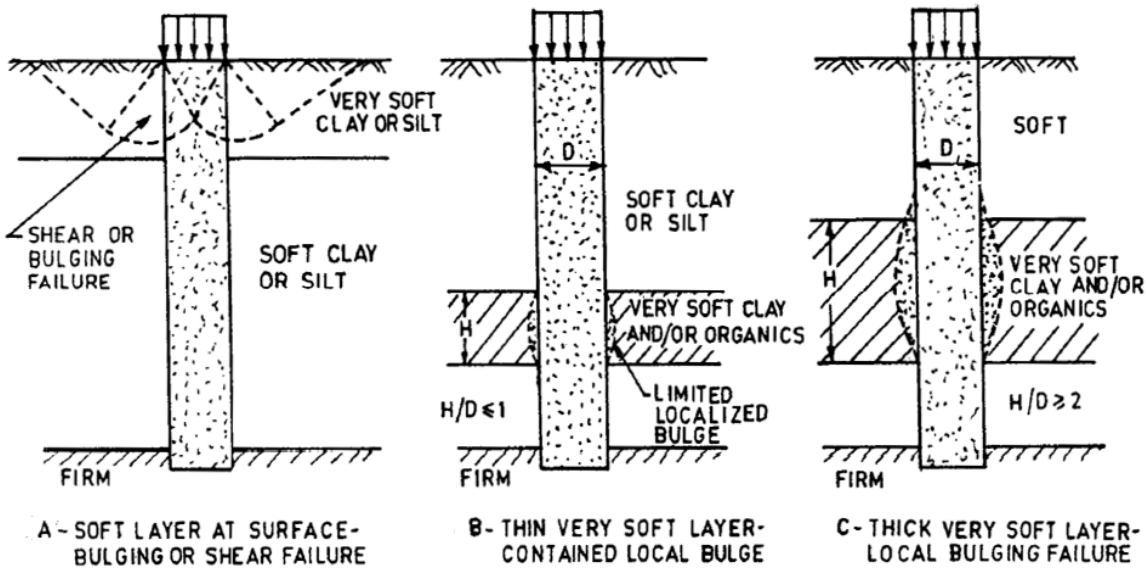

Figure 15-4 Failure modes of a single stone column in a nonhomogeneous cohesive soil a) surface bulging or shear failure, b) local bulge at thin very soft layer and c) local bulge at thick very soft layer [118]

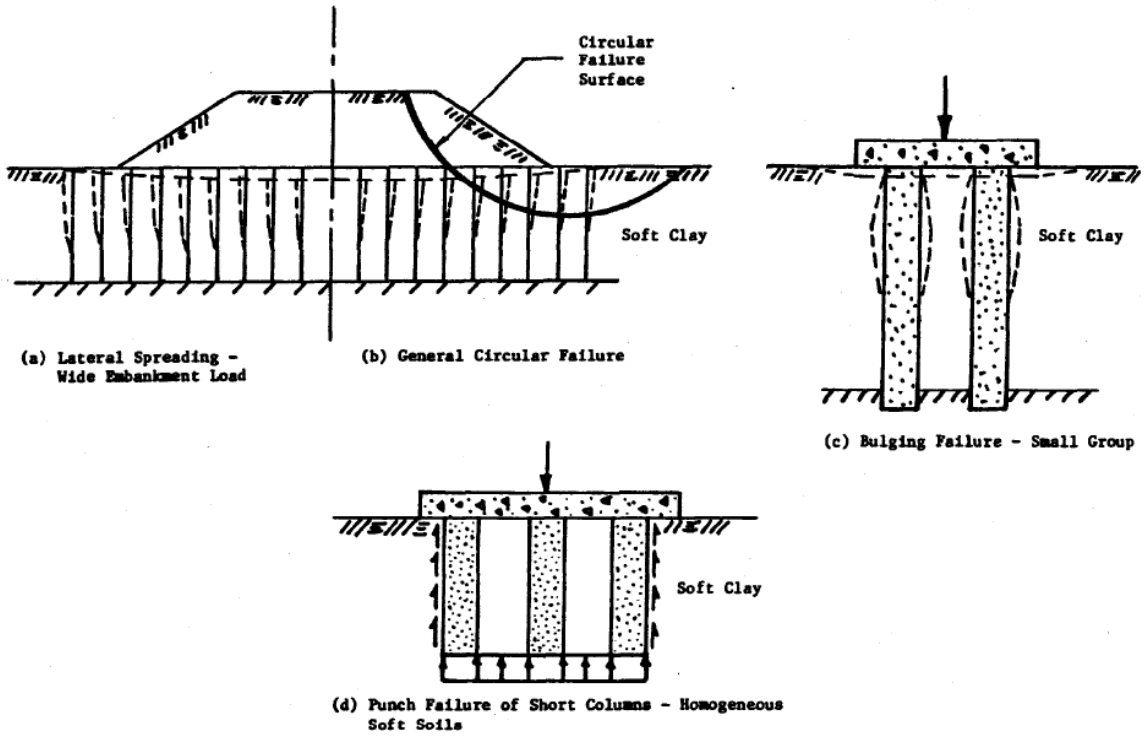

Figure 15-5 Failure modes of stone column groups [118]

Many theories are available to determine the ultimate bearing capacity of a single column surrounded by soft soils and most of them assume a triaxial stress state in the stone columns and failure occurs both in stone columns and the surrounding soil, whereas other methods uses empirical relationships [118]. Regarding the design of stone column groups, some design methods focus on the behavior of an isolated (single) stone column where the bearing capacity of a stone column group is controlled by the behavior of each individual stone column (behavior of individual stone columns are identical in a group of columns) and the number of the stone columns in the group; whereas other methods consider the overall behavior of an infinite grid of stone columns [111]. The following section introduces these methods considering different failure modes and group effects.

Note that the undrained shear strength c_u of the foundation soil, as the key soil property to be used in the bearing capacity analysis, can either be determined by applying the conventional unconsolidated undrained (UU) shear test or by applying the new procedure proposed in Chapter 16.

Failure Mode 1. General Bulging Failure for Single Long Column

The bulging failure shown in Figure 15-3 (a) usually occurs in the most generally constructed long stone columns (with length to diameter ratio equal or greater than 4 – 6) within the depth of the upper 3-diameters of the stone column. Either the cavity expansion theory [132] or the bearing capacity factor method [118] can be used to calculate the bearing capacity of stone column treated ground considering the general bulging failure.

Cavity expansion theory

A very conservative way to determine the bearing capacity of stone columns in homogenous soil considering general bulging failure is by applying classic plasticity theory, in which the failure of a stone column occurs when the lateral confining pressure σ_3 reaches the ultimate passive resistance mobilized by the surrounding soil as the stone column bulges against the soil [118]. In this case, the ratio of the ultimate vertical

stress q_{ult} (i.e. σ_1) to the ultimate lateral stress σ_3 is equal to the coefficient of passive earth pressure K_p which is a function of the internal friction angle of the stone column φ_s:

$$\sigma_1/\sigma_3 = K_p = \frac{1+\sin\varphi_s}{1-\sin\varphi_s} \tag{15-10}$$

$$q_{ult} = \sigma_3 \cdot \frac{1+\sin\varphi_s}{1-\sin\varphi_s} \tag{15-11}$$

where q_{ult} is the ultimate bearing stress that the stone column can sustain and the other parameters are previously defined.

Hughes and Withers [133] proposed a cavity expansion theory in which the bulging failure of a stone column is modeled as an infinitely long expanding cylindrical cavity (similar to the cavity in a pressure-meter test) [118] using elastic-plastic theory for frictionless material; Vesic [132] also proposed a cavity expansion theory taking into account both the friction and cohesion of soils. The ultimate lateral stress σ_3 of Vesic's cavity expansion theory is expressed as:

$$\sigma_3 = cF_c' + qF_q' \tag{15-12}$$

with

$$q = \frac{(1+2\cdot K_0)\cdot\sigma_v}{3} \tag{15-13}$$

$$\sigma_v = \gamma_c \cdot h \tag{15-14}$$

$$h = d_f + \frac{1}{2}D\tan(45^\circ + \frac{\varphi_s}{2}) \tag{15-15}$$

where c is the cohesion of the surrounding cohesive soil (equivalent to undrained shear strength), q is the mean stress at the failure depth, K_0 is the coefficient of earth pressure at rest ($K_0 = 1 - \sin\varphi_c$), φ_c is the friction angle of the surrounding soil (for clay under undrained condition $\varphi_c = 0$), σ_v is the overburden pressure, γ_c is the saturated or wet unit weight of the soil, h which is the depth where the bulging failure occurs can be estimated as a function of [134] the depth of the foundation structure (if any) below ground surface d_f, the diameter of the stone column D and the friction angle of the stone column φ_s as shown in Equation (15-15), F_c' and F_q' are cavity expansion factors determined using Figure 15-6 or Equation (15-16) and (15-17).

$$F_c' = \ln I_r + 1 \tag{15-16}$$

$$F_q' = (1+\sin\varphi_c)(I_r\sec\varphi_c)^{\frac{\sin\varphi_c}{1+\sin\varphi_c}} \tag{15-17}$$

The Rigidity Index shown in Figure 15-6 is determined as follows:

$$I_r = \frac{E}{2(1+\nu)(c+q\tan\varphi_c)} \tag{15-18}$$

where E is the modulus of elasticity of the surrounding soils in which the failure occurs (use an upper bound limit $E = 11c_u$ for soft to stiff non-organic soils; use an lower bound limit $E = 5c_u$ for very soft or organic soil with Plasticity Index greater than 30), ν is the Poisson's ratio (0.5 for undrained clay) and other parameters are previously defined.

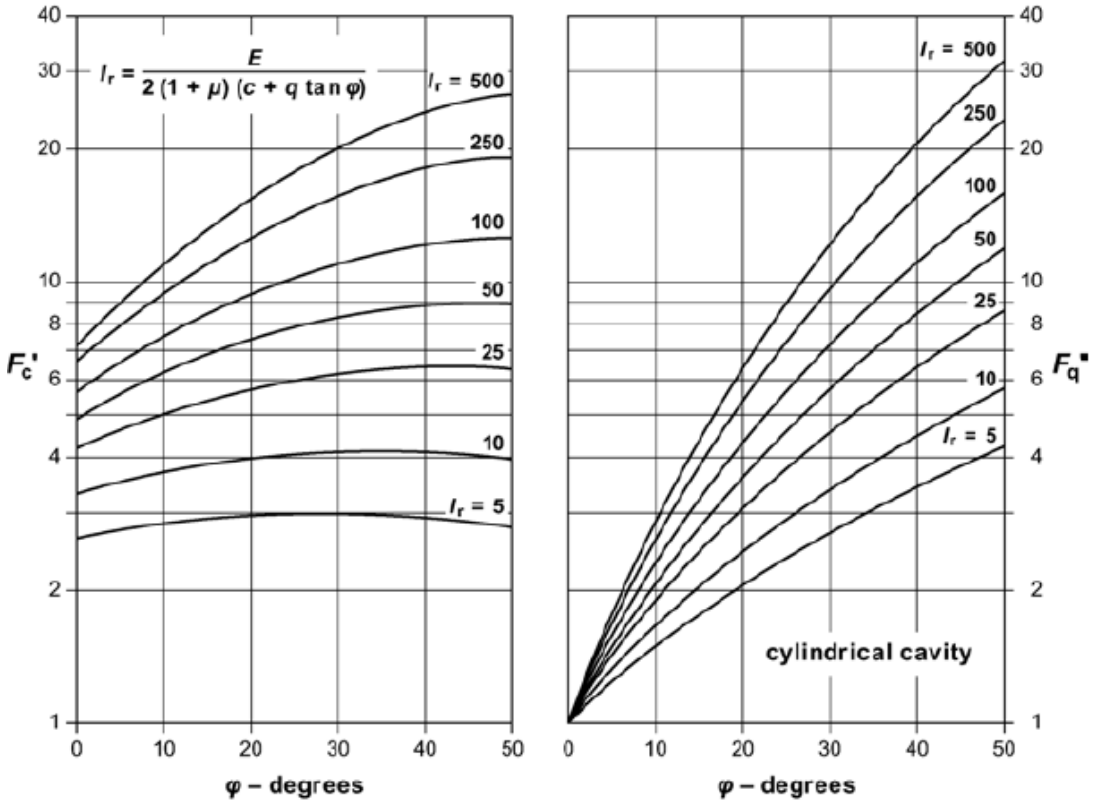

Figure 15-6 Cylindrical cavity expansion factors [111]

Bearing capacity factor method

Barksdale and Bachus [118] proposed a simple bearing capacity factor method on the basis of the Vesic's method to determine the bearing capacity of a single long column. In this method, the bearing capacity of a single column (either isolated or located within a group) is expressed as:

$$q_{ult} = c_u N_c \tag{15-19}$$

where q_{ult} is the ultimate stress that the stone column can carry, c_u is the undrained shear strength of the surrounding soil and N_c is the bearing capacity factor for the stone column determined based on back-calculation of field testing results [105]. Mitchell [135] provided a recommended value of $N_c = 25$ for stone columns constructed using the vibro-replacement method, whereas Datye et al. [136] suggested to use 25 to 30 for stone columns; however these analyses do not consider the strength of the surrounding soil which are more applicable in the case of foundations where settlement is the greatest concern rather than stability [118].

Barksdale and Bachus [118] indicated that N_c ranges from 18 to 22 depending on the stiffness of the surrounding soil. For soils with low stiffness, such as peats, organic cohesive soils and soft clays with Plasticity Index greater than 30, N_c of 18 is recommended; for soils with high stiffness, such as inorganic soft to stiff clays and silts, N_c of 22 is recommended. It should be noted that the strength of both soil and stone columns is considered in this analysis. In addition, a factor of safety equal to 3 is recommended for design [101].

For routine design, the ultimate bearing capacity of stone column groups can be estimated by multiplying the ultimate bearing capacity of a single stone column by the number of the columns in the group. In the case of the analysis for embankments or heavy tanks where bearing capacity is critical, a circular arc analysis should be performed to analyze the overall group effects on the stability of the structure and a minimum safety factor of 1.5 to 2 is recommended [118].

Failure Mode 2. Column Head Shear Failure for Single Long Column

Brauns [137] proposed a method which considered the passive earth pressure theory to determine the ultimate bearing stress of stone columns for shear failure that may occur at the near surface area similar to that shown in Figure 15-4 (a).

Brauns' Method

This failure mechanism of the Brauns' method as shown in Figure 15-7 assumed zero skin shear within the fracture surface and zero stress due to volume change

(conservation of volume). The ultimate vertical stress determined using this theory is expressed as:

$$q_{ult} = \sigma_{1,\max} = (q_s + \frac{2 \cdot c_u}{\sin(2 \cdot \delta)}) \cdot (1 + \frac{\tan(\frac{\pi}{4} + \frac{\varphi_s}{2})}{\tan\delta}) \cdot \tan^2(\frac{\pi}{4} + \frac{\varphi_s}{2}) \qquad (15\text{-}20)$$

Where q_{ult} is the ultimate vertical stress, q_s is the surcharge load at the ground surface, c_u is the undrained shear strength of the surrounding soil where failure occurs, φ_s is the friction angle of the stone column and δ is the angle of the shear failure cone which can be determined based on Figure 15-8.

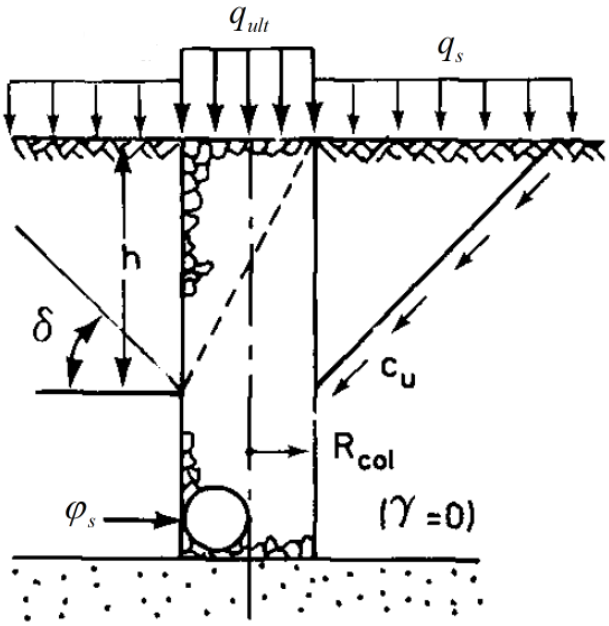

Figure 15-7 Shear failure of a single stone column near the column head [138]

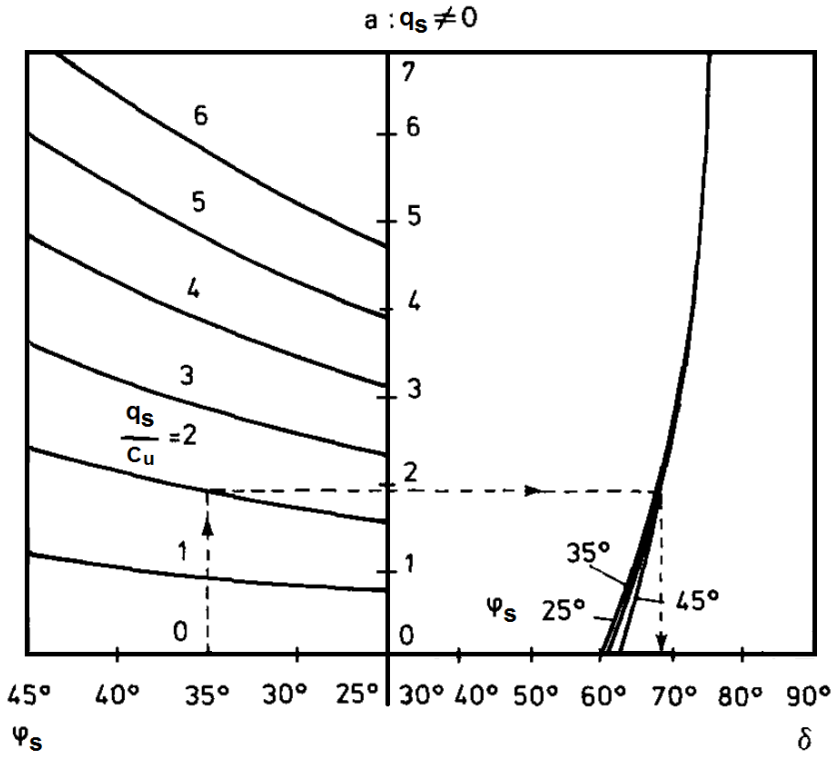

(a)

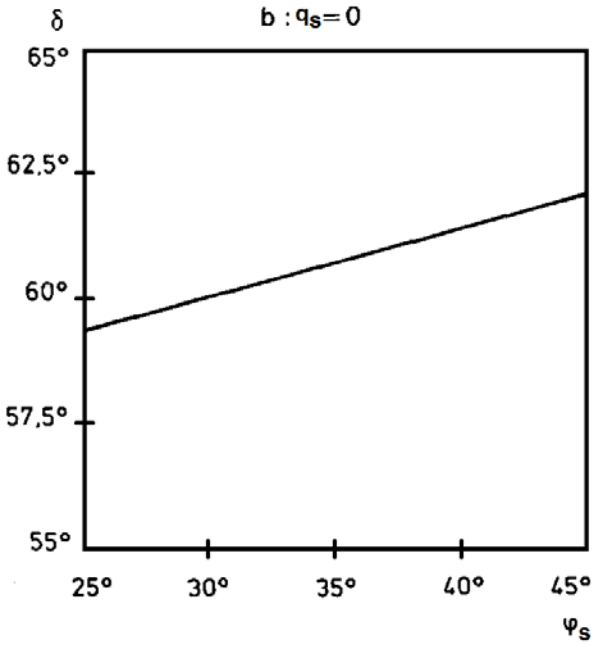

(b)

Figure 15-8 Determination of failure angle δ [137]

Failure Mode 3. Local Bulge Failure for Single Long Column

The local bulge failure mode occurs in long stone columns placed in nonhomogeneous cohesive soil when a very soft soil layer is present either at the surface or deep depth as shown in Figure 15-4. The ultimate bearing capacity of stone columns under these circumstances can be determined by using a semi-empirical method proposed by Barksdale and Bachus [118].

Barksdale and Bachus' Method

Barksdale and Bachus [118] proposed an empirical procedure to determine the ultimate lateral stress σ_3, and used the theory shown in Equation (15-11) to determine the ultimate vertical bearing stress q_{ult}.

For local bulge failure occurs at the surface layer, the ultimate lateral stress σ_3 can be estimated by:

$$\sigma_3 = 2c_u \tag{15-21}$$

where c_u is the undrained shear strength of the surrounding soil.

For local bulge failure occurs below a depth of 3-diameter of the stone column, the ultimate lateral stress σ_3 can be estimated by:

$$\sigma_3 = 9c_u \tag{15-22}$$

For the local bulge failure that occurs at a given depth below the surface and within the depth of 3-diameter of the stone column, the ultimate lateral stress σ_3 can be estimated by:

$$\sigma_3 = (2 + \frac{7h}{3D})c_u \tag{15-23}$$

where D is the diameter of the stone column and h is the depth where the stone column failure occurs [118].

Failure Mode 4. Shear and Punching Failure for Single Short Column

The failure of a short stone column may occur in the form of either general local shear failure at the near surface area as shown in Figure 15-3 (b) or punching failure as shown in Figure 15-3 (c).

The general local shear failure of a stone column treated ground under the surcharge load is shown in Figure 15-9; the bearing capacity of this case can be calculated based on the theorems of Drucker and Prager for the plane strain loading condition [118]:

$$q_{ult} = \frac{\gamma_c B}{2} N_r + cN_c + D_f \gamma_c N_q \tag{15-24}$$

where q_{ult} is the ultimate bearing stress, γ_c is the saturated or wet unit weight of the cohesive soil, B is the width of the loading area, c is the cohesion of the surrounding soil (equivalent to undrained shear strength), D_f is the depth of embedment and N_r, N_c and N_q are the bearing capacity factors given in Figure 15-10.

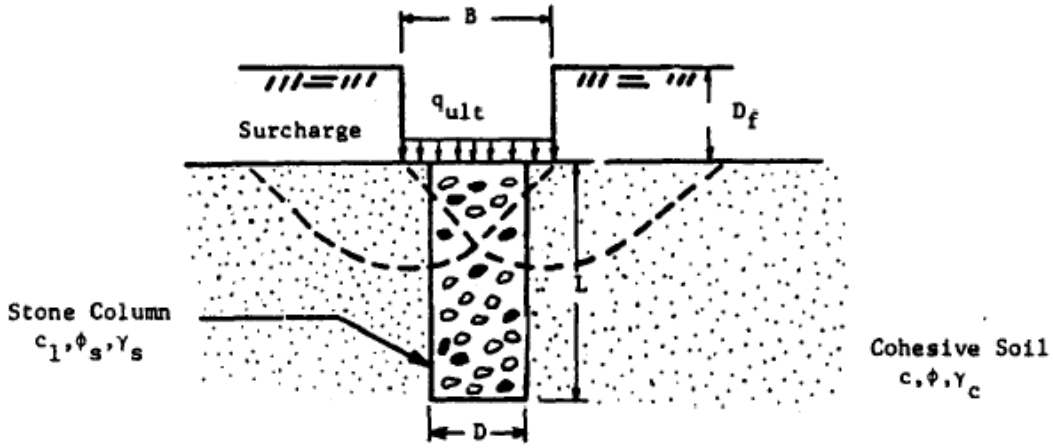

Figure 15-9 General local shear failure of a stone column treated ground [118]

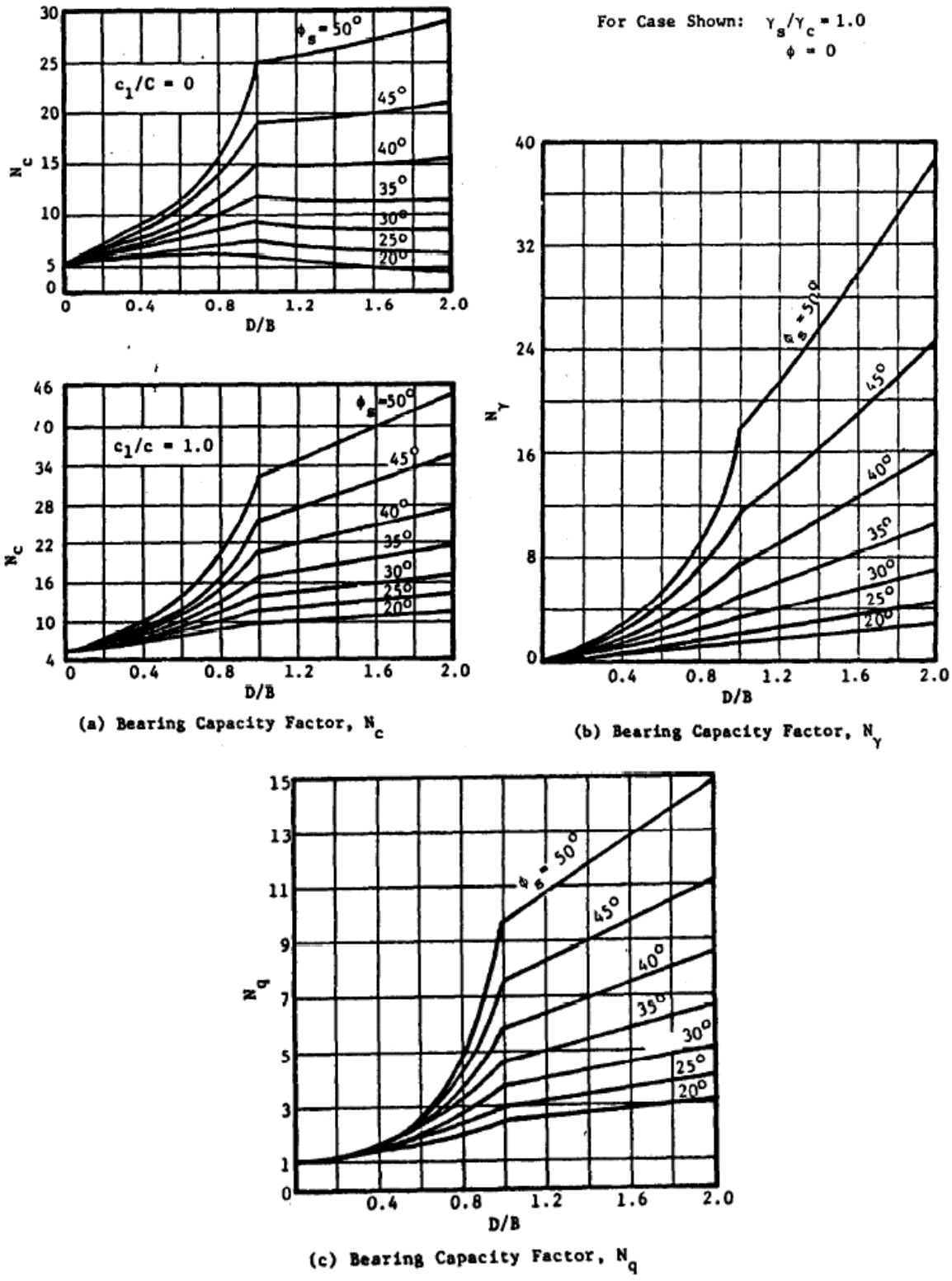

Figure 15-10 Bearing capacity factors for stone column treated soil [118]

The ultimate bearing capacity for punching failure can be calculated using the conventional bearing capacity theories considering the end bearing capacity of a stone column plus the skin friction along the side of the column [118].

Failure Mode 5. Shear Failure of Stone Column Groups

The method is applicable for small stone column groups placed in firm to strong cohesive type of soils with undrained shear strength greater than 600 – 800 psf under either a square or infinitely long rigid concrete footing as shown in Figure 15-11. Shear type failure which usually occurs in the form of a composite soil-stone column triangular failure wedge underneath the footing area is assumed for this type of stone column groups [118].

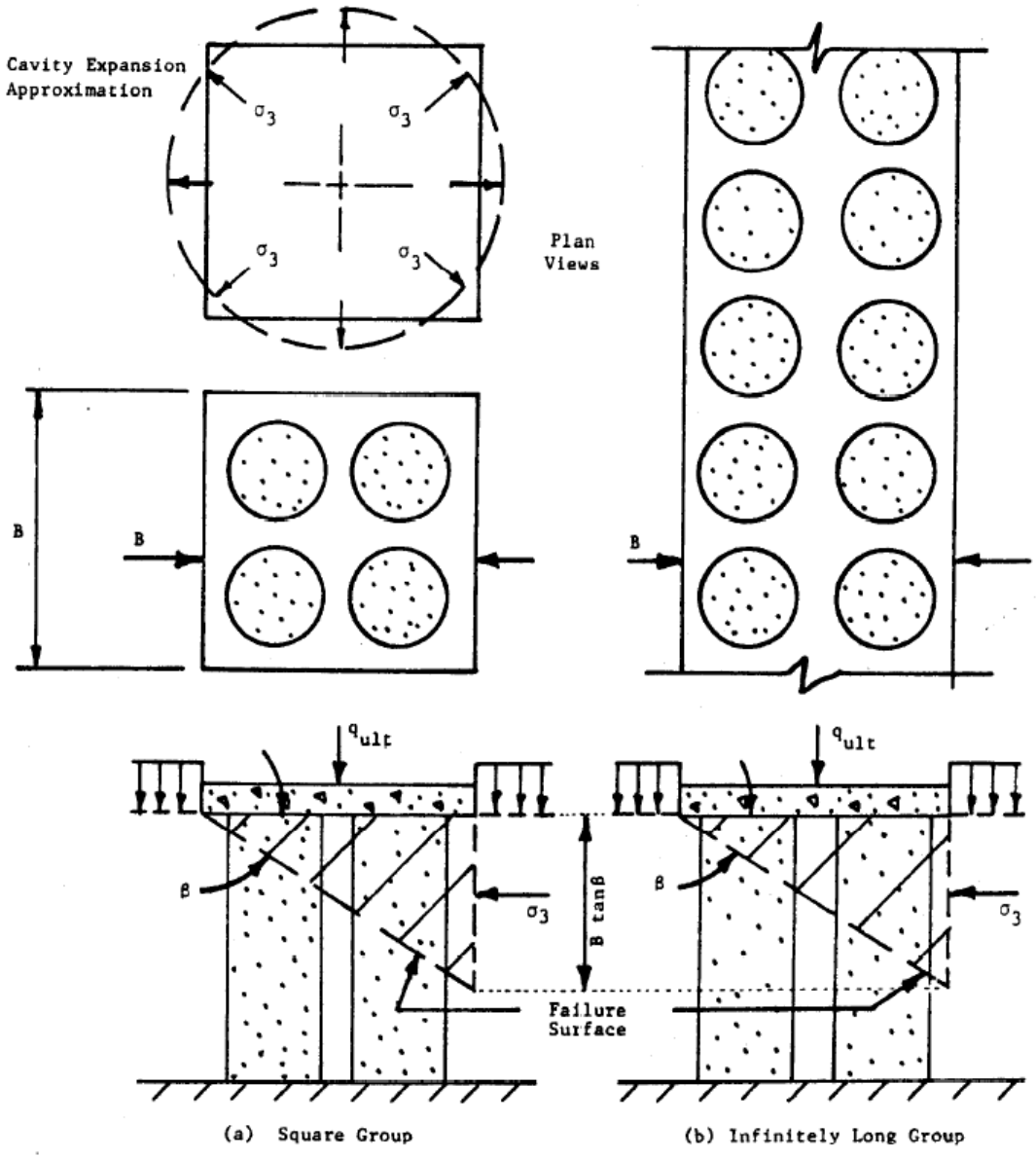

Figure 15-11 Shear failure of (a) square and (b) infinitely long stone column groups [118]

The ultimate vertical stress q_{ult} of the failure wedge depends on the shear strength of the composite soil-stone column wedge and the ultimate lateral resistance of the wedge σ_3. The parameters relative to the shear strength of the composite wedge are defined as:

$$\tan\varphi_{avg} = \mu_s a_s \tan\varphi_s \tag{15-25}$$

$$c_{avg} = (1 - a_s)c \tag{15-26}$$

where $\tan\varphi_{avg}$ is the tangent of the composite internal friction angle on the failure plane, μ_s is the ratio of stresses in the stone column to the stress over the unit cell as defined in Equation (15-9), a_s is the area replacement ratio defined in Equation (15-3), $\tan\varphi_s$ is the tangent of the stone column internal friction angle on the failure plane, c_{avg} is the composite cohesion on the failure plane and c is the cohesion (equivalent to undrained shear strength) of the surrounding cohesive soil. The angle of the failure surface β can be determined as:

$$\beta = 45° + \frac{\varphi_{avg}}{2} \tag{15-27}$$

$$\varphi_{avg} = \tan^{-1}(\mu_s a_s \tan\varphi_s) \tag{15-28}$$

The ultimate lateral pressure σ_3 for a square foundation can be determined using the Vesic [132] cavity expansion theory as shown from Equation (15-12) to (15-18), where Equation (15-15) can be modified to:

$$h = d_f + D\tan\beta \tag{15-29}$$

with

$$D = \sqrt{4A/\pi} \tag{15-30}$$

$$A = B^2 \text{ or } A = BL \tag{15-31}$$

where h is the depth of the failing wedge, D is the diameter of the failing cavity (i.e. width of the failing wedge), d_f is the depth of the foundation structure (if any) below ground surface, B is the length of a side of a square foundation structure or the width of a rectangular foundation structure and L is the length of the rectangular foundation structure.

The ultimate lateral pressure σ_3 for an infinitely long footing can be expressed as Equation (15-32) which is derived based on classical earth pressure theory [118]:

$$\sigma_3 = \frac{\gamma_c D\tan\beta}{2} + 2c_u \tag{15-32}$$

where γ_c is the saturated or wet unit weight of the cohesive soil, and the other parameters are previously defined.

Therefore, the ultimate vertical stress q_{ult} for a stone column group considering shear failure can be determined as:

$$q_{ult} = \sigma_3\tan^2\beta + 2c_{avg}\tan\beta \tag{15-33}$$

where σ_3 is calculated using either Equation (15-12) or (15-32) depending on the type of the footing (i.e. foundation structure) and all the other terms are previously defined. Note that the weight of the soil within the failure wedge is neglected which yields conservative results.

SETTLEMENT

One of the major benefits of using stone columns is to reduce settlement of a foundation upon loading. Numerous research studies have been conducted to develop methods for predicting settlement behavior of stone column reinforced soil [118, 122-126]. In general, most of these methods were assuming equal strain, using the unit cell concept and either based on pseudo-elastic or elasto-plastic theory. In many of the methods, the settlement of the untreated ground needs to be determined first using those conventional settlement analyses [101].

Several design methods were evaluated in the report by Barksdale and Bachus [118], such as the equilibrium, Priebe, Greenwood, incremental and the finite element methods. Specifically, the report [118] suggested that the equilibrium method can be used to provide an upper bound estimation of the settlement of reinforced ground; whereas the nonlinear finite element method can be used to determine a lower bound estimation. The best estimation should be the average of the two estimates.

In the FHWA report by Elias et al. [101], it was suggested that the equilibrium method gives an average or upper bound estimation and the Priebe's method can be used to provide a lower bound estimation for the settlement of stone column treated ground.

Therefore, in order to have a comprehensive idea which requires the knowledge of both upper and lower bound settlement estimations of stone column treated ground, the following of the section mainly focuses on elaborating the three methods introduced in the literature, which are the equilibrium, the finite element and the Priebe's methods.

Note that the compression index C_c of the foundation soil, as the key soil property to be used in the settlement analysis, can either be determined by performing the conventional oedometer test or by applying the new procedure proposed in Chapter 16.

Equilibrium Method

The equilibrium method provides a very simple and realistic approach for determining the reduction in settlement of stone column treated soil. This method is based on the following assumption: (1) the unit cell idealization, (2) force equilibrium in the unit cell, (3) equal strain (vertical settlement) assumption, and (4) a uniform vertical stress exits throughout the length of the stone column [118].

The vertical stress in the surrounding soil σ_c due to applied stress σ at the ground surface can be determined as:

$$\sigma_c = \mu_c \sigma \tag{15-34}$$

where these terms are already defined in Equation (15-8).

The change in the vertical stress $\Delta\sigma_c$ at the center of each soil layer can be estimated by the Boussinesq stress distribution theory as shown in Figure 15-12.

$$\Delta\sigma_c = I_z \sigma_c \tag{15-35}$$

where I_z is the influence factor determined using the Boussinesq stress distribution as shown in Figure 15-12. Besides using the Boussinesq stress distribution theory, there are other options such as the Newmark's chart method, Osterberg's Influence Chart method and Griffiths' influence factor method to determine the stress increase in soils. For simplicity, this report uses the Boussinesq solution.

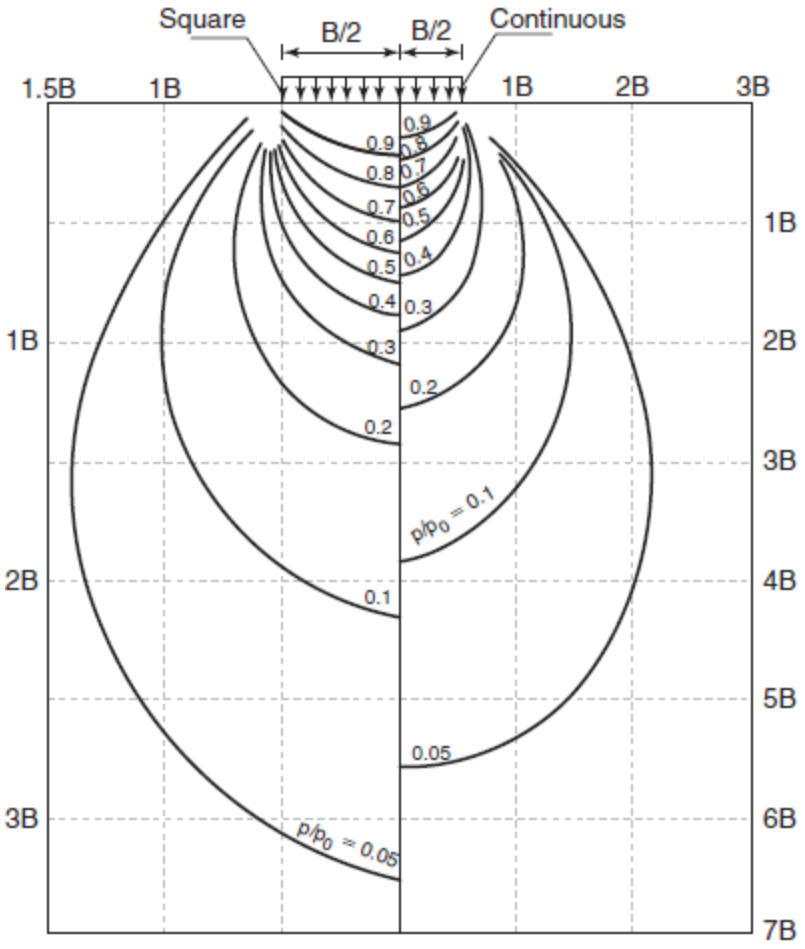

Figure 15-12 Stress distribution based on the Boussinesq elastic theory for a flexible foundation [127]

The conventional 1-d consolidation theory is expressed as:

$$S_t = (\frac{C_c}{1+e_0})\log_{10}(\frac{\bar{\sigma}_0+\Delta\sigma_c}{\bar{\sigma}_0}) \cdot H \tag{15-36}$$

where S_t is the primary consolidation settlement within a depth H of the stone column treated ground, H is the height of the stone column treated ground, $\bar{\sigma}_0$ is the average initial effective vertical stress in the soil layer, C_c is the compression index from a 1-d consolidation test and e_0 is the initial void ratio.

The ratio of settlement in the stone column treated ground to that in the untreated ground, S_t/S can be determined as:

$$\frac{S_t}{S} = \frac{\log_{10}(\frac{\bar{\sigma}_0+\mu_c\Delta\sigma}{\bar{\sigma}_0})}{\log_{10}(\frac{\bar{\sigma}_0+\Delta\sigma}{\bar{\sigma}_0})} \tag{15-37}$$

This equation essentially indicates that the level of improvement of settlement depends on: (1) the stress concentration ratio, SCR which is reflected through μ_c, (2) the average initial effective vertical stress in the soil (or the length of the stone column since $\bar{\sigma}_0$ increases with the increase of length of the stone column), (3) the applied stress σ.

For very large $\bar{\sigma}_0$ and small applied stress σ, the ratio of settlement rapidly approaches:

$$\frac{S_t}{S} = \frac{1}{[1+(SCR-1)\cdot a_s]} = \mu_c = \frac{1}{n} \tag{15-38}$$

where n is the settlement improvement ratio and all the terms are previously defined. The equation is shown graphically in Figure 15-13 which provides a slightly unconservative estimation of the settlement improvement and can be used for preliminary estimations. For the equilibrium method, a SCR of 4 – 5 is recommended based on the comparison between the calculated and measured settlement in field studies [118].

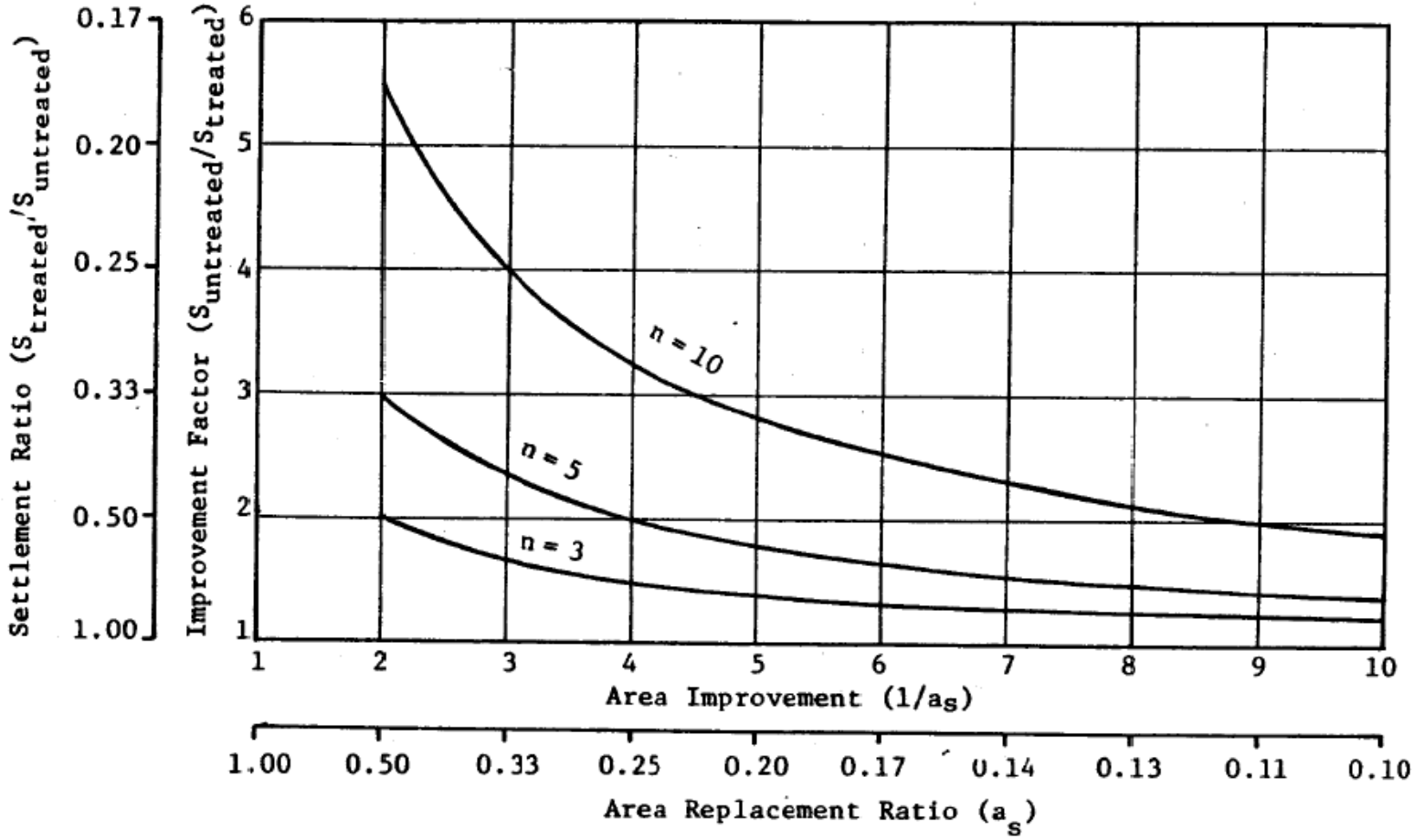

Figure 15-13 Maximum reduction in settlement that can be obtained using the equilibrium method [118]

Finite Element Method

The finite element method provides the most theoretical approach to model the stone column treated ground, in which nonlinear material properties, interface slip and suitable boundary conditions can all be modeled [118]. Barksdale and Bachus [118] conducted finite element modeling on the behavior of stone column treated ground to extend the early work into design chart for predicting primary consolidation settlement.

In this finite element study, computations of incremental and total stresses were conducted by solving a system of linear, incremental equilibrium equations. Eight node isoparametric material elements were used in the modeling; only one unit cell was modeled since the stress condition was uniform in the stone columns and soils. The interface element was set to be capable of modeling no slip, slip and separation by using the Mohr-coulomb failure theory, in order to define the maximum allowable shear at the interface between stone and soil particles. The stiffness of the system was allowed to vary after each load increment and iteration.

The finite element analyses which led to the development of design charts were divided into two sections: the first section dealt with low compressibility soils and the other focused on compressible cohesive soils. A low compressibility soil is defined as the soils that have a modulus ratio $E_s/E_c \leq 10$, where E_s and E_c are the average modulus of elasticity of the stone column and soil, respectively. A compressible cohesive soils is defined as the soils that have a modulus ratio $E_s/E_c > 10$.

Low compressibility soil

For low compressibility soil, such as stone column treated sand, silty sand and some silts, a linear elastic theory was used in the finite element modeling. The Poisson's ratio is assumed to be 0.30 for soil and 0.35 for stone. The finite element model based on the unit cell idealization is shown in Figure 15-14. Settlement prediction curves were developed for area replacement ratio of 0.1, 0.15 and 0.25; an example of the curve is shown in Figure 15-15 for an area replacement ratio of 0.1. Other curves that use different area replacement ratios can be found from Figure J-1 to Figure J-3 in

the Appendix J [118]. The curves are applicable for stone column length to diameter ratios L/D of 5, 10, 15 and 20.

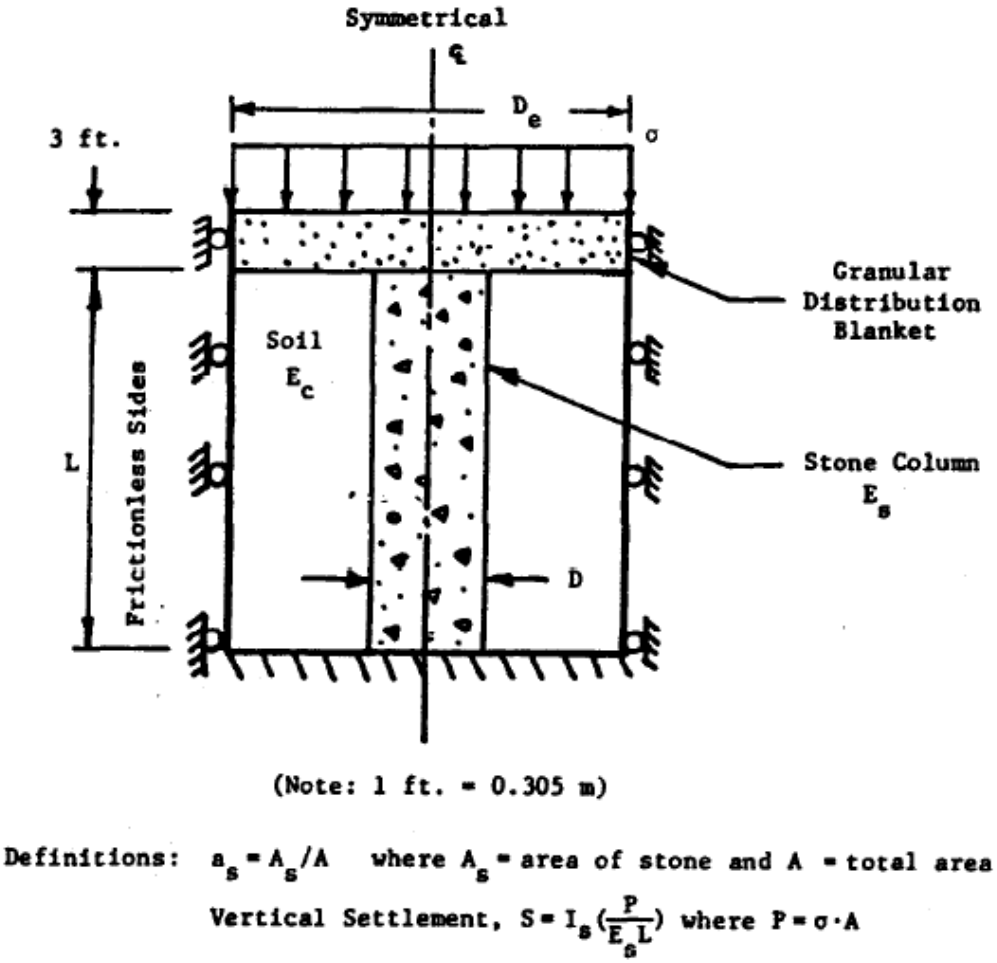

Figure 15-14 Unit cell model for low compressibility soil [118]

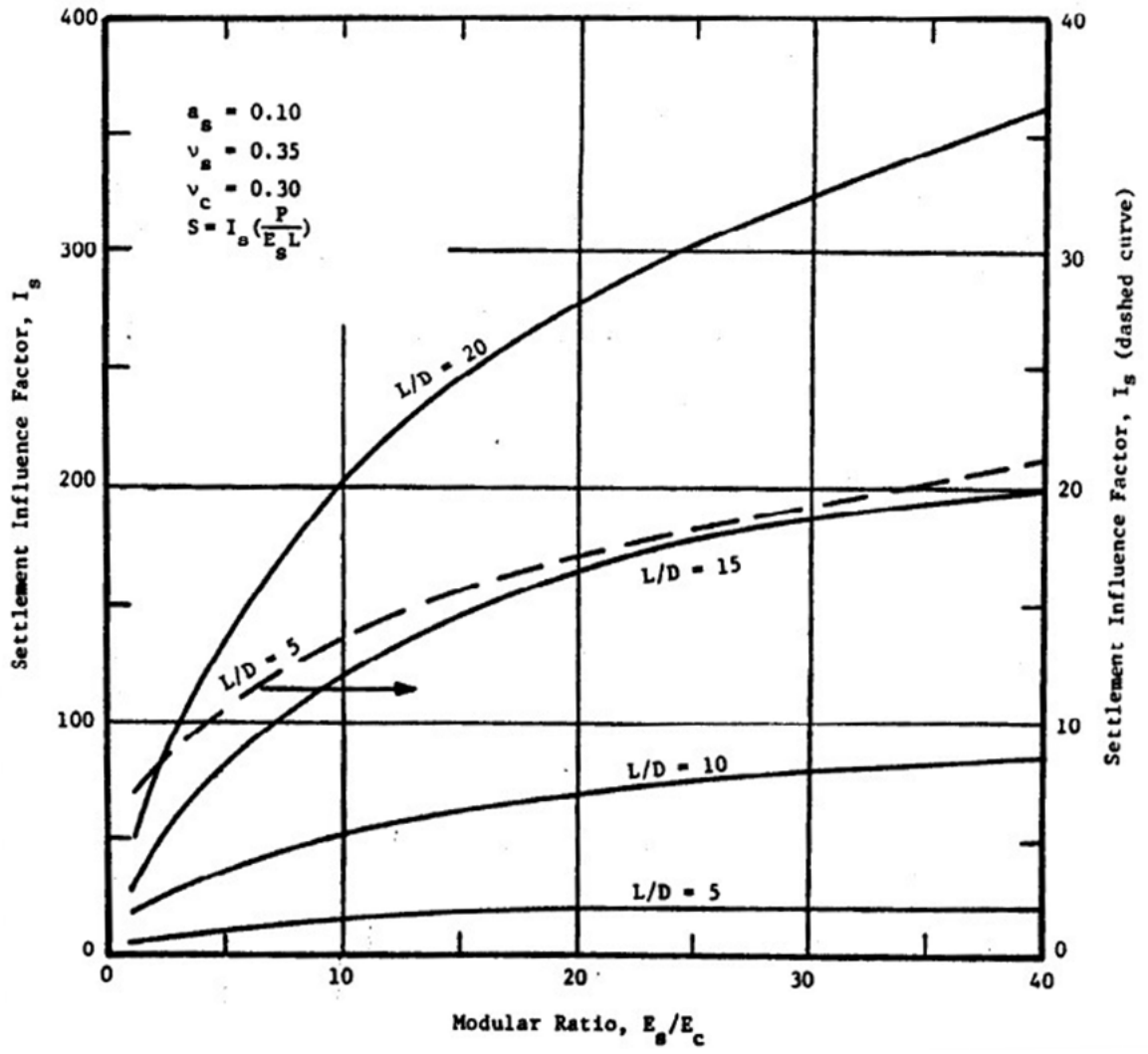

Figure 15-15 Settlement prediction curve for low compressibility soil with an area replacement ratio of 0.1 [118]

To predict the long-term primary consolidation settlement of the low compressibility soil, the drained modulus of elasticity of the cohesive soil needs to be used, which can be estimated using the following function if a drained triaxial test is not performed [118]:

$$E_c = \frac{(1+\nu)(1-2\nu)(1+e_0)\sigma_{va}}{0.435(1-\nu)C_c} \quad (15\text{-}39)$$

where E_c is the drained modulus of elasticity of the soil, e_0 is the initial void ratio, C_c is the compression index, ν is the Poisson's ratio (drained) and σ_{va} is the average of initial

and final stress state applied in the field (vertical stress). The selection of drained Poisson's ratio can be found in Figure 15-16.

Soil Consistency	Poisson's Ratio[1]
Very Soft to Soft[2,3]	0.35 - 0.45
Firm to Stiff[2]	0.30 - 0.35
Stiff Overconsolidated Clays	0.1 - 0.30

Notes: 1. For undrained loading use 0.45.
2. For normally consolidated clays.
3. For very soft to soft clays a value of 0.40-0.45 is recommended for calculating E_c for nonlinear finite element settlement analyses of stone column improved ground; for firm to stiff use at least $\nu_c = 0.35$.

Figure 15-16 Typical Poisson's ratio of clay under drained loading [118]

The stress dependent modulus of elasticity of stone column E_s is also required in the calculation, which is expressed as:

$$E_s = (\sigma_1 - \sigma_3)/\varepsilon_a \tag{15-40}$$

where $(\sigma_1 - \sigma_3)$ is the deviator stress under the applied load, σ_1 is the vertical stress in the column and σ_3 is the lateral stress in the column. It should be noted that both the at rest stress and the change in stress due to loading should be accounted for when calculating σ_1 and σ_3. The axial strain ε_a can be obtained from the stress-strain curve of a triaxial shear test on the stone column.

If a triaxial shear test or a field loading test is not available, the modulus of elasticity of stone column E_s can be determined using a hyperbolic expression developed by Duncan and Chang [128]:

$$E_s = K \cdot \sigma_\theta^n \cdot [1 - \frac{(\sigma_1 - \sigma_3)R_f}{(\frac{2(c \cdot \cos\varphi_s + \sigma_3 \sin\varphi_s)}{1 - \sin\varphi_s})}] \tag{15-41}$$

where E_s is the stress-dependent secant modulus of the stone (psi.), K, n are constants defining the initial modulus of the stone under low deviator stress, c is the cohesion of the stone which is often assumed as zero, φ_s is the friction angle of the stone, R_f is the failure ratio and $\sigma_\theta = \sigma_1 + \sigma_2 + \sigma_3$ (psi.). Without having specific test data, the following

parameters can be assumed where $K = 88.6$, $n = 1.14$, $R_f = 0.86$, $c = 0$ and $\varphi_s = 42° - 45°$. The settlement curves developed in this study were based on these values [118].

Compressible cohesive soil

For compressible cohesive soil, such as soft to firm clays, the soil was assumed to be elasto-plastic and the stones are stress dependent. The finite element model based on the unit cell idealization is shown in Figure 15-17. As shown in the figure, a soft boundary is placed around the unit cell in addition to the stone column and cohesive soil elements; this soft boundary is introduced to account for the effect of later bulging which induces lateral deformation at the support contributed by the sides of the unit cell. By trial and error using the finite element analysis, it was found that the use of a boundary of 1 in. thick with elastic modulus of 12 psi could successfully model the maximum lateral deformation induced by lateral spreading occurred in a unit cell; to obtain variation in the boundary stiffness, a rigid boundary with a modulus of 1000 psi was also used. The model shown in Figure 15-17 was developed by also considering a representative friction angle of $42°$ for the stone and $0°$ for the soil, a coefficient of at-rest earth pressure of 0.75 and a Poisson's ratio of 0.35 for both stones and soil. The modulus of elasticity and shear strength of the soil were assumed to be equal or less than 160 psi and 400 psf, respectively [118].

One example of the settlement prediction curves for compressible cohesive soil is shown in Figure 15-18. Other curves that use different area replacement ratios (ranging from 0.1 to 0.35) and column length to diameter ratios (ranging from 5 to 20) can be found from Figure J-4 to Figure J-12 in Appendix J [118]. As seen in the figure, settlement is a function of the average applied stress σ over the unit cell, modulus of elasticity of the soil E_c, area replacement ratio a_s, column length to diameter ratio L/D and boundary rigidity E_b. The modulus of elasticity of the soil can be determined again using Equation (15-39); also knowing the values of other parameters, the settlement of stone column improved ground can be determined using these prediction curves.

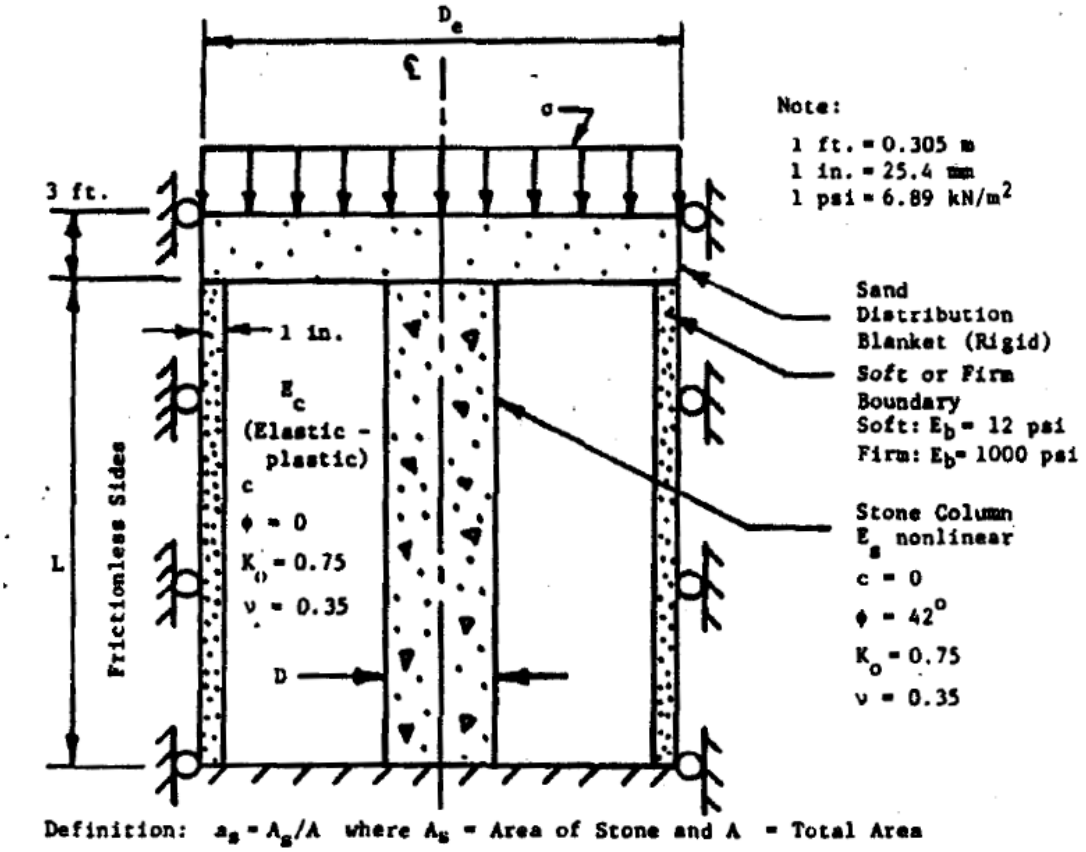

Figure 15-17 Unit cell model for compressible cohesive soil [118]

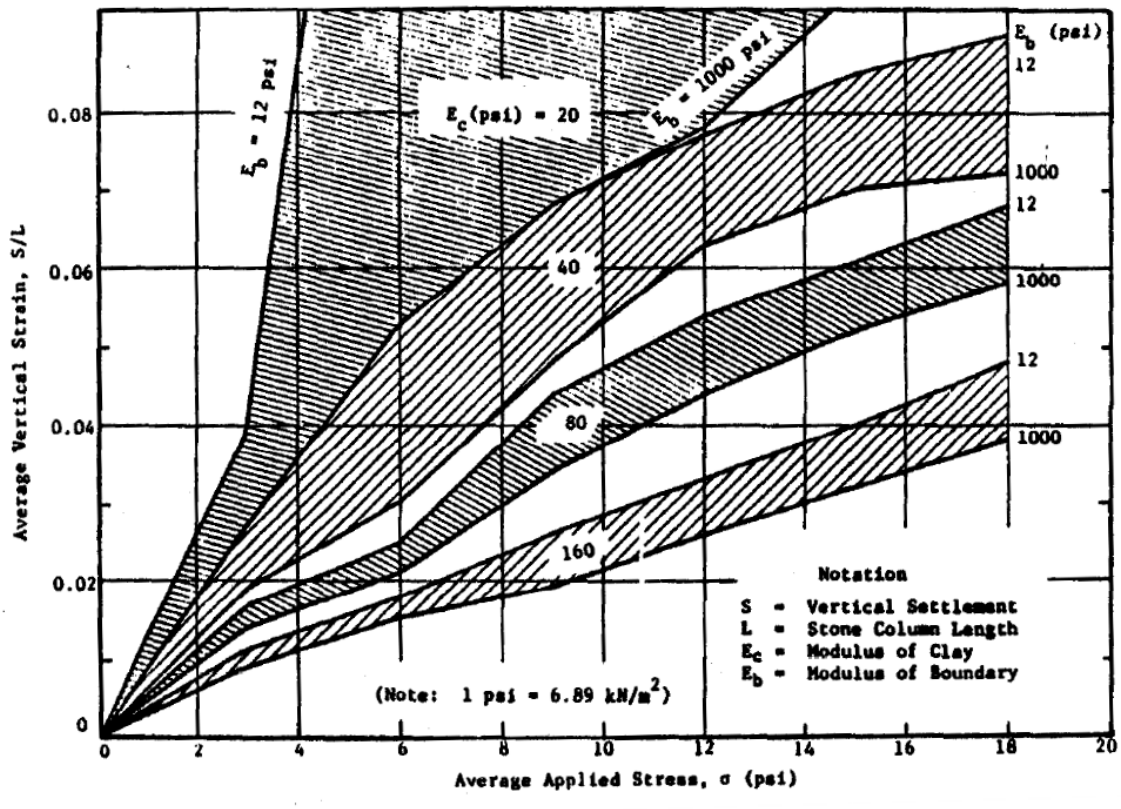

Figure 15-18 Settlement prediction curve for compressible cohesive soil with an area replacement ratio of 0.1 and *L/D* of 5 [118]

Priebe's Method

The Priebe's method is a semi-empirical method commonly used for predicting settlement design of stone columns and has been widely used in the industry, especially in Europe, by corporations such as Chambosse & Dobson (undated-a) with GKN Keller and the Vibroflotation Group [121, 129].

The Priebe's method has made a few assumptions for the analyses; the aggregates in a stone column are assumed to be plastic and incompressible; the soil in a unit cell is assumed to have elastic behavior; any change in the volume within the soil is due to the bulging of the column; the radial deformation in the soil is calculated using an infinitely long, elastic hollow cylinder solution; the bulk densities of both the stone column and the soil are neglected; the surrounding soil is assumed to be already displaced due to the inclusion of stone column which therefore results in a liquid state

(the coefficient of earth pressure $K = 1$) [118, 121, 129]. In addition, equal vertical strain (settlement) assumption and unit cell idealization are used. Based on the conservation of load and equal strain assumption, deformation and stresses in the elastic soil can be calculated systematically [130].

The following equations provide the derivation of the basic settlement improvement factor based on the aforementioned assumptions:

$$n_0 = 1 + \frac{A_s}{A}\left[\frac{1/2 + f(\nu, A_s/A)}{K_{aC} \cdot f(\nu, A_s/A)} - 1\right] \tag{15-42}$$

Where n_0 is the basic settlement improvement factor, A_s is the area of the stone column, A is the total area within a unit cell, K_{aC} is the Rankine's active earth pressure, which is a function of:

$$K_{aC} = \tan^2(45° - \varphi_s/2) \tag{15-43}$$

and $f(\nu, A_s/A)$ can be expressed as:

$$f(\nu, A_s/A) = \frac{(1-\nu)\cdot(1-A_s/A)}{1-2\nu+A_s/A} \tag{15-44}$$

where ν is the Poisson's ratio of the surrounding soil and φ_s is the friction angle of the stone column.

If a Poisson's ratio of $\nu = 1/3$ is used, Equation (15-42) becomes:

$$n_0 = 1 + \frac{A_s}{A}\left[\frac{5 - A_s/A}{4 \cdot K_{aC} \cdot (1 - A_s/A)} - 1\right] \tag{15-45}$$

The relationship between the basic settlement improvement factor n_0, the friction angle of the stone column material φ_s and the reciprocal area ratio A/A_s can be illustrated in the widely-known diagram as shown in Figure 15-19. In the end, the settlement of stone column improved ground can be calculated by using the improvement factor as:

$$S_t = S/n_0 \tag{15-46}$$

Where S_t is the settlement of the stone column treated ground and S is the settlement of the untreated ground which can be determined using conventional settlement analysis methods.

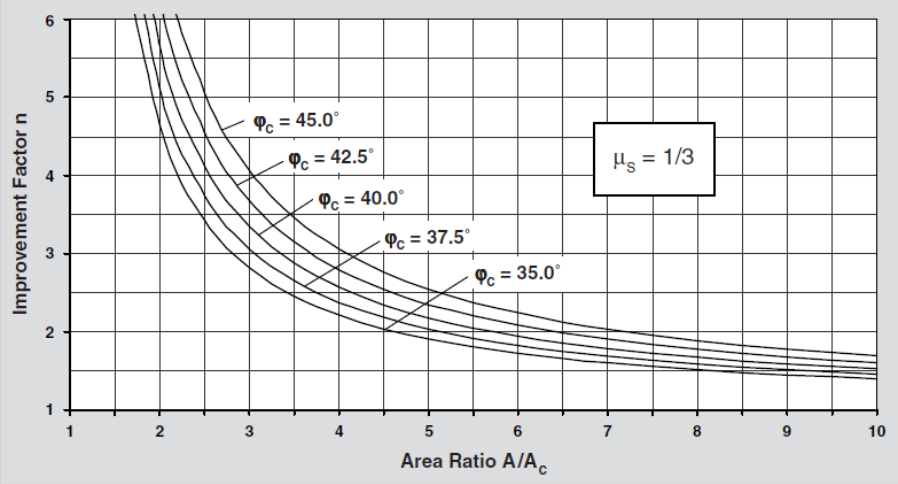

Figure 15-19 Design chart for stone column using Priebe's Method [129]

It should be noted that the above method is the original one published in 1976; there have been a few adaptions, extensions and supplements made in the 1995 version [129] which justify a more comprehensive application of this method, such as the consideration of the compressibility of stone column (resulting in slightly increased value of predicted settlement) , overburden (leading to a reduced value of predicted settlement) and compatibility control (prevents the compressibility of the stone column from being greater than the settlement of the composite structure). Overall, the consideration of these factors results in smaller values of predicted settlement (especially when the overburden is included) which may provide unconservative settlement predictions; therefore, it is considered that the calculation of the basic improvement factor n_0 is adequate for a lower bound settlement estimation.

Time Rate of Settlement

The inclusion of stone columns may significantly accelerate the process of the primary consolidation since the stone columns act like drainage paths. The report by Barksdale and Bachus [118] showed that the time rate of primary consolidation settlement of stone column treated ground could be estimated by using the sand drain consolidation theory, in which the primary consolidation settlement of a cohesive soil layer reinforced by stone column at time t can be expressed as:

$$S'_t = U \cdot S_t \tag{15-47}$$

where S'_t is the primary consolidation settlement at time t, S_t is the ultimate primary consolidation settlement and U is the average degree of consolidation considering both radial and vertical drainage, which is expressed as:

$$U = 1 - (1 - U_z)(1 - U_r) \tag{15-48}$$

where U_z is the degree of consolidation considering only vertical drainage and U_r is the degree of consolidation considering only radial drainage.

U_z can be determined by using Figure 15-20 and the vertical time factor T_z which is expressed by the following function:

$$T_z = \frac{C_v \cdot t}{(\frac{H}{N})^2} \tag{15-49}$$

where C_v is the coefficient of consolidation in the vertical direction, t is the elapsed time, H is the thickness of the soil layer and N is the number of permeable drainage surface at the top and/or the bottom of the layer ($N = 1$ for one-way draining and $N = 2$ for two-way draining).

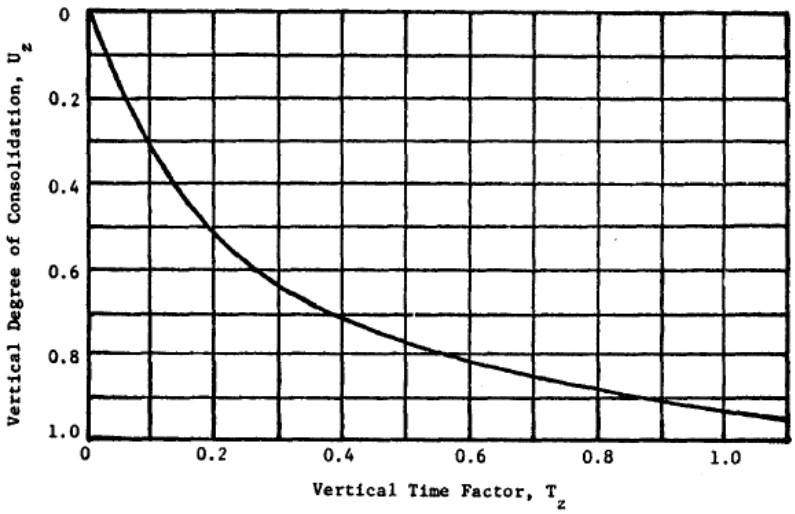

Figure 15-20 Determination of the degree of consolidation considering only vertical drainage [118]

U_r can be determined by using Figure 15-21 and the radial time factor T_r which is expressed by the following function:

$$T_r = \frac{C_{vr} \cdot t}{(D_e)^2} \tag{15-50}$$

where C_{v_r} is the coefficient of consolidation in the radial direction (which is usually 3 – 5 times greater than the coefficient of consolidation in the vertical direction), t is the elapsed time and D_e is the equivalent diameter of the unit cell. In Figure 15-21, the determination of U_r requires the calculation of n^* which can be expressed as:

$$n^* = D_e/D' \tag{15-51}$$

where D' is the reduced drain diameter which accounts for the "smear effects" in the surrounding soil (a reduction effect in the horizontal permeability of the soil around stone columns due to the remolding, disturbance and smear of the surrounding soil caused by the installation of stone columns). Literature [118] indicated that the research regarding the smear effects on the stone column was very limited; if not having enough information about the smear effect, it was tentatively recommended that the reduced drain diameter could be taken as from 1/2 to 1/15 of the original diameter of the stone column [118].

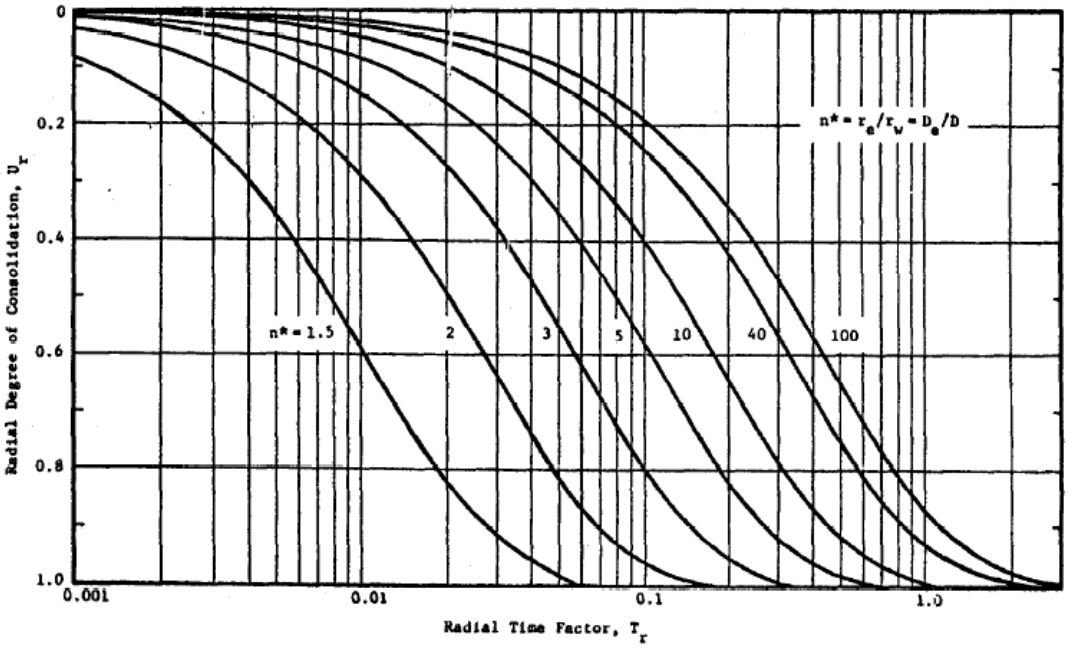

Figure 15-21 Determination of the degree of consolidation considering only radial drainage [118]

Secondary Compression Settlement

Once excess pore water pressure has dissipated at the end of the primary consolidation stage, the volume of soil body continues to decrease under loading due to the plastic deformation of the soil particles. The settlement of ground associated with this volume decrease is referred to as the secondary compression settlement. In the report by Barksdale and Bachus [118], a crude method was proposed to determine the secondary compression settlement based on a linear relationship between the secondary compression settlement and the logarithm of time by using the following function:

$$\Delta S = C_\alpha H \log_{10} \frac{t_2}{t_1} \tag{15-52}$$

where ΔS is the secondary compression settlement of the soil layer, C_α is the secondary compression index which is a physical constant evaluated by keeping the 1-d consolidation test beyond the primary consolidation stage, H is the thickness of the soil layer, t_1 is the time when the secondary compression stage starts (usually taken as the time when 90% of the primary consolidation settlement is achieved) and t_2 is the time of interest during the secondary compression stage.

Different from the primary consolidation settlement, the installation of stone columns does not accelerate the rate of secondary compression settlement. In the case where very soft clay and highly organic soils are present, the secondary compression settlement should be specially addressed since it can be even equal to or greater than the primary consolidation settlement [118]. Research [131] also found that the surcharge loading method can be used to effectively control the secondary compression settlement; sometimes, the applied surcharge loading should be greater than the ultimate service load in order to achieve greatest effectiveness.

CHAPTER 16

CHARACTERIZATION OF SOIL PROPERTIES

Foundation settlement is one of the main problems that lead to the bump-at-the-end-of-the-bridge. Ground improvement techniques such as the use of stone columns have been proven to reduce settlement and improve the bearing capacity of the ground. In order to achieve satisfactory design outcomes, it is always significant to carry out field investigations and laboratory experiments to characterize foundation soils and obtain key soil properties for design purposes.

In order to conduct laboratory testing and obtain strength and compressibility related soil properties for stone column design, it is often required to obtain undisturbed soil samples from bore holes which can be very complex and expensive; in addition, the traditional laboratory testing is difficult to conduct under field conditions.

This chapter considers the use of alternative methods as a means to expedite the testing process. The main objective is to develop non-destructive testing (NDT) technology that can be used under field conditions to determine and validate key soil properties.

BACKGROUND

Sahin [139] made important advancements in the use of NDT technology to determine key material properties of unbound aggregate materials which are usually used as base and subbase layers beneath pavements. In his research, Sahin [139] was able to use only two NDT measurements, such as Methylene Blue Value (MBV) and dielectric constant (DC) to estimate a variety of properties of unbound aggregate materials under a field condition, including the percent fine content (pfc), volumetric water content (θ), soil matric suction (h_m), dry unit weight (γ_d), resilient modulus and permanent deformation. The MBV and DC can be measured by performing the Methylene Blue Test (MBT) and percometer test, respectively. Both of the tests are considered with the following benefits, rapid (no complicated procedures involved), portable (all testing equipment can fit into a small toolbox), comprehensive (applicable

to a wide range of soils), simple (no advanced training required) and accurate with good repeatability. The core of this technology is the use of laboratory empirical relationships which must be established under laboratory conditions prior to the application under field conditions.

Although the aforementioned NDT technologies were conducted for predicting properties of unbound aggregate materials, it appears that there is great potential that the technologies can be applicable for other types of soil materials, such as clay and silts which are often found in the foundation underneath bridge embankments. The use of NDT technologies to estimate the strength and compressibility characteristics of foundation soils will be useful for the design of ground improvement techniques such as the use of stone columns.

PROPOSED PROCEDURE FOR ESTIMATING SOIL STRENGTH

As elaborated in the previous chapters, the undrained shear strength of foundation soils is one of the main properties to be used for the design of the bearing capacity of stone column treated ground. The undrained shear strength of a soil can be determined from the analysis of a Mohr circle as illustrated in Figure 16-1:

$$\sin\phi' = \frac{c_u}{c_u - \theta f h_m} \tag{16-1}$$

$$c_u = -h_m \theta f \frac{\sin\phi'}{1-\sin\phi'} \tag{16-2}$$

where c_u is the undrained shear strength of the soil, ϕ' is the effective internal friction angle of the soil, h_m is the matric suction of the soil, θ is the volumetric water content and f is the unsaturated shear strength factor which can be expressed as:

$$f = 1 + (\frac{S_r - 0.85}{0.15})(\frac{0.01}{\theta} - 1) \tag{16-3}$$

and

$$S_r = \frac{wG_s}{e_0} \tag{16-4}$$

$$w = \frac{\theta\gamma_w}{\gamma_d} \tag{16-5}$$

$$e_0 = \frac{G_s\gamma_w}{\gamma_d} - 1 \tag{16-6}$$

where S_r is the degree of saturation, θ is the volumetric water content, w is the gravimetric moisture content, e_0 is the void ratio of the soil, G_s is the specific gravity of the soil, γ_w is the unit weight of water (62.4 lb/ft^3) and γ_d is the dry unit weight of the soil.

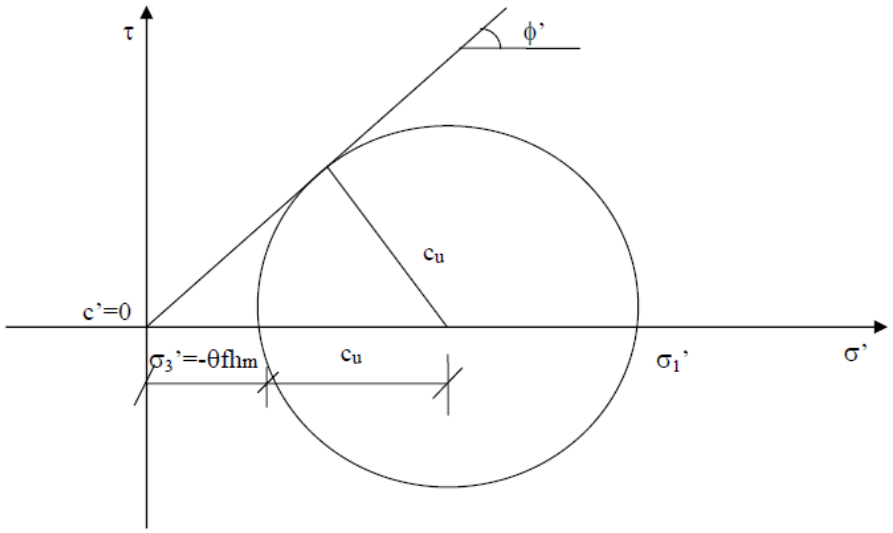

Figure 16-1 Mohr circle for the shear strength of unsaturated soils [140]

Therefore, it appears that the undrained shear strength c_u can be estimated if the following five parameters are known (shown in Figure 16-2):

- the effective internal friction angle ϕ';
- the specific gravity G_s;
- the matric suction h_m;
- the volumetric water content θ; and
- the dry unit weight of the soil γ_d.

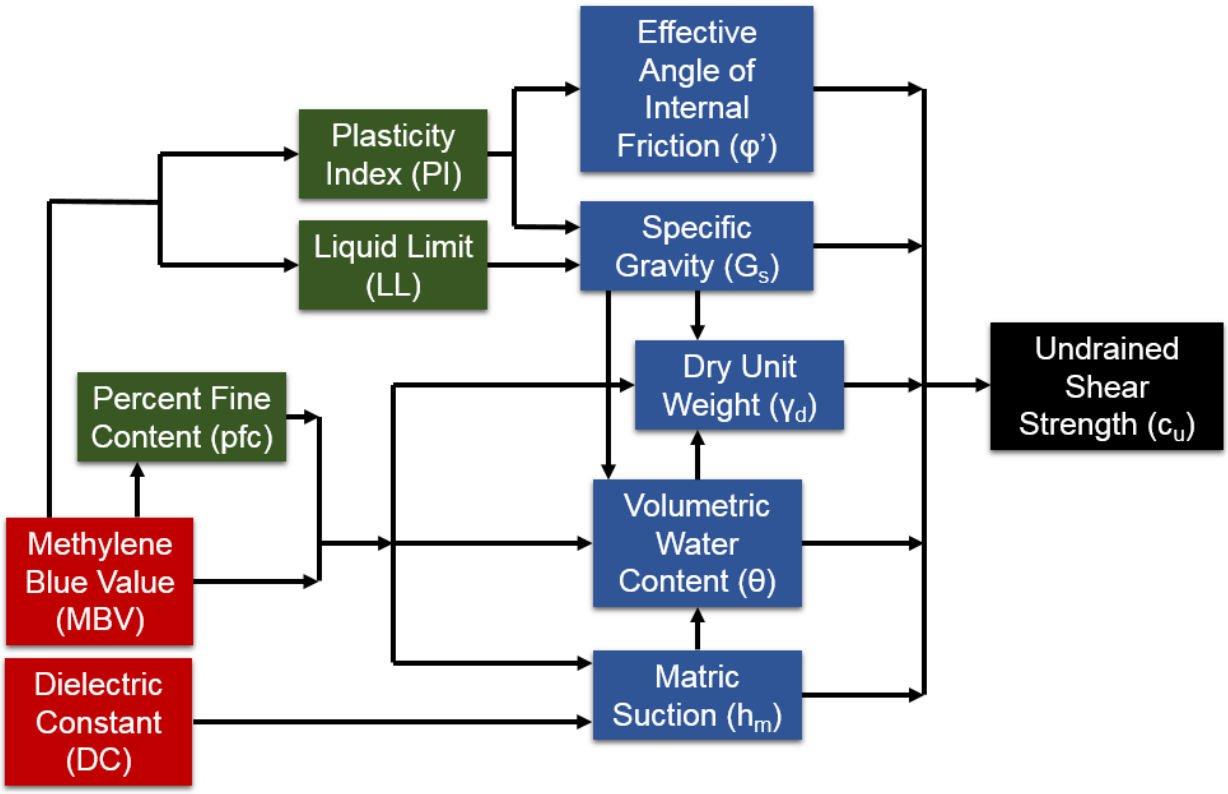

Figure 16-2 Flowchart of proposed field testing protocol for estimating c_u

As shown in Figure 16-2, the proposed field testing protocol considers the use of only two field measurements (i.e. MBV and DC) to estimate all of the five required parameters in order to predict the undrained shear strength c_u under a field condition, which can be achieved by using empirical relationships between the measurable parameters (i.e. MBV and DC) and the five required parameters established under laboratory conditions. The detailed procedures for establishing those empirical relationships under laboratory conditions are elaborated in Appendix K.

PROPOSED PROCEDURE FOR ESTIMATING SOIL COMPRESSIBILITY

In addition to predicting the undrained shear strength c_u under a field condition for calculating the bearing capacity of stone column treated ground, this chapter also provides a procedure to estimate the compression index C_c of cohesive foundation soils which is used for calculating the settlement of stone column treated ground. Conventionally, the compression index of a cohesive soil is determined by performing

an oedometer test under a laboratory condition which can be very time-consuming. If reliable empirical correlations can be established between the compression index and other soil properties, the process of determining compression index can be much faster and more cost-effective.

Past Experience

Over the last few decades, researchers have proposed a number of empirical relationships to relate the compression index to different soil properties, such as the one by Koppula (1981) [141]:

$$C_c = 0.009w + 0.005LL \tag{16-7}$$

the one by Yoon and Kim (2006) [142]:

$$C_c = -0.404 + 0.341e_0 + 0.006w + 0.004LL \tag{16-8}$$

and the one by Ozer et al. (2008)

$$C_c = 0.151 + 0.001225w + 0.193e_0 - 0.000258LL - 0.0699\gamma_d \tag{16-9}$$

where C_c is the compression index, w is the gravimetric moisture content, LL is the liquid limit, γ_d is the dry unit weight and e_0 is the initial void ratio of the soil which can be calculated as:

$$e_0 = \frac{n}{1-n} = \frac{\theta_{ws}}{1-\theta_{ws}} = \frac{G_s\gamma_w}{\gamma_d} - 1 \tag{16-10}$$

where n is the porosity and θ_{ws} is the volumetric water content at saturation which is defined in Equation (K-18).

These empirical relationships can be easily applied under a field condition to estimate the compression index since all the required parameters (i.e. w, LL, γ_d, G_s, e_0 and θ_{ws}) are predictable with only the measurements of MBV and DC following the procedures elaborated in Appendix K.

New Protocol

Besides using the pure empirical relationships (such as the ones shown in Equation (16-7) – (16-9)) previously proposed by other researchers, this research proposed a new protocol based on mechanistic-empirical relationships, in which the

compression index can be calculated in terms of a constrained modulus D based on the stress-strain relationship of a soil under a confined (1-D) compression test [143]:

$$D = \frac{\partial \bar{\sigma}_{axial}}{\partial \varepsilon_{axial}} = \frac{(1+e_0)\ln 10 \sigma_{va}}{C_c} = \frac{2.3(1+e_0)\sigma_{va}}{C_c} \quad (16\text{-}11)$$

and the relationship between constrained modulus D and Young's modulus E of the soil is:

$$D = \frac{E(1-\nu)}{(1+\nu)(1-2\nu)} \quad (16\text{-}12)$$

where e_0 is the initial void ratio, σ_{va} is the average of initial and final stress state applied in the field (vertical stress) and ν is the Poisson's ratio of the soil. The Young's modulus E of the soil can be calculated by using a nonlinear elastic model proposed by Lytton et al. (2005) [144]:

$$E = \frac{\sigma_{va}(1+\frac{0.4343}{Sw})}{0.435\gamma_h} \frac{(1+\nu)(1-2\nu)}{(1-\nu)} \quad (16\text{-}13)$$

therefore, the compression index can be expressed as:

$$C_c = \frac{(1+e_0)\gamma_h}{1+\frac{0.4343}{|S|w}} \quad (16\text{-}14)$$

where e_0 is the initial void ratio of the soil and can be determined using Equation (16-10) (which requires the knowledge of both the dry unit weight γ_d and the specific gravity G_s of the soil), γ_h is the suction compression index (related to the percent fine content pfc, plasticity index PI and liquid limit LL) and can be determined following the procedure elaborated in Appendix K, S is related to the slope of the SWCC and w is the gravimetric water content. As shown in Figure 16-3, the relation between volumetric water content θ and soil matric suction h_m can be expressed as [144]:

$$\frac{\theta}{1} = \frac{h_{m-intercept} - h_m}{|S|\frac{\gamma_w}{\gamma_d}} \quad (16\text{-}15)$$

rearranging Equation (16-15):

$$|S|\theta\frac{\gamma_w}{\gamma_d} = h_{m-\mathrm{intercept}} - h_m \quad (16\text{-}16)$$

since $w = \theta\frac{\gamma_w}{\gamma_d}$, Equation (16-16) becomes:

$$|S|w = h_{m-\mathrm{intercept}} - h_m \quad (16\text{-}17)$$

where $h_{m-\mathrm{intercept}}$ is the matric suction at the intersection with the vertical axis and it is a function of the percent fine content pfc:

$$h_{m-\mathrm{intercept}} = 5.622 + 0.0041(pfc) \quad (16\text{-}18)$$

and h_m is the soil matric suction which can be estimated under a field condition as elaborated in Appendix K.

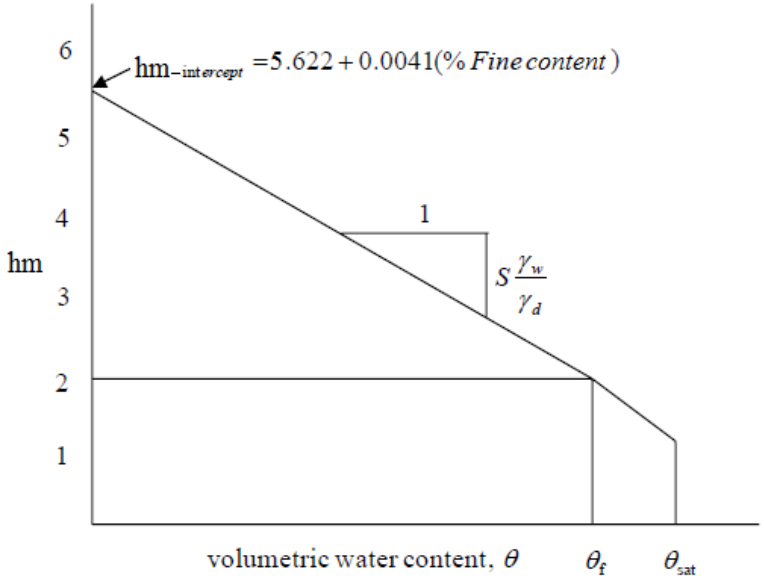

Figure 16-3 The SWCC of a clay soil [144]

To sum up, the compression index C_c can be estimated using Equation (16-14) if the following parameters are known:

- the matric suction h_m;
- the specific gravity G_s;
- the volumetric water content θ;
- the dry unit weight of the soil γ_d;
- the matric suction at intersection $h_{m-\mathrm{intercept}}$; and
- the suction compression index γ_h.

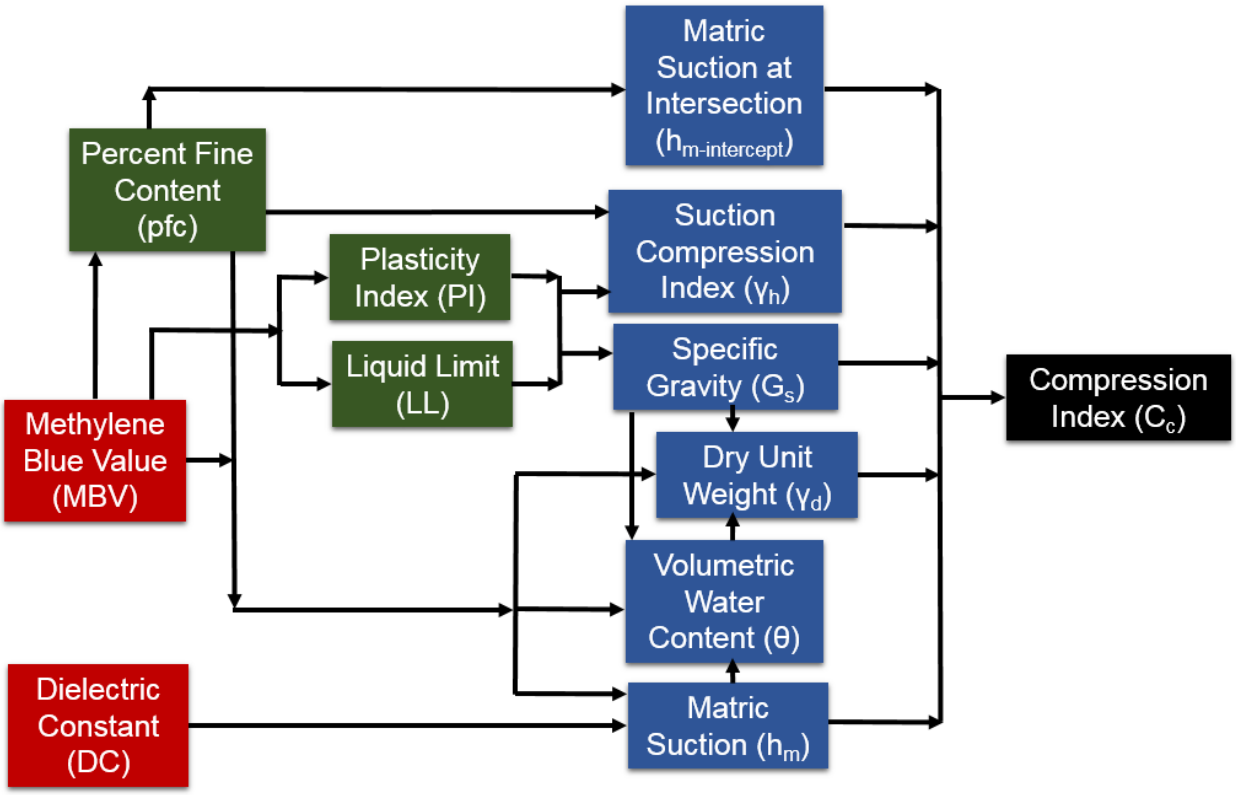

Figure 16-4 Flowchart of proposed field testing protocol for estimating C_c

As shown in Figure 16-4, the proposed field testing protocol considers the use of only two field measurements (i.e. MBV and DC) to estimate all the six required parameters in order to determine the compression index C_c under a field condition.

The empirical relationship shown in Equation (16-18) to determine the matric suction at intersection $h_{m-\mathrm{intercept}}$ is valid for clay soils as indicated in the report by Lytton et al. (2005) [144]. The charts shown from Figure K-12 – Figure K-20 to determine the suction compression index γ_h can also be directly used for natural clay soils since they are generated based on a large database of the Soil Survey Laboratory (SSL) of the Natural Resources Conservation Service of the U.S. Department of Agriculture. The procedures and empirical relationships to estimate the specific gravity G_s, the dry unit weight γ_d, the volumetric water content θ and the soil matric suction h_m under a field condition are elaborated in Appendix K. Again, it is important to note that those empirical relationships will have greater utilities under a field condition if they are established based on a wide range of soil types tested under laboratory conditions.

DEMONSTRATION OF PROPOSED PROCEDURES

This section consists of three major objectives:

1. Provide the results of the laboratory experiments;
2. Briefly demonstrate how to use the results to establish empirical relationships; and
3. Briefly demonstrate how the empirical relationships can be used to facilitate the estimation/characterization of soil properties using the NDT technologies.

Note that an Excel spreadsheet which contains all the laboratory experiment results and detailed information for establishing those empirical relationships will be provided to the practitioner (i.e. OKDOT engineers) to facilitate better understanding regarding how the empirical relationships are established using laboratory experiment results.

Laboratory Experiment Results

Three soil samples (Port, Kirkland and Osage) obtained from Oklahoma were used in the study to facilitate the development of the laboratory empirical relationships. In order to develop the empirical relationships that can be used under field conditions to estimate key soil properties, the following laboratory tests were performed:

1. the Atterberg limits test
2. the Methylene Blue Test
3. the specific gravity test
4. the percent fine content test
5. the percometer test
6. the filter paper test
7. the standard laboratory compaction test

Atterberg limits

Table 16-1 shows the Atterberg limits of the three soil samples obtained in Oklahoma.

Table 16-1 Atterberg limits

	Liquid limit	Plastic limit	Plasticity Index
Port	43.5	18.64	24.86
Kirkland	47	16.61	30.39
Osage	66.5	28.55	37.95

Methylene Blue Value

Table 16-2 shows the MBV of the three soil samples.

Table 16-2 MBV of the soil samples

	Sample	MBV	Average of MBV
Port	1	60.4	59.58
	2	59.2	
	3	58.7	
	4	60	
Kirkland	1	61.9	65.15
	2	65.4	
	3	66.1	
	4	67.2	
Osage	1	80.4	78.67
	2	77.6	
	3	78	

Specific gravity

Table 16-3 shows the specific gravity of the three soil samples.

Table 16-3 Specific gravity of the soil samples

	Port	Kirkland	Osage
Specific Gravity (G_s)	2.62	2.75	2.66

Percent fine content

Table 16-4 shows the pfc of the three soil samples.

Table 16-4 pfc of the soil samples

	Sample	Percent fine content, %	Average, %
Port	1	77.43	82.90
	2	87.14	
	3	82.54	
	4	78.04	
	5	89.37	
Kirkland	1	78.36	83.72
	2	80.37	
	3	82.88	
	4	89.22	
	5	87.78	
Osage	1	99.4	99.19
	2	97.25	
	3	99.59	
	4	100	
	5	99.72	

Dielectric constant and suction

Six 4-in diameter and 1.5-in height cylindrical soil samples were made for each soil to conduct percometer test and filter paper test (each test requires two soil samples). Dielectric constant and suction of the samples are shown in Table 16-5 and Table 16-6.

Table 16-5 Dielectric constant of the samples

	Sample	Total	Average
Port	1	27.2	28.48
	2	26.9	
	3	27.6	
	4	34.16	
	5	29.44	
	6	25.6	
Kirkland	1	35.18	33.29
	2	35.32	
	3	33.98	
	4	35.24	

	5	29.88	
	6	30.14	
Osage	1	37.68	33.96
	2	33.5	
	3	31.42	
	4	32.04	
	5	34.64	
	6	34.48	

Table 16-6 Matric suction of the samples

	Sample	**Matric suction, pF**	**Average matric suction, pF**
Port	1	3.56	3.49
	2	3.63	
	3	3.27	
Kirkland	1	3.73	3.71
	2	3.81	
	3	3.58	
Osage	1	3.61	3.42
	2	3.51	
	3	3.13	

Optimum water content and maximum dry unit weight

Table 16-5 shows the compaction curves from which the optimum moisture content and maximum dry unit weight of the three soil samples are determined as shown in Table 16-7.

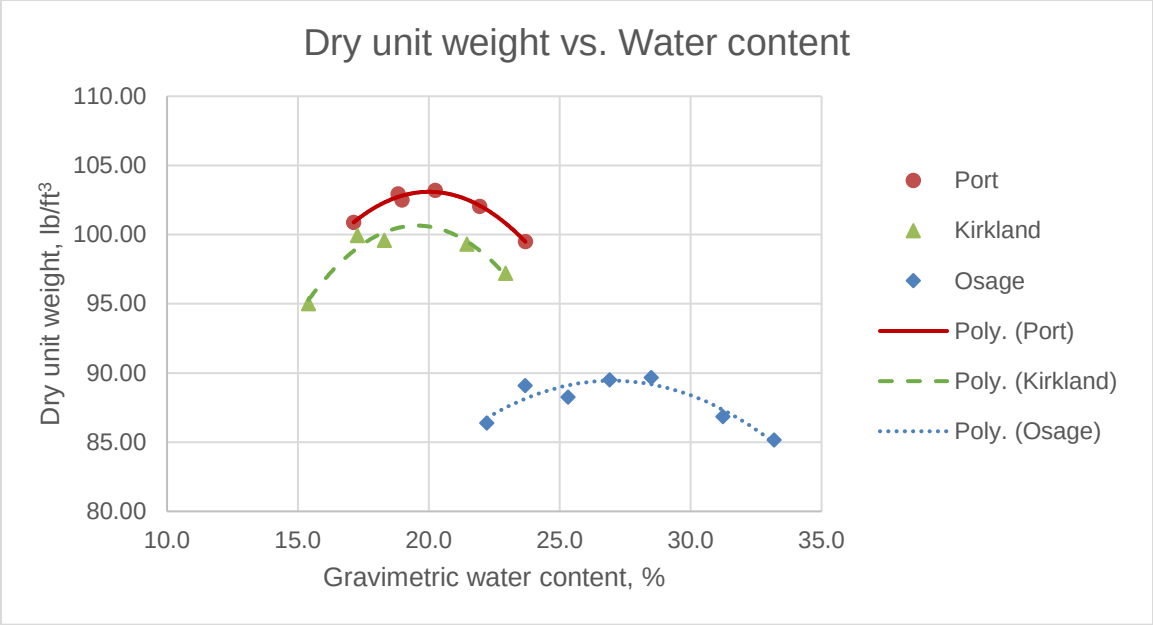

Figure 16-5 Compaction curves of the soil samples

Table 16-7 Optimum water content and maximum dry unit weight of the soil samples

	Optimum Water Content, %	Maximum Dry Unit Weight, lb./ft^3
Port	20.01	103.03
Kirkland	19.54	100.06
Osage	27.02	89.48

Establishment of Empirical Relationships

By using the results of the laboratory experiments for the three representative soils taken from Oklahoma, this section demonstrates examples of how to establish the empirical relationships that will be used to perform estimations of the strength and compressibility related soil properties under a field condition. Note that the empirical relationships developed within this section only have limited utilities due to the small sample database which is constrained by the scope of the research; therefore, they are developed for demonstration purposes only and greater utilities can be achieved if a

large number of soils samples are tested to cover a wide range of soil types in the interested local area.

Empirical relationships between Atterberg limits and MBV

As shown in Figure 16-6, the relationship between MBV and PI can be described by a linear relationship for the three samples:

$$PI = 0.6622MBV - 13.828 \quad (16\text{-}19)$$

and the relationship between MBV and LL shown in Figure 16-7 can also be described by a linear function:

$$LL = 1.2489MBV - 32.338 \quad (16\text{-}20)$$

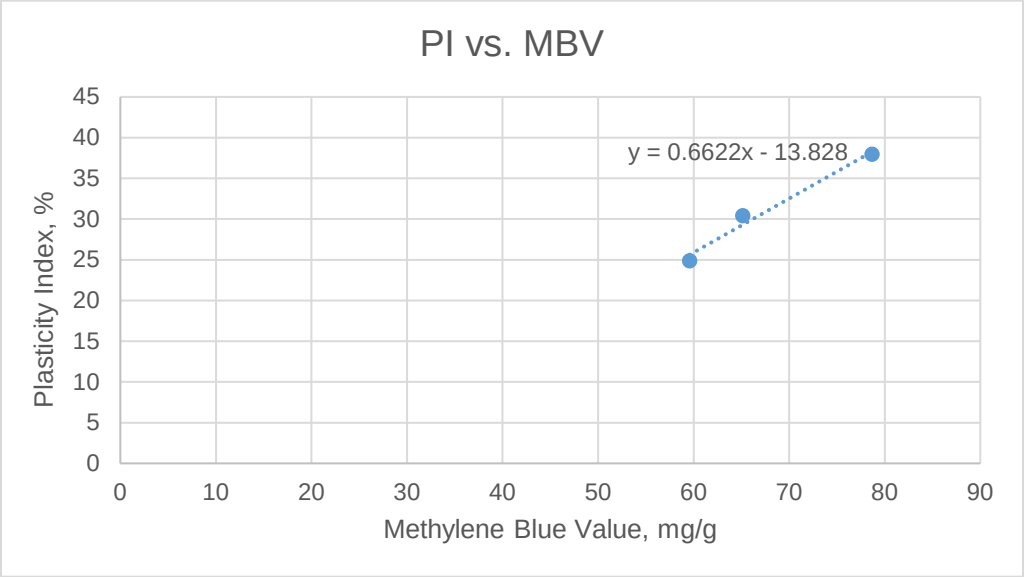

Figure 16-6 the correlation between MBV and PI for the three soil samples

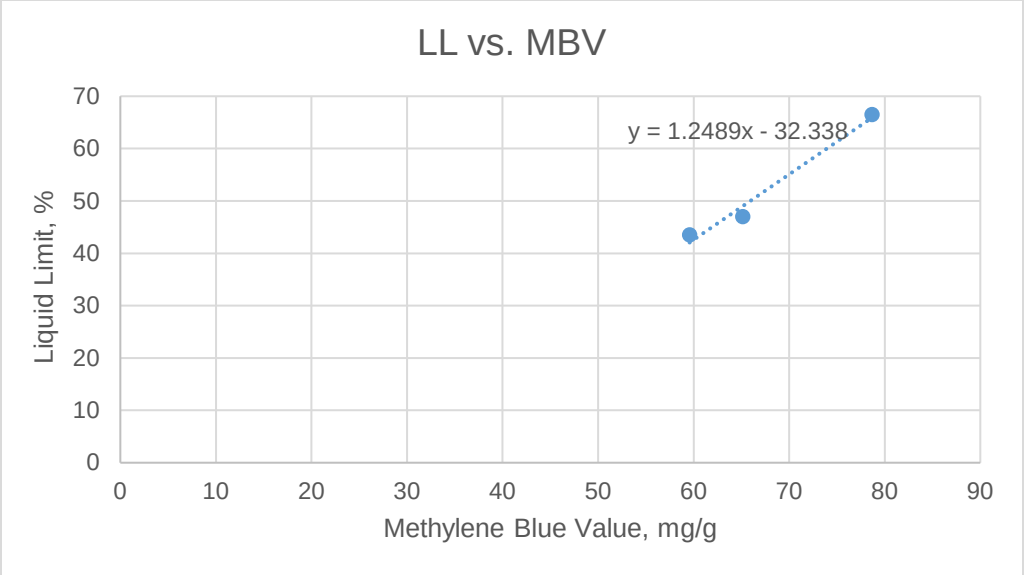

Figure 16-7 the correlation between MBV and LL for the three soil samples

Empirical relationship for predicting specific gravity

Laboratory experiment results of the specific gravity and Atterberg limits are summarized as shown in Table 16-8. These results are fitted to the mathematical function as shown in Equation (K-5), from which the fitting parameters β, γ and δ are determined as shown in Table 16-9.

Table 16-8 Specific gravity and Atterberg limits

	Port	Kirkland	Osage
Specific Gravity (G_s)	2.62	2.75	2.66
Liquid Limit (LL)	43.5	47	66.5
Plasticity Index (PI)	24.86	30.39	37.95
Approximate minimum liquid limit (L_0)	40		
Approximate maximum liquid limit (L_m)	70		
Approximate minimum plasticity index (P_0)	20		
Approximate maximum plasticity index (P_m)	40		

Table 16-9 Fitting parameters determined using the experiment results

Beta (β)	Gamma (γ)	Delta (δ)
0.057	3.24	-2.45

Once the fitting parameters are determined, the empirical function to calculate specific gravity of a soil can be formulated as:

$$G_s = \frac{2.55+2.91(0.057)\left(\frac{PI-20}{40-PI}\right)^{3.24}\left(\frac{LL-40}{70-LL}\right)^{-2.45}}{1+0.057\left(\frac{PI-20}{40-PI}\right)^{3.24}\left(\frac{LL-40}{70-LL}\right)^{-2.45}} \quad (16\text{-}21)$$

Empirical relationship for predicting pfc using MBV

As shown in Figure 16-8, the correlation between MBV and pfc can be described by the following function for the three samples:

$$pfc = 62.221\ln(MBV) - 173.33 \quad (16\text{-}22)$$

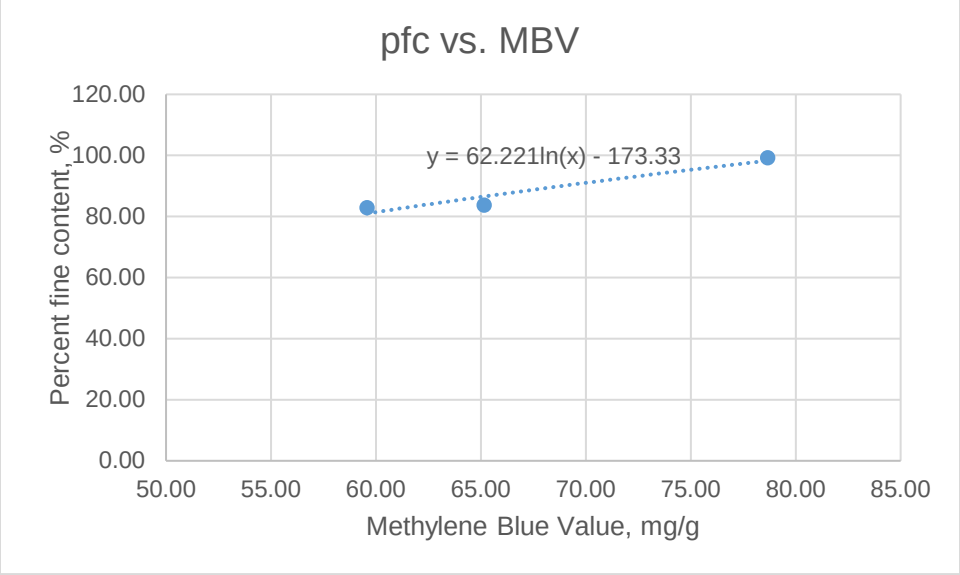

Figure 16-8 the correlation between MBV and pfc for the three soil samples

Empirical relationships for predicting ε_{sat} and ε_{min} to define SDCC

In order to establish the empirical relationships, it is necessary to determine $\varepsilon_{\min}$ and ε_{sat}, which can be calculated by applying the complex refraction index model (CRIM) (elaborated in Appendix K) based on the DC measurements of the soil samples.

Table 16-10 shows the results of the minimum and saturated DC calculated following the procedure elaborated previously. Figure 16-9 and Figure 16-10 show the correlations of $\varepsilon_{\min}$ vs. MBV and ε_{sat} vs. MBV, respectively. Both the empirical relationships can be represented by the quadratic functions shown in the figures. The relationship between $\varepsilon_{\min}$ and MBV is expressed as:

$$\varepsilon_{\min} = -0.0178MBV^2 + 2.414MBV - 71.026 \quad (16\text{-}23)$$

and the relationship between ε_{sat} and MBV is expressed as:

$$\varepsilon_{sat} = -0.0582MBV^2 + 8.4438MBV - 259.51 \quad (16\text{-}24)$$

Table 16-10 Determination of $\varepsilon_{\min}$ and ε_{sat}

	Measured DC of the soil (ε_r)	Specific Gravity (G_s)	Water content (w)	Dry unit weight (γ_d)	Volumetric solid content (θ_s)	Volumetric water content (θ)	Volumetric water content at saturation (θ_{ws})	DC of the solid (ε_s)	Minimum DC (ε_{min})	Saturated DC (ε_{sat})
Port	28.48	2.62	0.169	103.03	0.630	0.279	0.370	18.88	9.66	36.81
Kirkland	33.29	2.75	0.193	100.66	0.587	0.311	0.413	23.87	10.75	43.38
Osage	33.96	2.66	0.249	89.48	0.539	0.357	0.461	21.62	8.81	44.29

Sample calculation (take “Port” as an example):

Based on Equation (K-16) shown in Appendix K

The volumetric solid content θ_s:

$$\theta_s = \frac{\gamma_d}{G_s\gamma_w} = \frac{103.03}{2.62 \times 62.4} = 0.63$$

The volumetric water content θ:

$$\theta = \frac{w\gamma_d}{\gamma_w} = \frac{0.169 \times 103.03}{62.4} = 0.279$$

The DC of the solid ε_s:

$$\varepsilon_s = \left(\frac{\sqrt{\varepsilon_r} - 1 - (\sqrt{\varepsilon_w} - 1)\theta}{\theta_s} + 1\right)^2 = \left(\frac{\sqrt{28.48} - 1 - (\sqrt{81} - 1)0.279}{0.63} + 1\right)^2 = 18.88$$

Based on Equation (K-17) shown in Appendix K

The minimum DC $\varepsilon_{\min}$:

$$\varepsilon_{\min} = (1 + \theta_s(\sqrt{\varepsilon_s} - 1))^2 = (1 + 0.63(\sqrt{18.88} - 1))^2 = 9.66$$

Based on Equation (K-18) shown in Appendix K

The volumetric water content at saturation θ_{ws}:

$$\theta_{ws} = 1 - \theta_s = 1 - 0.63 = 0.37$$

The saturated DC ε_{sat}:

$$\varepsilon_{sat} = [(\sqrt{\varepsilon_s} - 1)\theta_s + (\sqrt{\varepsilon_w} - 1)\theta_{ws} + 1]^2 = [(\sqrt{18.88} - 1)0.63 + (\sqrt{81} - 1)0.37 + 1]^2$$
$$= 36.81$$

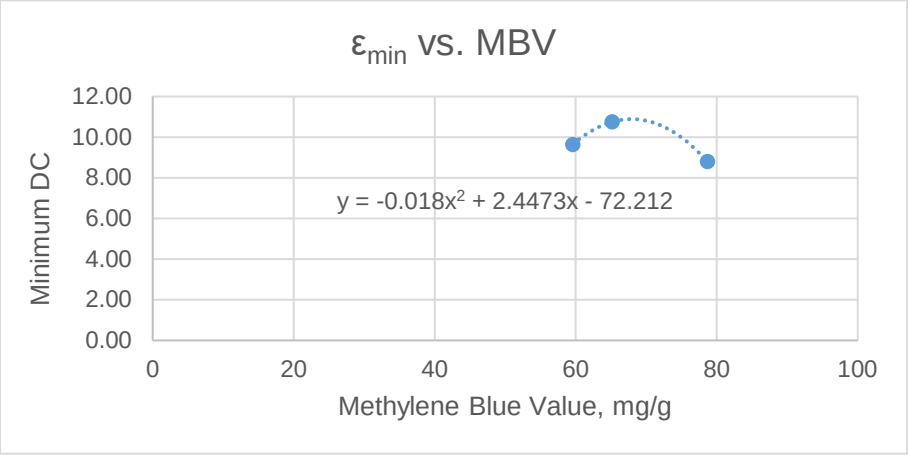

Figure 16-9 the correlation between MBV and ε_{min} for the three soil samples

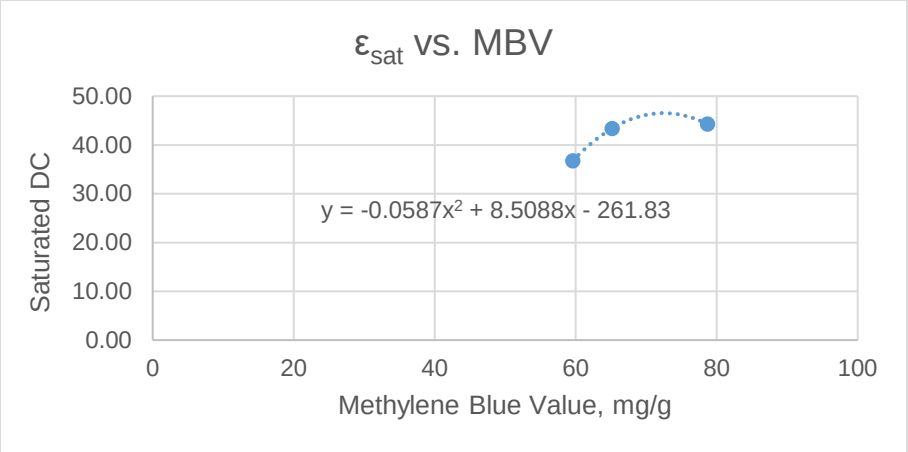

Figure 16-10 the correlation between MBV and ε_{sat} for the three soil samples

Empirical relationships for predicting fitting parameters to define SDCC

Once the three points of a SDCC (i.e. Point A, B and C as shown in Figure K-4) are determined by conducting laboratory experiments as aforementioned, they are fitted

to the general mathematical form as shown in Equation (K-6), from which the fitting parameters α and γ can be determined. Table 16-11 provides a summary of the three points of the SDCCs and Table 16-12 shows the fitting parameters α and γ determined for the three soil samples.

Table 16-11 the three points of the SDCCs for the soil samples

	Point A		Point B		Point C	
	Minimum DC (ε_{min})	**Maximum Suction (h_{max}), pF**	**Measured DC (ε_r)**	**Measured Matric Suction(h_m), pF**	**Saturated DC (ε_{sat})**	**Minimum Suction (h_{min}), pF**
Port	9.66	7	28.48	3.49	36.81	0
Kirkland	10.75	7	33.29	3.71	43.38	0
Osage	8.81	7	33.96	3.42	44.29	0

Table 16-12 the fitting parameters of the SDCCs of the soil samples

	α	γ	**MBV**	pfc**, %**
Port	0.449	2.868	59.58	82.90
Kirkland	0.177	7.741	65.15	83.72
Osage	0.448	1.930	78.67	99.19

Empirical relationships are established between the two fitting parameters and MBV and pfc using the neural network function in the statistical software JMP (detailed user guide is elaborated in Appendix M). The empirical prediction functions for α and γ are:

$$H_1 = TANH(0.5(a_1(MBV) + b_1(pfc) + c_1)) \quad (16\text{-}25)$$

$$\alpha, \gamma = m(H_1) + n \quad (16\text{-}26)$$

where H_1 is the hidden layer function and the coefficients in the prediction functions are shown in Table 16-13.

Table 16-13 coefficients in the empirical prediction functions

	α	γ
$\mathbf{a_1}$	0.22795851	-0.069916606

b_1	-0.266616429	0.085548558
c_1	9.551699184	-3.284691246
m	-0.900976768	-32.73418563
n	0.878226792	-2.935133574

Finally, using Equation (K-6), complete SDCCs can be plotted for the soil samples if α, γ, ε_{sat} and $\varepsilon_{\min}$ are predicted with only the measurements of MBV under a field condition as shown in Figure 16-11 (the three points of each sample are shown in the figure as well). As elaborated earlier, with also the measurements of DC, the SDCCs can be used to predict the matric suction h_m which is one of the required parameters to estimate the undrained shear strength and compression index of the soils.

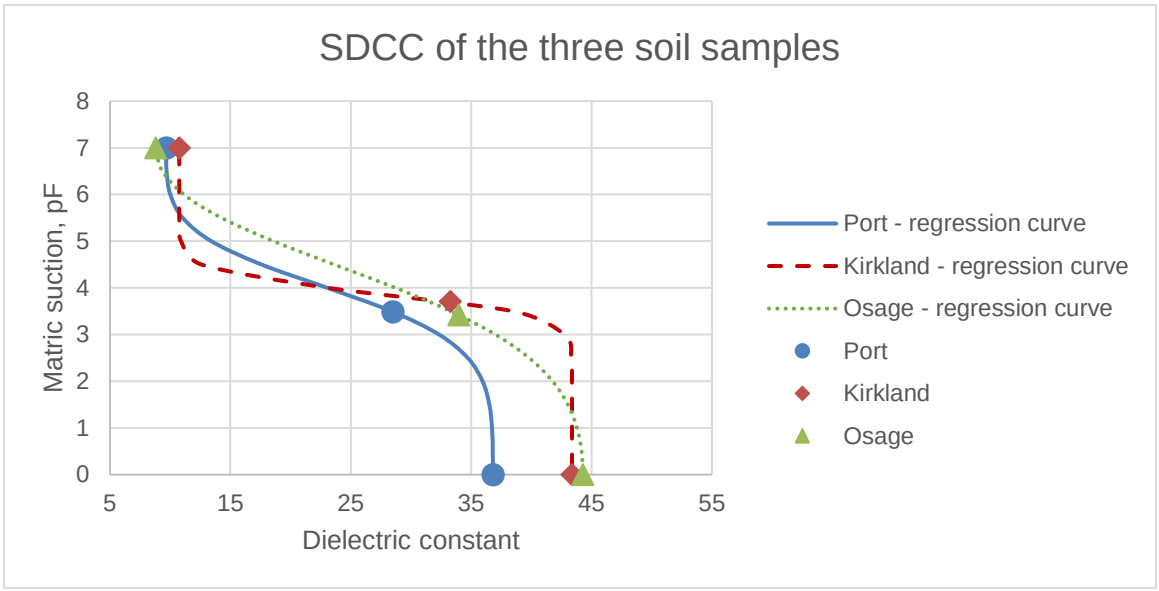

Figure 16-11 the SDCCs of the three soil samples

Empirical relationships for predicting required parameters to define SWCC

Once the three points of a SWCC (i.e. Point A, B and C as shown in Figure K-10) are determined by conducting laboratory experiments as aforementioned, they are fitted to the Fredlund and Xing model as shown in Equation (K-21) and (K-22), from which the fitting parameters a_f, b_f, c_f and h_r can be determined. Table 16-14 provides a summary

of the three points of the SWCCs and Table 16-15 shows the fitting parameters determined for the three soil samples.

Table 16-14 the three points of the SWCCs for the soil samples

	Point A		Point B		Point C	
	Minimum Volumetric Water Content	**Maximum Suction (h_{max}), pF**	**Measured Volumetric Water Content (θ)**	**Measured Matric Suction (h_m), pF**	**Saturated Volumetric Water Content (θ_{sat})**	**Minimum Suction (h_{min}), pF**
Port	0	7	0.279	3.49	0.370	0
Kirkland	0	7	0.311	3.71	0.413	0
Osage	0	7	0.357	3.42	0.461	0

Table 16-15 the fitting parameters of the SWCCs of the soil samples

	a_f	b_f	c_f	h_r	**MBV**
Port	11.250	1.050	-8.240	2.290	59.58
Kirkland	7.950	1.060	-7.000	1.500	65.15
Osage	6.950	1.070	-5.110	2.890	78.67

The four fitting parameters of each soil sample are plotted against their MBV as shown in Figure 16-12. The empirical correlations of a_f vs. MBV and c_f vs. MBV can be represented by linear functions as shown in Figure 16-12 (a) and (c), respectively; the correlations of b_f vs. MBV and h_r vs. MBV can be represented by quadratic functions as shown in Figure 16-12 (b) and (d), respectively. The empirical relationship between a_f and MBV is expressed as:

$$a_f = -0.1972MBV + 22.083 \quad (16\text{-}27)$$

The empirical relationship between b_f and MBV is expressed as:

$$b_f = -6 \times 10^{-5}MBV^2 + 0.0087MBV + 0.7289 \quad (16\text{-}28)$$

The empirical relationship between c_f and MBV is expressed as:

$$c_f = 0.1595MBV - 17.595 \quad (16\text{-}29)$$

The empirical relationship between h_r and MBV is expressed as:

$$h_r = 0.0128MBV^2 - 1.7393MBV + 60.447 \quad (16\text{-}30)$$

Once MBV is measured under a field condition, all the fitting parameters can be predicted using the empirical relationships.

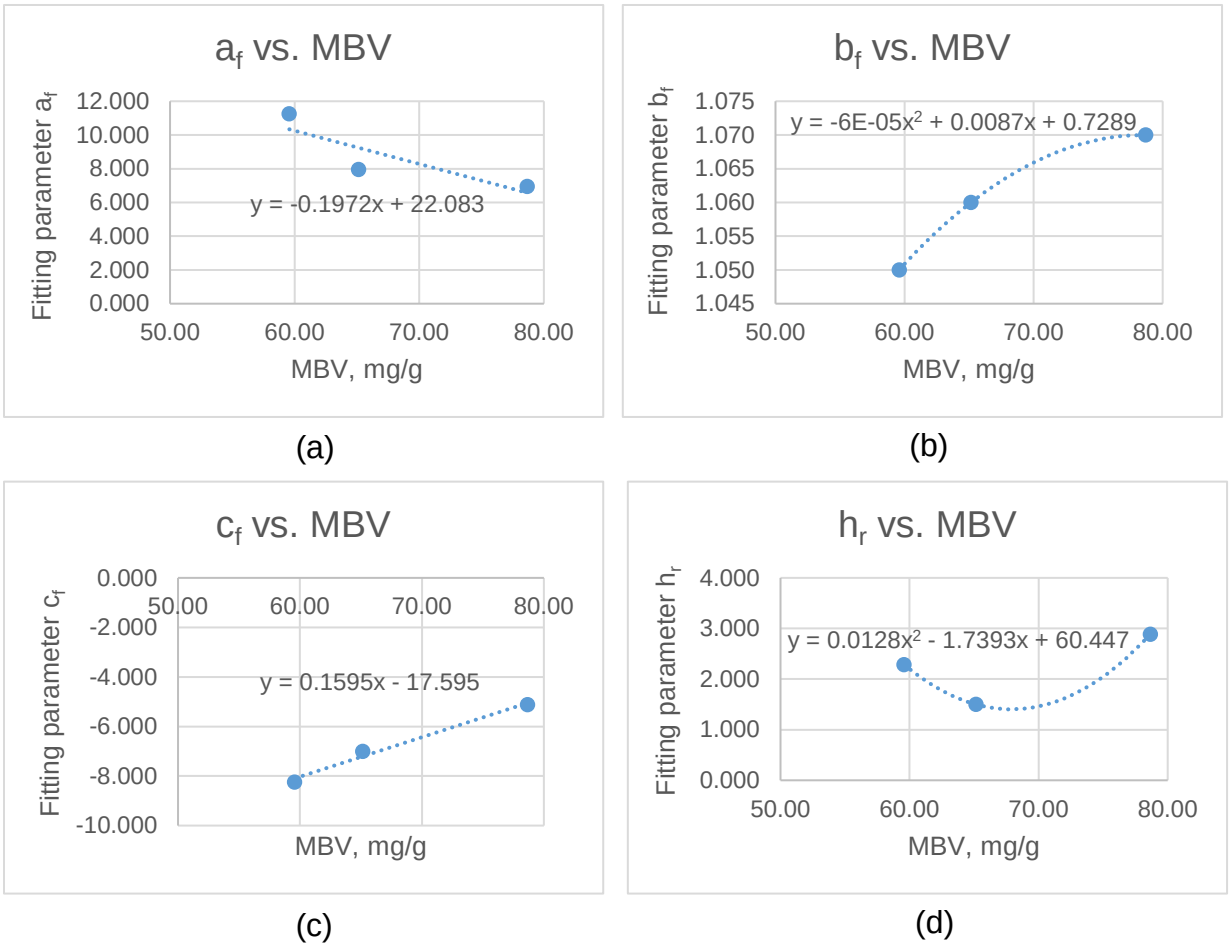

Figure 16-12 the empirical relationships between the four fitting parameters and MBV

In addition to the four fitting parameters, the saturated volumetric water content θ_{sat} is also required to define the SWCC of a soil. In order to obtain the required empirical relationships, the saturated volumetric water content θ_{sat} is correlated to the MBV, pfc and specific gravity G_s of the soil samples. The saturated volumetric water content for the three soil samples are calculated using Equation (K-31) as shown in Table 16-16.

Table 16-16 the saturated volumetric water content of the three soil samples

	Maximum dry unit weight, lb/ft^3	Specific Gravity (G_s)	Saturated volumetric water content (θ_{sat})	MBV	pfc, %
Port	103.03	2.62	0.370	59.58	82.90
Kirkland	100.66	2.75	0.413	65.15	83.72
Osage	89.48	2.66	0.461	78.67	99.19

Sample calculation (take “Port” as an example):

Based on Equation (K-31)

The saturated volumetric water content θ_{sat}:

$$\theta_{sat} = [1 - \frac{\gamma_{d-\max}}{(G_s\gamma_w)}] = [1 - \frac{103.03}{(2.62 \times 62.4)}] = 0.37$$

Empirical relationships are established between θ_{sat} and MBV, pfc and specific gravity G_s using the neural network function in the statistical software JMP as aforementioned. The empirical prediction functions for θ_{sat} are:

$$H_1 = TANH(0.5(a_1(MBV) + b_1(pfc) + c_1(G_s) + d_1)) \quad (16\text{-}31)$$

$$\theta_{sat} = m(H_1) + n \quad (16\text{-}32)$$

where H_1 is the hidden layer function and the coefficients in the prediction functions are shown in Table 16-17.

Table 16-17 coefficients in the empirical prediction functions

	θ_{sat}
a_1	0.1816298
b_1	-0.09726
c_1	1.6012614
d_1	-9.078068
m	0.130049
n	0.4722762

Finally, using Equation (K-21) and (K-22), complete SWCCs can be plotted for the soil samples once the four fitting parameters a_f, b_f, c_f, h_r and the saturated volumetric water content θ_{sat} are predicted with only the measurements of MBV (both pfc and specific gravity G_s can be estimated by MBV) under a field condition as shown in Figure 16-13 (the three points of each sample are shown in the figure as well). As elaborated earlier, once the SWCCs of the soil samples are obtained, with also the assist of the SDCCs from which the matric suction h_m of the soils are predicted, one is able to estimate the volumetric water content θ which is another required parameter used to estimate the undrained shear strength and compression index of the soils.

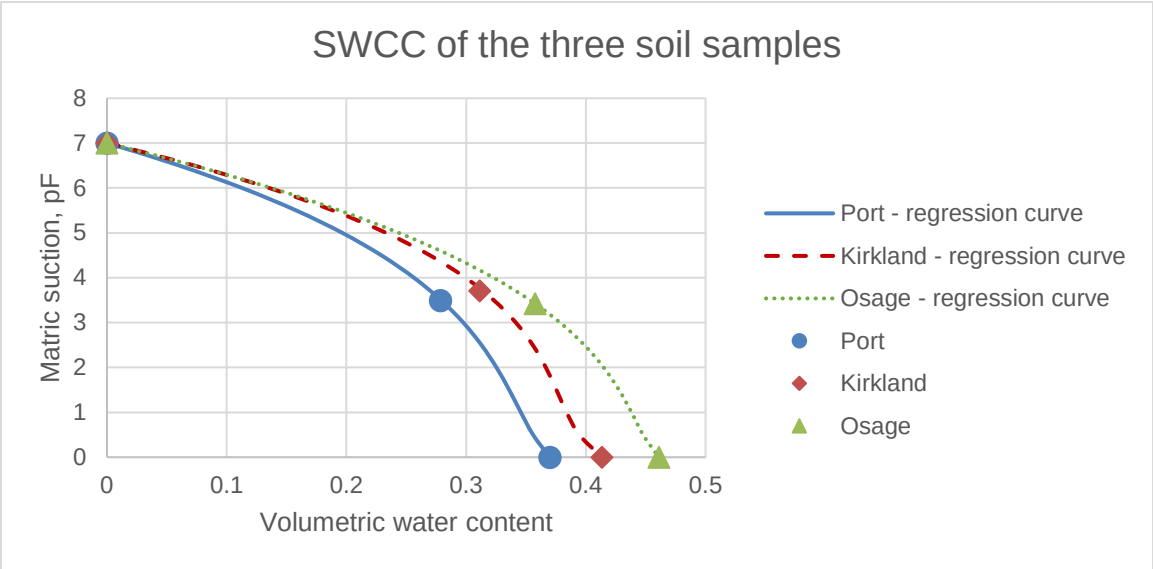

Figure 16-13 the SWCCs of the three soil samples

Empirical relationships for predicting dry unit weight

Once the standard laboratory compaction tests are performed for the three soil samples, the data points are fitted to the CCM shown in Equation (K-32), from which the fitting parameters a_d, b_d and n_d can be determined. The required laboratory experiment results to perform curve fitting are shown in Table 16-18. The fitted regression curves and the fitting parameters are shown in Figure 16-14 and Table 16-19, respectively.

Table 16-18 the required data points for compaction curve fitting

	Data point #	Water content, %	Dry unit weight, lb/ft^3	Volumetric water content	Saturated volumetric water content
Port	Point 1	17.13	100.89	0.28	0.37
	Point 2	18.82	102.94	0.31	0.37
	Point 3	18.97	102.51	0.31	0.37
	Point 4	20.24	103.21	0.33	0.37
	Point 5	21.94	102.04	0.36	0.37
	Point 6	23.69	99.50	0.38	0.37
Kirkland	Point 1	15.41	95.01	0.23	0.41
	Point 2	17.27	99.93	0.28	0.41
	Point 3	18.30	99.59	0.29	0.41
	Point 4	21.45	99.31	0.34	0.41
	Point 5	22.94	97.20	0.36	0.41
Osage	Point 1	22.22	86.37	0.31	0.46
	Point 2	23.68	89.09	0.34	0.46
	Point 3	25.31	88.26	0.36	0.46
	Point 4	26.91	89.50	0.39	0.46
	Point 5	28.50	89.67	0.41	0.46
	Point 6	31.23	86.85	0.43	0.46
	Point 7	33.19	85.17	0.45	0.46

Table 16-19 the fitting parameters of the CCMs of the soil samples

	a_d	b_d	n_d
Port	1.686771073	0.035955963	0.0088836
Kirkland	1.658890903	0.090392904	0.1091659
Osage	1.440218177	0.017872965	0.0062712

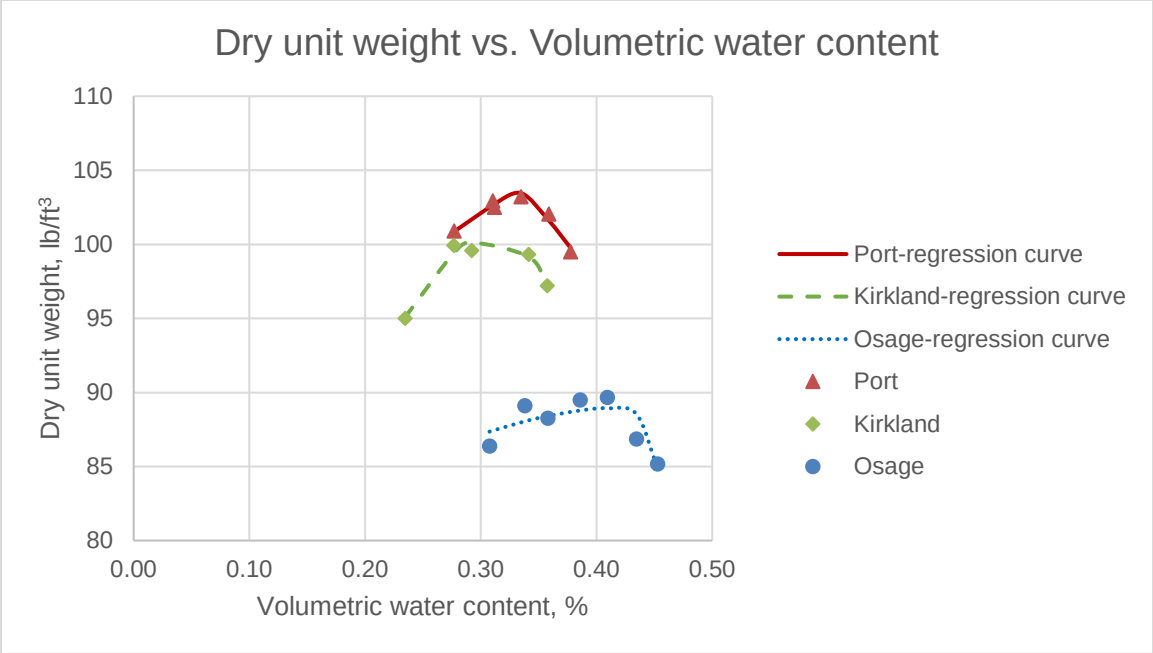

Figure 16-14 Regressed curves for the CCMs of the soil samples

In order to obtain the required empirical relationships for predicting the CCMs, the fitting parameters are correlated to the MBV, pfc and specific gravity G_s of the soil samples using the neural network function in the statistical software JMP as aforementioned. The empirical prediction functions for a_d, b_d and n_d are:

$$H_1 = TANH(0.5(a_1(MBV) + b_1(pfc) + c_1(G_s) + d_1)) \quad (16\text{-}33)$$

$$a_d, b_d, n_d = m(H_1) + n \quad (16\text{-}34)$$

where H_1 is the hidden layer function and the coefficients in the prediction functions are shown in Table 16-20.

Table 16-20 the fitting parameters of the CCMs of the soil samples

	a_d	b_d	n_d
a_1	0.099185396	-0.039174583	0.057947024
b_1	0.083715306	0.144640778	0.063143883
c_1	-1.824986435	-19.44194219	-50.73109753
d_1	-9.14215919	41.71321966	125.2064624
m	-0.195976385	-0.053774475	-0.069498463
n	1.593813729	0.047394686	0.040398477

Under a field condition, one is able to estimate the required fitting parameters to define the CCM using the empirical relationships shown in Equation (16-33) and (16-34) with only the measurements of MBV. The procedures to predict the saturated volumetric water content θ_{sat} and volumetric water content θ have been elaborated as aforementioned. Finally, one is able to obtain the dry unit weight γ_d of the soil using the CCM shown in Equation (K-32), which is one of the required parameters to estimate the undrained shear strength and compression index of the soils.

Estimation of Soil Properties

Once the empirical relationships are established, the following provides a brief demonstration of how to estimate the two key soil properties (i.e. the undrained shear strength c_u and the compression index C_c) using those relationships. The parameters required to conduct the estimations are (also illustrated in Figure 16-2 and Figure 16-4):

- the effective internal friction angle ϕ';
- the specific gravity G_s;
- the matric suction h_m;
- the volumetric water content θ; and
- the dry unit weight of the soil γ_d;
- the matric suction at intersection $h_{m-\mathrm{int}ercept}$; and
- the suction compression index γ_h.

For the purpose of demonstration, assuming that the MBV and DC are measured under a field condition for an unknown cohesive foundation soil which has properties similar to those of the three soil samples obtained from Oklahoma:

- MBV = 70 mg/g;
- DC = 25;

Task 1. Estimation of Effective Internal Friction Angle

Based on Equation (16-19):

$$PI = 0.6622MBV - 13.828 = 32.57$$

Based on Equation (16-20):

$$LL = 1.2489MBV - 32.338 = 55.09$$

Based on Equation (K-1):

$$\phi' = 0.0016PI^2 - 0.302PI + 36.208 = 28.07$$

Task 2. Estimation of Specific Gravity

Based on Equation (16-21):

$$G_s = \frac{2.55 + 2.91(0.057)\left(\frac{PI-20}{40-PI}\right)^{3.24}\left(\frac{LL-40}{70-LL}\right)^{-2.45}}{1 + 0.057\left(\frac{PI-20}{40-PI}\right)^{3.24}\left(\frac{LL-40}{70-LL}\right)^{-2.45}}$$

$$= \frac{2.55 + 2.91(0.057)\left(\frac{32.57-20}{40-32.57}\right)^{3.24}\left(\frac{55.09-40}{70-55.09}\right)^{-2.45}}{1 + 0.057\left(\frac{32.57-20}{40-32.57}\right)^{3.24}\left(\frac{55.09-40}{70-55.09}\right)^{-2.45}}$$

$$= 2.63$$

Task 3. Estimation of Matric Suction

1. Determine pfc using Equation (16-22)

$$pfc = 62.221\ln(MBV) - 173.33 = 62.221 \times \ln(70) - 173.33 = 91.02$$

2. Determine $\varepsilon_{\min}$ using Equation (16-23)

$$\varepsilon_{\min} = -0.0178MBV^2 + 2.414MBV - 71.026$$
$$= -0.0178 \times 70^2 + 2.414 \times 70 - 71.026$$
$$= 10.73$$

3. Determine ε_{sat} using Equation (16-24)

$$\varepsilon_{sat} = -0.0582MBV^2 + 8.4438MBV - 259.51$$
$$= -0.0582 \times 70^2 + 8.4438 \times 70 - 259.51$$
$$= 46.38$$

4. Determine fitting parameters α and γ for SDCC using Equation (16-25) and (16-26) and Table 16-13

$$H_1, \alpha = TANH(0.5(a_1(MBV) + b_1(pfc) + c_1))$$
$$= TANH(0.5(0.22795851(70) - 0.266616429(91.02) + 9.551699184))$$
$$= 0.5516$$

$$H_1, \gamma = TANH(0.5(a_1(MBV) + b_1(pfc) + c_1))$$
$$= TANH(0.5(-0.069916606(70) + 0.085548558(91.02) - 3.284691246))$$
$$= -0.1936$$

$$\alpha = m(H_1, \alpha) + n = -0.900976768 \times 0.5516 + 0.878226792 = 0.3812$$

$$\gamma = m(H_1, \gamma) + n = -32.73418563 \times (-0.1936) - 2.935133574 = 3.4034$$

5. Determine the matric suction using Equation (K-6)

$$\varepsilon_r = [\frac{\varepsilon_{sat}+\varepsilon_{\min}\alpha[\frac{h_m}{h_{\max}-h_m}]^{\gamma}}{1+\alpha(\frac{h_m}{h_{\max}-h_m})^{\gamma}}] \Rightarrow 25 = [\frac{46.38+10.73\times0.3812[\frac{h_m}{7-h_m}]^{3.4034}}{1+0.3812(\frac{h_m}{7-h_m})^{3.4034}}]$$

Solve for the only unknown in the function and found that

$$h_m = 4.1945\ pF$$

Task 4. Estimation of Volumetric Water Content

1. Determine the fitting parameters a_f, b_f, c_f and h_r using Equation (16-27) – (16-30)

$$a_f = -0.1972MBV + 22.083 = -0.1972 \times 70 + 22.083 = 8.279$$

$$b_f = -6 \times 10^{-5}MBV^2 + 0.0087MBV + 0.7289 = 1.0439$$

$$c_f = 0.1595MBV - 17.595 = 0.1595 \times 70 - 17.595 = -6.43$$

$$h_r = 0.0128MBV^2 - 1.7393MBV + 60.447$$
$$= 0.0128 \times 70^2 - 1.7393 \times 70 + 60.447 = 1.416$$

2. Determine saturated volumetric water content using Equation (16-31) and (16-32) and Table 16-17

$$H_1 = TANH(0.5(a_1(MBV) + b_1(pfc) + c_1(G_s) + d_1))$$
$$= TANH(0.5(0.1816298(70) - 0.09726(91.02) + 1.6012614(2.63) - 9.078068))$$
$$= -0.4642$$

$$\theta_{sat} = m(H_1) + n$$
$$= 0.130049 \times (-0.4642) + 0.4722762$$
$$= 0.4119$$

3. Determine the volumetric water content using Equation (K-21) and (K-22)

$$\theta = C(h) \times [\frac{\theta_{sat}}{[\ln[\exp(1) + (\frac{h_m}{a_f})^{b_f}]]^{c_f}}]$$

$$= [1 - \frac{\ln(1+\frac{4.1945}{1.416})}{\ln(1+\frac{7}{1.416})}] \times [\frac{0.4119}{[\ln[\exp(1) + (\frac{4.1945}{8.279})^{1.0439}]]^{-6.43}}]$$
$$= 0.252$$

Task 5. Estimation of Dry Unit Weight

1. Determine the fitting parameters a_d, b_d and n_d using Equation (16-33) and (16-34) and Table 16-20

$$H_1, a_d = TANH(0.5(a_1(MBV) + b_1(pfc) + c_1(G_s) + d_1))$$
$$= TANH(0.5(0.099185396(70) + 0.083715306(91.02) - 1.824986435(2.63) - 9.14215919))$$
$$= 0.30083$$

$$H_1, b_d = TANH(0.5(a_1(MBV) + b_1(pfc) + c_1(G_s) + d_1))$$
$$= TANH(0.5(\text{-}0.039174583(70) + 0.144640778(91.02) - 19.44194219(2.63) + 41.71321996))$$
$$= 0.46365$$
$$H_1, n_d = TANH(0.5(a_1(MBV) + b_1(pfc) + c_1(G_s) + d_1))$$
$$= TANH(0.5(0.057947(70) + 0.0631439(91.02) - 50.7311(2.63) + 125.20646))$$
$$= 0.66048$$
$$a_d = m(H_1, a_d) + n = -0.195976 \times 0.30083 + 1.5938137 = 1.53486$$
$$b_d = m(H_1, b_d) + n = -0.053774 \times 0.46365 + 0.0473947 = 0.02246$$
$$n_d = m(H_1, n_d) + n = -0.069498 \times 0.66048 + 0.0403985 = -0.0055$$

2. Determine the dry unit weight using Equation (K-32)

$$\gamma_d = (a_d[\text{csch}(\frac{\theta\theta_{sat}}{G_s(|\theta_{sat} - \theta|)})]^{n_d} - b_d[\text{csch}(\frac{\theta\theta_{sat}}{G_s(|\theta_{sat} - \theta|)})]) \times \gamma_w$$
$$= \left(\begin{matrix} 1.53486[\text{csch}(\frac{0.252 \times 0.4119}{2.63(|0.4119 - 0.252|)})]^{-0.0055} \\ -0.02246[\text{csch}(\frac{0.252 \times 0.4119}{2.63(|0.4119 - 0.252|)})] \end{matrix}\right) \times 62.4$$
$$= 89.43\ lb/ft^3$$

Task 6. Estimation of Matric Suction at Intersection

Based on Equation (16-18)

$$h_{m-\text{int}ercept} = 5.622 + 0.0041(pfc) = 5.622 + 0.0041(91.02) = 5.995\ pF$$

Task 7. Estimation of Suction Compression Index

1. Determine the mineralogical zone using Figure K-12.

$$PI = 32.57$$
$$LL = 55.09$$

Based on Figure K-12, the mineralogical zone is Zone II.

2. Determine $\frac{LL}{pfc}$, $Ac = \frac{PI}{pfc}$ and the volume change guide number γ_0 using Figure K-14

$$\frac{LL}{pfc} = \frac{55.09}{91.02} = 0.605$$
$$Ac = \frac{PI}{pfc} = \frac{32.57}{91.02} = 0.358$$
$$\gamma_0 = 0.05$$

3. Determine suction compression index using Equation (K-46)

$$\gamma_h = \gamma_0 \times \frac{pfc}{100} = 0.05 \times 0.9102 = 0.0455$$

Estimation of undrained shear strength

The undrained shear strength of a soil can be estimated using Equation (16-2) – (16-6):

$$e_0 = \frac{G_s \gamma_w}{\gamma_d} - 1 = \frac{2.63 \times 62.4}{89.43} - 1 = 0.835$$

$$w = \frac{\theta \gamma_w}{\gamma_d} = \frac{0.252 \times 62.4}{89.43} = 0.1758$$

$$S_r = \frac{wG_s}{e_0} = \frac{0.1758 \times 2.63}{0.835} = 0.5537$$

$$f = 1 + (\frac{S_r - 0.85}{0.15})(\frac{0.01}{\theta} - 1) = 1 + (\frac{0.5537 - 0.85}{0.15})(\frac{0.01}{0.252} - 1) = 2.897$$

$$h_m = 4.1945\ pF$$
$$= 10^{4.1945}\ cm\ of\ water\ column$$
$$= 6161\ inch\ of\ water\ column$$
$$= -222.36 psi$$

$$c_u = -h_m \theta f \frac{\sin\phi'}{1 - \sin\phi'}$$

$$= (222.36) \times 0.252 \times (2.897) \times \frac{\sin 28.07'}{1 - \sin 28.07'}$$
$$= 144.27\ psi$$

Therefore, the undrained shear strength of the soil is 144.27 psi.

Estimation of compression index

The compression index of a soil can be estimated using Equation (16-14) and (16-17):

$$|S|w = h_{m-\mathrm{int}ercept} - h_m = 5.995 - 4.1945 = 1.8005$$

$$C_c = \frac{(1+e_0)\gamma_h}{1+\frac{0.4343}{|S|w}} = \frac{(1+0.835)0.0455}{1+\frac{0.4343}{1.8005}} = 0.0673$$

Therefore, the compression index of the soil is 0.0673.

CHAPTER 17

EMBANKMENT CONSIDERATIONS

As concluded from the previous experience, keeping functional joint sealants and designing satisfactory concrete slab thickness to prevent slab cracking (access of water infiltration) at the BASs is the first step to prevent the underlying layer from erosion; second, designing appropriate surface drainage system to direct runoff water away from the BAS is also equally significant; last but not least important, applying adequate construction practices in the embankment is necessary to prevent the potential settlement and erosion issues.

This chapter focuses on reviewing the possible design details or construction practices and providing guidelines to address three elements of the embankment considerations:

1. Constructing embankment backfill wedge using suitable materials;
2. Applying proper treatment for the embankment; and
3. Implementing suitable subsurface drainage system and erosion protection practice.

EMBANKMENT BACKFILL WEDGE

The selection of the embankment backfill wedge material behind the abutment can significantly influence the performance of BASs considering its effect on the erosion or settlement related problems occurring underneath BASs.

The embankment backfill material should be selected based on the following considerations:

- Less compressibility to avoid settlement issues;
- Less erodibility to prevent erosion issues (Figure 17-1 shows the range of most erodible soils);
- Greater modulus to provide a strong support for the BAS; and
- Better drainability to facilitate subsurface drainage.

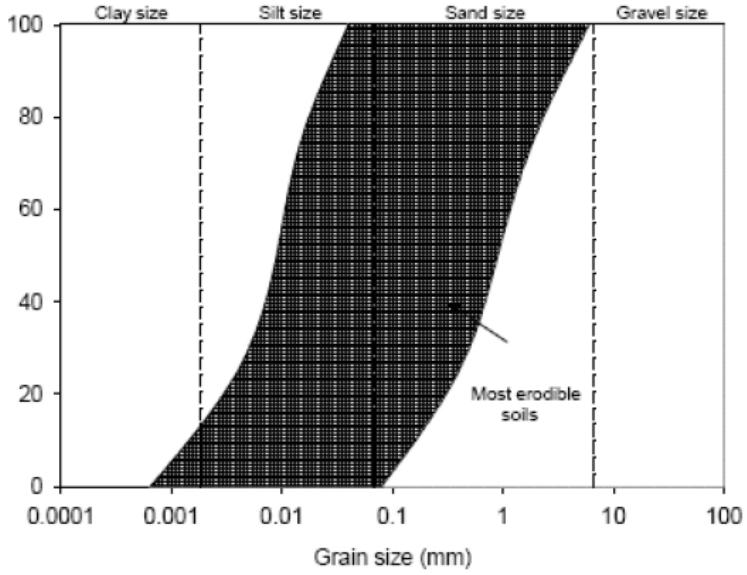

Figure 17-1 Grain size range of most erodible soils [68]

In the past, Oklahoma has been using granular materials as the backfill; however, due to the fact that the granular materials undergo significant amount of settlement upon wetting, now they have been gradually replaced by the controlled low strength material (CLSM) which is also referred to as the flowable fill. A detailed illustration of the CLSM underneath a BAS is shown in Figure 17-2. The CLSM has a couple of notable advantages comparing to granular backfill materials; first, it has negligible consolidation settlement attributed to its low compressibility; second, it does not require compaction that can be very difficult to conduct especially near the abutment wall; third, it has much less erodibility comparing to granular soils; fourth, it can provide adequate strength equivalent to or greater than well compacted granular soils. In addition, the permeability of CLSM can be designed with huge flexibility; it is recommended that the permeability of the CLSM should be designed at least greater than that of the surrounding soil to facilitate subsurface drainage [88].

In this regard, it appears that the use of CLSM as the backfill behind abutment is a viable option to provide satisfying performance with respect to preventing consolidation induced settlement problems as well as facilitating drainage. In the case where CLSM is designed with drainage capability (i.e. by appropriately designing its permeability) in combination with the use of well-designed subsurface drainage system underneath it,

accumulation of infiltrated runoff water at the bottom of a BAS (which may lead to erosion of the CLSM and exacerbation of the distress at the BAS) can be prevented. If the CLSM is designed impermeable, a drainable base layer and edge drains should be used to prevent infiltrated runoff water from accumulating underneath the BAS. Although the initial cost may be high, the application of CLSM is highly recommended considering all the aforementioned benefits.

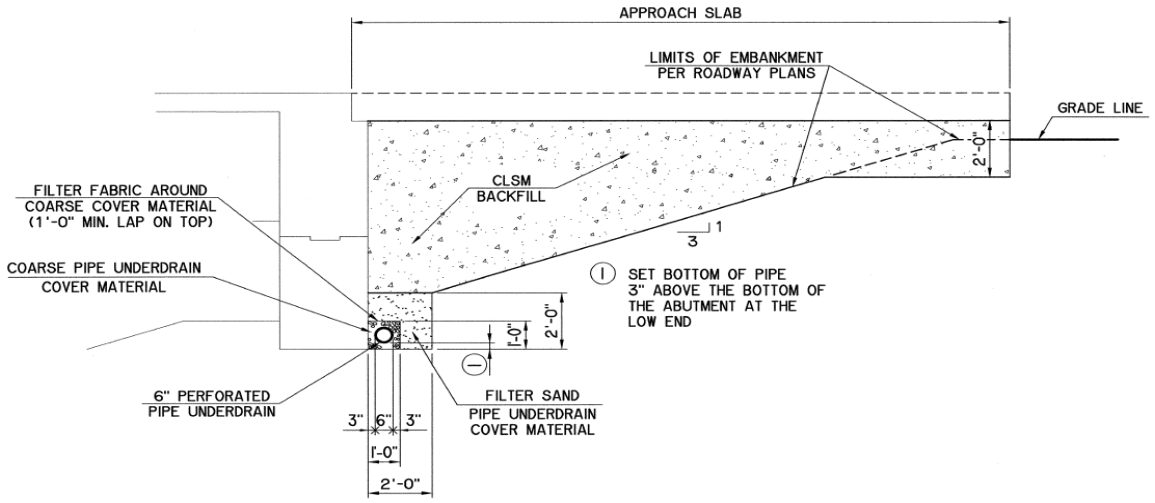

Figure 17-2 Subsurface drainage system in Oklahoma [2]

In addition to the CLMS, there are many other options that can potentially be used as the backfill material. Similarly to the use of CLMS, TxDOT promotes the use of cement stabilized sand (CSS) wedge as the backfill material. This type of material is less susceptible to moisture change and less erodible comparing to traditional granular materials. It was reported that this technique has been adopted by many districts in Texas as the standard practice [89].

One another viable option mentioned in literatures [68, 86, 90] is the use of the expanded polystyrene (EPS) geofoam (shown in Figure 17-3) which also provided excellent performance based on the past experience. This technique has been applied to geotechnical engineering for a few decades and the major advantages provided by this technique are reduced lateral earth pressure on the abutment, reduced vertical pressure on the foundation soil and associated settlement issues, greater resistance to temperature and moisture changes, ease of construction and cost-effective. Attributed

to the nature of lightweight, the application of EPS geofoam in the embankment can create zero net loading on the underlying foundation; this can be achieved by removing a specific amount of foundation soil and replacing them with EPS geofoam if design calculation is properly conducted. This can be extremely helpful and cost-effective for construction projects with high compressible soil layers in the foundation that can be very expensive and time-consuming to address.

Special attention needs to be paid to the drainage issue where a layer of granular materials should be placed between the EPS geofoam and the inclined embankment slope on which the geofoam structure is stepped; otherwise, the buoyancy effect caused by standing water can have negative influence on the performance of the EPS geofoam structure.

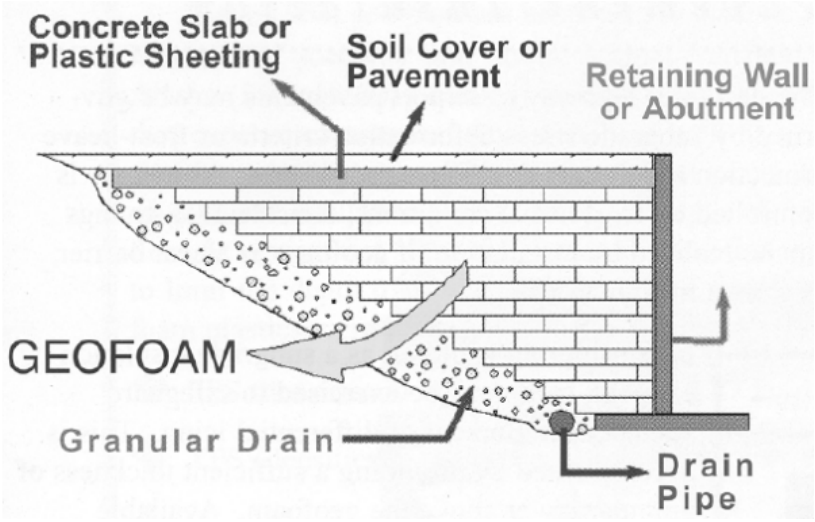

Figure 17-3 Details of EPS geofoam backfill [91]

In a research by White et al. [8], a Water Management Bridge Approach Model (WMBAM) was built under a laboratory condition and a series of laboratory testing was conducted for different backfill materials and practices using the WMBAM to simulate settlement and erosion conditions of the BAS when water was allowed to flow through the expansion joint between the BAS and the abutment. This research found that the use of porous backfill materials (poorly graded gravel) yielded very ideal results (zero settlement and voids) comparing to the use of other materials and practices (such as using granular backfill materials with and without the inclusion of geotextile

reinforcement). The model that used the porous backfill material is shown in Figure 17-4 and the grain size distribution of the porous material is shown in Figure 17-5. Although lacking an evaluation of the BAS performance under wheel load stress during the model testing (only the self-weight of the approach slab was applied to the backfill materials), this research still provided valuable information with respect to the potential utility of porous materials being used as the backfill.

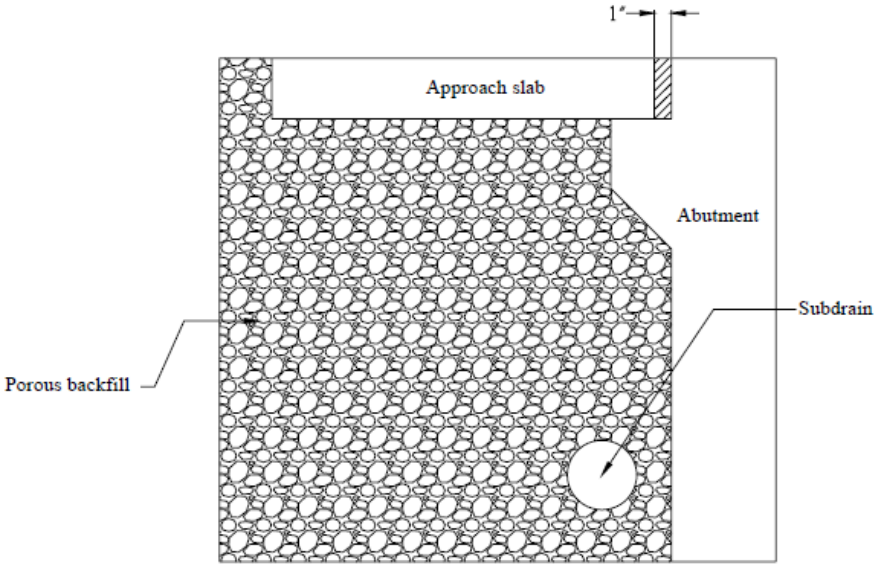

Figure 17-4 Porous backfill materials placed behind the abutment [8]

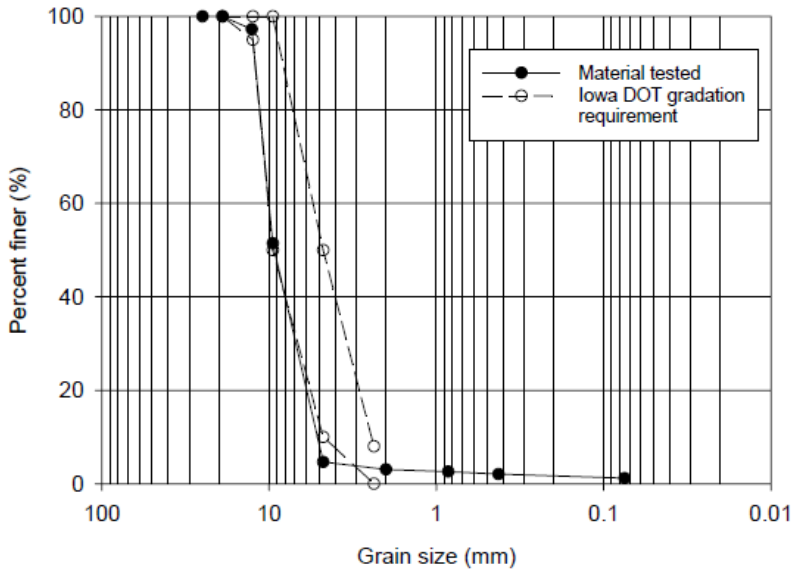

Figure 17-5 Grain size distribution for the porous backfill material [8]

Selection Criteria

Since the CLSM has become a standard practice in Oklahoma, it should be selected as the material for constructing embankment backfill wedge considering all the aforementioned benefits.

Oklahoma may also consider using the EPS geofoam as an alternative especially for the following conditions:

- If the weather condition in the construction site is not suitable to construct CLSM wedge;
- If the foundation of the embankment consists of extremely soft soil layers (e.g. peat) and it becomes too costly to address the settlement problem.

EMBANKMENT TREATMENT

Prevention of the differential settlement issue which helps to maintain smooth transition and minimize slab cracking at the BAS is not only affected by the design of the embankment backfill wedge, but also depends on the performance of the embankment on which the backfill wedge is stepped.

The most fundamental and efficient way to prevent consolidation induced settlement in the embankment area is to strictly ensure that the compaction effort is well achieved during construction of the embankment. According to a survey conducted by Hoppe which summarized the specifications of various DOTs [28]:

- At least 95% of standard proctor should be achieved when constructing the embankment;
- The compaction should be conducted with a lift thickness of 6 – 8 inches and the thinner the lift thickness, the less settlement potential.

To further increase the design reliability of embankment, especially for embankments that are more than 10 ft. in height [34], the use geosynthetic materials in the embankment will add additional confinement and stiffness to the embankment structure which will increase the stability of the embankment slope as well as providing erosion resistance [8]. Successful experience was reported in Wyoming [92] where it

was found that none of the ninety BASs which were constructed on geosynthetic reinforced embankments require any maintenance within 5 years of construction. In addition, research by Maddison et al. [93] indicated that, if columns (either stone columns or concrete columns) were used in the foundation to address compressible soil layers, placing a layer of geosynthetic material (such as geocell elements) at the base of the embankment (i.e. the interface between the embankment and the foundation) can significantly increase the stability and reduce settlement of the embankment structure. In addition to being used at each lift of the embankment, the geosynthetic materials are also frequently used as the slope protection layer to control erosion on the embankment slopes as shown in Figure 17-6.

Figure 17-6 Geocells used as slope protection layer [94]

In order to address the settlement issues in soft compressible foundation layers and ensure uniform transition at the BASs, concrete columns have been used in the embankment to support BASs as shown in Figure 17-7, which were mostly seen Louisiana [95, 96]. The design concept anticipates that a smooth transition will form between the bridge deck end and the pavement end, assuming that the long-term consolidation settlement of the concrete piles increase as the length of the piles decrease. Theoretically, the pile near the bridge end will develop the smallest amount of

settlement (negligible) comparable to the settlement underneath the abutment; the pile near the pavement end will develop the greatest amount of settlement which is closest to the settlement underneath the pavement.

However, field performance [96] indicated that inconsistent performance was observed for the pile-supported BASs due to the variations in the subsoil conditions. In fact, the design of pile-supported BASs can be very tricky and unreliable attributed to the difficulties in predicting the downdrag load induced settlement of the piles, which can vary significantly not only from one site to another, but also from one location to another for a single site. Even Louisiana has been considering replacing the pile-supported BAS solution due to the high cost (BAS usually ranges from 80 – 120 ft. in length) and the low predictability with respect to its performance [95]. Therefore, this option is not recommended.

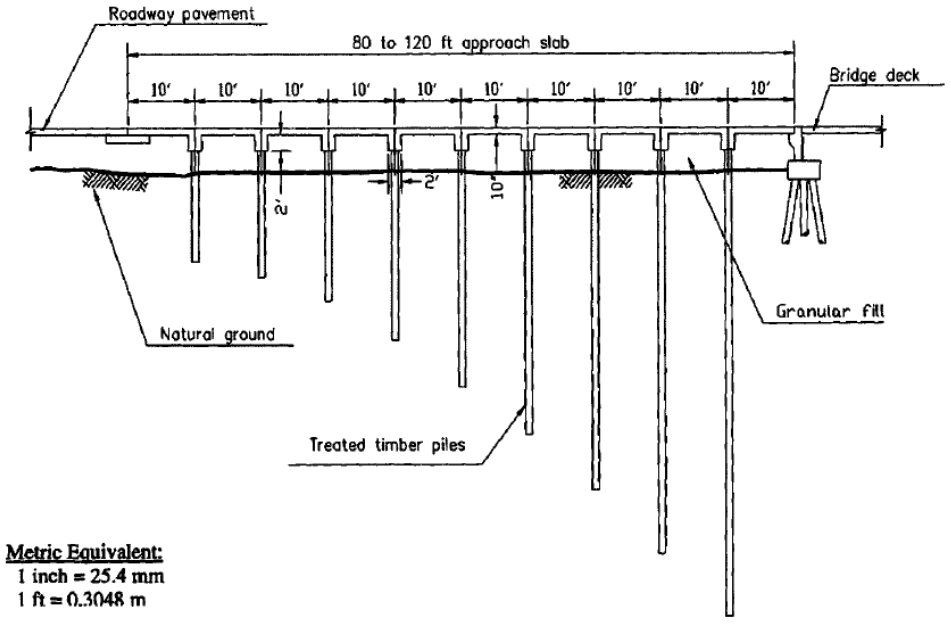

Figure 17-7 Column-supported BASs [96]

Another pile-supported BAS detail is from Illinois as shown in Figure 17-8. In this design detail, one end of the BAS is supported by the abutment and the other sits on a pile cap supported by a concrete column. Essentially, this BAS is designed to behave like a simply supported one-way slab [97] due to the use of the deep foundations at the two supporting ends (with negligible settlement), which indicates that the supporting

medium (i.e. the embankment) in between the two ends is actually functionally insignificant. Although the supporting medium may eventually settle over time if attention is not paid to minimize consolidation settlement or erosion issues, it may be still way too conservative to design a BAS like a simply supported bridge deck (e.g. being 15 in. in thickness and highly reinforced). In addition, without adequate support in between the two ends, the thick and highly reinforced BAS can still crack in the tension zone near the bridge deck-BAS joint (due to negative bending moment), which eventually leads to badly spalled transverse cracking band as was repetitively observed during many field investigations.

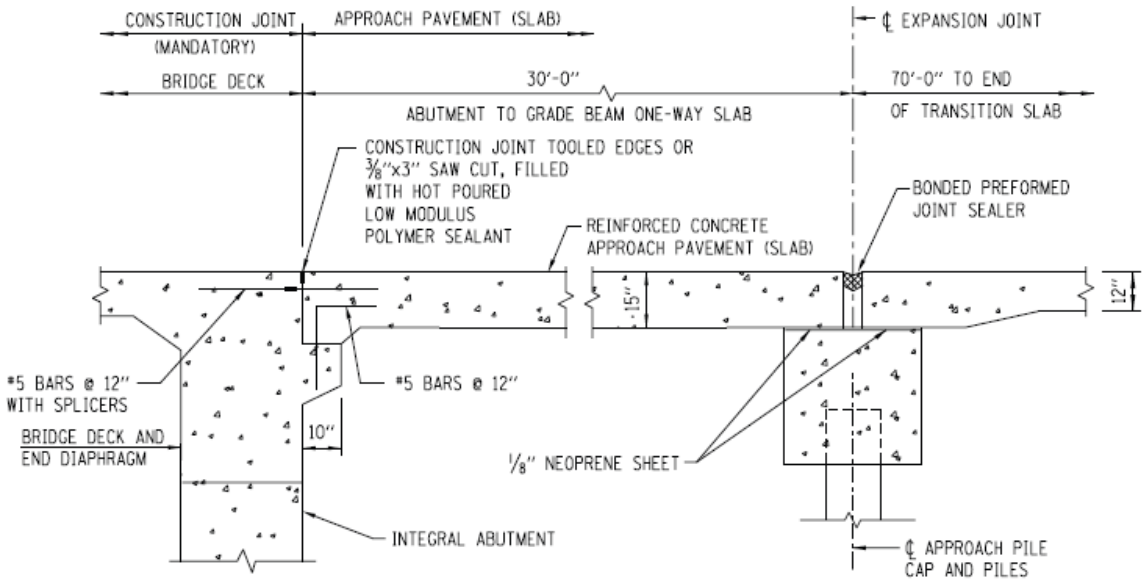

Figure 17-8 Illinois approach slab design details [97]

In order to provide a greater level of design assurance with respect to maintaining smooth transition at the BAS, this guideline also proposes a new design option to treat the embankment, which is the pile-supported backfill wedge option as shown in Figure 17-9. The aim of this design detail is to prevent differential settlement at the BAS by introducing the same deep foundation detail to support both the abutment and the BAS such that they have identical settlement performance. The concrete columns supporting the CLSM wedge should be designed with the same diameter and placed at the same depth in the bearing stratum of the foundation as the concrete column supporting underneath the abutment. In addition, if concrete columns are used

in the embankment to support CLSM and BAS, it is not necessary to apply any ground improvement technique (e.g. stone columns) at least in the area where concrete columns are placed.

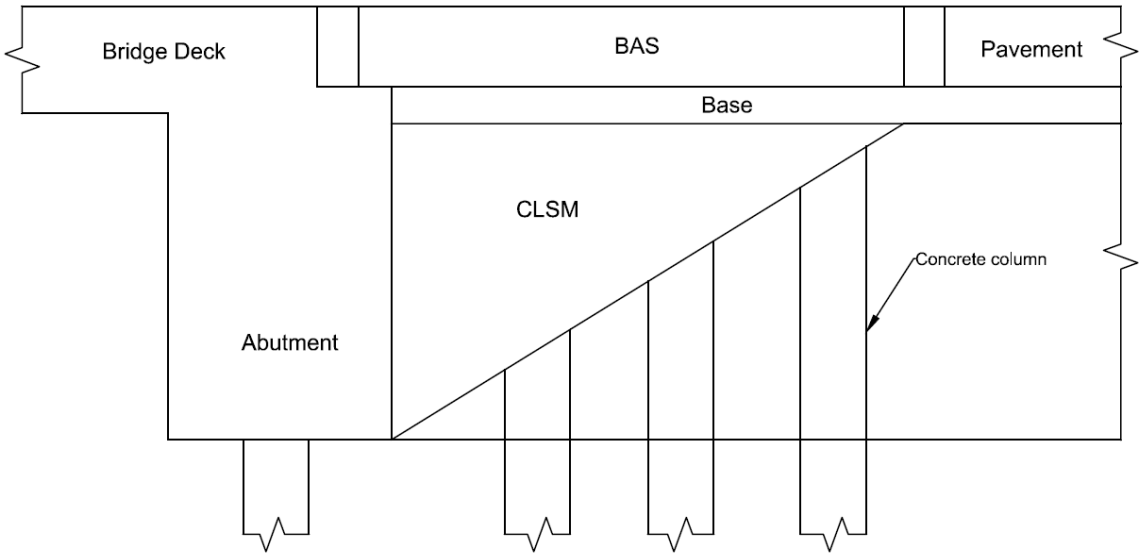

Figure 17-9 Concept of pile-supported backfill wedge option

Selection Criteria

The geosynthetic materials should be selected as an alternative for the embankment construction if:

- It requires to increase the design reliability (for stability, settlement and erosion prevention) for embankments that are higher than 10 ft.;
- The foundation are supported by columns, a layer of geosynthetic material should be placed at the interface between the foundation and the embankment.

The pile-supported backfill wedge option should be selected as an alternative for the embankment construction if:

- Weak and compressible layers are present in the foundation;
- The construction schedule cannot accommodate the long construction period associated with applying ground improvement techniques to address the weak and compressible layers;

- It requires to increase the design reliability with respect to minimizing the embankment and foundation settlement (this option is expected to provide the greatest reliability to maintain the smooth transition at the BAS);

SUBSURFACE DRAINAGE SYSTEM

With many efforts made to direct runoff water away from the surface of BASs, properly designed subsurface drainage system also plays a significant role in preventing the erosion of subsurface foundation materials.

Subsurface drainage in Oklahoma involves the use of a perforated pipe underdrain right underneath the CLSM wedge behind abutment, which is enclosed by filter sand, coarse underdrain cover material with filter fabric wrapping around. However, this standard design sometimes does not appear to prevent water from flowing underneath the abutment which creates substantial soil erosion problems such as the ones shown in Figure 17-10.

The research conducted by Miller et al. [66] investigated the erosion problem underneath the abutment and pointed out that the problem was due to a hydraulic short circuit (shown in Figure 17-11) developed underneath the abutment, which allowed water to bypass the drainage pipe and flow through the gap underneath the abutment leading to substantial erosion over time.

(a) (b)

Figure 17-10 Examples of erosion underneath abutment problem in Oklahoma [66]

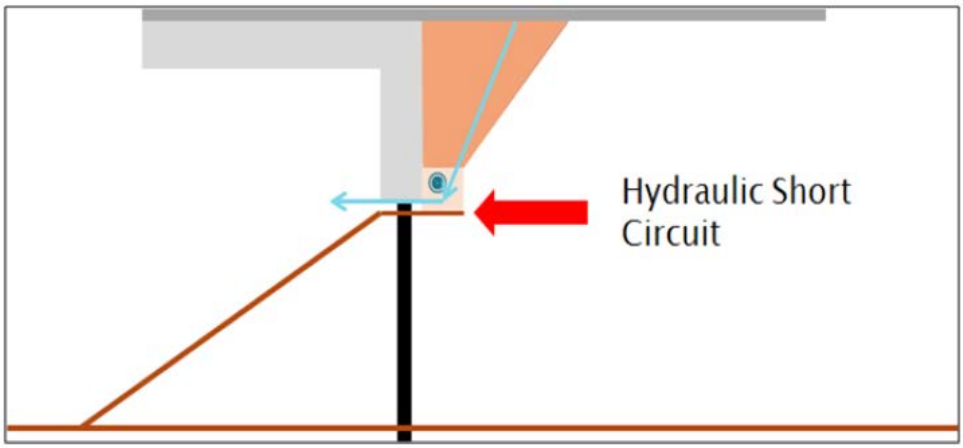

Figure 17-11 Hydraulic short circuit developing mechanism underneath the abutment drainage system [66]

Based on a previous field investigation where it was found that the use of water stop in the subsurface drainage system appeared to have good performance, Miller et al. [66] modified the standard details by introducing a geomembrane as a water stop at

the interface between the abutment and the underdrain cover material to prevent the erosion problem of the backfill material (mainly granular material) due to the developed hydraulic short circuit. A detail of such system is shown in Figure 17-12. This detail seems reasonable to solve the problem, though special attention needs to be paid to the vertical movement of the geomembrane relative to the abutment; geomembrane with high elongation potential may be used to address the issue [66].

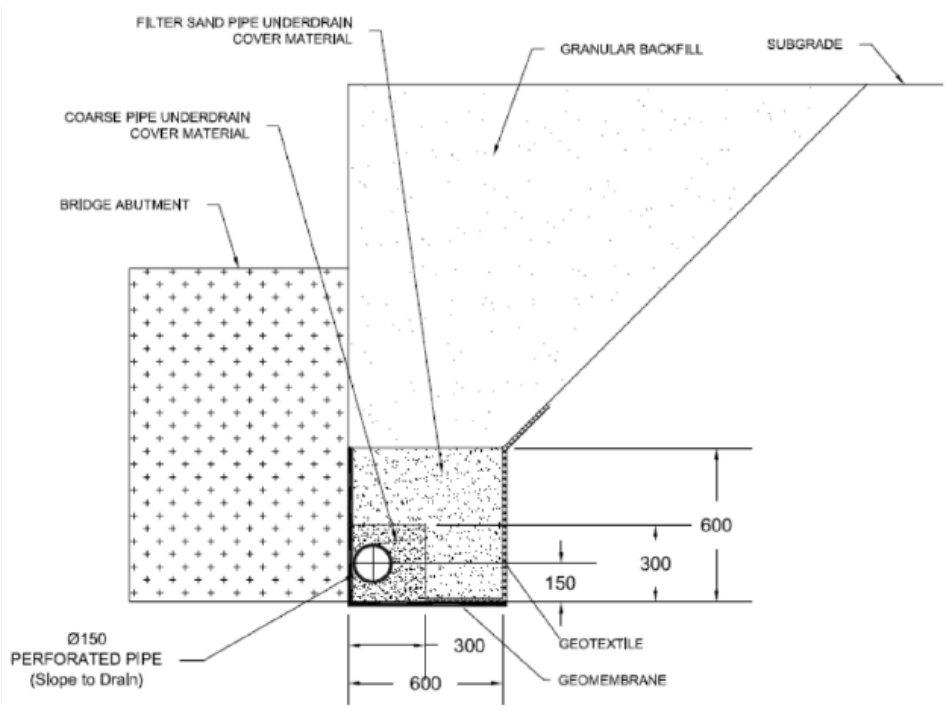

Figure 17-12 Abutment backfill drainage system with geomembrane proposed by Miller et al. [66]

Details from other state DOTs may also be adopted to address the subsurface drainage issue. White et al. [8] conducted laboratory testing and found that the use of a geocomposite vertical drain system as shown in Figure 17-13 significantly increased the capacity of drainage behind abutment. These geocomposite are made from different types of polymeric drainage cores which are covered by geo-textile filters. Once the geocomposite vertical drain system is installed at the face of the abutment, it behaves like an open channel to allow for drainage [86]. It appears that this approach may be

integrated into the design details of the subsurface drainage design of Oklahoma to better transport water into the pipe underdrain.

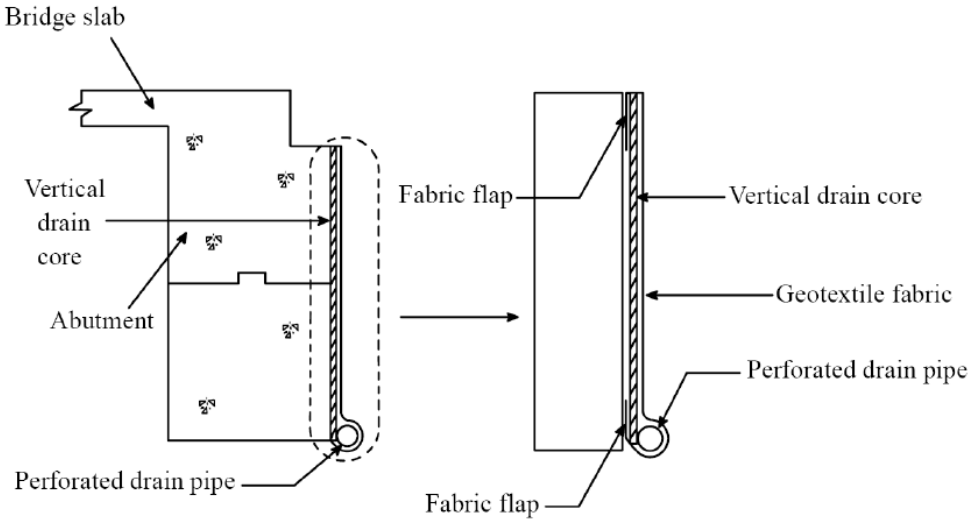

Figure 17-13 Schematic diagram of the use of vertical drain behind abutment [8]

Another practice which was proposed by the Colorado Department of Transportation (CDOT) to improve the subsurface drainage can be illustrated as shown in Figure 17-14. In this practice, the subsurface drainage pipe is placed at the bottom a "V" shape groove made behind the abutment wall; it appears that this practice can effectively prevent the hydraulic short circuit (which causes erosion at the bottom of the abutment) from occurring if the configuration of the groove and the capacity of the drainage pipe are well-designed. In addition to the drainage pipe placed at the bottom of the backfill, CDOT also placed another one at the shallow depth of the backfill behind the abutment, which helps to collect any water leaking into the expansion joint at the BAS-abutment connection. Also, a layer of polystyrene vertical drain is placed at the face of the abutment wall to direct any leaking water to the bottom drainage pipe. This subsurface drainage scheme seems to be very effective since it provides a double-insurance to prevent erosion from taking place underneath the abutment wall.

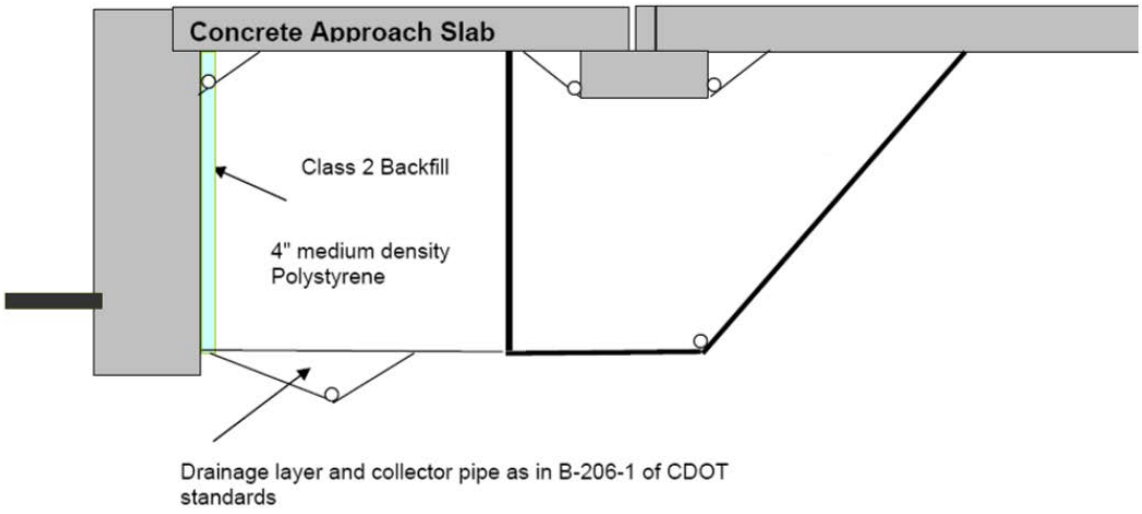

Figure 17-14 the subsurface drainage system provided by CDOT [87]

Selection Criteria

Since it is a standard practice in Oklahoma, the subsurface drainage system should be consistently applied in the embankment construction. This guideline recommends that the standard detail should be modified to include the features of the geomembrane water stop and the “V” shape groove as shown in Figure 17-12 and Figure 17-14, respectively.

The geocomposite vertical drain system may also be used if:

- The construction area is subjected to heavy rainfall;
- The practitioner wants to further increase the design reliability with respect to minimizing the erosion in the embankment.

APPENDIX I

DESIGN GUIDELINE AND EXAMPLE

This chapter provides examples and tools for designing stone columns. The examples provided specifically consider the case where the stone columns are used in the foundation soil of an embankment area which is used to support a bridge approach slab.

Prior to conducting the design of the stone columns, the following preliminary information need to be collected:

1. Limits of the treatment area;
2. key soil properties of the treatment area; in-situ or laboratory testing may be conducted to obtain the required data;
3. The stress exerted on top of the treatment area, including:
    - weight of the embankment
    - weight of the structure on top of the embankment, such as bridge approach slabs, wing walls and any bridge railings
    - traffic loading

EXAMPLE DESIGN FOR BEARING CAPACITY

This section provides a design example modified from the report by Barksdale and Bachus [152]. The objective of the example is to determine the number of stone columns needed that will provide sufficient ultimate bearing capacity for the given level of stress.

Step 1

1. Prepare preliminary information, including the treatment area, loading condition, soil properties for each soil layer and the stone column information.

    The preliminary information is shown Table I-1 and Table I-2.

Table I-1 Treatment area and loading condition

Embankment length, ft	50
Embankment width, ft	20
Embankment height, ft	8
Saturated unit weight of embankment material, pcf	125
Unit weight of concrete pavement, pcf	150
Thickness of concrete pavement, in	12
Wing wall and other structures, kips	50
Traffic loading, kips	150

Table I-2 Soil properties for bearing capacity calculation

Layer	Type	Depth	Thickness, ft	Undrained shear strength, psf	PI	Saturated unit weight, pcf
1	Soft clay	0 - 20 ft	20	500	20	100
2	Very soft clay	20 - 30 ft	10	250	40	100
3	Soft clay	30 - 35 ft	5	500	20	100
4	Firm bearing layer	> 35 ft	\	\	\	\

The friction angle of the stone column is assumed to be 40 degree.

2. Calculate the total factored stress Q_f on the treatment area.

The total dead load (DL) can be calculated as:

Embankment weight + Pavement weight + Wing wall and other structures

= (125*50*20*8)/1000 + (150*50*20*12/12)/1000 +50 = 1000+150+50

= 1200 kips.

The total live load (LL) is:

Traffic loading = 150 kips

The total factored load P_f can be calculated as:

P_f = 1.2 (DL+ 1.67 LL) = 1.2 × (1200 + 1.67 × 150) = 1741 kips

The total factored stress Q_f can be calculated as:

$Q_f = P_f/A_{total}$ = 1741 kips/(50 ft × 20 ft) = 1741 kips/1000 ft^2 = $1741psf$

Step 2

1. Determine the trial spacing, diameter and installation pattern for the stone columns.

   Trial column spacing $s = 6$ ft

   Trial column diameter $D = 3.5$ ft

   Trial installation pattern: equilateral triangular pattern ($C_1 = \pi/4$ for a square pattern and $C_1 = \pi/2\sqrt{3}$ for an equilateral triangular pattern).

2. Calculate area replacement ratio, area of each stone column and area of each unit cell.

   Area replacement ratio: $a_s = C_1(\frac{D}{s})^2 = \frac{\pi}{2\sqrt{3}}(\frac{3.5}{6})^2 = 0.308$

   Area of each stone column, ft^2: $A_s = \pi(\frac{D}{2})^2 = 9.62$ ft^2

   Area of each unit cell, ft^2: $A = A_s/a_s = 31.23$ ft^2

   Area of soil in each unit cell, ft^2: $A_c = A - A_s = 21.61$ ft^2

3. Estimate stress concentration ratio SCR and calculate ratio of stress in the stone column and the surrounding soil.

   Assume $SCR = 3$

   Ratio of stress in the stone column:

$$\mu_s = \frac{SCR}{1 + (SCR - 1) \cdot a_s} = \frac{3}{1 + 2 \cdot 0.308} = 1.856$$

   Ratio of stress in the surrounding soil:

$$\mu_c = \frac{1}{1 + (SCR - 1) \cdot a_s} = 0.619$$

Step 3

1. Identify the type of stone column (long or short stone column).

   Assuming the stone column is placed on top of the firm bearing layer and the length of the stone column is 35 ft. The length to diameter ratio L/D for the stone column is:

   $$L/D = 10 > 4$$

   Therefore, it is a long stone column.

2. Identify the possible failure mode.

   The possible failure mode for a long stone column:

   - General bulging failure
   - Column head shear failure
   - Local bulge failure occurs at very soft soil layer

Step 4

1. Determine the ultimate bearing stress for general bulging failure

   Cavity expansion theory:

   a. Determine the depth where bulge occurs, ft.:

   $$h = d_f + \frac{1}{2}D\tan(45^\circ + \frac{\varphi_s}{2}) = 0 + \frac{1}{2} \times 3.5 \times \tan(45^\circ + \frac{40^\circ}{2}) = 3.75 \text{ ft}$$

   b. Determine the overburden pressure σ_v:

   $$\sigma_v = \gamma_c \cdot h = 100 * 3.75 = 375 \text{ psf}$$

   c. Determine the mean stress at the failure depth q:

   $$q = \frac{(1 + 2 \cdot K_0) \cdot \sigma_v}{3} = \frac{(1 + 2 \cdot 1) \cdot 375}{3} = 375 \text{ psf}$$

   d. Determine the Rigidity Index I_r:

   $$I_r = \frac{E}{2(1 + \nu)(c + q\tan\varphi_c)} = \frac{11 \times 500}{2(1 + 0.5)(500 + 0)} = 3.67$$

   e. Determine cavity expansion factors F_c' and F_q' using determined Rigidity Index and Equation (15-16) and (15-17):

   $$F_c' = \ln I_r + 1 = 2.3$$

$$F_q' = (1 + \sin\varphi_c)(I_r \sec\varphi_c)^{\frac{\sin\varphi_c}{1+\sin\varphi_c}} = 1$$

f. Determine the ultimate lateral stress σ_3

$$\sigma_3 = cF_c' + qF_q' = 500 \times 2.3 + 375 \times 1 = 1525 \text{ psf}$$

g. Determine the ultimate bearing stress $q_{ult} = \sigma_3 \cdot \frac{1+\sin\varphi_s}{1-\sin\varphi_s}$

$$q_{ult} = \sigma_3 \cdot \frac{1 + \sin\varphi_s}{1 - \sin\varphi_s} = 1525 \times \frac{1 + 0.643}{1 - 0.643} = 1525 \times 4.6 = 7015 \text{ psf}$$

Bearing capacity factor method:

a. Select bearing capacity factor N_c for bulging failure occurs within the depth of the upper 3-diameter of the stone column, where a soft clay soil is present; based on the previous experience $N_c = 20$

b. Determine the ultimate bearing stress $q_{ult} = \sigma_3 \cdot \frac{1+\sin\varphi_s}{1-\sin\varphi_s}$

$$q_{ult} = c_u N_c = 500 * 20 = 10000 \text{ psf}$$

2. Determine the ultimate bearing stress for column head shear failure

Brauns' Method:

a. Determine angle of the shear failure cone based on Figure 15-8 for the case of surcharge load = 0

$$\delta = 61.5^\circ$$

b. Determine the ultimate bearing stress $q_{ult} = \sigma_3 \cdot \frac{1+\sin\varphi_s}{1-\sin\varphi_s}$

$$q_{ult} = \sigma_{1,\max} = (q_s + \frac{2 \cdot c_u}{\sin(2 \cdot \delta)}) \cdot (1 + \frac{\tan(\frac{\pi}{4} + \frac{\varphi_s}{2})}{\tan\delta}) \cdot \tan^2(\frac{\pi}{4} + \frac{\varphi_s}{2})$$

$$= (0 + \frac{2 \cdot 500}{\sin(2 \cdot 61.5^\circ)}) \cdot (1 + \frac{\tan(\frac{\pi}{4} + \frac{40^\circ}{2})}{\tan 61.5^\circ}) \cdot \tan^2(\frac{\pi}{4} + \frac{40^\circ}{2})$$

$$= 11843 \text{ psf}$$

3. Determine the ultimate bearing stress for local bulge failure to occur at very soft soil layer

Barksdale and Bachus' Method:

a. Determine the depth of very soft soil layer:

$$h = 20 > 3 \cdot D = 10.5 \text{ ft}$$

b. Determine the ultimate lateral stress σ_3, since the local bulge failure occurs below a depth of 3-diameter of the stone column, the ultimate lateral stress σ_3 can be estimated by applying Equation (15-22):

$$\sigma_3 = 9c_u = 9 \times 250 = 2250 \text{ psf}$$

c. Determine the ultimate bearing stress $q_{ult} = \sigma_3 \cdot \frac{1+\sin\varphi_s}{1-\sin\varphi_s}$

$$q_{ult} = \sigma_3 \cdot \frac{1+\sin\varphi_s}{1-\sin\varphi_s} = 2250 \times \frac{1+0.643}{1-0.643} = 2250 \times 4.6 = 10350 \text{ psf}$$

Step 5

1. Identify the most critical failure mode and the associated ultimate bearing stress in the stone column

   The stone column is most likely to fail due to general bulging failure.

   $$\sigma_s = q_{ult} = 7015psf$$

2. Determine the ultimate allowable bearing stress for the tributary soils σ_{c-ult} which can be estimated by:

   $$\sigma_{c-ult} = 5c_u = 5 \times 500 = 2500\text{psf}$$

3. Determine the stress for the tributary soils σ_c when the ultimate bearing stress in the stone column is achieved:

   $$\sigma_c = \mu_c\sigma = \mu_c\frac{\sigma_s}{\mu_s} = \mu_c\frac{q_{ult}}{\mu_s} = 0.619\frac{7015}{1.856} = 2340 \text{ psf} < \sigma_{c-ult}$$

   Therefore, the stress level in the tributary soil is satisfactory. If the condition is not satisfied, start over the design from **Step 2**.

Step 6

1. Calculate the ultimate load P_{ult} for each unit cell, with a factor of safety of 2:

   $$P_{ult} = \frac{\sigma_s A_s + \sigma_c A_c}{FS} = \frac{7015 \times 9.62 + 2340 \times 21.61}{2} = 59026 \text{ lb.}$$

2. Calculate the ultimate allowable stress Q_{ult} for each unit cell:

   $$Q_{ult} = \frac{P_{ult}}{A} = \frac{59026}{31.23} = 1890 \text{ psf}$$

3. Check the ultimate allowable stress Q_{ult} with the total factored stress Q_f

$$Q_f = 1741 \text{ psf} \leq Q_{ult} = 1890 \text{ psf}$$

Therefore, the design is valid.

BEARING CAPACITY CALCULATION WORKSHEET

Step 1

Soil layer 1

Type: soft clay Depth: 0 - 20 ft. Thickness, ft.: 20

Undrained shear strength c_u, psf: 500 PI: 20

Saturated unit weight γ_c, pcf: 100

Soil layer 2

Type: very soft clay Depth: 20 - 30 ft. Thickness, ft.: 10

Undrained shear strength c_u, psf: 250 PI: 40

Saturated unit weight γ_c, pcf: 100

Soil layer 3

Type: soft clay Depth: 30 - 35 ft. Thickness, ft.: 5

Undrained shear strength c_u, psf: 500 PI: 20

Saturated unit weight γ_c, pcf: 100

Soil layer 4

Type: firm bearing layer Depth: > 35 ft. Thickness, ft.: \

Undrained shear strength c_u, psf: \ PI: \

Saturated unit weight γ_c, pcf: \

Stone column

Internal angle of friction φ_s, degree : 40

Dead load (DL):

Embankment weight, kips: 1000 Pavement weight, kips: 150

Wing wall and other structures, kips: 50

Live load (LL):

Traffic loading, kips: 150

Total factored load P_f:

$$P_f = 1.2\ (\text{DL} + 1.67\ \text{LL}) = 1.2 \times (1200 + 1.67 \times 150) = 1741\ \text{kips}$$

Total factored stress Q_f:

$$Q_f = P_f/A_{total} = 1741 \text{ kips}/(50 \text{ ft} \times 20 \text{ ft}) = 1741 \text{ kips}/1000 \text{ ft}^2 = 1741 psf$$

Step 2

Trial column spacing s, ft: 6 Trial column diameter D, ft: 3.5

Trial installation pattern: equilateral triangular pattern

Area replacement ratio:

$$a_s = C_1(\frac{D}{s})^2 = \frac{\pi}{2\sqrt{3}}(\frac{3.5}{6})^2 = 0.308$$

Area of each stone column, ft^2:

$$A_s = \pi(\frac{D}{2})^2 = 9.62$$

Area of each unit cell, ft^2:

$$A = A_s/a_s = 31.23$$

Area of soil in each unit cell, ft^2: $A_c = A - A_s = 21.61$ in^2

Stress concentration ratio SCR: 3

Ratio of stress in the stone column:

$$\mu_s = \frac{SCR}{1 + (SCR - 1) \cdot a_s} = \frac{3}{1 + 2 \cdot 0.308} = 1.856$$

Ratio of stress in the surrounding soil:

$$\mu_c = \frac{1}{1 + (SCR - 1) \cdot a_s} = 0.619$$

Step 3

Length of the stone column, ft.: 35

Length to diameter ratio L/D for the stone column: 10

Long stone column ($L/D > 4$) or short stone column: Long stone column

Possible failure mode: General bulging failure, Column head shear failure, Local bulge failure occurs at very soft soil layer

Step 4

Failure Mode 1. General bulging failure

Cavity expansion theory:

Depth where bulge occurs, ft.:

$$h = d_f + \frac{1}{2}D\tan(45^\circ + \frac{\varphi_s}{2}) = 0 + \frac{1}{2} \times 3.5 \times \tan(45^\circ + \frac{40^\circ}{2}) = 3.75 \text{ ft}$$

Overburden pressure σ_v:

$$\sigma_v = \gamma_c \cdot h = 100 * 3.75 = 375 \text{ psf}$$

Mean stress at the failure depth q:

$$q = \frac{(1 + 2 \cdot K_0) \cdot \sigma_v}{3} = \frac{(1 + 2 \cdot 1) \cdot 375}{3} = 375 \text{ psf}$$

Rigidity Index I_r:

$$I_r = \frac{E}{2(1 + \nu)(c + q\tan\varphi_c)} = \frac{11 \times 500}{2(1 + 0.5)(500 + 0)} = 3.67$$

Cavity expansion factors F_c' and F_q':

$$F_c' = \ln I_r + 1 = 2.3$$

$$F_q' = (1 + \sin\varphi_c)(I_r \sec\varphi_c)^{\frac{\sin\varphi_c}{1+\sin\varphi_c}} = 1$$

Ultimate lateral stress σ_3

$$\sigma_3 = cF_c' + qF_q' = 500 \times 2.3 + 375 \times 1 = 1525 \text{ psf}$$

Ultimate bearing stress $q_{ult} = \sigma_3 \cdot \frac{1+\sin\varphi_s}{1-\sin\varphi_s}$

$$q_{ult} = \sigma_3 \cdot \frac{1 + \sin\varphi_s}{1 - \sin\varphi_s} = 1525 \times \frac{1 + 0.643}{1 - 0.643} = 1525 \times 4.6 = 7015 \text{ psf}$$

Bearing capacity factor method:

Bearing capacity factor N_c: 20

Ultimate bearing stress $q_{ult} = \sigma_3 \cdot \frac{1+\sin\varphi_s}{1-\sin\varphi_s}$

$$q_{ult} = c_u N_c = 500 * 20 = 10000 \text{ psf}$$

Failure Mode 2. Column head shear failure

Brauns' Method:

Determine angle of the shear failure cone based on Figure 15-8 for the case of surcharge load = 0

$$\delta = 61.5^{\circ}$$

Determine the ultimate bearing stress $q_{ult} = \sigma_3 \cdot \frac{1+\sin\varphi_s}{1-\sin\varphi_s}$

$$q_{ult} = \sigma_{1,\max} = (q_s + \frac{2 \cdot c_u}{\sin(2 \cdot \delta)}) \cdot (1 + \frac{\tan(\frac{\pi}{4} + \frac{\varphi_s}{2})}{\tan\delta}) \cdot \tan^2(\frac{\pi}{4} + \frac{\varphi_s}{2})$$

$$= (0 + \frac{2 \cdot 500}{\sin(2 \cdot 61.5^{\circ})}) \cdot (1 + \frac{\tan(\frac{\pi}{4} + \frac{40^{\circ}}{2})}{\tan 61.5^{\circ}}) \cdot \tan^2(\frac{\pi}{4} + \frac{40^{\circ}}{2})$$

$$= 11843 \text{ psf}$$

Failure Mode 3. Local bulge failure occurs at very soft soil layer

Barksdale and Bachus' Method:

Depth of very soft soil layer:

$$h = 20 > 3 \cdot D = 10.5 \text{ ft}$$

Ultimate lateral stress σ_3:

$$\sigma_3 = 9c_u = 9 \times 250 = 2250 \text{ psf}$$

Determine the ultimate bearing stress $q_{ult} = \sigma_3 \cdot \frac{1+\sin\varphi_s}{1-\sin\varphi_s}$

$$q_{ult} = \sigma_3 \cdot \frac{1+\sin\varphi_s}{1-\sin\varphi_s} = 2250 \times \frac{1+0.643}{1-0.643} = 2250 \times 4.6 = 10350 \text{ psf}$$

Step 5

The most critical failure mode: general bulging failure

Associated ultimate bearing stress in the stone column

$$\sigma_s = q_{ult} = 7015psf$$

Ultimate allowable bearing stress for the tributary soils σ_{c-ult}:

$$\sigma_{c-ult} = 5c_u = 5 \times 500 = 2500\text{psf}$$

Stress for the tributary soils σ_c when the ultimate bearing stress in the stone column is achieved:

$$\sigma_c = \mu_c\sigma = \mu_c\frac{\sigma_s}{\mu_s} = \mu_c\frac{q_{ult}}{\mu_s} = 0.619\frac{7015}{1.856} = 2340 \text{ psf} < \sigma_{c-ult}$$

Stress level in the tributary soil: satisfactory

Otherwise, start over the design from **Step 2**.

Step 6

Factor of safety: 2

Ultimate load P_{ult} for each unit cell:

$$P_{ult} = \frac{\sigma_s A_s + \sigma_c A_c}{FS} = \frac{7015 \times 9.62 + 2340 \times 21.61}{2} = 59026 \text{ lb.}$$

Ultimate allowable stress Q_{ult} for each unit cell:

$$Q_{ult} = \frac{P_{ult}}{A} = \frac{59026}{31.23} = 1890 \text{ psf}$$

Check the ultimate allowable stress Q_{ult} with the total factored stress Q_f

$$Q_f = 1741 \text{ psf} \leq Q_{ult} = 1890 \text{ psf}$$

The design is: valid

Otherwise, start over the design from **Step 2.**

EXAMPLE DESIGN FOR SETTLEMENT

Following the same example for designing bearing capacity, this section provides a guideline to determine the settlement of the stone column treated ground.

Step 1

1. Prepare preliminary information, including the treatment area, loading condition, soil properties for each soil layer and the stone column information.

In addition to the data shown in Table I-2, additional soil property information shown in Table I-3 is need to perform settlement calculation.

Table I-3 Additional soil properties for settlement calculation

Layer	Type	Depth	Thickness, ft	Compression index	Initial void ratio	Drained Poisson's ratio
1	Soft clay	0 - 20 ft	20	0.25	1.5	0.42

2	Very soft clay	20 - 30 ft	10	0.8	3.5	0.45
3	Soft clay	30 - 35 ft	5	0.25	1.5	0.42
4	Firm bearing layer	> 35 ft	\	\	\	\

2. Calculate the total factored stress Q_f on the treatment area.

Using the same loading condition shown in the bearing capacity design example, the total factored stress Q_f can be calculated as:

$$Q_f = P_f/A_{total} = 1741 \text{ kips}/(50 \text{ ft} \times 20 \text{ ft}) = 1741 \text{ kips}/1000 \text{ ft}^2 = 1741 psf$$

Step 2

1. Determine the trial spacing, diameter and installation pattern for the stone columns.

Trial column spacing $s = 6$ ft

Trial column diameter $D = 3.5$ ft

Trial installation pattern: equilateral triangular pattern ($C_1 = \pi/4$ for a square pattern and $C_1 = \pi/2\sqrt{3}$ for an equilateral triangular pattern).

2. Calculate area replacement ratio, area of each stone column and area of each unit cell.

Area replacement ratio: $a_s = C_1(\frac{D}{s})^2 = \frac{\pi}{2\sqrt{3}}(\frac{3.5}{6})^2 = 0.308$

Area of each stone column, ft^2: $A_s = \pi(\frac{D}{2})^2 = 9.62$ ft^2

Area of each unit cell, ft^2: $A = A_s/a_s = 31.23$ ft^2

Area of soil in each unit cell, ft^2: $A_c = A - A_s = 21.61$ ft^2

3. Estimate stress concentration ratio SCR and calculate ratio of stress in the stone column and the surrounding soil.

Assume $SCR = 3$

Ratio of stress in the stone column:

$$\mu_s = \frac{SCR}{1 + (SCR - 1) \cdot a_s} = \frac{3}{1 + 2 \cdot 0.308} = 1.856$$

Ratio of stress in the surrounding soil:

$$\mu_c = \frac{1}{1 + (SCR - 1) \cdot a_s} = 0.619$$

Step 3

1. Determine the primary consolidation settlement of the stone column treated ground using the Equilibrium Method:
    a. Calculate the initial effective vertical stress $\bar{\sigma}_0$ in the center of each soil layer (assuming water table is at the ground surface):

    Layer 1: $\bar{\sigma}_{0-1} = (100 \text{ pcf-}62.4 \text{ pcf}) \times 10 \text{ ft} = 376 \text{ psf}$

    Layer 2:

    $\bar{\sigma}_{0-2} = 100 \text{ pcf} \times 20 \text{ ft} + 100 \text{ pcf} \times 5 \text{ ft-}62.4 \text{ pcf} \times 25 \text{ ft} = 940 \text{ psf}$

    Layer 3: $\bar{\sigma}_{0-3} = (100 \text{ pcf-}62.4 \text{ pcf}) \times (20 \text{ ft} + 10 \text{ ft} + 2.5 \text{ ft}) = 1222 \text{ psf}$

    b. Estimate the change in the vertical stress $\Delta\sigma_c$ in the surrounding soil due to the embankment loading at the center of each soil layer by using the Boussinesq stress distribution theory:

    The vertical stress in the surrounding soil σ_c at the ground Surface:

    $\sigma_c = \mu_c \sigma = \mu_c Q_f = 0.619 \times 1741 \text{ psf} = 1078 \text{ psf}$

    Layer 1: $z/B = 10 \text{ ft}/50 \text{ ft} = 0.2B$

    From the Boussinesq solution shown in Figure 15-12, $I_{z-1} = 0.91$

    $$\Delta\sigma_{c-1} = I_{z-1}\sigma_c = 0.91 \times 1078 = 981 \text{ psf}$$

    Layer 2: $z/B = 25 \text{ ft}/50 \text{ ft} = 0.5B$ $I_{z-2} = 0.7$

    $$\Delta\sigma_{c-2} = I_{z-2}\sigma_c = 0.7 \times 1078 = 755 \text{ psf}$$

    Layer 3: $z/B = 32.5 \text{ ft}/50 \text{ ft} = 0.65B$ $I_{z-3} = 0.55$

    $$\Delta\sigma_{c-3} = I_{z-3}\sigma_c = 0.55 \times 1078 = 593 \text{ psf}$$

    c. Determine the primary consolidation settlement S_t of stone column treated ground for each layer

    Layer 1:

$$S_{t-1} = (\frac{C_c}{1+e_0})\log_{10}(\frac{\bar{\sigma}_0 + \Delta\sigma_c}{\bar{\sigma}_0}) \cdot H$$

$$= (\frac{0.25}{1+1.5})\log_{10}(\frac{376+981}{376}) \times 20 \times \frac{12 \text{ in}}{1 \text{ ft}} = 13.37$$

Layer 2:

$S_{t-2} = (\frac{C_c}{1+e_0})\log_{10}(\frac{\bar{\sigma}_0+\Delta\sigma_c}{\bar{\sigma}_0}) \cdot H = (\frac{0.8}{1+3.5})\log_{10}(\frac{940+755}{940}) \times 10 \times \frac{12 \text{ in}}{1 \text{ ft}} = 5.46$

Layer 3:

$$S_{t-3} = (\frac{C_c}{1+e_0})\log_{10}(\frac{\bar{\sigma}_0 + \Delta\sigma_c}{\bar{\sigma}_0}) \cdot H$$

$$= (\frac{0.25}{1+1.5})\log_{10}(\frac{1222+593}{1222}) \times 5 \times \frac{12 \text{ in}}{1 \text{ ft}} = 1.03$$

d. Determine the total primary consolidation settlement S_t of stone column treated ground:

$$S_t = S_{t-1} + S_{t-2} + S_{t-3} = 19.86 \text{ in}$$

e. Calculate the primary consolidation settlement S of untreated ground:

Layer 1: $\Delta\sigma_1 = I_{z-1}\sigma = 0.91 \times 1741 = 1584$ psf

$$S_1 = (\frac{C_c}{1+e_0})\log_{10}(\frac{\bar{\sigma}_0 + \Delta\sigma}{\bar{\sigma}_0}) \cdot H$$

$$= (\frac{0.25}{1+1.5})\log_{10}(\frac{376+1584}{376}) \times 20 \times \frac{12 \text{ in}}{1 \text{ ft}} = 17.21$$

Layer 2: $\Delta\sigma_2 = I_{z-2}\sigma = 0.7 \times 1741 = 1219$ psf

$$S_2 = (\frac{C_c}{1+e_0})\log_{10}(\frac{\bar{\sigma}_0 + \Delta\sigma}{\bar{\sigma}_0}) \cdot H$$

$$= (\frac{0.8}{1+3.5})\log_{10}(\frac{940+1219}{940}) \times 10 \times \frac{12 \text{ in}}{1 \text{ ft}} = 7.71$$

Layer 3: $\Delta\sigma_3 = I_{z-3}\sigma = 0.55 \times 1741 = 958$ psf

$$S_3 = (\frac{C_c}{1+e_0})\log_{10}(\frac{\bar{\sigma}_0 + \Delta\sigma}{\bar{\sigma}_0}) \cdot H$$

$$= (\frac{0.25}{1+1.5})\log_{10}(\frac{1222+958}{1222}) \times 5 \times \frac{12 \text{ in}}{1 \text{ ft}} = 1.51S$$

$$= S_1 + S_2 + S_3 = 26.43 \text{ in}$$

f. Calculate the improvement factor S/S_t (ratio of settlement in the untreated ground to that in the stone column treated ground):

$$S/S_t = \frac{26.43}{19.86} = 1.33$$

2. Determine the primary consolidation settlement of the stone column treated ground using the Finite Element Method:

   a. Calculate the drained modulus of elasticity of the soil:

      Layer 1:

      The Poisson's ratio (drained) ν can be estimated based on Figure 15-16; for this layer, $\nu = 0.42$ is adopted.

      Based on the calculation of the Equilibrium method, the initial average effective vertical stress is $\bar{\sigma}_{0-1} = 376$ psf and the change in the vertical stress in the surrounding soil due to embankment loading is $\Delta\sigma_{c-1} = 981$ psf, therefore the average of initial and final stress state applied in the field (vertical stress) σ_{va} is:

$$\sigma_{va} = \frac{\bar{\sigma}_0 + \Delta\sigma_c}{2} = 679 \text{ psf}$$

      Using Equation (15-39), the drained modulus of elasticity of the soil can be calculated as:

$$E_c = \frac{(1+\nu)(1-2\nu)(1+e_0)\sigma_{va}}{0.435(1-\nu)C_c} = \frac{(1+0.42)(1-2\times 0.42)(1+1.5)679}{0.435(1-0.42)0.25}$$
$$= 6115 \text{ psf} = 42.47 \text{ psi}$$

      Layer 2: $\nu = 0.45$ $\bar{\sigma}_{0-2} = 940$ psf $\Delta\sigma_{c-2} = 755$ psf

$$\sigma_{va} = \frac{\bar{\sigma}_0 + \Delta\sigma_c}{2} = 848 \text{ psf}$$

$$E_c = \frac{(1+\nu)(1-2\nu)(1+e_0)\sigma_{va}}{0.435(1-\nu)C_c} = \frac{(1+0.45)(1-2\times 0.45)(1+3.5)848}{0.435(1-0.45)0.8}$$
$$= 2891 \text{ psf} = 20.07\text{psi}$$

      Layer 3: $\nu = 0.42$ $\bar{\sigma}_{0-3} = 1222$ psf $\Delta\sigma_{c-3} = 593$ psf

$$\sigma_{va} = \frac{\bar{\sigma}_0 + \Delta\sigma_c}{2} = 908 \text{ psf}$$

$$E_c = \frac{(1+\nu)(1-2\nu)(1+e_0)\sigma_{va}}{0.435(1-\nu)C_c} = \frac{(1+0.42)(1-2\times 0.42)(1+1.5)908}{0.435(1-0.42)0.25}$$
$$= 8177 \text{ psf} = 56.78psi$$

   b. Estimate the modulus of elasticity of the stone column using Equation (15-41):

Without having specific test data, the following parameters can be assumed:

$K = 88.6$, $n = 1.14$, $R_f = 0.86$, $c = 0$ and $\varphi_s = 40°$.

Based on the example design for bearing capacity shown previously, for the most critical failure mode:

$\sigma_1 = 7015$ psf $\quad \sigma_2 = \sigma_3 = 1525$ psf

$$\sigma_\theta = \sigma_1 + \sigma_2 + \sigma_3 = 7015 + 1525 \times 2 = 10065 \text{ psf}$$

Therefore:

$$E_s = K \cdot \sigma_\theta^n \cdot [1 - \frac{(\sigma_1 - \sigma_3)R_f}{(\frac{2(c \cdot \cos\varphi_s + \sigma_3 \sin\varphi_s)}{1 - \sin\varphi_s})}]$$

$$= 88.6 \cdot 10065^{1.14} \cdot [1 - \frac{(7015 - 1525) \times 0.86}{(\frac{2(0 + 1525 \times \sin 40°)}{1 - \sin 40°})}] = 452857 \text{ psf} = 3145 \text{ psi}$$

c. Decide the compressibility of the soil:

If $E_s/E_c \leq 10$, it is low compressibility cohesive soil;

If $E_s/E_c > 10$, it is compressible cohesive soil.

Based on this rule, all the three layers are compressible cohesive soil.

d. Determine the average vertical strain using the design charts shown in Appendix J:

For this design example: $a_s = 0.308$ and $L/D = 10$; therefore, interpolate results by using Figure J-8 and Figure J-11 is needed.

The average applied stress: $\sigma = Q_f = 1741$ psf $= 12.09$ psi

Layer 1: $E_c = 42.47$ psi $\Delta\sigma_1 = 1584$ psf $= 11.00$ psi

Layer 2: $E_c = 20.07$ psi $\quad \Delta\sigma_2 = 1219$ psf $= 8.47$ psi

Layer 3: $E_c = 56.78$ psi $\quad \Delta\sigma_3 = 958$ psf $= 6.65$ psi

To be conservative, $E_b = 12$ psi is used as the modulus of the soft boundary for all the layers.

The average vertical strain S/L and settlement S can be estimated:

Layer 1: From Figure J-8 $S/L = 0.049$ where $a_s = 0.25$

From Figure J-11 $S/L = 0.022$ where $a_s = 0.35$

Therefore, $S/L = 0.0333$ for $a_s = 0.308$

$S_1 = L_1 \times 0.0333 = 20 \times 0.0333 \times (12\text{ in/1ft}) = 7.99$ in

Layer 2: From Figure J-8 $S/L = 0.062$ where $a_s = 0.25$

From Figure J-11 $S/L = 0.03$ where $a_s = 0.35$

Therefore, $S/L = 0.0434$ for $a_s = 0.308$

$S_2 = L_2 \times 0.0434 = 10\text{ ft} \times 0.0434 \times (12\text{ in/1ft}) = 5.21$ in

Layer 3: From Figure J-8 $S/L = 0.023$ where $a_s = 0.25$

From Figure J-11 $S/L = 0.01$ where $a_s = 0.35$

Therefore, $S/L = 0.0155$ for $a_s = 0.308$

$S_3 = L_3 \times 0.0155 = 5\text{ ft} \times 0.0155 \times (12\text{ in/1ft}) = 0.93$ in

e. Calculate the total settlement of the stone column treated ground:

$$S_t = S_1 + S_2 + S_3 = 14.13\text{ in}$$

f. Calculate the improvement factor S/S_t (ratio of settlement in the untreated ground to that in the stone column treated ground):

$$S/S_t = \frac{26.43}{14.13} = 1.87$$

3. Determine the primary consolidation settlement of the stone column treated ground using the Priebe's Method:

a. Calculate the improvement factor n_0:

The friction angle of the stone column is assumed to be 40°. The Rankine's active earth pressure:

$$K_{aC} = \tan^2(45° - \varphi_s/2) = \tan^2(45° - 40°/2) = 0.217$$

For Layer 1 & 3, the Poisson's ratio $\nu = 0.42$:

$$f(\nu, A_s/A) = \frac{(1-\nu)\cdot(1-A_s/A)}{1-2\nu+A_s/A} = \frac{(1-0.42)\cdot(1-0.308)}{1-2\times0.42+0.308} = 0.858$$

$$n_0 = 1 + \frac{A_s}{A}\left[\frac{1/2+f(\nu,A_s/A)}{K_{aC}\cdot f(\nu,A_s/A)} - 1\right] = 1 + 0.308\left[\frac{1/2+0.858}{0.217\cdot0.858} - 1\right] = 2.938$$

For Layer 2, the Poisson's ratio $\nu = 0.45$:

$$f(\nu, A_s/A) = \frac{(1-\nu)\cdot(1-A_s/A)}{1-2\nu+A_s/A} = \frac{(1-0.45)\cdot(1-0.308)}{1-2\times0.45+0.308} = 0.933$$

$$n_0 = 1 + \frac{A_s}{A}\left[\frac{1/2+f(\nu,A_s/A)}{K_{aC}\cdot f(\nu,A_s/A)} - 1\right] = 1 + 0.308\left[\frac{1/2+0.933}{0.217\cdot0.933} - 1\right] = 2.872$$

b. Calculate the primary consolidation settlement of untreated ground:

This has been previously determined by using the conventional 1-d consolidation theory:

$$S_1 = 17.21 \text{ in}$$

$$S_2 = 7.71 \text{ in}$$

$$S_3 = 1.51 \text{ in}$$

c. Calculate the primary consolidation settlement of stone column treated ground:

Layer 1: $S_{t-1} = \mathrm{S}_1/n_0 = 17.21/2.938 = 5.86$ in

Layer 2: $S_{t-2} = \mathrm{S}_2/n_0 = 7.71/2.872 = 2.68$ in

Layer 3: $S_{t-3} = \mathrm{S}_3/n_0 = 1.51/2.938 = 0.51$ in

Total: $S_t = S_{t-1} + S_{t-2} + S_{t-3} = 9.05$ in

d. Calculate the overall improvement factor S/S_t (ratio of settlement in the untreated ground to that in the stone column treated ground):

$$S/S_t = \frac{26.43}{9.05} = 2.92$$

4. Determine the lower and upper bounds of predicted primary consolidation settlements of stone column treated ground:

The upper bound settlement (by the Equilibrium Method):

$$S_t = 19.86 \text{ in}$$

The lower bound settlement (by the Priebe's Method):

$$S_t = 9.05 \text{ in}$$

The average of the settlements (for the lower and upper bounds):

$$S_t = \frac{19.86 + 9.05}{2} = 14.46 \text{ in}$$

The average of the settlements (for the three methods):

$$S_t = \frac{19.86 + 14.13 + 9.05}{3} = 14.35 \text{ in}$$

Therefore, it appears that the Finite Element Method provides settlement estimations that are reasonably close to the average of the three methods.

Step 4

1. Determine the time rate of settlement. Assuming t is at 100 day. Additional soil property information that is required for the calculation is shown in Table I-4.

Table I-4 Additional soil properties for time rate of settlement calculation

Layer	Type	Depth	Thickness, ft	Coefficient of consolidation in the vertical direction, ft^2/day	Coefficient of consolidation in the radial direction, ft^2/day
1	Soft clay	0 - 20 ft	20	0.04	0.12
2	Very soft clay	20 - 30 ft	10	0.08	0.24
3	Soft clay	30 - 35 ft	5	0.04	0.12
4	Firm bearing layer	> 35 ft	\	\	\

a. Determine the degree of consolidation U_z considering only vertical drainage by using Figure 15-20:

Layer 1: $T_z = \frac{C_v \cdot t}{(\frac{H}{N})^2} = \frac{0.04 ft^2/day \cdot 100 day}{(\frac{20}{2})^2} = 0.04$ $U_z = 0.15$

Layer 2: $T_z = \frac{C_v \cdot t}{(\frac{H}{N})^2} = \frac{0.08 ft^2/day \cdot 100 day}{(\frac{10}{2})^2} = 0.32$ $U_z = 0.65$

Layer 3: $T_z = \frac{C_v \cdot t}{(\frac{H}{N})^2} = \frac{0.04 ft^2/day \cdot 100 day}{(\frac{5}{2})^2} = 0.64$ $U_z = 0.83$

b. Determine the degree of consolidation U_r considering only radial drainage by using Figure 15-21:

The equivalent diameter D_e of a unit cell can be determined by using Equation (15-1) for an equilateral triangular pattern:

$$D_e = 1.05s = 1.05 \times 6 = 6.3 \text{ ft}$$

The reduced drain diameter D' is assumed to be 1/5 of the diameter of the stone columns:

$$D' = \frac{1}{5}D = \frac{1}{5} \times 3.5 = 0.7 \text{ ft}$$

$$n^* = D_e/D' = 6.3/0.7 = 9$$

Layer 1: $T_r = \frac{C_{v_r} \cdot t}{(D_e)^2} = \frac{0.12 ft^2/day \cdot 100 day}{(6.3)^2} = 0.302$ $U_r = 0.82$

Layer 2: $T_r = \frac{C_{v_r} \cdot t}{(D_e)^2} = \frac{0.24 ft^2/day \cdot 100 day}{(6.3)^2} = 0.605$ $U_r = 0.97$

Layer 3: $T_r = \frac{C_{v_r} \cdot t}{(D_e)^2} = \frac{0.12 ft^2/day \cdot 100 day}{(6.3)^2} = 0.302$ $U_r = 0.82$

c. Determine the average degree of consolidation considering both radial and vertical drainage U:

Layer 1: $U = 1 - (1 - U_z)(1 - U_r) = 1 - (1 - 0.15)(1 - 0.82) = 0.847$

Layer 2: $U = 1 - (1 - U_z)(1 - U_r) = 1 - (1 - 0.65)(1 - 0.97) = 0.99$

Layer 3: $U = 1 - (1 - U_z)(1 - U_r) = 1 - (1 - 0.83)(1 - 0.82) = 0.969$

d. Determine the primary consolidation settlement of a cohesive soil layer reinforced by stone column at the time $t = 100 day$:

As an example, the settlement of each layer calculated using the Finite Element Method is used to determine the time rate of settlement.

For the Finite Element Method:

$S_1 = 7.99$ in $\quad S_2 = 5.21$ in $\quad S_3 = 0.93$ in

$S_t = S_1 + S_2 + S_3 = 14.13$ in

Layer 1: $S'_{t1} = U \cdot S_1 = 0.847 \times 7.99 = 6.77$ in

Layer 2: $S'_{t2} = U \cdot S_2 = 0.99 \times 5.21 = 5.16$ in

Layer 3: $S'_{t3} = U \cdot S_3 = 0.969 \times 0.93 = 0.90$ in

Total: $S'_t = S'_{t1} + S'_{t2} + S'_{t3} = 6.77 + 5.16 + 0.9 = 12.83$ in

Step 5

1. Determine the secondary compression settlement ΔS that would occur $t_2 = 5$ year after construction.

Additional soil property information that is required for the calculation is the secondary compression index for each layer:

Layer 1: $C_\alpha = 0.005$

Layer 2: $C_\alpha = 0.01$

Layer 3: $C_\alpha = 0.005$

a. Determine t_1 which is the time when 90% of the primary consolidation settlement is achieved for each layer:

In order to achieve an average degree of consolidation $U = 0.9$considering both radial and vertical drainage for each layer, it is necessary to determine both U_r and U_z for each layer that would lead to $U = 0.9$; following the procedure showed in **Step 4,** it can be determined:

Layer 1: when $t = 130day$

$$T_r = \frac{C_{vr} \cdot t}{(D_e)^2} = \frac{0.12ft^2/day \cdot 130day}{(6.3)^2} = 0.393 \quad U_r = 0.88$$

$$T_z = \frac{C_v \cdot t}{(\frac{H}{N})^2} = \frac{0.04ft^2/day \cdot 130day}{(\frac{20}{2})^2} = 0.052 \quad U_z = 0.2$$

$$U = 1 - (1 - U_z)(1 - U_r) = 1 - (1 - 0.2)(1 - 0.88) = 0.904$$

Therefore, $t_1 = 130$ day for Layer 1.

Layer 2: when $t = 50day$

$$T_r = \frac{C_{vr} \cdot t}{(D_e)^2} = \frac{0.24ft^2/day \cdot 50day}{(6.3)^2} = 0.302 \quad U_r = 0.82$$

$$T_z = \frac{C_v \cdot t}{(\frac{H}{N})^2} = \frac{0.08ft^2/day \cdot 50day}{(\frac{10}{2})^2} = 0.16 \quad U_z = 0.47$$

$$U = 1 - (1 - U_z)(1 - U_r) = 1 - (1 - 0.47)(1 - 0.82) = 0.905$$

Therefore: $t_1 = 50$ day for Layer 2.

Layer 3: when $t = 65day$

$$T_r = \frac{C_{vr} \cdot t}{(D_e)^2} = \frac{0.12ft^2/day \cdot 65day}{(6.3)^2} = 0.197 \quad U_r = 0.64$$

$$T_z = \frac{C_v \cdot t}{(\frac{H}{N})^2} = \frac{0.04ft^2/day \cdot 65day}{(\frac{5}{2})^2} = 0.416 \quad U_z = 0.72$$

$$U = 1 - (1 - U_z)(1 - U_r) = 1 - (1 - 0.72)(1 - 0.64) = 0.899$$

Therefore: $t_1 = 65$ day for Layer 3.

b. Determine the secondary compression settlement ΔS that would occur $t_2 = 5$ year after construction for each layer:

Layer 1: $\Delta S_1 = C_\alpha H \log_{10} \frac{t_2}{t_1} = 0.005 \times 20 \text{ ft} \times \log \frac{5 \times 365 \text{ day}}{130 \text{ day}} = 0.115$

Layer 2: $\Delta S_2 = C_\alpha H \log_{10} \frac{t_2}{t_1} = 0.01 \times 10 \text{ ft} \times \log \frac{5 \times 365 \text{ day}}{50 \text{ day}} = 0.156$

Layer 3: $\Delta S_3 = C_\alpha H \log_{10} \frac{t_2}{t_1} = 0.005 \times 5 \text{ ft} \times \log \frac{5 \times 365 \text{ day}}{65 \text{ day}} = 0.036$

Total secondary settlement 5 years after construction:

$\Delta S = \Delta S_1 + \Delta S_2 + \Delta S_3 = 0.115 + 0.156 + 0.036 = 0.307 \text{ ft} = 3.68 \text{ in}$

SETTLEMENT CALCULATION WORKSHEET

Step 1

Soil layer 1

Type: soft clay Depth: 0 - 20 ft. Thickness, ft.: 20

Compression index C_c: 0.25 Initial void ratio: 1.5

Drained Poisson's ratio: 0.42

Soil layer 2

Type: very soft clay Depth: 20 - 30 ft. Thickness, ft.: 10

Compression index C_c: 0.8 Initial void ratio: 3.5

Drained Poisson's ratio: 0.45

Soil layer 3

Type: soft clay Depth: 30 - 35 ft. Thickness, ft.: 5

Compression index C_c: 0.25 Initial void ratio: 1.5

Drained Poisson's ratio: 0.42

Soil layer 4

Type: firm bearing layer Depth: > 35 ft. Thickness, ft.: \

Compression index C_c: \ Initial void ratio: \

Drained Poisson's ratio: \

Stone column

Internal angle of friction φ_s, degree : 40

Total factored stress Q_f: $Q_f = 1759psf$

Step 2

Trial column spacing s, ft: 6 Trial column diameter D, ft: 3.5

Trial installation pattern: equilateral triangular pattern

Area replacement ratio:

$$a_s = C_1(\frac{D}{s})^2 = \frac{\pi}{2\sqrt{3}}(\frac{3.5}{6})^2 = 0.308$$

Area of each stone column, ft^2:

$$A_s = \pi(\frac{D}{2})^2 = 9.62$$

Area of each unit cell, ft^2:

$$A = A_s/a_s = 31.23$$

Area of soil in each unit cell, ft^2:

$$A_c = A - A_s = 21.61 \text{ in}^2$$

Stress concentration ratio SCR: 3

Ratio of stress in the stone column:

$$\mu_s = \frac{SCR}{1 + (SCR - 1) \cdot a_s} = \frac{3}{1 + 2 \cdot 0.308} = 1.856$$

Ratio of stress in the surrounding soil:

$$\mu_c = \frac{1}{1 + (SCR - 1) \cdot a_s} = 0.619$$

Step 3

Primary consolidation settlement

Equilibrium Method:

a. Initial effective vertical stress $\bar{\sigma}_0$ in the center of each soil layer:

   Water table location: ground surface

   Layer 1: $\bar{\sigma}_{0-1} = (100 \text{ pcf-}62.4 \text{ pcf}) \times 10 \text{ ft} = 376 \text{ psf}$

   Layer 2: $\bar{\sigma}_{0-2} = 100 \text{ pcf} \times 20 \text{ ft} + 100 \text{ pcf} \times 5 \text{ ft-}62.4 \text{ pcf} \times 25 \text{ ft} = 940 \text{ psf}$

   Layer 3: $\bar{\sigma}_{0-3} = (100 \text{ pcf-}62.4 \text{ pcf}) \times (20 \text{ ft} + 10 \text{ ft} + 2.5 \text{ ft}) = 1222 \text{ psf}$

b. Change in the vertical stress $\Delta\sigma_c$ due to the embankment loading at the center of each soil layer:

   Surface: $\sigma_c = \mu_c\sigma = \mu_c Q_f = 0.619 \times 1741 \text{ psf} = 1078 \text{ psf}$

   Layer 1: $z/B = 10 \text{ ft}/50 \text{ ft} = 0.2B$ Figure 15-12: $I_{z-1} = 0.91$

   $$\Delta\sigma_{c-1} = I_{z-1}\sigma_c = 0.91 \times 1078 = 981 \text{ psf}$$

   Layer 2: $z/B = 25 \text{ ft}/50 \text{ ft} = 0.5B$ Figure 15-12: $I_{z-2} = 0.7$

   $$\Delta\sigma_{c-2} = I_{z-2}\sigma_c = 0.7 \times 1078 = 755 \text{ psf}$$

   Layer 3: $z/B = 32.5 \text{ ft}/50 \text{ ft} = 0.65B$ Figure 15-12: $I_{z-3} = 0.55$

   $$\Delta\sigma_{c-3} = I_{z-3}\sigma_c = 0.55 \times 1078 = 593 \text{ psf}$$

c. Primary consolidation settlement S_t of stone column treated ground for each layer:

Layer 1:

$$S_{t-1} = (\frac{C_c}{1+e_0})\log_{10}(\frac{\bar{\sigma}_0 + \Delta\sigma_c}{\bar{\sigma}_0}) \cdot H = (\frac{0.25}{1+1.5})\log_{10}(\frac{376+981}{376}) \times 20 \times \frac{12 \text{ in}}{1 \text{ ft}}$$
$$= 13.37$$

Layer 2:

$$S_{t-2} = (\frac{C_c}{1+e_0})\log_{10}(\frac{\bar{\sigma}_0+\Delta\sigma_c}{\bar{\sigma}_0}) \cdot H = (\frac{0.8}{1+3.5})\log_{10}(\frac{940+755}{940}) \times 10 \times \frac{12 \text{ in}}{1 \text{ ft}} = 5.46$$

Layer 3:

$$S_{t-3} = (\frac{C_c}{1+e_0})\log_{10}(\frac{\bar{\sigma}_0 + \Delta\sigma_c}{\bar{\sigma}_0}) \cdot H = (\frac{0.25}{1+1.5})\log_{10}(\frac{1222+593}{1222}) \times 5 \times \frac{12 \text{ in}}{1 \text{ ft}}$$
$$= 1.03$$

d. Total primary consolidation settlement S_t of stone column treated ground:

$$S_t = S_{t-1} + S_{t-2} + S_{t-3} = 19.86 \text{ in}$$

e. Primary consolidation settlement S of untreated ground for each layer:

Layer 1:

$$\Delta\sigma_1 = I_{z-1}\sigma = 0.91 \times 1741 = 1584 \text{ psf}$$
$$S_1 = (\frac{C_c}{1+e_0})\log_{10}(\frac{\bar{\sigma}_0 + \Delta\sigma}{\bar{\sigma}_0}) \cdot H = (\frac{0.25}{1+1.5})\log_{10}(\frac{376+1584}{376}) \times 20 \times \frac{12 \text{ in}}{1 \text{ ft}}$$
$$= 17.21$$

Layer 2:

$$\Delta\sigma_2 = I_{z-2}\sigma = 0.7 \times 1741 = 1219 \text{ psf} S_2 = (\frac{C_c}{1+e_0})\log_{10}(\frac{\bar{\sigma}_0 + \Delta\sigma}{\bar{\sigma}_0}) \cdot H$$
$$= (\frac{0.8}{1+3.5})\log_{10}(\frac{940+1219}{940}) \times 10 \times \frac{12 \text{ in}}{1 \text{ ft}} = 7.71$$

Layer 3:

$$\Delta\sigma_3 = I_{z-3}\sigma = 0.55 \times 1741 = 958 \text{ psf}$$
$$S_3 = (\frac{C_c}{1+e_0})\log_{10}(\frac{\bar{\sigma}_0 + \Delta\sigma}{\bar{\sigma}_0}) \cdot H = (\frac{0.25}{1+1.5})\log_{10}(\frac{1222+958}{1222}) \times 5 \times \frac{12 \text{ in}}{1 \text{ ft}}$$
$$= 1.51$$

f. Total primary consolidation settlement S of untreated ground:

$$S = S_1 + S_2 + S_3 = 26.43 \text{ in}$$

Primary consolidation settlement

Finite Element Method:

a. Drained modulus of elasticity of the surrounding soil:

Layer 1:

$$\sigma_{va} = \frac{\bar{\sigma}_0 + \Delta\sigma_c}{2} = \frac{376 + 981}{2} = 679 \text{ psf}$$

$$E_c = \frac{(1+\nu)(1-2\nu)(1+e_0)\sigma_{va}}{0.435(1-\nu)C_c} = \frac{(1+0.42)(1-2\times0.42)(1+1.5)670}{0.435(1-0.42)0.25}$$
$$= 6115 \text{ psf} = 42.47 \text{ psi}$$

Layer 2:

$$\sigma_{va} = \frac{\bar{\sigma}_0 + \Delta\sigma_c}{2} = \frac{940 + 755}{2} = 848 \text{ psf}$$

$$E_c = \frac{(1+\nu)(1-2\nu)(1+e_0)\sigma_{va}}{0.435(1-\nu)C_c} = \frac{(1+0.45)(1-2\times0.45)(1+3.5)848}{0.435(1-0.45)0.8}$$
$$= 2891 \text{ psf} = 20.07 \text{ psi}$$

Layer 3:

$$\sigma_{va} = \frac{\bar{\sigma}_0 + \Delta\sigma_c}{2} = \frac{1222 + 593}{2} = 908 \text{ psf}$$

$$E_c = \frac{(1+\nu)(1-2\nu)(1+e_0)\sigma_{va}}{0.435(1-\nu)C_c} = \frac{(1+0.42)(1-2\times0.42)(1+1.5)908}{0.435(1-0.42)0.25}$$
$$= 8177 \text{ psf} = 56.78\, psi$$

b. Modulus of elasticity of the stone column:

$K = 88.6$, $n = 1.14$, $R_f = 0.86$, $c = 0$ and $\varphi_s = 40°$.

$\sigma_1 = 7015$ psf $\quad \sigma_2 = \sigma_3 = 1525$ psf

$$\sigma_\theta = \sigma_1 + \sigma_2 + \sigma_3 = 7015 + 1525 \times 2 = 10065 \text{ psf}$$

$$E_s = K \cdot \sigma_\theta^n \cdot [1 - \frac{(\sigma_1 - \sigma_3)R_f}{(\frac{2(c \cdot \cos\varphi_s + \sigma_3 \sin\varphi_s)}{1 - \sin\varphi_s})}]$$

$$= 88.6 \cdot 10065^{1.14} \cdot [1 - \frac{(7015 - 1525) \times 0.86}{(\frac{2(0 + 1525 \times \sin40°)}{1 - \sin40°})}] = 452857 \text{ psf} = 3145 \text{ psi}$$

c. Decide the compressibility of the soil:

If $E_s/E_c \leq 10$, it is low compressibility cohesive soil;

If $E_s/E_c > 10$, it is compressible cohesive soil.

Layer 1: compressible cohesive soil

Layer 2: compressible cohesive soil

Layer 3: compressible cohesive soil

d. Average vertical strain and settlement for each layer:

$a_s = 0.308$ $L/D = 10$

Use Figure J-8 and Figure J-11 to interpolate results

Layer 1: $E_c = 42.47$ psi $E_b = 12$ psi $\Delta\sigma_1 = 1584$ psf $= 11.00$ psi

Layer 2: $E_c = 20.07$ psi $E_b = 12$ psi $\Delta\sigma_2 = 1219$ psf $= 8.47$ psi

Layer 3: $E_c = 56.78$ psi $E_b = 12$ psi $\Delta\sigma_3 = 958$ psf $= 6.65$ psi

Layer 1: $S/L = 0.0333$ for $a_s = 0.308$

$$S_1 = L_1 \times 0.0333 = 20 \times 0.0333 \times (12 \text{ in/1ft}) = 7.99 \text{ in}$$

Layer 2: $S/L = 0.0434$ for $a_s = 0.308$

$$S_2 = L_2 \times 0.0434 = 10 \text{ ft} \times 0.0434 \times (12 \text{ in/1ft}) = 5.21 \text{ in}$$

Layer 3: $S/L = 0.0155$ for $a_s = 0.308$

$$S_3 = L_3 \times 0.0155 = 5 \text{ ft} \times 0.0155 \times (12 \text{ in/1ft}) = 0.93 \text{ in}$$

e. Total settlement of the stone column treated ground

$$S_t = S_1 + S_2 + S_3 = 14.13 \text{ in}$$

Primary consolidation settlement

Priebe's Method:

a. Improvement factor n_0:

The Rankine's active earth pressure:

$$K_{ac} = \tan^2(45^\circ - \varphi_s/2) = \tan^2(45^\circ - 40^\circ/2) = 0.217$$

Layer 1 & 3:

$$f(\nu, A_s/A) = \frac{(1-\nu)\cdot(1-A_s/A)}{1-2\nu+A_s/A} = \frac{(1-0.42)\cdot(1-0.308)}{1-2\times0.42+0.308} = 0.858$$

$$n_0 = 1 + \frac{A_s}{A}\left[\frac{1/2 + f(\nu, A_s/A)}{K_{ac}\cdot f(\nu, A_s/A)} - 1\right] = 1 + 0.308\left[\frac{1/2+0.858}{0.217\cdot0.858} - 1\right] = 2.938$$

Layer 2:

$$f(\nu, A_s/A) = \frac{(1-\nu)\cdot(1-A_s/A)}{1-2\nu+A_s/A} = \frac{(1-0.45)\cdot(1-0.308)}{1-2\times 0.45+0.308} = 0.933$$

$$n_0 = 1 + \frac{A_s}{A}\left[\frac{1/2 + f(\nu, A_s/A)}{K_{ac}\cdot f(\nu, A_s/A)} - 1\right] = 1 + 0.308\left[\frac{1/2+0.933}{0.217\cdot 0.933} - 1\right] = 2.872$$

b. Primary consolidation settlement of untreated ground:

$$S_1 = 17.21 \text{ in}$$

$$S_2 = 7.71 \text{ in}$$

$$S_3 = 1.51 \text{ in}$$

c. Primary consolidation settlement of stone column treated ground:

Layer 1: $S_{t-1} = S_1/n_0 = 17.21/2.938 = 5.86$ in

Layer 2: $S_{t-2} = S_2/n_0 = 7.71/2.872 = 2.68$ in

Layer 3: $S_{t-3} = S_3/n_0 = 1.51/2.938 = 0.51$ in

Total: $S_t = S_{t-1} + S_{t-2} + S_{t-3} = 9.05$ in

Lower bound of primary consolidation settlements:

$$S_t = 9.05 \text{ in}$$

Upper bound of primary consolidation settlements:

$$S_t = 19.86 \text{ in}$$

Average of the settlements (for the three methods):

$$S_t = \frac{19.86 + 14.13 + 9.05}{3} = 14.35 \text{ in}$$

Step 4

Time rate of settlement at, t: 100 days

Soil layer 1

Type: soft clay Depth: 0 - 20 ft. Thickness, ft.: 20

Coefficient of consolidation in the vertical direction, ft^2/day: 0.04

Coefficient of consolidation in the radial direction, ft^2/day: 0.12

Soil layer 2

Type: very soft clay Depth: 20 - 30 ft. Thickness, ft.: 10

Coefficient of consolidation in the vertical direction, ft^2/day: 0.08

Coefficient of consolidation in the radial direction, ft^2/day: 0.24

Soil layer 3

Type: soft clay Depth: 30 - 35 ft. Thickness, ft.: 5

Coefficient of consolidation in the vertical direction, ft^2/day: 0.04

Coefficient of consolidation in the radial direction, ft^2/day: 0.12

Degree of consolidation U_z considering only vertical drainage:

Layer 1: $T_z = \frac{C_v \cdot t}{(\frac{H}{N})^2} = \frac{0.04 ft^2/day \cdot 100 day}{(\frac{20}{2})^2} = 0.04 \qquad U_z = 0.15$

Layer 2: $T_z = \frac{C_v \cdot t}{(\frac{H}{N})^2} = \frac{0.08 ft^2/day \cdot 100 day}{(\frac{10}{2})^2} = 0.32 \qquad U_z = 0.65$

Layer 3: $T_z = \frac{C_v \cdot t}{(\frac{H}{N})^2} = \frac{0.04 ft^2/day \cdot 100 day}{(\frac{5}{2})^2} = 0.64 \qquad U_z = 0.83$

Equivalent diameter D_e of a unit cell:

$$D_e = 1.05s = 1.05 \times 6 = 6.3 \text{ ft}$$

Reduced drain diameter D': 1/5 of the diameter of the stone columns

$$D' = \frac{1}{5} D = \frac{1}{5} \times 3.5 = 0.7 \text{ ft}$$

$$n^* = D_e / D' = 6.3 / 0.7 = 9$$

Degree of consolidation U_r considering only radial drainage:

Layer 1: $T_r = \frac{C_{vr} \cdot t}{(D_e)^2} = \frac{0.12 ft^2/day \cdot 100 day}{(6.3)^2} = 0.302 \quad U_r = 0.82$

Layer 2: $T_r = \frac{C_{vr} \cdot t}{(D_e)^2} = \frac{0.24 ft^2/day \cdot 100 day}{(6.3)^2} = 0.605 \quad U_r = 0.97$

Layer 3: $T_r = \frac{C_{vr} \cdot t}{(D_e)^2} = \frac{0.12 ft^2/day \cdot 100 day}{(6.3)^2} = 0.302 \quad U_r = 0.82$

Average degree of consolidation considering both radial and vertical drainage U:

Layer 1: $U = 1 - (1 - U_z)(1 - U_r) = 1 - (1 - 0.15)(1 - 0.82) = 0.847$

Layer 2: $U = 1 - (1 - U_z)(1 - U_r) = 1 - (1 - 0.65)(1 - 0.97) = 0.99$

Layer 3: $U = 1 - (1 - U_z)(1 - U_r) = 1 - (1 - 0.83)(1 - 0.82) = 0.969$

Ultimate primary consolidation settlement of each layer:

Layer 1: $S_1 = 7.99$ in

Layer 2: $S_2 = 5.21$ in

Layer 3: $S_3 = 0.93$ in

Time rate of settlement at the time $t = 100day$:

Layer 1: $S'_{t1} = U \cdot S_1 = 0.847 \times 7.99 = 6.77$ in

Layer 2: $S'_{t2} = U \cdot S_2 = 0.99 \times 5.21 = 5.16$ in

Layer 3: $S'_{t3} = U \cdot S_3 = 0.969 \times 0.93 = 0.90$ in

Total: $S'_t = S'_{t1} + S'_{t2} + S'_{t3} = 6.77 + 5.16 + 0.9 = 12.83$ in

Step 5

Secondary compression settlement at, t_2: 5 years

Secondary compression index:

Layer 1: $C_\alpha = 0.005$

Layer 2: $C_\alpha = 0.01$

Layer 3: $C_\alpha = 0.005$

Time t_1 when $U = 90\%$ of primary consolidation settlement occurs in each layer:

Layer 1: $t_1 = 130$ day

$T_r = \frac{C_{v_r} \cdot t}{(D_e)^2} = \frac{0.12ft^2/day \cdot 130day}{(6.3)^2} = 0.393 \qquad U_r = 0.88$

$T_z = \frac{C_v \cdot t}{(\frac{H}{N})^2} = \frac{0.04ft^2/day \cdot 130day}{(\frac{20}{2})^2} = 0.052 \qquad U_z = 0.2$

$U = 1 - (1 - U_z)(1 - U_r) = 1 - (1 - 0.2)(1 - 0.88) = 0.904$

Layer 2: $t_1 = 50$ day

$T_r = \frac{C_{v_r} \cdot t}{(D_e)^2} = \frac{0.24ft^2/day \cdot 50day}{(6.3)^2} = 0.302 \qquad U_r = 0.82$

$T_z = \frac{C_v \cdot t}{(\frac{H}{N})^2} = \frac{0.08ft^2/day \cdot 50day}{(\frac{10}{2})^2} = 0.16 \qquad U_z = 0.47$

$U = 1 - (1 - U_z)(1 - U_r) = 1 - (1 - 0.47)(1 - 0.82) = 0.905$

Layer 3: $t_1 = 65$ day

$T_r = \frac{C_{v_r} \cdot t}{(D_e)^2} = \frac{0.12ft^2/day \cdot 65day}{(6.3)^2} = 0.197 \qquad U_r = 0.64$

$T_z = \frac{C_v \cdot t}{(\frac{H}{N})^2} = \frac{0.04ft^2/day \cdot 65day}{(\frac{5}{2})^2} = 0.416 \qquad U_z = 0.72$

$U = 1 - (1 - U_z)(1 - U_r) = 1 - (1 - 0.72)(1 - 0.64) = 0.899$

Secondary compression settlement ΔS that would occur $t_2 = 5$ year in each layer:

Layer 1: $\Delta S_1 = C_\alpha H \log_{10} \frac{t_2}{t_1} = 0.005 \times 20 \text{ ft} \times \log \frac{5 \times 365 \text{ day}}{130 \text{ day}} = 0.115$

Layer 2: $\Delta S_2 = C_\alpha H \log_{10} \frac{t_2}{t_1} = 0.01 \times 10 \text{ ft} \times \log \frac{5 \times 365 \text{ day}}{50 \text{ day}} = 0.156$

Layer 3: $\Delta S_3 = C_\alpha H \log_{10} \frac{t_2}{t_1} = 0.005 \times 5 \text{ ft} \times \log \frac{5 \times 365 \text{ day}}{65 \text{ day}} = 0.036$

Total secondary settlement $t_2 = 5$ year after construction:

$\Delta S = \Delta S_1 + \Delta S_2 + \Delta S_3 = 0.115 + 0.156 + 0.036 = 0.307 \text{ ft} = 3.68 \text{ in}$

APPENDIX J

STONE COLUMN SETTLEMENT – FINITE ELEMENT METHOD DESIGN CHART

LOW COMPRESSIBILITY SOIL

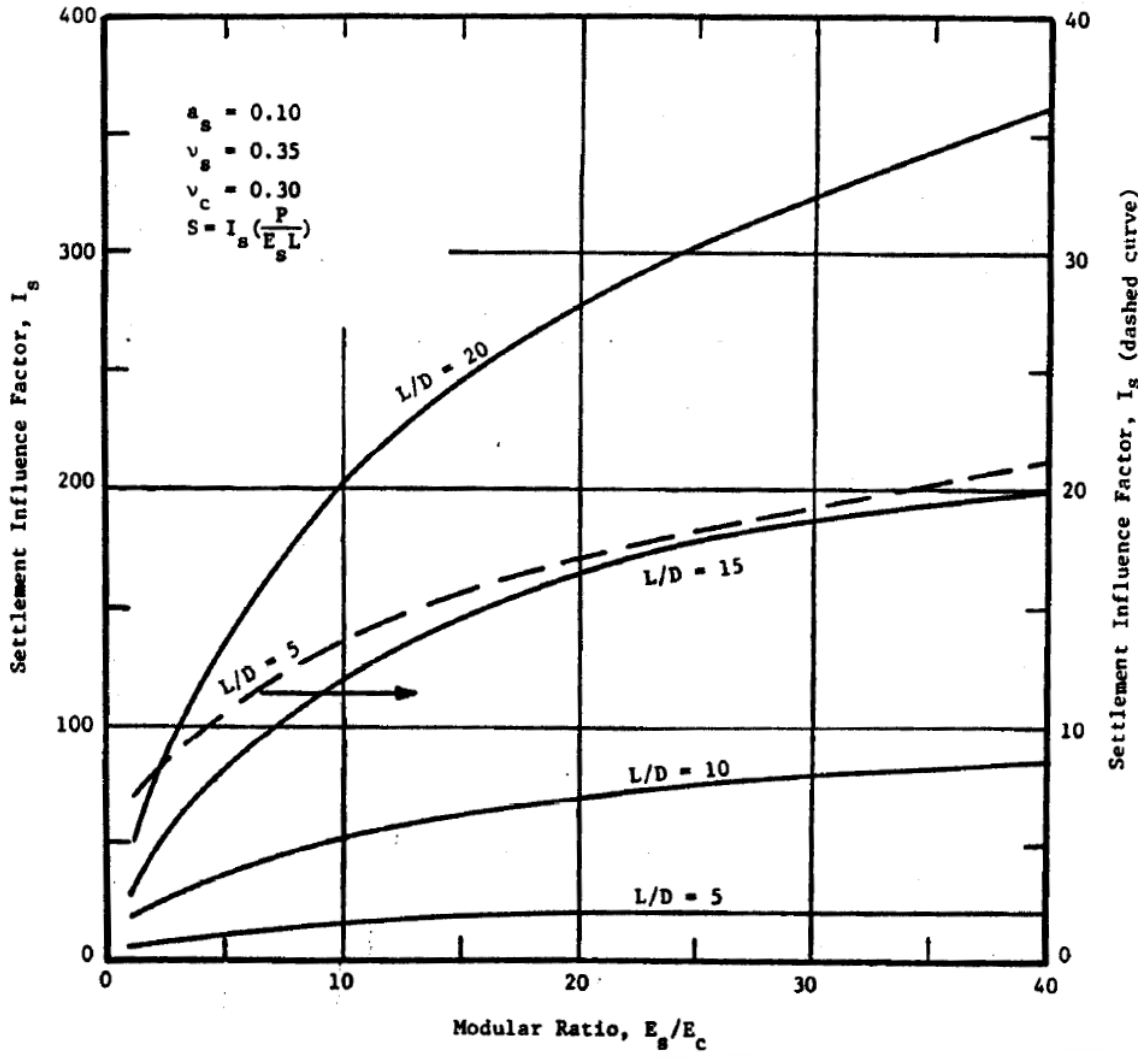

Figure J-1 Settlement prediction curve for low compressibility soil with an area replacement ratio a_s = 0.1 [118]

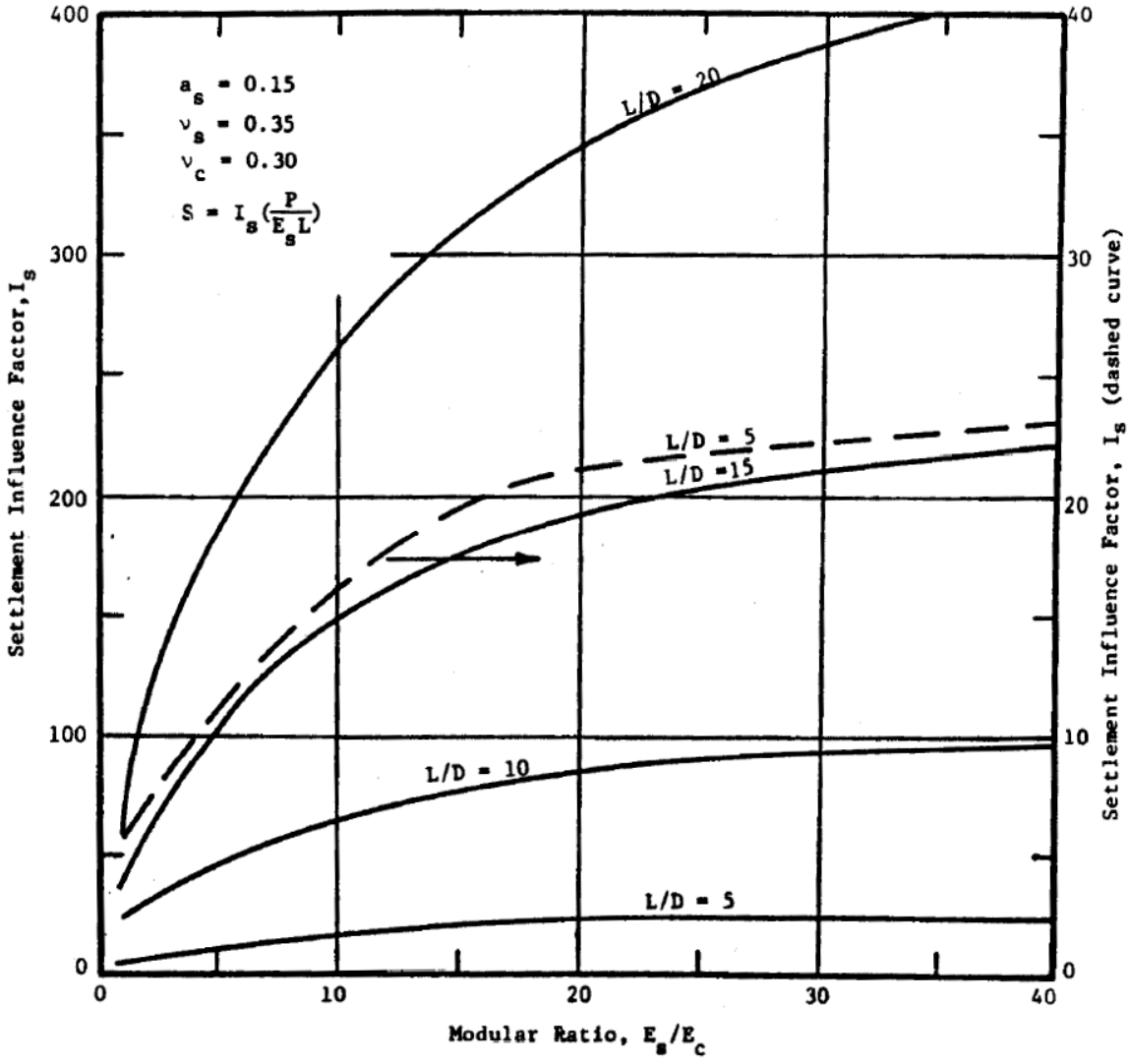

Figure J-2 Settlement prediction curve for low compressibility soil with an area replacement ratio a_s = 0.15 [118]

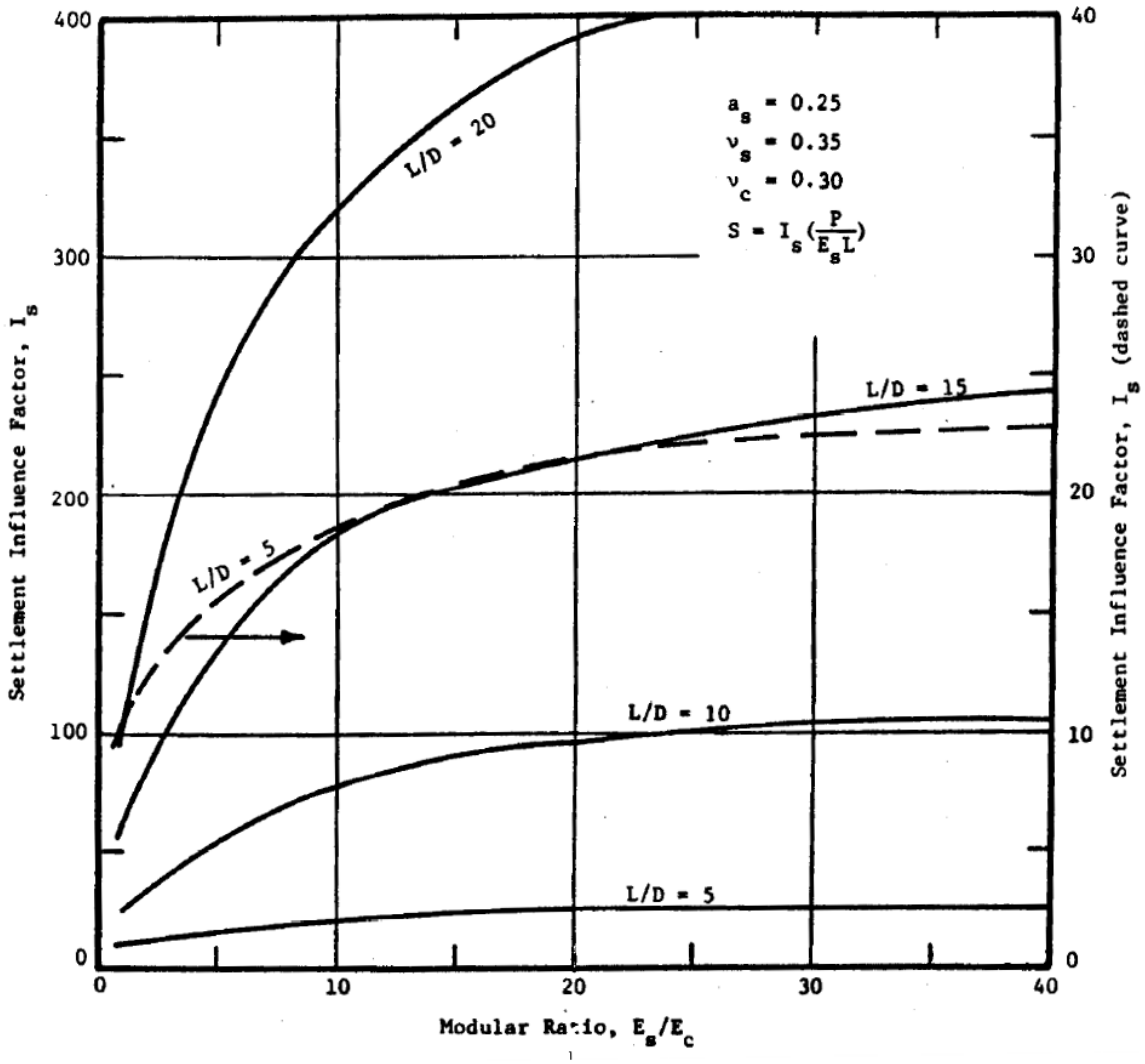

Figure J-3 Settlement prediction curve for low compressibility soil with an area replacement ratio a_s = 0.25 [118]

COMPRESSIBLE COHESIVE SOIL

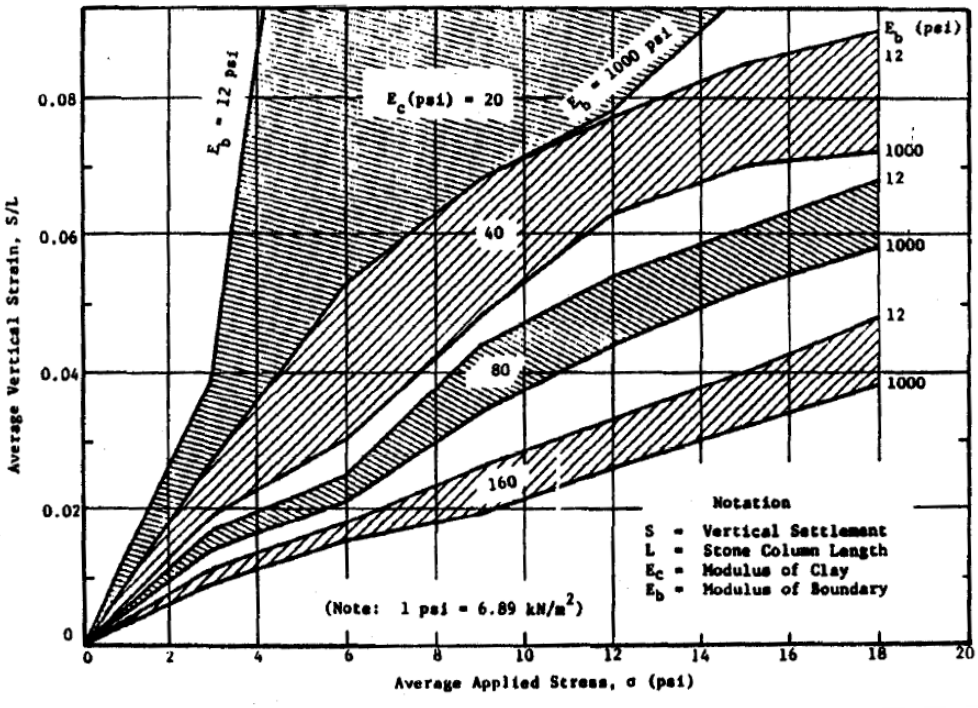

Figure J-4 Settlement prediction curve for compressible cohesive soil with an area replacement ratio a_s = 0.1 and L/D = 5 [118]

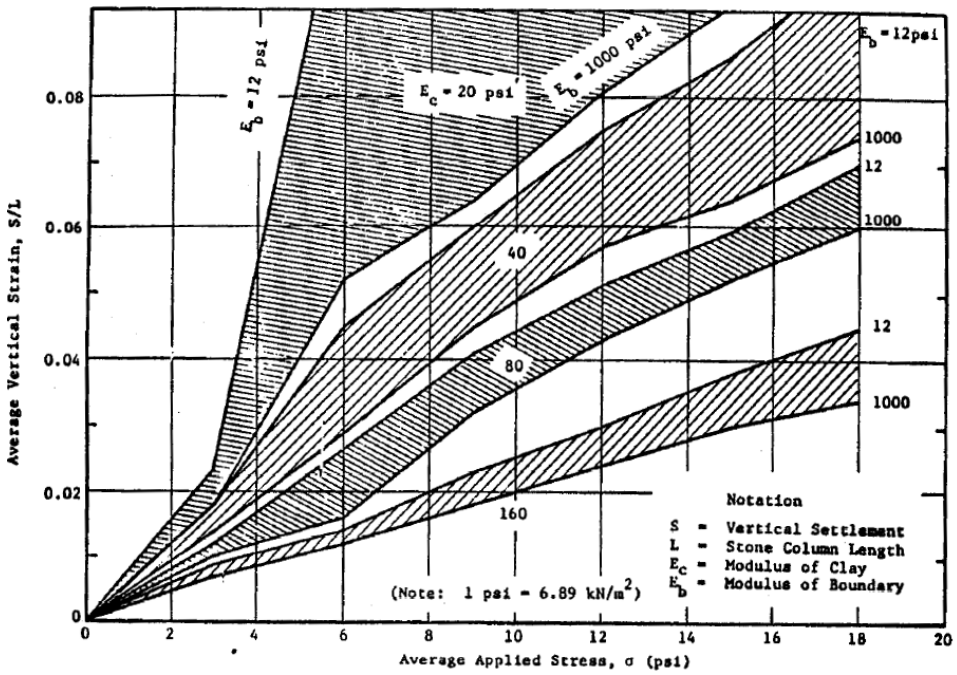

Figure J-5 Settlement prediction curve for compressible cohesive soil with an area replacement ratio a_s = 0.1 and L/D = 10 [118]

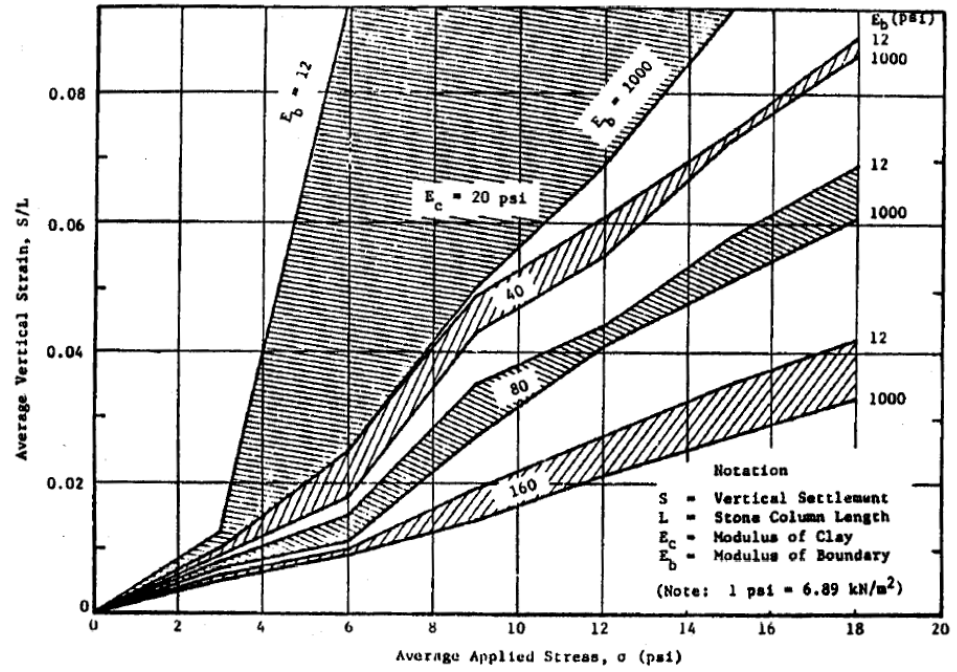

Figure J-6 Settlement prediction curve for compressible cohesive soil with an area replacement ratio a_s = 0.1 and L/D = 20 [118]

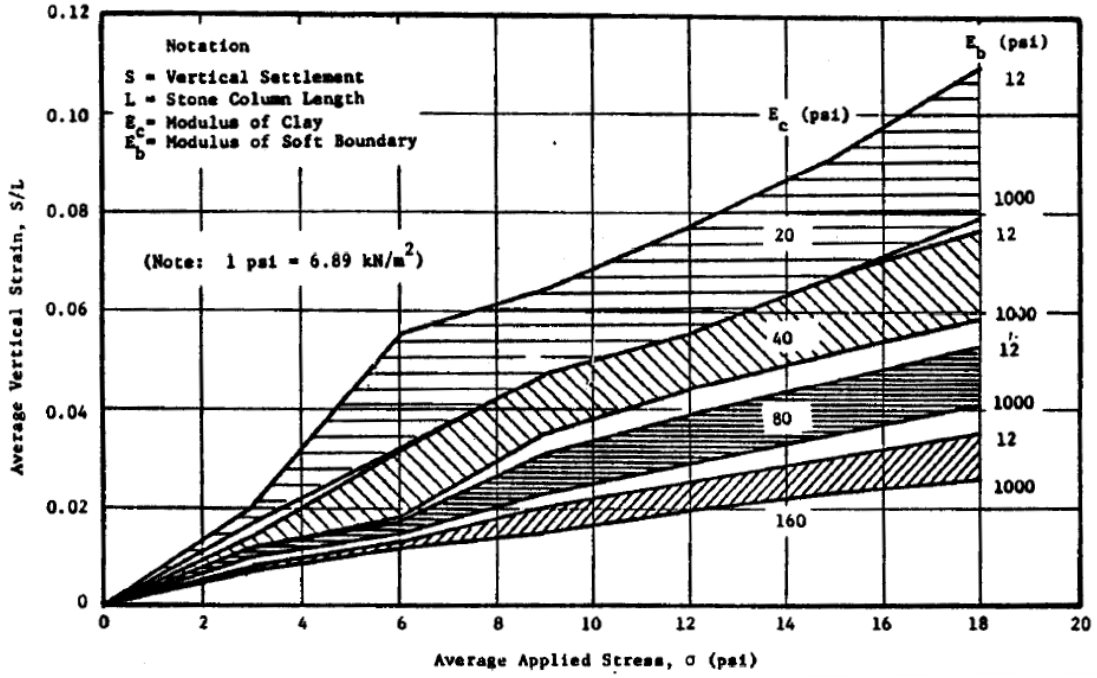

Figure J-7 Settlement prediction curve for compressible cohesive soil with an area replacement ratio a_s = 0.25 and L/D = 5 [118]

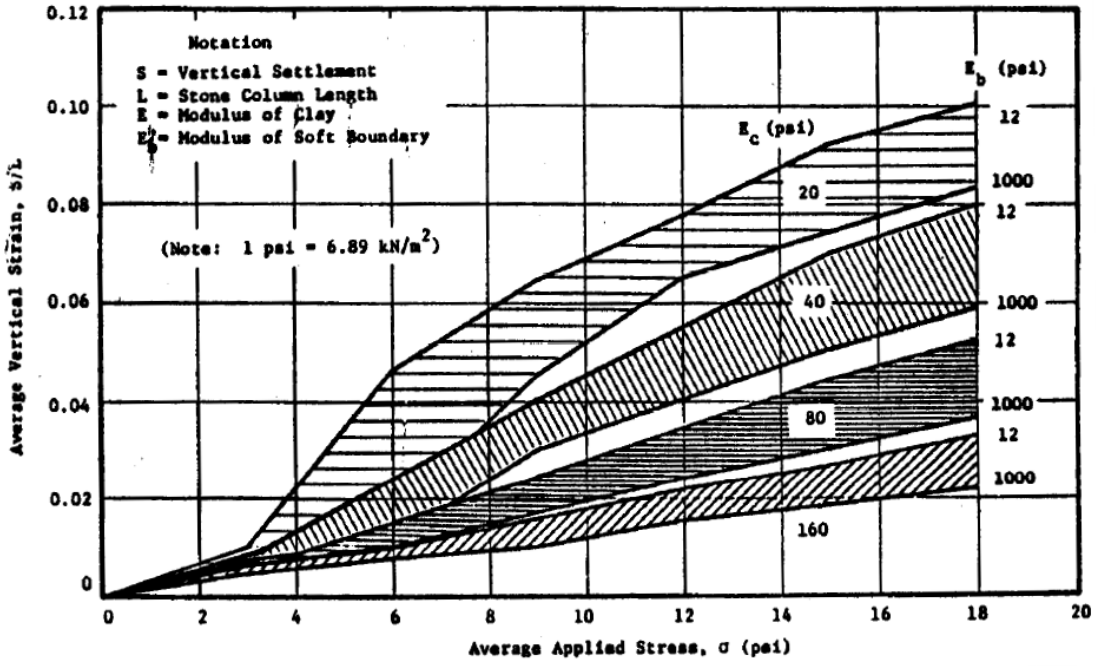

Figure J-8 Settlement prediction curve for compressible cohesive soil with an area replacement ratio a_s = 0.25 and L/D = 10 [118]

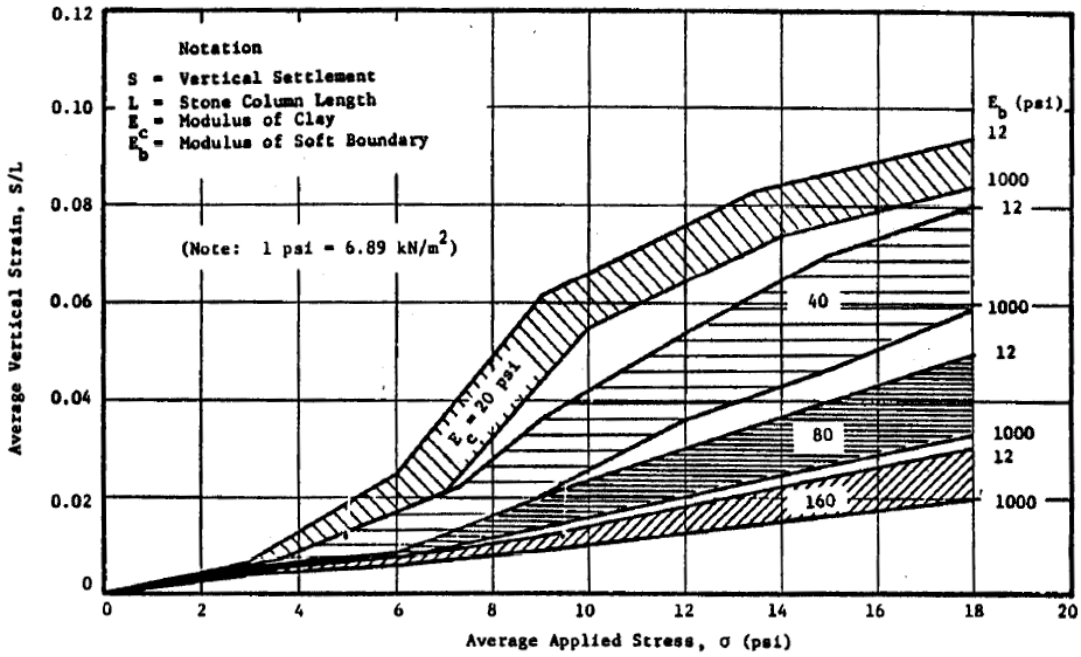

Figure J-9 Settlement prediction curve for compressible cohesive soil with an area replacement ratio a_s = 0.25 and L/D = 15 [118]

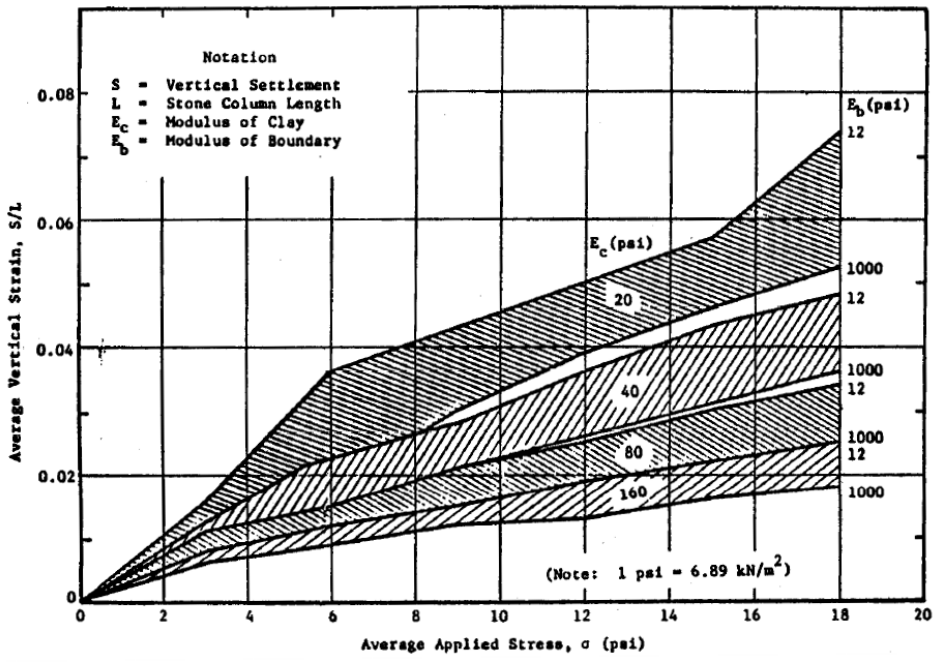

Figure J-10 Settlement prediction curve for compressible cohesive soil with an area replacement ratio a_s = 0.35 and L/D = 5 [118]

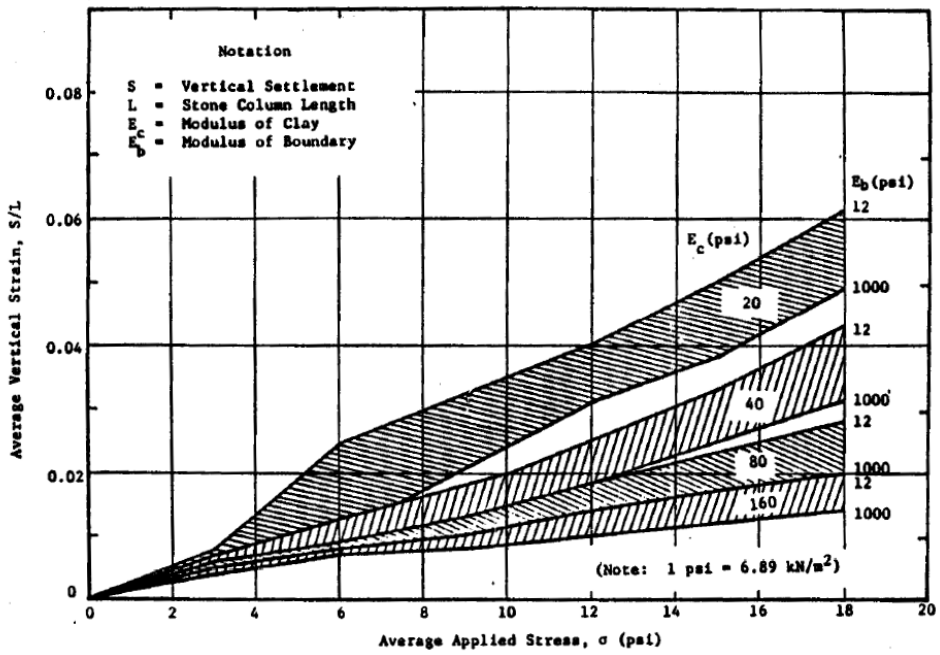

Figure J-11 Settlement prediction curve for compressible cohesive soil with an area replacement ratio a_s = 0.35 and L/D = 10 [118]

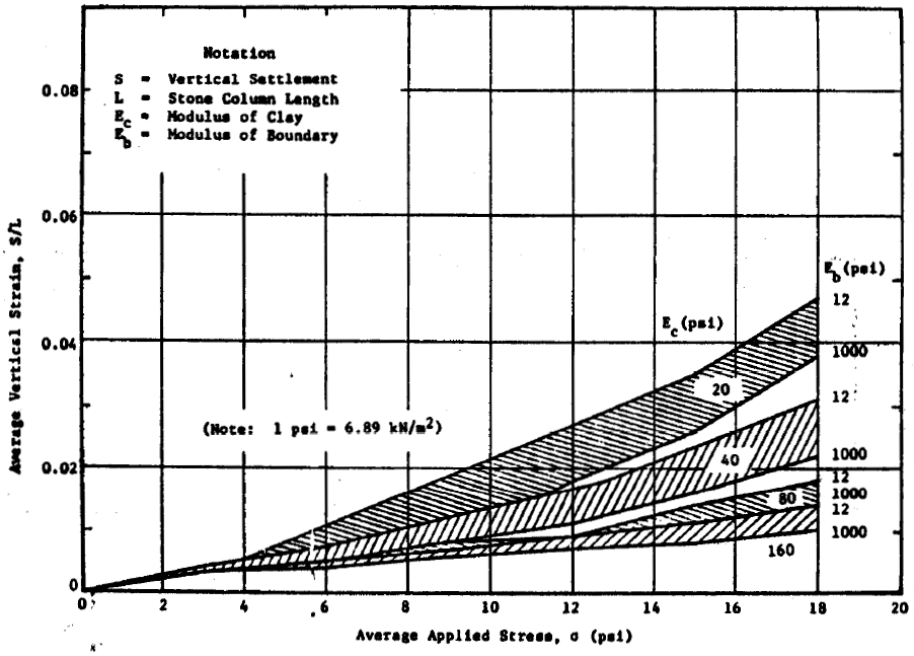

Figure J-12 Settlement prediction curve for compressible cohesive soil with an area replacement ratio a_s = 0.35 and L/D = 20 [118]

APPENDIX K

DETAILED PROCEDURES FOR CHARACTERIZATION OF SOIL PROPERTIES

This chapter provides detailed procedures for establishing empirical relationships under laboratory conditions and elaborates how the empirical relationships can be used to characterize soil properties using NDT technologies under field conditions.

Prediction of Effective Internal Friction Angle by Methylene Blue Test

The effective internal friction angle ϕ' of a soil can be determined under a laboratory condition by performing either consolidated-drained or consolidated-undrained triaxial shear test with the measurements of pore water pressure. Alternatively, ϕ' can also be estimated by applying empirical relationship based on the plasticity index (PI) of the soil, which can be expressed as [145]:

$$\phi' = 0.0016PI^2 - 0.302PI + 36.208 \quad \text{(K-1)}$$

where PI is the plasticity index and ϕ' is the effective internal friction angle of the soil. The PI of a soil can be determined under laboratory conditions by conducting standard Atterberg limits tests; alternatively, it can also be predicted by performing Methylene Blue Test (MBT) following Sahin's work [139].

A Methylene Blue Value (MBV) which provides an indication of the amount of fine content in a soil sample can be obtained by performing MBT. Experience indicates that it is the amount and characteristics of the fine content that govern the engineering properties (such as PI and ϕ') of a soil [139]; therefore, it is possible to estimate PI and calculate the effective internal friction angle ϕ' based on only the measurement of the MBV of a soil.

In contrast to the standard laboratory tests to determine PI and ϕ', the MBT can be performed under either a field or a laboratory condition within less than 10 min by using the testing apparatus shown in Figure K-1 which all can fit together into a portable kit. The testing apparatus kit consists of a colorimeter, a timer, two 45 mL plastic tube, a

micropipette, a 1.4 mL plastic tube, a plastic syringe, a 0.20 micrometers size filter, a 7.50 mL eyedropper, a bottle of methylene blue solution, a bottle of double distilled water and a high precision portable scale with 0.01 gram sensitivity [139].

Figure K-1 Methylene Blue Test apparatus [139]

A brief MBT testing procedure is shown in Figure K-2. The procedure consists of mixing the soil sample with methylene blue solution, diluting an aliquot of the mixed solution and measuring the MBV of the solution by using a colorimeter. The MBV provides a measurement of the color change of the methylene blue solution, which is affected by the amount and characteristics of the fine content in that soil sample. The test is not only rapid and simple, but also provides accurate and repeatable results [146]. The step-by-step MBT testing procedure can be found elsewhere [139].

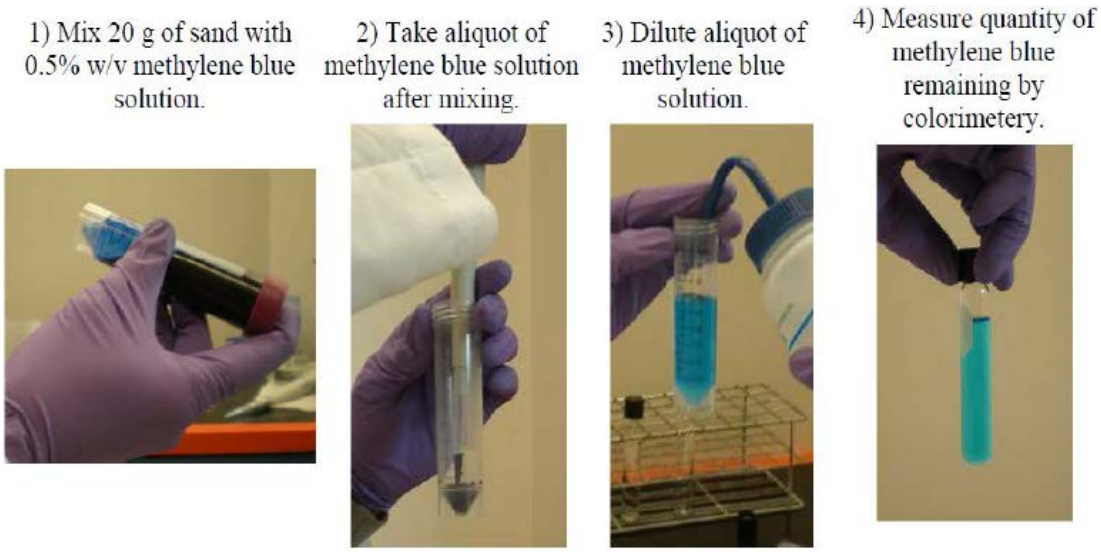

Figure K-2 Methylene Blue Test procedure [146]

Establishment of empirical relationships under laboratory conditions

In order to achieve the objective (using measured MBV to estimate PI and ϕ' under a field condition), an empirical relationship between MBV and PI must be established under a laboratory condition prior to the application of this technology under a field condition. Sahin [139] performed both MBT and Atterberg limits tests for a variety of base course aggregate materials under laboratory conditions and obtained the relationship between MBV and PI of the materials, which is shown in Figure K-3 with 90% confidence level boundaries.

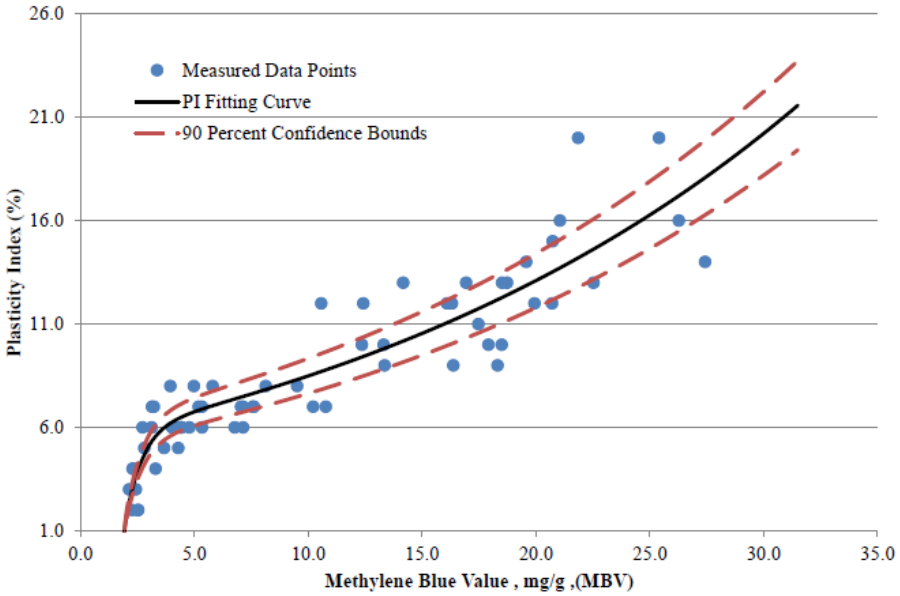

Figure K-3 The correlation between MBV and PI for base course materials [139]

Sahin [139] proposed an equation to characterize the relationship between MBV and PI of the base course materials, which is expressed as:

$$PI = 5.503e^{(0.04337MBV)} - 62.37 \cdot 10^{-5}e^{(-1.331MBV)} \quad \text{(K-2)}$$

where all the parameters are previously defined. Once the MBV is measured under a field condition, PI and ϕ' can be estimated by applying Equation (K-2) and Equation (K-1), respectively. Note that the relationship shown in Figure K-3 and the empirical function Equation (K-2) are only valid for the base course materials. In order to establish the specific empirical relationship for foundation soils, it is necessary to conduct laboratory experiments (i.e. MBT and Atterberg limits tests) on a large variety of foundation soils that cover the range of the typical soils found in the area of interest.

Prediction of Specific Gravity by Methylene Blue Test

The specific gravity of the most commonly found soil minerals ranges from 2.6 – 2.9 depending on the soil mineralogy and grain size [147]. Sahin [139] proposed a mathematical formulation to estimate the specific gravity of soils:

$$G_s = \frac{2.55+2.91(2.43)(\frac{PI-1}{22-PI})^{0.3076}(\frac{LL-1}{40-LL})^{-0.3525}}{1+(2.43)(\frac{PI-1}{22-PI})^{0.3076}(\frac{LL-1}{40-LL})^{-0.3525}} \quad \text{(K-3)}$$

where G_s is the specific gravity, PI is the plasticity index and LL is the liquid limit of the soil.

Sahin [139] also found the following relationship between MBV and LL of the tested base course materials:

$$LL = 14.64e^{(0.03371MBV)} - 24.99e^{(-1.149MBV)} \quad \text{(K-4)}$$

where all the parameters are previously defined. Similar to the empirical relationship between MBV and PI, the empirical relationship between MBV and LL shown in Equation (K-4) is only valid for the unbound base course materials, MBT and Atterberg limits tests should be performed under a laboratory condition on a large variety of foundation soils to find the empirical relationship between MBV and LL for foundation soils.

Establishment of empirical relationships under laboratory conditions

The specific gravity of a soil G_s can be easily estimated under a field condition by applying empirical relationship such as the one shown in Equation (K-3) once the PI and LL are estimated first (based on the measurements of MBV applying the empirical relationships such as the ones shown in Equation (K-2) and (K-4)). The empirical relationship shown in Equation (K-3) can be established based on the equation developed by Juárez-Badillo:

$$G_s = \frac{G_0 + G_m(\beta)(\frac{PI-P_0}{P_m-PI})^{\gamma}(\frac{LL-L_0}{L_m-LL})^{\delta}}{1+\beta(\frac{PI-P_0}{P_m-PI})^{\gamma}(\frac{LL-L_0}{L_m-LL})^{\delta}} \quad \text{(K-5)}$$

where G_0 is the minimum specific gravity (taken as 2.55), G_0 is the maximum specific gravity (taken as 2.91), P_0 is the approximate minimum plasticity index, P_m is the approximate maximum plasticity index, L_0 is the approximate minimum liquid limit, L_m is the approximate maximum liquid limit, β, and δ are fitting parameters. Note that P_0, P_m, L_0 and L_m are the approximate values of the true minimum or maximum values within the database of the laboratory experiment results. The approximate minimum values are determined by rounding down the true minimum values to 2 significant digits and the approaximate maximum values are determined by rounding up the true maximum values to 2 significant digits. For instance, if the true minimum plasticity index in the database is 44, then the approximate minimum plasticity index should be $P_0 = 40$; if the

true maximum plasticity index in the database is 79, then the approximate maximum plasticity index should be $P_m = 80$.

Prediction of Matric Suction by Soil Dielectric Characteristic Curve

The determination of soil matric suction h_m under a field condition relies on the use of the soil dielectric characteristic curve (SDCC) which is an S-shape curve that describes the correlation between the soil matric suction h_m and dielectric constant (DC) ε_r as shown in Figure K-4. Each soil material corresponds to a unique shape of SDCC curve due to the differences in soil properties. The general form of a SDCC can be expressed as [139]:

$$\varepsilon_r = \left[\frac{\varepsilon_{sat}+\varepsilon_{\min}\alpha\left[\frac{h_m}{h_{\max}-h_m}\right]^{\gamma}}{1+\alpha\left(\frac{h_m}{h_{\max}-h_m}\right)^{\gamma}}\right] \quad \text{(K-6)}$$

where ε_r is the DC of the soil, ε_{sat} is the saturated DC of the soil which is also the maximum DC and relates to the minimum potential of soil suction, $\varepsilon_{\min}$ is the minimum soil DC and relates to the maximum potential of soil suction, h_m is the soil matric suction, $h_{\max}$ is the maximum soil suction (equals to 1.45 x 10^5 psi or 10^6 kPa or 7 pF), α and γ are fitting parameters depending on the type of the soil.

If the SDCC of a soil is known (i.e. the fitting parameters α and γ are known), the matric suction h_m of the soil can be easily determined by a DC measurement using the known SDCC relationship. The DC of a soil can be measured by using a percometer as shown in Figure K-5. The percometer is a NDT instrument specifically designed for measuring the DC of a material. It can provide highly accurate and reliable DC measurements within 5 seconds once a good contact is achieved between the material and the measuring probe. The percometer with a surface probe is useful to make DC measurements for materials with smooth surfaces and the percometer with a tube probe is applicable for inserting into soft materials (e.g. foundation soils) which requires a minimum 3.94 in (10 cm) of penetration depth [139].

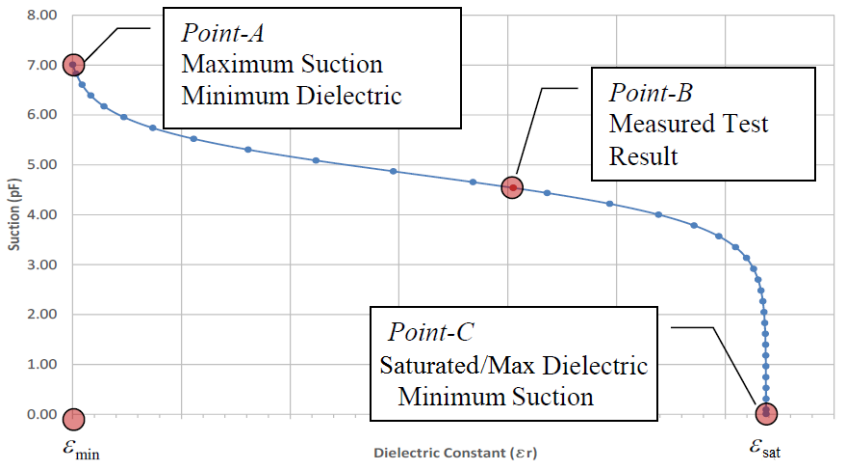

Figure K-4 A schematic illustration of the SDCC of a soil [139]

Figure K-5 Standard Adek Percometer™ with a surface probe and a tube probe [139]

However, very often, the SDCC of a soil is unknown under a field condition; in that case, it is necessary to determine all the unknown parameters (i.e. ε_{sat}, $\varepsilon_{\min}$, α and γ) in order to plot the SDCC of the soil. Sahin [139] has proposed empirical relationships to estimate the unknowns with only the measurements of MBV.

By conducting laboratory experiments (subsequently described) on a variety of base course materials, Sahin [139] found the following empirical relationship (shown in Figure K-6) between MBV and the saturated DC ε_{sat}:

$$\varepsilon_{sat} = 0.0334(MBV^2) - 0.1086(MBV) + 12.569 \qquad \text{(K-7)}$$

where all the parameters are previously defined.

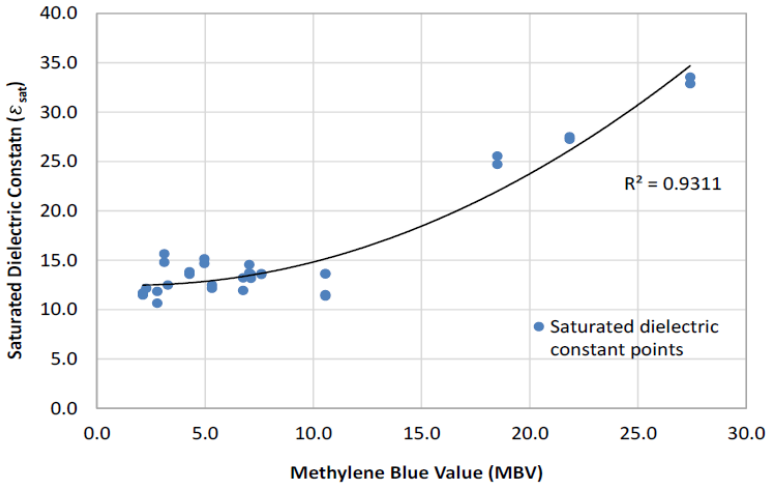

Figure K-6 Empirical relationship between MBV and ε_{sat} [139]

Similarly, the empirical relationship (shown in Figure K-7) between MBV and the minimum soil DC $\varepsilon_{\min}$ can be expressed as:

$$\varepsilon_{\min} = 0.1243\log(MBV) + 1.0668 \quad \text{(K-8)}$$

where all the parameters are previously defined.

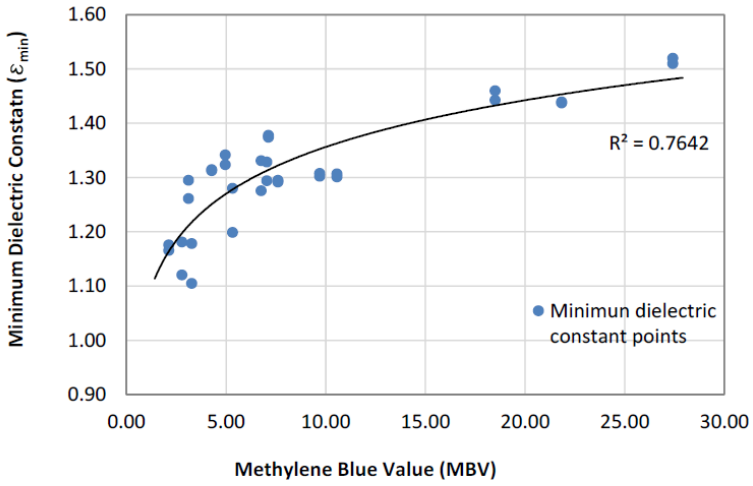

Figure K-7 Empirical relationship between MBV and $\varepsilon_{\min}$ [139]

The fitting parameters α and γ can also be estimated by using their empirical relationships with MBV and pfc (a parameter that can also be predicted by MBV). To estimate α, the following equations were proposed by Hakan [139]:

$$H_{1\alpha} = TANH(0.5(-0.478027(MBV) - 0.034582(pfc) + 8.923868)) \quad \text{(K-9)}$$

$$H_{2\alpha} = TANH(0.5(-0.207206(MBV) + 0.334387(pfc) - 8.088245)) \quad \text{(K-10)}$$

$$\alpha = 6.3772003(H_{1\alpha}) - 46.1404624(H_{2\alpha}) + 53.363999 \quad \text{(K-11)}$$

where $H_{1\alpha}$ and $H_{2\alpha}$ are hidden layer functions used to determine α and all the other parameters are previously defined. To estimate γ, the following equations were proposed [139]:

$$H_{1\gamma} = TANH(0.5(0.0897001(MBV) - 0.1597119(pfc) + 0.69592558)) \quad \text{(K-12)}$$

$$H_{2\gamma} = TANH(0.5(-0.0968849(MBV) - 0.020036(pfc) + 1.1379340)) \quad \text{(K-13)}$$

$$H_{3\gamma} = TANH(0.5(0.0668142(MBV) + 0.2112468(pfc) - 4.4814587)) \quad \text{(K-14)}$$

$$\gamma = 3.0066674(H_{1\gamma}) + 4.212358(H_{2\gamma}) + 3.211806(H_{3\gamma}) + 3.045290 \quad \text{(K-15)}$$

where $H_{1\gamma}$, $H_{2\gamma}$ and $H_{3\gamma}$ are hidden layer functions used to determine γ and all the other parameters are previously defined.

Establishment of empirical relationships under laboratory conditions

As noted previously, the core of this method is to establish empirical relationships (such as the ones shown in Equation (K-7) – (K-15)) under a laboratory condition in the first place and then use these relationships to expedite the process of characterizing soil properties under a field condition. This section provides the procedures for establishing the empirical relationships.

In order to establish the empirical relationships, a series of laboratory experiments should be performed, including:

1. the percometer test (to obtain the soil DC ε_r);
2. the filter paper test (to obtain the soil matric suction h_m);
3. the Methylene Blue Test (to obtain MBV of the soil);
4. the percent fine content test (to obtain pfc of the soil);
5. the standard laboratory compaction test (to obtain the dry unit weight γ_d and water content w); and
6. the specific gravity test (to obtain the specific gravity of the soil G_s).

Empirical relationships of ε_{sat} vs. MBV and ε_{min} vs. MBV

The percometer test is performed under a laboratory condition by using a surface probe percometer to obtain the DC ε_r of the soil samples. The detailed sample preparation and test procedures can be found elsewhere [139]. The main objective to

perform a percometer test is to determine the three main points (ε_r, ε_{sat} and $\varepsilon_{\min}$) of a SDCC as shown in Figure K-4, which are used to fit the general mathematical form of a SDCC (shown in Equation (K-6)) and perform regression analysis to obtain the two fitting parameters (i.e. α and γ).

ε_r is directly measured from a percometer test, based on which ε_{sat} and $\varepsilon_{\min}$ can be calculated by using a complex refraction index model (CRIM) following a two step-procedure. In the first step where an unsaturated condition is considered, the CRIM model can be expressed as:

$$\sqrt{\varepsilon_r} = [(\sqrt{\varepsilon_s} - 1)\theta_s + (\sqrt{\varepsilon_w} - 1)\theta + 1] \quad \text{(K-16)}$$

where ε_r is the measured composite DC, ε_s is the DC of the solid within the soil material, ε_w is the DC of water (which is a constant that equals to 81), $\theta_s = \frac{\gamma_d}{G_s\gamma_w}$ is the volumetric solid content of the soil, $\theta = \frac{w\gamma_d}{\gamma_w}$ is the volumetric water content and all the other parameters are previously defined. The goal of the first step which is to calculate the DC of the solid ε_s can be easily achieved once the volumetric solid content θ_s and volumetric water content θ are determined (unknown parameters γ_d, G_s, w can be determined under laboratory conditions). Once ε_s is determined, $\varepsilon_{\min}$ can be calculated using the following function:

$$\sqrt{\varepsilon_{\min}} = 1 + \theta_s(\sqrt{\varepsilon_s} - 1) \quad \text{(K-17)}$$

where all the parameters are previously defined.

In the second step where a saturated condition is considered, the CRIM model can be expressed as:

$$(\sqrt{\varepsilon_{sat}}) = [(\sqrt{\varepsilon_s} - 1)\theta_s + (\sqrt{\varepsilon_w} - 1)\theta_{ws} + 1] \quad \text{(K-18)}$$

where ε_{sat} is the saturated DC, $\theta_{ws} = 1 - \theta_s$ is the volumetric water content corresponds to the saturated condition and all the other parameters are previously defined.

The MBT is also performed under a laboratory condition, from which the MBV is obtained for each soil sample and is plotted against ε_{sat} and $\varepsilon_{\min}$ of the same soil sample as shown in Figure K-6 and Figure K-7, respectively. In this way, empirical relationships can be established for ε_{sat} vs. MBV and $\varepsilon_{\min}$ vs. MBV (such as the ones

shown in Equation (K-7) and (K-8)). As a result, ε_{sat} and $\varepsilon_{\min}$ can be easily estimated with only the measurements of MBV under a field condition.

Empirical relationships of α vs. (MBV & pfc) and γ vs. (MBV & pfc)

In order to establish the SDCC for a soil and determine the fitting parameters (i.e. α and γ) under a laboratory condition, it is also required to determine soil matric suction h_m by performing filter paper tests. The filter paper test is immediately conducted on the same samples after the completion of percometer tests under a laboratory condition. The detailed sample preparation and test procedures can be found elsewhere [139, 148]. Once all the required parameters are determined (ε_{sat}, $\varepsilon_{\min}$, ε_r and h_m) under a laboratory condition, the SDCC of the soil can be plotted and fitted to the general mathematical form as shown in Equation (K-6), from which the fitting parameters α and γ can be determined.

To facilitate the establishment of empirical relationships of α vs. (MBV & pfc) and γ vs. (MBV & pfc) (such as the ones shown in Equation (K-9) – (K-15) which can be used under a field condition to estimate α and γ), pfc test is also performed in addition to the MBT.

The pfc of a soil is defined as the ratio of the percent passing No.2 microns size to the percent passing No.200 sieve as shown in the following equation [139]:

$$pfc = \frac{\%-No.2 \text{ micron}}{\%-No.200 \text{ sieve}} \times 100 \qquad \text{(K-19)}$$

The pfc of a soil is measured by using a Horiba Laser Scattering Particle Size Distribution Analyzer (shown in Figure K-8) under a laboratory condition. The equipment is able to provide test results within 10 minutes with reasonable accuracy and repeatability. The detailed test procedure is elaborated elsewhere [139].

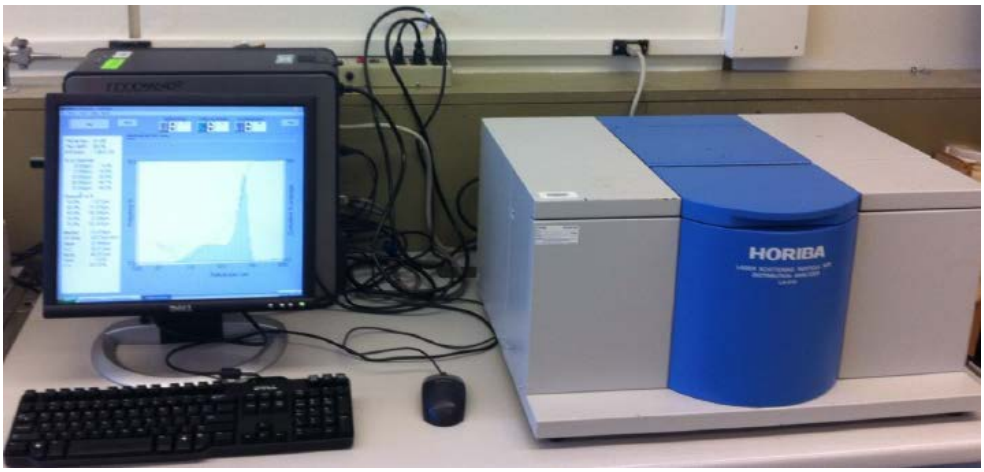

Figure K-8 Configuration of the Horiba LA-910 Particle Size Distribution Analyzer [139]

Once all of the required parameters are determined (i.e. α, γ, MBV and pfc) under the laboratory condition, neural network analyses are performed to obtain the empirical relationships by using a statistical software named as JMP which provides the most realistic mathematical relationship between the inputs and the empirical estimation models. Hakan [139] used JMP and successfully developed empirical relationships to estimate α and γ by inputting MBV and pfc as aforementioned. By using these empirical relationships, the fitting parameters α and γ of a soil can be easily estimated with only the measurements of MBV under a field condition (pfc can also be estimated with the measurement of MBV).

Empirical relationships between MBV and pfc

The equipment to measure pfc is not available under a field condition; therefore, it is necessary to establish empirical relationship between MBV and pfc under a laboratory condition as well in order to estimate pfc under a field condition with only the measurements of MBV.

Hakan [139] performed both MBT and pfc test for a variety of base course aggregate materials (same materials as aforementioned) and found a “C” shape correlation between the measured MBV and pfc as shown in Figure K-9.

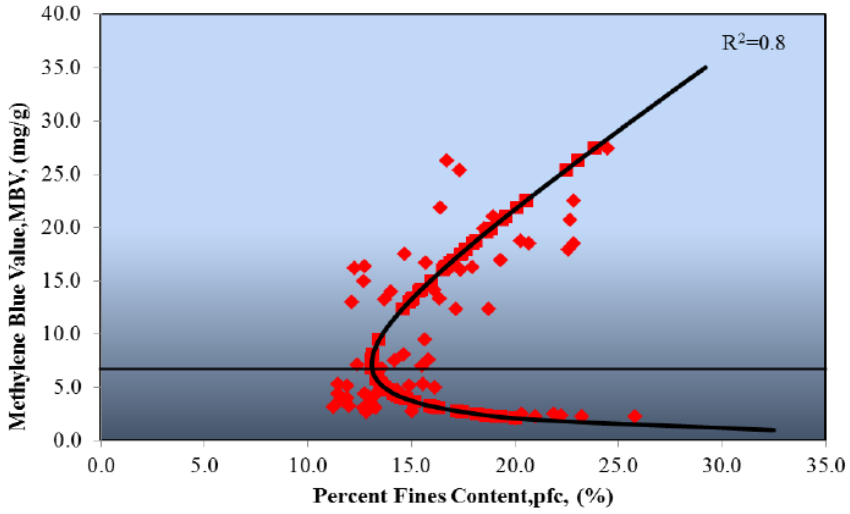

Figure K-9 the relationship between Methylene Blue Value and percent fines content [139]

Hakan [139] found that the "C" shape relationship can be best described by the following mathematical equation:

$$pfc = \frac{a_m}{(MBV)^{n_m}} + b_m(MBV) \quad \text{(K-20)}$$

where a_m, b_m and n_m are fitting parameters depending on the clay mineralogy, characteristics and fraction [139]. Although each type of aggregates corresponds to a unique set of fitting parameters, a single set of fitting parameters in which $a_m = 27.6$, $b_m = 1.55$ and $n_m = 0.92$ was obtained when all the data points (which corresponded to all the tested unbound aggregate materials) are fitted to Equation (K-20). In order to obtain the best empirical relationship, ideally, this single set of fitting parameters should be obtained through testing a large variety of soils that cover the typical range of the soil types found in the area of interest. Once the empirical relationship is obtained, pfc can be predicted using MBV measurements made under a field condition; the predicted pfc is used in the prediction of α and γ which are parameters required to form the SDCC of the soil (that is used to predict the soil matric suction h_m) under a field condition.

Prediction of Volumetric Water Content by Soil Water Characteristic Curve

The determination of volumetric water content θ under a field condition relies on the use of the soil water characteristic curve (SWCC) which is also an S-shape curve that describes the relation between the soil matric suction h_m and soil volumetric water content θ as shown in Figure K-10. Each soil material corresponds to a unique shape of SWCC curve due to the differences in soil properties. The Fredlund and Xing model [149] is one of the most commonly used models to characterize a SWCC, which is expressed as [139]:

$$\theta = C(h) \times \left[\frac{\theta_{sat}}{\left[\ln\left[\exp(1)+\left(\frac{h_m}{a_f}\right)^{b_f}\right]\right]^{c_f}}\right] \quad \text{(K-21)}$$

$$C(h) = \left[1 - \frac{\ln\left(1+\frac{h_m}{h_r}\right)}{\ln\left(1+\frac{7}{h_r}\right)}\right] \quad \text{(K-22)}$$

where θ is the volumetric water content, θ_{sat} is the saturated volumetric water content, h_m is the soil matric suction, a_f, b_f, c_f and h_r are all fitting parameters where a_f is related to the air entry value of the soil, b_f is a function of the rate of moisture extracted from the soil when the air entry value is exceeded, c_f is a function of the residual moisture content, h_r is related to the suction at the residual moisture content.

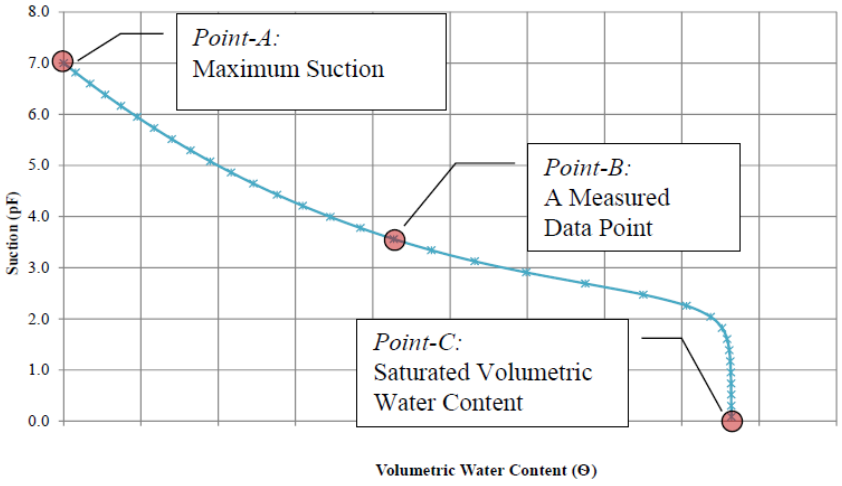

Figure K-10 A schematic illustration of the SWCC of a soil [139]

In order to determine the volumetric water content θ under a field condition, it is necessary to determine all the unknown parameters (i.e. h_m, a_f, b_f, c_f, h_r and θ_{sat}). The

last section already explained the detailed procedure to estimate the soil matric suction h_m by only performing MBT and percometer test under a field condition; the rest of the unknowns can also be predicted using the empirical relationships described as follows.

By conducting laboratory experiments on a variety of base course materials, Sahin [139] found the following empirical relationships between MBV and the fitting parameters:

$$a_f = 3.4994MBV^{0.0002} \quad \text{(K-23)}$$

$$b_f = 2.0044MBV^{-0.003} \quad \text{(K-24)}$$

$$c_f = 0.4956MBV^{-0.415} \quad \text{(K-25)}$$

$$h_r = 20MBV^{9.5E-06} \quad \text{(K-26)}$$

where all the other parameters are previously defined.

Sahin [139] also found that the saturated volumetric water content θ_{sat} has the following empirical relationship with the MBV, pfc and specific gravity G_s of the base course materials:

$$H_{1\theta_{sat}} = \tanh[\begin{matrix}0.5(0.1353107MBV + 0.14124964pfc \\ -2.67159193G_s + 4.689449)\end{matrix}] \quad \text{(K-27)}$$

$$H_{2\theta_{sat}} = \tanh[\begin{matrix}0.5(0.42673905MBV + 0.4791957pfc \\ -14.5836317G_s + 28.3844308)\end{matrix}] \quad \text{(K-28)}$$

$$H_{3\theta_{sat}} = \tanh[\begin{matrix}0.5(0.65761429MBV + 1.56633384pfc \\ -39.54978185G_s + 79.178564)\end{matrix}] \quad \text{(K-29)}$$

$$\theta_{sat} = \begin{matrix}0.214926485H_{1\theta_{sat}} + 0.27640261H_{2\theta_{sat}} \\ -0.12511932H_{3\theta_{sat}} + 0.30045553\end{matrix} \quad \text{(K-30)}$$

where $H_{1\theta_{sat}}$, $H_{2\theta_{sat}}$ and $H_{3\theta_{sat}}$ are hidden layer functions used to determine θ_{sat} and all the other parameters are previously defined.

Establishment of empirical relationships under laboratory conditions

In order to establish the empirical relationships (such as the ones shown in Equation (K-23) – (K-30)) for foundation soil materials, a series of laboratory experiments should be performed, including:

1. the filter paper test (to obtain the soil matric suction h_m and the volumetric water content θ);
2. the Methylene Blue Test (to obtain MBV of the soil);

3. the percent fine content test (to obtain pfc of the soil);
4. the standard laboratory compaction test (to obtain the maximum dry unit weight $\gamma_{d-\max}$); and
5. the specific gravity test (to obtain the specific gravity of the soil G_s).

In order to perform curve fitting and obtain the four fitting parameters of the SWCC for a soil, at least three points are required as shown in Figure K-10. Point A which is a known point corresponds to the maximum level of suction (where h_m equals to 1.45 x 10^5 psi or 10^6 kPa or 7 pF) and the minimum level of volumetric water content (where θ equals to 0). Point B is obtained by performing the filter paper test, from which both the matric suction and volumetric water content are measured once the test is finished. Point C corresponds to the minimum level of suction (where h_m equals to 0) and the maximum level of volumetric water content which is defined as the saturated volumetric water content θ_{sat}; the saturated volumetric water content can be calculated as:

$$\theta_{sat} = [1 - \frac{\gamma_{d-\max}}{(G_s \gamma_w)}] \quad \text{(K-31)}$$

where $\gamma_{d-\max}$ is the maximum dry unit weight of the soil and all the parameters are previously defined. Again, the statistical software JMP is used to construct the empirical relationship between θ_{sat} and MBV, pfc and G_s (such as the ones shown in Equation (K-27) – (K-30)).

Once the three points are determined, they are fitted to Equation (K-21) and (K-22) to obtain the four fitting parameters (i.e. a_f, b_f, c_f and h_r) for a soil. After testing a variety of soil materials, the empirical relationships (such as the ones shown in Equation (K-23) – (K-26)) between the fitting parameters and MBV then can be established which are useful under a field condition to determine the SWCC and the volumetric water content of the soil.

Prediction of Dry Unit Weight by Compaction Curve Model

The determination of dry unit weight γ_d under a field condition relies on the use of the compaction curve model (CCM) which is a C-shape curve that describes the relation

between the dry unit weight γ_d and soil volumetric water content θ as shown in Figure K-11. Each soil material corresponds to a unique shape of CCM curve due to the differences in soil properties. The general mathematical form of a CCM is expressed as [139]:

$$(\frac{\gamma_d}{\gamma_w}) = a_d[\mathrm{csch}(\frac{\theta\theta_{sat}}{G_s(|\theta_{sat}-\theta|)})]^{n_d} - b_d[\mathrm{csch}(\frac{\theta\theta_{sat}}{G_s(|\theta_{sat}-\theta|)})] \quad \text{(K-32)}$$

where a_d, b_d and n_d are fitting parameters depending on the soil type and all the other parameters are previously defined.

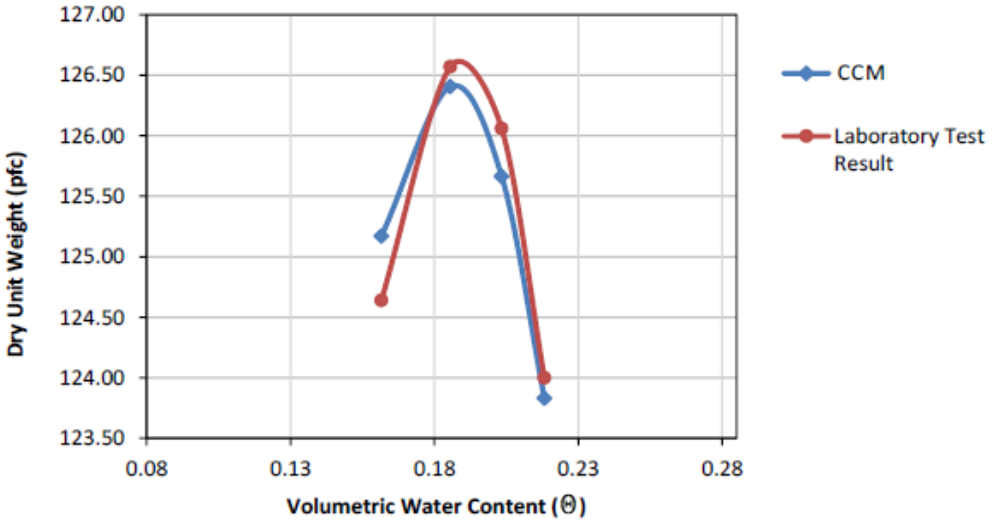

Figure K-11 A schematic illustration of the CCM of a soil in comparison with laboratory test results [139]

In order to estimate the dry unit weight γ_d under a field condition, it is necessary to determine all the unknown parameters (i.e. θ, θ_{sat}, a_d, b_d and n_d). The last section already explained the detailed procedures to estimate the volumetric water content θ (by using the SWCC) and saturated volumetric water content θ_{sat} (Equation (K-27) – (K-30)) under a field condition; the rest of the unknowns a_d, b_d and n_d can be estimated using the empirical relationships described as follows.

Sahin [139] found that the three fitting parameters can be estimated by the following functions:

$$H_{1a_d} = \tanh[\begin{matrix}0.5(0.40877300MBV + 0.21113984pfc \\ -8.72963215G_s + 16.336761)\end{matrix}] \quad \text{(K-33)}$$

$$H_{2a_d} = \tanh\left[\begin{matrix}0.5(-0.27242731MBV + 0.38117451pfc \\ +4.81581562G_s - 15.246911)\end{matrix}\right] \quad \text{(K-34)}$$

$$H_{3a_d} = \tanh\left[\begin{matrix}0.5(0.65761429MBV + 1.56633384pfc \\ -39.54978184G_s + 79.17856)\end{matrix}\right] \quad \text{(K-35)}$$

$$a_d = -0.7255499645H_{1a_d} + 0.2397642438H_{2a_d} + 0.8786388739H_{3a_d} + 1.88831833 \quad \text{(K-36)}$$

$$H_{1b_d} = \tanh\left[\begin{matrix}0.5(0.30481277MBV + 0.4712751pfc \\ -23.51993211G_s + 52.840434)\end{matrix}\right] \quad \text{(K-37)}$$

$$H_{2b_d} = \tanh\left[\begin{matrix}0.5(-0.05056449MBV - 0.11228127pfc \\ +27.55907692G_s - 71.931755)\end{matrix}\right] \quad \text{(K-38)}$$

$$H_{3b_d} = \tanh\left[\begin{matrix}0.5(-0.13331382MBV - 0.36012434pfc \\ +29.23482354G_s - 72.562443)\end{matrix}\right] \quad \text{(K-39)}$$

$$b_d = 0.10805394H_{1b_d} - 0.166763132H_{2b_d} + 0.160133497H_{3b_d} + 1.22496083 \quad \text{(K-40)}$$

$$H_{1n_d} = \tanh\left[\begin{matrix}0.5(-0.26235498MBV + 0.47405037pfc \\ -71.58187117G_s + 189.223422)\end{matrix}\right] \quad \text{(K-41)}$$

$$H_{2n_d} = \tanh\left[\begin{matrix}0.5(-0.78480185MBV - 0.75914733pfc \\ +56.24092591G_s - 133.107727)\end{matrix}\right] \quad \text{(K-42)}$$

$$H_{3n_d} = \tanh\left[\begin{matrix}0.5(-0.23889927MBV - 0.87246044pfc \\ -84.01782691G_s + 246.667662)\end{matrix}\right] \quad \text{(K-43)}$$

$$n_d = -0.013073056H_{1n_d} - 0.045526936H_{2n_d} + 0.013674419H_{3n_d} + 0.058352963 \quad \text{(K-44)}$$

where H_{1a_d}, H_{2a_d} and H_{3a_d} are hidden layer functions used to determine a_d, H_{1b_d}, H_{2b_d} and H_{3b_d} are hidden layer functions used to determine b_d, H_{1n_d}, H_{2n_d} and H_{3n_d} are hidden layer functions used to determine n_d and all the other parameters are previously defined.

Establishment of empirical relationships under laboratory conditions

In order to establish the empirical relationships shown in Equation (K-33) – (K-44), a series of laboratory experiments should be performed, including:

1. the standard laboratory compaction test (to obtain the dry unit weight γ_d and the volumetric water content θ);
2. the Methylene Blue Test (to obtain MBV of the soil);
3. the percent fine content test (to obtain pfc of the soil); and

4. the specific gravity test (to obtain the specific gravity of the soil G_s).

In order to perform curve fitting and obtain the three fitting parameters, the standard laboratory compaction test should be performed according to ASTM D698 the Standard Test Methods for Laboratory Compaction Characteristics of Soil Using Standard Effort (12400 ft-lbf/ft^3) [150]. At least four data points are required for each soil type to obtain a well-defined dry unit weight vs. volumetric water content curve. Again, the volumetric water content θ can be calculated as:

$$\theta = \frac{w\gamma_d}{\gamma_w} \tag{K-45}$$

where w is the gravimetric moisture content, γ_d is the dry unit weight of the soil and γ_w is the unit weight of water (62.4 lb/ft^3). The saturated volumetric water content θ_{sat} can be calculated using Equation (K-31). Once the dry unit weight vs. volumetric water content curve is plotted for laboratory results, the data points on the curve are fitted to the mathematical form of a CCM (shown in Equation (K-32)) to obtain the three fitting parameters a_d, b_d and n_d. Again, the statistical software JMP is used to construct the empirical relationships between the three fitting parameters and MBV, pfc and G_s.

Prediction of Suction Compression Index

The suction compression index γ_h equals to:

$$\gamma_h = \gamma_0 \times \frac{pfc}{100} \tag{K-46}$$

where γ_0 is the volume change guide number and pfc is the percent fine content. The determination of the volume change guide number is based on the procedure proposed by Lytton et al. (2005) [144]. The first step is to determine the mineralogical zone with the plasticity index PI and liquid limit LL of the soil by using Figure K-12. The next step is to determine the volume change guide number γ_0 using a series of charts (shown from Figure K-13 – Figure K-20), which requires the inputs of $\frac{LL}{pfc}$ and $Ac = \frac{PI}{pfc}$.

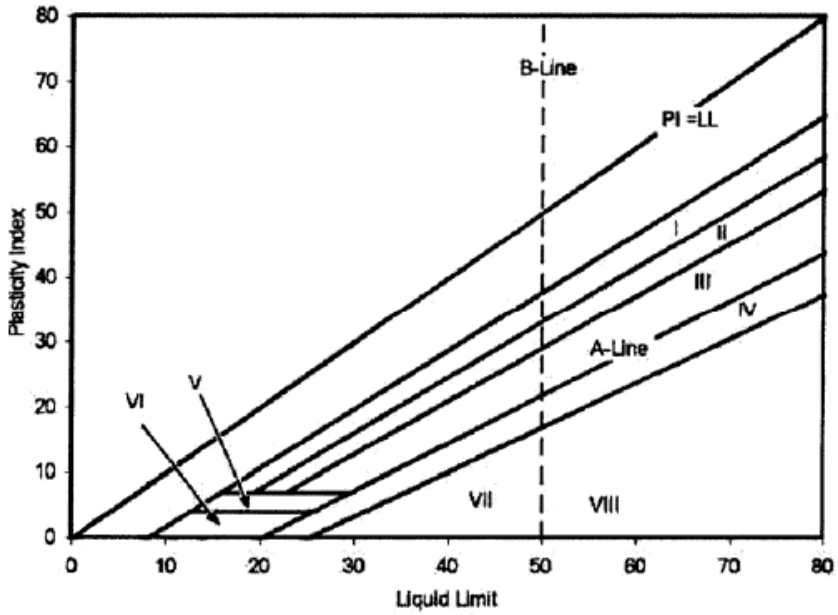

Figure K-12 Partitioning database on mineralogical types [144]

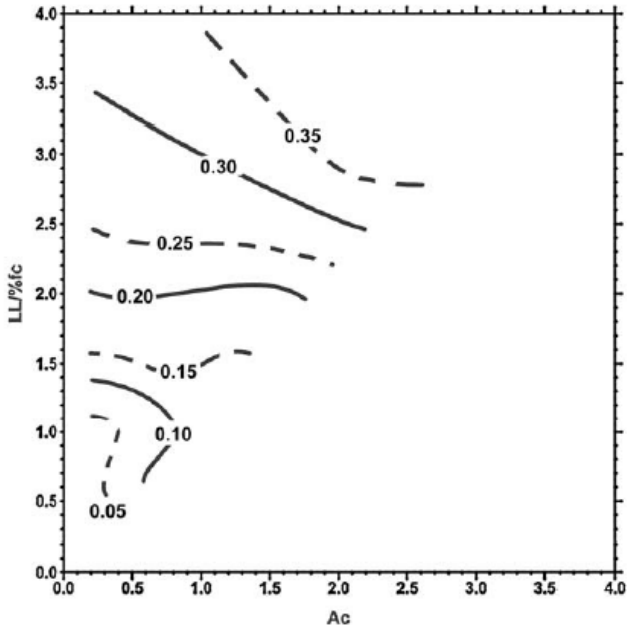

Figure K-13 Zone I Chart for Determining γ_0 [153]

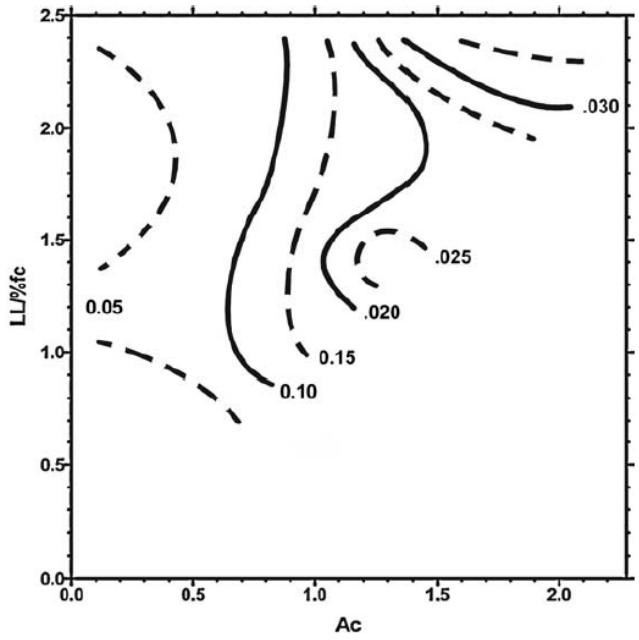

Figure K-14 Zone II Chart for Determining γ_0 [153]

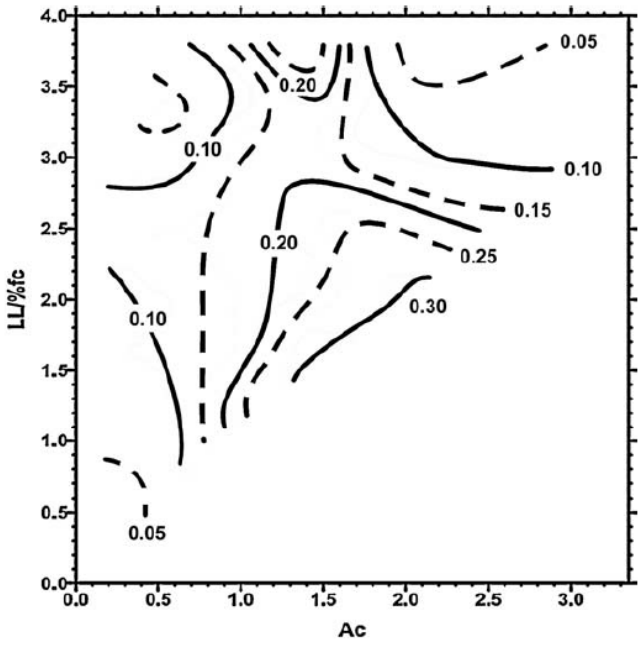

Figure K-15 Zone III Chart for Determining γ_0 [153]

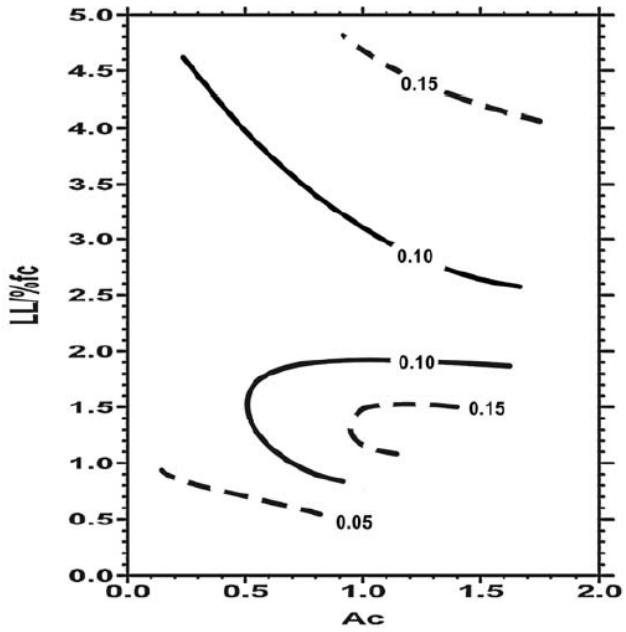

Figure K-16 Zone IV Chart for Determining γ_0 [153]

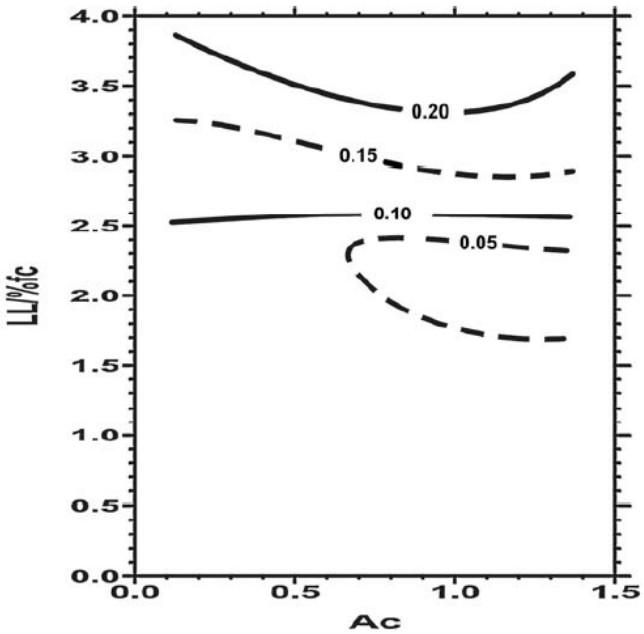

Figure K-17 Zone V Chart for Determining γ_0 [153]

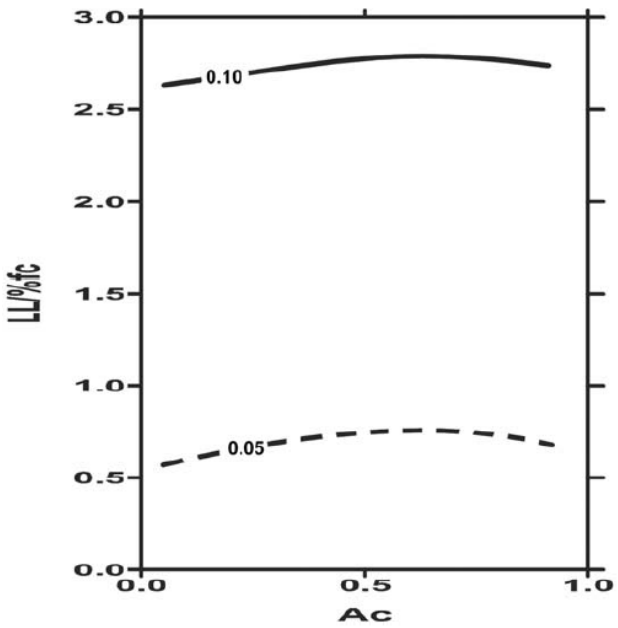

Figure K-18 Zone VI Chart for Determining γ_0 [153]

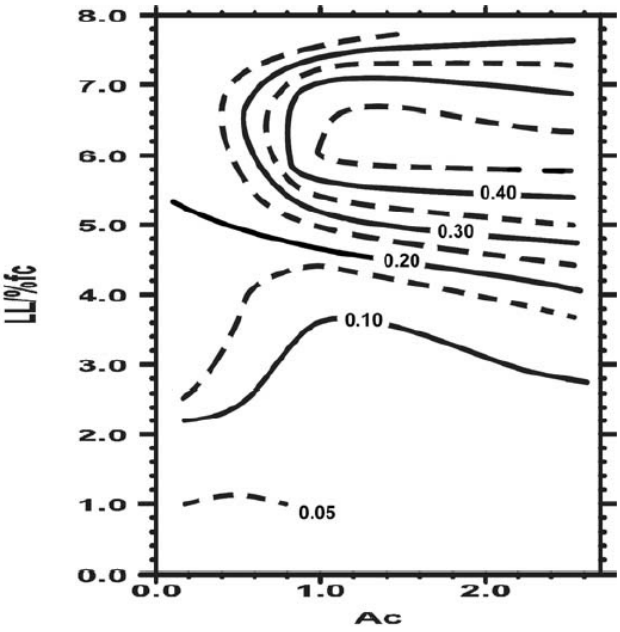

Figure K-19 Zone VII Chart for Determining γ_0 [153]

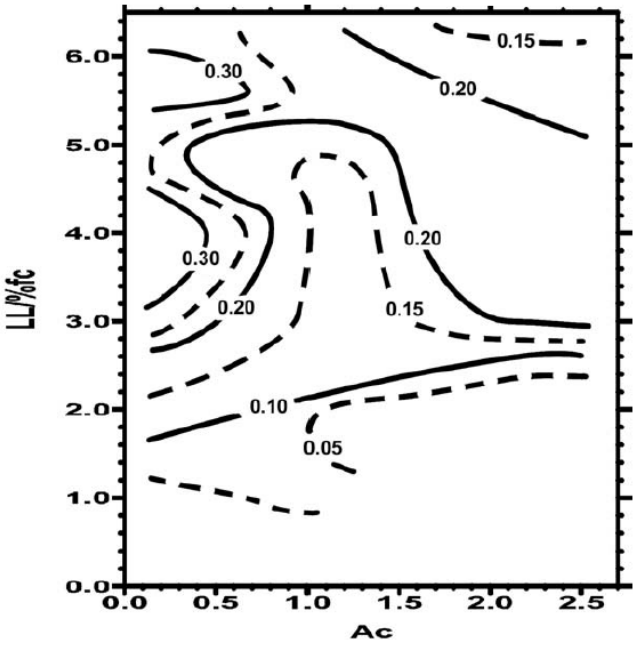

Figure K-20 Zone VIII Chart for Determining γ_0 [153]

APPENDIX L

BLANK WORKSHEET

BEARING CAPACITY CALCULATION

Step 1

Soil layer 1

Type:_____ Depth:_____ Thickness, ft.:_____

Undrained shear strength c_u, psf:_____ PI:_____

Saturated unit weight γ_c, pcf:_____

Soil layer 2

Type:_____ Depth:_____ Thickness, ft.:_____

Undrained shear strength c_u, psf:_____ PI:_____

Saturated unit weight γ_c, pcf:_____

Soil layer 3

Type:_____ Depth:_____ Thickness, ft.:_____

Undrained shear strength c_u, psf:_____ PI:_____

Saturated unit weight γ_c, pcf:_____

Soil layer 4

Type:_____ Depth:_____ Thickness, ft.:_____

Undrained shear strength c_u, psf:_____ PI:_____

Saturated unit weight γ_c, pcf:_____

Stone column

Internal angle of friction φ_s, degree :_____

Dead load (DL):

Embankment weight, kips:_____ Pavement weight, kips:_____

Wing wall and other structures, kips:_____

Live load (LL):

Traffic loading, kips:_____

Total factored load P_f:

$$P_f = 1.2\ (\text{DL} + 1.67\ \text{LL}) =$$

Total factored stress Q_f:

$$Q_f = P_f / A_{total} =$$

Step 2

Trial column spacing s, ft:_____ Trial column diameter D, ft:_____

Trial installation pattern:_____

Area replacement ratio:

$$a_s = C_1 (\frac{D}{s})^2 =$$

Area of each stone column, ft^2:

$$A_s = \pi (\frac{D}{2})^2 =$$

Area of each unit cell, ft^2:

$$A = A_s / a_s =$$

Area of soil in each unit cell, ft^2:

$$A_c = A - A_s =$$

Stress concentration ratio SCR:_____

Ratio of stress in the stone column:

$$\mu_s = \frac{SCR}{1 + (SCR - 1) \cdot a_s} =$$

Ratio of stress in the surrounding soil:

$$\mu_c = \frac{1}{1 + (SCR - 1) \cdot a_s} =$$

Step 3

Length of the stone column, ft.:_____

Length to diameter ratio L/D for the stone column:_____

Long stone column ($L/D > 4$) or short stone column:_____

Possible failure mode: _____

Step 4

Failure Mode 1. General bulging failure

Cavity expansion theory:

Depth where bulge occurs, ft.:

$$h = d_f + \frac{1}{2} D\tan(45^\circ + \frac{\varphi_s}{2}) =$$

Overburden pressure σ_v:

$$\sigma_v = \gamma_c \cdot h =$$

Mean stress at the failure depth q:

$$q = \frac{(1 + 2 \cdot K_0) \cdot \sigma_v}{3} =$$

Rigidity Index I_r:

$$I_r = \frac{E}{2(1+\nu)(c + q\tan\varphi_c)} =$$

Cavity expansion factors F_c' and F_q':

$$F_c' = \ln I_r + 1 =$$

$$F_q' = (1 + \sin\varphi_c)(I_r \sec\varphi_c)^{\frac{\sin\varphi_c}{1+\sin\varphi_c}} =$$

Ultimate lateral stress σ_3

$$\sigma_3 = cF_c' + qF_q' =$$

Ultimate bearing stress q_{ult}

$$q_{ult} = \sigma_3 \cdot \frac{1 + \sin\varphi_s}{1 - \sin\varphi_s} =$$

Bearing capacity method:

Bearing capacity factor N_c:_____

Ultimate bearing stress q_{ult}

$$q_{ult} = c_u N_c =$$

Failure Mode 2. Column head shear failure

Brauns' Method:

Determine angle of the shear failure cone based on Figure 15-8

$$\delta =$$

Determine the ultimate bearing stress q_{ult}

$$q_{ult} = \sigma_{1,\max} = (q_s + \frac{2 \cdot c_u}{\sin(2 \cdot \delta)}) \cdot (1 + \frac{\tan(\frac{\pi}{4} + \frac{\varphi_s}{2})}{\tan\delta}) \cdot \tan^2(\frac{\pi}{4} + \frac{\varphi_s}{2}) =$$

Failure Mode 3. Local bulge failure occurs at very soft soil layer

Barksdale and Bachus' Method:

Depth of very soft soil layer:

$$h = 20 > 3 \cdot D =$$

Ultimate lateral stress σ_3:

$$\sigma_3 = 9c_u =$$

Determine the ultimate bearing stress q_{ult}

$$q_{ult} = \sigma_3 \cdot \frac{1 + \sin\varphi_s}{1 - \sin\varphi_s} =$$

Step 5

The most critical failure mode:_____

Associated ultimate bearing stress in the stone column

$$\sigma_s = q_{ult} =$$

Ultimate allowable bearing stress for the tributary soils σ_{c-ult}:

$$\sigma_{c-ult} = 5c_u =$$

Stress for the tributary soils σ_c when the ultimate bearing stress in the stone column is achieved:

$$\sigma_c = \mu_c\sigma = \mu_c\frac{\sigma_s}{\mu_s} = \mu_c\frac{q_{ult}}{\mu_s} < \sigma_{c-ult}$$

Stress level in the tributary soil: satisfactory/unsatisfactory

If not satisfactory, start over the design from **Step 2**.

Step 6

Factor of safety: 2

Ultimate load P_{ult} for each unit cell:

$$P_{ult} = \frac{\sigma_s A_s + \sigma_c A_c}{FS} =$$

Ultimate allowable stress Q_{ult} for each unit cell:

$$Q_{ult} = \frac{P_{ult}}{A} =$$

Check the ultimate allowable stress Q_{ult} with the total factored stress Q_f

$$Q_f \leq \mathrm{Q_{ult}}$$

The design is: valid/invalid

If not valid, start over the design from **Step 2.**

SETTLEMENT CALCULATION

Step 1

Soil layer 1

Type:_____ Depth:_____ Thickness, ft.:_____

Compression index C_c:_____ Initial void ratio:_____

Drained Poisson's ratio:_____

Soil layer 2

Type:_____ Depth:_____ Thickness, ft.:_____

Compression index C_c:_____ Initial void ratio:_____

Drained Poisson's ratio:_____

Soil layer 3

Type:_____ Depth:_____ Thickness, ft.:_____

Compression index C_c:_____ Initial void ratio:_____

Drained Poisson's ratio:_____

Soil layer 4

Type:_____ Depth:_____ Thickness, ft.:_____

Compression index C_c:_____ Initial void ratio:_____

Drained Poisson's ratio:_____

Stone column

Internal angle of friction ϕ_s, degree :_____

Total factored stress Q_f: $Q_f =$

Step 2

Trial column spacing s, ft:_____ Trial column diameter D, ft:_____

Trial installation pattern:_____

Area replacement ratio:

$a_s = C_1(\frac{D}{s})^2 =$

Area of each stone column, ft^2:

$A_s = \pi(\frac{D}{2})^2 =$

Area of each unit cell, ft^2:

$A = A_s/a_s =$

Area of soil in each unit cell, ft^2: $A_c = A - A_s =$

Stress concentration ratio SCR:_____

Ratio of stress in the stone column:

$$\mu_s = \frac{SCR}{1 + (SCR - 1) \cdot a_s} =$$

Ratio of stress in the surrounding soil:

$$\mu_c = \frac{1}{1 + (SCR - 1) \cdot a_s} =$$

Step 3

Primary consolidation settlement

Equilibrium Method:

a. Initial effective vertical stress $\bar{\sigma}_0$ in the center of each soil layer:
   Water table location:_____
   Layer 1: $\bar{\sigma}_{0-1} =$
   Layer 2: $\bar{\sigma}_{0-2} =$
   Layer 3: $\bar{\sigma}_{0-3} =$
b. Change in the vertical stress $\Delta\sigma_c$ due to the embankment loading at the center of each soil layer:
   Surface: $\sigma_c = \mu_c\sigma = \mu_c Q_f =$
   Layer 1: $z/B =$ Figure 6-7: $I_{z-1} =$
   $\Delta\sigma_{c-1} = I_{z-1}\sigma_c =$
   Layer 2: $z/B =$ Figure 6-7: $I_{z-2} =$
   $\Delta\sigma_{c-2} = I_{z-2}\sigma_c =$
   Layer 3: $z/B =$ Figure 6-7: $I_{z-3} =$
   $\Delta\sigma_{c-3} = I_{z-3}\sigma_c =$

c. Primary consolidation settlement S_t of stone column treated ground for each layer:

Layer 1:

$$S_{t-1} = (\frac{C_c}{1+e_0})\log_{10}(\frac{\bar{\sigma}_0 + \Delta\sigma_c}{\bar{\sigma}_0}) \cdot H =$$

Layer 2:

$$S_{t-2} = (\frac{C_c}{1+e_0})\log_{10}(\frac{\bar{\sigma}_0 + \Delta\sigma_c}{\bar{\sigma}_0}) \cdot H =$$

Layer 3:

$$S_{t-3} = (\frac{C_c}{1+e_0})\log_{10}(\frac{\bar{\sigma}_0 + \Delta\sigma_c}{\bar{\sigma}_0}) \cdot H =$$

d. Total primary consolidation settlement S_t of stone column treated ground:

$$S_t = S_{t-1} + S_{t-2} + S_{t-3} =$$

e. Primary consolidation settlement S of untreated ground for each layer:

Layer 1:

$$\Delta\sigma_1 = I_{z-1}\sigma =$$

$$S_1 = (\frac{C_c}{1+e_0})\log_{10}(\frac{\bar{\sigma}_0 + \Delta\sigma}{\bar{\sigma}_0}) \cdot H =$$

Layer 2:

$$\Delta\sigma_2 = I_{z-2}\sigma =$$

$$S_2 = (\frac{C_c}{1+e_0})\log_{10}(\frac{\bar{\sigma}_0 + \Delta\sigma}{\bar{\sigma}_0}) \cdot H =$$

Layer 3:

$$\Delta\sigma_3 = I_{z-3}\sigma =$$

$$S_3 = (\frac{C_c}{1+e_0})\log_{10}(\frac{\bar{\sigma}_0 + \Delta\sigma}{\bar{\sigma}_0}) \cdot H =$$

f. Total primary consolidation settlement S of untreated ground:

$$S = S_1 + S_2 + S_3 =$$

Primary consolidation settlement

<u>Finite Element Method</u>:

a. Drained modulus of elasticity of the surrounding soil:

Layer 1:

$$\sigma_{va} = \frac{\bar{\sigma}_0 + \Delta\sigma_c}{2} =$$

$$E_c = \frac{(1+\nu)(1-2\nu)(1+e_0)\sigma_{va}}{0.435(1-\nu)C_c} =$$

Layer 2:

$$\sigma_{va} = \frac{\bar{\sigma}_0 + \Delta\sigma_c}{2} =$$

$$E_c = \frac{(1+\nu)(1-2\nu)(1+e_0)\sigma_{va}}{0.435(1-\nu)C_c} =$$

Layer 3:

$$\sigma_{va} = \frac{\bar{\sigma}_0 + \Delta\sigma_c}{2} =$$

$$E_c = \frac{(1+\nu)(1-2\nu)(1+e_0)\sigma_{va}}{0.435(1-\nu)C_c} =$$

b. Modulus of elasticity of the stone column:

$K =$, $n =$, $R_f =$, $c =$ and $\varphi_s =$

$\sigma_1 =$ $\sigma_2 = \sigma_3 =$

$$\sigma_\theta = \sigma_1 + \sigma_2 + \sigma_3 =$$

$$E_s = K \cdot \sigma_\theta^n \cdot [1 - \frac{(\sigma_1 - \sigma_3)R_f}{(\frac{2(c \cdot \cos\varphi_s + \sigma_3 \sin\varphi_s)}{1 - \sin\varphi_s})}] =$$

c. Decide the compressibility of the soil:

If $E_s/E_c \leq 10$, it is low compressibility cohesive soil;

If $E_s/E_c > 10$, it is compressible cohesive soil.

Layer 1:_____

Layer 2:_____

Layer 3:_____

d. Average vertical strain and settlement for each layer:

$a_s =$ $L/D =$

Use Figure J-8 and Figure J-11 to interpolate results

Layer 1: $E_c =$ $E_b =$ $\Delta\sigma_1 =$

Layer 2: $E_c =$ $E_b =$ $\Delta\sigma_2 =$

Layer 3: $E_c =$ $E_b =$ $\Delta\sigma_3 =$

Layer 1: $S/L =$ for $a_s =$

$$S_1 = L_1 \times \mathrm{S}/L =$$

Layer 2: $S/L =$ for $a_s =$

$$S_2 = L_2 \times \mathrm{S}/L =$$

Layer 3: $S/L =$ for $a_s =$

$$S_3 = L_3 \times \mathrm{S}/L =$$

e. Total settlement of the stone column treated ground

$$S_t = S_1 + S_2 + S_3 =$$

Primary consolidation settlement

Priebe's Method:

a. Improvement factor n_0:

The Rankine's active earth pressure:

$$K_{aC} = \tan^2(45° - \phi_s/2) =$$

Layer 1 & 3:

$$f(\nu, A_s/A) = \frac{(1-\nu)\cdot(1-A_s/A)}{1-2\nu+A_s/A} =$$

$$n_0 = 1 + \frac{A_s}{A}\left[\frac{1/2 + f(\nu, A_s/A)}{K_{aC}\cdot f(\nu, A_s/A)} - 1\right] =$$

Layer 2:

$$f(\nu, A_s/A) = \frac{(1-\nu)\cdot(1-A_s/A)}{1-2\nu+A_s/A} =$$

$$n_0 = 1 + \frac{A_s}{A}\left[\frac{1/2 + f(\nu, A_s/A)}{K_{aC}\cdot f(\nu, A_s/A)} - 1\right] =$$

b. Primary consolidation settlement of untreated ground:

$$S_1 =$$

$$S_2 =$$

$$S_3 =$$

c. Primary consolidation settlement of stone column treated ground:

Layer 1: $S_{t-1} = S_1/n_0 =$

Layer 2: $S_{t-2} = S_2/n_0 =$

Layer 3: $S_{t-3} = S_3/n_0 =$

Total: $S_t = S_{t-1} + S_{t-2} + S_{t-3} =$

Lower bound of primary consolidation settlements:

$$S_t =$$

Upper bound of primary consolidation settlements:

$$S_t =$$

Average of the settlements (for the three methods):

$$S_t =$$

Step 4

Time rate of settlement at, t:_____ days

Soil layer 1

Type:_____ Depth:_____ Thickness, ft.:_____

Coefficient of consolidation in the vertical direction, ft^2/day:_____

Coefficient of consolidation in the radial direction, ft^2/day:_____

Soil layer 2

Type:_____ Depth:_____ Thickness, ft.:_____

Coefficient of consolidation in the vertical direction, ft^2/day:_____

Coefficient of consolidation in the radial direction, ft^2/day:_____

Soil layer 3

Type:_____ Depth:_____ Thickness, ft.:_____

Coefficient of consolidation in the vertical direction, ft^2/day:_____

Coefficient of consolidation in the radial direction, ft^2/day:_____

Degree of consolidation U_z considering only vertical drainage:

Layer 1: $T_z = \frac{C_v \cdot t}{(\frac{H}{N})^2} =$ $U_z =$

Layer 2: $T_z = \frac{C_v \cdot t}{(\frac{H}{N})^2} =$ $U_z =$

Layer 3: $T_z = \frac{C_v \cdot t}{(\frac{H}{N})^2} =$ $U_z =$

Equivalent diameter D_e of a unit cell:

$$D_e = 1.05s =$$

Reduced drain diameter D':_____ of the diameter of the stone columns

$$D' = \frac{1}{5}D =$$

$$n^* = D_e/D' =$$

Degree of consolidation U_r considering only radial drainage:

Layer 1: $T_r = \frac{C_{vr} \cdot t}{(D_e)^2} =$ $U_r =$

Layer 2: $T_r = \frac{C_{vr} \cdot t}{(D_e)^2} =$ $U_r =$

Layer 3: $T_r = \frac{C_{vr} \cdot t}{(D_e)^2} =$ $U_r =$

Average degree of consolidation considering both radial and vertical drainage U:

Layer 1: $U = 1 - (1 - U_z)(1 - U_r) =$

Layer 2: $U = 1 - (1 - U_z)(1 - U_r) =$

Layer 3: $U = 1 - (1 - U_z)(1 - U_r) =$

Ultimate primary consolidation settlement of each layer:

Layer 1: $S_1 =$

Layer 2: $S_2 =$

Layer 3: $S_3 =$

Time rate of settlement at the time $t = day$:

Layer 1: $S'_{t1} = U \cdot S_1 =$

Layer 2: $S'_{t2} = U \cdot S_2 =$

Layer 3: $S'_{t3} = U \cdot S_3 =$

Total: $S'_t = S'_{t1} + S'_{t2} + S'_{t3} =$

Step 5

Secondary compression settlement at, t_2:_____ years

Secondary compression index:

Layer 1: $C_\alpha =$

Layer 2: $C_\alpha =$

Layer 3: $C_\alpha =$

Time t_1 when $U = 90\%$ of primary consolidation settlement occurs in each layer:

Layer 1: $t_1 =$ day

$T_r = \frac{C_{vr} \cdot t_1}{(D_e)^2} =$ $U_r =$

$T_z = \frac{C_v \cdot t_1}{(\frac{H}{N})^2} =$ $U_z =$

$U = 1 - (1 - U_z)(1 - U_r) \approx 0.9$

Layer 2: $t_1 =$ day

$T_r = \frac{C_{vr} \cdot t_1}{(D_e)^2} =$ $U_r =$

$T_z = \frac{C_v \cdot t_1}{(\frac{H}{N})^2} =$ $U_z =$

$U = 1 - (1 - U_z)(1 - U_r) \approx 0.9$

Layer 3: $t_1 =$ day

$T_r = \frac{C_{vr} \cdot t_1}{(D_e)^2} =$ $U_r =$

$T_z = \frac{C_v \cdot t_1}{(\frac{H}{N})^2} =$ $U_z =$

$U = 1 - (1 - U_z)(1 - U_r) \approx 0.9$

Secondary compression settlement ΔS that would occur $t_2 =$ year in each layer:

Layer 1: $\Delta S_1 = C_\alpha H \log_{10} \frac{t_2}{t_1} =$

Layer 2: $\Delta S_1 = C_\alpha H \log_{10} \frac{t_2}{t_1} =$

Layer 3: $\Delta S_1 = C_\alpha H \log_{10} \frac{t_2}{t_1} =$

Total secondary settlement $t_2 =$ year after construction:

$\Delta S = \Delta S_1 + \Delta S_2 + \Delta S_3 =$

SOIL PROPERTIES CHARACTERIZATION

Input

MBV:_____

DC:_____

Task 1. Estimation of Effective Internal Friction Angle

Plasticity index PI:_____

$$PI = a \times MBV + b =$$

Refer to Equation (16-19), the coefficients a and b can be determined using the given Excel spreadsheet (see tab "**Task 1**" of the spreadsheet) based on laboratory experiment results.

Liquid limit LL:_____

$$LL = a \times MBV + b =$$

Refer to Equation (16-20), the coefficients a and b can be determined using the given Excel spreadsheet (see tab "**Task 1**" of the spreadsheet) based on laboratory experiment results.

Effective internal friction angle ϕ':_____

Using Equation (K-1):

$$\phi' = 0.0016PI^2 - 0.302PI + 36.208 =$$

Task 2. Estimation of Specific Gravity

Specific graveity G_s:_____

$$G_s = \frac{2.55 + 2.91(\beta)(\frac{PI - P_0}{P_m - PI})^{\gamma}(\frac{LL - L_0}{L_m - LL})^{\delta}}{1 + \beta(\frac{PI - P_0}{P_m - PI})^{\gamma}(\frac{LL - L_0}{L_m - LL})^{\delta}} =$$

Refer to Equation (16-21), the three fitting parameters (i.e. β, γ and δ) can be determined using the given Excel spreadsheet (see tab "**Task 2**" of the spreadsheet) based on laboratory experiment results.

Task 3. Estimation of Matric Suction

Percent fine content pfc:_____

$$pfc = a \times \ln(MBV) + b =$$

Refer to Equation (16-22), the coefficients a and b can be determined using the given Excel spreadsheet (see tab "**Task 3a**" of the spreadsheet) based on laboratory experiment results.

Minimum soil DC $\varepsilon_{\min}$:_____

$$\varepsilon_{\min} = a \times MBV^2 + b \times MBV + c =$$

Refer to Equation (16-23), the coefficients a, b and c can be determined using the given Excel spreadsheet (see tab "**Task 3b**" of the spreadsheet) based on laboratory experiment results.

Saturated soil DC ε_{sat}:_____

$$\varepsilon_{sat} = a \times MBV^2 + b \times MBV + c =$$

Refer to Equation (16-24), the coefficients a, b and c can be determined using the given Excel spreadsheet (see tab "**Task 3b**" of the spreadsheet) based on laboratory experiment results.

SDCC fitting parameter α:_____

SDCC fitting parameter γ:_____

$$H_1, \alpha = TANH(0.5(a_1(MBV) + b_1(pfc) + c_1)) =$$

$$H_1, \gamma = TANH(0.5(a_1(MBV) + b_1(pfc) + c_1)) =$$

$$\alpha = m(H_1, \alpha) + n =$$

$$\gamma = m(H_1, \gamma) + n =$$

Refer to Equation (16-25) and (16-26) and Table 16-13, the coefficients (i.e. a_1, b_1, c_1, m and n) for calculating α and γ can be found in the given Excel spreadsheet (see tab "**Task 3c**" of the spreadsheet).

Matric suction h_m:_____

Using Equation (K-6)

$$\varepsilon_r = [\frac{\varepsilon_{sat} + \varepsilon_{\min}\alpha[\frac{h_m}{h_{\max} - h_m}]^\gamma}{1 + \alpha(\frac{h_m}{h_{\max} - h_m})^\gamma}]$$

Solve for the only unknown (i.e. the matric suction) in this function

$$h_m = \qquad pF$$

Task 4. Estimation of Volumetric Water Content

SWCC fitting parameter a_f:_____

SWCC fitting parameter b_f:_____

SWCC fitting parameter c_f:_____

SWCC fitting parameter h_r:_____

$$a_f = a \times MBV + b =$$

$$b_f = a \times MBV^2 + b \times MBV + c =$$

$$c_f = a \times MBV + b =$$

$$h_r = a \times MBV^2 + b \times MBV + c =$$

Refer to Equation (16-27) – (16-30), the coefficients a, b and c for calculating the four SWCC fitting parameters can be determined using the given Excel spreadsheet (see tab "**Task 4**" of the spreadsheet) based on laboratory experiment results.

Saturated volumetric water content θ_{sat}:_____

$$H_1 = TANH(0.5(a_1(MBV) + b_1(pfc) + c_1(G_s) + d_1)) =$$

$$\theta_{sat} = m(H_1) + n =$$

Refer to Equation (16-31) and (16-32) and Table 16-17, the coefficients (i.e. a_1, b_1, c_1, d_1, m and n) for calculating θ_{sat} can be found in the given Excel spreadsheet (see tab "**Task 4**" of the spreadsheet).

Volumetric water content θ:_____

Using Equation (K-21) and (K-22)

$$\theta = C(h) \times [\frac{\theta_{sat}}{[\ln[\exp(1) + (\frac{h_m}{a_f})^{b_f}]]^{c_f}}] =$$

Task 5. Estimation of Dry Unit Weight

CCM fitting parameter a_d:_____

CCM fitting parameter b_d:_____

CCM fitting parameter n_d:_____

$$H_1, a_d = TANH(0.5(a_1(MBV) + b_1(pfc) + c_1(G_s) + d_1)) =$$
$$H_1, b_d = TANH(0.5(a_1(MBV) + b_1(pfc) + c_1(G_s) + d_1)) =$$
$$H_1, n_d = TANH(0.5(a_1(MBV) + b_1(pfc) + c_1(G_s) + d_1)) =$$
$$a_d = m(H_1, a_d) + n =$$
$$b_d = m(H_1, b_d) + n =$$
$$n_d = m(H_1, n_d) + n =$$

Refer to Equation (16-33) and (16-34) and Table 16-20, the coefficients (i.e. a_1, b_1, c_1, d_1, m and n) for calculating fitting parameter (a_d, b_d and n_d) can be found in the given Excel spreadsheet (see tab "**Task 5**" of the spreadsheet).

Dry unit weight γ_d:_____

Using Equation (K-32)

$$\gamma_d = (a_d[\text{csch}(\frac{\theta\theta_{sat}}{G_s(|\theta_{sat} - \theta|)})]^{n_d} - b_d[\text{csch}(\frac{\theta\theta_{sat}}{G_s(|\theta_{sat} - \theta|)})]) \times \gamma_w =$$

Task 6. Estimation of Matric Suction at Intersection

Matric suction at intersection $h_{m-\mathrm{int}ercept}$:_____

Using Equation (16-18)

$$h_{m-\mathrm{int}ercept} = 5.622 + 0.0041(pfc) = \qquad pF$$

Task 7. Estimation of Suction Compression Index

Mineralogical zone:_____

Determine the mineralogical based on plasticity index and liquid limit using Figure K-12.

Volume change guide number γ_0:_____

Calculate $\frac{LL}{pfc}$ and Ac, determine γ_0 for the specific mineralogical zone using Figure K-13 – Figure K-20.

$$\frac{LL}{pfc} =$$

$$Ac = \frac{PI}{pfc} =$$

$$\gamma_0 =$$

Suction compression index γ_h:_____

Using Equation (K-46)

$$\gamma_h = \gamma_0 \times \frac{pfc}{100} =$$

Estimation of Undrained Shear Strength

Initial void ratio of the soil e_0:_____

Using Equation (16-6)

$$e_0 = \frac{G_s \gamma_w}{\gamma_d} - 1 =$$

Gravimetric moisture content w:_____

Using Equation (16-5)

$$w = \frac{\theta \gamma_w}{\gamma_d} =$$

Degree of saturation S_r:_____

Using Equation (16-4)

$$S_r = \frac{wG_s}{e_0} =$$

Unsaturated shear strength factor f:_____

Using Equation (16-3)

$$f = 1 + (\frac{S_r - 0.85}{0.15})(\frac{0.01}{\theta} - 1) =$$

Matric suction h_m, psi:_____

$$\begin{aligned} h_m &= \quad pF \\ &= \quad cm\ of\ water\ column \\ &= \quad inch\ of\ water\ column \\ &= \quad psi \end{aligned}$$

Undrained shear strength c_u, psi:_____

Using Equation (16-2)

$$c_u = -h_m \theta f \frac{\sin\phi'}{1 - \sin\phi'} =$$

Estimation of Compression Index

Estimation of $|S|w$:_____

Using Equation (16-17)

$|S|w = h_{m-\mathrm{int}ercept} - h_m =$

Compression index C_c:_____

Using Equation (16-14)

$C_c = \frac{(1+e_0)\gamma_h}{1+\frac{0.4343}{|S|w}} =$

APPENDIX M

JMP USER GUIDE AND EXAMPLE DEMONSTRATION

This section provides a demonstration of how to use the neural network function in the statistical software JMP to construct empirical functions. The user may need to purchase JMP in order to get full access to all the functions in the software. Alternatively, the practitioner can apply the procedure elaborated in Appendix N to determine the regression coefficients by executing Matlab codes.

Example: Referring to the given Excel spreadsheet tab "**Task 3C**", then read "**Step 3**" and "**Step 4**" of the instruction.

Inputs: MBV and pfc as shown in "**Table 3**" in tab "**Task 3C**" of the Excel spreadsheet.

Targets: α and γ as shown in "**Table 3**" in tab "**Task 3C**" of the Excel spreadsheet.

Objective: Use the neural network function in the "JMP" software and the information summarized in "**Table 3**" to construct empirical relationships for " α vs. MBV & pfc " and " γ vs. MBV & pfc ", such that one can use MBV and pfc to estimate either α or γ.

Procedure:

1. Launch the "JMP" software;
2. Select File > New > Data Table to create a new table;
3. Copy the data from "**Table 3**" and paste them into the table just created as shown in Figure M-1;

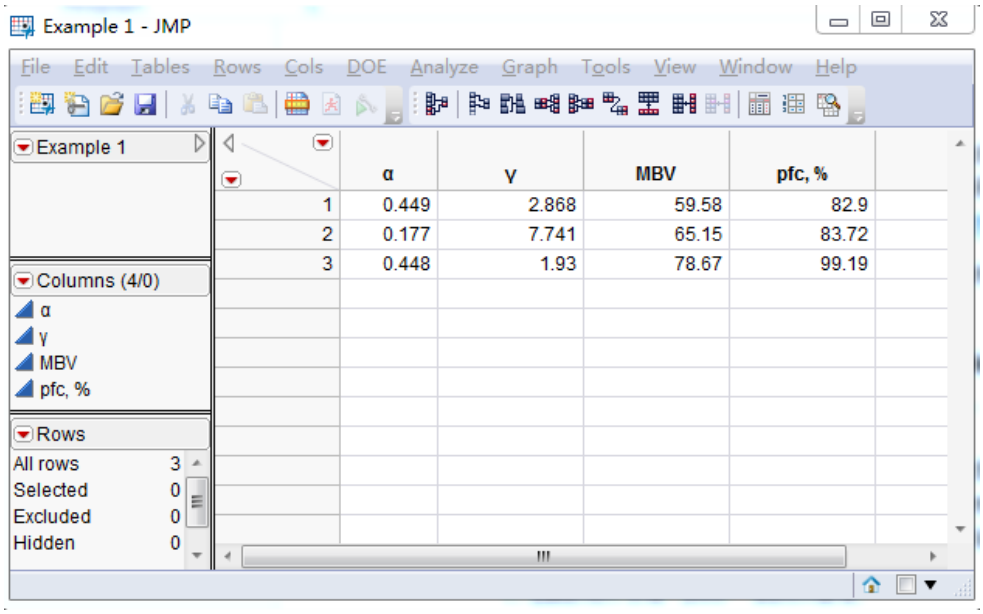

Figure M-1 Copy and paste the required information into JMP

4. Select **Analyze** > **Modeling** > **Neural**;
5. Assign α (target) to the **Y, Response** role and assign MBV and pfc (inputs) to the **X, Factor** role as shown in Figure M-2, then click **OK;** (The empirical relationship of γ vs. MBV & pfc can be established in the same way by setting γ to the **Y, Response** role and assign MBV and pfc (inputs) to the **X, Factor** role);

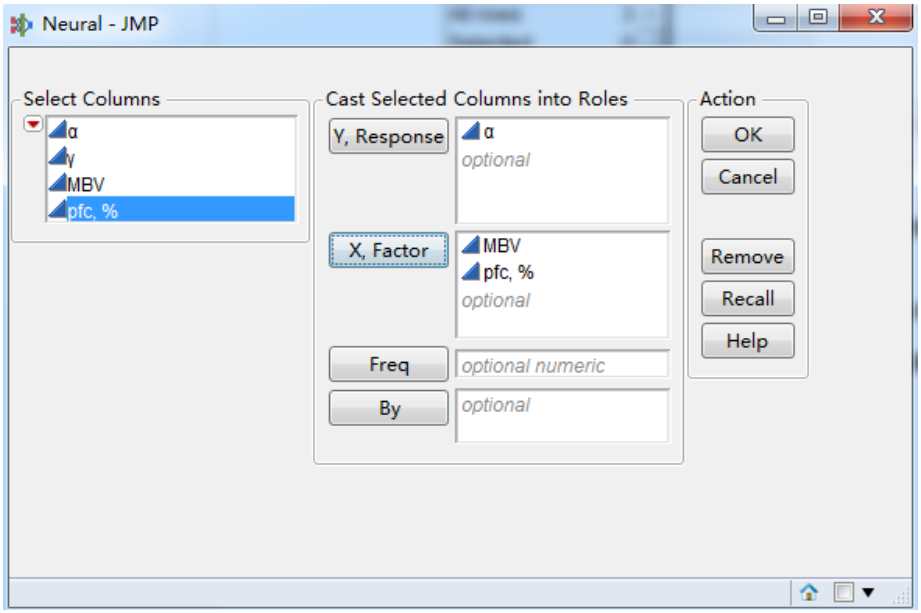

Figure M-2 Select target and inputs for the neural network function

6. Once the window as shown in Figure M-3 pops out, edit the **Hidden Nodes** to 1 (can be modified to different values if 1 does not generate a good empirical model) , then click **Go;**

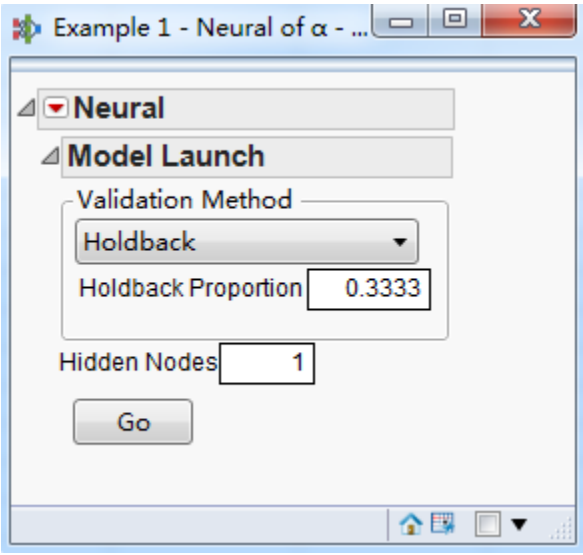

Figure M-3 Model launch

7. The neural network training results will pop out as shown in Figure M-4;

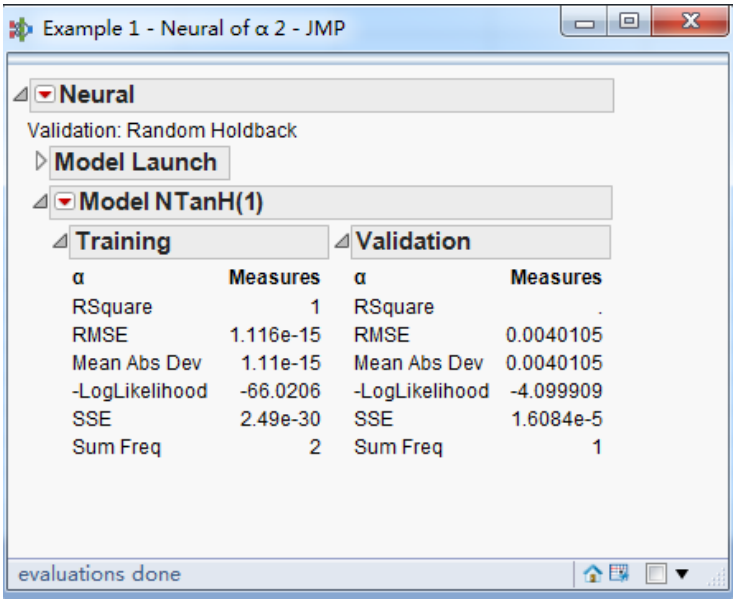

Figure M-4 Result of neural network training

8. Left click on **Model NTanH (1),** select **Save Fast Formulas**, a new column will be created in the table previously formed as shown in Figure M-5;

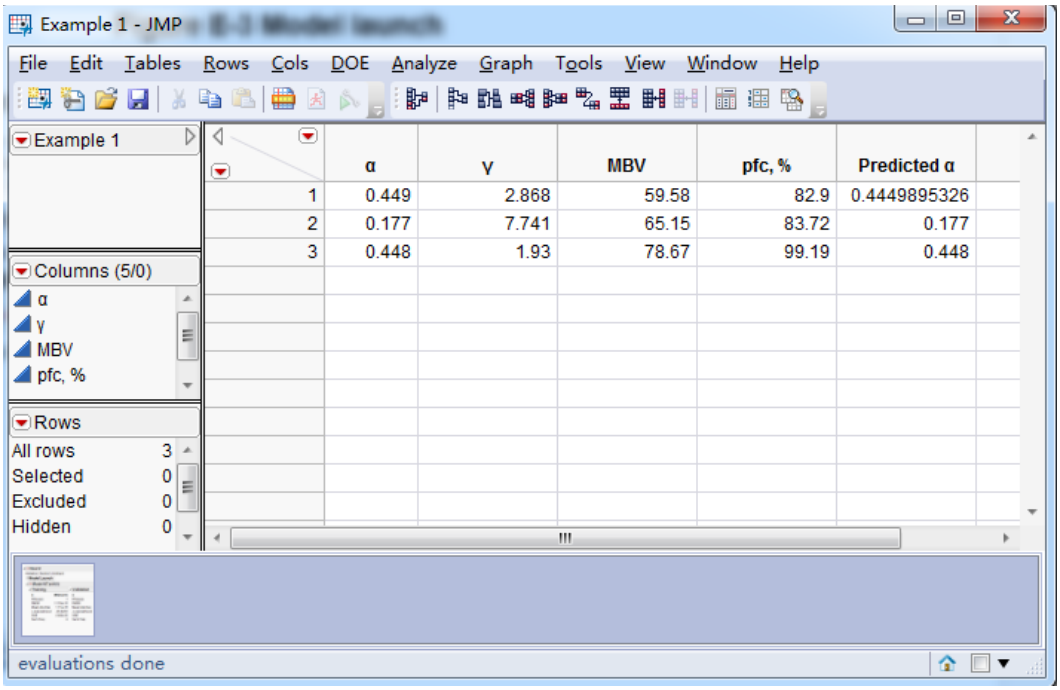

Figure M-5 Predicted target values

9. Check the values in the new column "**Predicted** α", if the predicted α values in this column are reasonably closed to the target α values in the first column, then, Left click again on **Model NTanH (1),** select **Make SAS DATA Step,** the following will pop out as shown Figure M-6;

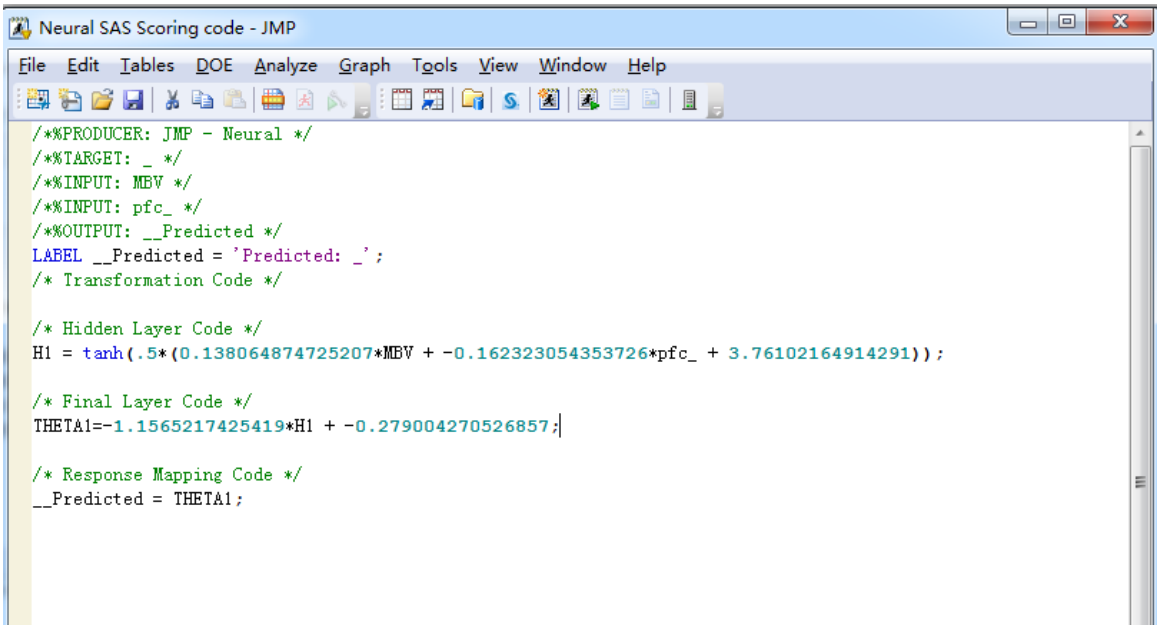

Figure M-6 Make SAS DATA Step

10. Identify the coefficients in the hidden layer functions as shown in Figure M-7 and copy these coefficients into "**Table 4**" in tab "**Task 3C**" of the given Excel spreadsheet;

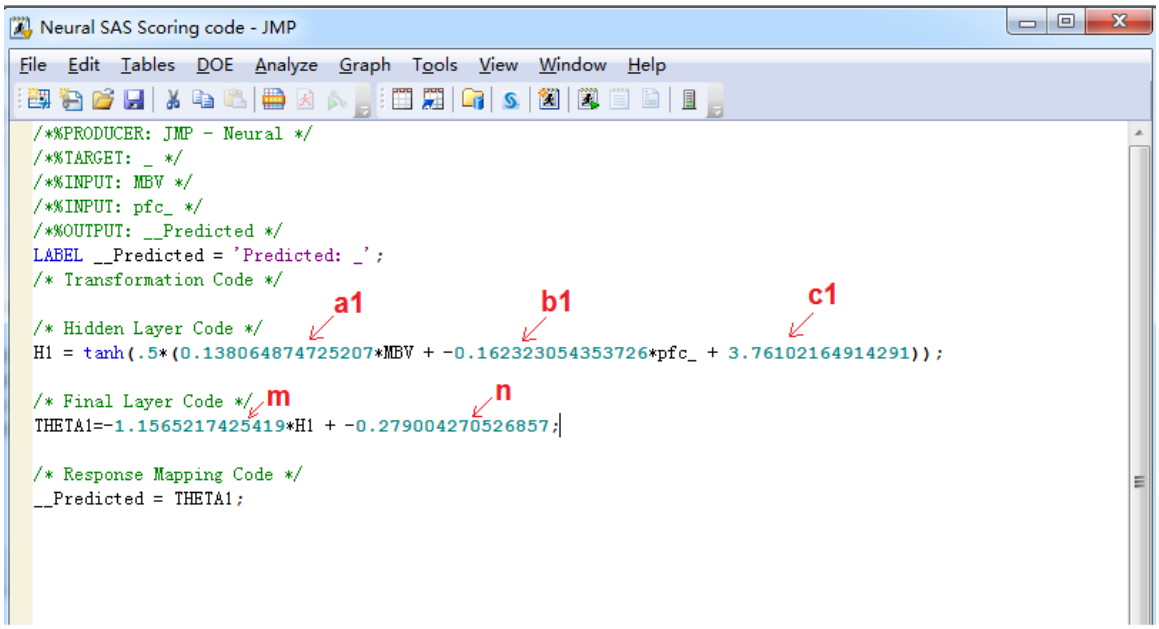

Figure M-7 Identification of regression coefficients

11. Check "**Table 5**" in tab "**Task 3C**" of the given Excel spreadsheet, the total tolerance for predicting α should be less than 0.001; otherwise, repeat the neural network analysis by left clicking on **Neural**, select **Script** and then **Redo Analysis** as shown in Figure M-8 until the tolerance is satisfactory.

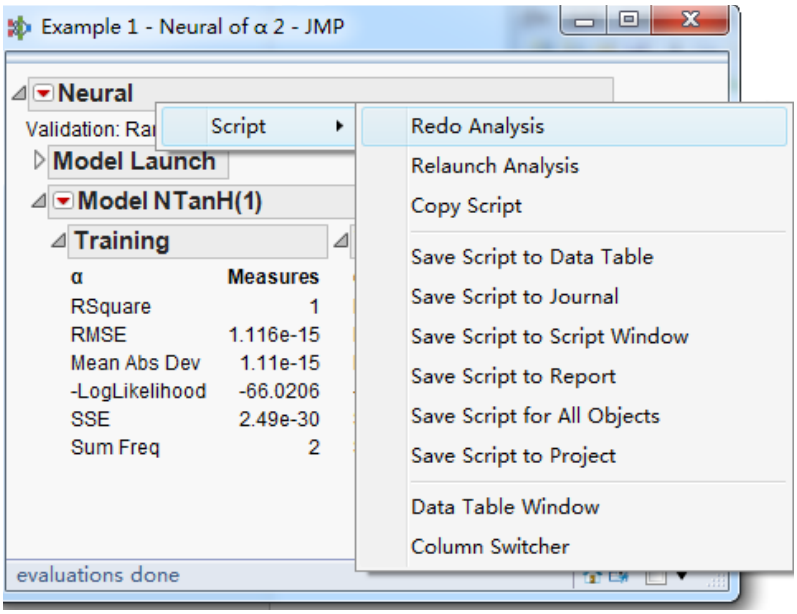

Figure M-8 Redo Analysis

APPENDIX N

MATLAB CODE USER GUIDE AND EXAMPLE DEMONSTRATION

This chapter provides guidelines and demonstrates an example of how to use the Matlab code (as an alternative method to the JMP software) to determine the unknown coefficients in the empirical relationships using laboratory experiment results. This Matlab code is written such that it is applicable for all the tasks elaborated in the Excel spreadsheet (i.e. **Task 3C**, **Task 4** and **Task 5**).

Example: Referring to the given Excel spreadsheet tab "**Task 3C**", the Matlab code should be performed once all the required information are summarized in Table 3 as elaborated in "**Step 3**" of the instruction in the spreadsheet.

Prerequisite: In Table 4 of the Excel spreadsheet tab "**Task 3C**", the user needs to input initial guess of the coefficients.

Procedure:

1. Launch the "Matlab" software and open the Matlab code;
2. Click "Run" to run the Matlab code, the following window will pop out;

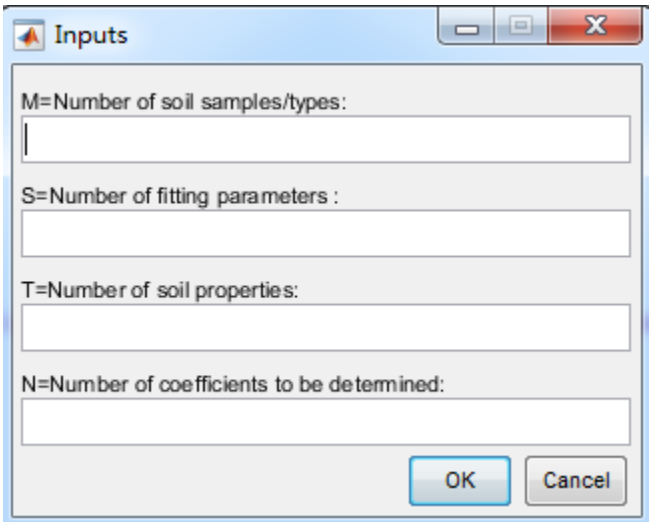

Figure N-1 Inputs window 1

3. Referring to the Table 3 in the Excel spreadsheet, input the number of soil samples/types which is 3 in this example (i.e. Port, Kirkland and Osage), the number of fitting parameters which is 2 in this example (i.e. α and γ), the number of soil properties which is 2 in this example (i.e. MBV and pfc) and the number of coefficients to be determined which is 5 in this example (i.e. a_1, b_1, c_1, m, n);
4. Click “OK”, the following window will pop out as shown in Figure N-2 (tables are blank initially). Copy the soil properties, fitting parameters (found in Table 3 in the Excel spreadsheet) and the initial guess of coefficients (found in Table 4 in the Excel spreadsheet) and paste them into “Soil Property Matrix”, “Fitting Parameter Matrix” and “Initial Guess of Coefficient Matrix”, respectively as shown in Figure N-2;

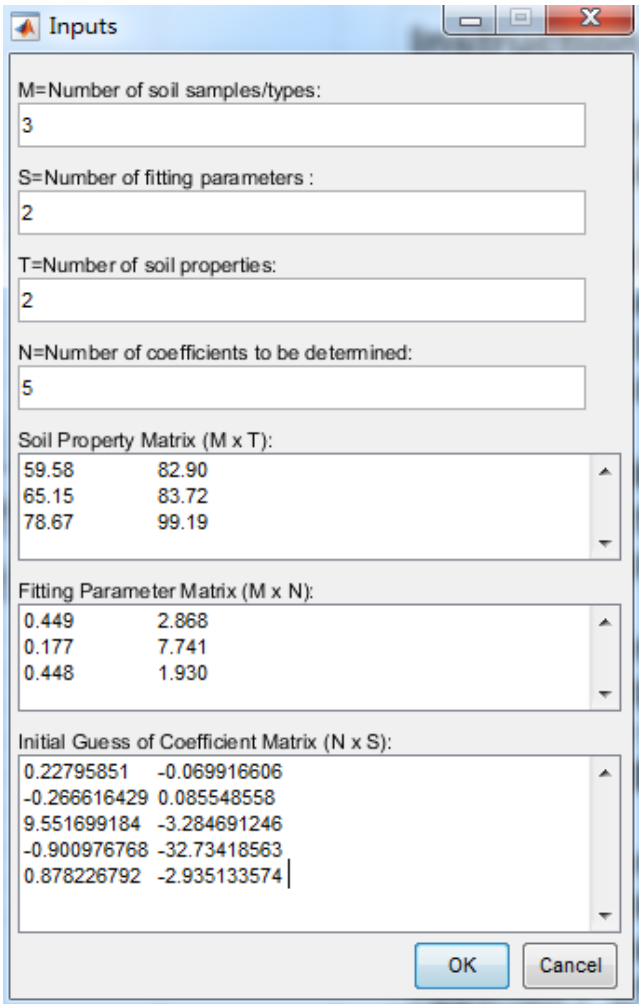

Figure N-2 Inputs window 2

5. Click “OK”, the Matlab will perform calculations automatically and the final results of the coefficients will pop out as shown in Figure N-3;

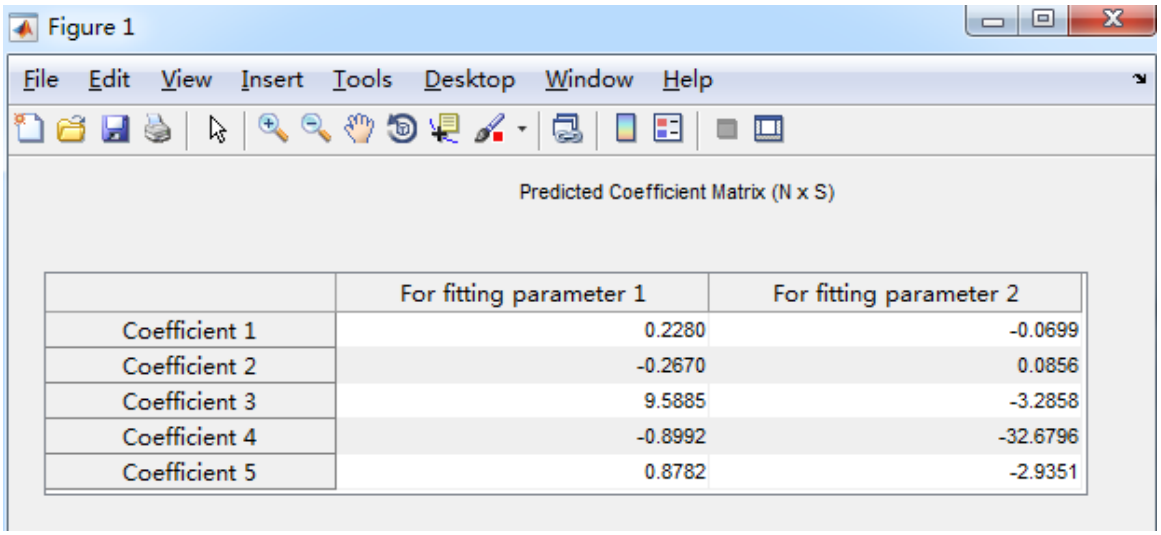

	For fitting parameter 1	For fitting parameter 2
Coefficient 1	0.2280	-0.0699
Coefficient 2	-0.2670	0.0856
Coefficient 3	9.5885	-3.2858
Coefficient 4	-0.8992	-32.6796
Coefficient 5	0.8782	-2.9351

Figure N-3 Predicted Coefficient Matrix

6. Copy the final results shown in the Figure N-3 and paste them into Table 4 of the Excel spreadsheet;
7. Referring to “**Step 4**” of the instruction, the total tolerances for predicting the two fitting parameters (i.e. α and γ) found in Table 5 of the Excel spreadsheet should be less than 0.001; otherwise, the user needs to modify the initial guess of the coefficients and repeat the procedure elaborated in this chapter until the tolerances are met.

REFERENCES

1. Nevels, J.B., *Final Report of the Approach Embankment Settlement Investigation for Federal Aid Project No. NHY-013N(014)*. 2011.
2. Oklahoma, D., *Standard specifications for highway construction*. 2009, Oklahoma City.
3. Brown, R.W. and S.S. Reed, *Evaluation of the Uretek Deep Injection (UDI) Process for Improving Performance of Cardinal Drive (US 69 North Frontage Road) Beaumont, TX*, in *Pilot Project Report*. 2011, Texas Department of Transportation and Ureteck USA, inc.
4. Schmalzer, P., *LTPP Manual for Falling Weight Deflectometer Measurements*. 2006, FHWA-HRT-06-132.
5. Zollinger, C.J., et al. *Innovative approach to pavement rehabilitation analysis and design of runway (R/W) 15L-33R at George Bush Intercontinental Airport (IAH) in Houston, TX*. in *Eighth International Conference on Concrete Pavement*s. 2005.
6. Miller, G.A., et al., *APPLIED APPROACH SLAB SETTLEMENT RESEARCH, DESIGN/CONSTRUCTION.* 2013.
7. Dupont, B. and D.L. Allen, *Movements and Settlements of Highway Bridge Approaches.* 2002.
8. White, D., et al., *Identification of the best practices for design, construction, and repair of bridge approaches*. 2005.
9. Greimann, L.F., et al., *Integral Bridge Abutment-to-Approach Slab Connection*. 2008.
10. Tayabji, S.D., D. Ye, and N. Buch, *Precast concrete pavement technology*. 2013: Transportation Research Board.
11. Merritt, D.K., et al., *Construction of the Iowa Highway 60 Precast Prestressed Concrete Pavement Bridge Approach Slab Demonstration Project*. 2007.
12. Merritt, D.K., B.F. McCullough, and N.H. Burns, *Construction and Preliminary Monitoring of the Georgetown, Texas Precast Prestressed Concrete Pavement*. 2002, Citeseer.
13. Merritt, D., B. Frank McCullough, and N. Burns, *Precast prestressed concrete pavement pilot project near Georgetown, Texas.* Transportation Research Record: Journal of the Transportation Research Board, 2003(1823): p. 11-17.
14. Larrazabal, E., *Precast Concrete (PC) Pavement Tests on Taxiway DD at Laguardia Airport.* 2004.
15. Switzer, W., et al. *Overnight Pavement Replacement Using Precast Panels and Conventional Subgrade Material - Washington Dulles International Airport Case Study in Airfield Pavements. Challenges and New Technologies*. in *Airfield Pavements. Challenges and New Technologies*. 2004.
16. Farrington, R., et al. *Overnight Concrete Pavement Replacement Using a Precast Panel and Expanding Polymer Positioning Technique - Washington Dulles International Airport Case Study in Airfield Pavements. Challenges and New Technologies*. in *Airfield Pavements. Challenges and New Technologies*. 2004.

17. Tayabji, S. and K. Hall, *Precast Concrete Panels for Repair and Rehabilitation of Jointed Concrete Pavements.* CPTP TechBrief, 2008.
18. Association, N.P.C., *Jointed precast concrete pavement (JPrCP)*. 2011, National Precast Concrete Association: http://precast.org/wp-content/uploads/2011/11/PCPSbrochure.pdf.
19. Ye, D., *Personal communication*. 2016.
20. Merritt, D.K., et al., *The Feasibility of Using Precast Concrete Panels to Expedite Highway Pavement Construction*. 2000: Center for Transportation Research, University of Texas at Austin.
21. Merritt, D.K. and S. Tayabji, *Precast Prestressed Concrete Pavement for Reconstruction and Rehabilitation of Existing Pavements*. 2009.
22. Merritt, D., R. Rogers, and R. Rasmussen, *Construction of a Precast Prestressed Concrete Pavement Demonstration Project on Interstate 57 near Sikeston, Missouri*. 2008, FHWA-HIF-08-009. Washington, DC: Federal Highway Administration.
23. Merritt, D.K., P. MCCULLOUGH, and N.H. Burns, *Design-construction of a precast, prestressed concrete pavement for interstate 10, El Monte, California.* PCI journal, 2005. **50**(2): p. 18-27.
24. Tayabji, S., *Precast Concrete Pavement Technology ~ Rapidly Evolving*, in *International Society for concrete pavements*. 2011.
25. Sun, P., *A new protocol for evaluating concrete curing effectiveness*. 2013, Texas A&M University.
26. Sun, P. and D.G. Zollinger, *Concepts to Enhance Specification and Inspection of Curing Effectiveness in Concrete Pavement Design and Construction.* Transportation Research Record: Journal of the Transportation Research Board, 2015(2504): p. 124-132.
27. Ma, S., *Bridge approach slab analysis and design incorporating elastic soil support*. 2011, University of Missouri--Columbia.
28. Hoppe, E.J., *Guidelines for the use, design, and construction of bridge approach slabs*. 1999.
29. Shi, X., et al., *Finite element analysis of concrete approach slab on soil embankment*. 2004.
30. Cai, C., et al., *Structural performance of bridge approach slabs under given embankment settlement.* Journal of Bridge Engineering, 2005. **10**(4): p. 482-489.
31. Puppala, A.J., et al., *Recommendations for design, construction, and maintenance of bridge approach slabs: Synthesis report*. 2009, University of Texas at Arlington.
32. Dunn, K.H.A., G.H. Rodes, T.H., and Zieher, J.J., *Performance Evaluation of Bridge Approaches.* Wisconsin Department of Transportation, 1983.
33. Thiagarajan, G., et al., *Bridge Approach Slabs for Missouri DOT: Looking at Alternative and Cost Efficient Approaches*. 2010.
34. Luna, R., *Evaluation of Bridge Approach Slabs, Performance and Design*. 2004.
35. Miller, G.A., et al., *Applied approach slab settlement research, design/construction*. 2013, University of Oklahoma: Oklahoma Department of Transportation.

36. Northeast, P., *Guideline for Accelerated Bridge Construction Using Precast/Prestressed Concrete Elements Including Guideline Details*. 2014, Report No. PCINE-14-ABC. Precast/Prestressed Concrete Institute, Chicago, IL.
37. Schmitz, M.E., et al., *Use of controlled low-strength material as abutment backfill*. 2004, Kansas Department of Transportation.
38. Guide, M.E.P.D., *A Manual of Practice.* American Association of State Highway and Transportation Officials, 2008.
39. Pierce, L.M. and G. McGovern, *Implementation of the AASHTO Mechanistic-Empirical Pavement Design Guide and Software*. 2014.
40. su Jung, Y., et al., *Subbase and subgrade performance investigation and design guidelines for concrete pavement.* 2010.
41. Tayabji, S., D. Ye, and F. Motamed, *Final Report, Proposed Process for Design of Precast Concrete Pavements Sacramento, California*. 2012, Fugro Consultants, Inc.
42. Jang, S.H., *Automated crack control analysis for concrete pavement construction*. 2005, Texas A&M University.
43. Thiagarajan, G., J. Myers, and C. Halmen, *Field Evaluation of Alternative and Cost-Efficient Bridge Approach Slabs*. 2013.
44. Jung, Y. and D. Zollinger, *New laboratory-based mechanistic-empirical model for faulting in jointed concrete pavement.* Transportation Research Record: Journal of the Transportation Research Board, 2011(2226): p. 60-70.
45. su Jung, Y., D. Zollinger, and A. Wimsatt, *Test method and model development of subbase erosion for concrete pavement design.* Transportation Research Record: Journal of the Transportation Research Board, 2010(2154): p. 22-31.
46. Bari, M.E. and D.G. Zollinger, *New concepts for the assessment of concrete slab interfacial effects in pavement design and analysis.* International Journal of Pavement Engineering, 2016. **17**(3): p. 233-244.
47. Bakhsh, K.N. and D. Zollinger. *Faulting Prediction Model for Design of Concrete Pavement Structures*. in *Geo-Shanghai 2014*. 2014.
48. Jung, Y., D. Zollinger, and B. Ehsanul, *Improved mechanistic-empirical continuously reinforced concrete pavement design approach with modified punchout model.* Transportation Research Record: Journal of the Transportation Research Board, 2012(2305): p. 32-42.
49. Darter, M., *Design of zero-maintenance plain jointed pavements.* Federal Highway Administration, Washington DC, 1977.
50. Ioannides, A.M., L. Khazanovich, and J.L. Becque, *Structural evaluation of base layers in concrete pavement systems.* Transportation Research Record, 1992(1370).
51. Buch, N., *Precast Concrete Panel Systems for Full-Depth Pavement Repairs. Field Trials*. 2007.
52. Smith, P.J., *Replacement of Bridge Approach Slabs and Super-Structure In Two Consecutive Weekends, Rt. 46 Over Broad St., Clifton, NJ*. 2011, The Fort Miller Co. Inc: New Jersey.
53. Mishra, T., P. French, and Z. Sakkal, *Engineering a better road: Use of two-way prestressed, precast concrete pavement for rapid rehabilitation.* PCI journal, 2013. **58**(1): p. 129-141.

54. Highways, M. and T. Commission, *Missouri Standard Specifications for Highway Construction, 2004*. 2016: Missouri Highways and Transportation Commission.
55. Dailey, C.L., *Instrumentation and early performance of an innovative prestressed precast pavement system*. 2006, University of Missouri--Columbia.
56. LLC, C.A., *Concrete bridge approach pavements: a survey of state practices*. 2010, Wisconsin Highway Research Program Rigid Pavements Technical Oversight Committee.
57. Phares, B.M., et al., *Identification and evaluation of pavement-bridge interface ride quality improvement and corrective strategies.* Rep. No. Federal Highway Administration (FHWA)/Ohio (OH)-2011/1, Washington, DC, 2011.
58. Nadermann, A., L. Greimann, and B. Phares, *Instrumentation and Monitoring of Precast Bridge Approach Tied to an Integral Abutment Bridge in Bremer County.* 2010.
59. Bautista, F.E. and I. Basheer, *Jointed Plain Concrete Pavement (JPCP) Preservation and Rehabilitation Design Guide*, in *Office of Pavement Design Pavement Design & Analysis Branch*. 2008.
60. Corporation, D.C., *Rapid cure sealant demonstrates remarkable success*. 1999: Available from Internet:<http://www.dowcorning.com/content/publishedlit/62283A01.pdf>.
61. Purvis, R.L. and M.P. Burke, *Bridge deck joint performance: A synthesis of highway practice*. Vol. 319. 2003: Transportation Research Board.
62. Milner, M.H. and H.W. Shenton III, *Survey of Past Experience and State-of-the-Practice in the Design and Maintenance of Small Movement Expansion Joints in the Northeast.* AASHTO Transportation System Preservation Technical Services Program (TSP2) Report, 2014. **242**.
63. su Jung, Y., D.G. Zollinger, and S.D. Tayabji, *Best Practices for Concrete Pavement Transition Design and Construction*. 2007: Texas Transportation Institute, Texas A&M University System.
64. Seo, J., H. Ha, and J.-L. Briaud, *Investigation of settlement at bridge approach slab expansion joint: Numerical simulations and model tests*. 2002.
65. Briaud, J., R. JAMES, and S. Hoffman, *SETTLEMENT OF BRIDGE APPROACHES (THE BUMP AT THE END OF THE BRIDGE)*. 1997.
66. Miller, G.A., et al., *APPLIED APPROACH SLAB SETTLEMENT RESEARCH, DESIGN/CONSTRUCTION.* 2011.
67. Ziehl, P., M. EIBatanouny, and M.K. Jones, *In-Situ Monitoring of Precast Concrete Approach Slab Systems*. 2015, South Carolina Department of Transportation Federal Highway Administration.
68. Lenke, L.R., *Settlement Issues--Bridge Approach Slabs*. 2006.
69. Hopkins, T.C., *Settlement of highway bridge approaches and embankment foundations*. 1969, University of Kentucky.
70. Arsoy, S., R.M. Barker, and J.M. Duncan, *The behavior of integral abutment bridges*. Vol. 3. 1999: Virginia Transportation Research Council Charlottesville, VA.
71. Mahmood, I.U., *Evaluation of causes of bridge approach settlement and development of settlement prediction models*. 1990.

72. Horvath, J.S., *Integral-abutment bridges: problems and innovative solutions using EPS geofoam and other geosynthetics.* Res. Rpt. No. CE/GE-00, 2000. **2**.
73. Schaefer, V.R., J.C. Koch, and S. Dakota, *Void development under bridge approaches*. 1992: South Dakota Department of Transportation, Office of Research.
74. Kerokoski, O., *Soil-structure interaction of long jointless bridges with integral abutments*. 2006.
75. Hoppe, E.J., *Field study of integral backwall with elastic inclusion*. 2005.
76. Hoppe, E.J. and S.L. Eichenthal, *Thermal response of a highly skewed integral bridge*. 2012.
77. White, H., *Wingwall type selection for integral abutment bridges: Survey of current practice in the United States of America*. 2008: Transportation Research and Development Bureau, New York State Department of Transportation.
78. Manual, N.B., *New York State Department of Transportation*. 2014.
79. DOT, N., *STRUCTURES MANUAL* in *Substructures*. 2008: https://www.nevadadot.com/uploadedFiles/NDOT/About_NDOT/NDOT_Divisions/Engineering/Structures/Chapter18.pdf.
80. Jones, C. and F. Sims, *Earth pressure against the abutments and wing walls of standard motorway bridges.* Geotechnique, 1975. **25**(4): p. 731-742.
81. Thompson, T.A., *Passive earth pressures behind integral bridge abutments.* 1999.
82. Kalayci, E., S.A. Civjan, and S.F. Breña, *Parametric study on the thermal response of curved integral abutment bridges.* Engineering Structures, 2012. **43**: p. 129-138.
83. Wahls, H.E., *Design and construction of bridge approaches*. Vol. 159. 1990: Transportation Research Board.
84. ODOT, C., *Material Specifications.* Ohio Department of Transportation, Office of Contracts, Columbus, OH, 2008.
85. Transportation, P.D.o., *Bridge Design Standards*. 2014: Pennsylvania.
86. Jayawickrama, P., et al., *Water Intrusion in Base/Subgrade Materials at Bridge Ends.* 2005.
87. Abu-Hejleh, N., et al., *Flowfill and MSE Bridge Approaches: Performance, Coast, and Recommendations for Improvements*. 2006, Colorado Department of Transportation, Research Branch.
88. Association, N.R.M.C., *Guide Specification for Controlled Low Strength Materials (CLSM).* Specification Guide, 2006.
89. Seo, J.B., *The bump at the end of the bridge: an investigation*. 2005, Texas A&M University.
90. Yeh, S.-T. and C. Su, *EPS, FLOW FILL AND STRUCTURE FILL FOR BRIDGEABUTMENTBACKnLL.* 1995.
91. Lutenegger, A.J. and M. Ciufetti, *Full-Scale Pilot Study to Reduce Lateral Stresses in Retaining Structures Using GeoFoam.* Final report, project No. RSCH010-983 Vermont DOT, University of Massachusetts, Amherst, MA, 2009.
92. Edgar, T.V., J.A. Puckett, and B. Rodney, *Effects of geotextiles on lateral pressure and deformation in highway embankments.* Geotextiles and Geomembranes, 1989. **8**(4): p. 275-292.

93. Maddison, J., et al., *Design and performance of an embankment supported using low strength geogrids and vibro concrete columns.* Geosynthetics: Applications, design and construction, De Groot, Den Hoedt, and Termaat, eds, 1996: p. 325-332.
94. Polska, G.G., *Everything tailor-made Slope protection*.
95. Shi, X., et al., *Design of ribbed concrete approach slab based on interaction with the embankment.* Transportation Research Record: Journal of the Transportation Research Board, 2005(1936): p. 181-191.
96. Bakeer, R.M., et al., *Performance of pile-supported bridge approach slabs.* Journal of Bridge Engineering, 2005. **10**(2): p. 228-237.
97. Authority, I.S.T.H., *Design Manual for Tollway Transportation Structures and Facilities*, I.S.T.H. Authority, Editor. 2008.
98. Hu, W., *Physical modelling of group behaviour of stone column foundations*. 1995, University of Glasgow.
99. Ayadat, T., *Collapse of stone column foundations due to inundation.* 1990.
100. Aguado, P., et al., *Recommendations for the design, calculation, construction and quality control of stone columns*. 2011, the French geotechnical union association: http://www.cfms-sols.org/sites/default/files/recommandations/Recommandations-CB-ENGLISH.pdf.
101. Elias, V., et al., *Ground Improvement Technical Summaries, Volume II, Demonstration Project 116.* US Department of Transportation, Federal Highway Administration, Publication No. FHWA-SA-98-086, 1998.
102. Niroumand, H., *From Research to Practice in Stone Columns and Reinforced Stone Columns as Soil Improvement Techniques* 2012: LAP Lambert Academic Publishing.
103. Pitt, J.M., et al., *Highway applications for rammed aggregate piers in Iowa soils*. 2003.
104. Raju, V., R. Hari Krishna, and R. Wegner. *Ground improvement using vibro replacement in Asia 1994 to 2004-a 10 year review*. in *5th International Conference on Ground Improvement Techniques, Kuala Lumpur*. 2004.
105. Townsend, F.C. and J.B. Anderson, *A compendium of ground modification techniques*. 2004.
106. Priebe, H.J., *The application of Priebe's method to extremely soft soils,"floating "foundations and proof against slope or embankment failure.* Ground engineering, 2005.
107. Raju, V., et al. *Vibro replacement for the construction of a 15 m high highway embankment over a mining pond*. in *Malaysian Geotechnical Conference*. 2004.
108. Wehr, J., *Keller Workshop*. 2013, www.kellerholding.com: http://kellerbrasil.com.br/pdf/Brazil%20Workshop%20Keller%20Wehr%202013.pdf.
109. Taube, M.G. and J.R. Herridge, *Stone Columns for Industrial Fills*. 2002: Cuddy, Pennsylvania.
110. Foundation, K., *Keller Foundation Brochure*, in *http://www.keller-uk.com/contentfiles/files/Keller%20F_%20brochure%20Dec2010.pdf*. 2010.

111. Kirsch, K. and F. Kirsch, *Ground improvement by deep vibratory methods*. 2010: CRC Press.
112. Egan, D., W. Scott, and B. McCabe. *Installation effects of vibro replacement stone columns in soft clay*. in *Proceedings of the 2nd International Workshop on the Geotechnics of Soft Soils, Glasgow*. 2008.
113. Mani, K. and N. K, *A study on ground improvement using stone column technique.* International Journal of Innovative Research in Science, Engineering and Technology, 2013. **2**(11).
114. McCabe, B.A., et al. *A review of the settlement of stone columns in compressible soils*. in *Ground improvement and geosynthetics. Proceedings of sessions of GeoShanghai 2010, Shanghai, China, 3-5 June, 2010.* 2010. American Society of Civil Engineers (ASCE).
115. Farrell, T. and A. Taylor. *Rammed aggregate pier design and construction in California-performance, constructability, and economics*. in *Structural Engineers Association of California Convention Proceedings. Placerville, CA. and liquefied behavior, Journal Geotech. Geoenviron. Engineering*. 2004.
116. Bilgin, Ö., K. Arens, and M. Salveter, *Analysis of Aggregate Pier Systems for Stabilization of Subgrade Settlement*. 2014.
117. Handy, R., D. White, and K. Wissmann, *Concentric stress zones near rammed aggregate piers.* Manuscript in preparation–draft to be provided upon request, 2002.
118. Barksdale, R.D. and R.C. Bachus, *Design and Construction of Stone Columns Volume I*. 1983.
119. YILDIZ, M., *DETERMINATION OF STRESS CONCENTRATION FACTOR IN STONE COLUMNS BY NUMERICAL MODELLING*. 2013, MIDDLE EAST TECHNICAL UNIVERSITY.
120. Hu, W., D. Wood, and W. Stewart. *Ground improvement using stone column foundation: results of model tests*. in *International Conference on ground Improvement Techniques*. 1997.
121. Douglas, S.C.P., *A web-based information system for geoconstruction technologies and performance of stone column reinforced ground*. 2012.
122. Hughes, J., N. Withers, and D. Greenwood, *A field trial of the reinforcing effect of a stone column in soil.* Geotechnique, 1975. **25**(1): p. 31-44.
123. Goughnour, R. and A. Bayuk, *Analysis of stone column-soil matrix interaction under vertical load.* Coll. Int. Renforcements des Sols, 1979: p. 279-285.
124. Balaam, N. and J. Booker, *Effect of stone column yield on settlement of rigid foundations in stabilized clay.* International journal for numerical and analytical methods in geomechanics, 1985. **9**(4): p. 331-351.
125. Balaam, N. and H.G. Poulos. *The behaviour of foundations supported by clay stabilised by stone columns*. in *European Conference on Soil Mechanics and Foundation Engineering, 8th, 1983, Helsinki, Finland*. 1983.
126. Greenwood, D. and G. Thomson, *Ground Stabilisation: Deep compaction and grouting*. 1983: Telford.
127. Briaud, J.-L., *Geotechnical engineering: unsaturated and saturated soils*. 2013: John Wiley & Sons.

128. Duncan, J.M. and C.-Y. Chang, *Nonlinear analysis of stress and strain in soils.* Journal of the soil mechanics and foundations division, 1970. **96**(5): p. 1629-1653.
129. Priebe, H.J., *The design of vibro replacement.* Ground engineering, 1995. **28**(10): p. 31.
130. BUSCHMEIER, B. and F. MASSE, *Discusión sobre las diferencias de la metodología de diseño entre las inclusiones granulares y las inclusiones rígidas.* 2012.
131. Rutledge, P.C. and S.J. Johnson, *Review of Uses of Vertical Sand Drains.* Highway Research Board Bulletin, 1958(173).
132. Vesic, A.S., *Expansion of cavities in infinite soil mass.* Journal of Soil Mechanics & Foundations Div, 1972. **98**(sm3).
133. Hughes, J. and N. Withers, *Reinforcing of soft cohesive soils with stone columns.* Ground engineering, 1974. **7**(3).
134. BEŞLER, O.F., *A SOIL IMPROVEMENT CASE STUDY USING RAMMED STONE COLUMN SYSTEMS*. 2013, MIDDLE EAST TECHNICAL UNIVERSITY.
135. Mitchell, J.K., *State-of-the-art Report on Soil Improvement.* 10th Int. Conf. in Soil Mechanics and Foundation Engineering, Stockholm, 1981.
136. Datye, K.R. and S. S. Nagaraju, *Behavior of Foundations on Ground Improved with Stone ColumnS.* 9th International Conference on Soil Mechanics and Foundation Engineering, Tokyo, 1977. **Proceedings**.
137. Brauns, J. *Initial bearing capacity of stone column and sand piles*. in *Proc. Symp.„Soil Reinforcing and Stabilizing Techniques in Engineering Practise", Sydney*. 1978.
138. Soyez, B., *Méthodes de dimensionnement des colonnes ballastées.* Bulletin de liaison des Laboratoires des Ponts et Chaussées, 1985. **135**(135): p. 35-51.
139. Sahin, H., *Nondestructive Test Methods for Rapid Assessment of Flexible Base Performance in Transportation Infrastructures*. 2014.
140. Long, X., *Prediction of shear strength and vertical movement due to moisture diffusion through expansive soils*. 2006, Texas A&M University.
141. Koppula, S., *Statistical estimation of compression index.* ASTM Geotechnical Testing Journal, 1981. **4**(2).
142. Yoon, G.L. and B.T. Kim, *Regression analysis of compression index for Kwangyang marine clay.* KSCE Journal of Civil Engineering, 2006. **10**(6): p. 415-418.
143. Kulhawy, F.H. and P.W. Mayne, *Manual on estimating soil properties for foundation design*. 1990, Electric Power Research Inst., Palo Alto, CA (USA); Cornell Univ., Ithaca, NY (USA). Geotechnical Engineering Group.
144. Lytton, R., C. Aubeny, and R. Bulut, *Design Procedure for Pavements on Expansive Soils: Volume 1*. 2005.
145. Holtz, R.D. and W.D. Kovacs, *An introduction to geotechnical engineering*. 1981.
146. Bakhsh, K.N. and D. Zollinger, *Design Methodology for Subgrades and Bases Under Concrete Roads and Parking Lots Test Methods & Results of Erosion Potential of Commonly Used*. 2014, Ready Mixed Concrete (RMC) Research and Education Foundation: Texas Transportation Institute.

147. Das, B., *Principles of geotechnical engineering. Cengage Learning.* Stamford, CT, 2010.
148. AUBENY, C., R. BULUT, and R. LYTTON, *Design Procedure for Pavements on Expansive Soils: Volume 2.* 2006.
149. Fredlund, D.G. and A. Xing, *Equations for the soil-water characteristic curve.* Canadian geotechnical journal, 1994. **31**(4): p. 521-532.
150. Standard, A., *D698. Standard test methods for laboratory compaction characteristics of soil using standard effort 12 400 ft-lbf/ft3 600 kN-m/m3. West Conshohocken (PA): ASTM International; 2011*.
151. Covar, A.P. and R.L. Lytton, *Estimating Soil Swelling Behavior Using Soil Classification Properties.* ASCE Geotechnical Special Technical Publication No. 115, 2001.
152. Barksdale, R. and R. Bachus, *Design and Construction of Stone Columns Volume II, Appendixes.* 1983.
153. Covar, A.P. and R.L. Lytton, *Estimating Soil Swelling Behavior Using Soil Classification Properties.* ASCE Geotechnical Special Technical Publication No. 115, 2001.